University of Nevada, Reno

High Resolution Paleolake-Level and Paleoclimate Reconstruction from Integrated Geologic, Glacial, Tectonic, and Hydrologic Modeling of the south-eastern Sierra Nevada

A dissertation submitted in partial fulfillment of
the requirements for the degree of Doctor of
Philosophy in Hydrology

by

Steven N. Bacon

Dr. Rina Schumer/Dissertation Advisor

May, 2020

Copyright by Steven N. Bacon 2020
All Rights Reserved

THE GRADUATE SCHOOL

We recommend that the dissertation
prepared under our supervision by

Steven N. Bacon

Entitled

High Resolution Paleolake-Level and Paleoclimate Reconstruction from Integrated Geologic, Glacial, Tectonic, and Hydrologic Modeling of the south-eastern Sierra Nevada

be accepted in partial fulfillment of
the requirements for the degree of

DOCTOR OF PHILOSPHY

Rina A. Schumer, Ph.D., Advisor

Thomas F. Bullard, Ph.D., Committee Member

David L. Decker, Ph.D., Committee Member

Seshadri Rajagopal, Ph.D., Committee Member

Adam Z. Csank, Ph.D., Graduate School Representative

David W. Zeh, Ph.D., Dean, Graduate School

May, 2020

ABSTRACT

A new approach to developing a continuous paleolake-level curve for Owens Lake in the south-eastern Sierra Nevada during last 50,000 years integrates lake-core data and shoreline geomorphology with wind-wave and sediment entrainment modeling of lake-core sedimentology that is corrected for tectonic ground deformation. An 11,500-year time-series of reconstructed changes in precipitation and snowpack was then produced from a watershed-lake water balance model of the paleo-Owens River-Lake system. Paleoclimate simulations were performed at 100-yr time steps using adjusted 800-meter historical climate data. The water balance model developed in this dissertation improves on existing paleohydrologic models for the region through use of a continuous lake-level calibration curve and incorporation of (1) a paleotemperature dataset corresponding with local glacial deposits; (2) changes in paleo-solar insolation; (3) glacial ice/perennial snow accumulation; (4) salinity of paleolake water; and (5) surface runoff gains and losses. The simulation of hydroclimate during the Holocene is summarized by precipitation ranging from ~74 to 159% of historical baseline (WY1896–2015) with temperature anomalies ranging from -1.5 to 0.31°C. One of the principle findings of this research is the south-eastern Sierra Nevada was cooler and persistent droughts were not as severe during the late Holocene compared to previous estimates made from paleohydrologic modeling of other lakes in the region that are controlled by tree-ring proxy records. The application of elevated temperatures and lack of accounting for losses from snow sublimation and snow storage, plus losses from channel percolation in other models produces overestimates in the severity of droughts. The new Holocene hydroclimate record can be used to support other

paleoclimate archives in the western U.S. by providing high-resolution quantitative estimates of regional hydroclimate variability.

DEDICATION

This dissertation is dedicated to my Mom for always believing in me and encouraging me to follow my dream of pursuing a Ph.D degree.

ACKNOWLEDGEMENTS

Undertaking this Ph.D. has been a truly fulfilling experience for me that would not have been possible without the support I received from many people. I would like to first express my appreciation and thanks to my primary supervisor Dr. Rina Schumer for all the support and guidance she gave me. Without her encouragement in finding quantitative solutions to solve complex geologic and hydrologic problems, this Ph.D. would not have been completed in a timely manner. Many thanks also to my committee members: Dr. Thomas Bullard, Dr. Adam Csank, Dr. David Decker, and Dr. Seshadri 'Shey' Rajogopal who graciously provided their time and expertise in helping me achieve a Ph.D. In particular, I want to acknowledge Dr. Bullard for his patience along with his invaluable advice and feedback on my research and for always being so supportive of my work. I am especially grateful to Dr. Decker for his continuous moral support. Lastly, I want to thank Dr. Laurel Saito, former Director of the Graduate Program of Hydrologic Sciences, for giving me a chance in the program.

I gratefully acknowledge the funding received towards my Ph.D. from partial support of the General Frederick Lander Endowment, National Institutes for Water Resources/U.S. Geological Survey #G16AP00069, and National Science Foundation EAR #1252225. I want to also acknowledge Dr. Grace McCarley Holder and the Great Basin Unified Air Pollution Control District (GBUAPCD) for partial funding throughout the duration of geologic and hydrologic research of Owens Lake basin. Sincere thanks are also given to Mr. Matt Boggs and the Naval Air Warfare Center Weapons Division at China Lake for field support and partial funding (U.S. Government Contract #N68936–09–D–0040) during research of China Lake basin and the paleo-Owens River system.

Lastly, I want to acknowledge the Division of Earth and Ecosystem Sciences (DEES) and the Vice President for Research Office of the Desert Research Institute (DRI) for partial support of my research. I want to thank former DEES director Dr. Beverly Ramsey and current DEES director Mr. Tim Minor for their enthusiastic support. In addition, I want to acknowledge DRI for providing sabbatical support that allowed me to solely focus on research efforts for a six-month period.

I greatly appreciate the support received through the collaborative work undertaken during my dissertation. A special thanks to Dr. Nicholas Lancaster, Dr. Scott Stine, Dr. Edward Rhodes, and Dr. Grace McCarley Holder for their assistance in deciphering the late Holocene Owens Lake shoreline record. My thanks also go out to the support I received from the collaborative work on characterizing the tectonic setting of Owens Lake basin – much thanks to Dr. Bullard, Dr. Amanda Keen-Zebert, Dr. Angela Jayko, and Dr. David Decker. In addition, I want to acknowledge the collaborative work on the late Quaternary Owens Lake water-level record with Dr. Angela Jayko, Dr. Lewis Owen, Mr. Scott Lindvall, Dr. Edward Rhodes, Dr. Schumer, and Dr. Decker. Lastly, I want to acknowledge the collaborative work with Dr. Rina Schumer on the watershed-lake hydrologic modeling of the paleo-Owens River system.

I am especially grateful to many of my colleagues at DRI whom also provided moral and technical support. I want to thank Ms. Jenny Chapman and Ms. Julie Miller for being understanding during projects when my academic schedule posed a conflict. I am also thankful for the positive support from Dr. Jim Thomas and Dr. Ron Hershey in the DRI hallways. I want to thank Mr. Charles Morton for processing gridded climate data in a useable format and Mr. Chris Garner for providing Mono Lake basin export records. I

also want to acknowledge Mr. Chris Pearson who was always so helpful and provided me with much needed MATLAB coding support throughout my dissertation. Furthermore, I want to acknowledge Dr. Ken Adams for assisting with sampling beach ridges in Owens Lake basin for luminescence analysis; and Dr. Keen-Zebert and the DRI E.L. Cord Luminescence Laboratory. Lastly, I want to thank Mr. Roger Kriedberg for editorial review of two published manuscripts as part of my dissertation and Ms. Maria Vasquez for document formatting support.

I would also like to give a heartfelt thank you to Dr. Raymond "Bud" Burke and Dr. Silvio Pezzopane who were my master's thesis mentors at Humboldt State University and good friends. They both were instrumental in guiding me in the early days of my geologic research of Owens Lake basin beginning in January 1999. And finally, to Alexandra, who has been by my side throughout this Ph.D. and a constant voice of inspiration in reminding me to hurry up and finish. Plus, my young son Bradley for being a breath of fresh air and an additional voice in reminding me to hurry up and finish my dissertation!

Table of Contents

LIST OF TABLES

CHAPTER 1:

CHAPTER 2:

CHAPTER 3:

CHAPTER 4:

LIST OF FIGURES

INTRODUCTION:

CHAPTER 1:

CHAPTER 2:

CHAPTER 3:

CHAPTER 4:

INTRODUCTION

Climate change may impact water resources in the western U.S. through increased ambient air temperatures and regionally extensive drought conditions (Seager et al., 2007; Dai et al., 2004; Cayan et al., 2010; Dai, 2013). In the arid and semi-arid regions of the western U.S., where up to 70% of the annual river discharge is supplied by snowmelt, the loss of alpine snowpack represents one of the most significant potential impacts of climate warming (Serreze et al., 1999; Howat and Tulaczyk, 2005). Snowmelt accounts for the majority of the annual streamflow in the Sierra Nevada and the first sign of global climate change will likely be an earlier start to spring snowmelt and runoff related to warming winter ambient air temperatures and shrinking snow cover (Dettinger and Cayan, 1995; Howat and Tulaczyk, 2005). Less snow cover and earlier snowmelt in the Sierra Nevada, coupled with reduced precipitation from variable atmospheric circulation patterns are all factors that will potentially impact the water resources of California and other drylands of the western U.S. (e.g., Harpold et al., 2017; Hatchet, 2018; Hatchett and McEvoy, 2018).

Understanding past hydroclimatic change provides insight into present and future drought risk (e.g., Stakiv, 2011). Instrumental records of precipitation, temperature, and surface-water flow in many areas of the western U.S. are often limited to the past century, but long-term estimates of streamflow variability are critical for managing water resources and mitigating impacts of floods and droughts (e.g., Enzel and Wells, 1997; Meko et al., 2001; Saito et al., 2008; 2015; Rice et al., 2009; Dettinger et al., 2011). Deciphering patterns of background natural hydroclimate variability from underlying anthropogenic forcing is only possible from understanding periods of rapid climate

change during the recent to distant geologic past (Mayewaski et al., 2004). The overarching goal of this dissertation is to shed new light on southern Sierra Nevada hydroclimate in the form of precipitation and snowpack reconstruction for the last 11,500 years (Holocene) from the integration of detailed lacustrine, glacial, and tectonic records with a coupled watershed-lake water balance model that is appropriate for an alpine and snow-dominated hydrologic system.

PALEOHYDROLOGIC MODELING OF WATERSHED-LAKE SYSTEMS

Shoreline geomorphic features and associated deposits from paleolakes record large hydrologic changes to lake systems through the relationship between the basin water budget and the surface area for the paleolake system at specific shorelines of known age (Smith and Street-Perrott, 1983; Street-Perrott and Harrison, 1985; Mifflin and Wheat, 1979). The use of shoreline records in the Great Basin of the western U.S. from dated shoreline landforms and/or deposits offer an exceptional method for identifying past hydrologic changes in paleolakes at millennial time scales, and rarely, at centennial time scales (e.g., Reheis et al., 2014 and references therein). Sedimentologic and geomorphic indicators of former lake levels can be preserved for millennia and accurately measured across broad areas, thus allowing reconstruction of long paleoclimate records provided tectonic effects and/or isostatic rebound can be incorporated (Reheis et al., 2014). The spatiotemporal distribution of paleolakes and lake-level histories in the western U.S. has also been used as a proxy for migration of the North American polar jet stream and associated hydroclimatic conditions between 35°N and 43°N latitudes, which in turn have been used to infer North Pacific atmospheric

circulation patterns across the western U.S. during the late Quaternary (last ~40,000 years) (Enzel et al., 1989; 2003; Benson et al., 1990, 1996, 2002; Enzel and Wells, 1997; Negrini, 2002; Zic et al., 2002; Kirby et al., 2012, 2015; Lyle et al., 2012; Antinao and McDonald, 2013; Munroe and Laabs, 2013; Garcia et al., 2014; Oster et al., 2015; Reheis et al., 2014; McGee et al., 2018; Morrill et al., 2018; Hatchett et al., 2019; Hudson et al., 2019; Knott et al., 2019) (Figure 1).

Most geomorphic and geologic studies focused on reconstructing lake levels are either limited to periods with relative highstands because of a lack of preserved landforms and outcrop evidence for lower water levels due to shoreline erosion and burial from fluctuating lake levels (e.g., Adams, 2007; Bartov et al., 2007), or rely on inferences from stratigraphy exposed in lower parts of lake basins without shoreline constraints (e.g., Negrini et al., 2006). Many western U.S. paleolake records are derived from proxy evidence (e.g., geochemical, biological, particle size) in lake sediment cores to infer climate change (e.g., Benson, 1994; 2004; Benson and Thompson, 1987; Benson et al., 1996; 1997; 2002; Smith and Bischoff, 1997; Negrini et al., 2000; Kirby et al., 2012; Zimmerman et al., 2011; Blunt and Negrini, 2016; Noble et al., 2016; Roza et al., 2016), despite large uncertainty in inference on water depth and level (e.g., Smith et al., 1997; Reheis et al., 2014). Synthesis of shoreline data and lake core records reduces this uncertainty and produces more complete records (Wells et al., 2003; Bacon et al., 2006; Negrini et al., 2006; Reheis et al., 2012; 2014; Benson et al., 2013). Geology-based lake-level records, however, afford only qualitative assessments of regional hydroclimate variability from the relative duration and magnitude of water-level oscillations.

Quantitative estimates of long-term moisture patterns sufficient to drive regional- to global-scale paleoclimate atmospheric models (e.g., McGee et al., 2018) can be derived from paleohydrologic modeling of coupled watershed-lake systems. However, these models are typically controlled by discontinuous lake stage records derived from incomplete records of either dated landforms or inferences from outcrop evidence. These hydrologic models simulate short time periods during which lakes were at their relative highstands (e.g., Matsubara and Howard, 2009; Yu et al., 2015; Barth et al., 2016) or in rare cases during relative lowstands (e.g., Hatchett et al., 2015; 2016). As a result, most model simulations are restricted to discrete periods that lack a complete record of a given lake-level cycle, thereby providing discontinuous estimates of paleoclimate variability in the context of climate change at multidecadal to multicentennial scales.

STUDY AREA

This dissertation builds on the state-of-the-art in watershed-lake hydrologic modeling for paleohydroclimate reconstruction through the novel incorporation of multidisciplinary datasets and analyses. The study area, the paleo-Owens River system on the eastern escarpment of the southern Sierra Nevada in eastern California (Figure. 1), has been extensively studied because a robust record of climate change is preserved in lacustrine sediment and shoreline geomorphic features in Owens Lake basin and downstream China and Searles Lake basins (e.g., Smith and Pratt, 1957; Reheis et al., 2014; Phillips, 2008) and in glacial deposits in the Sierra Nevada (e.g., Burbank, 1991; Clark and Gillespie, 1997; Bowerman and Clark, 2011; Phillips, 2016, 2017). Owens Valley is a region of active tectonics—as demonstrated by the Mw 7.5–7.9 Owens Valley

earthquake in 1872, the third largest historical earthquake in California (Beanland and Clark, 1994). As a result, the late Pleistocene and Holocene geomorphic history and spatial extent of Owens Lake shorelines have also been studied to resolve tectonic deformation because the lake basin is crossed by a complex array of five primary faults zones (e.g., Carver, 1970; Slemmons et al., 2008).

The Sierra Nevada forms one of the principal rain shadows in the western U.S. with its highest crest elevations of 3400–4300 m occurring between ~36°N and 38°N latitudes. The entire range was extensively glaciated during the Pleistocene, and many small glaciers and snowfields persist in sheltered cirques at high elevations (Moore and Moring, 2013). The Owens River watershed is sensitive to arid to semi-arid hydroclimate variability. It is the single largest watershed draining the eastern Sierra Nevada and contains over 230 km of range crest spanning the highest elevations. Owens Lake basin is relatively shallow because of high sedimentation from the Owens River and surrounding alluvial fans. Therefore, small changes in streamflow inputs associated with changes in the magnitude of snowpack and rate of snowmelt are amplified in the lake basin because of its shallow hypsometric configuration, therefore landforms and associated deposits produced from subtle lake-level fluctuations are more likely to be preserved across the landscape.

OVERVIEW OF CHAPTERS

The rich paleoclimate record in the seismically active setting of Owens Valley presented an opportunity to develop a new approach in paleohydrologic modeling that integrates available geomorphic, stratigraphic, and tectonic information into improved

models of hydrologic change. The dissertation is comprised of four chapters collectively aimed at characterizing the hydroclimate that controlled Holocene lake-level and snowpack variations within the paleo-Owens River system.

The primary goal of chapter 1 was to produce a continuous water-level record of Owens Lake for the late Holocene. An approach was developed to provide water-level estimates in the absence of shoreline evidence by integrating landform, outcrop, and existing lake core data with wind-wave and sediment entrainment modeling of lake core sedimentology. Radiocarbon (^{14}C) and luminescence dating of sandy deposits was used to refine the late Holocene lake-level history of Owens Lake by dating four previously undated shoreline features above the historical highstand water level in 1872–1878 AD. The new luminescence ages of shorelines coincide with wetter and cooler climate during the Neopluvial (~3.6 ka, thousand years ago), Medieval Pluvial (~0.8 ka), and Little Ice Age (~0.35 ka). Radiocarbon dates from stumps below the historical highstand also indicate two periods of lowstands at ~0.89 and 0.67 ka during the Medieval Climatic Anomaly.

A commonly used approach to estimate erosion potential within intertidal to open water coastal environments for coastal protection and habitat rehabilitation (e.g., USACE, 1984; 2002) and the distribution of sediment texture at the lake bottom (e.g., Håkanson, 1977) was applied to model the wind-wave characteristics and threshold lake-water depths required for the sedimentology previously described in sediment lake core OL-97 (Smoot et al., 2000). Prior to the calculation of threshold lake-water depth, the lake bottom was first reconstructed because of the seismically active setting of the lake basin. The lake bottom was reconstructed by accounting for settlement from consolidation and

subsidence from active faulting based on slip rates on nearby active faults. The approach presented in Chapter 1 is novel because the elevation of water levels was reconstructed from the age of deposition of specific stratigraphic units of a certain sediment texture in lake cores. The construction of a comprehensive lake-level curve based on integrating shoreline and subsurface geologic information from lake cores with geotechnical and fluid dynamic methods is, to my knowledge, the first of its kind in paleolake-level reconstruction.

Chapter 2 focuses on characterizing the vertical slip distribution between five of the primary faults in Owens Lake basin. New slip rates for two uncharacterized faults in the lake basin were calculated based on new luminescence ages of ~40 ka for a vertically faulted, highstand beach ridge in Owens Valley. Slip rates for all faults were used in a differential fault-block model to estimate vertical tectonic deformation across the basin. This allowed reconstruction of absolute elevations for various strata, the lake bottom, and lake overflow positions through time to produce a continuous lake-level curve that is corrected for tectonic ground deformation.

Chapter 3 builds upon the work in Chapters 1 and 2 by extending the Owens Lake water-level record from 4000 to 50,000 years and revises the previous lake-level curve of Bacon et al. (2006). The differential fault-block model in Chapter 2 was used to perform tectonic reconstruction of stratigraphic sites, plus lake bottom and overflow channel positions. Previous sediment core age-depth models for sediment lake cores OL-84B and OL-90 (Benson et al., 1996, 1997, 2002) were also revised by accounting for sediment compaction and using no reservoir correction for open basin conditions, which reduced

discrepancies of lake-level oscillations between the Owens Lake lake-level and lake-core proxy records.

The work in Chapter 3 also incorporates new ^{14}C and luminescence age dating of shoreline stratigraphic sites and subsurface geotechnical investigations in the overflow channel of Owens Lake basin that yielded stratigraphic and geochronologic information to define the timing of potential episodes of overflow. New luminescence ages of beach ridges and fluvial-deltaic and alluvial sediment filling the overflow channel established the first spatiotemporal connections between Early-Middle Holocene (~8.4–6.4 ka) and latest Pleistocene (~12.8–11.6 ka) shorelines and overflow levels of Owens Lake, thereby reducing the uncertainty between the late Pleistocene overflow records of Owens Lake (Bacon et al., 2006; Reheis et al., 2014) and downstream lake basins (Orme and Orme, 2008; Phillips, 2008; Smith, 2009; Rosenthal et al., 2017). One of the new significant findings in Chapter 3 is the occurrence of shorelines that can be directly linked to spillway channel incision and show episodes of Owens Lake overflow are much younger than previously recognized.

This dissertation culminates with Chapter 4, describing development of a Thornthwaite-based monthly, coupled watershed-lake hydrologic model of the paleo-Owens River system. The model reconstructs post-glacial precipitation patterns and the buildup of snowpack at 100-year time steps in the south-eastern Sierra Nevada during the last 11,500 years. The model is calibrated to the continuous lake-level record of Owens Lake developed in Chapters 1 and 3 and incorporates (1) a mean global paleo-temperature dataset adjusted to local paleotemperature depression estimates from glacial deposits in the watershed; (2) changes in paleo-solar insolation driven by orbital forcing;

(3) a glacial ice/perennial snow accumulation model component based on paleo-equilibrium line altitudes (i.e., summer paleo-snowline); and (4) changes in salinity of paleolake water.

The paleohydrologic modeling produced continuous precipitation and snowpack reconstruction from calibration with lake-level variations and glacial deposits. The paleohydrologic modeling demonstrated that glacial ice and perennial snow accumulation are essential components for simulation of a snow-dominated hydrologic system, because incoming solar radiation drives snowmelt. As a result, changes in solar insolation from orbital forcing are essential model boundary conditions that should be incorporated in paleohydrologic models, because these changes significantly affect the water balance in a snow-dominated hydrologic system. Furthermore, by accounting for losses from snow sublimation, as well as runoff losses from channel percolation and riparian evapotranspiration on alluvial fans, it appears that Holocene droughts were not as severe as estimates from previous paleohydrologic studies in the Sierra Nevada that were either based on inferred discharge or temperature or both from tree-ring records. The reduction in drought severity shown in this dissertation is related to increases in simulated precipitation required to balance the losses from snow sublimation and channel percolation across the watershed, in combination with accounting for changes in solar insolation.

The notable results of paleohydrologic modeling in Chapter 4 indicate the persistent megadroughts in the late Holocene were wetter and cooler during the Medieval Climate Anomaly and Little Ice Age than previously estimated. The modeling also suggests drought during the entire Holocene was characterized by precipitation between

74 and 90% of historical baseline climate and snowpack at ~50–200% of present-day extent. Paleoclimate simulations at 100-year time steps that are based on the integration of a continuous lake-level curve and a watershed-lake water balance model that accounts for glacial ice/perennial snow accumulation is, to my knowledge, the first of its kind.

VALUE OF RESEARCH

The physiographic and hydrologic setting of the Owens River watershed is optimally located to record long-term atmospheric circulation patterns that modulate streamflow and lake-level variations in the southwestern U.S. (e.g., Redmond and Koch, 1991). The development of a continuous lake-level record ultimately reduces the inherited geologic uncertainty that is typically associated with past studies of lake-level reconstructions, thereby further reducing the uncertainty in model boundary conditions in watershed-lake hydrologic models commonly used to reconstruct paleo-precipitation. The use of an integrated record of paleohydrologic change with a watershed-lake hydrologic model appropriate for a snow-dominated hydrologic system creates a long-term dataset that can be used to validate and/or refine previous estimates of precipitation variations, as well as atmospheric circulation models developed from the spatiotemporal extent of other paleolakes in the western U.S. (e.g., Lyle et al., 2012; Hudson et al., 2019).

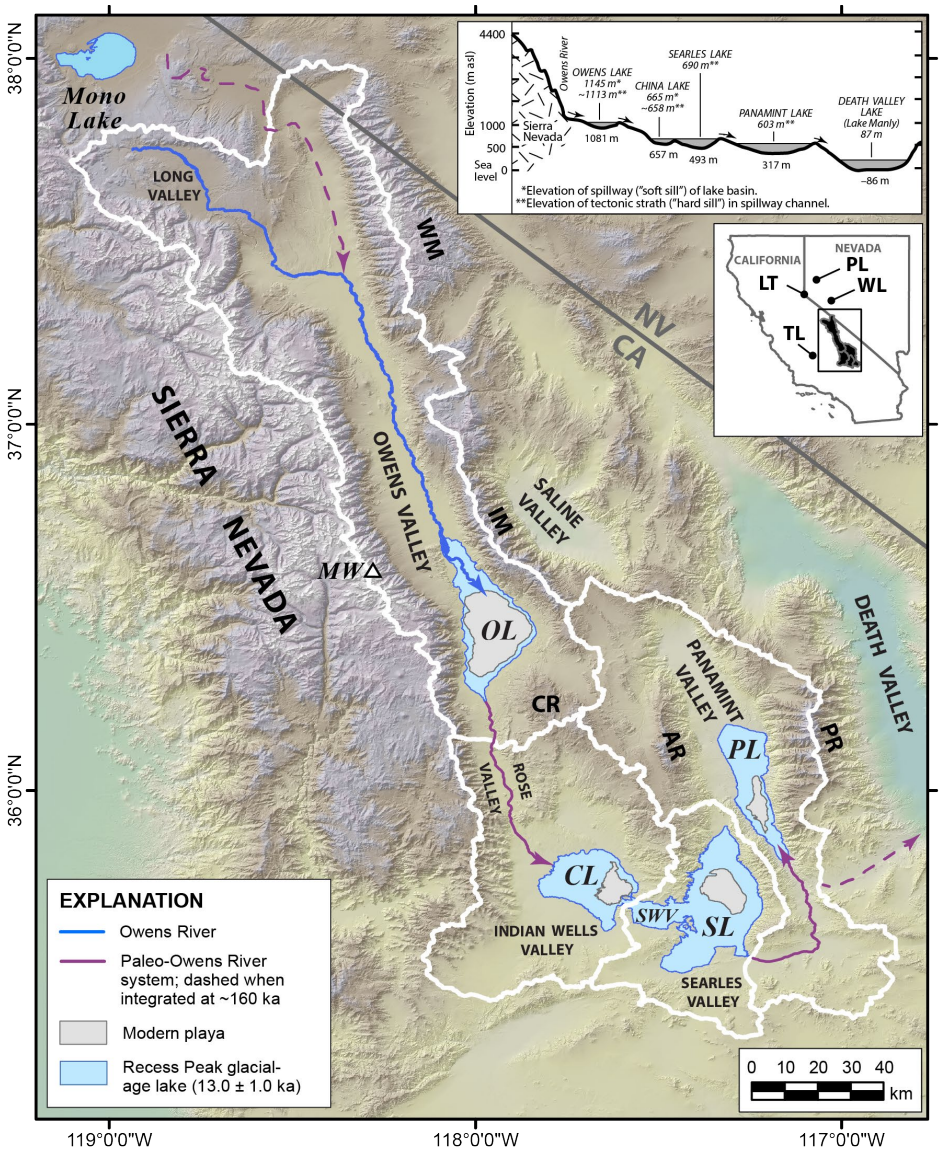

Figure 1. Major physiographic features along the eastern escarpment of the southern Sierra Nevada, eastern California in relation to modern playas and pluvial Owens Lake, and other lakes of the paleo-Owens River system during the Recess Peak glaciation (Bacon et al., 2006; Orme and Orme, 2008; Hoffman, 2009; Rosenthal et al., 2017). Age of Recess Peak glaciation is from Phillips (2016, 2017). Inset is graphical profile of the chain of lakes downstream of Owens Lake showing the elevations of hard and soft sills, plus playa bottoms of each lake basin (modified after Smith and Bischoff, 1997). Watershed boundaries of lake basins are shown for: CL – China Lake; OL – Owens Lake; PL – Panamint Lake; SL – Searles Lake; and SWV – Salt Wells Valley. Mountain ranges are also shown on the map: AR – Argus Range CR – Coso Range; IM – Inyo Mountains; PR – Panamint Range; WM – White Mountains. Other lakes discussed in text include: LT – Lake Tahoe; TL – Tulare Lake; PL – Pyramid Lake; and WL – Walker Lake.

REFERENCES

Adams, K.D. (2007). Late Holocene sedimentary environments and lake-level fluctuations at Walker Lake, Nevada, USA. *Geological Society of America Bulletin* 119, 126–139.

Antinao, J.J., and McDonald, E. (2013). An enhanced role for the Tropical Pacific on the humid Pleistocene-Holocene transition in southwestern North America. *Quaternary Science Reviews* 78, 319–341.

Bacon, S.N., Burke, R.M., Pezzopane, S.K., Jayko, A.S. (2006). Last glacial maximum and Holocene lake levels of Owens Lake, eastern California, USA. *Quaternary Science Reviews* 25/11-12, 1264–1282.

Barth, C., Boyle, D.P., Hatchett, B.J., Bassett, S.D., Garner, C.B., Adams, K.D. (2016). Late Pleistocene climate inferences from a water balance model of Jakes Valley, Nevada (USA). *Journal of Paleolimnology*, DOI 10.1007/s10933-016-9897-z.

Bartov, Y., Enzel, Y., Porat, N., Stein, M. (2007). Evolution of the late Pleistocene-Holocene Dead Sea Basin from sequence stratigraphy of fan deltas and lake-level reconstruction. *Journal of Sedimentary Research* 77, 680–692.

Beanland, S., and Clark, M.M. (1994). The Owens Valley fault zone, eastern California, and surface rupture associated with the 1872 earthquake. U.S. Geological Survey Bulletin 1982, 29 p.

Benson, L. (1994). Carbonate deposition, Pyramid Lake subbasin, Nevada; 1, Sequence of formation and elevational distribution of carbonate deposits (tufas). *Palaeogeography, Palaeoclimatology, Palaeoecololgy* 109, 55–87.

Benson, L. (2004). Western Lakes. In: Gillespie, A.R., Porter, S.C., Atwater, B.F. (Eds.), The Quaternary Period in the United States. Elsevier, New York, pp. 185–204.

Benson, L.V., and Thompson, R.S. (1987). The physical record of lakes in the Great Basin. In: Ruddiman, W.F., Wright Jr., H.E. (Eds.), North America and Adjacent Oceans during the Last Deglaciation. Geological Society of America, Boulder, CO, United States, pp. 241–260.

Benson, L.V., Currey, D.R., Dorn, R.I., Lajoie, K.R., Oviatt, C.G., Robinson, S.W., Smith, G.I., Stine, S. (1990). Chronology of expression and contraction of four Great Basin lake systems during the past 35000 years, *Palaeogeography, Palaeoclimatology, Palaeoecology* 78, 241–286.

Benson, L.V., Burdett, J.W., Kashgarian, M., Lund, S.P., Phillips, F.M., Rye, R.O. (1996). Climatic and hydrologic oscillations in the Owens Lake basin and the adjacent Sierra Nevada, California. *Science* 274, 746–749.

Benson, L., Burdett, J., Lund, S., Kashgarian, M., Mensing, S. (1997). Nearly synchronous climate change in the Northern Hemisphere during the last glacial termination. *Nature* 388, 263–265.

Benson, L., Kashgarian, M., Rye, R., Lund, S., Paillet, F., Smoot, J., Kester, C., Mensing, S., Meko, D., Lindstrom, S. (2002). Holocene multidecadal and multicentennial droughts affecting northern California and Nevada. *Quaternary Science Reviews* 21, 659–682.

Benson, L.V., Smoot, J.P., Lund, S.P., Mensing, S.A., Foit Jr., F.F., Rye, R.O. (2013). Insights from a synthesis of old and new climate-proxy data from the Pyramid and Winnemucca lake basins for the period 48 to 11.5 cal ka. *Quaternary International* 310, 62–82.

Blunt, A., and Negrini, R.M. (2016). Latest Pleistocene through Holocene lake levels from the TL05-4 cores, Tulare Lake, CA. *Quaternary International* 387, 122–130.

Bowerman, N.D., and Clark, D.H. (2011). Holocene glaciation of the central Sierra Nevada, California. *Quaternary Science Reviews* 30, 1067–1085.

Burbank, D.W. (1991). Late Quaternary snowline reconstructions for the southern and central Sierra Nevada, California and a reassessment of the "Recess Peak Glaciation". *Quaternary Research* 36, 297–306.

Cayan, D., Das, T., Pierce, D., Barnett, T., Tyree, M., Gershunov, A. (2010). Future dryness in the southwest United States and the hydrology of the early 21st century drought. *Proc. Natl. Acad. Sci. U.S.A.*, 107(50), 21,271–21,276.

Clark, D.H., and Gillespie, A.R. (1997). Timing and significance of late-glacial and Holocene cirque glaciation in the Sierra Nevada, California. *Quaternary International* 38/39, 21–38.

Dai, A. (2013). Increasing drought under global warming in observations and models. *Nat. Clim. Change*, 3(1), 52–58.

Dai, A., Trenberth, K.E., Qian, T. (2004). A global dataset of Palmer Drought Severity Index for 1870–2002: Relationship with soil moisture and effects of surface warming. *Journal of Hydrometeorology* 5(6), 1117–1130.

Dettinger, M.D. and Cayan, D.R., (1995). Large-scale atmospheric forcing of recent trends toward early snowmelt runoff in California. *Journal of Climate*, 8(3), 606–623.

Dettinger, M.D., Ralph, F.M., Das, T., Neiman, P.J., Cayan, D.R. (2011). Atmospheric rivers, floods and the water resources of California. *Water* 3, 445–478.

Enzel, Y., and Wells, S.G., 1997. Extracting Holocene paleohydrology and paleoecology information from modern extreme flood events: An example from southern California. Geomorphology 19, 203–226.

Enzel, Y., Cayan, D.R., Anderson, R.Y., Wells, S.G. (1989). Atmospheric circulation during Holocene lake stands in the Mojave Desert: evidence of regional climate change. *Nature* 341, 44–48.

Enzel, Y., Wells, S.G., Lancaster, N., 2003. Late Pleistocene lakes along the Mojave River, southeast California. In: Enzel, Y., Wells, S.G., Lancaster, N. (Eds.), Paleoenvironments and Paleohydrology of the Mojave and Southern Great Basin Deserts, Geological Society of America Special Paper 368, pp. 61–77.

Garcia, A.L., Knott, J.R., Mahan, S.A., Bright, J. (2014). Geochronology and paleoenvironment of pluvial Harper Lake, Mojave Desert, California, USA. *Quaternary Research* 81, 305–317.

Håkanson, L. (1977). The influence of wind, fetch, and water depth on the distribution of sediments in Lake Väern, Sweden. Canadian Journal of Earth Sciences 14, 397–412.

Harpold, A.A., Dettinger, M., Rajagopal, S. (2017). Defining snow drought and why it matters. *Eos* 98, doi:10.1029/2017EO068775.

Hatchett, B.J., (2018). Snow level characteristics and impacts of a spring typhoon-originating atmospheric river in the Sierra Nevada, USA. *Atmosphere* 9, 233, doi:10.3390/atmos9060233.

Hatchett, B.J., and McEvoy, D.J., (2018). Exploring the origins of snow droughts in the northern Sierra Nevada, California. *American Meteorological Society* 22, 1–13. doi:10.1175/EI-D-17-0027.1.

Hatchett, B.J., Boyle, D.P., Putnam, A.E., Bassett, S.D. (2015). Placing the 2012–2015 California-Nevada drought into a paleoclimatic context: Insights from Walker Lake, California-Nevada, USA. *Geophysical Research Letters* 42. doi:10.1002/2015GL065841.

Hatchett, B. J., Boyle, D. P., Garner, C. B., Kaplan, M. L., Putnam, A. E., Bassett, S. (2016). Magnitude and frequency of wet years under a megadrought climate in the western Great Basin, USA, *Quaternary Science Reviews* 152, 197–202.

Hatchett, B.J., Boyle, D.P., Garner, C.B., Kaplan, M.L., Bassett, S.D., Putnam, A.E. (2019). Sensitivity of a western Great Basin terminal lake to winter northeast Pacific storm track activity and moisture transport. In Starratt, S.W., and Rosen, M.R., (Eds.), From Saline to Freshwater: The Diversity of Western Lakes in Space and Time: Geological Society of America Special Paper 536, doi.org/10.1130/2018.2536(05).

Hoffman, W.R. (2009). Late Pleistocene slip rate along the Panamint Valley fault zone, eastern California. Unpublished M.Sc. Thesis, The Pennsylvania State University, 81 p.

Howat, I.M., and Tulaczyk, S. (2005). Trends in spring snowpack over a half-century of climate warming in California, USA. *Annals of Glaciology* 40, 151–156.

Hudson, A.M., Hatchett, B.J., Quade, J., Boyle, D.P., Bassett, S.D., Ali, G., De los Santos, M.G. (2019). North-south dipole in winter hydroclimate in the western United States during the last deglaciation. *Scientific Reports* 9, 4826, doi.org/10.1038/s41598-019-41197-y.

Kirby, M.E., Zimmerman, S.R.H., Patterson, W.P., Rivera, J.J. (2012). A 9170-year record of decadal-to-multi-centennial scale pluvial episodes from the coastal Southwest United States: a role for atmospheric rivers? *Quaternary Science* Reviews 46, 57–65.

Kirby, M.E., Knell, E.J., Anderson, W.T., Lachniet, M.S., Silveira, E., Palermo, J.,Hiner, C.A., Eeg, H., Arevalo, A., Lucero, R., Murrieta, R. (2015). Evidence for Insolation and Pacific Forcing of Late Glacial through Holocene Climate in the Central Mojave Desert (Silver Lake, CA), *Quaternary Research* 84, 174–186.

Knott, J.R., Liddicoat, J.C., Coe, R.S., Negrini, R.M. (2019). Radiocarbon and paleomagnetic chronology of the Searles Lake Formation, San Bernardino County, California, USA. In: Starratt, S.W., Rosen, M.R. (Eds.), From Saline to Freshwater: The Diversity of Western Lakes in Space and Time: Geological Society of America Special Paper 536, doi.org/10.1130/2018.2536(06).

Lyle, M., Heusser, L., Ravelo, C., Yamamoto, M., Barron, J., Diffenbaugh, N.S., Herbert, T., Andreasen, D. (2012). Out of the tropics: The Pacific, Great Basin lakes, and

late Pleistocene water cycle in the western United States. *Science* 337, 1629–1633.

Matsubara, Y., and Howard, A.D. (2009). A spatially explicit model of runoff, evaporation, and lake extent: Application to modern and late Pleistocene lakes in the Great Basin region, western United States. *Water Resources Research* 45, W06425.

Mayewski, P.A. et al., (2004). Holocene climate variability. *Quaternary Research* 62, 243–255.

McGee, D., Moreno-Chamarro, E., Wetlandsall, J., Galbraith, E.D. (2018). Western U.S. lake expansions during Heinrich stadials linked to Pacific Hadley circulation. Science Advances 4, eaav0118, DOI: 10.1126/sciadv.aav0118.

Meko, D.M., Therrell, M.D., Baisan, C.H., Hughes, M.K. (2001). Sacramento River flow reconstructed to A.D. 869 from tree rings: *Journal of the American Water Resources Association* 37(4) 1029–1040.

Mifflin M.D., and Wheat M.M. (1979). Pluvial lakes and estimated pluvial climates of Nevada. Nevada Bureau of Mines and Geology Bulletin 94: University of Nevada, Reno, 57 pp.

Moore, J.G., and Moring B.C. (2013). Range wide glaciation in the Sierra Nevada, California. *Geosphere* 9, 1804–1818.

Morrill, C., Lowry, D.P., Hoell, A. (2018). Thermodynamic and dynamic causes of pluvial conditions during the Last Glacial Maximum in western North America. *Geophysical Research Letters* 45, 335–345.

Munroe, J.S. and Laabs, B.J.C. (2013). Late Pleistocene history of Pluvial Lake Franklin, Northeastern Nevada, U.S.A., *Geological Society of America Bulletin* 125, 322–342.

Negrini, R.M., Erbes, D.B., Faber, K., Herrera, A.M., Roberts, A.P., Cohen, A.S., Wigand, P.E., Foit, F.F.J. (2000). A paleoclimate record for the past 250,000 years from Summer Lake, Oregon, USA: I. Chronology and magnetic proxies for lake level. *Journal of Paleolimnology* 24, 125–149.

Negrini, R.M. (2002). Pluvial lake sizes in the northwestern Great Basin throughout the Quaternary period. In: Hershler, R., Madsen, D.B., Currey, D. (Eds.), Great Basin Aquatic Systems History: Smithsonian Contributions to the Earth Sciences, vol. 33. Smithsonian Institution Press, Washington, D.C, pp. 11–52.

Negrini, R.M., Wigand, P.E., Draucker, S., Gobalet, K., Gardner, J.K., Sutton, M.Q., Yohe, R.M. (2006). The Rambla highstand shoreline and the Holocene lake-level history of Tulare Lake, California, USA. *Quaternary Science Reviews* 25, 1599–1618.

Noble, P.J., Ball, G.I., Zimmerman, S.H., Maloney, J., Smith, S.B., Kent, G., Adams, K.D., Karlin, R.E., Driscoll, N. (2016). Holocene paleoclimate history of Fallen Leaf Lake, CA, from geochemistry and sedimentology of well-dated sediment cores. *Quaternary Science Reviews* 131, 193–210.

Orme, A.R. and Orme, A.J. (2008). Late Pleistocene shorelines of Owens Lake, California, and their hydroclimatic and tectonic implication, in Reheis, M.C., Hershler, R., and Miller, D.M., eds., Late Cenozoic Drainage History of the Southwestern Great Basin and Lower Colorado River Region: Geologic and Biotic Perspectives: Geological Society of America Special Paper 439, p. 207–226.

Oster, J.L., Montañez, I.P., Santare, L.R., Sharp, W.D., Wong, C., Cooper, K.M. (2015). Stalagmite records of hydroclimate in central California during termination 1. *Quaternary Science Reviews* 127, 199–214.

Phillips, F.M. (2008). Geological and hydrological history of the paleo-Owens River drainage since the late Miocene, in Reheis, M.C., Hershler, R., and Miller, D.M., eds., Late Cenozoic Drainage History of the Southwestern Great Basin and Lower Colorado River Region: Geologic and Biotic Perspectives: Geological Society of America Special Paper 439, p. 115–150.

Phillips F.M. (2016). Constraints on cosmogenic nuclide production rates by samples from the Sierra Nevada, California: I. Late Pleistocene glacial chronology. *Quaternary Geochronology* 35, 119–129.

Phillips F. (2017). Glacial chronology of the Sierra Nevada, California, from the Last Glacial Maximum to the Holocene. *Geographical Research Letters* 43, 527–552, doi:10.18172/cig.3233.

Redmond, K.T., and Koch, R.W. (1991). Surface climate and streamflow variability in the western United States and their relationship to large scale circulation indices. *Water Resources Research* 27, 2381–2399.

Reheis, M.C., Adams, K.D., Oviatt, C.G., Bacon, S.N. (2014). Pluvial lakes in the Great Basin of the western United States – A view from the outcrop. *Quaternary Science Reviews* **97**, 33-57.

Rice, J., Woodhouse, C., Lukas, J., (2009). Science and decision-making: Water management and tree-ring data in the western United States. *Journal of the American Water Resources Association* 45(5): 1248–1259.

Rosenthal, J.S., Meyer, J., Palacios-Fest, M.R., Young, D.C., Ugan, A., Byrd, B.F., Goblet, K., Giacomo, J. (2017). Paleohydrology of China Lake basin and the context of early human occupation in the northwestern Mojave Desert, USA. *Quaternary Science Reviews* 176, 112–139.

Roza, J., Jackson, B., Heaton, E., Negrini, R. (2016). Paleomagnetic secular variation and environmental magnetism of Holocene-age sediments from Tulare Lake, CA. *Quaternary Research* 85, 391–398.

Saito, L., Biondi, F., Salas, J.D., Panorska, A.K., Kozubowski, T.J., (2008). A watershed modeling approach to streamflow reconstruction from tree-ring records. *Environmental Research Letters* 3 (2), 024006 (6pp).

Saito, L., Biondi, F., Devkota, R., Vittori, J., Salas, J.D., (2015). A water balance approach for reconstructing streamflow using tree-ring proxy records. *Journal of Hydrology* 529, 535–547.

Seager R. et al., (2007). Model projections of an imminent transition to a more arid climate in southwestern North America. *Science* 316, 1181–1184.

Serreze, M.C., Clark, M.P., Armstrong, R.L., McGinnis, D.A., Pulwarty, R.S. (1999). Characteristics of the western United States snowpack from snowpack telemetry (SNOTEL) data. *Water Resource Research* 35, 2145–2160.

Slemmons, D.B., Vittori, E., Jayko, A.S., Carver, G.A., Bacon, S.N. (2008). Quaternary fault and lineament map of Owens Valley, Inyo County, eastern California: Geological Society of America Map and Chart 96, 25 p.

Smith, G.I. (2009). Late Cenozoic geology and lacustrine history of Searles Valley, Inyo and San Bernardino Counties, California. U.S. Geological Survey Professional Paper 1727, 115 p.

Smith, G.I. and Pratt, W.P. (1957). Core logs from Owens, China, Searles, and Panamint Basins, California. US Geological Survey Bulletin 1045-A, 1–62.

Smith, G.I., Street-Perrott, F.A. (1983). Pluvial lakes of the western United States. (H. E. Jr. Wright, Ed.), In "Late-Quaternary environments of the United States vol. 1" (S. C. Porter, Ed.), pp. 190–212. Minneapolis, University of Minnesota Press.

Smith, G.I., and Bischoff, J.L. (1997). Core OL-92 from Owens Lake: project rationale, geologic setting, drilling procedures, and summary. In: Smith, G.I., Bischoff, J.L. (Eds.), An 800,000-year Paleoclimatic Record from Core OL-92, Owens Lake, southeast California, Geological Society of America Special Paper 317, pp. 1–8.

Smith, G.I., Bischoff, J.L., Bradbury, J.P. (1997). Synthesis of the paleoclimatic record from Owens Lake Core OL-92. In: Smith, G.I., Bischoff, J.L. (Eds.), An 800,000-year Paleoclimatic Record from Core OL-92, Owens Lake, southeast California, Geologic Society of America Special Paper 317, pp. 143–160.

Smoot, J.P., Litwin, R.J., Bischoff, J.L., Lund, S.P. (2000). Sedimentary record of the 1872 earthquake and ‘‘Tsunami’’ at Owens Lake, southeast California. *Journal of Sedimentary Geology* 135, 241–254.

Stakhiv, E.Z. (2011). Pragmatic approaches for water management under climate change uncertainty. *Journal of the American Water Resources Association* 47(6), 1183–1196.

Street-Perrott, F.A., and Harrison, S.P. (1985). Lake levels and climate reconstruction, *in*: Paleoclimate Analysis and Modeling, ed., Hecht, A.D., John Wiley and Sons, New York, pp. 291–340.

U.S. Army Corps of Engineers (USACE) (1984). Shore Protection Manual, Volume 1. U.S. Army Engineer Waterways Experiment Station, Vicksburg, MS, U.S.A., 502 p.

U.S. Army Corps of Engineers (USACE) (2002). Coastal Engineering Manual. Washington D.C., U.S. Corps of Engineers, Engineer Manual 1110-2-1100, Part II and III.

Yu, Z, Dong, W., Jiang, P. (2015). Temperature and rainfall estimates for past 18000 years in Owens Valley, California with a coupled catchment-lake model. Hydrology and Earth Systems Sciences Discussions 12, 6505–6539.

Zic, M., Negrini, R.M., Wigand, P.E. (2002). Evidence of synchronous climate change across the Northern Hemisphere between the Northern Atlantic and the Northwestern Great Basin, United States. *Geology* 30, 635–638.

Zimmerman, S.R.H., Hemming, S.R., Hemming, N.G., Tomascak, P.B., Pearl, C. (2011). High-resolution chemostratigraphic record of late Pleistocene lake-level variability, Mono Lake, California. *Geological Society of America Bulletin* 123, 2320–2334.

CHAPTER 1

A CONTINUOUS 4000-YEAR LAKE-LEVEL RECORD OF OWENS LAKE, SOUTH-CENTRAL SIERRA NEVADA, CALIFORNIA, USA

Steven N. Bacon[a], Nicholas Lancaster[a], Scott Stine[b], Edward J. Rhodes[c], and Grace A. McCarley Holder[d]

[a]Desert Research Institute, Division of Earth and Ecosystem Sciences, 2215 Raggio Parkway, Reno, NV 89512, USA
[b]California State University East Bay, Department of Geography and Environmental Studies, Hayward, CA 94542, USA
[c]University of Sheffield, Department of Geography, Sheffield, United Kingdom
[d]Great Basin Unified Air Pollution Control District, Bishop, CA 93514, USA

Reproduced with permission from:
Bacon, S.N., Lancaster, N., Stine, S., Rhodes, E.J., and McCarley Holder, G.A., 2018. A continuous 4000-year lake-level record of Owens Lake, south-central Sierra Nevada, California, USA. Quaternary Research 90, 276–302. doi:10.1017/qua.2018.50.

Copyright 2018 Cambridge University Press.

ABSTRACT

Reconstruction of lake-level fluctuations from landform and outcrop evidence typically involves characterizing periods with relative highstands. We developed a new approach to provide water-level estimates in the absence of shoreline evidence for Owens Lake in eastern California by integrating landform, outcrop, and existing lake core data with wind-wave and sediment entrainment modeling of lake core sedimentology. We also refined the late Holocene lake-level history of Owens Lake by dating four previously undated shoreline features above the water level (1096.4 m) in AD 1872. The new ages coincide with wetter and cooler climate during the Neopluvial (~3.6 ka), Medieval Pluvial (~0.8 ka), and Little Ice Age (~0.35 ka). Dates from stumps below 1096 m also indicate two periods of lowstands at ~0.89 and 0.67 ka during the Medieval Climatic Anomaly. The timing of modeled water levels associated with 22 mud and sand units in lake cores agree well with shoreline records of Owens Lake and nearby Mono Lake, as well as with proxy evidence for relatively wet and dry periods from tree-ring and glacial records within the watershed. Our integrated analysis provides a continuous 4000-yr lake-level record showing the timing, duration, and magnitude of hydroclimate variability along the south-central Sierra Nevada.

1. INTRODUCTION

The delineation and dating of shoreline features typically provides information on the areal extent and age of lakes at their relative highstands during oscillating lake-level cycles. Most studies focused on reconstructing lake levels are either limited to periods with relative highstands because of a lack of preserved landforms and outcrop evidence for lower water levels (e.g., Adams, 2007; Bartov et al., 2007) or rely on inferences from stratigraphy exposed in lower parts of lake basins without shoreline constraints (e.g., Negrini et al., 2006). Lacustrine sediment cores are useful in identifying changes in relative lake levels from proxy evidence (e.g., sediment size, geochemistry, biology) (e.g., Benson, 2004), but there is large uncertainty in use of proxy evidence to infer corresponding water depths and associated water levels (e.g., Smith, 1997; Reheis et al., 2014). When shoreline data and lake core records are combined, a coupled data synthesis yields stronger and more complete records (Bacon et al., 2006; Reheis et al., 2014). Further, if these data sets are integrated using a method to provide constraining water levels in the absence of shoreline evidence of both high and low water levels, a continuous lake-level record can be developed.

Application of monthly, watershed-lake hydrologic models have been used for the Sierra Nevada and Great Basin to infer paleoclimate variability for the region. The hydrologic models are commonly controlled by lake stage records derived from either dated landforms or inferences from outcrop evidence. These hydrologic models typically include simulations encompassing short time periods during which lakes were at their relative highstands (e.g., Matsubara and Howard, 2009; Yu et al., 2015; Barth et al., 2016) or in rare cases during relative lowstands (e.g., Hatchett et al., 2015; 2016). As a

result, most of the model simulations are restricted to discrete periods that lacked a complete record of a given lake-level cycle, thereby offering discontinuous estimates of paleoclimate variability in the context of climate change at multidecadal to multicentennial scales.

The primary goal of our investigation is to refine the late Holocene portion of the lake-level record of Owens Lake, previously developed by Bacon et al. (2006) and included in Reheis et al. (2014), to test a new approach in developing a continuous lake-level record. Our objectives are three-fold: (1) to present geomorphic evidence and numerical age constraints for four previously undated shoreline features below the late Holocene highstand shoreline at an elevation of ~1108 m and for two lowstands below the historical lake level at ~1096 m; (2) to develop a new modeling approach to estimate lake levels in the absence of shoreline evidence by integrating shoreline and lake core data sets with threshold lake-water depth estimates from wind-wave and sediment entrainment modeling of lake core OL97 sedimentology; and (3) to construct a continuous lake-level curve for the late Holocene to assess hydroclimate variability in the region.

2. GEOLOGIC AND HYDROLOGIC SETTING

The Owens River watershed includes Owens Valley, an approximately 15–40 km wide and 200 km long graben in the southwestern Great Basin in east-central California. The watershed is on the eastern side of the south-central Sierra Nevada that forms one of the principal rain shadows in the western U.S. The watershed has a drainage area of ~8515 km^2 and is bounded by the crests of the Sierra Nevada Range to the west, White-

Inyo Mountains to the east, and the Coso Range to the south and east (Figure 1). The northern extent of the watershed is defined by a drainage divide with Mono Lake basin. Crests of the Sierra Nevada and White-Inyo Mountains rise more than 3000 m above the floor of Owens Valley, with Mount Whitney at an elevation of 4421 m west of the town of Lone Pine (Figure 1). The northern extent of the Owens River is within Long Valley and extends to the south where it drains into Owens Lake basin.

Owens Lake occupies a topographically closed basin contained by a sill at an elevation of ~1145 m at the south end of the basin. Owens Lake basin is relatively shallow because of high sedimentation rates from the Owens River and surrounding alluvial fans (Figure 1). Snowmelt from the Sierra Nevada accounts for most of the annual streamflow in the watershed (Hollet et al., 1991). Therefore, small changes in streamflow inputs associated with changes in the magnitude of snowpack and rate of snowmelt are amplified in the lake basin because of its shallow-hypsometric configuration compared to other lakes on the eastern side of the Sierra Nevada that are much deeper (e.g., Lake Tahoe, Pyramid Lake, Walker Lake, and Mono Lake) or west side lakes that are sourced from larger and forested watersheds at lower elevations (e.g., Tulare Lake) (Figure 1).

During the period AD 1872–1878, Owens Lake was a perennial, closed-basin lake that covered more than 280 km^2 with a historical maximum lake level at 1096.4 m and a water depth of 14.9 m (Gale, 1914; Lee, 1915). Major water diversions in Owens Valley began after AD 1913 with construction of the Los Angeles aqueduct system that transported surface water from the Owens River watershed and Mono Lake basin (since AD 1941) more than 320 km to the south for distribution (Hollett et al., 1991). Owens

Lake first began depositing salts onto the lake floor in AD 1921 because of these diversions, and by AD ~1931, Owens Lake had desiccated and become a playa (Smith et al., 1997).

3. Late Pleistocene and Holocene Lake-Level History

Owens Lake has been the focus of numerous paleohydrologic studies because of a robust record of climate change preserved in lacustrine sediments and shoreline geomorphic features. Most of these studies focused on resolving the late Pleistocene history of pluvial Owens Lake through analyses of sediment cores with records going back ~800,000 yr BP (e.g., Smith and Pratt, 1957; Newton, 1991; Lund et al., 1993; Benson et al., 1996, 1997, 2004; Smith et al., 1997 and references therein; Mensing, 2001) and shoreline features as old as ~140,000 yr BP (Carver, 1970; Beanland and Clark, 1994; Bacon et al., 2006; Bacon and Pezzopane, 2007; Jayko and Bacon, 2008; Orme and Orme, 2008). The age, distribution, and paleoclimatic context of the younger and lowest-elevation shorelines that encompass Owens Lake basin, however, have not been the primary focus of previous studies. Previous descriptions and geologic mapping of areas within Owens Lake basin do not provide sufficient resolution to characterize the middle to late Holocene lacustrine stratigraphy in the basin, because they either lack numerical ages (e.g., Gale, 1914; Lee, 1915; Stinson, 1977; Stone et al., 2000, 2004; Jayko, 2009) or were performed during site-specific studies focused on older and higher shorelines (e.g., Bacon and Pezzopane, 2007; Jayko and Bacon, 2008; Orme and Orme, 2008). Only inferred surface ages for the lowest shorelines (Bacon et al., 2006) and sediment-core proxy evidence spanning the last 1000 years (Li et al., 2000; Smoot et al.,

2000) and for most of the Holocene (Newton, 1991; Smith et al., 1997; Benson et al., 2002; Benson, 2004) addressed the middle to late Holocene history of Owens Lake and hydroclimate variability in the region.

4. TECTONIC SETTING

Understanding the rates and style of tectonic deformation within seismically active lake basins provides information to correlate shoreline features, as well as to accurately reconstruct past lake levels. Owens Valley is a region of active tectonics, as demonstrated by the M7.5–7.75 AD 1872 Owens Valley earthquake (Beanland and Clark, 1994). The southern section of the Owens Valley fault (OVF) extends along the entire western margin of Owens Lake basin (Figure 1). During the AD 1872 earthquake, normal-oblique displacements produced subsidence in the depocenter area of Owens Lake that created a seismic seiche (i.e., tsunami), raised the western shoreline, and shifted the position of the eastern shoreline of the lake several hundred meters to the west (Smoot et al., 2000). Predominantly eastside-down vertical fault slip of 0.5–1.0 m (Slemmons et al., 2008; Haddon et al., 2016) coupled with natural variability in the height of constructional shoreline features of about 1.0 m have produced a range in elevation of up to ~1.5 m for shoreline features of similar age that are younger than the penultimate event on the southern OVF of 9500 ± 500 cal yr BP (Bacon et al., 2006; Bacon and Pezzopane, 2007).

5. METHODS

5.1. Geomorphic Mapping

We mapped fluvial, deltaic, and shoreline features between the lower Owens River meander belt and northern sector of Owens Lake basin to establish geomorphic information on the late Holocene lake-level history. Mapping delineated landforms from georeferenced satellite imagery and aerial photography. Map unit contacts were digitally created directly on base layers in a geographic information systems (GIS) platform. Digitizing unit boundaries was done at a fixed map scale of 1:4000 using a series of color satellite imagery with 0.5 and 1.0 m resolution from the years AD 2006 and 2008, respectively, in addition to color aerial photography with 0.3 m resolution acquired in AD 2011.

Mapping of geomorphic features was based on tonal, textural, and topographic qualities (e.g., differences in surface color, degree of dissection and channel network development) plus presence and density of vegetation (e.g., Bull, 1991). Landforms were classified into geomorphic units following a modified version of the categorization scheme of Peterson (1981). Landform surface characteristics including magnitude of bar-and-swale microtopography and the elevation position of landform surfaces in relation to active channels (i.e., degree of dissection and relief), along with the degree of desert pavement (i.e., surface gravel density) and desert varnish (i.e., manganese oxide coatings) development helped differentiate younger landforms from older ones (e.g., McFadden et al., 1989). Documenting these types of surface features and weathering characteristics

combined with the age and elevation of specific shorelines from published studies and/or from this study enabled separation of primary landform feature types into distinct geomorphic units with an associated age class (Figure 2).

Seven primary landform feature types were identified including alluvial fans, deltaic, eolian, fluvial, lacustrine, playa, and other. These primary feature types were further separated into fifty-three distinct geomorphic map units with a corresponding surface age when applicable (Figure 2). Abbreviated descriptors for Quaternary feature types (e.g., Qfl, fluvial; Qf, alluvial fan; Qd, deltaic) were numbered 1 through increasing value (e.g., 1 to 5), representing oldest to youngest geomorphic surfaces. Playa features of the dry bed of Owens Lake (Qpl) were separated into silt crust, salt crust, and sand-covered surface landform units (Qpl(si), Qpl(salt), and Qpl(s), respectively). Lacustrine features (Ql) also were separated into shoreline landform units consisting of beach ridges and lake plains (Ql(br) and Ql(p), respectively). Deltaic features were further separated into delta bar and delta plain landform units (Qd(b) and Qd(p), respectively). Eolian features (Qe) were differentiated into five distinct landform units including active dunes, active sand sheets, sand sheets with coppice dunes, intermediate between active sand sheets and sand sheets with coppice dunes, and vegetated dunes (Qe(d), Qe(ss), Qe(ssc), Qe(ss/ssc), and Qe(vd), respectively). The remaining map units include recent colluvium (Qc) associated with bluffs (i.e., terrace risers and wave-formed scarps) of the lower Owens River meander belt and fluvial-deltaic system (Figure 2), along with late Holocene flood deposits (Qfd) and undifferentiated bedrock (Bx) (Figure 5).

5.2. Radiocarbon Analysis

We used radiocarbon analysis to directly date detrital charcoal within beach rock from a natural stream channel cut across a beach ridge at 1103 m to constrain the age of a shoreline at this elevation. Analyses were also performed to constrain the age of lake levels below 1096 m by dating carbonized wood of a tufa-coated stump preserved on the playa floor, and to date carbonized wood of an additional stump from a buried soil exposed in alluvium (Table 1). The radiocarbon ages are reported in radiocarbon years before present (^{14}C yr BP) and have been calibrated to calendar years before present (cal yr BP) using the CALIB7.1 program (Stuiver and Reimer, 1993; Stuiver et al., 2017) with the IntCal13 data set (Reimer et al., 2013). All samples were prepared and processed for AMS dating at either the Center for Accelerator Mass Spectrometry (CAMS) of the Lawrence Livermore National Laboratory or at Lamont-Doherty Geological Observatory.

5.3. Luminescence Analysis

We used infrared stimulated luminescence (IRSL) analysis to directly date sediments of a beach ridge at 1108 m and to constrain the ages of erosional shoreline features at 1101 and 1099 m by dating sediment within an eolian dune ridge complex. Two samples from a natural stream channel cut across the 1108 m beach ridge, and six samples from two boreholes (borehole-1 and -2) at the top of two dune ridges were recovered (Table 2). Samples were collected in steel tubes tapped into sand-rich horizons in natural exposures or hand-augered at the crest of dune features, where in situ gamma spectrometer measurements were made at each sample position to determine dose rate. All samples were prepared and processed at the University of California, Los Angeles

(UCLA) luminescence laboratory. Dating was based on the post-IR_{50}-$IRSL_{225}$ single-grain luminescence dating method (Rhodes, 2015). This method has been used recently to date alluvial fan deposits lacking quartz south of Owens Valley in the northern Mojave Desert (e.g., Dolan et al., 2016) and enables accurate dating of feldspar grains with a precision equal in many cases to radiocarbon analysis of detrital charcoal – thereby allowing the dating of previously undateable strata and landforms (see Rhodes (2015) and Appendix A for description of the post-IR_{50}-$IRSL_{225}$ technique).

The IRSL determinations indicated that a high degree of signal resetting had taken place, since the majority of grains provided a common IR_{50} equivalent dose value when an over dispersion of 15% was incorporated. This additional uncertainty value accounts for between-grain variability caused by effects including slight variations in burial dose rate. For most samples, IRSL dating results are consistent for duplicates or stratigraphically close locations (compare the following sample pairs: KD12-01 and KD12-02; KD12-12 and KD12-14; KD12-16 and KD12-17), as well as between IR_{50} and PIR-IR_{225} determinations (Table 2). Of the eight samples measured, two samples did not follow these trends (i.e., KD12-08 and KD12-10 from the borehole-1 site). It seems likely that the lowermost sample (KD12-10) from this site was collected from alluvial fan sediments underlying the dune and lake plain during the augering process. It remains unclear why the upper sample (KD12-08) at this location provided an apparent discrepancy between IR_{50} and PI-RIR_{225} results (300 ± 20 and 1000 ± 150 yr, respectively), but this probably relates to the small number of grains providing PI-RIR signals at 225°C. Furthermore, although fading uncorrected PIR-IR_{225} has been shown to agree with independent age control in several studies, in some cases, residuals associated

with thermal transfer arising from high pre-heat temperatures can result in age overestimation (Buyalert et al., 2011; Chen et al., 2013; Li et al., 2014). Therefore, the corrected IR_{50} ages in borehole-1 appear to be the more reliable estimate for this sector of Owens Lake basin, therefore all the corrected IR_{50} ages are considered the representative ages in the study.

5.4. Lake Bottom Sediment Entrainment Modeling

5.4.1. Wind-Wave Model

Application of wind-wave and sediment entrainment models are commonly used to estimate erosion potential within intertidal to open water coastal environments for coastal protection and habitat rehabilitation (e.g., USACE, 1984; 2002; Teeter et al., 2001; Rohweder et al., 2008; Fagherazzi and Wiberg, 2009). These types of models have also been used in lacustrine environments to estimate the distribution of sediment texture at the lake bottom (e.g., Håkanson, 1977), as well as to quantify potential impacts to water quality and clarity from resuspension of sediment, plus nutrients, heavy metals, and other toxic substances for water resource management (e.g., Reardon et al., 2016; Ji, 2017). In this study, we apply a similar approach to model the wind-wave characteristics and threshold lake-water depths required for the sedimentology described in core OL97. Our approach is calibrated by modeling the historical section in core OL97 with limnological conditions for the period AD 1872–1878 when Owens Lake was at its historical maximum water level.

Wind-driven sediment entrainment occurs when water depth is shallow enough to effectively transfer the momentum of wind-waves from the water surface to the sediment-

water interface (Håkanson and Jansson, 2002; Reardon et al., 2016). Wind waves and the fluid shear stresses they produce within the water column are the main mechanism responsible for sediment erosion and resuspension when the critical shear stress of bottom sediment is exceeded (e.g., Fagherazzi and Wiberg, 2009). The wind-wave model we used is based on linear wave theory and consists of a series of analytical solutions for estimating deep-water wave characteristics, including: significant wave height, wave length, spectral peak wave period, maximum orbital wave velocity, and critical shear stress (USACE, 1984; 2002; Rohweder et al., 2008).

An initial step in the modeling procedure is to determine the wave characteristics of wave height, period, and length in deep water. The shape of wind waves is predominately controlled by the intensity and duration of wind shear across open water surfaces, therefore wind velocity and fetch are the principal variables used to determine wave characteristics that control the magnitude of the boundary velocity below the wave crest at a specified depth. Modeling of intermediate to shallow wind-waves (e.g., USACE, 2002; Le Roux, 2010) was not performed in this study because sediment cores were extracted from the depocenter area of Owens Lake basin (Figure 1).

5.4.2. Wind

Wind direction in Owens Lake basin is strongly controlled by the orientation and topography of Owens Valley, which has a wind regime with two primary directional sectors of N-NNW and S-SSE (Lancaster et al., 2015). We relied on the classification of wind potential to produce dust raising events in Owens Lake basin to characterize wind in the wind-wave model. Data from three continuous meteorological stations around Owens

Lake playa operating from AD 1988–1991 show that high and extreme-high wind events in Owens Lake basin have hourly average wind speeds of ≥7 and ≥18 m/s, respectively, with extreme-high wind events occurring only a few times per year having wind gusts in excess of 22 m/s mostly from the N-NNW (Zhong et al., 2008). Furthermore, measured wind speeds of 15–17 m/s for fetch-limited water bodies have previously been used in wind-wave models because these magnitudes generate waves causing sediment erosion and resuspension (e.g., Rohweder et al., 2008; Fagherazzi and Wiberg, 2009).

5.4.3. Fetch

Fetch is the unobstructed distance traveled by wind or waves across open water (e.g., Fagherazzi and Wiberg, 2009). Limited fetch conditions existed at Owens Lake during AD 1872–1878, because of the lakes limited size having fetch lengths of ~17 and ~5 km at the core OL97 site from N-NNW and S-SSE directed winds, respectively. The 17 km fetch length was also used in the wind-wave model to simulate wave characteristics for the higher pre-historical water levels, because the difference in fetch between the 1096 and 1108 m lake levels is negligible (Figure 1). Similarly, the same fetch length was used for lower lake levels associated with the deposition of very coarse sand to fine pebble (2–4 mm) described in core OL97 to provide maximum potential water depths estimates for the larger particles sizes.

5.4.4. Critical Shear Stress

Critical shear stress represents the threshold for the initiation of potential particle motion when the drag force of flowing water against a particle exceeds the gravitational

force holding it in place. The routine used to calculate the critical shear stress is based on the methods described in USACE (2002), which accounts for laminar flow along a flat lake bottom surface, as well as particle size and density in water with a specific density and viscosity. A flat lake bottom slope was confirmed around the core OL97 site by a calculation of 0.025° in a GIS platform from a digital elevation model (DEM) that was created from contours digitized by Mihevc et al. (1997) from the bathymetric map of Owens Lake surveyed in February, AD 1913 (Gale, 1914; Lee; 1915). The salinity of Owens Lake water of 60.4 g/l in AD 1872–1878 (Winkle and Eaton, 1910) was used to calculate a water density of 1045.8 kg/m^3 and kinematic viscosity of 1.235 m^2/s at a temperature of 15°C using MATLAB code of the MIT seawater thermophysical properties library (Sharqawy et al., 2010; Nayar et al., 2016). Sediment characteristics were assumed to have a density of quartz (2650 kg/m^3), well sorted, and rounded with particle diameters ranging from mud-sized (0.0625–0.002 mm) to fine pebble (4 mm) that coincide with the boundaries between the size classes of the Wentworth (1922) scale.

6. RESULTS

6.1. Geomorphology of Late Holocene Shoreline Features

6.1.1. Shoreline Features

Four late Holocene (pre-historical) shorelines surrounding Owens Lake playa at elevations of ~1108, 1103, 1101, and 1099 m were first recognized and investigated as part of a study to characterize dune fields in Owens Lake basin (Lancaster and McCarley-Holder, 2013; Lancaster et al., 2015). These shoreline features are the focus of the study presented here and include well-preserved, gravelly and sandy beach ridges and lake

plains in the northern and southern margins of the lake basin where there was sustained perennial stream discharge from the Owens River and/or low-gradient alluvial fan sedimentation during their formation. In contrast, the shoreline features on the western and eastern margins of the basin associated with these lake levels are mostly wave-formed strandlines (i.e., wave-formed scarps or shoreline scarps) developed at the toe of steep and active alluvial fans or near fan apexes, with fewer constructional beach-ridge remnants. Two primary lacustrine landform units were identified in the Owens Lake basin that include beach ridges [Ql(br)] and lake plains [Ql(p)] (Figure 2).

Lacustrine beach ridges are defined as relict, semiparallel, as well as multiple wave- and wind-built landforms that formed in response to seasonal water-level changes (Otvos, 2000). The height and dimensions of beach ridges relative to still water levels in lake basins are principally controlled by slope angle, wave conditions, lake-level ranges, and wind-induced rise in water level (Otvos, 2000). Surface cover on these features in Owens Lake basin ranges from a lag of well-rounded gravel underlain by well-stratified, well-sorted, massive to stratified coarse sand and gravel on poorly-developed and younger-aged features to surfaces with a desert pavement composed of gravel that are underlain by well-rounded, well-stratified, and well-sorted sand and gravel on better developed and older-aged features.

The lake plain surfaces represent former lake bottoms within the lower-foreshore and near-shore bathymetric environmental zones of the lake shore. Different-aged lake plains can be identified as the intervening area between well-developed beach ridges that often contain small-relief shoreline scarps formed by recessional stands of the lake (Peterson, 1981). Surface cover on the lake plain features in Owens Lake basin ranges

from a desert pavement composed of gravel underlain by well-rounded, well-stratified, and well-sorted sands to gravels on well-developed and older-aged features to surfaces either having a soluble salt-rich crust, platy tufa, or a lag of sandy gravel that are all underlain by massive silts and sands on the lower elevation and younger-aged features.

The best preserved and most-complete geomorphic record of late Holocene-aged shoreline features below an elevation of ~1110 m is located in the northwest corner of the playa basin near the surface rupture of the active OVF (Figure 1). At this locality and in many other areas along the northern and southern margins of the basin, there are up to four well-developed shorelines in the form of beach ridges and wave-formed strandlines at elevations of ~1108, 1103, 1101, and 1099 m, plus historical shoreline features at and below 1096 m (Figures 3 and 4A).

6.1.2. Deltaic Features

Two landform units identified near the mouth of the Owens River where it enters Owens Lake basin consist of delta bar and delta plain feature-types (Figure 2). Delta plains are commonly associated with delta bars and collectively can indicate the mean lake level associated with the deltaic system (e.g., Einsele, 2000). The deltaic units are inset into a broad and dissected fluvial-deltaic plain last occupied by an early Holocene (~8000 cal yr BP) highstand at 1120 m (Bacon et al., 2006; Bacon and Pezzopane, 2007). Subsequent middle to late Holocene regressive water levels have formed a prograding delta complex that extends south from the entrenched channel of the Owens River meander belt to the floor of the playa. The morphostratigraphic position and elevation of each delta bar and plain map unit coincide with shorelines at 1108, 1103, 1101, and

1099 m, plus historical shoreline features at and below the 1096 m shoreline last occupied during the period AD 1872–1878 (Gale, 1914) (Figure 2). The bulk of the entrenched portion of the delta complex formed at the 1101, 1099, and 1096 m (historical) water levels. The unconfined and telescoping morphometry of the southern extent of the delta complex across the playa floor formed in response to falling water levels at and below ~1093 m beginning in AD 1884–1894 (e.g., Lee, 1915).

6.2. Late Holocene Shorelines

6.2.1. Neopluvial Highstand at 1108 m (3800–3600 cal yr BP)

Shoreline features identified at and near the elevation of 1108 m occur as relatively narrow areas preserved on gentle slopes fringing the playa basin. The best developed example of a beach ridge at 1108 m is in the northeastern sector of the lake basin within the Swansea embayment (Figures 1 and 5). Here, the beach ridge along with discontinuous wave-formed strandlines are preserved at the base of a latest Pleistocene to early Holocene beach ridge complex (Bacon et al., 2006; Orme and Orme, 2008). The 1108 m beach ridge has well-developed and broad heights of up to ~2 m dissected by alluvial channels. The surface of the beach ridge and associated lake plain in this area is covered by few small shrubs and a layer of sub-rounded to well-rounded gravel that is underlain by mostly stratified coarse sand and gravel composed of Paleozoic metasedimentary lithologies (Figure 5A). The 1108 m lake plain surfaces in other parts of the map area are also commonly poorly preserved from either erosion by younger alluvial fans or burial by eolian dunes between the elevations of 1103 or 1108 m (e.g., Figure 2).

The lake plain surfaces are also moderately vegetated and have a surface cover consisting of a lag of sub-rounded to well-rounded gravel underlain by massive sands.

The 1108 m shoreline previously was inferred to be ~3500 cal yr BP by Bacon et al. (2006), based on relative degree of preservation, geomorphic, and topographic cross-cutting relations, as well as regional paleoclimate proxy evidence. Luminescence analysis of two duplicate samples from a sandy layer within interbedded sand and gravel deposits of the 1108 m beach ridge at the Swansea site (Figure 5B) gave IR_{50} ages of 3620 ± 260 and 3490 ± 290 yr BP, supporting this interpretation (Table 2).

The soil-geomorphic characteristics of the 1108 m beach ridge at the Swansea site also indicate that the beach ridge is relatively younger than adjacent and higher latest Pleistocene to early Holocene shoreline features at the Swansea site. The surface of the 1108 m beach ridge has a moderately developed desert pavement with weakly to moderately developed desert varnish and subsurface rubification (i.e., reddening) coatings on gravel clasts, a thin vesicular A (Av) horizon (e.g., McFadden et al., 1998), and a ~30-cm thick, weakly developed soil with carbonate (k) and Avk/Bwk/Ck profile lacking soil structure (e.g., Birkeland, 1999). These soil characteristics are similar to descriptions made on gravelly late Holocene alluvial fans in the southwestern U.S. (McDonald et al., 2003; Bacon et al., 2010).

A mean age of ~3560 ± 370 yr and supporting soil-geomorphic characteristics provide direct evidence that water levels reached an elevation as high as 1108 m in Owens Lake basin during the late Holocene. Around this time, lakes and glaciers expanded in the south-central Sierra Nevada during a period of wetter conditions

commonly referred to as the Neopluvial (or Neoglacial) (e.g., Stine, 1990; 1994; Konrad and Clark, 1998; Bowerman and Clark, 2011; Street et al., 2012; 2013).

6.2.2. Medieval Pluvial Highstand at 1103 m (810–790 cal yr BP)

The 1103 m shoreline features occur as relatively narrow areas on gentle slopes fringing the basin that commonly are eroded by younger alluvial fans or buried by sand dunes (e.g., Figure 2). The 1103 m beach ridges [Ql6(br)] have heights of less than 1 m and a surface that is moderately to poorly vegetated and covered by a lag of well-rounded, coarse sand to gravel, except along the eastern margin of the lake basin where surfaces are typically covered by a lag of angular to sub-rounded gravel. Beach ridge and lake plain deposits consist mostly of massive to poorly-stratified coarse sand to gravel or fine-grained sediment with silt- and salt-rich crusts in areas east of the Owens River delta, extending as far south as Keeler. The 1103 m shoreline features are poorly-developed and commonly in the form of wave-formed strandlines developed on bluffs within the lower Owens River meander belt and across older lacustrine and alluvial features that encompass the basin, whereas beach ridges are commonly preserved on inactive and dissected areas of alluvial fans (e.g., Figure 2).

Age control of the 1103 m shoreline is from detrital charcoal sampled within a natural exposure at Carrol Creek where it crosses a beach ridge at 1103 m on the northwestern margin of the lake basin (Figures 1 and 6). Similar to other well-preserved beach ridge complexes in the basin (e.g., Figure 3), the Carrol Creek site has up to four well-developed shorelines in the form of beach ridges and wave-formed strandlines preserved at elevations of ~1108, 1103, 1101, and 1099 m, plus historical shoreline

features at and below 1096 m (Figures 1 and 4B). The charcoal sample was preserved in beach rock near the surface below the crest of a well-developed sandy beach ridge. Radiocarbon analysis of the charcoal yielded a date of 870 ± 40 ^{14}C yr BP [910–700 cal yr BP] with a median probability age of 780 cal yr BP (Table 1).

The ^{14}C age of ~780 cal yr BP provides direct evidence that water levels reached an elevation as high as 1103 m in Owens Lake basin during a major wet interval during the MCA in the western Great Basin, known as the Intervening Pluvial (Cook et al., 2010) or Medieval Pluvial (Adams et al., 2015; Hatchett et al., 2015). The bristlecone pine tree-ring chronologies in the nearby White Mountains support a short period of extreme hydroclimate variability at this time with a 10–49 yr wet and anomalously cold interval centered at ~840 cal yr BP (Leavitt, 1994; Hughes and Graumlich, 1996; Cook et al., 2010; Bale et al., 2011; Salzer et al., 2014).

6.2.3. Little Ice Age Highstands at 1101 and 1099 m (440–280 cal yr BP)

The 1101 and 1099 m shoreline features are the lowest pre-historical shorelines preserved in the lake basin. These features occur as a relatively narrow band of closely-spaced beach ridges and intervening lake plains on gentle slopes or as wave-formed strandlines on relatively steeper slopes, where both feature-types are commonly eroded by younger alluvial fans or buried by eolian dunes (e.g., Figure. 2). The 1101 m beach ridge typically has heights of less than ~1.5 m, whereas the 1099 m beach ridge is less developed and more discontinuous with heights of less than ~1 m. An example of the paired beach ridges is preserved on a well-developed barrier spit 150–200 m wide and extending ~3.5 km across the floor of the playa in the southern sector of the lake basin

near Olancha (Figure 1). The beach ridges in the basin typically have a surface covered by a lag of sandy gravel underlain by massive to poorly stratified coarse sand to gravel with silt. The associated lake plain surfaces are typically covered by coarse sand to granules with rare gravel and a coating of platy tufa in areas of the delta complex and along the western and southern margins of the lake basin, whereas surfaces along the eastern playa margin consist mostly of fine-grained sediment with silt- and salt-rich crusts.

Age constraints for the 1101 and 1099 m shorelines are derived from cross-cutting relations of wave-formed scarps with dated eolian sediment from a vegetated dune complex known as the Lizard Tail Dunes. The Lizard Tail Dunes consist of a set of 4–6 m high, parallel, and vegetated linear dune ridges that accumulated adjacent to a ~1103 m wave-formed scarp and lake plain in the northeastern margin of the lake basin, locally burying the scarp (Figures 1, 2, and 7). The outer (landward) vegetated dune ridge appears cut by two over-steepened slopes or notches that range in height from 0.5 to 1.5 m along the southwestern face of the dune ridge (Figures 7 and 8). Such features are absent on other vegetated dunes or active dunes in Owens Lake basin above 1103 m (Lancaster and McCarley-Holder, 2013; Lancaster et al., 2015). The over-steepened slopes are within 0.5 to 0.7 m of the 1101 and 1099 m shorelines (Figure 8) and we interpret them as wave-formed scarps formed at the 1101 and 1099 m lake stages. In addition, a similar zone of over-steepened slopes occurs at the base of the inner (lakeward) dune ridge at the Lizard Tail Dunes site (Figures 7 and 8). Here, the inner dune ridge has a lag of well to moderately rounded, disk-shaped gravel over massive sand at the toe of over-steepened slopes that are collectively situated at an elevation of

~1097 m, within 1 m of the historical water level of Owens Lake during the period AD 1872–1878. This area also was affected by the 1872 AD tsunami wave observed to have run-up ~60 m east of the shoreline along the northeastern margin of the lake (Smoot et al., 2000).

Luminescence sampling from hand-auger boreholes (1 and 2) at the crests of the vegetated dune ridges bounding the erosional 1101 m and 1099 m strandlines constrains the ages of the wave-formed scarps (Figures 7 and 8). Six samples were collected from several depths down to the base of the dunes using a sand auger, with a special sampler to allow collection of undisturbed samples that were not exposed to daylight. Luminescence analysis yielded six IR_{50} and PIR-IR_{225} ages, of which the IR_{50} IRSL ages are considered the representative age of sediment at the site (Table 2). The inner dune ridge was sampled to a depth of 2.5 m at the site of borehole-1 and produced two ages of 300 ± 20 yr and 5000 ± 210 yr at depths of 0.75 m and 2.0 m, respectively (Table 2). The lower sample at 2.0 m depth likely reflects the age of distal alluvial fan deposits underlying the dunes and 1103 m lake plain, rather than the basal age of the dune (Figure 8). The outer dune ridge was sampled to a depth of 4.0 m at the site of borehole-2 and produced four ages. The upper two samples at depths of 0.87 and 2.0 m yielded ages of 400 ± 30 and 420 ± 30 yr, respectively, whereas the lower two samples at depths of 3.0 and 3.74 m yielded ages of 710 ± 40 and 620 ± 30 yr, respectively. Although the ages of the lower two samples are not in stratigraphic order, the ages are within 20 yr of their uncertainty (Table 2; Figure 8).

Morphostratigraphic position, uniform sandy texture, and IR_{50} ages indicate three periods of sand accumulation at the borehole sites. The first period of sand accumulation occurred at 670 ± 80 yr (Unit A) and buried the 1103 m lake plain and was followed by a

second period of sand accumulation at 410 ± 40 yr (Unit B) (Figure 8). The mean age of ~780 cal yr BP from the 1103 m beach ridge supports the ages at the base of eolian deposits (Unit A) that buried the 1103 m lake plain. The unit A ages indicate sand dune accumulation after a recession of at least ~5 m from the 1103 m water level down to an elevation below ~1098 m. Sand dune accumulation ceased after ~410 yr when fluctuating lake-levels reached the elevations of 1101 and 1099 m to form erosional shoreline features on the outer dune ridge of the Lizard Tail Dunes. A third and last period of sand accumulation occurred at 300 ± 20 yr (Unit C) and formed the outer dune ridge above ~1098 m (Figure 8). This accumulation was followed by shoreline erosion at elevations from 1096 to 1097 m during the period AD 1872–1878. In addition, the oldest age on alluvium at the base of the inner dune ridge indicates that Owens Lake water levels were below ~1097 m at 5000 ± 210 yr. The ages of the 1101 and 1099 m shorelines are constrained to 360 ± 80 yr, based on cross-cutting relations of wave-formed scarps with dated eolian sediment.

The 1101 and 1099 m shorelines developed during a time of variable and extreme hydroclimatic conditions with mostly cooler temperatures in the Owens River watershed (e.g., Scuderi, 1987b; Salzer et al., 2014). This period generally corresponds to a period of glacier advance in the Sierra Nevada and across North America during the Little Ice Age (LIA) (e.g., Bowerman and Clark, 2011; Solomina et al., 2016) (Figure 11).

6.2.4. Medieval Climatic Anomaly Lowstands (1050–550 cal yr BP)

Radiocarbon analysis of in situ terrestrial vegetation at two different sites at and below 1096 m gives age information for periods of extremely low water levels in Owens

Lake basin. The lower elevation site is at ~1085 m on the playa floor at a spring mound near the northeastern margin of the perennial brine pool in the basin (Figure 1). Here, we sampled carbonized wood from a tufa-coated rooted stump in playa sediments that yielded a date of 990 ± 60 ^{14}C yr BP [1050–760 cal yr BP] with a median probability age of 890 cal yr BP (Table 1). The higher elevation site is a natural exposure of a preserved alluvial terrace within the entrenched channel of the Ash Creek alluvial fan at ~1096 m in the western margin of the lake basin (Figure 1). The Ash Creek site is situated locally below wave-formed strandlines and lake plains at 1103 and 1101 m, whereas historical shoreline features are situated ~150 m east of the site at ~1096 m. Here, we sampled carbonized wood from a stump rooted in a buried soil developed on sandy alluvium on the south wall of the stream channel that yielded a date of 720 ± 70 ^{14}C yr BP [780–550 cal yr BP] with a median probability age of 670 cal yr BP (Table 1).

The age and elevations of dated rooted stumps provide new information on the timing and limiting elevations for pre-historical water levels in Owens Lake basin. After accounting for ~1 m of subsidence from the AD 1872 earthquake, the location and age of the tufa-coated stump at the Brine Pool site indicates that water levels were below ~1086 m prior to ~890 cal yr BP. We interpret the age of the stump to record the time of death of the shrub during a rise in lake level that killed the shrub at ~890 cal yr BP, an event followed by precipitation of a coating of tufa on the submerged remains of the vegetation. The location and age of the stump at Ash Creek indicates a period of surface stability and soil formation at ~1096 m, thus requiring lower lake levels at ~670 cal yr BP.

The low lake levels of Owens Lake constrained to ~890 cal yr BP occurred during the first episode of extreme and persistent drought during the Medieval Climatic

Anomaly (MCA-1) – first identified at Mono Lake with ~200 yr of low lake levels prior to ~840 cal yr BP (Stine, 1994). Similarly, the period of low lake levels constrained to ~670 cal yr BP that followed the Medieval Pluvial highstand of Owens Lake occurred during the second episode of extreme and persistent drought during the MCA-2, also identified at Mono Lake (Stine, 1994). The lowstands of Owens and Mono Lakes from 1050 to 550 cal yr BP coincided with extended drought conditions documented in other parts of the western Great Basin (e.g., Mensing et al., 2008; Cook et al., 2010).

6.2.5. Historical Maximum Shoreline at 1096 m (AD 1872–1878)

The earliest land survey in the region was the Van Schmidt Public Land Survey in AD 1856. The elevation of the water surface of Owens Lake was not recorded during this survey, but the lake area was measured at ~288 km^2 (Lee, 1915). Three well-preserved and conspicuous historical shoreline features encompassing Owens Lake playa were previously identified at elevations of ~1096, 1093, and 1091 m (e.g., Figure 4). The oldest of these shorelines formed during a period of stable water levels at a historical maximum elevation of 1096.4 m with a corresponding lake area of 287.7 km^2 in AD 1872 (Gale, 1914; Lee, 1915; Mihevc et al., 1997), a similar lake area compared to that measured earlier in AD 1856.

The historical maximum lake levels created laterally continuous and small-scale shoreline features around most of the margin of Owens Lake playa in the form of wave-formed strandlines, beach ridges, lake plains, and discontinuous low-relief shoreline dunes (e.g., Figures 2 and 4). The ~1096 m beach ridge has crest heights of less than 1.5 m and a surface covered by mostly coarse sand to granules with gravel and sparse

vegetation (e.g., Figure 4). Surfaces of the ~1096 m lake plain consist of moderately continuous and sandy areas with tightly spaced recessional strandlines with local areas on the floor of the playa that expose underlying fine-grained lacustrine sediments as a result of wind deflation (e.g., Figure 2). The lake plain surfaces are typically covered by coarse sand to granules with fine gravel in areas near the Owens River delta, and western and southern margins of the playa, whereas surfaces along the eastern and southeastern margins of the playa commonly consist of silt- and salt-rich crusts underlain by fine-grained lacustrine sediment.

6.2.6. Post-Water Diversion Shorelines Below 1096 m (AD 1884–1931)

In addition to the ~1096 m shoreline features, other shoreline features formed during the period AD 1884–1894 at an elevation of ~1093 m and at a slightly lower lake level of ~1091 m in AD 1912 (Gale, 1914; Lee, 1915; Mihevc et al., 1997). The ~3 m drop from its historical maximum lake level to ~1093 m was primarily the result of >25% less input to the lake from stream diversions in Owens Valley between AD 1884 and 1894. During this period, Owens Lake had relatively stable water levels and a slight rise in salinity of 72.5 g/l because of the balance between stream diversions and a period of relatively wet climatic conditions in the late AD 1880s and early 1890s (Winkle and Eaton, 1910; Lee, 1915). This wet period terminated at the onset of 10 yr of severe drought between AD 1895 and 1905 that, combined with continued stream diversions, caused an additional drop in water level of ~6 m to an elevation of 1086.6 m with a corresponding lake area of ~170 km^2 (Lee, 1915). Owens Lake became hypersaline during the drought with a salinity of 213.6 g/l by AD 1906 (Winkle and Eaton, 1910).

The biological productivity of Owens Lake was severely impacted at this time because the once prevalent brine shrimp and alkali fly populations of the lake became extirpated (Herbst and Prather, 2014) when salinity of the lake exceeded ~133 g/l (e.g., Dana and Lenz, 1986). The drought was terminated by an extreme wet period (AD 1905–1917), known as the 20th century North American pluvial (Cook et al., 2011) that raised the surface of Owens Lake by ~4.5 m to an elevation of ~1091 m by May 1, AD 1912 (Lee, 1915). Owens Lake water levels began to decline after AD 1913, even during the wet period, because of the beginning of major tributary stream and Owens River diversions to the Los Angeles aqueduct system, and by AD 1931 the lake had become a salt playa (Smith et al., 1997).

The post-diversion water levels formed conspicuous recessional shoreline features around and on the floor of Owens Lake basin that are mostly preserved along the northwestern, western, and southwestern margins of the playa as sandy lake plains and beach ridges and wave-formed strandlines. The beach ridges at ~1093 and 1091 m generally have crest heights of less than 1 m and a surface covered by coarse sand to granules with gravel and sparse vegetation (Figure 4). Surfaces of the ~1093 and 1091 m lake plains consist mostly as discontinuous and thin sandy areas with tightly spaced recessional strandlines between wind-deflated areas that expose fine-grained sediments (e.g., Figure 2).

6.3. Reevaluation of Sediment Core OL97

Reevaluation of stratigraphic and lithologic descriptions and ^{14}C dates from three shallow sediment cores (OL97PC-2, OL97A, OL97C) was performed in light of the new

age constraints on late Holocene shorelines from this study to provide an additional record of late Holocene lake-level variations. The OL97 cores ranged from 2.5 to 5.64 m long and were extracted from Owens Lake playa in AD 1997 (Li et al., 2000; Smoot et al., 2000). The OL97 core sites were placed at an elevation of ~1083 m close to the depocenter of the lake basin and near the OL92 core site of Smith and Bischoff (1997) and ~1 m higher and south-southwest of core OL84B of Benson et al. (1997) (Figure 1).

The late Holocene stratigraphic sections of the OL97 cores differ from earlier cores (OL84B; OL87D; OL90; OL92) taken from Owens Lake in that they are composed of interbedded sand and mud layers in contrast to either having a thick section of sand or mud (Lund et al., 1993; Smith and Bischoff, 1997), thereby offering an opportunity to develop an association between the sedimentology (i.e., sediment texture, bedding) described in the cores and the corresponding water level. To do this, standard sediment core methodology (e.g., Smith et al., 1997) and ^{14}C calibration were first applied to develop a composite age-depth model from reported sedimentology and ^{14}C dates from the cores. Secondly, sediment texture information from the cores in combination with a simple method for calculating deterministic wind-wave characteristics for deep water sediment entrainment (USACE, 1984; 2002) was used to estimate threshold lake-water depth to entrain different size particles at the bottom of Owens Lake, which in turn was used to reconstruct lake levels.

6.3.1. Sediment Core Age-Depth Model

The OL97 cores were initially analyzed by Li et al. (2000) to infer hydroclimatic variability during the past 1000 yr based on measured variations in acid-leachable

concentrations of Mg and Li, as well as $\delta^{18}O$ values. The cores also were examined by Smoot et al. (2000) to document seismic-induced wave (i.e., tsunami) deposits in a lacustrine setting. Li et al. (2000) did not rely on ^{14}C dates from the cores because dated sediments determined to be historical in age yielded a reservoir age of ~1000 yr. Instead, Li et al. (2000) developed an age-depth model based on using paleomagnetic secular variations (PSV). Smoot et al. (2000) also acknowledged the uncertainty in the reservoir estimation and applied a ~1000 yr correction to ^{14}C dates from several mud units to establish age control in the cores.

The sediment in OL97 cores consist of sand units with thin beds and lenses of ostracode-rich sand and mud drapes, with mud layers having thin, pinch-and-swell sand laminae (Smoot et al., 2000). The sand units were interpreted by Smoot et al. (2000) to be primarily deposited by storm waves as oscillatory ripples, whereas the mud drapes accumulated during quiet-water periods. In addition, they interpreted less common 10–30 cm thick mud units with laminations of graded sand or silt to represent periods of deeper-water conditions. A total of eleven mud units (Historical and A–J) and interbedded sand units were qualitatively described in the cores, of which seven mud units (Historical and A, C, D, F, H, J) were ^{14}C dated (Smoot et al., 2000).

We developed a new composite age-depth model from the three cores to estimate mean calendar ages for mud units with multiple ^{14}C dates (e.g., A, D, J), as well as to assign interpolated ages to undated mud and sand units described in the cores (Table 3; Figure 9A). Although slight variations in sedimentation rate are evident from the age and corresponding depths of mud units in the cores, we chose to model a linear and constant rate of sedimentation to best match independent age constraints from shoreline evidence

(Table 3). A 1000-yr reservoir correction was applied to all ^{14}C conventional dates to account for older carbon, based on a date of 1050 ± 40 ^{14}C yr BP on organics from a historical mud unit in core OL97PC-2 that was underlain by a pebbly sand deposited during a tsunami in AD 1872 (Smoot et al., 2000). This reservoir age estimate was supported by high Pb concentrations within the mud layers that bound the sandy tsunami deposit, produced from the operation of silver/lead-smelting plants near Owens Lake during AD 1869–1878 (Li et al., 2000; Smoot et al., 2000).

The new composite age-depth model of core OL97 is also supported by the total inorganic content (TIC) record from core OL84B since ~4000 cal yr BP (Benson et al., 2002; Benson, 2004). The TIC content in the lake core is used as a proxy for relative water level, where low values indicate lake expansion and high values represent contraction. Given the uncertainty of the different age-depth models of cores OL84B and OL97, the TIC record in core OL84B sediments shows the same number and approximate age of prominent peaks with low values (1–10) to the number and age of mud units (A–J) in composite core OL97, demonstrating correspondence between the two core sites of the frequency of late Holocene Owens Lake expansion (Figure 9B).

6.3.2. Sedimentation Rates

Sediment in lacustrine settings consolidates with burial, requiring normalization of sediment thickness based on dry density or water content to allow direct comparison of recent and ancient sedimentation rates (e.g., Martin and Rice, 1981; Davidson et al., 2004). To evaluate the late Holocene sedimentation rate from core OL97 we used the water contents of ~62.7–51.3 wt.% at depths of 1–24.61 m for silty clay layers reported

in nearby core OL92 (Friedman et al., 1997) to account for consolidation. The normalized water content versus depth data was fitted by a logarithmic trend line (r^2 = 0.96), similar to the presentation of compression test data of soil, where the void ratio of a soil decreases linearly with the logarithm of pressure (Handy and Spangler, 2007). The sedimentation rate of this study is 120 cm/ky, based on the age-depth model with ^{14}C dates corrected for reservoir effects, but increases to 130 cm/ky when accounting for consolidation of up to 0.34 m at the observed field depth of 5.64 m.

6.4. Threshold Lake-Water Depth Analysis

The erosion potential of lake bottom sediments was assessed by modeling the threshold lake-water depths required to best match sedimentology described in core OL97 for the calibration period AD 1872–1878. The wind wave-generated bottom shear stress at the water-sediment boundary and critical shear stress for bottom erosion were calculated after the methods of USACE (1984; 2002). The hourly average wind speeds of 7 and 18 m/s for strong breeze and whole gale conditions, respectively, along with a maximum fetch length of 17 km were used in the model to simulate two wind event scenarios that would potentially define the effective wave base at the core OL97 site. The wave characteristic calculated by the wind-wave model include significant wave height (Hs), spectral peak wave period (Tp), and wave length (L). The wave characteristics driven by wind speeds of 7 and 18 m/s have values ranging from (Hs=0.53 m; Tp=2.85 s; L=12.70 m) to (Hs=1.41 m; Tp=3.94 s; L=24.24 m), respectively. The wave characteristics at the wind speed of 7 m/s produced bottom shear stresses of 4.29–0.008 Pa at depths ranging from 2 to 8 m, whereas the wind speed of 18 m/s

produced values of 4.1–0.13 Pa at greater depths ranging from 6 to 17 m (Figure 10A). The critical bottom shear stresses were also calculated for seven particle sizes ranging from clay (0.002 mm) to fine pebble (4.0 mm) (Figure 10A). The threshold lake-water depth to initiate sediment entrainment was determined by iterating water depth until the ratio between the bottom shear stress below the wave crest and the critical bottom shear stress to entrain a given particle size exceeded 1.0.

Deposits characterized as mud typically contain particles less than 0.0625 mm (coarse silt/very fine sand) in size with mud units having particles mostly less than 0.005 mm in size (very fine silt) (Ehlers and Blatt, 1982) (Figure 10B). The mud units described in the OL97 and nearby OL92 cores were previously inferred to represent periods of relatively deeper water conditions at depositional depths of 12–14 m, whereas the interbedded and coarser-grained sediment composed of sands and granules represent relatively shallower water depths of ~7 m (Smith, 1997; Smoot et al., 2000). In contrast, Li et al. (2000) interpreted the mud units in the OL97 cores as being deposited in a shallow-water setting based on proxy evidence of high salt content peaks measured within the mud units. Our sediment entrainment modeling, however, shows that the threshold lake-water depth of mud-sized particles (0.0625–0.002 mm) under waves driven by wind events of 7 and 18 m/s at Owens Lake during AD 1872–1878 potentially reached depths between ~5–7 m and ~12–16 m, respectively (Figure 10B). The modeling also shows that under the same wind events, the sandy sediment composed of very coarse sand to very fine granule/fine pebble (2–4 mm) was potentially entrained at depths between ~2–3 and ~6–8 m, respectively (Figure 10B). The range of particle sizes assigned to the mud and sand units in the model agrees with the particle size distributions

directly measured in several nearby cores with similar sedimentary units (e.g., Lund et al., 1993). The lake-water depth analysis presented here, however, would have a higher resolution if core OL97 data included measured particle size distributions at closely-spaced sample intervals.

6.5. Lake-Level Reconstruction

We evaluated the threshold lake-water depth analysis for accuracy during calibration by comparing the modeled water depths and corresponding lake-level elevations with the measured lake-level elevation and equivalent water depth in AD 1872–1878. To do this, the elevation of the lake bottom of Owens Lake during this time relative to the depth of the historical mud unit and the core OL97 site elevation of 1083 m was reconstructed by accounting for settlement from consolidation and subsidence from active faulting. Settlement was estimated by correcting for consolidation, as previously discussed. Subsidence at the core site was estimated from combining the vertical slip rates for the Sierra Nevada frontal fault of 0.25 ± 0.05 m/ky (Le et al., 2007) and for the OVF near Lone Pine of 0.12 ± 0.04 m/ky (Bacon and Pezzopane, 2007) to provide a total subsidence rate of 0.37 ± 0.09 m/ky across Owens Lake basin, given that the core OL97 site is located east and on the hanging wall of both fault zones (Figure 1).

Accounting for depth, settlement, and application of a maximum subsidence rate of 0.46 m/ky to the historical mud unit, along with the difference between the elevation of the core OL97 site and the historical maximum lake level of 1096.4 m (Gale, 1914; Lee, 1915), provided a water depth of 14.2 m. The equivalent particle size at this depth is

0.013 mm (fine silt) based on the threshold lake-water depth analysis during a high-extreme wind event of 18 m/s (Figure 10B). Applying the same corrections to the depth of the historical mud unit and adding a threshold lake-water depth ~14 ± 2 m for mud units yields a modeled lake level of 1096.2 ± 2 m (Table 3). The results of this analysis yielded a mean modeled lake level similar to the observed water level of Owens Lake in AD 1872. The reconstructed lake levels associated with pre-historical mud and sand units were calculated the same as the modeled historical lake level, requiring up to 1.92 m of correction for consolidation and subsidence at a depth of 5.64 m. The assignment of modeled water depths of ≥14 ± 2 m for mud units and ≤8 ± 2 m for sandy/pebbly (1–4 mm) units yielded reconstructed lake levels of 1092.5–1098 m and 1085–1092 m, respectively (Table 3). The range of threshold lake-water depths for the mud and sand units of this study is similar to the depositional depths of 12–14 m for the mud units in core OL97 inferred by Smoot et al. (2000), as well as the range in depositional depths of 7–14 m for the interbedded sandy and silty clay sediment in nearby core OL92 inferred by Smith (1997).

7. DISCUSSION

7.1. Refined Late Holocene Lake-Level Record of Owens Lake

Here we update a summary of late Holocene Owens Lake fluctuations previously reported in Reheis et al. (2014) and based on Bacon et al. (2013) with new limiting age constraints for water levels below 1096 and 1086 m, as well as estimates of the timing and elevation of lake levels without shoreline constraints from a new age-depth model and threshold lake-water depth modeling of sedimentology in core OL97. Integration of

these new data offers a comprehensive and continuous characterization of the lake-level history of Owens Lake that, in turn, allows refinement of the late-Holocene portion of the lake-level curve (Figure 11). The following discussion includes an accuracy assessment of the refined lake-level record by comparing the results of this study to the shoreline record of Mono Lake, as well as descriptions of modeled water-level variations of Owens Lake in the context of hydroclimate variability inferred from temperature- and precipitation-sensitive tree-ring chronologies and glacial records in the watershed.

7.2. Comparisons Between Core OL97 and Owens and Mono Lake Shoreline Records

High-resolution sediment-core records have been obtained from major lake basins along the eastern Sierra Nevada (e.g., Owens, Mono, Walker, Pyramid, Tahoe) to infer the frequency of decadal-centennial hydroclimate variability during the Holocene (e.g., Benson, 2004, and references therein). Lake-level records from the region also have been used to evaluate temporal correspondence between highstands and regional-to-global climate change (e.g., Munroe and Laabs, 2013). Our new modeling approach presents an example of how to directly link lake core and shoreline lake-level data sets to produce continuous constraints on the timing, duration, and magnitude of oscillating water levels in terminal lake basins.

Geomorphic- and outcrop-based lake-level data provide independent control on the accuracy of core-based proxy interpretations (Reheis et al., 2014). As a result, we assessed the accuracy of our modeling approach by evaluating temporal correspondence of 22 sand and mud units in core OL97 to the revised shoreline record of Owen Lake. We also compared the core OL97 and shoreline chronologies of Owens Lake to the well-

constrained shoreline record of Mono Lake to further demonstrate temporal correspondence of lake-level fluctuations between adjacent terminal lake systems (Table 4).

7.2.1. Core OL97 and Owens Lake Shoreline Records

The age of Owens Lake highstand shorelines of ~3560 yr, 780 cal yr BP, and 360 yr, as well as 78 cal yr BP for the historical lake level are within the range of ages for mud units J, C, A, and historical (hist.) in core OL97, respectively (Table 4; Figure 11). Conversely, the timing of lowstands at ~890 cal yr BP, 670 cal yr BP/ 670 yr, and 410 yr are within the range of ages for sand units 4, 3, and 2, respectively (Table 4; Figure 11). The ages of the seven sand and mud units of core OL97 and timing of Owens Lake water levels from geomorphic evidence have significant temporal correspondence ($r^2 = 0.9985$, $p < 0.001$), thereby demonstrating that the use of an ~1000-yr reservoir correction to ^{14}C dates and development of a new age-depth model for core OL97 sediment was warranted.

7.2.2. Core OL97 and Mono Lake Shoreline Records

The watersheds of Owens and Mono lake basins are situated along the eastern side of the Sierra Nevada crest and share a common west-east oriented drainage divide (Figure 1). The late Holocene lake-level record of Mono Lake is constrained by stratigraphic analysis of deltaic and shoreline deposits, as well as dating of buried stumps and woody material within interbedded fluvial layers exposed along stream banks (Stine, 1990; 1994). Similar to Owens Lake, the timing of Mono Lake lowstands and highstands coincide with the age of sand and mud units in core OL97. The ages of Mono Lake

highstands at ~3770, 1670, 1370, 870, 510, 340, and 60 cal yr BP are within the range of ages for mud units J, F, E, C, B, A, and hist., respectively (Table 4). Further, the ages of Mono Lake lowstands at ~1810, 1060, 675, 420, and 190 cal yr BP are within the range of ages for sand units 7, 4, 3, 2, and 1, respectively (Table 4). The ages of the twelve sand and mud units of core OL97 and timing of Mono Lake water-level variations from stratigraphic evidence have significant temporal correspondence ($r^2 = 0.9988$, $p < 0.001$). In addition, seven of the twelve Mono Lake lowstands and highstands are represented in the shoreline record of Owens Lake (Table 4). A comparison between the shoreline records of Owens and Mono Lakes shows significant temporal correspondence ($r^2 = 0.9976$, $p < 0.001$), indicating that even with inherited geologic and dating uncertainties in the different studies, both records show that each lake basin responded in a similar manner to hydroclimatic forcing during the late Holocene.

7.3. Late Holocene Hydroclimate Variability

Hydroclimate (e.g., precipitation and temperature) extremes in the western U.S. are strongly affected by large-scale atmospheric circulation patterns that are modulated by interannual-decadal connections in the tropical Pacific, known as the El Niño–Southern Oscillation (ENSO) (e.g., Dettinger et al., 1995; Cayan et al., 1999). The hydroclimate extremes are commonly reflected as interannual-interdecadal streamflow variability and persistence within snowmelt-dominated, dryland regions (e.g., Redmond and Koch, 1991; Vogel et al., 1998; Pagano and Garen, 2005). The relatively close correspondence between large-scale precipitation patterns and tree-ring variation patterns

in some studies has demonstrated the utility of extending the history of precipitation patterns (and perhaps their climatic forcings) into the pre-instrumental past (Dettinger et al., 1998).

7.3.1. Hydroclimate Variability from Tree-Ring Chronologies

Numerous studies in the western U.S. and Sierra Nevada have developed tree-ring reconstructions to infer precipitation variability and drought, streamflow, lake-level fluctuations, and snow water equivalent (e.g., Cook et al., 1999; 2004 Meko and Woodhouse, 2011; Graham and Hughes, 2007; Adams et al., 2015; Belmecheri et al., 2015). In the Owens River watershed, tree-ring studies have provided records of hydroclimate variability of up to ~8000-yr long from precipitation reconstructions (e.g., Hughes and Graumlich, 1996; Hughes et al., 2002; Berkelhammer and Stott, 2008; Bale et al., 2011), temperature reconstructions (e.g., Scuderi, 1987a,b; Scuderi, 1993; Salzer et al., 2009, 2014), and reconstructions of both precipitation and temperature (e.g., LeMarche, 1974; Tolwinski-Ward et al., 2015).

To assess the role of hydroclimate variability in controlling lake-level variations of Owens Lake, we used several tree-ring records of up to ~4000-yr long from the Owens River watershed to provide paleoclimatic proxy information (Figure 12). These tree-ring time series were aggregated into discrete time intervals that match the ages of sand and mud units of core OL97. Temperature-sensitive tree-ring chronologies from a site west of Owens Lake in the south-eastern Sierra Nevada were used for temperature information. This tree-ring record was developed from relic logs of foxtail pine (*P. balfouriana* Grev. and Balf.) with ^{14}C dates and reflects warm and cold intervals inferred from changes in

timberline (Scuderi, 1987a,b), that also have corresponding temperature anomalies (Scuderi, 1993) (Table 4). An additional temperature-sensitive tree-ring chronology from bristlecone pine (*P. longaeva* Bailey) from the White Mountains was used and is based on the correlation of ring widths to summer (JAS) temperature meteorological data to estimate temperature anomalies relative to modern temperature (Salzer et al., 2014) (Table 4; Figure 12B).

The same time-series aggregation also was performed for the precipitation-sensitive tree-ring chronologies developed from the Methuselah Walk bristlecone pine series from the White Mountains. These chronologies are based on either the correlation of ring widths to precipitation meteorological data (Hughes and Graumlich, 1996) (Figure 12C) or from analysis of carbon isotope ratios ($\delta^{13}C$) in cellulose that have been correlated to summer (JJA) precipitation meteorological data (Bale et al., 2011) (Figure 12A). The reported precipitation values of the tree-ring records were converted into percent-of-normal precipitation relative to the length of the records shown in Table 4 to provide a simple index with which to compare the precipitation anomalies to the timing of sand and mud deposition in core OL97.

Notable trends in the data set are from the temperature and precipitation tree-ring records from the White Mountains. These tree-ring records show that on average the mean and range in temperature anomaly and percent-of-normal precipitation values relative to the 6-yr moving mean have correspondence between sand and mud units in core OL97. The temperature anomaly values associated with the ages of sand and mud units are 0.37 ± 0.67°C and 0.29 ± 0.48 °C, respectively. These data show that the mean and range in temperature anomaly values associated with the sand units are ~25% greater

compared to the values for mud units (Table 4). The tree-ring precipitation records have relatively similar relations to the temperature anomaly data set, where the ~4000-yr long record of Hughes and Graumlich (1996) displays corresponding percent-of-normal precipitation values for sand and mud units of 100.8 ± 14.8% and 99.9 ± 9.7%, respectively. These data indicate that mean precipitation for both the sand and mud units is similar, but the range in precipitation associated with the age of sand units is ~35% greater compared to the values for mud units (Table 4). The ~1000-yr long $\delta^{13}C$-based tree-ring record of Bale et al. (2011) also has similar trends of percent-of-normal precipitation with values for sand and mud units of 98.3 ± 50.0% and 93.8 ± 32.5%, respectively. The ~4000-yr long tree-ring record shows that mean precipitation associated with the age of sand units was ~5% greater than mud units but displayed a ~35% greater range in precipitation associated with sand units compared to mud units (Table 4).

7.3.2. Hydroclimate Variability from Glacial Records

In the Sierra Nevada, the advance and retreat of glaciers are especially sensitive to changes in winter precipitation and summer temperature (Gillespie and Clark, 2011). We used the Holocene glacial record from alpine lakes in the central Sierra Nevada to assess the role of alpine hydroclimate variability in controlling lake-level variations of Owens Lake (Bowerman and Clark, 2011) (Figure 12). The reported ages of glacier maxima inferred from lake-core evidence below the Palisades Glacier in the Owens River watershed at 3300 ± 100, ~2800, ~2200, ~1600, ~700, and 210 ± 40 cal yr BP were compared to both the age of corresponding sand and mud units of core OL97 and the tree-ring records from the Owens River watershed (Table 4). Evaluation of these records

showed that the timing of four of the six glacier maxima corresponded to the age of sand units in core OL97. Further, comparison of the timing of glacier maxima to the tree-ring record in the southeastern Sierra Nevada (Scuderi,1987a,b) also shows temporal correspondence between lowering of timberline during cold intervals and sand deposition in core OL97. These relations are supported by the timing of when glaciers in the central Sierra Nevada reached their Holocene maximum extent at 210 ± 40 cal yr BP during the latter half of the LIA (LIA-1) (Bowerman and Clark, 2010), which was also a time that corresponded to sand deposition in Owens Lake basin (Figure 11; Table 4).

Tree-ring records from the White Mountains provided a more continuous record of hydroclimate variability during periods of glacier maxima. The glacial record has corresponding temperature anomaly values of 0.41 ± 0.72°C and percent-of-normal precipitation values of 100.0 ± 15.2% from the record of Hughes and Graumlich (1996) and 102.5 ± 50.0% from the record of Bale et al. (2011) (Table 4). The ~4000-yr long tree-ring records showed that the range in both temperature and precipitation which corresponded to periods of glacier maxima were ~30% greater than the range of values for the entire record (Table 4).

7.4. Hydrologic Response of Owens Lake to Hydroclimate Variability

Comparisons of the frequency of sand and mud deposition in core OL97 to the tree-ring and glacial records in the Owens River watershed display a complex pattern of hydroclimate variability: wet/cold, wet/warm, dry/cold, or dry/warm (Table 4; Figure 12). Data analysis revealed relatively good temporal correspondence between the magnitude of temperature and precipitation variability and the timing of sand and mud deposition in

Owens Lake basin. Our analysis demonstrated that sand deposition (i.e., lowstands) occurred mostly during periods with higher hydroclimate variability, whereas mud deposition (i.e., highstands) occurred primarily during times with lower hydroclimate variability. These relations link the hydrologic response of the Owens River-Lake system to two general patterns of hydroclimatic forcing during the late Holocene.

Contemporary stream discharge and water-level changes in lake basins of the Sierra Nevada are largely modulated by the magnitude of snowpack and rate of snowmelt runoff (e.g., Howat and Tulacyak, 2005). Recent observations of snow drought conditions in the Sierra Nevada (Harpold et al., 2017; Hatchett and McEvoy, 2018) may provide one of many possible hydrologic forcing mechanisms to explain the temporal pattern of late Holocene hydroclimate variability reflected in the lake-level record of Owens Lake, as well as in the glacier maxima record of the central Sierra Nevada (Bowerman and Clark, 2010). Snow drought in the context of hydrologic systems is either classified as “dry snow drought” because of a lack of winter precipitation or “warm snow drought,” where warmer-than-normal temperatures prevent precipitation from accumulating on the landscape as snowpack. Warm snow drought conditions in the Sierra Nevada often influence significant winter flooding, early snowmelt runoff, reduce summer streamflow, and cause a decrease in perennial snow accumulation (Dettinger and Cayan, 1995; Harpold et al., 2017; Hatchett and McEvoy, 2018).

Warm snow droughts can force the hydrologic balance of river-lake systems to respond with a net lowering of lake levels over decadal-multidecadal timescales with persistent warm climate conditions, even during periods with near-normal winter precipitation. Recent hydrologic modeling of the Walker Lake basin (Figure 1), directly

north of Mono Lake, demonstrates that a variety of frequencies and magnitudes of wetter years linked to total moisture transport and atmospheric river events can interrupt MCA-like megadroughts, while still producing regressive lake levels consistent with documented MCA lowstands and drought durations (Hatchett et al., 2015; 2016). The Walker Lake modeling results under a megadrought climate offer a large-scale pattern of potential hydroclimate regimes that may explain the apparent correspondence of Owens Lake lowstands to the timing of glacier maxima, including the Holocene maximum extent during the LIA, during periods with higher hydroclimate variability. We encourage further research of the hydroclimate required to support Holocene glaciers and snow persistence in the Sierra Nevada to better understand the hydrology of regional river-lake systems.

7.4.1. Lake-Level Oscillations of Owens Lake During the Late Holocene

Many studies in the western U.S. have performed paleo-hydrological modeling along the north-central Sierra Nevada of megadrought climatic conditions to reconstruct precipitation (e.g., Graham and Hughes, 2007; Kleppe et al., 2011) or to identify potential storm track activity and moisture transport during the late Holocene (e.g., Hatchett et al., 2015; 2016; 2018). Our results, based on integrated lake-core and shoreline records, showed that 75% of the ~4000-yr long record of core OL97 is represented by eleven periods of primarily sandy deposition corresponding to modeled lake levels that were ~4–11 m below the historical maximum (Figure 11). The corresponding lowstands and tree-ring records indicated that periods with low stream discharge to the lake were mostly controlled by persistent and higher hydroclimate variability that lasted on average

~290 yr with a maximum duration of ~620 yr centered at ~3260 cal yr BP, soon after the Neopluvial highstand and a minimum of ~60 yr centered at ~2105 cal yr BP (Table 3). The frequency and duration of Owens Lake lowstands were also in general agreement with periods of severe multidecadal to multicentennial droughts (i.e., megadroughts) documented in the western Great Basin and south-central Sierra Nevada during the late Holocene (e.g., Stine, 1994; Benson et al., 2002; Mensing et al., 2008; 2013; Cook et al., 2010).

The remaining 25% of the Owens Lake record was characterized by eleven periods of mostly mud deposition corresponding to lake levels that were ~4 m below and up to ~12 m above the historical maximum (Figure 11). The corresponding highstands were primarily controlled by relatively high stream discharge to the lake during periods with persistent and lower hydroclimate variability that lasted on average for ~80 yr with a maximum duration of ~230 yr centered at ~2250 cal yr BP and a minimum of ~20 yr centered at ~800 cal yr BP during the Medieval Pluvial highstand (Table 3). The integrated core OL97 and shoreline records showed that Owens Lake highstands coincided with periods of global-scale climate change with transgressions of up to ~25 m during the Neopluvial (or Neoglacial), ~18 m during the Medieval Pluvial of the MCA, and ~11–13 m during the LIA-1 (Figure 11).

8. CONCLUSIONS

We refined the late Holocene Owens Lake lake-level history by mapping, as well as ^{14}C and luminescence dating of four previously undated shorelines above the historical maximum lake level of ~1096 m last occupied during AD 1872–1878. Dates of

3560 ± 370 yr from a beach ridge at 1108 m, 910–700 cal yr BP from a beach ridge at 1103 m, and a constraining age of 360 ± 80 yr for erosional shorelines at 1101 and 1099 m coincide with periods of persistent and mostly lower hydroclimate variability during the Neopluvial, Medieval Pluvial, and LIA, respectively. New dates from rooted stumps below the historical lake level also indicated two periods of low water levels associated with persistent and higher hydroclimate variability ending at ~890 cal yr BP and that occurred ~670 cal yr BP, nearly synchronous with the timing of eolian sand deposition in Owens Lake basin and multi-centennial lowstands documented nearby at Mono Lake during the MCA.

Reevaluation of core OL97 data and application of a ~1000-yr reservoir correction enabled us to produce a new age-depth model for Owens Lake sediments during the past ~4000 yr. Our new age-depth model of OL97 data and interpretation of mud units as being deposited in deep lakes coupled with threshold lake-water depth estimates from wind-wave sediment entrainment modeling have produced a lake-level record of Owens Lake that agrees well with proxy evidence of climate change from lake-level constraints of dated shorelines of Owens and Mono Lakes, as well as from tree-ring and glacial records from sites within the Owens River watershed. The strong correspondence of the timing of modeled lake-level variations of Owens Lake from this analysis with watershed-paleoclimatic proxy records of hydroclimate variability provide confidence in the approach developed in this study to estimate the timing, duration, and magnitude of regional climate change. Our integrated approach to generate a continuous lake-level record with well-constrained oscillating water levels will afford a unique

opportunity to perform hydrologic water-balance modeling of the Owens watershed-lake system and characterize the pattern of hydroclimate variability along south-central Sierra Nevada during the past ~4000 yr.

9. ACKNOWLEDGEMENTS

Funding for this work was provided by the Great Basin Unified Air Pollution Control District (GBUAPCD) with contributions from the General Frederick Lander Endowment, as well as by the National Institutes for Water Resources/U.S. Geological Survey #G16AP00069 and National Science Foundation EAR #1252225 to S. Bacon. The authors acknowledge Sondra Grimm of GBUAPCD for assistance with fieldwork. Many discussions with Thomas Bullard throughout the study and his review of an earlier version of the manuscript are gratefully appreciated. We also thank Roger Kreidberg for editorial review of an earlier version of the manuscript. We acknowledge Adam Csank for providing the Hughes and Graumlich (1996) Methuselah bristlecone pine tree-ring chronology. The authors thank Ken Adams, Robert Negrini, and *QR* Editors for providing constructive and thoughtful reviews that greatly improved the manuscript.

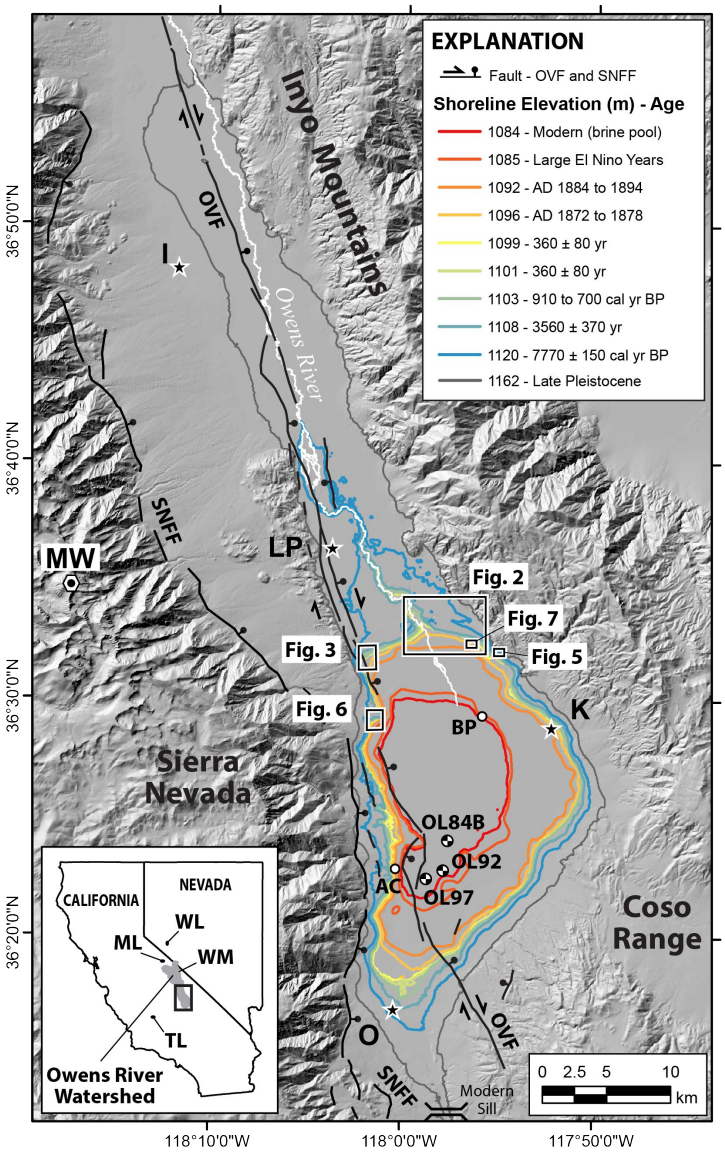

Figure 1. Map of the southern Owens River watershed showing the elevation of well-developed Holocene shorelines (1084–1120 m) and late Pleistocene highstand shoreline (~1162 m) of Owens Lake from this study and Bacon et al. (2006). The modern extent of Owens Lake playa below an elevation of ~1096 m, the Owens Valley fault (OVF), and Sierra Nevada Frontal fault (SNFF) are shown. Rectangles show areal extent of maps and imagery on following figures. White circles are the locations of study sites described in text: AC – Ash Creek; BP – Brine Pool. Location of lake core OL84B, OL92, and OL97 sites are shown. Inset map shows the boundary of the Owens River watershed along the eastern side of the south-central Sierra Nevada in eastern California. Major physiographic and hydrologic features and towns shown on the maps include: I – Independence; K – Keeler; LP – Lone Pine; ML – Mono Lake; MW – Mount Whitney Peak (el. 4421 m); O – Olancha; TL – Tulare Lake; WL – Walker Lake; WM – White Mountains.

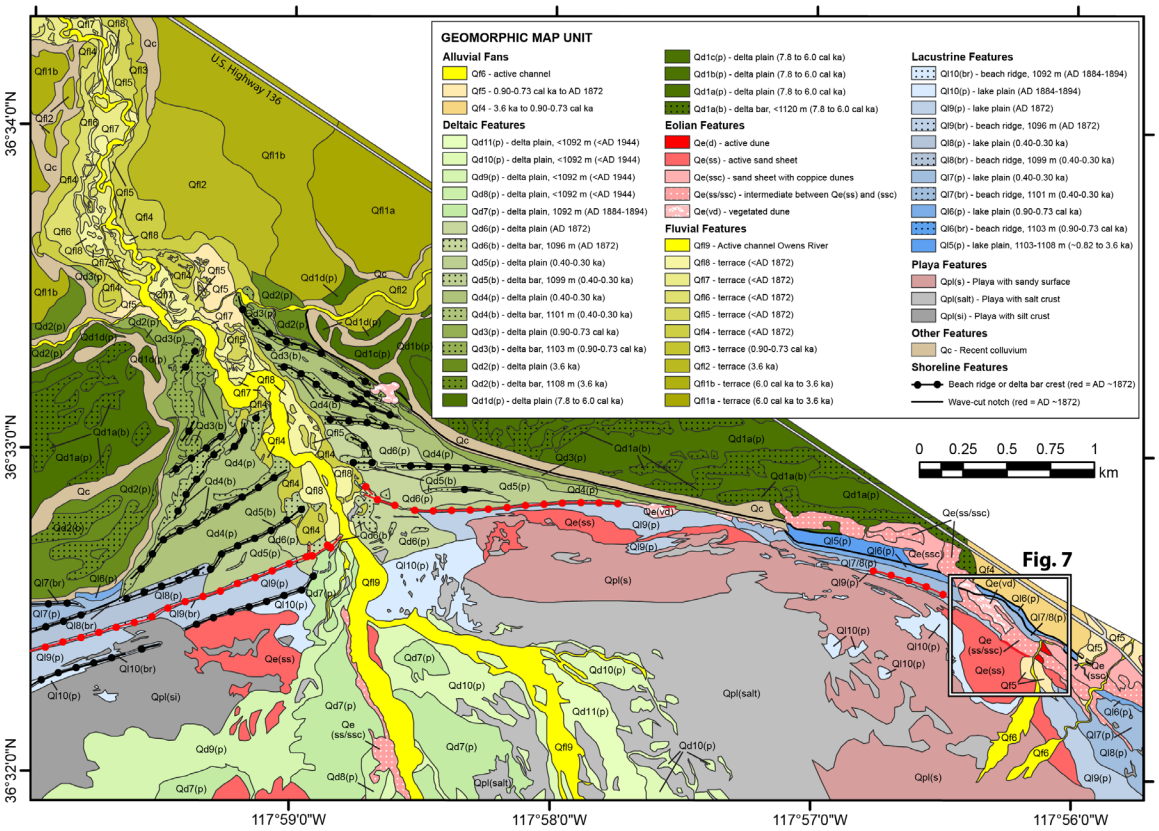

Figure 2. Detailed geomorphic map of the north-northeastern sector of Owens Lake basin showing the age and distribution of alluvial fan, deltaic, eolian, fluvial, lacustrine, playa, and other landform feature-types. Age control is from directly dated shoreline features from Bacon et al. (2006) and results of this study, as well as from cross-cutting relations with undated landforms. Inset box shows areal extent of the Lizard Tail Dune study site. Shoreline features formed by historical lake levels during AD 1872–1878 are shown in red.

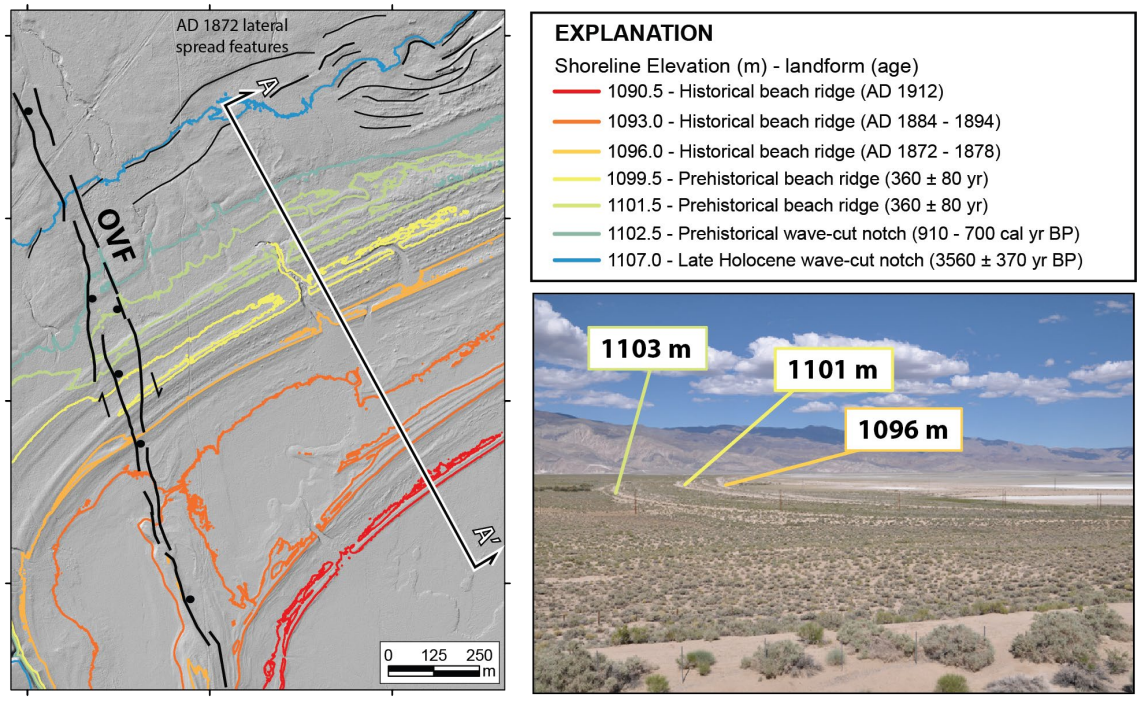

Figure 3. Hillshade map and elevation contours showing the best preserved and complete geomorphic record of late Holocene-aged shoreline features below an elevation of ~1110 m. The trace of the AD 1872 surface rupture of the Owens Valley fault (OVF) and secondary-faulting from lateral-spreading during the earthquake (Carver, 1970) are shown in the northwest corner of Owens Lake basin (Figure 1). Location of geomorphic profile transect A–A' (Figure 4) is shown. Photograph shows the 1103, 1101, and 1096 m shorelines and playa, view to the east with Inyo Mountains in distance. Hillshade and contours from 0.5 meter resolution airborne laser swath mapping digital topographic data from EarthScope (2011).

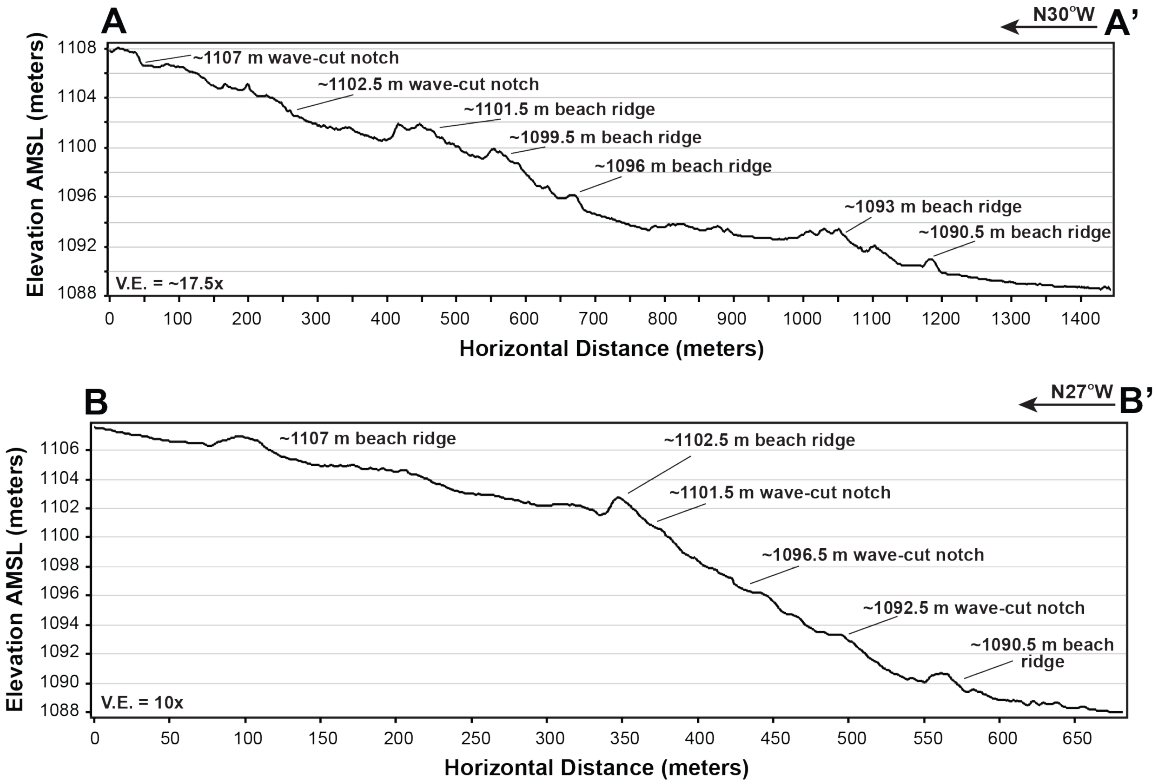

Figure 4. Geomorphic profiles of late Holocene-aged shoreline features below an elevation of ~1110 m along transect A–A' at the northwest corner of Owens Lake basin (Figure 3) and B–B' at the Carrol Creek study site along the western margin of the lake basin (Figures 1 and 6). Profiles were developed from 0.5 meter resolution airborne laser swath mapping digital topographic data from EarthScope (2011).

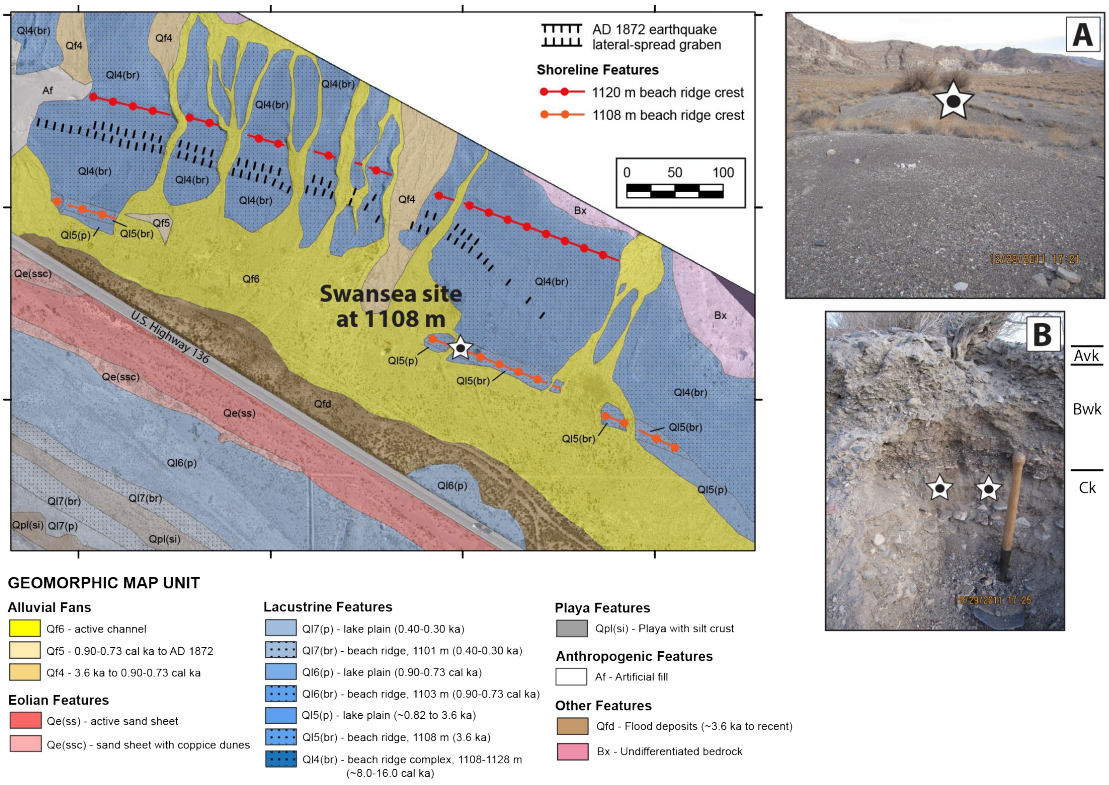

Figure 5. Geomorphic map of the Swansea Embayment northwest of Keeler (Figure 1) showing well-developed beach ridge and lake plain features at elevations of 1120 and 1108 m, along with a prominent graben formed from lateral spreading during the AD 1872 earthquake (Carver, 1970). Star on photographs: (A) shows the location of infrared stimulated luminescence (IRSL) sampling within a channel cut across the crest of the 1108 m beach ridge, view to the southeast; and (B) shows interbedded sands and gravels, as well as location of duplicate IRSL samples within a sandy layer on northwest-facing channel wall that returned ages of 3490 ± 260 and 3620 ± 260 yr. Entrenching tool is shown for scale. Annotations on the photograph of general soil-geomorphic horizons are also shown.

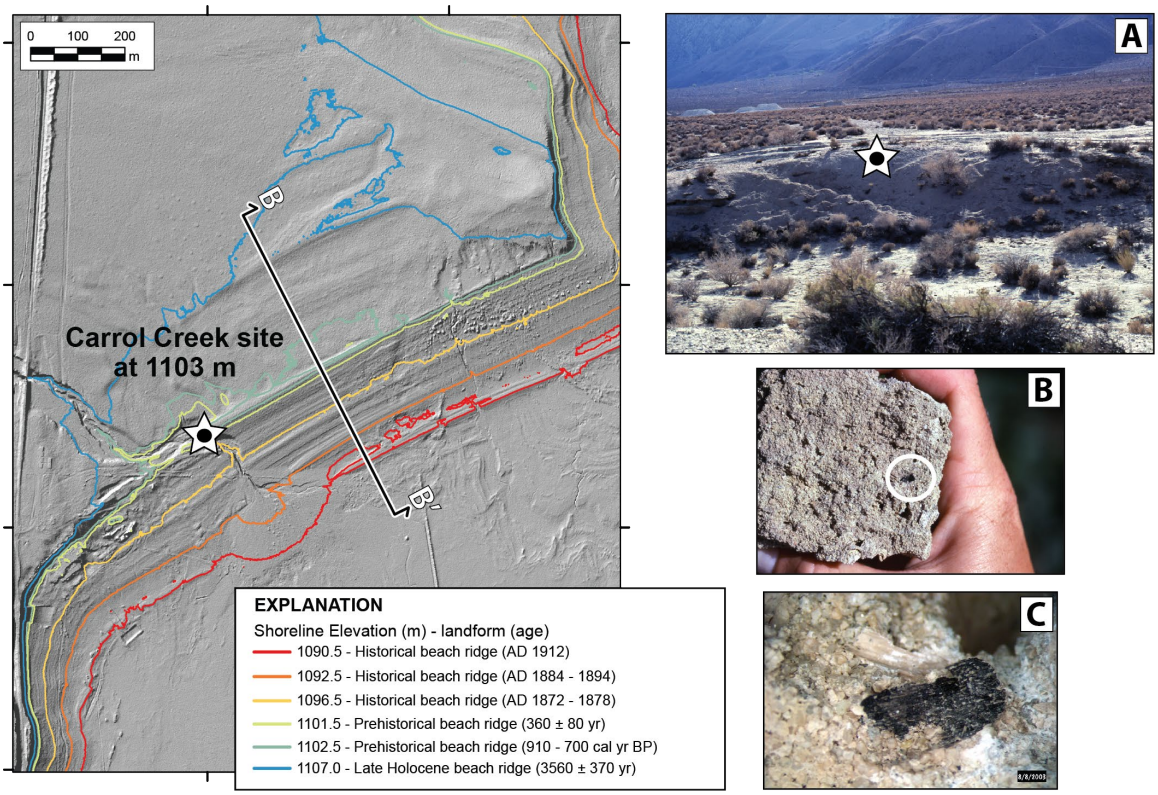

Figure 6. Hillshade map and elevation contours showing a well-preserved and complete geomorphic record of late Holocene-aged shoreline features below an elevation of ~1110 m at the Carrol Creek site on the western margin of Owens Lake basin (Figure 1). Location of geomorphic profile transect B–B' (Figure 4) is shown. Star on photographs: (A) shows the sample location of detrital charcoal at the crest of the 1103 m shoreline on the southwest face of the incised channel; (B and C) show close-up views of detrital charcoal in beach rock that yielded a ^{14}C age of 910–700 cal yr BP, indicating Owens Lake had a Medieval Pluvial highstand during an intervening period of the Medieval Climate Anomaly. Hillshade and contours from 0.5 meter resolution airborne laser swath mapping digital topographic data from EarthScope (2011).

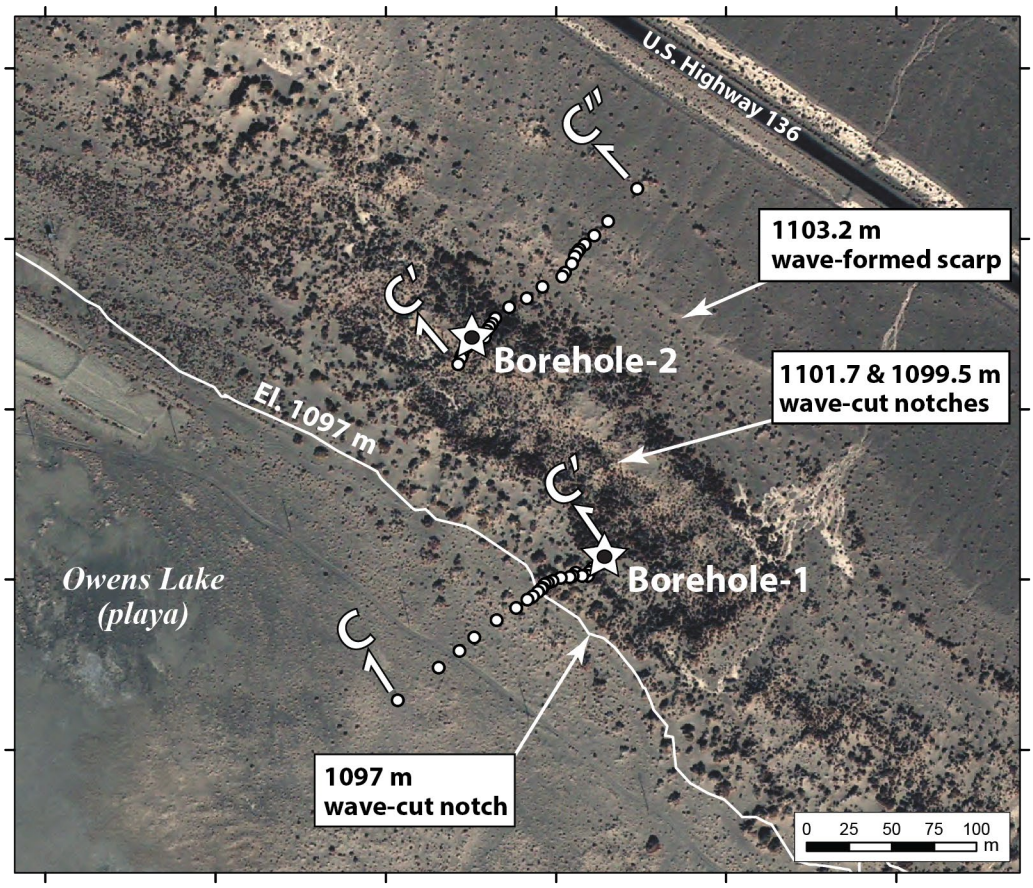

Figure 7. Aerial imagery of the Lizard Tail Dune site on the northeastern margin of Owens Lake basin (Figures 1 and 2) showing a vegetated, parallel linear dune system that has developed on the 1103 m lake plain. Wave-formed scarps at an elevation of 1103.2 m across distal alluvial fans, as well as wave-formed notches at 1099.5 and 1101.7 m on the outer dune ridge are shown. The location of wave-formed notches and beach ridges at ~1097 m formed by historical lake levels during AD 1872–1878 is shown at the base of the inner (basin ward) dune ridge. The locations of boreholes-1 and -2 (stars), as well as transects C–C' and C–C" are shown across the crests of inner and outer dune ridges, respectively.

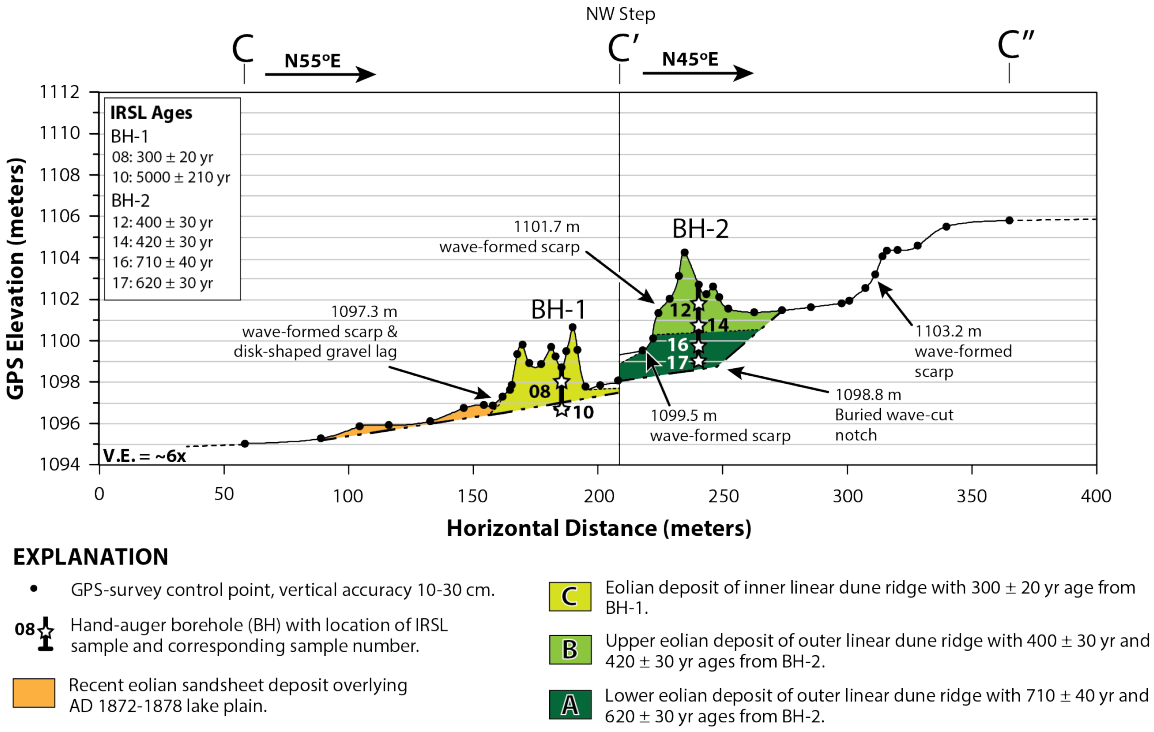

Figure 8. Geologic cross section along transect C–C'–C" (Figure 7) of the Lizard Tail Dune site showing eolian depositional units (A–C) and the location of infrared stimulated luminescence (IRSL) ages from hand-auger boreholes (BH)-1 and -2 at the crest of the inner and outer linear dune ridges, respectively. Erosional shoreline features at the elevations of 1103.2, 1101.7, 1099.5, and 1097.3 m are also shown. The ~1101 and 1099 m wave-formed scarps are constrained to 360 ± 80 yr, based on cross-cutting relations between the shoreline features and IRSL ages from dated sediments of the inner and outer dune ridges at the site.

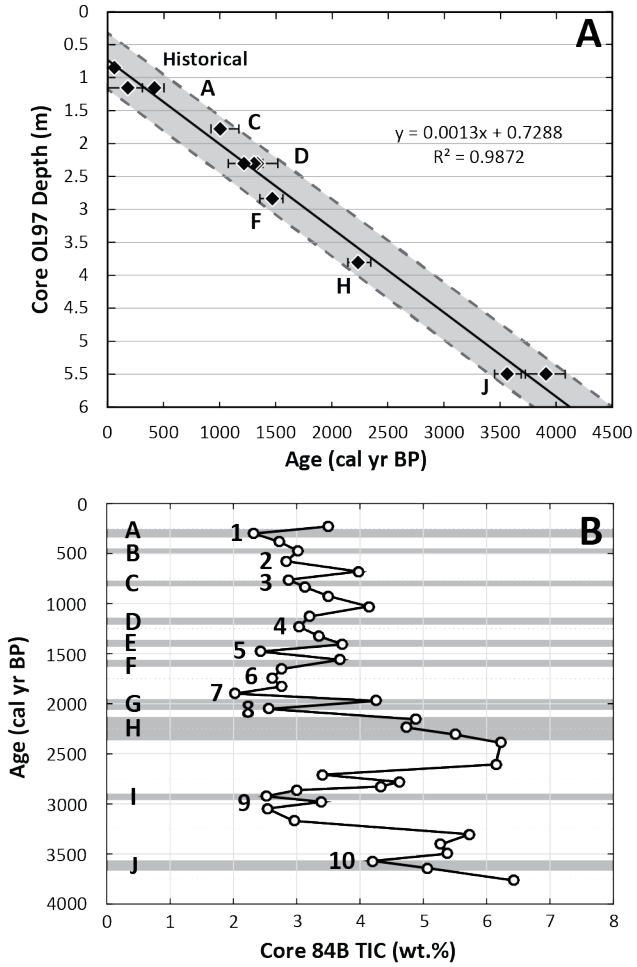

Figure 9. Plots showing: (A) composite age-depth model with 1000-yr reservoir correction developed from reevaluation of data from Owens Lake sediment cores (OL97PC-2, OL97A, and OL97C) of Li et al. (2000) and Smoot et al. (2000). Age of reported dated mud units in cores is shown, and depth has been corrected for consolidation. Shaded area shows the 95% confidence interval of ^{14}C ages, and (B) comparison of the total inorganic content (TIC) record of core OL84B (Benson et al., 2002; Benson, 2004) and sedimentologic record of core OL97. Given the different age-depth models of the cores, there is strong correspondence of the frequency of late Holocene Owens Lake expansion inferred from the age of peaks with low TIC values (1–10) in core OL84B and age of mud units (A–J) in core OL97.

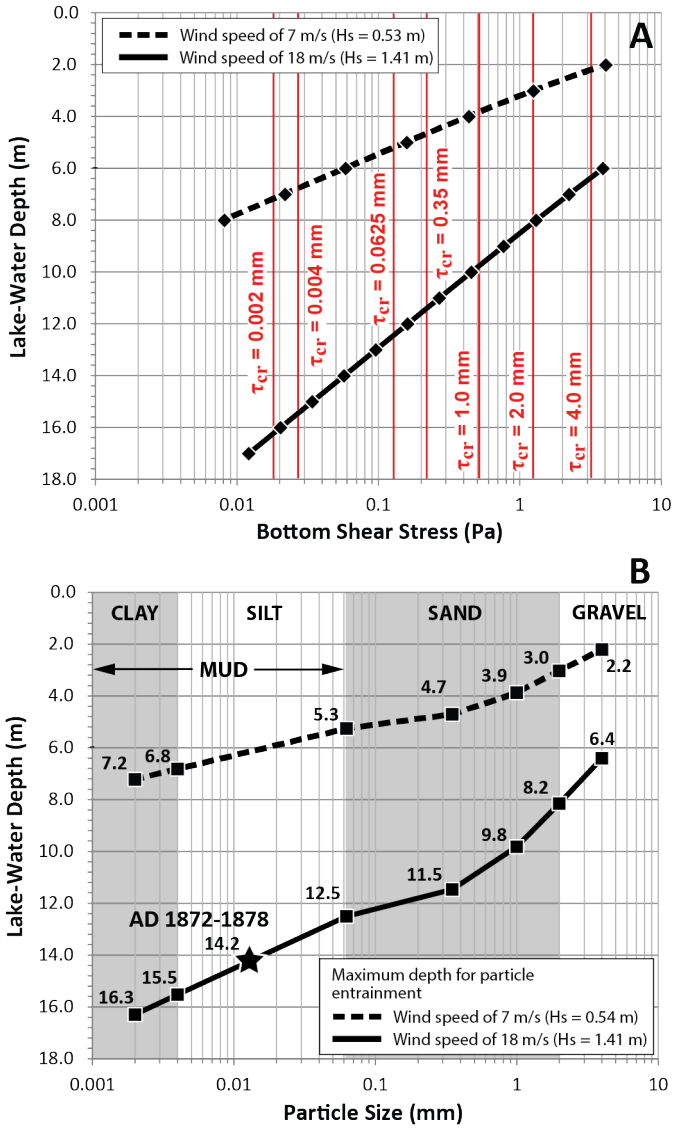

Figure 10. Plots showing: (A) bottom shear stress at specific depths and critical shear stress (τ_{cr}) for bottom erosion of particles ranging from clay (0.002 mm) to very fine granule/fine pebble (4 mm), and (B) threshold lake-water depth to entrain the range of particle sizes. Average wind speeds associated with strong breeze (7 m/s) and whole gale (18 m/s) conditions, along with a maximum fetch length of ~17 km in AD 1872–1878 AD were used in the model to generate wind waves having significant wave heights (Hs) of 0.54 and 1.41 m, based on deterministic wind-wave and sediment entrainment modeling of deep water conditions (USACE, 1984; 2002). The observed lake-water depth of 14.2 m in AD 1872–1878 AD is shown with a star.

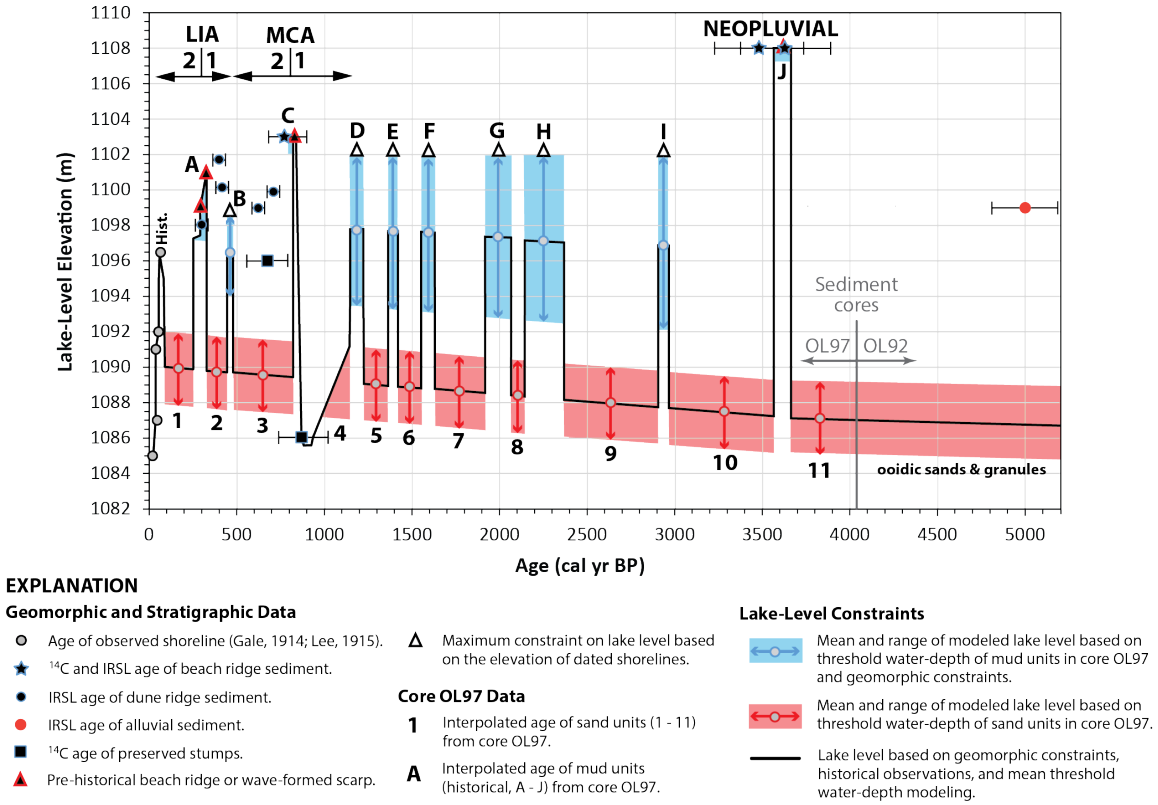

Figure 11. Integrated lake-level record of Owens Lake from a new age-depth model of core OL97 sediment and data from nearby core OL92, threshold lake-water depth analysis, and new numerical ages for the 1108, 1103, 1101, 1099 m shorelines, plus lowstands constrained to below 1096 and 1086 m. The age of mud (historical, A–J) and sand (1–11) units of core OL97 previously described by Smoot et al. (2000) are shown in relation to a range of potential lake levels based on threshold lake-water depth analysis of muddy and sandy/pebbly units driven by a wind speed 18 m/s. The elevation and age of numerical ages from ^{14}C and infrared stimulated luminescence dating, as well as elevation constraints for water levels based on cross-cutting relations with dated geomorphic features are shown. The periods of the early (1) and late (2) Medieval Climate Anomaly (MCA) and Little Ice Age (LIA), as well as the Neopluvial (or Neoglacial) are shown in relation to the lake-level record.

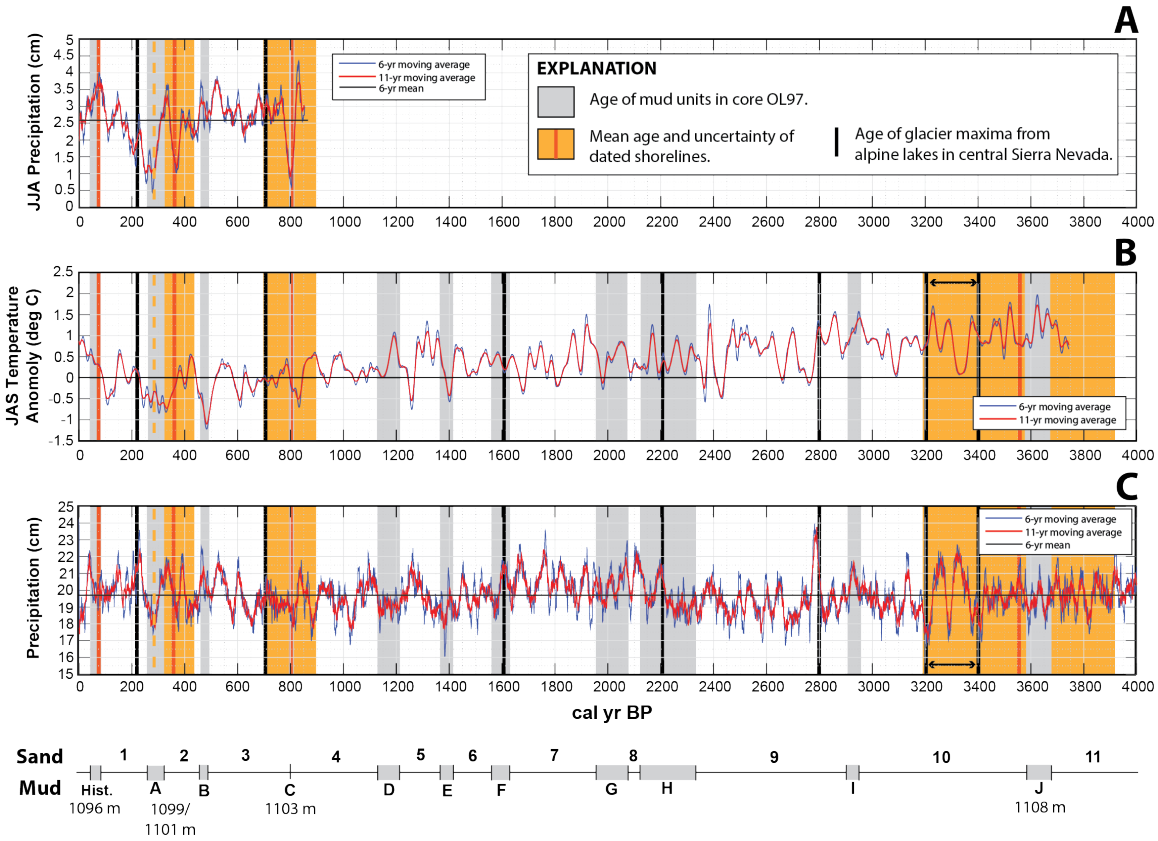

Figure 12. Comparison of mud (Historical, A–J) and sand (1–11) unit ages from reevaluation of core OL97 data previously described by Smoot et al. (2000), plus the ages of shorelines at 1096, 1099, 1101, 1103, and 1108 m of this study with the White Mountain bristlecone pine tree-ring records: (A) precipitation reconstruction based on $\delta^{13}C$ during the past 850 yr (Bale et al, 2011); (B) temperature reconstruction during the past 3750 yr (Salzer et al., 2014); and (C) precipitation reconstruction during the past 4000 yr (Hughes and Graumlich, 1996). The timing of glacier maxima from alpine lake-core proxy evidence is also shown (Konrad and Clark, 1998; Bowerman and Clark, 2011).

Table 1. Radiocarbon dating results and calibrations.

Site	Landform (soil/deposit)	Latitude (°N)	Longitude (°W)	Elevation[a] (m)	Material dated	Lab number[b]	Date[c] (^{14}C yr BP)	Calendar age[d] (cal yr BP)	Median probability[e] (cal yr BP)
Ash Creek	Distal alluvial fan (buried soil)	36.381	-118.011	1096.0	Carbonized wood	LDGO1719B	720 ± 70	770–550 (99.2%) 780–775 (0.8%)	670
Carrol Creek	Beach ridge (beach rock)	36.484	-118.027	1102.5	Charcoal	CAMS99099	870 ± 40	830–700 (75.7%) 910–850 (24.3%)	780
Brine Pool	Playa (near spring mound)	36.474	-117.926	1086.0[f]	Carbonized wood	CAMS16621	990 ± 60	1000–760 (97.3%) 1050–1030 (2.7%)	890

[a]Elevation source: Ash Creek site from U.S. Geological Survey 10 m DEM; Carrol Creek site from Earthscope (2011) LiDAR DEM; Brine Pool site from 1 m DEM from Mihevc et al. (1997).
[b]CAM = Center for Accelerator Mass Spectrometry, Lawerence Livermore National Laboratory, Livermore, CA; LDGO = Lamont-Doherty Geological Observatory, Columbia University, Palisades, NY.
[c]Accelerator mass spectrometry (AMS) analysis was performed on samples.
[d]Radiocarbon date is calibrated at ±2σ using CALIB7.1 program (Stuiver and Reimer, 1993) with the IntCal13 data set (Reimer et al., 2013); percent probability is shown for each age range.
[e]Median probability of the calibrated age falling within the reported range as calculated by CALIB7.1 program.
[f]Elevation adjusted ~1 m to account for subsidence from the AD 1872 earthquake.

Table 2. Results of single-grain post-IR IRSL dating of fine sand in Owens Lake basin.

Site	Landform	Latitude (°N)	Longitude (°W)	Elevation[a] (m)	Field number	Depth (m)	IR_{50} age[b,c] (years)	1 σ[c] uncertainty	PIR-IR_{225} age[b] (years)	1 σ uncertainty
Swansea	Beach ridge	36.533	-117.916	1108.7	KD12-01	0.46	3490	± 260	3690	± 260
Swansea	Beach ridge	36.533	-117.916	1108.7	KD12-02	0.46	3620	± 260	3620	± 270
Borehole-1	Dune	36.542	-117.938	1098.6	KD12-08	0.75	300	± 20	1000	± 150
Borehole-1	Alluvial fan	36.542	-117.938	1098.6	KD12-10	2.00	5000	± 210	7870	± 360
Borehole-2	Dune	36.543	-117.939	1102.7	KD12-12	0.87	400	± 30	500	± 150
Borehole-2	Dune	36.543	-117.939	1102.7	KD12-14	2.00	420	± 30	580	± 150
Borehole-2	Dune	36.543	-117.939	1102.7	KD12-16	3.00	710	± 40	600	± 150
Borehole-2	Dune	36.543	-117.939	1102.7	KD12-17	3.73	620	± 30	620	± 150

[a]Elevation of surface of sample site. Elevation surveyed with GPS with real-time differential correction with 10-30 cm vertical accuracy.

[b]Ages are presented as years before AD 2012.

[c]IR_{50} ages are considered the representative age of sediment in the northeast sector of Owens Lake basin.

Table 3. Interpolated ages for sand and mud units in sediment core OL97, reconstructed lake-level elevations based on threshold lake-water depth modeling of core OL97 sedimentology, and elevation and ages of shorelines in Owens Lake basin.

Sediment core unit[a]	Depth (m)	Thickness (m)	Duration[b] (yr)	Interpolated mud unit age[c] (cal yr BP)	Consolidation (m)	Maximum subsidence (m)	Minimum mean lake-level elevation (mud)[d] (m)	Maximum mean lake-level elevation (sand)[d] (m)	Geomorphic shoreline elevation (m)	Model lake-level elevation (m)	Age of shoreline / lake-level constraint
mud (hist.)	0.85	0.04	34	70	0.000	0.03	1096.2	–	1096.4[e]	–	78[g]
sand 1	1.06	0.21	188	258	0.004	0.11		1090.1	–	1090.1 ± 2.0	–
mud A	1.15	0.09	71	328	0.002	0.15	1096.0	–	1099, 1101	–	360 ± 80[h]
sand 2	1.31	0.16	127	455	0.004	0.21		1089.9	<1099[f]	1089.9 ± 2.0	410 ± 40[h]
mud B	1.35	0.04	32	486	0.001	0.22	1095.9	–	<1099[f]	1096.5 ± 2.6	–
sand 3	1.73	0.38	305	791	0.016	0.37		1089.7	<1096[f]	1089.7 ± 2.0	670 +110/-120[g]; 670 ± 80[h]
mud C	1.75	0.02	16	807	0.001	0.38	1095.6	–	1103	–	780 +80/-130[g]
sand 4	2.16	0.41	332	1139	0.022	0.53		1089.4	1086[f]	–	890 +160/-130[g]
mud D	2.25	0.09	73	1212	0.005	0.57	1095.3	–	<1102[f]	1097.7 ± 4.4	–
sand 5	2.44	0.19	155	1367	0.011	0.64		1089.2	–	1089.2 ± 2.0	–
mud E	2.50	0.06	49	1416	0.004	0.66	1095.2	–	<1102[f]	1097.6 ± 4.4	–
sand 6	2.67	0.17	139	1555	0.011	0.73		1089.1	–	1089.1 ± 2.0	–
mud F	2.75	0.08	66	1621	0.005	0.76	1095.0	–	<1102[f]	1097.6 ± 4.4	–
sand 7	3.15	0.40	330	1951	0.029	0.91		1088.8	–	1088.8 ± 2.0	–
mud G	3.30	0.15	124	2075	0.011	0.97	1094.7	–	<1102[f]	1097.4 ± 4.7	–
sand 8	3.37	0.07	58	2133	0.005	1.00		1088.6	–	1088.6 ± 2.0	–
mud H	3.65	0.28	233	2366	0.022	1.11	1094.5	–	<1102[f]	1097.3 ± 4.8	–
sand 9	4.29	0.64	536	2901	0.057	1.35		1088.1	–	1088.1 ± 2.0	–
mud I	4.35	0.06	50	2952	0.005	1.37	1094.0	–	<1102[f]	1097.0 ± 5.0	–
sand 10	5.08	0.73	616	3568	0.071	1.65		1087.6	–	1087.6 ± 2.0	–
mud J	5.20	0.12	101	3669	0.012	1.70	1093.5	–	1108	–	3560 ± 370[h]
sand 11	5.64	0.44	373	4042	0.045	1.87	–	1087.3	–	1087.3 ± 2.0	–

[d]Mean lake-level elevations have an uncertainty of ± 2.0 m.

[g]Radiocarbon age cal yr BP (Table 1).

[h]IRSL age years (Table 2).

Table 4. Comparison of the age of sand and mud units in sediment core OL97 to dated shorelines in Owens and Mono Lakes and paleoclimatic proxy data from tree-ring and glacial records in the Owens River watershed.

Lake-level records					Paleoclimatic proxy records					
	Owens Lake			Mono Lake	Tree-ring records from south-eastern Sierra Nevada		Tree-ring records from White Mountains			Central Sierra Nevada
Sediment core unit[a]	Mean age of core unit[a]	Lake-level elevation	Age of lake level	Age of lake level[g]	Cold/warm intervals[h]	Temperature anamoly[i]	Temperature anamoly[j]	Precipitaton[k]	δ^{13}C Precipitaton[l]	Glacier maxima from alpine lakes[m]
	(cal yr BP)	(m)	(cal yr BP)	(cal yr BP)	(cal yr BP)	(°C)	(°C)	(% normal)	(% normal)	(cal yr BP)
mud (hist.)	50 ± 20	1096.4[b]	78[e]	60 ± 30[1]	–	–	0.46 ± 0.22	104 ± 9	125 ± 20	–
sand 1	160 ± 90	1090.1 ± 2.0[c]	–	190 ± 100[2]	~140[3]	0.1 ± 1.32	-0.04 ± 0.71	103 ± 17	95 ± 60	210 ± 40
mud A	290 ± 40	1099, 1101[d]	360 ± 80[f]	340 ± 40[1]	–		-0.52 ± 0.40	98 ± 11	70 ± 45	–
sand 2	390 ± 60	1089.9 ± 2.0[c]	410 ± 40[f]	420 ± 40[2]	~340[3]	0.2 ± 1.46	-0.08 ± 0.64	100 ± 12	90 ± 50	–
mud B	470 ± 20	1096.5 ± 2.6[c]	–	510 ± 40[1]	500 ± 120[3]	–	-0.73 ± 0.37	105 ± 9	120 ± 25	–
sand 3	640 ± 150	<1096[d]	670 +110/-120[e]; 670 ± 80[f]	580 ± 30[2] 770 ± 90[2]	660 ± 110[3]	1.03 ± 0.15	-0.06 ± 0.52	99 ± 14	110 ± 40	~700
mud C	800 ± 10	1103[d]	780 +80/-130[d]	~870[1]	–	–	-0.04 ± 0.37	95 ± 6	60 ± 40	–
sand 4	970 ± 170	1086[d]	890 +160/-130[d]	1060 ± 190[2]	910 ± 150[4]	-1.12	0.15 ± 0.47	99 ± 14	–	–
mud D	1180 ± 40	1097.7 ± 4.4[c]	–	–	1170 ± 50[4]	-1.23	0.46 ± 0.62	96 ± 6	–	–
sand 5	1290 ± 80	1089.2 ± 2.0[c]	–	–	–	–	0.46 ± 0.89	100 ± 14	–	–
mud E	1390 ± 20	1097.6 ± 4.4[c]	–	~1370[1]	–	-1.95	-0.07 ± 0.62	96 ± 13	–	–
sand 6	1490 ± 70	1089.1 ± 2.0[c]	–	–	1480 ± 200[3]	–	0.40 ± 0.40	99 ± 10	–	–
mud F	1590 ± 30	1097.6 ± 4.4[c]	–	~1670[1]	–	1.45	0.37 ± 0.25	102 ± 9	–	~1600
sand 7	1790 ± 170	1088.8 ± 2.0[c]	–	~1810[2]	–	-1.60	0.41 ± 1.10	104 ± 16	–	–
mud G	2010 ± 60	1097.4 ± 4.7[c]	–	–	–	–	0.49 ± 0.37	103 ± 13	–	–
sand 8	2100 ± 30	1088.6 ± 2.0[c]	–	–	–	–	0.23 ± 0.23	106 ± 10	–	–
mud H	2250 ± 120	1097.3 ± 4.8[c]	–	–	–	–	0.45 ± 0.81	99 ± 13	–	~2200
sand 9	2630 ± 270	1088.1 ± 2.0[c]	–	–	2680 ± 100[3]	–	0.65 ± 1.10	98 ± 23	–	~2800
mud I	2930 ± 30	1097.0 ± 5.0[c]	–	–	–	–	1.10 ± 0.47	103 ± 7	–	–
sand 10	3260 ± 310	1087.6 ± 2.0[c]	–	–	–	–	0.89 ± 0.91	99 ± 16	–	3300 ± 100
mud J	3620 ± 50	1108[d]	3560 ± 370[f]	3770 ± 120[1]	3580 ± 100[4]	–	1.20 ± 0.77	98 ± 11	–	–
sand 11	3860 ± 190	1087.3 ± 2.0[c]	–	–	–	–	1.02 ± 0.41	101 ± 16	–	–

[a]Sedimentary units in cores OL97 previosly described by Smoot et al. (2000) with new age-depth model of this study (Table 3).
[b]Maximum lake level measured during AD 1872–1878 (Gale, 1914).
[c]Modeled-level based on threshold lake-water depth modeling (Table 3).
[d]Lake-level constraint based on geomorphic or stratigraphic relations.
[e]Radiocarbon age cal yr BP (Table 1).
[f]IRSL age years (Table 2).
[g]Stine (1990, 1994); [1]highstand; [2]lowstand.
[h]Scuderi (1987a,b); [3]cold and [4]warm intervals inferred from changes in timberline.
[i]Scuderi (1993); extreme temperature anomoly for 20-yr moving means.
[j]Salzer et al. (2014); [k]Hughes and Graumlich (1996); [l]Bale et al. (2011); [m]Bowerman and Clark (2011).

10. REFERENCES

Adams, K.D., 2007. Late Holocene sedimentary environments and lake-level fluctuations at Walker Lake, Nevada USA. *Geological Society of America Bulletin* 119, 126–139.

Adams, K.D., Negrini, R.M., Cook, E.R., Rajagopal, S., 2015. Annually resolved late Holocene paleohydrology of the southern Sierra Nevada and Tulare Lake, California. *Water Resources Research,* DOI 10.1002/2015WR017850.

Bacon, S.N., and Pezzopane, S.K., 2007. A 25,000-year record of earthquakes on the Owens Valley fault near Lone Pine, California: Implications for recurrence intervals, slip rates, and segmentation models. *Geological Society of America Bulletin* 119/7, 823–847.

Bacon, S.N., Burke, R.M., Pezzopane, S.K., Jayko, A.S., 2006. Last glacial maximum and Holocene lake levels of Owens Lake, eastern California, USA. *Quaternary Science Reviews* 25/11-12, 1264–1282.

Bacon, S.N., McDonald, E.V., Caldwell, T.G., Dalldorf, G.K., 2010. Timing and distribution of alluvial fan sedimentation in response to strengthening of late Holocene ENSO variability in the Sonoran Desert, southwestern Arizona, USA. *Quaternary Research* 73, 425-438.

Bacon, S.N., Lancaster, N., Stine, S., Rhodes, E.J., Holder, G.A.M., 2013. Refined late Holocene lake-level history of Owens Lake, east-central California. Geological Society of America Annual Meeting, Abstracts with Programs, 45 (7), 552.

Bale, R.J., Roberston, I., Salzer, M.W., Loader, J.J., Leavitt, S.W., Gagen, M., Harlan, T.P., McCarroll, D., 2011. An annually resolved bristlecone pine carbon istope chronology for the last millennium. *Quaternary Research* 76, 22–29.

Bartov, Y., Enzel, Y., Porat, N., Stein, M., 2007. Evolution of the late Pleistocene-Holocene Dead Sea Basin from sequence stratigraphy of fan deltas and lake-level reconstruction. *Journal of Sedimentary Research* 77, 680–692.

Barth, C., Boyle, D.P., Hatchett, B.J., Bassett, S.D., Garner, C.B., Adams, K.D., 2016. Late Pleistocene climate inferences from a water balance model of Jakes Valley, Nevada (USA). *Journal of Paleolimnology*, DOI 10.1007/s10933-016-9897-z.

Bartlein, P.J., Harrison, S.P., Brewer, S., Connor, S., Davis, B.A.S., Gajewski, K., Guiot, J., Harrison-Prentice, T.A., Henderson, A., Peyron, O., Prentice, I.C., Scholze, M., Seppa, H., Shuman, B., Sugita, S., Thompson, R.S., Viau, A.E., Williams, J., Wu, H., 2010. Pollen-based continental climate reconstructions at 6 and 21 ka: a global synthesis. *Climate Dynamics*, DOI: 10.1007/s00382-010-0904-1.

Beanland, S., and Clark, M.M., 1994. The Owens Valley fault zone, eastern California, and surface rupture associated with the 1872 earthquake. U.S. Geological Survey Bulletin 1982, 29 p.

Belmecheri, S., Babst, F., Wahl, E.R., Stahle, D.W., and Trouet, V., 2015. Multi-century evaluation of Sierra Nevada snowpack. *Nature Climate Change* 6(2–3), doi:10.1038/nclimate2809.

Benson, L., 2004. Western Lakes. In: Gillespie, A.R., Porter, S.C., Atwater, B.F. (Eds.), The Quaternary Period in the United States. Elsevier, New York, pp. 185–204.

Benson, L.V., Burdett, J.W., Kashgarian, M., Lund, S.P., Phillips, F.M., Rye, R.O., 1996. Climatic and hydrologic oscillations in the Owens Lake basin and the adjacent Sierra Nevada, California. *Science* 274, 746–749.

Benson, L., Burdett, J., Lund, S., Kashgarian, M., Mensing, S., 1997. Nearly synchronous climate change in the Northern Hemisphere during the last glacial termination. *Nature* 388, 263–265.

Benson, L., Kashgarian, M., Rye, R., Lund, S., Paillet, F., Smoot, J., Kester, C., Mensing, S., Meko, D., Lindstrom, S., 2002. Holocene multidecadal and multicentennial droughts affecting northern California and Nevada. *Quaternary Science Reviews* 21, 659–682.

Berkelhammer, M., Stott, L.D. 2008. Recent and dramatic changes in Pacific storm trajectories recorded in $\delta^{18}O$ from bristlecone pine tree ring cellulose. *Geochemistry, Geophysics, Geosystems* 9, Q04008.

Birkeland, P.W., 1999. Soils and Geomorphology, 3rd ed., Oxford Univ. Press, New York, p. 372 p.

Bowerman, N.D., and Clark, D.H., 2011. Holocene glaciation of the central Sierra Nevada, California. *Quaternary Science Reviews* 30, 1067–1058.

Bull, W.B., 1991. Geomorphic Response to Climate Change. Oxford University Press, New York, 326 p.

Buyalert, J., Thiel, C., Murray, A.S., Vendenberghe, D.A.G., Yi, S., Lu, H., 2011. IRSL and post-IR IRSL residual doses recorded in modern dust samples from the Chinese loess plateau. *Geochronometria* 38, 432–440.

Carver, G.A., 1970. Quaternary tectonism and surface faulting in Owens Lake basin, California. Technical Report AT2, MacKay School of Mines, University of Nevada, Reno, 103 p.

Chen, Y., Sheng-Hua, L., Li, B., 2013. Residual doses and sensitivity change of post IR IRSL signals from potassium feldspar under different bleaching conditions. *Geochronometria* 40, 229–238.

Cook E.R., Meko, D.M., Stahle, D.W., Cleaveland, M.K., 1999. Drought reconstructions for the continental United States. *Journal of Climate* 12, 1145–1162.

Cook, E.R., Woodhouse, C., Eakin, C.M., Meko, D.M., and Stahle, D.W., 2004. Long-term aridity changes in the western United States. *Science* 306, 1015–1018.

Cook, E.R., Seager, R., Heim, Jr. R.R., Vose, R.S., Herweijer, C., Woodhouse, C., 2010. Megadrought in North America: placing the IPCC projections of hydroclimate change in a long-term paleoclimate context. *Journal of Quaternary Science* 25, 48–61.

Cook, B.I., Seager, R., Miller, R.L., 2011. On the causes and dynamics of the Early Twentieth-Century North American Pluvial. *Journal of Climate* 24, 5043–5060.

Dana, G.L., and Lenz, P.H., 1986. Effects of increasing salinity on an *Artemia* population from Mono Lake, California. *Oecologia* 68, 428–436.

Davidson, G.R., Carnley, M., Lange, T., Galicki, S.J., Douglas, A., 2004. Changes in sediment accumulation rate in oxbow lake following late 9th century clearing of land for agricultural use: A ^{210}Pb, ^{137}Ce, and ^{14}C study in Mississippi, USA. *Radiocarbon* 46, 755–764.

Davis, O.K., 1999. Pollen analysis of a late-glacial and Holocene sediment core from Mono Lake, Mono County, California. *Quaternary Research* 52, 243–249.

Dettinger, M.D., Ghil, M., and Keppenne, C.L., 1995. Interannual and interdecadal variability of United States surface-air temperatures, 1910–1987. *Climate Change* 31, 35–66.

Dettinger, M.D., Cayan, D.R., Diaz, H.F., Meko, D.M., 1998. North-south precipitation patterns in western North America on interannual-to-decadel timescales. Journal of Climate 11, 3095–3111.

Dolan, J.F., McAuliffe, L.J., Rhodes, E.J., McGill, S.F., Zinke, R., 2016. Extreme multi-millennial slip rate variations on the Garlock fault, California: Strain super-cycles, potentially time-variable fault strength, and implications for system-level earthquake occurrence. *Earth and Planetary Science Letters* 446, 123–136.

EarthScope, 2011. Owens Valley fault zone LiDAR Survey, Plate Boundary Observatory operated by UNAVCO for EarthScope (http://www.earthscope.org).

Ehlers, E.G., and Blatt, H., 1982. Petrology: Igneous, Sedimentary, and Metamorphic. W.H Freeman and Company, New York, 732 p.

Einsele, G., 2000. Sedimentary Basins: Evolution, Facies, and Sediment Budget, second ed. Springer, New York, NY 804 p.

Fagherazzi, S., and Wiberg, P.L., 2009. Importance of wind conditions, fetch, and water levels on wave-generated shear stresses in shallow intertidal basins. *Journal of Geophysical Research* 114, F03022.

Friedman, I., Bischoff, J.L., Johnson, A., Tyler, S.W., Fitts, J.P., 1997. Movement and diffusion of pore fluids in Owens Lake sediment: An 800-k.y. record of saline/fresh cycles in core OL-92. In: Smith, G.I., Bischoff, J.L. (Eds.), An 800,000-year Paleoclimatic Record from Core OL-92, Owens Lake, Southeast California. Geological Society of America Special Paper 317, pp. 49–66.

Gale, H.S., 1914. Salines in the Owens, Searles, and Panamint basins, southeastern California. U.S. Geology Survey Bulletin 580-L, pp. 251–323.

Gillespie, A.R., and Clark, D.H., 2011. Glaciations of the Sierra Nevada, California, USA. Developments in Quaternary Science 15, 447–462. 10.1016/B978-0-444-53447-7.00034-9.

Graham, N.E., Hughes, M.K., 2007. Reconstructing the medieval low stands of Mono Lake, Sierra Nevada, California, USA. *Holocene* 17, 1197–1210.

Haddon, E.K., Amos, C.B., Zielke, O., Jayko, A.S., Bürgmann, R., 2016. Surface slip during large Owens Valley earthquakes, *Geochem. Geophys. Geosyst.,* 17, 2239–2269, doi:10.1002/2015GC006033.

Håkanson, L., 1977. The influence of wind, fetch, and water depth on the distribution of sediments in Lake Väern, Sweden. *Canadian Journal of Earth Sciences* 14, 397–412.

Håkanson, L., and Jansson, M., 2002. Principles of Lake Sedimentology, The Blackburn Press, New Jersey, 316 p.

Handy, R.L., and Spangler, M.G., 2007. Geotechnical Engineering: soil and foundation principles and practice, 5th ed. McGraw-Hill, New York, NY, 904 p.

Harpold, A.A., Dettinger, M., and Rajagopal, S. 2017. Defining snow drought and why it matters. *Eos*, 98, doi:10.1029/2017EO068775.

Hatchett, B.J., Boyle, D.P., Putnam, A.E., Bassett, S.D., 2015. Placing the 2012-2015 California-Nevada drought into a paleoclimatic context: Insights from Walker Lake, California-Nevada, USA. *Geophysical Research Letters* 42, doi:10.1002/2015GL065841.

Hatchett, B.J., Boyle, D.P., Garner, C.B., Kaplan, M.L., Putnam, A.E., Bassett, S., 2016. Magnitude and frequency of wet years under a megadrought climate in the western Great Basin, USA, *Quaternary Science Reviews* 152, 197-202.

Hatchett, B.J., Boyle, D.P., Garner, C.B., Kaplan, M.L., Bassett, S.D., Putnam, A.E., 2018. Sensitivity of a western Great Basin terminal lake to winter northeast Pacific storm track activity and moisture transport. In Starratt, S.W., and Rosen, M.R., (Eds.), From Saline to Freshwater: The Diversity of Western Lakes in Space and Time: Geological Society of America Special Paper 536, in press, doi.org/10.1130/2018.2536(XX).

Hatchett, B.J., and McEvoy, D.J., 2018. Exploring the origins of snow droughts in the northern Sierra Nevada, California. *American Meteorological Society*, doi:10.1175/EI-D-17-0027.1, in press.

Herbst, D.B., and Prather, M., 2014. Owens Lake – from dustbowl to mosaic of salt water habitats. *Lakeline* 34, 34–38.

Hollett, K.J., Danskin, W.R., McCafferey, W.F., Walti, C.L., 1991. Geology and water resources of Owens Valley, California. U.S. Geological Survey Water-Supply Paper 2370-B, 77 p.

Howat, I.M., and Tulaczyk, S., 2005. Trends in spring snowpack over a half-century of climate warming in California, USA. *Annals of Glaciology* 40, 151–156.

Hughes, M.K., and Graumlich, L.J., 1996. Multimillennial dendroclimatic studies from the western United States. In: Bradley, R.S., Jones, P.D., and Jouzel, J. (eds.), Climatic variations and forcing mechanisms of the last 2000 years. Berlin: Springer Verlag, pp. 109–124.

Hughes, M.K., Funkhouser, G., and Ni, F., 2002. The ancient bristlecone pines of Methuselah Walk, California, as a natural archive of past environment. *PAGES News* 10, 16–17.

Jayko, A.S., 2009. Surficial geologic map of the Darwin Hills 30' x 60' quadrangle, Inyo County, California: U.S. Geological Survey Scientific Investigations Map 3040, 20 p. pamphlet, 2 plates, scale 1:100,000.

Jayko, A.S. and Bacon, S.N., 2008. Late Quaternary MIS 6-8 shoreline features of pluvial Owens Lake, Owens Valley, eastern California. In: Reheis, M.C., Hershler, R., and Miller, D.M., (Eds.), Late Cenozoic Drainage History of the Southwestern Great Basin and Lower Colorado River Region: Geologic and Biotic Perspectives: Geological Society of America Special Paper 439, pp. 185–206.

Kleppe, J.A., Brothers, D.S., Kent, G.M., Biondi, F., Jensen, S., Driscoll, N.W., 2011. Duration and severity of medieval drought in the Lake Tahoe basin. *Quaternary Science Reviews* 30, 3269–3279.

Konrad, S.K., and Clark, D.H., 1998. Evidence for and early Neoglacial glacier advance from rock glaciers and lake sediments in the Sierra Nevada, California, USA. *Arctic and Alpine Research* 30, 272–284.

Lancaster, N., and Bacon, S., 2012. Late Holocene stratigraphy and chronology of the Keeler Dunes area. Final Report Prepared by the Desert Research Institute for the Great Basin Unified Air Pollution Control District (November 13, 2012), 19 p.

Lancaster, N., and McCarley-Holder, G., 2013. Decadal-scale evolution of a small dune field: Keeler Dunes, California 1944–2010. *Geomorphology* 180–181, 281–291.

Lancaster, N., Baker, S., Bacon, S., McCarley-Holder, G., 2015. Owens Lake dune fields: Composition, sources of sand, and transport pathways. *Catena* 134, 41–49.

LaMarche, V.C. Jr. (1974). Paleoclimatic inferences from long tree-ring records. *Science* 183, 1043–1048.

Le Roux, J.P., 2010. Sediment entrainment under fully developed waves as a function of water depth, boundary layer thickness, bottom slope and roughness. *Sedimentary Geology* 223, 143–149.

Le, K., Lee, J., Owen, L.A., Finkel, R., 2007. Late Quaternary slip rates along the Sierra Nevada frontal fault zone, California: Evidence for slip partitioning across the western margin of the Eastern California shear zone/Basin and Range Province. *Geological Society of America Bulletin* 119, 240–256.

Lee, C.H., 1915. Report on hydrology of Owens Lake basin and the natural soda industry as affected by the Los Angeles Aqueduct diversion. Report written by City Hydraulic Engineer, Los Angeles, California.

Leavitt, S.W., 1994. Major wet interval in the White Mountains Medieval Warm Period evidenced in $\delta^{13}C$ of bristlecone pine tree rings. *Climatic Change* 26, 299–307.

Li, H., Bischoff, J.L., Ku, T., Lund, S.P., Stott, L.D., 2000. Climate variability in east-central California during the past 1000 years reflected by high-resolution geochemical and isotopic records from Owens Lake sediments. *Quaternary Research* 54, 187–197.

Li, B., Roberts, R.G., Jacobs, Z., 2013. On the dose dependency of the bleachable and non-bleachable components of IRSL from K-feldspar: Improved procedures for luminescence dating of Quaternary Sediments. *Quaternary Geology* 17, 1–13.

Lund, S.P., Newton, M.S., Hammond, D.E., Davis, O.K., Bradbury, J.P., 1993. Late Quaternary stratigraphy of Owens Lake, California. In: Benson, L.V., (Ed.), Proceedings on the Workshop "Ongoing Paleoclimatic Studies in the Northern Great Basin. U.S. Geological Survey Circular 1119, p. 47–52.

Marcott, S.A., Shakun, J.D., Clark, P.U., Mix, A.C., 2013. A reconstruction of regional and global temperature for the past 11,300 years. *Science* 339, 1198–1201.

Martin E.A. and Rice, C.A., 1981. Sampling and analyzing sediment cores for ^{210}Pb geochronology. U.S. Geological Survey, Open-File Report 81–983.

Matsubara, Y., and Howard, A.D., 2009. A spatially explicit model of runoff, evaporation, and lake extent: Application to modern and late Pleistocene lakes in the Great Basin region, western United States. *Water Resources Research* 45, W06425.

McDonald, E.V., McFadden, L.D., Wells, S.G., 2003. Regional response of alluvial fans to the Pleistocene-Holocene climatic transition, Mojave Desert, California: In Enzel, Y., Wells, S.G., Lancaster, N., (Eds.), Paleoenvironments and paleohydrology of the Mojave and southern Great Basin Deserts. Geological Society of America Special Paper 368, p. 189–205.

McFadden, L.D., Ritter, J.B., Wells, S.G., 1989. Use of multiparameter relative-age methods for age estimation and correlation of alluvial-fan surfaces on a desert piedmont, eastern Mojave Desert, California. *Quaternary Research* 32, 276–290.

McFadden, L.D., McDonald, E.V., Wells, S.G., Anderson, K., Quade, J., Forman, S.L., 1998. The vesicular layer and carbonate collars of desert soils and pavements: formation, age and relation to climate change. *Geomorphology* 24, 101–145.

Meko, D.M. and Woodhouse, C.A., 2011. Application of streamflow reconstruction to water resources management, *in* Dendroclimatology: Progress and Prospects (eds. M.K. Hughes, T.W. Swetnam, H.F. Diaz). Springer, pp. 231-261.

Mensing, S.A., 2001. Late-glacial and early Holocene vegetation and climate change near Owens Lake, eastern California. *Quaternary Research* 55, 57–65.

Mensing, S.A., Smith, J., Norman, K.B., Allen, M., 2008. Extended drought in the Great Basin of western North America in the last two millennia reconstructed from pollen records. *Quaternary International* 188, 79–89.

Mensing, S.A., Sharpe, S.E., Tunno, I., Sada, D.W., Thomas, J.M., Starratt, S., Smith, J., 2013. The Lake Holocene Dry Period: multiproxy evidence for an extended drought between 2800 and 1850 cal yr BP across the central Great Basin, USA. *Quaternary Science Reviews* 78, 266–282.

Mihevc, T.M., Cochran, G.F., Hall, M., 1997. Simulation of Owens Lake water levels. Report prepared by the Water Resources Center, Desert Research Institute for the Great Basin Unified Air Pollution Control District, June 1997, Publication No. 41155, 71 p.

Munroe, J.S., and Laabs, B.J., 2103. Temporal correspondence between pluvial lake highstands in the southwestern US and Heinrich Event 1. *Journal of Quaternary Science* 28, 49–58.

Nayar, K.G., Sharqawy, M.H., Banchik, L.D., Lienhard V., J.H., 2016. Thermophysical properties of seawater: A review and new correlations that include pressure dependence. *Desalination* 390, 1– 24. doi:10.1016/j.desal.2016.02.024.

Negrini, R.M., Wigand, P.E., Draucker, S., Gobalet, K., Gardner, J.K., Sutton, M.Q., Yohe, R.M., 2006. The Rambla highstand shoreline and the Holocene lake-level history of Tulare Lake, California, USA. *Quaternary Science Reviews* 25, 1599–1618.

Newton, M.S., 1991. Holocene stratigraphy and magnetostratigraphy of Owens and Mono Lakes, eastern California. Unpublished Ph.D. Thesis, University of Southern California, Los Angeles, 330 p.

Orme, A.R. and Orme, A.J., 2008. Late Pleistocene shorelines of Owens Lake, California, and their hydroclimatic and tectonic implication. In: Reheis, M.C., Hershler, R., and Miller, D.M., (Eds.), Late Cenozoic Drainage History of the Southwestern Great Basin and Lower Colorado River Region: Geologic and Biotic Perspectives: Geological Society of America Special Paper 439, p. 207–226.

Otvos, E.G., 2000. Beach ridges – definitions and significance. *Geomorphology* 32, 83–108.

Pagano, T., and Garen, D., 2005. A recent increase in western U.S. streamflow variability and persistence. *Journal of Hydrometeorology* 6, 173–179.

Peterson, F.F., 1981. Landforms of the Basin and Range province: defined for soil surveys. Nevada agriculture experiment station, University of Nevada, Reno, Technical Bulletin 28, 52 p.

Reardon, K.E., Moreno-Casas, P.A., Bombardelli, F.A., Schladow, S.G., 2016. Seasonal nearshore sediment resuspension and water clarity at Lake Tahoe. *Lake and Reservoir Management* 32, 132–145.

Redmond, K.T., and Koch, R.W., 1991. Surface climate and streamflow variability in the western United States and their relationship to large scale circulation indices. *Water Resources Research* 27, 2381–2399.

Reheis, M.C., Adams, K.D., Oviatt, C.G., Bacon, S.N., 2014. Pluvial lakes in the Great Basin of the western United States – A view from the outcrop. *Quaternary Science Reviews* 97, 33-57.

Reimer, P., Bard, E., Bayliss, A., Beck, J., Blackwell, P., Ramsey, C., Van der Plicht, J., 2013. IntCal13 and marine13 radiocarbon age calibration curves 0–50,000 years cal BP. *Radiocarbon* 55, 1869–1887.

Rhodes, E.J., 2015. Dating sediments using potassium feldspar single-grain IRSL: Initial methodological considerations: *Quaternary International* 362, 14–22.

Rohweder, J., Rogala, J.T., Johnson, B.L., Anderson, D., Clark, S., Chamberlin, F., Runyon, K., 2008. Application of wind fetch and wave models for habitat rehabilitation and enhancement projects. U.S. Geological Survey Open-File Report 2008–1200, 43 p.

Salzer, M.W., Bunn, A.G., Graham, N.E., Hughes, M.K., 2014. Five millennia of paleotemperature from tree-rings in the Great Basin, USA. *Climate Dynamics* 42, 1517–1526.

Scuderi, L.A., 1987a. Late Holocene upper timberline variation in the southern Sierra Nevada. *Nature* 325, 242–244.

Scuderi, L.A., 1987b. Glacier variations in the Sierra Nevada, California, as reflected to a 1200-year tree-ring chronology. *Quaternary Research* 27, 220–231.

Scuderi, L.A., 1993. A 2000-year tree ring record of annual temperatures in the Sierra Nevada Mountains. *Science* 259, 1433–1436.

Sharqawy, M.H., Lienhard, J.H., Zubair, S.M., 2010. Thermophysical properties of seawater: a review of existing correlations and data. *Desalination and Water Treatment* 16, 354–380. doi:10.5004/dwt.2010.1079.

Slemmons, D.B., Vittori, E., Jayko, A.S., Carver, G.A., Bacon, S.N., 2008. Quaternary fault and lineament map of Owens Valley, Inyo County, eastern California, 25 p., Geological Society of America Map and Chart 96.

Smith, G.I., 1997. Stratigraphy, lithologies, and sedimentary structures of Owens Lake core OL-92. In: Smith, G.I., Bischoff, J.L. (Eds.), An 800,000-year Paleoclimatic Record from Core OL-92, Owens Lake, Southeast California. Geological Society of America Special Paper 317, pp. 9–24.

Smith, G.I. and Pratt, W.P., 1957. Core logs from Owens, China, Searles, and Panamint Basins, California. US Geological Survey Bulletin 1045-A, 1–62.

Smith, G.I., Street-Perrott, F.A., 1983. Pluvial lakes of the western United States. In: Porter, S.C. (Ed.), The Late Pleistocene. Univ. Minn. Press, Minneapolis, pp. 190–212.

Smith, G.I., and Bischoff, J.L., 1997. Core OL-92 from Owens Lake: Project rationale, geologic setting, drilling procedures, and summary. In: Smith, G.I., Bischoff, J.L. (Eds.), An 800,000-year Paleoclimatic Record from Core OL-92, Owens Lake, Southeast California. Geological Society of America Special Paper 317, pp. 1–8.

Smith, G.I., Bischoff, J.L., Bradbury, J.P., 1997. Synthesis of the Paleoclimatic record from Owens Lake core OL-92. In: Smith, G.I., Bischoff, J.L. (Eds.), An 800,000-year Paleoclimatic Record from Core OL-92, Owens Lake, Southeast California. Geological Society of America Special Paper 317, pp. 143–160.

Smoot, J.P., Litwin, R.J., Bischoff, J.L., Lund, S.P., 2000. Sedimentary record of the 1872 earthquake and ‘‘Tsunami’’ at Owens Lake, southeast California. *Journal of Sedimentary Geology* 135, 241–254.

Solomina, O.N., Bradley, R.S., Jomelli, V., Geirsdottir, A., Kaufman, D.S., Koch, J., McKay, N.P., Masiokas, M., Miller, G., Nesje, A., Nicolussi, K., Owen, L.A., Putnam, A.E., Wanner, H., Wiles, G., Yang, B., 2016. Glacier fluctuations during the past 2000 years. *Quaternary Science Reviews* 149, 61–90.

Stine, S., 1990. Late Holocene fluctuations of Mono Lake, eastern California. *Paleogeography, Paleoclimatology, and Paleoecology* 78, 333–381.

Stine, S., 1994. Extreme and persistent drought in California and Patagonia during Medieval time. *Nature* 339, 546–549.

Stinson, M.C., 1977. Geology of the Keeler 15’ quadrangle, Inyo County, California, California Division of Mines and Geology Map Sheet 38, scale 1:62,500.

Stone, P., Dunne, G.C., Moore, J.G., Smith, G.I., 2000. Geologic map of the Lone Pine 15’ quadrangle, Inyo County, California, U.S. Geological Survey Scientific Investigations Map 2617, scale 1:64,000.

Stone, P., Dunne, G.C., Conrad, J.E., Swanson, B.J., Stevens, C.H., Valin, V.C., 2004. Geologic map of the Cerro Gordo Peak 7.5’ quadrangle, Inyo County, California, U.S. Geological Survey Scientific Investigations Map 2851, scale 1:24,000.

Street, J.H., Anderson, R.S., Paytan, A., 2012. An organic geochemical record of Sierra Nevada climate since the LGM from Swamp Lake Yosemite. *Quaternary Science Reviews* 40, 89–106.

Street, J.H., Anderson, R.S., Rosenbauer, R.J., Paytan, A., 2013. *n*-Alkane evidence for the onset of wetter conditions in the Sierra Nevada, California (USA) at the mid-Holocene transition, ~3.0 ka. *Quaternary Research* 79, 14–23.

Stuiver, M. and Reimer, P.J., 1993. Extended ^{14}C data base and revised CALIB 3.0 ^{14}C age calibration program. In Stuiver, M., Long, A. Kra, R.S., (Eds.), Calibration 1993. *Radiocarbon* 35, 215–230.

Stuiver, M., Reimer, P.J., and Reimer, R.W., 2017. CALIB 7.1 [WWW program] at http://calib.org, accessed 2017-2-21.

Tolwinski-Ward, S.E., Tingley, M.P., Evans, M.N., Hughes, M.K., Nychka, D.W. 2015. Probabilistic reconstructions of local temperature and soil moisture from tree-ring data with potentially time-varying climatic response. *Climate Dynamics* 44, 791–806.

Yu, Z., Dong, W., Jiang, P., 2015. Temperature and rainfall estimates for past 18000 years in Owens Valley, California with a coupled catchment-lake model. *Hydrology and Earth System Sciences* 12, 6505–6539.

U.S. Army Corps of Engineers, 1984. Shore Protection Manual, Volume 1. U.S. Army Engineer Waterways Experiment Station, Vicksburg, MS, U.S.A., 502 p. U.S. Army Corps of Engineers, 2002. Coastal Engineering Manual. Washington D.C., U.S. Corps of Engineers, Engineer Manual 1110-2-1100, Part II and III.

Vogel, R.M., Tsai, Y., and Limbrunner, J.F., 1998. The regional persistence and variability of annual streamflow in the United States. *Water Resources Research,* 34, 3445–3459.

Wentworth, C.K., 1922. A scale of grade and class terms for clastic sediments. *Journal of Geology* 30, 377–392.

Winkle, W.V., and Eaton, F.M., 1910. Quality of the surface waters of California. U.S. Geological Survey, Water-Supply Paper 237, 142 p.

Zhong, S., Li, J., Whiteman, C.D., Bian, X., Yao, W., 2008. Climatology of high wind events in the Owens Valley, California. *Monthly Weather Review* 136, 3536–3552.

CHAPTER 2

SPATIOTEMPORAL PATTERNS OF DISTRIBUTED SLIP IN SOUTHERN OWENS VALLEY INDICATED BY DEFORMATION OF LATE PLEISTOCENE SHORELINES, EASTERN CALIFORNIA

Steven N. Bacon[a†], Thomas F. Bullard[a], Amanda K. Keen-Zebert[a], Angela S. Jayko[b], and David L. Decker[a]

[a]Desert Research Institute, 2215 Raggio Parkway, Reno, Nevada 89512, USA
[b]U.S. Geological Survey, U.C. White Mountain Research Station, Bishop, California 93514, USA

Reproduced with permission from:
Bacon, S.N., Bullard, T.F., Keen-Zebert, A.K., Jayko, A.S., and Decker, D.L., 2019. Spatiotemporal patterns of distributed slip in southern Owens Valley indicated by deformation of late Pleistocene shorelines, eastern California. Geological Society of America Bulletin. doi.org/10.1130/B35247.1.

Copyright 2019 Geological Society of America.

ABSTRACT

High-resolution elevation surveys of deformed late Pleistocene shorelines and new luminescence dating provide improved constraints on spatiotemporal patterns of distributive slip between normal and strike-slip faulting in southern Owens Valley, eastern California. A complex array of five subparallel faults, including the normal Sierra Nevada frontal fault (SNFF) and the normal-oblique Owens Valley fault (OVF), collectively form an active pull-apart basin that has developed within a dextral transtensional shear zone. Spatiotemporal patterns of slip are constrained by post-IR-IRSL dating of a 40.0 ± 5.8 ka highstand beach ridge that is vertically faulted and tilted up to 9.8 ± 1.8 m and an undeformed suite of 11–16 ka beach ridges. The tectono-geomorphic record of deformed beach ridges and alluvial fans indicates that both normal and dextral faulting occurred between the period of ~16 and 40 ka, whereas dextral faulting has been the predominant style of slip since ~16 ka. A total extension rate of 0.7 ± 0.2 mm/yr resolved in the N72°E direction across all faults in Owens Lake basin is within error of geodetic estimates, suggesting extension has been constant during intervals of 10^1–10^4 yr. A new vertical slip rate of 0.13 ± 0.04 m/k.y. on the southern OVF from deformed 160 ± 32 ka shoreline features also suggests constant slip for intervals up to 10^5 yr when compared to paleoseismic vertical slip rates from the same fault segment. This record supports a deformation mechanism characterized by steady slip and long interseismic periods of 8–10 k.y. where the south-central OVF and SNFF form a parallel fault system.

1. INTRODUCTION

Owens Lake basin in southern Owens Valley, eastern California (Figure 1), has been the focus of numerous paleohydrologic studies because a robust record of climate change is preserved in lacustrine sediment and shoreline geomorphic features (e.g., Smith and Pratt, 1957; Smith and Street-Perrott, 1983; Smith and Bischoff, 1997; Bacon et al., 2006, 2018; Jayko and Bacon, 2008; Orme and Orme, 2008; Reheis et al., 2014). The late Pleistocene and Holocene geomorphic history and spatial extent of Owens Lake shorelines also have been studied to resolve tectonic deformation in the lake basin (Carver, 1970; Lubetkin and Clark, 1988; Beanland and Clark, 1994; Bacon and Pezzopane, 2007; Jayko and Bacon, 2008; Orme and Orme, 2008). The lake basin is crossed by a complex array of five primary faults that have formed a well-developed, pull-apart basin with a deep, rhombus-shaped depocenter area created by normal-oblique faulting (Carver, 1970; Slemmons et al., 2008) (Figures 1 and 2). The primary faults in the lake basin generally strike clockwise of local Sierra Nevada-North American plate motion vectors along the eastern margin of the Sierra Nevada microplate, and therefore display a releasing geometry that accommodates dextral oblique slip in a transtensional regime (Unruh et al., 2003) (Figure 1).

Ground-based trilateration networks have demonstrated that the deformation field within south-central Owens Valley is broadly distributed and complicated. Between certain stations, more strain is accumulating than could be determined by slip rates on known active faults (Savage and Lisowski, 1995) or by global positioning system (GPS) data (McCaffrey, 2005). Since these geodetic surveys were performed, slip rates on known faults in Owens Valley have been revised; and new faults in the Owens Lake

basin have been identified and characterized based on numerical age constraints, tectono-geomorphic and paleoseismologic studies, and geophysical surveys (Bacon et al., 2005; Kirby et al., 2006, 2008; Bacon and Pezzopane, 2007; Le et al., 2007; Jayko and Bacon, 2008; Slemmons et al., 2008; Amos et al., 2013a; Haddon et al., 2016). The geologic information on fault behavior, however, is incomplete on some of the primary faults, thereby the spatiotemporal patterns of both distributive slip in Owens Lake basin and slip partitioning in Owens Valley are poorly understood.

The primary goal of our investigation is to provide information to better understand how elastic strain accumulation is released through an array of closely spaced and overlapping faults along the eastern escarpment of the Sierra Nevada. In this study, we (1) performed new survey-controlled measurements of deformed shorelines in the lake basin; (2) obtained new numerical ages of a faulted and tilted highstand beach ridge; (3) applied a differential fault-block model to reconstruct absolute shoreline elevations to determine vertical slip and subsidence rates; and (4) estimated rates of extension in Owens Lake basin in order to evaluate long-term slip patterns in comparison with geodetic estimates. Our new data integrated with previous slip rate and paleoseismic records are also used to propose a model for south-central Owens Valley where normal and strike-slip faults appear to have long interseismic periods (8–10 k.y.) and constant slip rates. This is in contrast to other regions of the Basin and Range province outboard of the Sierra Nevada microplate and areas south of the Garlock fault where temporal clustering of earthquakes and transient patterns of slip have been more typical during the Holocene (e.g., Pérouse and Wernicke, 2016).

2. Geologic and Hydrologic Setting

The Owens Valley is a tectonic graben on the east side of the south-central Sierra Nevada that consists of steep alluvial fans and a broad axial meander belt of the Owens River that flows to the south and terminates in Owens Lake basin. The valley is bounded to the north and south by large volcanic centers including the Long Valley caldera and Coso volcanic field, respectively, as well as the smaller Big Pine volcanic field (BPVF) that includes late Pleistocene basaltic cinder cones and lava flows sourced mostly from range-front faults in the central part of the valley (Figure 1). Late Pleistocene to Holocene lacustrine landforms are preserved in the southern part of the valley, and glacial deposits occur throughout the upper elevations in the Sierra Nevada with lateral moraines extending to the valley floor as far south as the latitude of ~36.5°N (e.g., Moore and Moring, 2013) (Figure 1B).

Crests of the Sierra Nevada and White-Inyo Mountains rise more than 3000 m above Owens Valley and form one of the principal rain shadows in the western U.S. (Figure 1B). Owens Lake basin is relatively shallow because of high sedimentation rates from the Owens River and surrounding alluvial fans. Snowmelt from the Sierra Nevada accounts for most of the annual streamflow in the watershed (Hollet et al., 1991). Owens Lake occupies a topographically closed basin contained by a modern sill at an elevation of ~1145 m at the south end of the valley (Figure 2). The lake is currently a terminal playa resulting from historical stream diversions for water resources beginning in A.D 1913 (Gale, 1914).

During much of the late Pleistocene, Owens Lake was a perennial freshwater lake that periodically overflowed to the south through a well-developed overflow channel to

form a chain of pluvial lakes and simultaneously occupying one or more of the four successively lower-elevation lake basins (i.e., China, Searles, Panamint, and Death Valley) during pluvial periods with greater moisture flux across the region (Smith and Street-Perrott, 1983; Jayko and Bacon, 2008; Jayko et al., 2008; Phillips, 2008; Rosenthal et al., 2017) (Figure 1). Late Pleistocene shoreline and lake-core records indicate that Owens Lake had extreme lake-level fluctuations in response to hydroclimatic variability coinciding with glaciations and climate change in the Sierra Nevada. In addition, a record of shallow oscillating lake levels has been documented from stratigraphic studies of late Pleistocene and Holocene deposits (e.g., Benson et al., 1996, 1997, 2002; Smith and Bischoff, 1997; Li et al., 2000; Smoot et al., 2000; Bacon et al., 2006, 2018; Orme and Orme, 2008).

3. TECTONIC SETTING

The Owens Valley graben consists of several range-bounding fault zones, which include the normal Sierra Nevada frontal fault (SNFF) to the west, and the normal-oblique White Mountains (WMF) and Inyo Mountains (IMF) faults to the east, as wells as the active normal-oblique Owens Valley fault (OVF) along the axis of the valley (Figure 1). These faults collectively accommodate a portion of the ~20 to 25% of dextral shear inboard of the San Andreas plate boundary along a regional zone at the western edge of the extensional Basin and Range Province north of the Garlock fault (Argus and Gordon, 1991; Bennett et al., 1999; Wernicke et al., 2000; Oldow et al., 2001). This zone of dextral shear is locally accommodated by clockwise rotation of crustal blocks that has produced structural basins and oblique components of slip that are commonly partitioned

into subparallel strike-slip and dip-slip faults (Wesnousky and Jones, 1994; Wesnousky, 2005a,b). The regional zone north of the Garlock fault is sometimes termed the southern Walker Lane belt (WLB) or northern Eastern California shear zone (ECSZ) and consists of three major subparallel strike-slip fault systems: the Death Valley-Fish Lake Valley, Hunter Mountain-Panamint Valley, and Owens Valley-Little Lake fault zones (e.g., Dokka and Travis, 1990; Wesnousky, 2005a; Dixon and Xie, 2018) (Figure 1A). The spatiotemporal patterns of strike-slip faulting within the WLB were generally steady during the past ~75–150 k.y., whereas normal faulting along the northern and eastern margins of the Basin and Range has been distributed and transient (Pérouse and Wernicke, 2016). A recent change of greater seismic activity localized along north-south fault belts within the WLB and ECSZ, however, occurred during the Holocene and historical times indicating a recent trend of transient fault behavior in the form of temporal clustering of earthquakes (e.g., Rockwell et al., 2000; Dolan et al., 2007; Oskin et al., 2008; Ganev et al., 2010b; Pérouse and Wernicke, 2016).

Owens Valley is a region of active tectonics—as demonstrated by the M_w 7.5–7.9 Owens Valley earthquake in A.D. 1872, the third largest historical earthquake in California, that had a ~113–120 km surface rupture with an average dextral offset of 6.0 ± 2.0 m and 1.0 ± 0.5 m of normal slip (Beanland and Clark, 1994; Bacon and Pezzopane, 2007; Slemmon et al., 2008; Hough and Hutton, 2008; Haddon et al., 2016) (Figures 1 and 2). Tectonic-geomorphic studies and kinematic models indicate that normal-oblique shear is partitioned and distributed north of the OVF in northern Owens Valley along three primary zones including SNFF, Volcanic Tableland on the eastern flanks of the Long Valley caldera, and the WMF (Pinter, 1995; Reheis and Dixon, 1996;

Kirby et al., 2006; Lee et al., 2009; Phillips and Majkowski, 2011; Nagorsen-Rinke et al., 2013; Ferrill et al., 2016; Haddon et al., 2016) (Figure 1A). Regional fault maps and kinematic models in the south show a structural connection across the Coso volcanic field between the southern termination of the historical OVF rupture and the dextral Little Lake fault (LLF) in Indian Wells Valley (Peltzer et al., 2001; Unruh et al., 2002, 2003; Monastero et al., 2005; Frankel et al., 2008; Amos et al., 2013a, b) (Figure 1). The LLF has similar seismo-tectonic characteristics, tectonic geomorphology, and dextral slip rate compared to the OVF (e.g., Roquemore and Zellmer, 1983; Amos et al., 2013b), including the occurrence of historical surface rupture on short fault segments associated with A.D. 1982 M4.9 and A.D. 1995 M5.4 earthquakes (Roquemore and Zellmer, 1983; Hauksson et al., 1995). The complexity of the slip distribution within the LLF zone was demonstrated by the A.D. 2019 M7.1 Ridgecrest earthquake that produced a ~50 km long surface rupture along the eastern margin of Indian Wells Valley and into Searles Valley, which was not previously mapped as the primary fault in the valley (GEER, 2019) (Figure 1A).

Previous studies in Owens Valley have mainly focused on characterizing the seismic hazards on the OVF because of its historic large magnitude event. Dextral slip rates for the OVF vary from site to site along the entire fault length with values ranging from ~0.5 to 4.5 m/k.y. (Lubetkin and Clark, 1988; Beanland and Clark, 1994; Zehfuss et al., 2001; Lee et al., 2001; Bacon and Pezzopane, 2007; Kirby et al., 2008; Haddon et al., 2016). Ground- and space-based geodetic data across the region based on an elastic half-space models estimate dextral shear rates on the OVF of ~2.5 to 8.5 mm/yr (Savage and Lisowski, 1995; Thatcher et al., 1999; Dixon et al., 1995, 2000; Gan et al., 2000; Miller

et al., 2001; McClusky et al., 2001; Zeng and Shen, 2014). Alternatively, Dixon et al. (2003) calculated a lower GPS geodetic rate of 2.1 ± 0.7 mm/yr for the OVF based on an elastic-viscoelastic, half-space model. More recently, Jha (2010) calculated even lower rates of 1.1 ± 0.7 mm/yr from GPS data and block modeling that accounts for viscoelastic, postseismic relaxation effects following the A.D. 1872 earthquake. This geodetic slip rate is similar to the two-event paleoseismic slip rate of 1.0 ± 0.5 mm/yr on the southern OVF from fault trench investigations (Bacon and Pezzopane, 2007), as well as the geologic slip rate of 1.1 ± 0.5 mm/yr for the entire OVF based on analysis of high-resolution topographic data (Haddon et al., 2016). The sum of geologic dextral slip rates across the southern WLB at the latitude of south-central Owens Valley (~36.5°N) is similar to dextral shear measured by GPS in the region and shows that about ~1 mm/yr (~10%) of dextral slip is distributed on the OVF (Bacon and Pezzopane, 2007; Lee et al., 2009).

4. METHODS

4.1. Shoreline Geomorphology and Sedimentology

Documentation of deformed shoreline features in Owens Lake basin is based on field observations and mapping of lacustrine and alluvial geomorphology in relation to previously identified faults and new tectono-geomorphic features identified in this study. Landforms and map unit contacts were digitally created directly on georeferenced satellite imagery in a geographic information systems (GIS) platform. Lacustrine landforms were classified following the categorization schemes of Peterson (1981) and Otvos (2000). We made field descriptions of selected geologic exposures to establish lacustrine sequence stratigraphy and sedimentological characteristics. Lithofacies and

facies associations were classified in the field according to grain size, sedimentary structure, and as lateral and vertical stratigraphic position (e.g., Einsele, 2000).

4.1.1. Shoreline Elevation Control

Elevation control of shoreline features was determined with a Trimble GPS Pathfinder® ProXRT receiver with differential correction services. Measurements of elevation during surveying had a vertical accuracy of ±80 cm. Geomorphic features reported in previous studies were resurveyed to keep elevation data within the same georeferenced frame and to minimize the error associated with different surveying methods. Previous studies had elevation control based on either total-station surveys (Orme and Orme, 2008; Slemmons et al., 2008) or hand-held GPS units cross-checked with 1:24,000 topographic quadrangle maps and 10 m digital elevation models (DEMs) (Bacon et al., 2006; Jayko and Bacon, 2008).

4.1.2. Natural Variability of Shoreline Elevations

Natural variability in the height of constructional shorelines is a characteristic of beach ridges and other similar features that needs to be considered when using these types of landforms as piercing points to measure ground deformation in tectonically active lake basins. Detailed topographic surveys in the Lahontan Lake basin, Nevada have shown that the natural variability of beach ridges was within 2.5 m in elevation when spatially compared to shoreline features of the same lake level (Adams and Wesnousky, 1998). This range is slightly less for Owens Lake basin because its smaller area during highstands that produced less effective fetch conditions controlled by the

narrow physiography of Owens Valley compared to the larger and broader Lahontan Lake basin (e.g., Bacon et al., 2006). We determined that the natural variability of highstand constructional shorelines in Owens Valley is up to 2.0 m based on our GPS survey of one continuous beach ridge with a mean elevation of ~1166 m across a distance of ~1.75 km at the Centennial Flat study site (Figure 3). The surveyed beach ridge is in the southern lake basin and has a maximum fetch of ~70 km from north-northwest directed winds. The range in natural variability of beach ridges at lower elevations with shorter fetches is estimated to be on the order of ~1–2 m.

4.2. Luminescence Dating

We used infrared stimulated luminescence (IRSL) analysis to directly date shoreline sediments of a deformed beach ridge at the Centennial Flat study site in the southeastern sector of Owens Lake basin at elevations ranging from ~1156 to 1166 m (Figures 2 and 3). Three samples were collected in tubes driven horizontally into sand-rich deposits in natural exposures, ensuring no light exposure, and analyzed at the Desert Research Institute Luminescence Laboratory (DRILL). Dating was based on the post-IR-$IRSL_{225}$ single-grain luminescence dating method (e.g., Rhodes, 2015). This method has been used recently to date alluvial fan deposits in the northern Mojave Desert (Dolan et al., 2016) and eolian dune and beach ridge deposits in Owens Lake basin (Bacon et al., 2018) that lack quartz. The method enables more reliable accurate dating of feldspar grains with a precision equal in many cases to radiocarbon analysis of detrital charcoal – thereby allowing the dating of previously undateable strata and landforms (Rhodes, 2015). Coarse grained (220–300 μm) potassium feldspar was isolated by removing

carbonates, organics, magnetic sub-fractions, and mineral separation with lithium heterotungstate. The feldspar portion of the sample was then etched in hydrofluoric acid to remove the outer layer of the grains affected by irradiation from α particles, and the remaining sample was then sieved again to remove any grains that were reduced to <220 μm by etching.

4.2.1. Post-IR-IRSL Analysis

The total dose absorption (De) for all samples was measured on single grain aliquots of feldspar using a single aliquot regenerative-dose (SAR) technique (Murray and Wintle, 2000, 2003), modified for measuring a post-IR-IRSL signal from single grains of potassium feldspar using a 225°C measurement (e.g., Thomsen et al., 2008; Rhodes, 2015). An exponential function was used to fit regeneration curves. Routine screening criteria included rejection of aliquots that had net signals <3 standard deviations above background; natural signals that did not intersect saturating growth curves; failure to produce, within 20%, the same signal ratio from identical regeneration doses given at the beginning and end of the SAR sequence—suggesting inaccurate sensitivity correction (recycling test), a maximum test dose error of >20%, and maximum paleodose error of >30%. We measured at least 900 single grains for each sample. A minimum of 62 accepted De determinations were used in age modeling. The total equivalent dose or burial dose (Db) for each sample was modeled using the central age model (CAM) of Galbraith et al. (1999) that models the central tendency taking into account over-dispersion of the population and the error associated with each aliquot measurement.

Samples for dose rate (Dr) were dried and milled to a fine, flour consistency and sent to ALS Geochemistry in Reno, Nevada for geochemical analysis of U, Th, and K_2O. U and Th samples were fused with lithium borate and measured with ICP-MS. K_2O was measured on bulk sample with ICP-AES and converted to % K. Dose rates (Gy/ka) were calculated using the conversion factors of Liritzis et al. (2013) and are shown to two decimal places, and ages were calculated prior to rounding. A water content of 2 ± 1% (expressed as the percentage of the mass of dry sediment) was used for all samples, estimated for the burial lifetime based on the measured water content of samples. Internal K was estimated to be 10 ± 2 following Smedley et al., (2012). Central values are given for dose rates, and errors are incorporated into that given for the total dose rate. Cosmic dose rates (Gy/ka) were calculated according to Prescott and Hutton (1994). Dose rate and final age calculations were made using DRAC (Durcan et al., 2015). Ages are expressed as thousands of years before A.D. 2015 and are rounded to the nearest 10 years (Table 1).

5. Faults In Owens Lake Basin

We used a modified version of Slemmons et al. (2008) map to show the orientation and style of faulting associated with faults in Owens Lake basin (Figure 2). The following section includes general descriptions and fault mapping of the Keeler, Owens River-Centennial Flat, and Central Owens Lake faults. The Owens Valley, Sierra Nevada Frontal, southern Inyo Mountains, and Sage Flat faults have either published slip rate or recurrence information or both; these data are summarized and used in estimating the rates of extension, as well as establishing the distribution of slip across the lake basin.

5.1. Keeler Fault

The Keeler fault (KF) is a northwest striking fault with an orientation of about N20°W that parallels historical shorelines and the northeastern playa margin near Keeler, and roughly parallels the Owens River-Centennial Flat fault (OR-CFF) and OVF (Slemmons et al., 2008) (Figure 2). The KF was first described in detail from seismic reflection data as a southward branching flower structure within lacustrine sediments having east-side-down sense of slip with a dip of ~85°NE (Neponset Geophysical Company and Aquila Geosciences, Inc., 1997). Earlier aeromagnetic surveys in the lake basin also identified a structural feature with a similar strike in the same location of the KF, but that also extends to the north-northwest into Owens Valley with a change to valley-down sense of slip known as the IMF (Pakiser et al., 1964) (Figure 2).

New mapping on the playa surface in the area of the subsurface location of the KF shows the fault is expressed as a lineament defined by deflected stream channels and confined channels on the west side of the lineament, indicating relief on the playa surface and confirming an east-side-down sense of vertical slip (Figure 3). The southeast projection of the KF across the playa, and nearby beach terraces and alluvial plains also coincides with a change in shoreline geomorphology in the area of the southern end of the southern Inyo Mountains fault (SIMF). The location of the KF near the SIMF is defined by an abrupt change from constructional beach ridges at 1114–1131 m on the southwest to either a lack of corresponding shorelines or a prominent scarp of the SIMF (Figure 3). Locally, the range in elevation of the scarp face is similar to adjacent beach ridges at ~1127–1131 m, therefore we interpret the SIMF scarp to be a wave-modified fault scarp. Further to the southeast, the trace of the KF is at the base of a linear

escarpment within the Coso Range forming a left-step along strike. The location of the linear escarpment occurs near the lowest elevation of an eastward-tilted highstand beach ridge at an elevation of 1157.7 m (Figure 3).

5.2. Owens River and Centennial Flat Faults

The ORF and CFF form two segments of a single northwest-striking fault that closely parallels the OVF with an orientation of N30°W and a west-side-down sense of slip and dip of ~85°SW (Figure 2). The ORF segment projects across the floor of Owens Lake playa and northward toward the mouth of the Owens River and the IMF near Lone Pine, whereas the CFF segment extends southward across beach terraces and alluvial plains of the lake basin before projecting further south in the Coso Range (Slemmons et al., 2008) (Figure 2). The CFF is well-defined by linear drainage patterns and escarpments within the Coso Range (Jayko, 2009). The sense of normal-oblique slip on the ORF is indicated by surface fault mapping on the playa surface by Carver (1970) and subsurface information showing southward branching flower structures within lacustrine sediments from seismic reflection data across the playa (Neponset Geophysical Company and Aquila Geosciences, Inc., 1997). A component of recent dextral slip on the CFF also is confirmed by three fault plane solutions of pure strike-slip faulting on northwest striking nodal planes associated with the A.D. 2009 M4.7, M5.0, and M5.2 Olancha earthquake swarm that occurred on the CFF in Owens Lake basin (Holzer et al., 2010) (Figure 3).

5.3. Central Owens Lake Fault

The Central Owens Lake fault (COLF) is a zone of short and discontinuous fault segments with mostly northwest-side-down vertical slip that likely transfer slip between the OVF and OR-CFF, and as a result is not considered a primary fault in the lake basin (Slemmons et al., 2008) (Figure 2). The geometry of the COLF also suggests that it collectively accommodates subsidence during rupturing events on the OVF or OR-CFF because most fault segments coincide with the lowest elevations in the depocenter area of the lake basin (Carver, 1970). A southern branch of the COLF, however, forms a parallel and linear zone of poorly-defined distributed faults across mostly alluvial plains in the lake basin, as well as a well-defined narrow graben on the piedmont displacing late to middle Pleistocene fans on the northern Coso Range (Jayko, 2009) (Figure 2). This graben appears to be structurally connected to the southern end of the OVF where dextral shear in the area has formed large-scale plunging anticlinal forms within Coso Formation (~2 Ma) rocks and overlying early to middle Pleistocene alluvium (Frankel et al., 2008; Jayko, 2009) (Figure 2).

5.4. Owens Valley Fault

The southern segment of the OVF extends along the entire western margin of Owens Lake basin with a strike of N40°E and dip of 85°E (Figure 2). During the A.D. 1872 earthquake, normal-oblique displacements produced subsidence in the depocenter area of Owens Lake that created a seismic seiche, raised the western shoreline, and shifted the position of the eastern shoreline of the lake several hundred meters to the west (Smoot et al., 2000). A predominantly eastside-down vertical fault slip of 0.5–1.0 m and

decreasing dextral slip to the south of up to 2.0 m defined the deformation field along the southern end of the historical rupture (Slemmons et al., 2008; Haddon et al., 2016). There are no published slip rates on the OVF in the lake basin, but the Holocene vertical slip rate from tectonic geomorphology and paleoseismic trench data for the southern OVF near Lone Pine is 0.12 ± 0.04 m/k.y. and the interseismic periods between the three latest surface rupture events are on the order of 8–10 k.y. (Lubetkin and Clark, 1988; Bacon and Pezzopane, 2007).

5.5. Sierra Nevada Frontal Fault

The Olancha segment of the SNFF in Owens Lake basin strikes N4°E, dips ~75°NE, and includes discontinuous faults and lineaments (Slemmons et al., 2008; USGS, 2016) (Figures 1B and 2). In general, the SNFF scarps are poorly preserved because of erosion by high-gradient alluvial fans and highstand water levels of pluvial Owens Lake. The degree of SNFF activity, however, is indicated by a few well-defined and prominent fault scarps that occur as short segments on older alluvial surfaces near fan apexes, as well as steep-sided and linear bedrock escarpments with triangular facets along the range front. There are no published slip rates for the Olancha segment of the SNFF in the lake basin, but the long-term vertical slip rate for the nearby Independence segment of the SNFF in south-central Owens Valley is 0.25 ± 0.05 m/k.y. from offset and dated alluvial fans up to ~124 ka (Le et al., 2007). Paleoseismic data is also lacking for the SNFF in Owens Valley and lake basin, therefore recurrence for range-front faulting is poorly understood.

5.6. Southern Inyo Mountains Fault

The SIMF in Owens Lake basin strikes N45°E, dips 85°NE, and is well-defined along the range front of the Inyo Mountains where it exhibits mountain-side-down, oblique dextral offsets of Quaternary and Tertiary alluvial deposits east of Keeler (Stone et al., 2004; Jayko, 2009) (Figures 2 and 3). Latest Quaternary fault activity is indicated by compound fault scarps and normal-dextral oblique displacement from two surface rupture events since 13,100 ± 200 cal yr B.P. and a single-event dextral offset of 2.2 ± 0.8 m of an alluvial channel. Combining the age and offset results in an oblique slip rate of 0.1–0.3 m/k.y. (Bacon et al., 2005). A vertical slip rate for the SIMF from tectonic geomorphology and paleoseismology also can be estimated from Bacon et al. (2005). Surface rupture evidence of the most recent event includes well-preserved 0.65 ± 0.2 m depressions and single-event scarps—which, when combined with the minimum age of 10,840 ± 260 cal yr BP for the penultimate event in natural wash exposures, yield a vertical slip rate of 0.06 ± 0.02 m/k.y. The most recent event on the SIMF is considered to be latest Holocene in age because of the well-preserved and youthful scarps and depressions. The tectonic geomorphology and paleoseismology of the SIMF suggest an interseismic period of 8–10 k.y. between the most recent and penultimate events.

The mapped length of latest Quaternary faulting along the SIMF is at least 12 km. The southern extent of the mapped trace bifurcates to the south into mostly discontinuous lineaments that strike N10°W across alluvial fans (Figure 3). The apparent termination of the SIMF to the south is a complex of short and linear fault scarps that are mostly west-side-down and wave-modified near the intersection with the KF (Figure 3). To the northwest, segments of the fault zone in the lake basin have a curve linear map pattern

along the range front, whereas in the valley, the map pattern is left-stepping along linear and short sections of the range front (Figure 2). Given the northwesterly strike, mostly northeast dip, and location of faults on the margin of the lake basin, the SIMF is likely an independent seismogenic source that accommodates dextral shear in southeastern Owens Valley (Bacon and Pezzopane, 2007).

5.7. Sage Flat Fault

The Sage Flat fault (SFF) is a northerly striking fault in the Haiwee Reservoir area of southern Owens Lake basin (Jayko, 2009) (Figure 2). The fault is ~10 km long and locally forms a half graben that bounds the northern half of the overflow channel in the sill area of the lake basin. Tectono-geomorphic and paleoseismic trench data on the western SFF demonstrate that the main fault is east-side-down with a dip of ~75°NE, shows evidence for normal-dextral oblique slip, and has had late Quaternary activity—most recently a surface rupture event between 25.7 ± 1.7 and 30.1 ± 1.3 ka (Amos et al., 2013a). Displacement and geochronologic data from trench exposures provide an estimate of dip slip maximum rate of 0.09 ± 0.01 m/k.y. and evidence of a relatively long interseismic period of ~28 k.y. since the most recent event on the SFF (Amos et al., 2013a).

6. Deformed Shorelines In Owens Lake Basin

Measurements of deformed landform features commonly provide datums from which to estimate fault slip rate, fault activity, as well as the direction and amount of displacement on faults (e.g., McCalpin, 1996; Lettis and Kelson, 2000). Deformation of shorelines in Owens Lake basin is commonly expressed as fault offsets, short lengths of

monoclinal warping, and broad warping or uniform tilting (Carver, 1970). Two of the oldest and highest shorelines in Owens Valley are primarily erosional but include a few preserved constructional features that show progressive deformation. Elevations of the two shorelines referred to as the 1160 and 1180 m shorelines are lower on the east side of the lake basin at ~1155 and 1180 m and higher on the west side at ~1165 and 1200 m. Evidence of both shorelines is sparse along the western margin of the valley and lake basin at the base of the Sierra Nevada. We attribute the lack of shoreline evidence to erosion and burial from younger, late Pleistocene-Holocene alluvial fans and construction activities related to the Los Angeles Aqueduct system. In contrast, the 1160 and 1180 m shorelines are preserved as the erosional remnants of prominent, wave-formed scarps and platforms, and beach ridges on the eastern and southern margins of the lake basin and at the base of the Inyo Mountains.

The ~1180-m shoreline is constrained to an age of 160 ± 32 ka (Jayko and Bacon, 2008) and is discussed in the following section. The ~1160-m shoreline, however, lacks direct age control and a detailed analysis of its spatial extent. For these reasons, determining the age and extent of the ~1160-m shoreline is the primary focus of our study. We examined three sites to correlate, directly date, and measure the amount of deformation of the 1160-m shoreline and associated lacustrine features in relation to nearby faults (Figure 2).

6.1. Centennial Flat Study Site

The best preserved and most complete geomorphic record of historical to late Pleistocene shorelines in Owens Valley is located in the southeastern sector of the lake

basin along the flank of the Coso Range near Centennial Flat (Jayko and Bacon, 2008; Orme and Orme, 2008; Jayko, 2009) (Figures 2 and 3). The Centennial Flat study site consists of a well-preserved beach terrace comprised of a suite of undeformed beach ridges having crest elevations at 1114, 1120, 1127, 1129, and 1131 m, and a higher and prominent deformed beach ridge (i.e., ~1160 m shoreline) (Carver, 1970; Orme and Orme, 2008) (Figures 3 and 4A, B). Following Carver's (1970) work, the area was later described by Orme and Orme (2008) as having wave-formed scarps and headlands with cliffs developed on Pliocene-age Coso Formation rocks, and a gravelly beach ridge that is tilted northeastward across a distance of ~5.2 km; the beach ridge and the wave-cut notches were measured with a total station to have up to ~10 m of deflection between the elevations of ~1157 and 1167 m. We made a refined estimate of the amount of tilting for the area by using a high-precision GPS to measure only the crest elevations of the same deformed beach ridge. This GPS survey yielded up to ~8 m of deflection between ~1158 and 1166 m (Figure 3).

6.1.1. Tectonic Geomorphology of the Centennial Flat Area

The beach ridge plain of the Centennial Flat study site includes two remnant beach terraces with poorly-preserved surfaces covered with eroded beach rock and platy lithoid tufa mounds at elevations between ~1142 and 1155 m that show progressive deformation and eastward tilting, similar in magnitude to the nearby ~1160 m beach ridge (Figures 3 and 4C). The lower of the two beach terraces extends for ~4 km across the site, whereas the higher terrace extends for ~1.5 km (Figure 3). In contrast, the suite of lower beach ridges with surveyed crest elevations of ~1114, 1120, 1127, 1129, and

1131 m across a distance of ~3 km have consistent elevations across the site that are within the ~1–2 m range of natural variability of lower constructional shoreline features in the valley. An age for the lower shoreline feature is provided by a ^{14}C date of 15.2 ± 0.32 cal kyr B.P. from a freshwater mussel (*Anodonta californiensis*) shell fragment within sediment of the ~1114 m beach ridge (Orme and Orme, 2008). In addition, a prominent and steeply-sloping beach ridge complex within the Swansea embayment northwest of Keeler consists of upper ridges at GPS elevations of ~1119, 1124, and 1129 m with ^{14}C dates from bivalve and gastropod shells of ~11 to 16 cal kyr B.P. (Bacon et al., 2006; Orme and Orme, 2008) (Figure 2). The similarity of the number and age of beach ridges between the Swansea embayment and Centennial Flat site also suggests a lack of measurable ground deformation within the eastern lake basin, because the beach ridges at the Swansea embayment are situated in a sheltered setting that likely had less effective fetch conditions, thereby yielding elevations within the ~1–2 m range of natural variability of lower shorelines in the valley.

The tightly spaced beach ridges at ~1127, 1129, and 1131 m at the Centennial Flat site change to wave-formed scarps in an area that coincides with the southern projection of the KF defined by geophysical surveys (Slemmons et al., 2008) and well-defined deflected playa stream channels (Figure 3). The change in shoreline feature type suggests that the wave-formed scarps are controlled by the intersection of the KF and the southern extent of the SIMF (Figure 3). In the northern Centennial Flat area, relative uplift in the area is indicated near the fault intersection by preservation of a narrow, gravelly beach terrace at ~1135 m bounded by short fault segments (Carver, 1970; Jayko, 2009). The front edge of the terrace surface ranges in elevation from ~1135 to 1136 m over ~1.5 km,

indicating a lack of measurable tilting along the strike of the SIMF (Figure 3). The small beach terrace remnant is covered by a moderately-developed desert pavement with moderately-developed desert varnish and subsurface rubification (i.e., reddening) on a mixture of limestone and basalt gravel clasts. The surface is underlain by a ~1–2 m thick, carbonate-cemented beach terrace deposit (e.g., beach rock) that has well rounded, gravelly beach-face facies with well-stratified, lakeward dipping tabular beds (i.e., forests) (Figures 3 and 4D–F). There is no age control for these deposits, but the terrace-deposit package is underlain by an abrasion platform formed on alluvium that has at least one easily recognizable buried soil.

6.1.2. Ground Deformation of the ~1160 m Highstand Beach Ridge

Geomorphic analysis of the natural variability of beach ridges and consideration of faulting in the area has allowed us to refine previous estimates of the style of ground deformation of the highstand beach ridge at the Centennial Flat study site. Along the crest of the beach ridge nearest the CFF, six GPS elevations (vertical accuracy ±45–60 cm) ranged from 1164.6 to 1166.6 m. These measurements yield a mean elevation of 1165.7 ± 1.4 m for the southwestern half of the beach ridge (Figure 3). Additional measurements of the same beach ridge in areas to the northeast are at elevations of 1163.0, 1161.3, and 1157.7 m (accuracy ±44–66 cm); these higher elevations exceed the 2 m value associated with natural variability of constructional shoreline features. As a result, we attribute the differences in elevation of the beach ridge at the northeastern locations to ground deformation.

The preservation and apparent eastward tilting of the ~1160 m highstand beach ridge indicate that the area of the Centennial Flat study site is a tilted fault block with up to ~4 m of deflection over a distance of 3.8 km between the KF and CFF (Figure 3). The difference in elevation of the same beach ridge across the KF, however, represents ~3.5 m of vertical separation on the KF (Figure 3). Furthermore, the absence of lower shoreline features on the hanging walls of the CFF and KF also indicates relative motion across the faults, where the absence of shorelines appears to be the result of burial or erosion by alluvium sourced from the Coso Range on the offset block of both faults (Figures 2 and 3).

6.1.3. Geochronology and Stratigraphy of the ~1160 m Highstand Beach Ridge

The ~1160 m shoreline was previously inferred to be 24.7 ± 1.5 cal kyr B.P. by Bacon et al. (2006) based on a ^{14}C date on lithoid tufa-cemented beach gravel in the Alabama Hills at ~1155 m (Lubetkin and Clark, 1988), and less than ~18 to 27 cal kyr B.P. from ^{14}C dates on packrat middens in the Inyo Mountains that constrain the shoreline to below ~1155 m during this time (Koehler and Anderson, 1994) (Figure 2). Previous studies have demonstrated the potential uncertainty in using ^{14}C dates from tufa to constrain the age of shorelines because tufa can be contaminated by younger, post-depositional carbon from pedogenic processes or by syndepositional older carbon from lake water (e.g., Lubetkin and Clark, 1988; Bischoff et al., 1993). At the time of these earlier studies, there was uncertainty in the magnitude of vertical deformation across Owens Valley and no direct age control of deposits associated with ~1160 m shoreline features. We performed post-IR-IRSL analysis on three samples from

deposits of the ~1160 m beach ridge at the Centennial Flat study site to establish the first numerical ages of the second highest shoreline in Owens Valley (Figure 3).

The ~1160 m beach ridge at the Centennial Flat study site has a surface covered by a moderately-developed desert pavement with moderately-to-poorly developed desert varnish and subsurface rubification coatings on mostly limestone gravel clasts. Shoreline deposits are continuously exposed in 5–6 m high outcrops along a wash between the elevations of ~1150 and 1165 m (Figure 3). The lacustrine section is capped by gravelly beach rock and a base defined by a cobble lag on an abrasion platform formed on alluvium with two buried soils that exhibit increasing soil development with depth (Figures 3 and 5A-C). Three IRSL samples were taken from beach ridge and beach terrace deposits that lacked evidence of bioturbation. Duplicate samples were taken from a sandy layer at ~1156 m within a horizontal bed associated with sand-rich, back-ridge (i.e., back-barrier) lagoon facies overlain by well rounded, sandy to gravelly beach ridge facies with landward dipping tabular beds (i.e., backsets) (Figure 5A, B). The duplicate samples yielded post-IR-IRSL dates of 36.51 ± 3.21 and 43.39 ± 3.65 ka (Table 1). The third sample was taken from beach terrace deposits at an elevation of ~1163 m, about 130 m upstream from the duplicate sample site. The sample is from well-rounded, gravelly sand beach-face facies with well-stratified foresets (Figure 5A, D). The third sample returned a post-IR-IRSL date of 40.09 ± 3.13 ka (Table 1).

The stratigraphic relations between the beach ridge, back-ridge lagoon, and beach face deposits represent a transgressive (TS-1) and regressive (RS-1) sequence associated with one lake-level cycle, similar to other late Pleistocene highstand shoreline deposits described in Lahontan Lake basin (e.g., Adams and Wesnousky, 1998). Site stratigraphy

shows that this lake-level cycle had two periods with relatively stable water levels vertically separated by ~9 m. The earlier period is indicated by the beach ridge and back-ridge lagoon deposits at a basal elevation of ~1156 m and the later period constructed the prominent beach ridge up to ~1165 m (Figure 5A-C).

6.1.4. Paleohydroclimatic Context of ~40 ka Owens Lake

Several independent lines of evidence exist for a deep, late Pleistocene Owens Lake. The mean post-IR-IRSL date of 40.0 ± 5.8 ka (referred to as ~40 ka) and geomorphic surface characteristics provide direct evidence that the second highest shoreline in Owens Valley is late Pleistocene in age. Supporting stratigraphic evidence for a deep lake at this time is from Owens Lake sediment cores. Sediment in lake cores from the depocenter area of the basin (Figure 2) show the highest weight percent of clay deposition since ~130 kyr B.P. occurs at 39.5–43 kyr B.P. from core OL92 (Smith and Bischoff, 1997; Litwin et al., 1999), as well as evidence of two glacier advances at 49.0–45.1 and 42.8–39.0 kyr B.P. based on the rock flour record in composite core OL90/92 (Bischoff and Cummins, 2001). Additional proxy records in the lake cores support an increase in sediment flux, and, thus, water flux to the lake after ~40 kyr B.P. in response to either glacial activity (Bishoff and Cummins, 2001) or erosion from increased runoff and alluvial deposition in the watershed near Lone Pine at 32–44 ka (Benn et al., 2006). The ~40 ka beach ridge and evidence of a major transgression up to its highstand at ~1160 m occurred prior to the most intense and prolonged glacial advance in the Sierra Nevada during the Tioga Glaciation from 30.5 to 15.0 ka, equivalent to marine isotope

stage 2 (MIS 2) (e.g., Bishoff and Cummins, 2001; Phillips et al., 2009; Gillespie and Clark, 2011; Rood et al., 2011; Moore and Moring, 2013).

Soil development at the Centennial Flat site also provides an indication of geomorphic conditions at the site prior to the ~40 ka transgression of Owens Lake. Two well-developed buried soils formed on alluvium beneath the ~1160 m shoreline deposits indicate mostly alluvial fan deposition at the site followed by landscape stability after the regression of the higher and older pluvial lake (i.e., ~1180 m shoreline) between ~160 and 40 ka. A period of alluvial fan aggradation near Lone Pine at 80–86 ka (Benn et al., 2006) provides additional support for basin-wide alluvial fan aggradation during an interglacial period in southern Owens Valley.

6.2. Keeler Beach Ridge Study Site

We performed a new investigation of shoreline features and cross-cutting relations with alluvial fans on the west flank of the Inyo Mountains to assess the style of deformation near Keeler. Previous studies documented wave-formed scarps and an associated platform on older alluvial fans in the area (Carver, 1970; Beanland and Clark, 1994; Bacon et al., 2005; 2006; Orme and Orme, 2008; Jayko, 2009). Two sets of wave-formed scarps with heights up to ~10 m that bound a prominent highstand beach terrace (i.e., platform) are preserved near the axis of dissected alluvial fans. A thin veneer of small coalescing alluvial fans derived from adjacent scarps and upslope areas locally covers the beach terrace. Elevations from our GPS survey of the front and back edges of the beach terrace over ~2 km, average 1145 ± 1 and 1150 ± 1 m, respectively, indicating a lack of measurable north-south tilting in the area.

The best-preserved geomorphic record of historical to late Pleistocene shorelines near Keeler is at the newly described Keeler beach ridge study site (Figures 2 and 6). The highstand beach terrace is locally composed of a beach ridge at ~1156 m along the back edge of the terrace within a ~220 m wide area between wave-formed scarps (Figure 6A). The study site encompasses an area that includes widespread recent to late Holocene alluvial fan deposition, remnants of a ~1113 m beach ridge and associated terrace, a late Holocene (~3.5 ka) beach ridge at ~1108 m, and lower historical to latest Holocene shoreline features (e.g., Bacon et al., 2018) (Figure 6). We infer that the ~1113 m beach ridge at the site was formed by the same lake level that constructed the ~1114 m at the Centennial Flat study site based on similar elevations, lateral continuity, and geomorphic surface characteristics. In addition, several short, left-stepping faults of the north-south striking branch of the SIMF lie ~250 m east of the wave-formed scarps at the site (Carver, 1970). The fault scarps are east facing and well-defined, but lack large vertical offsets (Bacon et al., 2005; Jayko, 2009) (Figures 2 and 6A). The wave-formed scarps and beach terrace, plus faults at the site, cross dissected alluvial fans (Qf1) that lack surface evidence of shorelines above ~1156 m.

6.2.1. Geomorphology and Stratigraphy

The ~1156 m beach ridge has a broad, convex topographic profile and is locally crossed by sinuous alluvial channels. Back ridge topography consists of prominent depressions and wave-formed scarps developed across the Qf1 fan (Figure 6B, C). The beach ridge surface is covered by a moderately-developed desert pavement with moderately-to-poorly developed desert varnish and subsurface rubification coatings on

mostly limestone gravel clasts. The ~1156 m beach ridge near Keeler has surface characteristics similar to the deformed ~40 ka beach ridge of the Centennial Flat study site (e.g., Figure 4A).

Beach deposits rarely are observed in natural exposures of the highstand beach terrace near Keeler, but a gravel quarry and natural wash exposures provide subsurface evidence for at least two lake cycles (Figures 6 and 7). Deep quarry excavations at the front edge of the beach terrace and face of the lower wave-formed scarp show a thick section of shoreline deposits consisting of well-rounded and well-sorted gravel beach facies that are cemented to form beach rock. Exposures in quarry walls show the gravelly beach rock is underlain by less indurated and well-sorted, massive sands, as well as overlain by a thick sequence of colluvium derived from the wave-formed scarp to the west. Natural wash exposures also show the gravelly beach rock forms a buttress unconformity with older alluvium between GPS elevations of 1140 ± 1 and 1145 ± 1 m on the east. Other natural wash exposures of the beach terrace east of the quarry excavations show the stratigraphy of two beach ridges at elevations of ~1148 and ~1156 m that were deposited above an abrasion platform on older alluvium (Figure 7A).

The surface of the lower beach ridge appears to be slightly eroded, given the relatively planar surface and lack of a well-formed ridge crest in the area. A GPS elevation of 1148.2 ± 0.2 m was measured for the lower beach ridge. The lower beach ridge is underlain by a ~2–3 m thick section of well-rounded gravelly beach ridge facies with horizontal tabular beds (i.e., topsets) and backsets that laterally grade into silty, sand-rich, back-ridge lagoon facies (Figure 7B). In contrast, the higher beach ridge is unmodified. The GPS elevations (accuracy of ±14–28 cm) of four points at the crest of

the higher beach ridge ranged from 1155.1 to 1155.8 m, resulting in a mean elevation of 1155.5 ± 0.4 m (Figure 6A). The ~1156 m beach ridge is underlain by a ~4–5 m thick section of well-rounded gravelly beach ridge facies comprised of backsets near the base and foresets near the top of the section. The lateral and vertical position of this gravelly facies below the crest of the ~1156 m beach ridge indicates a transgressive-regressive sequence (Figure 7C). Both ~1148 and ~1156 m beach ridge deposits are cemented with depositional carbonate to form beach rock.

6.2.2. Age Estimates and Correlations of Shoreline Deposits

We used cross-cutting stratigraphic relations between beach and alluvial deposits, relative degree of beach rock cementation, and correlation to other similar beach ridges in the lake basin to estimate the relative ages of the beach ridge and shoreline sediment at the site. A ~5 m thick section of gravelly beach rock along the front edge of the beach terrace appears to be overlain by the ~2–3 m thick deposits associated with the ~1148 m beach ridge (Figure 7A). The lower depositional contacts of both deposits are at different elevations. The lower and lateral contact of the ~5-m-thick deposit is defined by a buttress unconformity (Figure 7A). In addition, the relative degree of beach rock cementation between the two deposits is different, with the ~5 m thick beach deposit exhibiting thicker and more indurated calcium carbonate coatings compared to the beach rock of the ~1148 and ~1156 m beach ridge deposits.

The stratigraphic evidence points to at least two lake-level cycles. The older lake-level cycle is represented by the ~5 m thick section of gravelly beach rock between ~1140 and 1145 m. The buttress unconformity that is present on older alluvium at these

elevations is interpreted as a relict (buried) wave-formed scarp. The latest lake-level cycle at the site is represented by the shoreline deposits of the ~1148 and ~1156 m beach ridges. This lake-level cycle had relatively stable water levels beginning at a GPS elevation of 1145.7 ± 0.2 m, indicated by the horizontal and laterally continuous basal contact of the ~1148 m beach ridge and back-ridge lagoon deposits (Figure 7). A short period of stable water levels is required for the accumulation and preservation of fine-grained lagoon deposits and subsequent burial by gravelly beach deposits. The burial indicates a transgression of up to ~10 m that was followed by another period of stable water levels that generated shoreline erosion at the distal margin of the Qf1 alluvial fans and construction of the higher and well-preserved ~1156 m beach ridge.

Shoreline features can be correlated within lake basins based on their elevation and geomorphic characteristics if the geomorphic processes that created the shorelines are understood (Oviatt, 2000), and if ground deformation is considered. The Keeler beach ridge study site shares similar geomorphologic and stratigraphic characteristics with the deformed ~40 ka beach ridge at the Centennial Flat study site (e.g., Figure 5). Notable characteristics include: (1) similar vertical and lateral stratigraphic evidence of one lake-level cycle; (2) the same number of stable water levels and difference in elevation (~9–10 m) between a lower sequence of beach ridge and back-ridge lagoon deposits and a higher, well-formed beach ridge; (3) similar degree of depositional carbonate (i.e., beach rock) cementation of beach ridge and terrace deposits; and (4) similar degrees of desert pavement and varnish development. The major difference between the two study sites is the elevations of the similar shoreline deposits and features. We attribute this difference in elevation to relative ground deformation between the two sites.

6.3. Moffat Ranch Road Alluvial Fan Study Site

We studied erosional shoreline features and their cross-cutting relations with a dated alluvial fan on the north flank of the Alabama Hills near Moffat Ranch road to assess ground deformation of additional ~40.0 ka shoreline features in the northwestern sector of the lake basin (Figures 2 and 8). An alluvial fan in this area west of the OVF was shown previously to have wave-formed scarps at ~1162 m cutting a late Pleistocene distal alluvial fan and paleo-lateral spread features above this elevation (Slemmons et al., 2008). The alluvial fan (Qf1) was inferred to be older than ~25 cal kyr B.P. by Bacon et al. (2003) based on soil-geomorphic characteristics, as well as the characteristics of inset alluvial fans (Qf2) and fan delta (Qfd2) deposits that grade to the ~1160 m shoreline inferred to be Tioga Glaciation age equivalent (Figure 8). Subsequent to the initial study, cosmogenic ^{10}Be surface exposure ages of 80–86 ka were obtained for the Qf1 fan (Benn et al., 2006). The surface and soil-geomorphic characteristics and cross-cutting relations with younger fans described in Slemmons et al. (2008) support the exposure ages of Benn et al. (2006).

The new age constraint of ~40 ka for the ~1160 m shoreline from our study refines the age of the inset Qf2 alluvial fans, Qfd2 fan delta deposits, and wave-formed scarps in the Moffat Ranch Road area (Figure 8). In addition, the elevation of the wave-formed scarps at the site were resurveyed during our study. The GPS elevations of three points at the distal margin of the Qf1 fan ranged from 1159.8 to 1160.7 m with measurements having a vertical accuracy of ±42–52 cm. These measurements provide a revised mean elevation for the wave-formed scarps of 1160.3 ± 0.8 m (Figure 8).

7. Lake-Level Reconstruction of Deformed Shorelines

Lacustrine shoreline landforms have previously been used to resolve the magnitude and rates of ground deformation because these types of features are useful geomorphic paleohorizonal datums (e.g., Oviatt, 2000). Understanding the rates and styles of tectonic deformation within seismically active lake basins provides information to correlate shoreline features, as well as to reconstruct past lake levels to their original formational positions. Alternatively, when there is a lack of fault or ground displacement information, shoreline features and lacustrine deposits have been used as piercing points to measure cyclic-lithospheric deformation (i.e., isostatic rebound) due to surface loading of lakes in the Great Basin (e.g., Crittenden, 1963; Mifflin and Wheat, 1979; Currey, 1982; Bills and May, 1987, Bills et al., 1994, 2007; Adams et al., 1999; Currey and Sack, 2009; Chen and Maloof, 2017), as well as cyclic-ground deformation associated with volcanic activity (e.g., Locke and Meyer, 1994; Pierce et al., 2002; Hildreth and Fierstein, 2016). The dating and measurement of fault offsets determined from shoreline features and associated deposits also have been used to estimate slip rates and paleoseismicity for assessing seismic hazards (e.g., Machette et al., 1991; Adams et al., 1999; Knott et al., 2002; Caskey et al., 2004; Bacon and Pezzopane, 2007; Oldow and Singleton, 2008). Fault offsets are also used to characterize the style of tectonic deformation for structural models and long-term basin evolution (e.g., Reheis et al., 2014; Hopkins and Dawers, 2016).

Available coseismic and postseismic observations bear little resemblance to the topography of Owens Valley that was built in response to crustal extension, yet the topography is the direct result of repeated earthquakes on closely spaced faults (e.g., Thompson and Parsons, 2017). Geologic field measurements provide valuable

information on the relative displacement across faults, but typically provide little or no direct information on the absolute elevations of offset surfaces (Martel et al., 2014). Reconstruction of deformed shorelines in the northern Basin and Range have commonly been performed in broad pluvial lake basins (e.g., Lahonton and Bonneville Lakes) where faulting and warping of shorelines are accommodated by single normal fault systems, and isostatic crustal flexure and rebound of relatively thin crust (e.g., Bills et al., 1994, 2000; Adams et al., 1999; Hampel and Hetzel, 2006). We infer that ground deformation associated with isostatic rebound from loading of Owens Lake is negligible because southern Owens Valley is a narrow graben crossed by an array of several faults and is underlain by relatively thick crust along the eastern escarpment of the Sierra Nevada (e.g., Saleeby et al., 2013; Martel et al., 2014; Unruh et al., 2014). Instead, we consider gravitational loading is the driving force acting on the crust and that isostatic reloading is the primary mechanism that controls the shear stresses acting on faults from both tectonic plate motions and by the process of faulting itself (e.g., Koseluk and Bischke, 1981; Ruff, 2002; Thompson and Parsons, 2017).

7.1. Differential Fault-Block Model

The conceptual elements and results of two models that are based on isostasy and crustal lithospheric rheology were relied upon in our study to support a straightforward approach in reconstructing the absolute elevation of the ~40 ka shoreline for differential fault-block movement. The first model was based on numerical modeling to characterize Basin and Range extensional faulting in light of coeseimic and post-seismic deformation measured prior to and after the A.D. 1954 M7.2 Fairview Peak and M6.8 Dixie Valley

earthquake sequence in the central WLB (Thompson and Parsons, 2017). The second model was based on an ensemble of mechanical analyses to identify the ratio of uplift to subsidence from range-front faulting along the eastern escarpment of the Sierra Nevada, including Owens Valley (Martel et al., 2014).

Modeling of postseismic deformation on normal faults in the central WLB following the A.D. 1954 earthquakes simulate a broad and asymmetric uplift pattern under the footwall that matches level-line and GPS survey observations made up to 60 years later. Final simulations in the model allows repeated earthquakes to mimic observed deformation over many millions of years that effectively replicate the distinctive signature of uplifted and bent ranges within the hanging walls of faults (Thompson and Parsons, 2017). The same style of postseismic uplift of footwall areas modeled for the A.D. 1954 earthquake sequence was also identified in Owens Valley at the latitude of Lone Pine where leveling surveys across the SNFF, OVF and IMF were measured from A.D. 1925–1928 to 1974, about 50 to 100 years after the A.D. 1872 earthquake (Savage and Lisowski, 1980; 1995; Figure 2). The leveling data shows constant differential uplift rates up to 1.8 mm/yr that increase uniformly with distance west of the OVF trace until reaching the SNFF trace, a distance of ~12.5 km. Normal slip on both the OVF and SNFF were required in an elastic half-space dislocation model of repeated measurements from a trilateration network spanning the valley to match the observed eastward-tilted uplift pattern on the OVF-SNFF fault block (Savage and Lisowski, 1995). The documented differential uplift in Owens Valley demonstrates that the postseismic effects of surface faulting and active strain accumulation is translated across the entire OVF-SNFF fault block and that both faults are structurally connected.

Modeling of range-front faulting along the SNFF system also suggest the occurrence of differential surface displacements across the fault, where ~66–85% of the current escarpment relief is from subsidence of the grabens east of the Sierra Nevada, with only ~15–34% resulting from footwall uplift near the crest (Martel et al., 2014). The fault-block models and observed transient uplift patterns in Owens Valley collectively support differential fault-block motion across normal faults. We use this mechanism to resolve differential surface offsets to reconstruct shorelines to their original (i.e., undeformed) elevation across closely spaced faults.

7.1.1. Reconstruction of ~40 ka Shoreline Features

The Moffat Ranch road study site provides geomorphic evidence of shoreline erosion and fan delta deposition at ~1160 m attributed to the ~40 ka lake level (e.g., Slemmons et al., 2008). The wave-formed scarps at the Moffat Ranch road site are ~0.5–1.0 km west of the OVF (Figure 8) and ~11.5 km east of the SNFF (Figures 1 and 2). Both faults have slip rates estimated from previous studies, thereby providing independent information. Lake levels are reconstructed by multiplying the net vertical slip rate of the fault block containing shoreline features by the age of the shoreline to solve for the magnitude and direction of vertical deformation. The ~1160 m shoreline features at the Moffat Ranch road site are situated on the footwall block of the OVF that produces relative uplift, as well as on the hanging wall block of the SNFF that produces relative subsidence during earthquakes. To account for long-term differential fault-block motion, a net ground deformation rate was estimated by adding an uplift rate (i.e., positive value) for the southern OVF near Lone Pine of 0.12 ± 0.04 m/k.y. (Bacon

and Pezzopane, 2007) and a subsidence rate (i.e., negative value) for the SNFF of 0.25 ± 0.05 m/k.y. (Le et al., 2007) (Table 2; Figures 9 and 10). The result is a net subsidence rate of 0.13 ± 0.09 m/k.y. for the fault block, which is within the uncertainty of subsidence rates estimated when the possible uplift to subsidence ratios for hanging wall and footwall deformation for the SNFF and OVF were applied (e.g., Martel et al., 2014). This net subsidence rate, when multiplied by the mean age of 40.0 ± 5.8 ka for the shoreline, resulted in an estimated 5.2 ± 3.7 m of subsidence at the site. Adding this value to the mean elevation of the wave-formed scarps of 1160.3 ± 0.8 m to correct for subsidence yielded a reconstructed shoreline elevation of 1165.5 ± 4.5 m, similar to the mean elevation of 1165.7 ± 1.4 m along the southwestern half of the deformed beach ridge at the Centennial Flat study site. We used the highest elevation of 1165.7 ± 1.4 m from the deformed shoreline to (1) represent the position of the ~40 ka lake level at the Moffat Ranch Road site and (2) the paleohorizontal datum for assessing ground deformation of similar shoreline features identified in other parts of the lake basin (Figure 11A).

7.1.2. Reconstruction of ~15 ka Shoreline Features

We used the same approach for determining the ~40 ka paleo-horizontal datum to assess potential ground deformation within the western sector of the lake basin since 15 ka by reconstructing the water level associated with the lowest undeformed beach ridges identified at the Centennial Flat and Keeler Beach ridge sites at ~1113–1114 m (Figures 3 and 6). Stratigraphic and geochronologic data from a paleoseismic study on the OVF near Lone Pine was used to provide constraints on the age and elevation of a

~15 ka lake level that was identified in fault trenches (Bacon and Pezzopane, 2007) (Figure 11B). Trench exposures on the hanging wall of the fault revealed fluvial-deltaic deposits with carbonized willow/cottonwood (*Salix* sp.) twigs at an elevation of 1111.6 ± 0.2 m. Radiocarbon dates on three twigs yielded a mean age of 15.0 ± 0.5 cal kyr B.P. for the deposit, whereas the deposit elevation provided a maximum constraint on the position of a lake level at this time (Bacon et al., 2006; Bacon and Pezzopane, 2007). The mean age is similar to the age of 15.2 ± 0.3 cal kyr B.P. for the ~1114 m beach ridge at the Centennial Flat study site (Orme and Orme, 2008). We therefore interpret the ~15.0 cal kyr B.P. deposit in the fault trench as representing the fluvial-deltaic facies of the lacustrine system that also constructed the ~15.2 cal kyr B.P. beach ridge. The apparent difference in elevation between the fluvial-deltaic deposit and beach ridges is attributed to near-field deformation within the hanging wall of the OVF (Figure 11B).

We reconstructed the ~15 ka water level from the fault trench data to model ground deformation across the lake basin. This was first attempted by using a total subsidence rate of ~0.37 m/k.y. across the hanging wall blocks of the SNFF and OVF (Table 2). This approach produced ~5.5 m of uniformly distributed subsidence in lake basin since ~15 ka, but this magnitude of subsidence is not reflected in the shoreline geomorphology, which consists of a laterally continuous suite of ~11–16 ka beach ridges at ~1114 to 1131 m. In a second approach using only the OVF to produce the observed deformation, the reconstructed water level from fault trench data was supported by stratigraphic and geomorphic evidence. The reconstructed water level was calculated using a subsidence rate of 0.12 ± 0.04 m/k.y. for hanging-wall deformation on the OVF, as well as the mean age of 15.0 ± 0.5 cal kyr B.P. and elevation of 1111.6 ± 0.2 m for the

fluvial-deltaic deposit. Multiplying the subsidence rate and age yields an estimated subsidence of 1.8 ± 0.6 m since ~15 ka. When added to the deposit elevation, the reconstructed water level is 1113.4 ± 0.8 m. This reconstructed ~15 ka lake level is within error of the elevations of beach ridges in the eastern lake basin west of the KF at 1113.6 ± 0.2 m and east of the fault at 1112.5 ± 0.6 m (Figures 3 and 6). The difference in the elevations between the reconstructed water level and the beach ridges (1.1 ± 0.8 m) bounding the KF is within the natural variability of low-elevation beach ridges in the lake basin (Figure 11B). We attribute the natural variability at the ~1114 m shoreline sites to variable fetch conditions within different sectors of the lake basin.

8. Basin-Wide Ground Deformation

The style of faulting and slip rates on the OR-CFF and KF, and the magnitude of ground deformation have not been previously characterized in Owens Lake basin. The difference in elevation and age of the ~40 ka beach ridge at the Centennial Flat study site was used as the piercing point and age to estimate vertical separation across faults and calculate vertical slip and subsidence rates. The ~1166 m paleo-horizontal datum also was used to determine the total amount of basin-wide deformation in the areas of the OR-CFF and KF, and the eastern margin of the lake basin. The slip rates are regarded as neotectonic or geologic vertical slip rates as opposed to paleoseismic slip rates (e.g., McCalpin, 1996), because the slip and timing per event histories on the OR-CFF and KF are unknown.

To evaluate the extensional slip distribution in Owens Valley, we calculated slip rates on the OR-CFF and KF and combined them with other faults having slip rate

information (Table 2). This evaluation resolves only the long-term vertical slip distribution across the lake basin because confident piercing points to estimate dextral offsets on the OR-CFF and KF have not been identified. Measurements of absolute vertical deformation are controlled by the 1165.7 ± 1.4 m paleohorizontal datum of the ~40 ka shoreline.

8.1. Subsidence Rate in Eastern Owens Lake Basin

We resolved ground deformation in the area of the Keeler beach ridge study site relative to nearby faults and the ~1166 m paleo-horizontal datum of the ~40 ka beach ridge. The prominent beach terrace and ~1156 m beach ridge are situated on the footwall of the SIMF and hanging wall of the KF (B–B'; Figure 10). The subsidence at the site is 10.2 ± 1.8 m based on the difference between the elevations of 1155.5 ± 0.4 m for the Keeler beach ridge and the paleo-horizontal datum (1165.7 ± 1.4 m) of the ~40 ka shoreline. The subsidence value when combined with the age of the beach ridge yields a total subsidence rate of 0.26 ± 0.06 m/k.y. for the site.

Geomorphic and stratigraphic piercing points from the ~40 ka beach ridge and shoreline deposits that are underlain by an abrasion platform provide an additional estimate of subsidence that can be used to validate our approach in reconstructing the absolute elevation of shorelines from differential fault-block motion. The combined elevations of the base of lowstand beach ridge deposits and highstand beach ridge crests of 1156.0 ± 0.2 m and 1165.7 ± 1.4 m from the Centennial Flat site and 1146.7 ± 0.2 m and 1155.5 ± 0.4 m from the Keeler beach ridge site collectively show a mean of 9.8 ± 1.8 m of subsidence across the fault blocks of the OR-CFF, KF, and SIMF in the

eastern lake basin (Figure 11A). The magnitude of subsidence and age of the ~40 ka beach ridge and deposits together yield a total subsidence rate of 0.24 ± 0.06 m/k.y., similar to the mean rate from the Keeler beach ridge site that was calculated by the paleo-horizontal datum. We consider the subsidence rate of ~0.24 m/k.y. from both geomorphic and stratigraphic markers, however, as a better constrained estimate because it includes the range of possible piercing points from deposition and erosion along a shoreline. The two different markers taken together represent a mean subsidence estimate because beach ridges typically form above mean water level, whereas abrasion platforms form below mean water level (e.g., Oviatt, 2000). We infer that the measured ground deformation in the eastern sector of the lake basin is accommodated by differential fault block movement between the KF and SIMF, and basin-wide subsidence, which has produced up to ~10 m of cumulative subsidence in areas east of Keeler (Figure 11A).

8.2. Vertical Slip Rate on the Keeler Fault

The sense and magnitude of slip on the KF was estimated by an apparent northeast-side-down vertical separation of the ~40 ka beach ridge at a left-step onto a steep, east-facing escarpment within the low-relief hills of the Coso Range (Figure 3). Mean elevations of the beach-ridge crest bounding the KF are 1161.3 ± 0.8 m from two points south of the fault and 1157.7 ± 0.4 m from one point on the north side of the fault, yielding a vertical separation of 3.6 ± 1.2 m (Figure 11A). Supporting evidence of vertical separation on the KF as opposed to eastward tilting is indicated by differences in surface gradient of the deformed beach ridge. The slope of the beach ridge crest across the KF is 0.17° taken over a distance of ~1000 m between the ~1161 and 1158 m

reference points. This value is greater than the slope of 0.096° measured across a distance of ~2400 m between the elevations of ~1165 and 1161 m on the northeastern half of the beach ridge (Figure 3). We interpret the higher slope to represent a vertical offset across the KF, whereas the lower slope is mostly from eastward tilting of the fault block between the OR-CFF and KF.

The vertical slip rate for the KF is calculated using a vertical separation of 3.6 ± 1.2 m and mean age of 40.0 ± 5.8 ka for the offset beach ridge combined with a fault dip of ~85° from geophysical subsurface data (Neponset Geophysical Company and Aquila Geosciences, Inc., 1997). These values yield a vertical slip rate of 0.09 ± 0.03 m/k.y. (Table 2; Figures 9 and 10). Total cumulative subsidence in the areas adjacent to the KF is resolved relative to the ~1166 m paleohorizontal datum of the ~40 ka beach ridge. The amount of total subsidence on the footwall of the KF is 4.4 ± 2.2 and on the hanging wall of the KF is 8.0 ± 1.8 m. The cumulative fault slip and basin-wide subsidence along the southeastern lake basin is accommodated by both the apparent eastward tilt of the fault block between the OR-CFF and faulting on the KF since ~40 ka (Figure 11A).

8.3. Vertical Slip Rate on the Centennial Flat Fault

The elevation of the ~40 ka beach ridge in the Centennial Flat study area provides fault slip information on the CFF segment and style of deformation on the fault block between the OR-CFF and KF (Figures 2 and 3). The mean elevation of 1165.7 ± 1.4 m measured by GPS for the southwestern half of the beach ridge nearest the CFF is similar to the mean paleohorizontal datum elevation of 1166 ± 5 m estimated from the

differential vertical slip on the OVF-SNFF fault block at the Moffat Ranch road site. This implies that there has been negligible vertical ground deformation on the footwall of the CFF within ~2 km of the fault trace (Figure 3). The northeastern half of the beach ridge, however, is uniformly tilted to the east with increasing subsidence in areas closest to the KF (Figure 11A). The tilting is accommodated by footwall deformation on the CFF, whereas the hanging-wall forms the eastern margin of a graben with the OVF (B–B'; Figure 10).

Fault offset of the beach ridge cut by the CFF cannot be resolved because the ~40 ka beach ridge is not preserved on the hanging wall. Thus, direct calculation of a slip rate for the CFF is precluded. To account for the lack of a piercing point, we assigned a total subsidence rate of 0.24 ± 0.06 m/k.y. from the difference in elevation between the beach ridges and abrasion platforms of the ~40 ka shoreline as a representative slip rate for the CFF to balance the apparent deformation field in this part of the lake basin (Table 2; Figures 9 and 10).

8.3.1. Owens Valley Fault Graben

The OVF and OR-CFF form a graben that coincides with the depocenter of the lake basin (B–B'; Figure 10). The graben accommodates the highest rates of subsidence in the lake basin (net rate of 0.36 ± 0.1 m/k.y.) based on the summation of the mean subsidence rates for the footwalls of the OVF and CFF (Table 2; Figure 9). The high subsidence rate of the graben is reflected in the geomorphology of the southern lake basin. A well-preserved sequence of shorelines, including the ~40 ka shoreline, is not present in this area; but there is a well-developed and continuous wave-formed scarp that

crosses late to middle Pleistocene or older alluvium at elevations of ~1170–1180 m attributed to shoreline erosion from the ~160 ka and earlier pluvial Owens Lakes, and a few isolated areas with remnant wave-formed scarps at lower elevations (e.g., Jayko and Bacon, 2008; Slemmons et al., 2008). The graben area contains Holocene alluvial fans (e.g., Jayko, 2009), indicating both aggradation of alluvial sediment within a predominately subsiding area of the basin and base-level changes associated with an overall lowering of lake levels during the Holocene (Bacon et al., 2006; 2018).

9. DISCUSSION

9.1. Late Pleistocene Vertical Slip Rate on the Owens Valley Fault

In light of our new results, it is informative to revisit previous studies on the higher and older ~1180 m shoreline. Jayko and Bacon (2008) published a reconnaissance-level investigation of the highest and oldest preserved shoreline features in Owens Valley above the ~40 ka shoreline. Erosional remnants of the older shoreline at 1200 ± 4 m along the Alabama Hills and at 1180 ± 2 m at the base of the Inyo Mountains near Lone Pine that bound the OVF provide piercing points to determine a vertical separation of ~20 ± 4 m across the fault (A–A'; Figure 10). The age of the lake associated with the older shoreline is constrained by a ^{36}Cl exposure age on an eroded lithoid tufa mound (Jayko and Bacon, 2008) at a GPS elevation of 1174.4 ± 0.8 m. The tufa mound is associated with sandy embayment deposits near Centennial Flat Wash in southern Owens Lake basin (Figure 3). The 160 ± 32 ka age is equivalent to the Tahoe Glaciation (MIS 6) in the Sierra Nevada (e.g., Phillips et al., 2009; Gillespie and Clark, 2011; Rood et al., 2011). An estimated late Pleistocene vertical slip rate of 0.13 ± 0.04 m/k.y. on the OVF

near Lone Pine is derived from the displacement and geochronologic data of Jayko and Bacon (2008). This long-term slip rate for the OVF is similar to the short-term slip rate from deformed latest Pleistocene to Holocene deposits in paleoseismic trenches and alluvial fans on the same fault segment (Lubetkin and Clark, 1988; Bacon and Pezzopane, 2007). This suggests relatively constant vertical slip from ~160 ka to present, similar to the dextral slip component on the OVF over the same period (Haddon et al., 2016).

9.2. Rates of Extension across Owens Lake Basin

To compare geologic-based normal and dextral slip rates in Owens Valley to geodetic-based rates, we estimated extension rates across Owens Lake basin to identify changes in spatiotemporal patterns in vertical slip rates. The physiography of the basin reflects long-term horizontal extension and resultant subsidence by exhibiting nearly ~3340 m of relief across a distance of ~35 km between Mt. Whitney on the crest of the Sierra Nevada and the playa floor of Owens Lake (Figure 1B). A ground-based trilateration network installed to measure strain accumulation in central and southern Owens Valley resolves 1.0 ± 0.3 mm/yr of extension normal to the axis of the valley in the N72°E direction (Savage and Lisowski, 1995). Geodetic measurements from GPS arrays also yield a similar rate of extension of ~1 mm/yr in a N65°E direction between the SNFF and Fish Lake Valley fault at the latitude of northern Owens Valley (Bennett et al., 2003; Wesnousky, 2005a) (Figure 1A). Both rates are similar to the sum of geologic-derived extension rates from several faults across the same area (Ganev et al., 2010a). We estimated the total extension rate across the lake basin by summing the extension rates of

primary faults from previous studies and new rates for faults from our study (Table 2). We calculated extension rates from dip slip rates and resolved relative to the N72°E direction to match the measured extension direction from the trilateration network (Figure 9). Summing the extension rates of the primary faults resulted in a total rate of extension of 0.7 ± 0.2 mm/yr (Table 2). Thus, the long-term extension rate derived from geologic slip rates calculated for an interval of up to ~40 k.y. is within the lower range of geodetic estimates (Figure 9).

9.3. Distribution of Normal-Oblique Slip in Owens Valley

Geodetic and kinematic models of transtensional slip along the eastern margin of the southern Sierra Nevada microplate require a significant amount of normal-oblique shear within Owens Valley (Dokka and Travis, 1990; Savage et al., 1990; Dixon et al., 1995, 2000, 2003; Reheis and Dixon, 1996; Miller et al., 2001; Unruh et al., 2003). Geologic oblique slip and extension rates from the major dextral and normal fault systems across the southern WLB at the latitudes of northern and southern Owens Valley are in general agreement with contemporary, space-based geodetic data (Dixon et al., 2003; Lee et al., 2001, 2009; Ganev et al., 2010a; Haddon et al., 2016). The spatiotemporal pattern of geologic slip rates on normal and normal-oblique faults provides insight on the distribution of extension and dextral shear in Owens Valley. Non-steady slip is reflected in Owens Valley by late Quaternary normal slip rates that increase northward from Owens Lake basin to northern Owens Valley (Berry, 1997; Kirby et al., 2006; Frankel et al., 2008; Le et al., 2007; Amos et al., 2013a,b). Normal-oblique slip rates on the OVF apparently show spatiotemporal variations along strike with rates of

~1.0 m/k.y. on the southern OVF since ~25 ka (Lubetkin and Clark, 1988; Bacon and Pezzopane, 2007; Haddon et al., 2016) and rates up to ~2.8–4.5 m/k.y. on the northern OVF during the past ~55–80 k.y. (Kirby et al., 2008; Pérouse and Wernicke, 2016). The apparent nonsteady distribution of dextral slip on the OVF may be related to a variety of processes including, but not limited to short- and long-term variations of strain distribution related to evolving fault segments (Haddon et al., 2016), an incomplete accounting for all faults responsible for distributing slip at slip rate sites, uncertainties of dating deposits and landforms used in slip rate derivations, and comparison of paleoseismic- and geologic-derived slip rates. Tectono-geomorphic analysis of the entire OVF, however, shows steady dextral slip that decreases slightly on the northern OVF over periods up to 10^5 yr when all available age control for offset landforms in the BPVF are used (Haddon et al., 2016; Figure 1B).

9.3.1. Distributed Faulting in Northern Owens Valley

Available paleoseismological records in Owens Valley provide insight into the apparent discrepancy of transient patterns of slip on the OVF. The penultimate and antepenultimate events on the southern OVF identified in seven fault trenches and in tectonic geomorphology near Lone Pine are well constrained at ~8.6–10.4 cal kyr B.P. and poorly constrained at ~14–24 cal kyr B.P., respectively, suggesting long interseismic periods of 8–10 k.y. (Bacon and Pezzopane, 2007) (Figure 1B). In addition, a fault trench investigation on the northern OVF near Big Pine identified a younger penultimate event at 3.0–4.1 ka (Lee et al., 2001) (Figure 1B). Given the different event chronologies for the southern and northern OVF, Bacon and Pezzopane (2007) speculated that the ~3.5 ka

penultimate event on the northern OVF is likely associated with distributed faulting from the most recent event on the southern WMF at ~2–5 ka (dePolo et al., 1993)—based on small vertical offsets, timing coincidence, close proximity, and rupture setting (Figure 1B).

A model of temporal clustering of paleoearthquakes on parallel faults in the valley near Big Pine where the SNFF, OVF, and WMF are closely spaced and overlap may explain the apparent transient character of greater dextral slip rates on the northern OVF since ~80 ka documented by Kirby et al., (2008) (Figure 1B). The long-term vertical slip rate of ~0.24 ± 0.04 m/k.y. from offset alluvial fans and cinder cone on the Fish Springs normal fault splay of the OVF in the BPVF also indicates a two-fold increase in vertical slip rate since ~300 ka compared to the southern OVF (Martel et al., 1987; Zehfuss et al., 2001) (Figure 1B). The vertical slip rate of the Fish Springs fault splay is similar to the vertical slip rates of the SNFF and CFF in southern Owens Valley (Table 2), suggesting that a greater component of vertical slip is distributed on the northern OVF in the area. We propose that the apparent two- to three-fold increase in both normal and dextral slip can be explained by cumulative offsets from primary surface rupture on the OVF and distributed faulting and/or triggered slip from nearby adjacent faults, as well as possible extensional ground deformation within the BPVF associated with six episodes of volcanic eruptions between ~17 and 80 ka, and several more since ~300 ka (e.g., Martel et al., 1987; Blondes et al., 2008; Vazquez and Woolford, 2015). Therefore, the apparent transient behavior on the northern OVF since ~80 ka, may not be representative of the entire fault system, but a product of the seismo-tectonic and volcanic settings of central Owens Valley (e.g., Haddon et al., 2016).

9.4. Spatiotemporal Patterns of Slip Partitioning in Owens Valley

In south-central Owens Valley, transtension is accommodated by slip partitioning between two subparallel faults in the valley: the normal SNFF with a curvilinear map pattern (i.e., Independence fault or segment) and the linear and near-vertical, normal-oblique OVF (Zoback, 1989; Wesnousky and Jones, 1994; Wesnousky, 2005b; Le et al., 2007), whereas slip partitioning in Owens Lake basin is between five subparallel faults across a large step-over along the north-striking range-front of the Sierra Nevada (e.g., Carver, 1970; Slemmons et al., 2008) (Figures 1 and 2). Tectono-geomorphic evidence shows the distribution of slip across the lake basin is partitioned between normal faults including the SNFF (i.e., Olancha fault segment); COLF; OR-CFF; KF; and normal-oblique faults comprising the OVF and SIMF (B-B'; Figure 10). Deformation within Owens Valley has been interpreted to be either accommodated by oblique fault slip that is spatially partitioned into normal and dextral components within a single stress field (Wesnousky and Jones, 1994; Le et al., 2007) or by temporally partitioned slip into normal and dextral components within cyclic normal and strike-slip stress fields (Zoback, 1989; Bellier and Zoback, 1995). It is beyond the scope of our study to evaluate the two proposed hypotheses of slip partitioning in Owens Valley, but we provide geologic-based information for spatiotemporal changes of the distribution of faulting on the primary faults in Owen Lake basin.

The relative ground deformation between the tilted and faulted ~40 ka beach ridge and undeformed ~11–16 ka beach ridges demonstrate spatiotemporal patterns of slip partitioning between normal and oblique faulting in Owens Lake basin in the last ~40 k.y. The magnitude and similarity in subsidence rates of ~0.25 m/k.y. between the eastern

sector of Owens lake basin and the dip slip rates of the SNFF and CFF, suggest that extensional faulting and fault-block tilting were the primary mechanisms that accommodated subsidence in the eastern lake basin during the period ~40 to 16 ka (Figure 11A). The dominant slip vector during the latest period from ~16 ka to present, however, was associated primarily with normal-oblique faulting on the OVF and SIMF base on a lack of measurable subsidence and faulting in the eastern lake basin (Figure 11B). Historical and paleoseismic evidence support mostly strike-slip faulting in the lake basin and show that the last two large earthquakes on the OVF, including the A.D. 1872 event, and the last two moderate surface rupturing events on the SIMF occurred since ~12 ka (Bacon et al., 2005; Bacon and Pezzopane, 2007). Instrumental data also show a recent locus of post-A.D. 1872 earthquake dextral slip in the lake basin partitioned along the eastern margin of the OVF and OR-CFF graben. This slip partitioning is reflected as pure strike-slip faulting that occurred on the CFF segment during the A.D. 2009 Olancha earthquake swarm (Holzer et al., 2010) (Figure 3).

The tectono-geomorphic data from southern Owens Valley and lake basin provide evidence of spatiotemporal changes in slip partitioning between normal and strike-slip faulting (e.g., Zoback, 1989; Wesnousky and Jones, 1994). Although we demonstrated such changes in slip partitioning, the geologic and geodetic extension rates for the same area are within their uncertainties (Figure 9). In general, this implies that extension involving normal and normal-oblique faulting in Owens Lake basin has been constant during intervals of 10^1–10^4 yr. Furthermore, the new long-term vertical slip rates on the southern OVF from deformed ~160 ka shoreline features also support constant normal-oblique faulting in south-central Owens Valley during intervals up to 10^5 yr when

compared to the paleoseismic vertical slip rate derived over the past ~25 k.y. (Bacon and Pezzopane, 2007) and tectono-geomorphology of the OVF (Haddon et al., 2016).

9.4.1. Potential Effects of Slip Partitioning on Earthquake Cycles

There is a growing body of evidence of clustered strike-slip earthquake activity and transient slip during the Holocene on the Garlock fault (Dolan et al., 2016), on the southern Panamint Valley fault, north of the Garlock fault and east of Owens Valley (McAuliffe et al., 2013), and on Mojave faults in the ECSZ, south of the Garlock fault (e.g., Rockwell et al., 2000; Dawson et al., 2003; Dolan et al., 2007; Oskin et al., 2008; Ganev et al., 2010b; Pérouse and Wernicke, 2016) (Figure 1A). The paleoseismic records of the OVF and SIMF, however, indicate a lack of latest Quaternary temporal clustering of strike-slip earthquakes in central and southern Owens Valley. This implies elastic strain accumulation is released during moderate to large surface rupture events separated by long interseismic periods of 8–10 k.y. over the last two earthquake cycles (Bacon et al., 2005; Bacon and Pezzopane, 2007).

Coseismic stress perturbations cause visco-elastic relaxation of the lower crust and the upper mantle, contributing to time-dependent stress transfer onto nearby faults across variable timescales (e.g., Stein, 1999). These perturbations can either increase or decrease the stress field (e.g., Zoback, 1989; Malservisi et al., 2001; Oskin and Iriondo, 2004; Steacy et al., 2005; Verdecchia and Carena, 2016). Several studies in the ECSZ south of the Garlock fault have suggested that transient changes of the relative strength of regional fault systems may control spatiotemporal clustering of large earthquakes on closely spaced fault systems due to the effects of stress perturbations within the ductile

shear zone from strain hardening during tectonic loading and weakening during postseimic relaxation (Dolan et al., 2007, 2016; Oskin et al., 2008). Strain hardening may also occur from pinning of brittle fault tips against a kinematically incompatible intersecting fault, such as occurs where right-lateral faults of the ECSZ intersect with the left-lateral Garlock fault (Oskin et al., 2008) (Figure 1A).

We attribute the differences between the spatiotemporal behavior of strike-slip faults along the southeastern margin of the Sierra Nevada microplate (i.e., block) and in other structural domains of the ECSZ (e.g., Mojave block) to variations in the kinematics that control upper crustal deformation (Unruh et al., 2002; 2003; 2014). Dextral shear east of the Sierra Nevada microplate is accommodated by transtensional slip partitioning via three fault systems within prominent grabens north of the Garlock fault (Zoback, 1989; Wesnousky and Jones, 1994; Unruh et al., 2003), whereas dextral shear in the ECSZ is accommodated by up to six parallel strike-slip fault systems (e.g., Dixon and Xie, 2018) (Figure 1A). The paired SNFF and OVF system in central-southern Owens Valley is also nearest the margin of the southern Sierra Nevada microplate where faults along the eastern escarpment may extend to depths of 20–40 km (Martel et al., 2014) in areas of active seismogenic crustal thinning above upwelling of asthenosphere (Saleeby et al., 2013; Unruh et al., 2014). The seismo-tectonic setting of Owens Valley also differs from Panamint Valley and Death Valley, as well as areas of the central WLB northeast of Owens Valley that are outboard of the Sierra Nevada microplate. Consequently, dextral shear outboard of Owens Valley is accommodated much differently where faults have faster slip rates and evidence of multiple earthquakes (i.e., shorter recurrence) during the Holocene (Frankel et al., 2007, 2008; McAuliffe et al., 2013; Angster et al., 2019)

(Figure 1A). Although the paleoseismic records of faults outboard of the Sierra Nevada microplate imply an overall increased pattern of Holocene activity within the southern WLB, there has been a sequence of large-scale historical faulting events since the A.D. 1872 earthquake extending from the central WLB to the ECSZ (e.g., Wallace, 1984; Peltzer et al., 2001). Five of the historical fault ruptures occurred in grabens adjacent to the Sierra Nevada microplate and bounding the A.D 1872 fault trace. Collectively, the surface rupture lengths, including the A.D. 2019 M7.1 Ridgecrest earthquake, total nearly 70% of the ~335-km long eastern escarpment of the southern Sierra Nevada between the latitudes of the Long Valley caldera/northern Owens Valley and Garlock fault (USGS, 2016; GEER, 2019; Figure 1A).

The spatiotemporal patterns of elastic strain accumulation that is partitioned between the SNFF and OVF in Owens Valley are poorly understood because the paleoseismology of the SNFF is unknown. What we can infer from the paleoseismic evidence on the OVF is that strike-slip faulting events similar in size to the A.D. 1872 earthquake have not been clustered over the past ~20 k.y. (Bacon and Pezzopane, 2007). If long interseismic periods between large surface rupture events (~100 km long) are a typical pattern on the central and southern OVF it may explain the apparent constant slip rates over the past ~160 k.y. (e.g., Haddon et al., 2016). We hypothesize that the two-dimensional geometry between the west-dipping SNFF and vertical OVF forms a kinematically incompatible fault intersection at depth that may cause stress perturbations that effect the relative strength of the two faults, analogous to the intersection between the Garlock and ECSZ faults (e.g., Oskin et al., 2008). We also note that the northern and southern fault tips of the parallel segments of the SNFF and OVF end within the BPVF

and near the Coso volcanic center, respectively, which may also affect the overall stress distributions controlling fault strength by increased heat flow and dilation from magmatic intrusions during the late Pleistocene (e.g., Prejean et al., 2002) (Figure 1). The fault strength of the SNFF is considerably stronger (approximately two orders of magnitude) than the OVF under a single stress field, based on stress transformation laws (Jones and Wesnousky, 1992) and a simple physical model (Wesnousky and Jones, 1994; Le et al., 2007). This implies that the OVF has relatively greater potential in producing rupture events than the SNFF, and if so, the interseismic periods on the SNFF could be up to 10–20 k.y., which are typical of northern Basin and Range normal faults (Pérouse and Wernicke, 2016). Only paleoseismic data, however, can determine the duration of the latest interseismic periods on the SNFF. Nonetheless, the integration of paleoseismic and geologic records of fault behavior for closely spaced faults has potential for identifying the processes that might control the apparent transient changes in slip and rate at scales of 10^4–10^5 yr (e.g., Mueller, 2017).

10. CONCLUSIONS

New stratigraphic analysis, luminescence dating, and accurate elevations of a highstand beach ridge were used to measure ~9–10 m of ground deformation and derive slip rates on previously uncharacterized faults in Owens Lake basin. We attribute the magnitude of deformation to the cumulative effects of faulting, uniform tilting, and basin-wide subsidence since construction of the 40.0 ± 5.8 ka beach ridge. This contrasts with a lower suite of ~11–16 ka beach ridges that are not deformed by measurable tilting. The style of slip and magnitude of ground deformation in the lake basin suggest that both normal and dextral

slip interseismic periods have controlled the overall style of deformation across the valley between ~16 and 40 ka. In contrast, geologic and geomorphic data indicate dextral faulting on the OVF and SIMF has been dominant since ~16 ka. Normal-oblique slip on the southern OVF also has been constant during periods of up to 10^5 yr based on a vertical slip rates estimated from deformed shorelines and paleoseismic data. The total extension rate of 0.7 ± 0.2 mm/yr across primary faults in the lake basin is within error of contemporary geodetic estimates, suggesting that normal and dextral faulting in south-central Owens Valley also has been constant during intervals of at least 10^1–10^4 yr. Our approach in reconstructing water levels by accounting for differential fault-block motion provides information to characterize the distribution of transtensional faulting across a major releasing step-over in the WLB-ECSZ. The approach also can be used to correct lake-stage and overflow records for ground deformation on closely spaced faults to produce accurate input data for paleoclimate hydrologic models in the western U.S.

11. ACKNOWLEDGEMENTS

The authors acknowledge K. Adams for field discussions and assistance with luminescence sampling at the Centennial Flat study site. We thank R. Schumer for field assistance with GPS measurements and R. Kreidberg for editorial review. Discussion of GPS geodetic modeling of faults in Owens Valley with W. Hammond is also acknowledged. We thank M. Reheis and two *GSA Bulletin* anonymous reviewers for their comments and critiques that greatly improved the manuscript. Funding for this work was partially provided by U.S. Government Contract #N68936–09–D–0040, National Science

Foundation EAR #1252225, and Vice President for Research Office of the Desert Research Institute to S. Bacon.

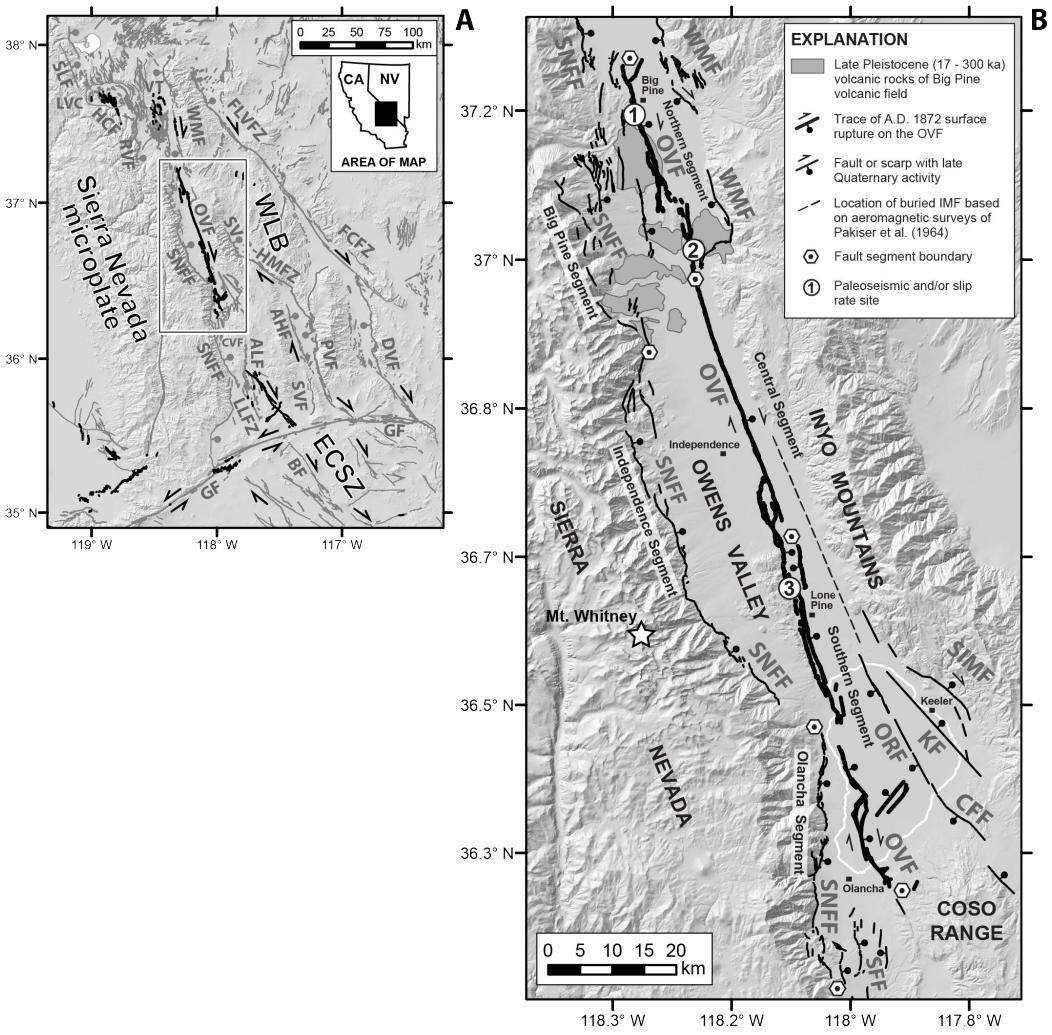

Figure 1. (A) Map of major Quaternary faults in the southern Walker Lane belt (WLB) along the southeastern margin of the Sierra Nevada microplate and Eastern California shear zone (ECSZ) in eastern California (modified after USGS, 2016). Faults shown in black are historical ruptures between A.D. 1872 and 2019. Faults (F) and fault zones (FZ): AHF – Ash Hill; BW – Blackwater; DV, Death Valley; FC, Furnace Creek; FLV – Fish Lake Valley; G – Garlock; HCF – Hilton Creek; LL – Little Lake; MLF – Mono Lake; OV – Owens Valley; PV – Panamint Valley; RV – Round Valley; SNF – Sierra Nevada Frontal; SIM – southern Inyo Mountains; SLF – Silver Lake; SV – Searles Valley; SV-HM, Saline Valley-Hunter Mountain; and WM – White Mountain. Volcanic features: CVF – Coso volcanic field; LVC – Long Valley Caldera; and VT – Volcanic tableland. (B) Map of primary faults and rocks of the Big Pine volcanic field in south-central Owens Valley. The A.D. 1872 Owens Valley fault rupture and fault segments of the OVF and SNFF are shown (modified from Bacon and Pezzopane, 2007). Faults (F): CF – Centennial Flat; K – Keeler; and SF – Sage Flat. Numbers show sites on OVF referred to in text of 1 – Kirby et al. (2008); 2 – Lee et al. (2001); and 3 – Bacon and Pezzopane (2007).

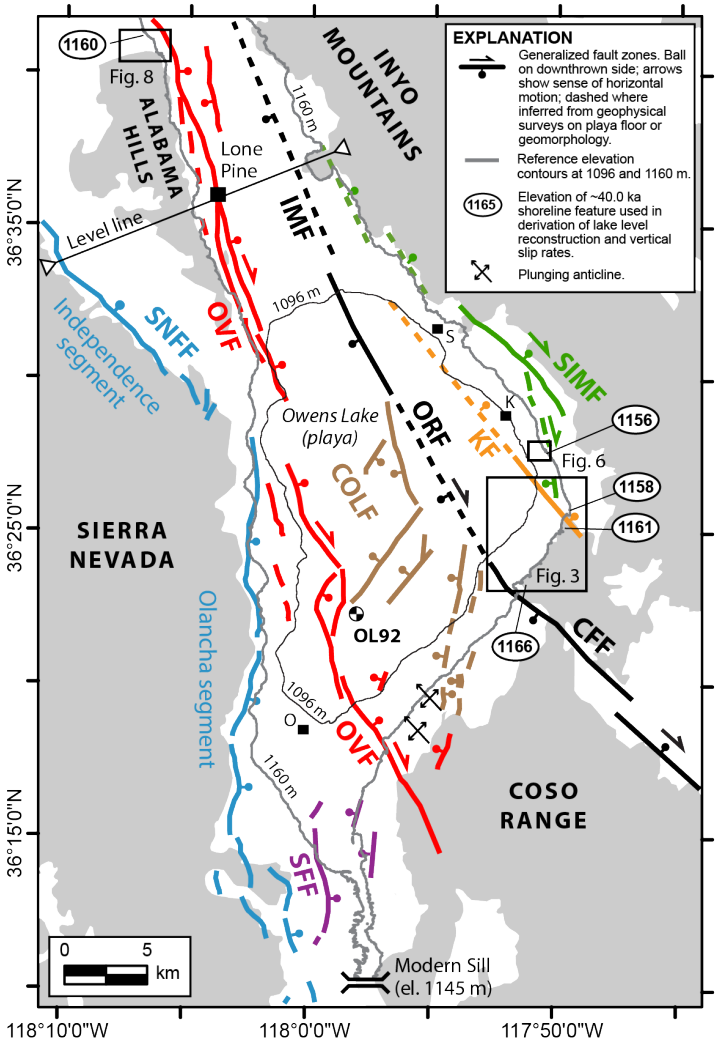

Figure 2. Map of primary faults in Owens Lake basin and elevations of deformed shoreline features (~1156 to 1166 m) used to estimate the magnitude of ground deformation and slip rates across faults in the lake basin. Faults are modified after Bacon et al. (2005) and Slemmons et al. (2008). Faults: CFF – Centennial Flat fault; COLF – Central Owens Lake fault; IMF – Inyo Mountain fault; KF – Keeler fault; ORF – Owens River fault; OVF – Owens Valley fault; SIMF – southern Inyo Mountains fault; and SNFF – Sierra Nevada Frontal fault. The location of the Sage Flat fault (SFF) after Jayko (2009) and Amos et al. (2013a) is also shown. Plunging anticlines from Frankel et al. (2008). Reference elevation contours at 1096 and 1160 m represent the margin of Owens Lake playa and the approximate location of ~40.0 ka shoreline features, respectively. Modern sill is also shown relative to the 1160 m elevation that defines the overflow channel of the basin. Sediment lake core OL92 of Smith and Bischoff (1997) is shown relative to the depocenter area of the lake basin. Approximate location of transect for repeat leveling surveys near Lone Pine of Savage and Lisowski (1980; 1995) is also shown. Lone K – town of Keeler; S – Swansea embayment; and O – town of Olancha.

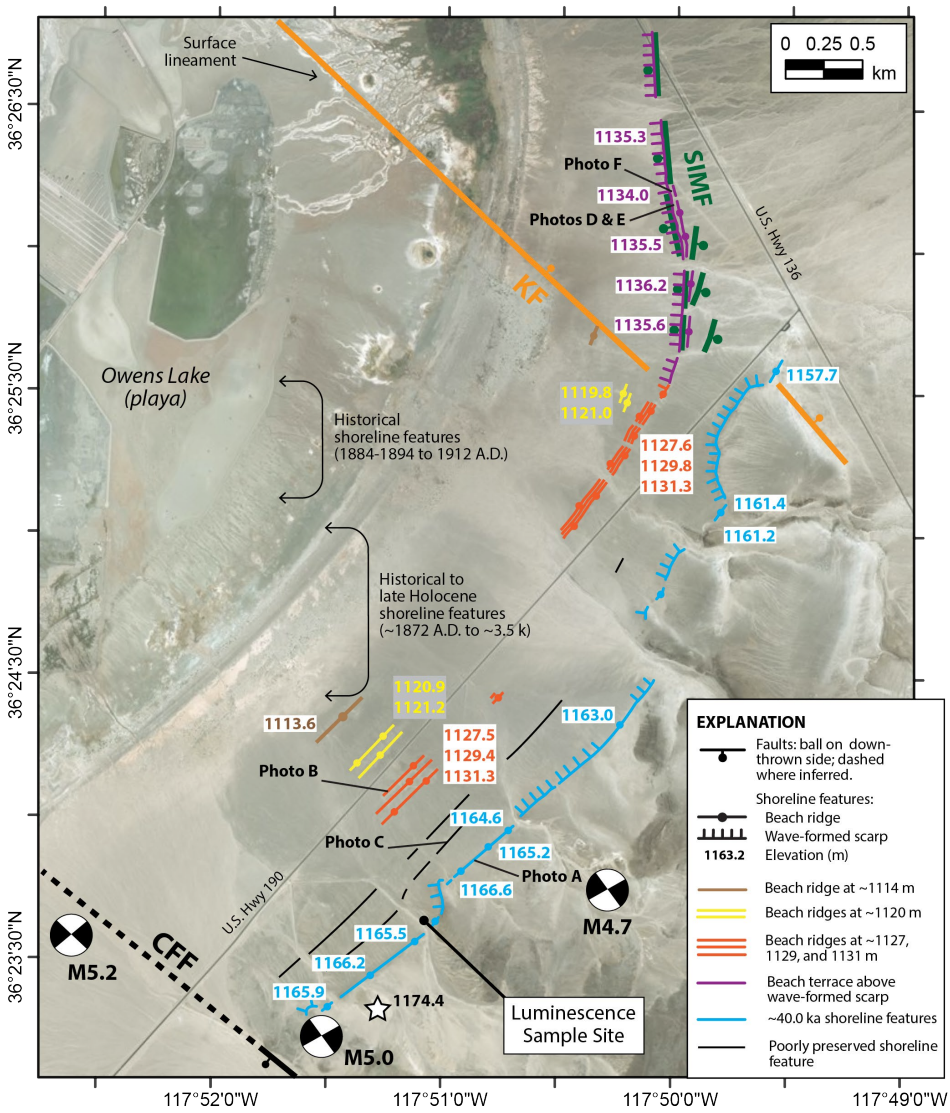

Figure 3. Map of the Centennial Flat study site showing the location of primary faults and elevations of shoreline features in the southeastern sector of Owens Lake basin (Figure 2). Faults: CFF – Centennial Flat fault; KF – Keeler Fault; and SIMF – Southern Inyo Mountains fault. Elevation of deformed highstand beach ridge at elevations ~1158 to 1167 m first characterized is shown. High-precision GPS measurements are shown color coded to match specific shoreline feature and presented in meters above mean sea level. The location of luminescence sampling within a natural wash exposure of the deformed beach ridge is also shown. The location and age of historical to late Holocene shorelines are from Bacon et al. (2018). Epicenters, magnitudes, and focal mechanisms of the A.D. 2009 Olancha earthquake swarm on the CFF are shown (Holzer et al., 2010). Sites of photographs of shoreline features referenced with letters on Figure 4 are also shown. Star shows location and corrected elevation of ^{36}Cl surface exposure sample site of ~160 ka tufa mound of Jayko and Bacon (2008).

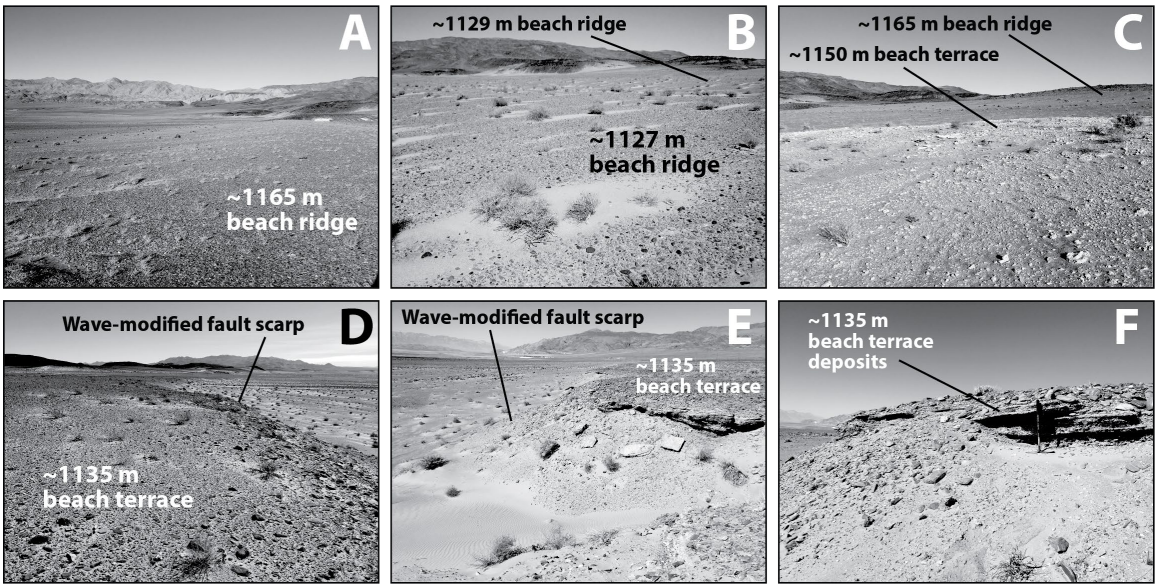

Figure 4. Photographs of shoreline features at the Centennial Flat study site (Figure 3): (A) highstand beach ridge at an elevation of ~1165 m, view to the northeast; (B) lower beach ridges at ~1127 and 1129 m, view to the southeast; (C) poorly preserved (relict) beach terrace with platy tufa, and location of ~1165 m highstand beach ridge in distance, view to the southeast; (D and E) wave-modified fault scarps of the southern Inyo Mountains fault and beach terrace at ~1135 m, views to the south and north, respectively; and (F) beach terrace deposits exposed in ephemeral wash at ~1135 m show lakeward dipping forest beds of well-sorted and well-rounded sand and gravel.

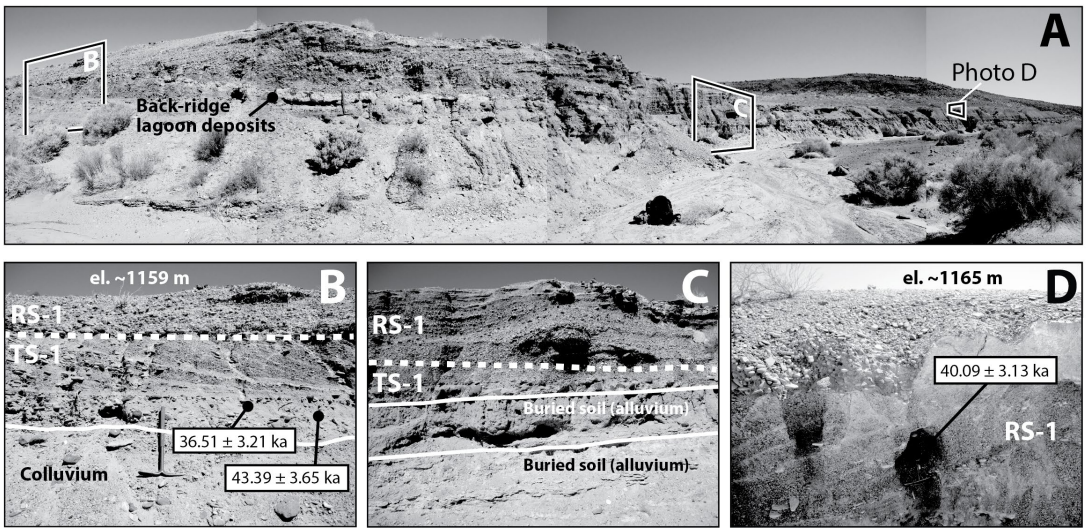

Figure 5. Photographs of natural wash exposure at the Centennial Flat study site (Figure 3): (A) continuous exposure of beach ridge and back-ridge lagoon deposits with backsets and forest beds underlain by alluvium with buried soils. Location of photographs B-D from site-specific areas are shown; (B) luminescence sample site and ages from the base of sand-rich beach ridge with backset beds and back-ridge lagoon facies of a transgressive sequence (TS-1). Stratigraphic section also shows a regressive sequence (RS-1) with forest beds defining one lake-level cycle at the site; (C) beach ridge sediment underlain by alluvium with buried soils. Contact between the shoreline and alluvial deposits is defined by a well-developed abrasion platform with a lag of gravel and cobbles; (D) luminescence sample site and age of sand-rich forest beds within regressive sequence (RS-1) of upper beach ridge at ~1165 m.

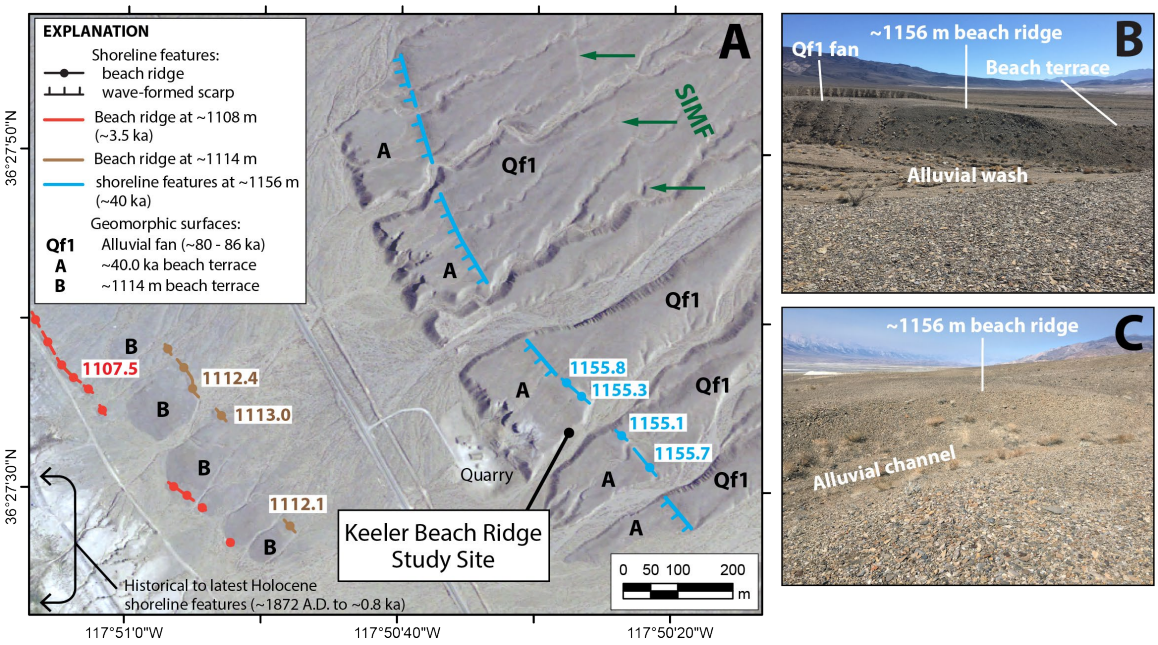

Figure 6. Imagery and photographs of shoreline features and fault lineaments near the Keeler beach ridge study site (Figure 2): (A) map showing shoreline features and location of GPS measurements. A preserved beach ridge at ~1156 m is shown in relation to prominent beach terraces, Qf1 fans, and short east-facing fault scarps of the southern Inyo Mountains fault (SIMF) (green arrows). The ~1156 m beach ridge is assigned a correlative ~40.0 ka age based on similar stratigraphic and surface characteristics, plus morpho-stratigraphic position with the Qf1 fan surface to other shoreline features at the Centennial Flat and Moffat Ranch study sites; (B) photograph of ~1156 m beach ridge in relation to Qf1 fan and beach terrace surfaces, view to the southeast; and (C) photograph of ~1156 m beach ridge crossed by a sinuous channel and presence of back-ridge depression. The location and age of historical to late Holocene (~3.5 ka) shorelines are from Bacon et al. (2018) and the location of the SIMF is from Bacon et al. (2005) and Jayko (2009).

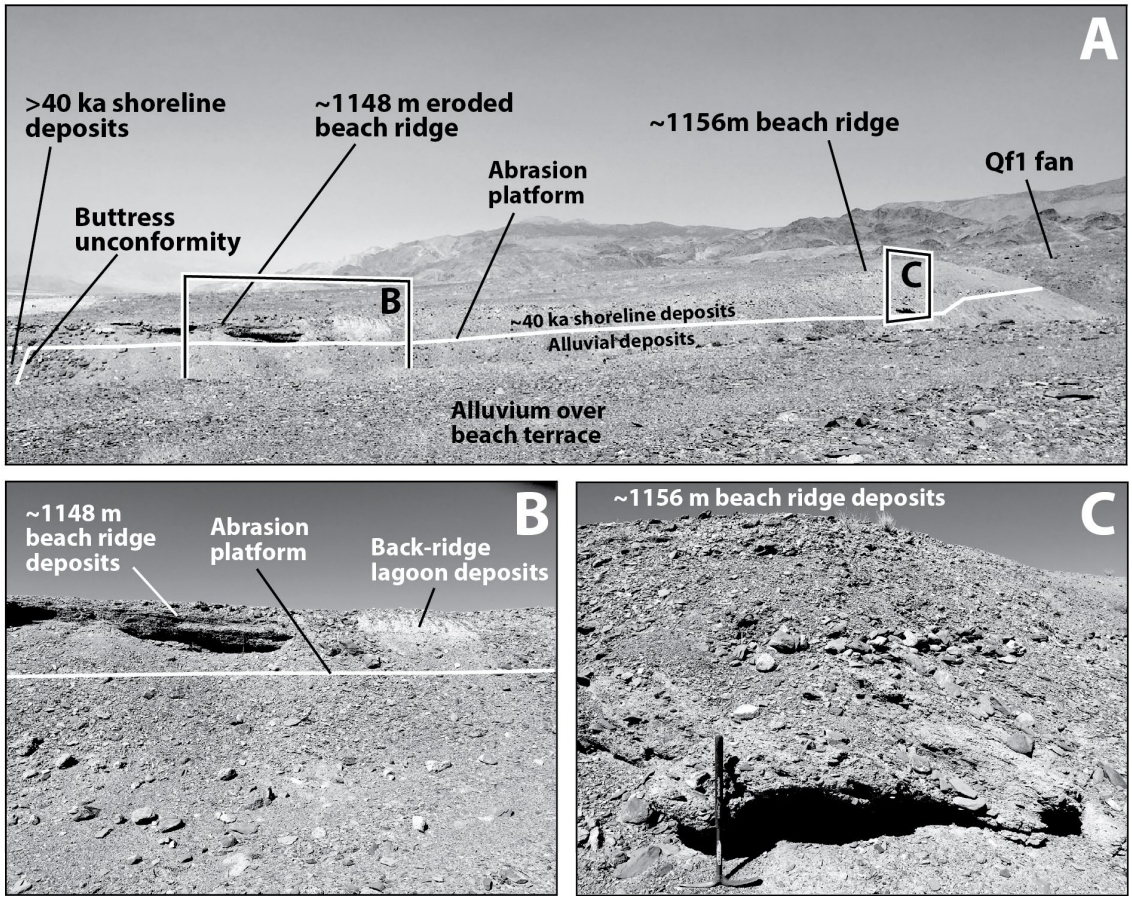

Figure 7. Photographs of natural wash exposure at the Keeler beach ridge site (Figure 6): (A) continuous exposure of ~40 ka beach ridge and back-ridge lagoon deposits with backsets and forest beds underlain by abrasion platform developed on older alluvium with buried soils, view to northwest. Approximate location of buttress unconformity between >40 ka shoreline deposits and older alluvium is also shown. Location of photographs B and C from site-specific areas are shown; (B) lower beach ridge and back-ridge lagoon deposits with backset beds at an elevation of ~1148 m; and (C) higher beach ridge deposits at an elevation of ~1156 m, pick for scale. Section contains a package of basal backset and upper forest beds that define a transgressive and regressive sequence related to one lake-level cycle at the site.

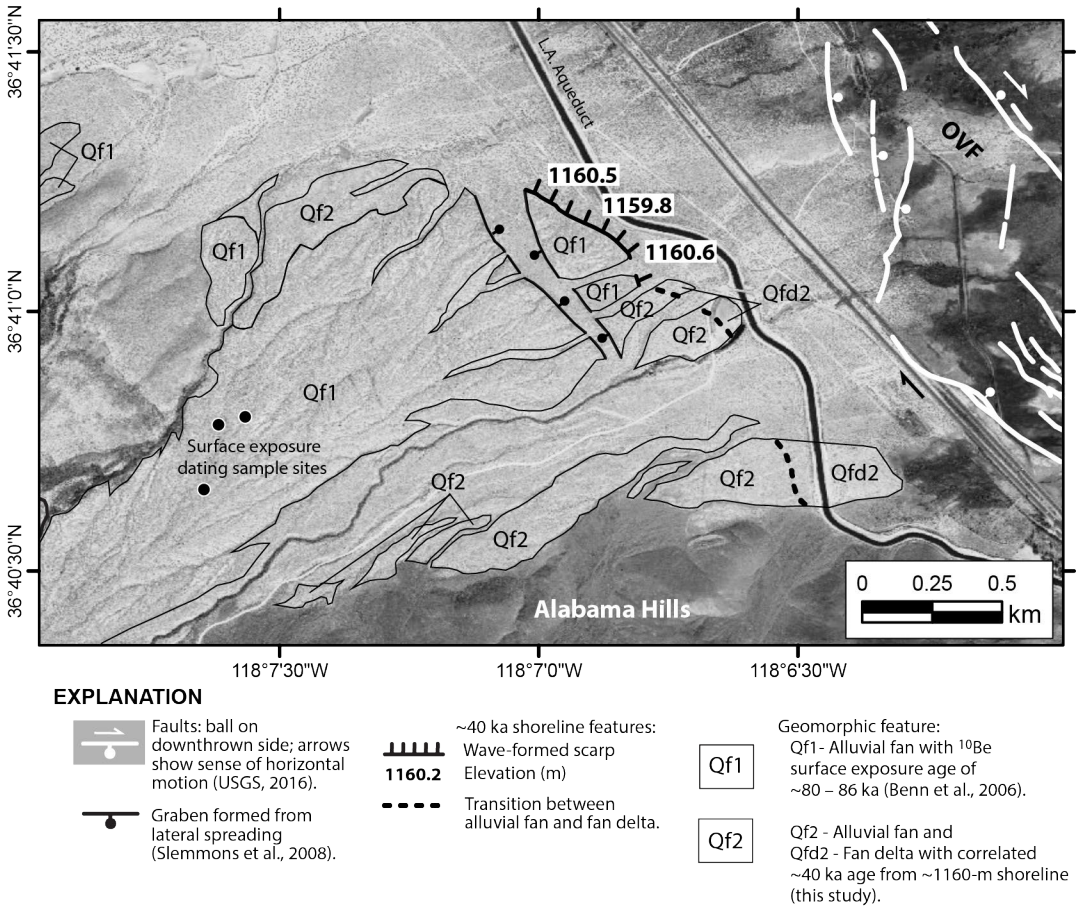

Figure 8. Map of Moffat Ranch Road site north of the Alabama Hills showing distribution of Qf1 and Qf2 alluvial fan and Qdf2 delta fan surfaces, lateral-spread graben, and shoreline features of Bacon et al. (2003) and Slemmons et al. (2008) (Figure 2). Surface exposure sample sites and age of ~80–86 ka for Qf1 surface are also shown (Benn et al., 2006). The Qf2 and Qdf2 surfaces are inset to the Qf1 surface and grade to the elevation of ~40 ka wave-formed scarps at ~1160 m. The location of GPS measurements are shown at the toe of wave-formed scarps. The Owens Valley fault (OVF) is shown east of the site (USGS, 2016). The Moffat Ranch Road site lies on the footwall of the OVF and the hanging wall of the Sierra Nevada Frontal fault (SNFF) to the west.

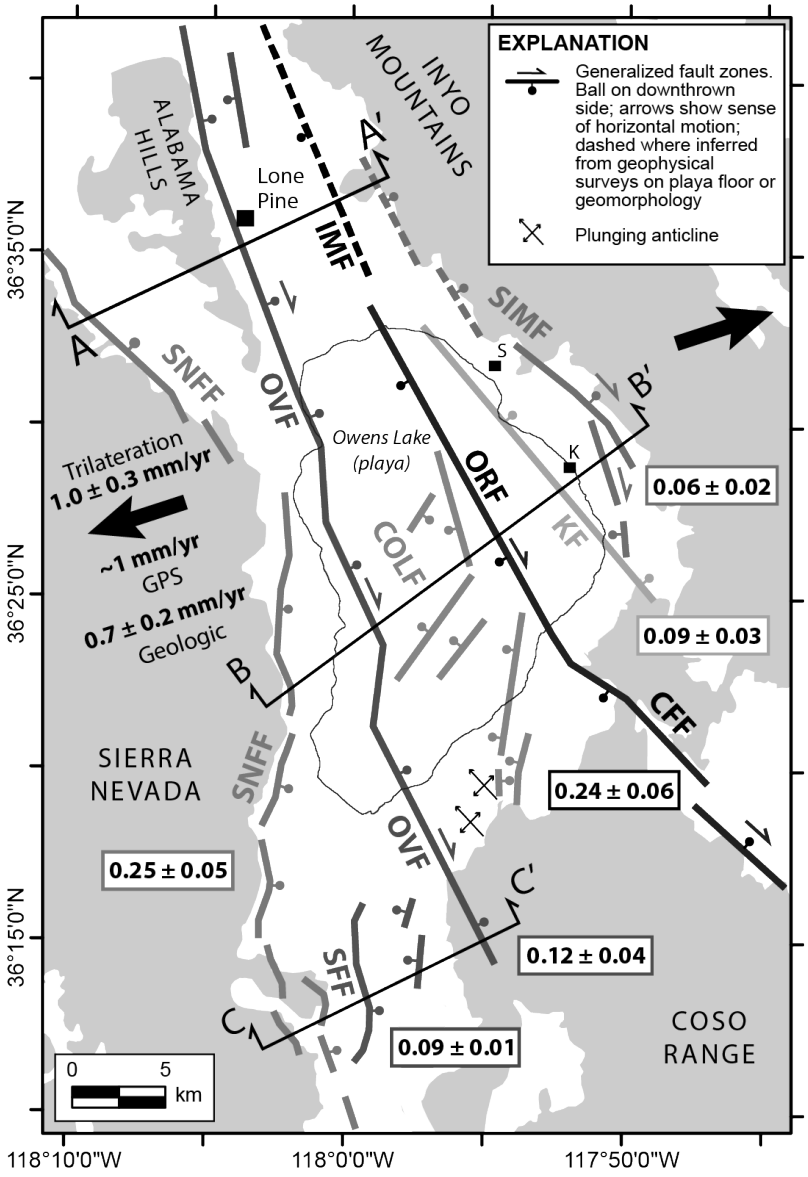

Figure 9. Generalize fault map of Owens Lake basin showing slip rates from this study and previous investigations. Faults: CFF – Centennial Flat fault; COLF – Central Owens Lake fault; IMF – Inyo Mountains fault; KF – Keeler fault; ORF – Owens River fault; OVF – Owens Valley fault; SFF – Sage Flat fault; SIMF – southern Inyo Mountains fault; and SNFF – Sierra Nevada Frontal fault. Extension direction at N72°E normal to Owens Valley is shown with geologic extension rate from this study and geodetic extension rates from trilateration networks in the valley (Savage and Lisowski, 1995) and global position system (GPS) arrays across northern Owens Valley (Ganev et al., 2010a). The location of transects A-A', B-B', and C-C' used in cross sections are shown. K – town of Keeler; and S – Swansea embayment.

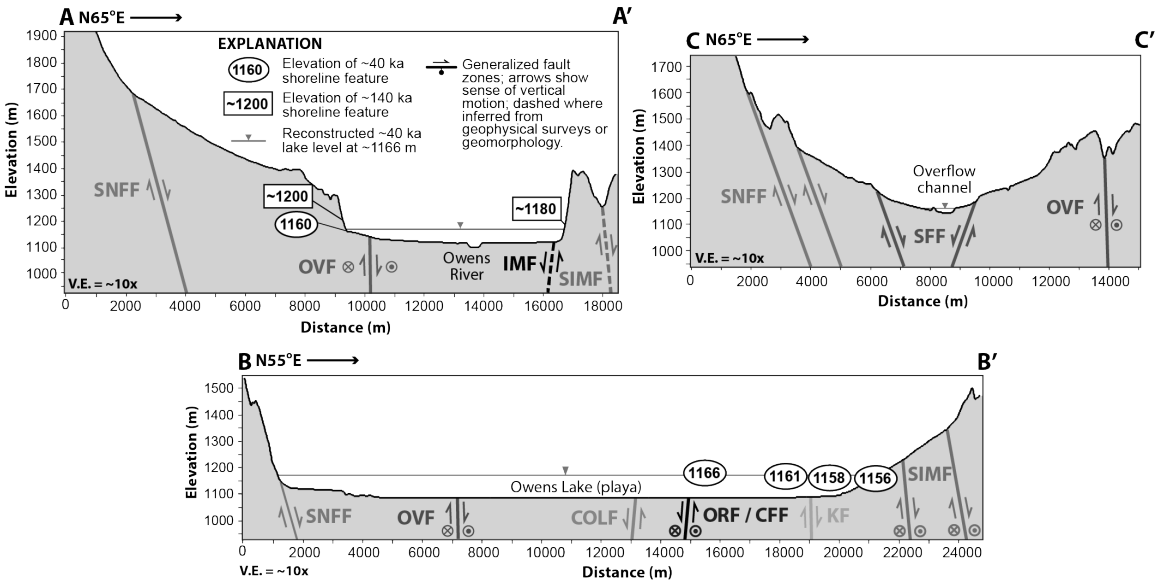

Figure 10. Cross sections showing orientation of faults and sense of slip, and reconstructed water levels of the ~40 highstand pluvial lake in Owens Lake basin. Faults: CFF – Centennial Flat fault; COLF – Central Owens Lake fault; IMF – Inyo Mountains fault; KF – Keeler fault; ORF – Owens River fault; OVF – Owens Valley fault; SFF – Sage Flat fault; SIMF – southern Inyo Mountains fault; and SNFF – Sierra Nevada Frontal fault. Fault orientations are apparent dip based on fault strike across transects. Inferred locations of KF and SIMF on transect A-A' are from Pakiser et al. (1964) and Bacon et al. (2005).

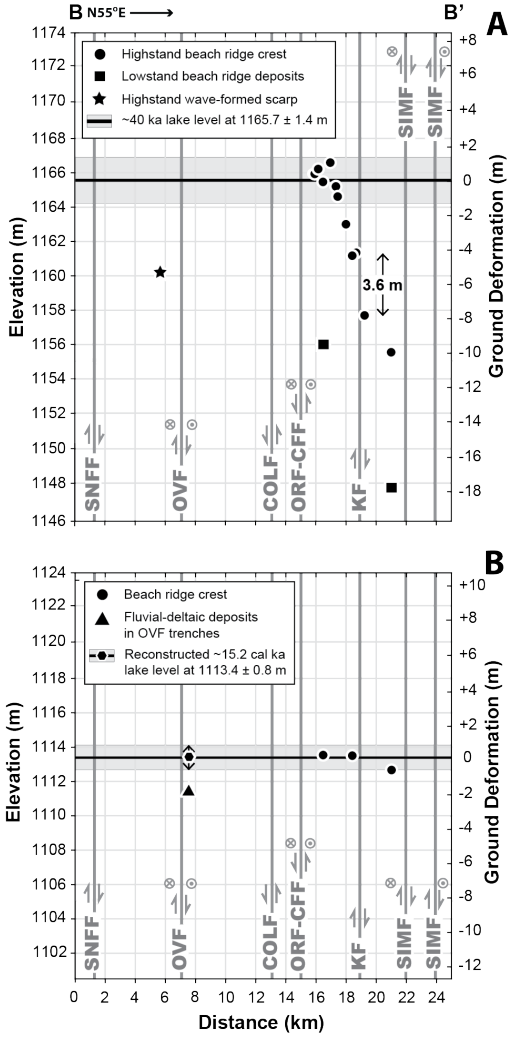

Figure 11. Plots showing the elevation of: (A) deformed ~40 ka shoreline features and lowstand beach ridge deposits and (B) ~15 cal kyr B.P. shorelines features and deformed fluvial-deltaic deposits. The elevation of shoreline features and deposits are projected onto transect B-B' and shown in relation to the generalized location of faults in Owens Lake basin (Figure 9). Magnitude of ground deformation shown is ~10 m subsidence relative to the ~40 ka reconstructed water level (i.e., paleohorizontal datum) and ~3.6 m fault separation on the KF of the ~40 ka beach ridge crests. The elevation and age of fluvial deltaic deposits on the hanging wall of the OVF are from paleoseismic fault trench data (Bacon and Pezzopane, 2007). Faults: CFF – Centennial Flat fault; COLF – Central Owens Lake fault; IMF – Inyo Mountains fault; KF – Keeler fault; ORF – Owens River fault; OVF – Owens Valley fault; SFF – Sage Flat fault; SIMF – southern Inyo Mountains fault; and SNFF – Sierra Nevada Frontal fault. Actual dips of faults are not shown. Vertical sense of slip is indicated by arrows. Lateral slip is indicated by crosses (away) and dots (towards). The elevation errors from GPS survey of shoreline features and deposits are less than width of symbols.

Table 1. Results of single-grain post-ir-rsl dating of fine sand from beach deposits of ~1160 m highstand shoreline in Owens Lake Basin.

Sample number	Depth (m)	Altitude (m)	N accepted (N analyzed)[a]	Over-dispersion (%)	D_b (Gy)[b]	U (ppm)[c]	Th (ppm)[c]	K (%)[c]	External beta dose rate wet (Gy/ka)	External gamma dose rate wet (Gy/ka)	Cosmic dose rate (Gy/ka)[d]	Total dose rate (Gy/ka)[e]	Age (ka)[f]
OLB001	2.3	1156	62 (1100)	46	124.06 ± 8.06	1.99	4.74	2.55	2.14	1.06	0.20	3.40 ± 0.20	36.51 ± 3.21
OLB002	2.5	1156	71 (1000)	41	149.89 ± 8.19	1.54	3.07	2.84	2.26	1.01	0.19	3.45 ± 0.22	43.39 ± 3.65
OLB003	1.8	1163	68 (900)	44	122.12 ± 7.07	2.80	5.38	1.93	1.81	1.03	0.21	3.05 ± 0.16	40.09 ± 3.13

Sample location: 36.395°N, -117.852E (OLB001 and OLB002); 36.394°N, -117.851E (OLB003).

[a] n is the number of D_e determinations accepted after screening; in parentheses are the total number of aliquots measured.

[b] The error shown on the burial dose, D_b, is the error modeled with the central age model (CAM) (Galbraith et al., 1999).

[c] U and Th samples were fused with lithium borate and measured with ICP-MS. K_2O was measured on bulk sample with ICP-AES and converted to % K.

[d] Cosmic dose rates (Gy/ka) are calculated according to Prescott and Hutton (1994).

[e] Dose rates (Gy/ka) were calculated using the conversion factors of Liritzis et al. (2013) and are shown rounded to two decimal places; ages were calculated using values prior to rounding; central values are given for dose rates and errors are incorporated into that given for the total dose rate. Water content of 2% ± 1% was used for all dose-rate calculations.

[f] Luminescence ages were calculated using DRACv1.2 (Durcan et al., 2015) and are expressed as thousands of years before 2015 and rounded to the nearest year. Error is 1 sigma.

Table 2. Summary of fault characteristics and dip slip and extension rates for Owens Lake Basin.

Fault zone	Strike (°)	Dip (°)	Vertical offset (m)	Dip-slip rate (m/k.y.)	Extension rate‡ (mm/yr)	Source
Keeler fault (KF)	N20W	85NE	3.6 ± 1.2†	0.09 ± 0.03†	0.08 ± 0.03	This study
Centennial Flat fault (CFF)	N30W	85SW	—	0.24 ± 0.06#	0.23 ± 0.06	This study
Southern Owens Valley fault (OVF)	N40W	85NE	—	0.12 ± 0.04	0.12 ± 0.04	Bacon and Pezzopane (2007)
Southern Sierra Nevada frontal fault (SNFF)	N4E	75E	—	0.25 ± 0.05	0.22 ± 0.04	Le et al. (2007)
Southern Inyo Mountains fault (SIMF)	N45W	80NE	—	0.06 ± 0.02	0.05 ± 0.02	Bacon et al. (2005)
SUM					0.7 ± 0.2	This study

†Vertical slip rate is calculated using vertical separation, dip of fault, and post-IR-IRSL mean age of 40.0 ± 5.8 for the Centennial Flat beach ridge.

#Assigned vertical slip rate that matches total subsidence along the eastern margin of lake basin in order to achieve negligible ground deformation of ~40 ka beach ridge on the footwall block of the CFF.

‡Extension rates are calculated using fault dip and strike, and resolved relative to N72°E direction as defined by geodetic trilateration networks in central and southern Owens Valley (Savage and Lisowski, 1995).

12. REFERENCES

Adams, K.D., and Wesnousky, S.G., 1998, Shoreline processes and the age of the Lake Lahontan highstand in the Jessup embayment, Nevada: Geological Society of America Bulletin, v. 110, p. 1318–1332.

Adams, K.D., Wesnousky, S.G., and Bills, B.G., 1999, Isostatic rebound, active faulting, and potential geomorphic effects in the Lake Lahontan basin, Nevada and California: Geological Society of America Bulletin, v. 111, p. 1739–1756.

Amos, C.B., Lutz, A.T., Jayko, A.S., Mahan, S.A., Burch Fisher, G., and Unruh, J.R., 2013a, Refining the southern extent of the 1872 Owens Valley earthquake rupture through paleoseismic investigations in the Haiwee Area, southeastern California: Bulletin of the Seismological Society of America, v. 103, p. 1022–1037.

Amos, C.B., Brownlee, S.J., Rood, D.H., Burch Fisher, G., Bürgmann, R., Renne, P.R., and Jayko, A.S., 2013b, Chronology of tectonic, geomorphic, and volcanic interactions and the tempo of fault slip near Little Lake, California: Geological Society of America Bulletin, v. 125, p. 1187–1202.

Angster, S.J., Wesnousky, S.G., Figueiredo. Owen, L.A., and Hammer, S.J., 2019, Late Quaternary slip rates for faults of the central Walker Lane (Nevada, USA): Spatiotemporal strain release in a strike-slip fault system: Geosphere, v. 15, p. 1460–1478.

Argus, D.F., and Gordon, R.G., 1991, Current Sierra Nevada-North America motion from very long baseline interferometry: Implications for the kinematics of the western United States: Geology, v. 19, p. 1085–1088.

Bacon, S.N., and Pezzopane, S.K., 2007, A 25,000-year record of earthquakes on the Owens Valley fault near Lone Pine, California: Implications for recurrence intervals, slip rates, and segmentation models: Geological Society of America Bulletin, v. 119, p. 823–847.

Bacon, S.N., Pezzopane, S.K., Burke, R.M., 2003, Paleoseismology on the Owens Valley fault and latest Quaternary stratigraphy in Owens Valley near Lone Pine, eastern California: U.S. Geological Survey, National Earthquake Hazards Reduction Program (NEHRP) Final Technical Report, 42 p. http://erp-web.er.usgs.gov/reports/abstract/2002/ni/02hqgr0003.pdf

Bacon, S.N., Jayko, A.S., and McGeehin, J.P., 2005, Holocene and latest Pleistocene oblique dextral faulting on the southern Inyo Mountains fault, Owens Lake basin, California: Bulletin of the Seismological Society of America, v. 95, p. 2472–2485.

Bacon, S.N., Burke, R.M., Pezzopane, S.K., and Jayko, A.S., 2006, Last glacial maximum and Holocene lake levels of Owens Lake, eastern California, USA: Quaternary Science Reviews, v. 25, p. 1264–1282.

Bacon, S.N., Lancaster, N., Stine, S., Rhodes, E.J., and McCarley Holder, G.A., 2018, A continuous 4000-year lake-level record of Owens Lake, south-central Sierra Nevada, California, USA: Quaternary Research, v. 90, p. 276–302.

Beanland, S., and Clark, M.M., 1994, The Owens Valley fault zone, eastern California, and surface rupture associated with the 1872 earthquake: U.S. Geological Survey Bulletin 1982, 29 p.

Bellier, O., and Zoback, M.L., 1995, Recent state of stress change in the Walker Lane zone, western Basin and Range Province, United States: Tectonics, v. 14, p. 564–593.

Benn, D.I., Owens, L.A., Finkel, R.C., and Clemmens, S., 2006, Pleistocene lake outburst floods and fan formation along the eastern Sierra Nevada, California: implications for the interpretation of intermontane lacustrine records: Quaternary Science Reviews, no. 25, p. 2729–2748.

Bennett, R.A., Davis, J.L., and Wernicke, B.P., 1999, Present-day pattern of Cordilleran deformation in the western United States: Geology, v. 27, no. 4, p. 371–374.

Bennett, R.A., Wernicke, B.P., Niemi, N.A., Friedrich, A.M., Davis, J.L., 2003, Contemporary strain rates in the northern Basin and Range province from GPS data: Tectonics, v. 22, doi:10.1029/2001TC001355.

Benson, L.V., Burdett, J.W., Kashgarian, M., Lund, S.P., Phillips, F.M., Rye, R.O., 1996. Climatic and hydrologic oscillations in the Owens Lake basin and adjacent Sierra Nevada, California: Science, v. 274, p. 746–748.

Benson, L., Burdett, J., Lund, S., Kashgarian, M., Mensing, S., 1997. Nearly synchronous climate change in the Northern Hemisphere during the last glacial termination: Nature, v. 388, p. 263–265.

Benson, L., Kashgarian, M., Rye, R., Lund, S., Paillet, F., Smoot, J., Kester, C., Mensing, S., Meko, D., Lindstrom, S., 2002. Holocene multidecadal and multicentennial droughts affecting northern California and Nevada: Quaternary Science Review, v. 21, p. 659–682.Berry, M.E., 1997, Geomorphic analysis of late Quaternary faulting on Hilton Creek, Round Valley and Coyote Warp faults, east-central Sierra Nevada, California, USA: Geomorphology, v. 20, p. 177–195.

Berry M.E., 1997, Geomorphic analysis of late Quaternary faulting on Hilton Creek, Round Valley and Coyote warp faults, east-central Sierra Nevada, California, USA: Geomorphology, v. 20, p. 177–195.

Bills, B.G., and May, G.M., 1987, Lake Bonneville: Constraints on lithospheric thickness and upper mantle viscosity from isostatic warping of Bonneville, Provo and Gilbert stage shorelines: Journal of Geophysical Research, v. 92, p. 11,493–11,508.

Bills, B.G., Currey, D.R., and Marshall, G.A., 1994, Viscosity estimates for the crust and upper mantle from patterns of lacustrine shoreline deformation in the eastern Great Basin: Journal of Geophysical Research, v. 99, p. 22,059–22,086.

Bills, B.G., Adams, K.D., and Wesnousky, S.G., 2007, Viscosity structure of the crust and upper mantle in western Nevada from isostatic rebound patterns of the late Pleistocene Lake Lahontan high shoreline: Journal of Geophysical Research Solid Earth, v. 112, p. 1–18.

Bischoff, J.L., and Cummins, K., 2001, Wisconsin glaciation of the Sierra Nevada (79,000-15,000 yr B.P.) as recorded by rock flour in sediments of Owens Lake, California: Quaternary Research, v. 55, p. 14–24.

Bischoff, J.L., Stine, S., Rosenbauer, R.J., Fitzpatrick, J.A., Stafford Jr., T.W., 1993, Ikaite precipitation by mixing of shoreline springs and lake water, Mono Lake, California, USA: Geochimica et Cosmochimica Acta, v. 57, p. 3855–3865.

Blondes, M.S., Reiners, P.W., Ducea, M.N., Singer, B.S., and Chesley, J., 2008, Temporal–compositional trends over short and long time-scales in the basalts of the Big Pine Volcanic Field, California: Earth and Planetary Science Letters, v. 269, p. 140–154.

Carver, G.A., 1970, Quaternary tectonism and surface faulting in Owens Lake basin, California: Reno, University of Nevada, MacKay School of Mines Technical Report AT2, 103 p.

Caskey, S.J., Bell, J.W., Ramelli, A.R., and Wesnousky, S.G., 2004, Historic surface faulting and paleoseismicity in the area of the 1954 Rainbow Mountain-Stillwater earthquake sequence, central Nevada: Bulletin of the Seismological Society of America, v. 94, p. 1255–1275.

Chen, C.Y., and Maloof, A.C., 2017, Revisiting the deformed high shoreline of Lake Bonneville: Quaternary Science Reviews, v. 159, p. 169–189.

Crittenden, M., 1963, New data on the isostatic deformation of Lake Bonneville: U.S. Geological Survey Professional Paper 454.

Clark, D.H., and Gillespie, A.R., 1997, Timing and significance of late-glacial and Holocene cirque glaciation in the Sierra Nevada, California: Quaternary International, v. 38/39, p. 21–38.

Currey, D.R., 1982. Lake Bonneville: selected features of relevance to neotectonic Analysis. U.S. Geological Survey Open-File Report 82-1070.

Currey, D.R., and Sack, D., 2009, Hemiarid Lake Basins: Geomorphic Patterns. In: Parsons, A.J., Abrahams, A.D. (Eds.), Geomorphology of Desert Environments. Springer, Netherlands, pp. 489–514.

Dawson, T.E., McGill, S.F., and Rockwell, T.K., 2003, Irregular recurrence of paleoearthquakes along the central Garlock fault near El Paso Peaks, California: Journal of Geophysical Research, v. 108, p. 2356–2385.

dePolo, C.M., Clark, D.G., Slemmons, D.B., and Ramelli, A.R., 1991, Historic surface faulting in the Basin and Range Province, western North America: Implications for fault segmentation: Journal of Structural Geology, v. 13, p. 123–136.

dePolo, C.M., Pippen, W.A., and Johnson, P.A., 1993, Contemporary tectonics, seismicity, and potential earthquake sources in the White Mountain seismic gap, west-central Nevada and east-central California, USA: Tectonophysics, v. 225, p. 271–299.

Dixon, T.H., Robaudo, S., Lee, J., and Reheis, M.C., 1995, Constraints on present day Basin and Range deformation from space geodesy: Tectonics, v. 14, p. 755–772.

Dixon, T. H., Miller, M., Farina, F., Wang, H., Johnson, J., 2000, Present-day motion of the Sierra Nevada block and some tectonic implications for the Basin and Range province, North American Cordillera: Tectonics, v. 19, p. 1–24.

Dixon, T.H., Norabuena, E., and Hotaling, L., 2003, Paleoseismology and global positioning system: Earthquake-cycle effects and geodetic versus geologic fault slip rates in the Eastern California shear zone: Geology, v. 31, p. 55–58.

Dixon, T.H., and Xie, S., 2018, A kinematic model for the evolution of the Eastern California Shear Zone and Garlock Fault, Mojave Desert, California: Earth and Planetary Science Letters, v. 494, p. 60–68.

Dokka, R.K., and Travis, C.J., 1990, The role of the Eastern California shear zone in accommodating Pacific-North American plate motion: Geophysical Research Letters, v. 17, p. 1323–1326.

Dolan, J.F., Bowman, D.D., and Sammis, C.G., 2007, Long-range and long-term fault interactions in southern California: Geology, v. 35, p. 855–858.

Dolan, J.F., McAuliffe, L.J., Rhodes, E.J., McGill, S.F., Zinke, R., 2016. Extreme multi-millennial slip rate variations on the Garlock fault, California: Strain super-cycles, potentially time-variable fault strength, and implications for system-level earthquake occurrence: Earth and Planetary Science Letters, v. 446, p. 123–136.

Dreger, D.S., Tkalčič, H., and Johnston, M., 2000, Dilational processes accompanying earthquakes in the Long Valley Caldera: Science, v. 288, p. 122–125.

Durcan, J.A., King, G.E., Duller, G.A.T., 2015, DRAC: Dose rate and age calculator for trapped charge dating: Quaternary Geochronology, v. 28, p. 54–61.

Einsele, G., 2000, Sedimentary Basins: Evolution, Facies, and Sediment Budget (2nd edition): New York, Springer-Verlag, 804 p.

Ferrill, D.A., Morris, A.P., McGinnis, R.N., Smart, K.J., Watson-Morris, M.J., and Wigginton, S.S., 2016, Observations on normal-fault scarp morphology and fault system evolution of the Bishop Tuff in the Volcanic Tableland, Owens Valley, California, U.S.A.: Lithosphere, v. 8, p. 238–253.

Frankel, K.L., Brantley, K.S., Dolan, J.F., Finkel, R.C., Klinger, R.E., Knott, J.R., Machette, M.N., Owen, L.A., Phillips, F.M., Slate, J.L., and Wernicke, B.P., 2007, Cosmogenic 10Be and 36Cl geochronology of offset alluvial fans along the northern Death Valley fault zone: Implications for transient strain in the eastern California shear zone: Journal of Geophysical Research, v. 112, B06407.

Frankel, K.L., Glazner, A.F., Kirby, E., Monastero, F.C., Strane, M.D., Oskin, M.E., Unruh, J.R., Walker, J.D., Anandakrishnan, S., Bartley, J.M., Coleman, D.S., Dolan, J.F., Finkel, R.C., Greene, D., Kylander-Clark, A., Morrero, S., Owen,

L.A., and Phillips, F., 2008, Active tectonics in the eastern California shear zone, *in* Duebendorfer, E.M., and Smith, E.I., eds., Field Guide to Plutons, Volcanoes, Faults, Reefs, Dinosaurs, and Possible Glaciation in Selected Areas of Arizona, California, and Nevada: Geological Society of America Field Guide 11, p. 43–81.

Galbraith, R.F., Roberts, R.G., Laslett, G.M., Yoshida, H., Olley, J.M., 1999, Optical dating of single grains of quartz from Jinmium rock shelter, northern Australia. Part I: experimental design and statistical models: Archaeometry, v. 41, p. 339–364.

Gale, H.S., 1914, Salines in the Owens, Searles, and Panamint basins, southeastern California. U.S. Geology Survey Bulletin 580-L, p. 251–323.

Gan, W., Svarc, J.L., Savage, J.C., and Prescott, W.H., 2000, Strain accumulation across the Eastern California Shear Zone at latitude 36°30'N: Journal of Geophysical Research, v. 105, p. 16229–16236.

Ganev, P.N., Dolan, J.F., Frankel, K.L., and Finkel, R.C., 2010a, Rates of extension along the Fish Lake Valley fault and transtensional deformation in the Eastern California shear zone-Walker Lane belt: Lithosphere, v. 2, p. 33–49.

Ganev, P.N., Dolan, J.F., Blisniuk, K., Oskin, M., and Owen, L.A., 2010b, Paleoseismologic evidence for multiple Holocene earthquakes on the Calico fault: Implications for earthquake clustering in the Eastern California shear zone: Lithosphere, v. 2, p. 287–298.

GEER [Geotechnical Extreme Event Reconnaissance], 2019. Preliminary report on the engineering and geological effects of the July 2019 Ridgecrest earthquake sequence, p. 77.

Gillespie, A.R., and Clark, D., 2011, Glaciations in the Sierra Nevada, California, USA: Developments in Quaternary Science, v. 15, p. 447–462.

Haddon, E.K., Amos, C.B., Zielke, O., Jayko, A.S., Bürgmann, R., 2016, Surface slip during large Owens Valley earthquakes: Geochemical, Geophysical, Geosystems, v. 17, p. 2239–2269.

Hauksson, E., Hutton, K., Kanamori, H., Jones, L., Mori, J., Hough, S., and Roquemore, G., 1995, Preliminary report on the 1995 Ridgecrest earthquake sequence in eastern California: Seismological Research Letters, v. 66 p. 54–60.Hampel, A., and Hetzel, R., 2006, Response of normal faults to glacial-interglacial fluctuations

of ice and water masses on Earth's surface: Journal of Geophysical Research, v. 111, p. B06406, doi:10.1029/2005JB004124.

Hildreth, W., and Fierstein, J., 2016, Long Valley Caldera lake and reincision of Owens River Gorge: U.S. Geological Survey Scientific Investigations Report 2016–5120, 63 p.

Hollett, K.J., Danskin, W.R., McCafferey, W.F., Walti, C.L., 1991, Geology and water resources of Owens Valley, California. U.S. Geological Survey Water-Supply Paper 2370-B, 77 p.

Holzer, T.L., Jayko, A.S., Hauksson, E., Fletcher, J.P.B., Noce, T.E., Bennett, M.J., Dietel, C.M., and Hudnut, K.W., 2010, Liquefaction caused by the 2009 Olancha, California (USA), M5.2 earthquake: Engineering Geology, v. 116, p. 184–188.

Hopkins, M.C., and Dawers, N.H., 2016, Vertical deformation of lacustrine shorelines along breached relay ramps, Catlow Valley fault, southeastern Oregon, USA: Tectonophysics, v. 674, p. 89–100.

Hough, S.E., and K. Hutton, 2008, Revisiting the 1872 Owens Valley, California, earthquake: Bulletin Seismological Society of America, v. 98, p. 931–949.

Jayko, A.S., 2009, Surficial geologic map of the Darwin Hills 30' x 60' quadrangle, Inyo County, California: U.S. Geological Survey Scientific Investigations Map 3040, 20 p. pamphlet, 2 plates, scale 1:100,000.

Jayko, A.S. and Bacon, S.N., 2008, Late Quaternary MIS 6-8 shoreline features of pluvial Owens Lake, Owens Valley, eastern California, In: Reheis, M.C., Hershler, R., and Miller, D.M., eds., Late Cenozoic Drainage History of the Southwestern Great Basin and Lower Colorado River Region: Geologic and Biotic Perspectives: Geological Society of America Special Paper 439, p. 185–206.

Jayko, A.S., Forester, R.M., Kaufman, D.S., Phillips, F.M., Yount, J.C., McGeehin, J., Mahan, S.A., 2008, Late Pleistocene lakes and wetlands, Panamint Valley, Inyo County, California. In: Reheis, M.C., Hershler, R., Miller, D.M., eds., Late Cenozoic Drainage History of the Southwestern Great Basin and Lower Colorado River Region: Geologic and biotic perspectives, Geological Society of America Special Paper 439, p. 151–184.Jellinek, A.M., Manga, M., and Saar, M.O., 2004, Did melting glaciers cause volcanic eruptions in eastern California? Probing the mechanics of dike formation: Journal of Geophysical Research, v. 109, B09206, doi:10.1029/2004JB002978.

Jha, S., 2010, Block kinematics and slip rates in the southern Walker Lane estimated from GPS data: Unpublished M.S. Thesis, University of Nevada, Reno, 51 pp.

Jones, C.H., and Wesnousky, S.G., 1992, Variations in strength and slip rate along the San Andreas Fault system: Science, v. 256, p. 83–86.Karow, T., and Hampel, A., 2010, Slip rate variations on faults in the Basin-and-Range Province caused by regression of Late Pleistocene Lake Bonneville and Lake Lahontan: International Journal of Earth Science, v. 99, p. 1941–1953.

Kirby, E., Burbank, D. W., Reheis, M., and Phillips, F., 2006, Temporal variations in slip rate of the White Mountain fault zone, eastern California: Earth Planetary Science Letters, v. 248, p. 168–185, doi:10.1016/j.epsl.2006.05.026.

Kirby, E., Anandakrishnan, S., Phillips, F., and Marrero, S., 2008, Late Pleistocene slip rate along the Owens Valley fault, eastern California: Geophysical Research Letters, v. 35, L01304, doi:10.1029/2007GL031970.

Knott, J.R., Tinsley, J.C. III, and Wells, S.G., 2002, Are the benches at Mormon Point, Death Valley California, USA, scarps or strandlines?: Quaternary Research, v. 58, p. 352–360.

Koehler, P.A., Anderson, R.S., 1994, Full-Glacial shoreline vegetation during the maximum highstand at Owens Lake, California: Great Basin Naturalist, v. 54, p. 142–149.

Koseluk, R.A., and Bischke, R.E., 1981, An elastic rebound model for normal fault earthquakes: Journal of Geophysical Research, n. 86, p. 1081–1090.

Kutterolf, S., Schindlebeck, J.C., Jegen, M., Freundt, A., and Straub, S.M., 2019, Milankovitch frequencies in tephra records at volcanic arcs: The relation of kyr-scale cyclic variations in volcanism to global climate changes: Quaternary Science Reviews, v. 204, p. 1–16.

Le, K., Lee, J., Owen, L.A., and Finkel, R., 2007, Late Quaternary slip rates along the Sierra Nevada frontal fault zone, California: Evidence for slip partitioning across the western margin of the Eastern California shear zone/Basin and Range Province: Geological Society of America Bulletin, v. 119, p. 240–256.

Lee, J., Spencer, J., and Owen, L., 2001, Holocene slip rates along the Owens Valley fault, California: Implications for the recent evolution of the Eastern California shear zone: Geology, v. 29, p. 819–822.

Lee, J., Stockli, D.F., Owen, L.A., Finkel, R.C., and Kislitsyn, R., 2009, Exhumation of the Inyo Mountains, California: Implications for the timing of extension along the western boundary of the Basin and Range Province and distribution of dextral fault slip rates across the eastern California shear zone: Tectonics, v. 28, TC1001, doi:10.1029/2008TC002295.

Lettis, W.R., and Kelson, K.I., 2000, Applying geochronology in paleoseismology, in Noller, J.S., Sowers, J.M., and Lettis, W.R., eds., Quaternary Geochronology: Methods and Applications: AGU Reference Shelf Volume 4: Washington D.C., American Geophysical Union, p. 479–496.

Li, H., Bischoff, J.L., Ku, T., Lund, S.P., Stott, L.D., 2000, Climate variability in east-central California during the past 1000 years reflected by high-resolution geochemical and isotopic records from Owens Lake sediments. Quaternary Research, v. 54, p. 187–197.

Liritzis, I., Stamoulis, K., Papachristodoulou, C., Ioannides, K., 2013, A re-evaluation of radiation dose-rate conversion factors: Mediterranean Archaeology and Archaeometry, v. 13, p. 1–15.

Litwin, R.J., Smoot, J.P., Durika, N.J., and Smith, G.I., 1999, Calibrating Late Quaternary terrestrial climate signals: radiometrically dated pollen evidence from the southern Sierra Nevada, USA: Quaternary Science Reviews, v. 18, p. 1151–1171.

Locke, W.W., and Meyer, G.A., 1994, A 12,000-year record of vertical deformation across the Yellowstone caldera margin: The shorelines of Yellowstone Lake: Journal of Geophysical Research: Solid Earth, v. 99, p. 20,079–20,094.

Lubetkin, L.K.C., and Clark, M.M., 1988, Late Quaternary activity along the Lone Pine fault, eastern California: Geological Society of America Bulletin, v. 100, p. 755–766.

Machette, M.N., Personius, S.F., Nelson, A.R., Schwartz, D.P., and Lund, W.R., 1991, The Wasatch fault zone, Utah, segmentation and history of Holocene earthquakes: Journal of Structural Geology, v. 13, p. 137–149.

Malservisi, R., Furlong, K.P., and Dixon, T.H., 2001, Influence of the earthquake cycle and lithospheric rheology on the dynamics of the Eastern California shear zone: Geophysical Research Letters, v. 28, p. 2731–2734, doi: 10.1029/2001GL013311.

Martel, S.J., Harrison, T.M., and Gillespie, A.R., 1987, Late Quaternary vertical displacement rate across the Fish Springs fault, Owens Valley fault zone, California: Quaternary Research, v. 27, p. 113–129.

Martel, S.J., Stock, G.M., and Ito, G., 2014, Mechanics of relative and absolute displacements across normal faults and implications for uplift and subsidence along the eastern escarpment of the Sierra Nevada, California; Geosphere, v. 10, p. 243–263.

McAuliffe, L.J., Dolan, J.F., Kirby, E., Rollins, C., Haravitch, B., Alm, S., and Rittenour, T.M., 2013. Paleoseismology of the southern Panamint Valley fault: Implications for regional earthquake occurrence and seismic hazard in southern California: Journal of Geophyscial Research: Solid Earth, v. 118, p. 5126–5146.

McCaffrey, R., 2005, Block kinematics of the Pacific–North America plate boundary in the southwestern United States from inversion of GPS, seismological, and geologic data: Journal of Geophysical Research, v. 110, B07401–B07427.

McCalpin, J.P., 1996, Application of paleoseismic data to seismic hazard assessment and neotectonic research, in McCalpin, J.P., ed., Paleoseismology: International Geophysics Series Volume 62: New York, Academic Press, p. 439–493.

McClusky, S.C., Bjornstad, S.C., Hager, B.H., King, R.W., Meade, B.J., Miller, M.M., Monastero, F.C., and Souter B.J., 2001, Present day kinematics of the Eastern California Shear Zone from a geodetically constrained block model: Geophysical Research Letters, v. 28, p. 3369–3372.

Mifflin, M.D., and Wheat, M.M., 1979, Pluvial lakes and estimated pluvial climates of Nevada: Nevada Bureau of Mines and Geology Bulletin 94, p. 57.Miller, M.M., Johnson, D.J., Dixon, T.H., and Dokka, R.K., 2001, Refined kinematics of the Eastern California Shear Zone from GPS observations, 1993-1994: Journal of Geophysical Research, v. 106, p. 2245–2263.

Monastero, F.C., Miller, J.S., Unruh, J.R., Adams, M.C., and Richards-Dinger, K., 2005, The Coso geothermal field: A nascent metamorphic core complex: Geological Society of America Bulletin, v. 117, p. 1534–1553, doi: 10.1130/B25600.1.

Moore, J.G., and Moring B.C., 2013, Rangewide glaciation in the Sierra Nevada, California: Geosphere, v. 9, p. 1804–1818.

Mueller, K., 2017, Variation in slip rates on active faults: Natural growth or stress transients?: Geology, v. 45, p. 287–288.

Murray, A.S., and Wintle, A.G. 2000, Luminescence dating of quartz using an improved single-aliquot regenerative-dose protocol: Radiation Measurements, v. 32, p. 57–73.

Murray, A.S., and Wintle, A.G., 2003, The single-aliquot regenerative dose protocol: potential for improvements in reliability: Radiation Measurements, v. 37, p. 377–381.

Nagorsen-Rinke, S., Lee, J., and Calvert, A., 2013, Pliocene sinistral slip across the Adobe Hills, eastern California–western Nevada: Kinematics of fault slip transfer across the Mina deflection: Geosphere, v. 9, p. 37–53.

Neponset Geophysical Company and Aquila Geosciences, Inc., 1997, Final Report Phase 3 and Phase 4 seismic program, Owens Lake, Inyo County, California: Prepared for the Great Basin Unified Air Pollution Control District, Bishop, California, 55 p.

Oldow, J.S., and Singleton, E.S., 2008, Application of terrestrial laser scanning in determining the pattern of late Pleistocene and Holocene fault displacement from the offset of pluvial lake shorelines in the Alvord extensional basin, northern Great Basin, USA: Geosphere, n. 4, p. 536–563.

Oldow, J.S., Aiken, C.L.V., Hare, J.L., Ferguson, J.F., and Hardyman, R.F., 2001, Active displacement transfer and differential block motion within the central Walker Lane, western Great Basin: Geology, v. 29, p. 19–22.

Orme, A.R., and Orme, A.J., 2008, Late Pleistocene shorelines of Owens Lake California, and their hydroclimatic and tectonic implications, in Reheis, M.C., Hershler, R., and Miller, D.M., eds., Late Cenozoic Drainage History of the Southwestern Great Basin and Lower Colorado River Region: Geologic and Biotic Perspectives: Geological Society of America Special Paper 439, p. 207–226.

Oskin, M., and Iriondo, A., 2004, Large-magnitude transient strain accumulation on the Blackwater fault, Eastern California shear zone: Geology, v. 32, p. 313–316.

Oskin, M., Perg, L., Shelf, E., Strane, M., Gurney, E., Singer, B., and Zhang, X., 2008, Elevated shear zone loading rate during an earthquake cluster in eastern California: Geology, v. 36, p. 507–510.

Otvos, E.G., 2000, Beach ridges – definitions and significance: Geomorphology, v. 32, p. 83–108.

Oviatt, C.G., 2000. Lacustrine features and global climate change, in Noller, J.S., Sowers, J.M., and Lettis, W.R., eds., Quaternary Geochronology: Methods and Applications: AGU Reference Shelf Volume 4: Washington D.C., American Geophysical Union, p. 470–478.

Pakiser, L.C., Kane, M.F., and Jackson, W.H., 1964, Structural geology and volcanism of Owens Valley region, California—a geophysical study: U.S. Geological Survey Professional Paper 438, 65 p.

Peltzer, G., Crampe, F., Hensley, S., and Rosen, P., 2001, Transient strain accumulation and fault interaction in the Eastern California shear zone: Geology, v. 29, p. 975–978.

Pérouse, E., and Wernicke, B.P., 2016, Spatiotemporal evolution of fault slip rates in deforming continents: The case of the Great Basin region, northern Basin and Range province: Geosphere, v. 13, p. 112–135.

Peterson, F.F., 1981, Landforms of the Basin and Range province: defined for soil surveys: Nevada Agriculture Experiment Station, University of Nevada, Reno, Technical Bulletin 28, 52 p.

Phillips, F.M., 2008, Geological and hydrological history of the paleo-Owens River drainage since the late Miocene, in Reheis, M.C., Hershler, R., and Miller, D.M., eds., Late Cenozoic Drainage History of the Southwestern Great Basin and Lower Colorado River Region: Geologic and Biotic Perspectives: Geological Society of America Special Paper 439, p. 115–150.

Phillips, F.M., Zreda, M., Plummer, M.A., Elmore, D., and Clark, D.H., 2009, Glacial geology and chronology of Bishop Creek and vicinity, eastern Sierra Nevada, California: Geological Society of America Bulletin, v. 121, p. 1013–1033.

Phillips F. M. and Majkowski L., 2011, The role of low-angle normal faulting in active tectonics of the northern Owens Valley, California: Lithosphere, v. 3, p. 22–36.

Pierce, K.L., Cannon, K.P., Meyer, G.A., Trebesch, M.J., and Watts, R.D., 2002, Post-glacial inflation-deflation cycles, tilting, and faulting in the Yellowstone Caldera based on Yellowstone Lake shorelines. U.S. Geological Survey Open-file Report 02–0142, 30 p.

Pinter, N., 1995, Faulting on the Volcanic Tableland, California: The Journal of Geology, v. 103, p. 73–83.

Prejean, S., Ellsworth, W., Zoback, M., and Waldhauser, F., 2002, Fault structure and kinematics of the Long Valley Caldera region, California, revealed by high-accuracy earthquake hypocenters and focal mechanism stress inversions: Journal of Geophysical Research, v. 107, doi:10.1029/2001JB001168.

Prescott, J.R. and Hutton, J.T., 1994, Cosmic ray contributions to dose rates for luminescence and ESR dating: Large depths and long-term time variations: Radiation Measurements, v. 23, p. 497–500.

Reheis, M.C., and Dixon, T.H., 1996, Kinematics of the Eastern California shear zone: Evidence for slip transfer from Owens and Saline Valley fault zones to Fish Lake Valley fault zone: Geology, v. 24, p. 339–342.

Reheis, M.C., Adams, K.D., Oviatt, C.G., Bacon, S.N., 2014, Pluvial lakes in the Great Basin of the western United States – A view from the outcrop: Quaternary Science Reviews, v. 97, p. 33–57.

Rockwell, T.K., Lindvall, S., Herzberg, M., Murbach, D., Dawson, T., and Berger, G., 2000, Paleoseismology of the Johnson Valley, Kickapoo, and Homestead Valley faults: Clustering of earthquakes in the Eastern California shear zone: Bulletin of the Seismological Society of America, v. 90, p. 1200–1236.

Rhodes, E.J., 2015, Dating sediments using potassium feldspar single-grain IRSL: Initial methodological considerations: Quaternary International, v. 362, p. 14–22.

Rood, D.H., Burbank, D.W., and Finkel, R.C., 2011, Chronology of glaciations in the Sierra Nevada, California, from ^{10}Be surface exposure dating: Quaternary Science Reviews, v. 30, p. 646–661.

Roquemore, G.R., and Zellmer, J.T., 1983, Ground cracking associated with 1982 magnitude 5.2 Indian Wells Valley earthquake, Inyo County: California Geology: v. 36, p. 197–200.

Rosenthal, J.S., Meyer, J., Palacios-Fest, M.R., Young, D.C., Ugan, A., Byrd, B.F., Goblet, K., Giacomo, J., 2017, Paleohydrology of China Lake basin and the context of early human occupation in the northwestern Mojave Desert, USA. Quaternary Science Reviews, v. 176, p. 112–139.

Roquemore, G.R., and Zellmer, J.T., 1983, Ground cracking associated with 1982 magnitude 5.2 Indian Wells Valley earthquake, Inyo County: California Geology, v. 36, no. 9, p.197–200.

Ruff, L.J., 2002, State of stress within the Earth: in Lee, W.H.C., Kanamori, H., Jennings, P.C., and Kisslinger, C., eds., Part A: International Handbook of Earthquake and Engineering Seismology: Academic Press, p. 539–557.

Saleeby, J., Saleeby, Z., and Le Pourhiet, L., 2013, Epeirogenic transients related to mantle lithosphere removal in the southern Sierra Nevada region, California: Part II. Implications of rock uplift and basin subsidence relations: Geosphere, v. 9, p. 394–425.

Savage, J.C., and Lisowski, M., 1980, Deformation in Owens Valley: Bulletin of the Seismological Society of America, v. 70, p. 1225–158.

Savage, J.C., and Lisowski, M., 1995, Strain accumulation in Owens Valley: Bulletin of the Seismological Society of America, v. 85, p. 151–158.

Savage, J.C., Lisowski, M., and Prescott, W.H., 1990, An apparent shear zone trending north-northwest across the Mojave Desert into Owen sValley: Geophysical Research Letters, v. 17, p. 2113–2116.

Slemmons, D.B., Vittori, E., Jayko, A.S., Carver, G., and Bacon, S.N., 2008, Quaternary Fault and Lineament Map of Owens Valley, Inyo County, eastern California: Geological Society of America Map and Chart Series 96, 25 pp., scale 1:100,000.

Smedley, R.K., Duller, G.A.T., Pearce, N.J.G., Roberts, H.M., 2012, Determining the K-content of single-grains of feldspar for luminescence dating: Radiation Measurements, v. 47, p. 790–796.

Smith, G.I. and Pratt, W.P., 1957, Core logs from Owens, China, Searles, and Panamint Basins, California: U.S. Geological Survey Bulletin 1045-A, 1–62.

Smith, G.I., and Street-Perrott, F.A., 1983, Pluvial lakes of the western United States. In: Wright, Jr., H.E., Porter, S.C. (Eds.), Late-Quaternary Environments of the United States, vol. 1. University of Minnesota Press, Minneapolis, p. 190–212.

Smith, G.I., and Bischoff, J.L., 1997, Core OL-92 from Owens Lake: Project rationale, geologic setting, drilling procedures, and summary, in Smith, G.I., and Bischoff, J.L., eds., An 800,000-Year Paleoclimatic Record from Core OL-92, Owens Lake, Southeast California: Geological Society of America Special Paper 317, p. 1–8.

Smoot, J.P., Litwin, R.J., Bischoff, J.L., and Lund, S.P., 2000, Sedimentary record of the 1872 earthquake and ‘‘Tsunami’’ at Owens Lake, southeast California: Journal of Sedimentary Geology, v. 135, p. 241–254.

Steacy, S., Gomberg, J., and Cocco, M., 2005, Introduction to special section: Stress transfer, earthquake triggering, and time-dependent seismic hazard: Journal of Geophysical Research, v. 110, B05S01, doi:10.1029/2005JB003692.

Stein, R.S., 1999, The role of stress transfer in earthquake occurrence: Nature, v. 402, p. 605–609.

Stone, P., Dunne, G.C., Conrad, J.E., Swanson, B.J., Stevens, C.H., and Valin, V.C., 2004, Geologic map of the Cerro Gordo Peak 7.5' quadrangle, Inyo County, California: U.S. Geological Survey, Geologic Science Investigation Map I-2851, scale 1:24,000.Thatcher, W., Foulger, G., Julian, B., Svarc, J., Quilty, E., and Bawden, G., 1999, Present day deformation across the Basin and Range province, western United States: Science, v. 283, p. 1715–1718.

Thatcher, W., Foulger, G.R., Julian, B.R., Svarc, J.L., Quilty, E., and Bawden, G.W., 1999, Present-day deformation across the Basin and Range province, western United States: Science, v. 283, 1714–1718.

Thompson, G.A., and Parsons, T., 2017, From coseismic offsets to fault-block mountains: Proceedings of the National Academy of Sciences, n. 114, p. 9820–9825.

Thomsen, K.J, Murray, A.S., Jain, M., Botter-Jensen, L., 2008, Laboratory fading rates of various luminescence signals from feldspar-rich sediment extracts: Radiation Measurements, v. 43, p. 1474–1486.

USGS (United States Geological Survey and California State Geological Survey), 2016, Quaternary fault and fold database for the United States, accessed June, 2016 from USGS web site: https://earthquake.usgs.gov/hazards/qfaults/.

Unruh, J.R., Hauksson, E., Monastero, F.C., Twiss, R.J., and Lewis, J.C., 2002, Seismotectonics of the Coso Range–Indian Wells Valley region, California: Transtensional deformation along the southeastern margin of the Sierran microplate, in Glazner, A.F., Walker, J.D., and Bartley, J.M., eds., Geologic Evolution of the Mojave Desert and Southwestern Basin and Range: Geological Society of America Memoir 195, p. 277–294.

Unruh, J., Humphrey, J., and Barron, A., 2003, Transtensional model of Sierra Nevada frontal fault system, eastern California: Geology, vol. 31, p. 327–330.

Unruh, J., Hauksson, E., Jones, C.H., 2014, Internal deformation of the southern Sierra Nevada microplate associated with foundering lower lithosphere, California: Geosphere, v. 10, p. 107–128.

Vazquez, J.A., and Woolford, J.M., 2015, Late Pleistocene ages for the most recent volcanism and glacial-pluvial deposits at Big Pine volcanic field, California, USA, from cosmogenic ^{36}Cl dating: Geochem. Geophys. Geosyst., v. 16, p. 2812–2828.

Verdecchia, A., and Carena, S., 2016, Coulomb stress evolution in a diffuse plate boundary: 1400 years of earthquakes in eastern California and western Nevada, USA: Tectonics, v. 35, p.1793–1811.

Wallace, R.E., 1984, Patterns and timing of late Quaternary faulting in the Great Basin Province and relation to some regional tectonic features: Journal of Geophysical Research, v. 89, p. 5763–5769.

Wernicke, B.P., Friedrich, A.M., Niemi, N.A., Bennett, R.A., and Davis, J.L., 2000, Dynamics of plate boundary fault systems from Basin and Range Geodetic Network (BARGEN) and geologic data: GSA Today, v. 10, no. 11, p. 1–7.

Wesnousky, S.G., 2005a, Active faulting in the Walker Lane: Tectonics, v. 24, p. 1–35.

Wesnousky, S.G., 2005b, The San Andreas and Walker Lane fault systems, western North America: transpression, transtension, cumulative slip and the structural evolution of a major transform plate boundary: Journal of Structural Geology, v. 27, p. 1505–1512.

Wesnousky, S.G., and Jones, C.H., 1994, Oblique slip, slip partitioning, spatiotemporal changes in the regional stress field, and the relative strength of active faults in the Basin and Range, western United States: Geology, v. 22, p. 1031–1034.

Zehfuss, P.H., Bierman, P.R., Gillespie, A.R., Burke, R.M., and Caffe, M.W., 2001, Slip rates on the Fish Springs fault, Owens Valley, California, deduced from cosmogenic 10Be and 26Al and soil development on fans: Geological Society of America Bulletin, v. 113, p. 241–255.

Zeng, Y., and Shen, Z., 2014, Fault network modeling of crustal deformation in California constrained using GPS and geologic observations: Tectonophysics, v. 612/613, p. 1–17.

Zoback, M.L., 1989, State of stress and modern deformation on the northern Basin and Range Province: Journal of Geophysical Research, v. 94, p. 7105–7128.

CHAPTER 3

A 50,000-YEAR RECORD OF LAKE-LEVEL VARIATIONS AND OVERFLOW FROM OWENS LAKE, EASTERN CALIFORNIA, USA

Steven N. Bacon[a†], Angela S. Jayko[b], Lewis A. Owen[c], Scott C. Lindvall[d], Edward J. Rhodes[e], Rina A. Schumer[a], and David L. Decker[a]

[a]Desert Research Institute, Reno, Nevada 89512, USA
[b]U.S. Geological Survey, U.C. White Mountain Research Station, Bishop, California 93514, USA
[c]Department of Marine, Earth, and Atmospheric Sciences, North Carolina State University, Raleigh, North Carolina 27695, USA
[d]Lettis Consultants International, Inc., Valencia, California 91335, USA
[e]Department of Geography, University of Sheffield, Sheffield, United Kingdom

Reproduced with permission from:
Bacon, S.N., Jayko, A.S., Owen, L.A., Lindvall, S.C., Rhodes, E.J., Schumer, R.A., and Decker, D.L., 2020. A 50,000-year record of lake-level variations and overflow from Owens Lake, eastern California, USA. Quaternary Science Reviews. doi.org/10.1016/j.quascirev.2020.106312.

Copyright 2020 Elsevier Ltd.

ABSTRACT

A continuous lake-level curve was constructed for Owens Lake, eastern California by integrating lake-core data and shoreline geomorphology with new wind-wave and sediment entrainment modeling of lake-core sedimentology. This effort enabled refinement of the overflow history and development of a better understanding of the effects of regional and global climate variability on lake-levels of the paleo-Owens River system during the last 50,000 years. The elevations of stratigraphic sites, plus lake bottom and spillway positions were corrected for vertical tectonic deformation using a differential fault-block model to estimate the absolute hydrologic change of the watershed-lake system. New results include ^{14}C dating of mollusk shells in shoreline deposits, plus post-IR-IRSL dating of a suite of 5 beach ridges and OSL dating of spillway alluvial and deltaic deposits in deep boreholes. Geotechnical data show the overflow area is an entrenched channel that had erodible sills composed of unconsolidated fluvial-deltaic and alluvial sediment at elevations of ~1113–1165 m above mean sea level. Owens Lake spilled most of the time at or near minimum sill levels, controlled by a bedrock sill at ~1113 m. Nine major transgressions at ~40.0, 38.7, 23.3, 19.3, 15.6, 13.8, 12.8, 11.6, and 10.5 ka reached levels ~10–45 m above the bedrock sill. Several major regressions at or below the bedrock sill from 36.9–28.5 ka, and at ~17.8, 12.9, and 10.4–8.8 ka indicate little to no overflow during these times. The latest period of overflow occurred ~10–20 m above the bedrock sill between ~8.4 and 6.4 ka that was followed by closed basin conditions after ~6.4 ka. Previous lake core age-depth models were revised by accounting for sediment compaction and using no reservoir correction for open basin conditions, thereby reducing discrepancies between Owens

Lake shoreline and lake-core proxy records. The integrated analysis provides a continuous 50 ka lake-level record of hydroclimate variability along the south-central Sierra Nevada that is consistent with other shoreline and speloethem records in the southwestern U.S.

1. INTRODUCTION

Fluctuation of paleo-lake levels preserve a record of coeval climate and drainage-basin change in the Great Basin of the western U.S. Lake levels in closed basins fluctuate in response to the balance between precipitation and evaporative processes in the watershed (Street-Perrott and Harrison, 1985). The sediments and landforms of pluvial lakes are sensitive recorders of these balances, thereby provide information on the magnitudes and rates of climatic change that influence lake level. Numerous geomorphic and exposure-based sedimentological studies in the Great Basin have focused on developing lake-level reconstructions (e.g., Reheis et al., 2014). These types of studies are commonly used to infer regional paleohydroclimate variability at multiple time scales (e.g., Mifflin and Wheat, 1979; Enzel et al., 1989; 2003; Broeker et al., 2009). The spatiotemporal distribution of paleolakes and lake-level histories in the southwestern U.S. have also been used as a proxy for migration of the North American polar jet stream (NAPJS) and associated hydroclimatic conditions between 35°N and 43°N; which in turn have been used to infer North Pacific atmospheric circulation patterns across the western U.S. during the late Quaternary (Enzel et al., 1989; 2003; Benson et al., 1990, 1995, 2003; Enzel and Wells, 1997; Negrini, 2002; Zic et al., 2002; Lyle et al., 2012; Antinao and McDonald, 2013; Munroe and Laabs, 2013; Garcia et al., 2014; Kirby et al., 2014, 2015; Oster et al., 2015; Reheis et al., 2014; McGee et al., 2018; Morrill et al., 2018; Hatchett et al., 2019; Hudson et al., 2019; Knott et al., 2019).

The Owens River watershed includes Owens Valley, an ~15–40 km wide and 200 km long tectonic graben within the southwestern Great Basin in eastern California (Figure 1). This graben lies along the eastern escarpment of the south-central Sierra

Nevada. The Sierra Nevada forms one of the principal rain shadows in the western U.S. with its highest crest elevations of 3400–4300 m occurring between ~36°N and 38°N. The entire range was heavily glaciated during the Pleistocene, and many small glaciers and snowfields persisted through the early 2000's in sheltered cirques at high elevations (Basagic and Fountain, 2011; Gillespie and Clark, 2011; Moore and Moring, 2013). The physiographic and hydrologic setting of the Owens River watershed is optimally located to record long-term atmospheric circulation patterns that modulate streamflow and lake-level variations in the southwestern U.S. (e.g., Redmond et al., 1991; Dettinger et al., 1998). Combining the older geomorphic and lacustrine sediment archives of Owens Lake into an integrated record of hydrologic change provides a long-term dataset that can be used to validate and/or refine atmospheric circulation models developed from the spatiotemporal extent of other paleolakes in the western U.S. (e.g., Lyle et al., 2012; Oster et al., 2015; Lachniet et al., 2014; McGee et al., 2018; Hudson et al., 2019).

The primary goals of this investigation are: 1) to augment the Middle–Early Holocene to late Pleistocene portion of the lake-level record of Owens Lake previously developed by Bacon et al. (2006) and updated in Reheis et al. (2014). This information is combined with improved shoreline and paleo-spillway reconstructions that show the timing and duration of surface flow to downstream basins that contained China and Searles Lakes (Figure 1); and 2) to assess the correlation of global climate events with the late Quaternary hydroclimate variability inferred from this lake level and paleo spillway record. In order to accomplish this we: (a) present new radiocarbon (^{14}C) and luminescence ages for beach ridges and shoreline stratigraphic sites in Owens Lake basin; (b) use previously unpublished and published subsurface geotechnical data and

luminescence ages from the overflow channel of Owens Lake to directly link shoreline and spillway levels; (c) reconstruct the elevation of shorelines, spillway channels and lake bottoms to absolute positions by applying a differential fault-block model; (d) estimate lake levels in the absence of shoreline evidence by applying wind-wave and sediment entrainment modeling of lake-core sedimentology to estimate threshold lake-water depth and produce a continuous lake-level curve; and (e) evaluate temporal correspondence between the shoreline record and lake-core proxies of Owens Lake in identifying trends of hydroclimatic variability related to climate change over the past 50 ka at both watershed- and global-scales.

One of the significant new observations is the occurrence of shorelines that can be directly linked to spillway channel incision and that show episodes of Owens Lake overflow are much younger (latest Pleistocene and Early Holocene), than previously recognized. Gaining a better understanding of the spatiotemporal hydrologic connections between Owens Lake and downstream lakes of the paleo-Owens River system is the first step in assessing the hydroclimate variability of the south-central Sierra Nevada and region. This can then be used for more quantitative watershed-lake paleohydrological modeling.

2. Background of Paleo-Owens River System

2.1. Geologic and Hydrologic Settings

The Owens River watershed has a drainage area of ~8515 km^2 and is bounded by the crests of the Sierra Nevada on the west, White-Inyo Mountains on the east, and the Coso Range on the southeast. Crests of the Sierra Nevada and White-Inyo Mountains rise

>3000 m above mean sea level (masl) in southern Owens Valley, with Mount Whitney (at an elevation of 4421 m) rising ~3280 m above the valley floor. The northern and southern parts of the watershed share drainage divides with the watersheds of Mono and China Lake basins, respectively. The northern reach of the Owens River is within the Long Valley caldera and its southern extent drains into Owens Lake (Figure 1). During the period AD 1872–1878, Owens Lake was a perennial, closed-basin lake that covered >280 km^2 with a historical maximum lake level at 1096.4 m and a water depth of 14.9 m (Gale, 1914; Lee, 1915). Major water diversions in Owens Valley began after AD 1913 with construction of the Los Angeles aqueduct system that transported surface water from the Owens River watershed and Mono Lake basin (since AD 1941) >320 km to the south for distribution (Hollett et al., 1991). Owens Lake first began depositing salts onto the lake floor in AD 1921 because of these diversions, and by AD ~1931, Owens Lake had desiccated and become a playa (Smith and Bischoff, 1997).

Owens Lake occupies a topographically closed basin contained by a modern spillway across its drainage divide (i.e., sill) at the south end of the basin. The majority of contemporary annual streamflow in the Owen River watershed is from rain and snowmelt runoff from ~20% of the drainage area on the eastern slopes of Sierra Nevada (Hollet et al., 1991). Discharge from the Owens River watershed is required to support downstream lakes in China and Searles basins, even during pluvial periods, because of high rates of evaporation from valleys bottoms and low runoff from surrounding mountains due to rain shadow positions and a lack of high elevations in both watersheds (e.g., Smith and Street-Perrott, 1983; Jannik et al., 1991; Phillips, 2008). During much of the Pleistocene when periods with greater moisture flux and cooler temperatures occurred across the region,

Owens Lake was a perennial freshwater lake that periodically overflowed its sill to form a chain of pluvial lakes occupying one or more of four successively lower-elevation lake basins (Gale, 1914; Smith and Street-Perrott, 1983; Jannik et al., 1991; Menking, 1995; Phillips, 2008; Knott et al., 2019) (Figure 1). Shoreline and sediment-core records from lakes in the paleo-Owens River system indicate that pluvial Owens Lake had relatively high water levels during the late Pleistocene coinciding with deglaciations and exceptionally wet periods in the Sierra Nevada. Owens Lake has previously been inferred to have overflowed into China-Searles and Panamint Lakes, as many as 2 to 3 times between ~20 and 12 ka (Benson et al., 1996, 1997; 1998; 2002; Phillips et al., 1996; Smith et al., 1997; Bishoff and Cummins, 2001; Jayko et al., 2008; Orme and Orme, 2008; Phillips, 2008; Hoffman, 2009; Kirby and McDonald, 2016; Rosenthal et al., 2017; Knott et al., 2019) (Figure 1). Previous research also indicates that overflow from Owens Lake to support downstream lakes likely ceased after 11–12 ka based on shoreline stratigraphic studies in China Lake basin (Rosenthal et al., 2017). Owens Lake was considered to be the terminal lake in the system during the Holocene with mostly moderate to shallow water levels into historical times according to geomorphic shoreline records (Bacon et al., 2006; 2018) and lake-core evidence (Newton, 1991; Smith et al., 1997; Li et al., 2000; Smoot et al., 2000; Benson et al., 2002).

2.2. Neotectonic Setting

Tectonic forces in extensional regimes generally act to create internally drained basins separated by highlands or mountain ranges (e.g., Peterson, 1981). Orographic focusing of precipitation on uplands creates runoff that supports lakes or wetlands in

basins during periods with greater moisture flux (e.g., Cohen, 2003). Drainage-basin integration can be thought of as the balance between climate and tectonics, with climate-driven processes acting to fill a basin with sediment and tectonics acting to create both accommodation space through subsidence in depocenter areas and either uplift or subsidence of spillways (e.g., Reheis et al., 2014). The physiography of the paleo-Owens River drainage reflects active tectonic processes associated with several north- to northwest-striking principal strike-slip faults and northeast-striking connecting normal faults known as the southern Walker Lane belt (WLB) (Wesnousky and Jones, 1994; Wesnousky, 2005a,b).

Owens Valley is a region of active tectonics, as demonstrated by the M_w7.5–7.9 AD 1872 Owens Valley earthquake (Beanland and Clark, 1994; Hough and Hutton, 2008; Haddon et al., 2016). Owen Lake basin is crossed by five principal faults that collectively have formed a well-developed, pull-apart basin with a deep, rhombus-shaped depocenter area developed by dextral-oblique faulting (Slemmons et al., 2008). Faults in the lake basin include the range-bounding normal SNFF on the west and the dextral-oblique southern Inyo Mountains fault (SIMF) on the east, plus the active dextral-oblique OVF along the axis of the valley and lake basin (Figure 2). The southern section of the OVF extends along the entire western margin of the lake basin. During the AD 1872 earthquake, dextral-oblique displacements produced subsidence in the depocenter area of Owens Lake that created a seismic seiche, raised the western shoreline, and shifted the position of the eastern shoreline of the lake several hundred meters to the west (Smoot et al., 2000). Other faults that accommodate slip within the pull-apart basin are the normal Owens River-Centennial Flat fault (OR-CFF) and normal Keeler fault (KF) (Figure 2).

Deformation of shorelines in Owens Lake basin is commonly expressed as fault offsets, short lengths of monoclinal warping, and broad warping or uniform tilting (Carver, 1970). Two of the oldest and highest shorelines in Owens Valley are primarily erosional but include a few preserved constructional features that show progressive deformation. Elevations of the two shorelines referred to as the 1160 and 1180 m shorelines have dates of 40.0 ± 5.8 ka and 160 ± 32 ka that are both lower on the east side of the lake basin at ~1155 and 1180 m and higher on the west side at ~1162 and 1200 m, respectively (Jayko and Bacon, 2008; Bacon et al., 2019a).

3. MATERIALS AND METHODS

Geomorphic- and exposure-based studies that construct lake-level curves use a variety approaches with a range of uncertainties, but all involve plotting the age of landforms and/or deposits with respect to altitude to constrain the position of water levels from either specific stratigraphic facies, fossils, and archeological sites (e.g., Stine, 1990; Oviatt, 1997; 2015; Licciardi, 2001; Bacon et al., 2006; Adams, 2007; Bartov et al., 2007; Reheis et al., 2014), carbonate (tufa) deposits (e.g., Benson et al., 2013; Ibarra et al., 2014; Hudson et al., 2017), or direct ages from beach ridges (e.g., Rades et al., 2015; Bacon et al., 2018; Adams and Rhodes, 2019a,b).

3.1. Radiocarbon Dating

We integrated 47 new and previously published radiocarbon (^{14}C) ages from Owens Lake to refine prior reconstructions of water levels for the lake over the last 50 ka. Thirteen previously unpublished accelerator mass spectrometry (AMS) ages from

samples of aquatic and semi-aquatic bivalve and gastropod shells, ostracode valves, lithiod tufa (carbonate), and charcoal from Owens Lake basin and its overflow channel are from this study and Black and Veatch (2013), whereas 34 previously published AMS and conventional ages from similar material, plus carbonized wood and organic sediment (bulk organic carbon) from around the basin were collectively used in our study to reconstruct a refined lake-level curve of Owens Lake (Beanland and Clark, 1994; Koehler, 1995; Bacon et al., 2006, 2018; Bacon and Pezzopane, 2007; Orme and Orme, 2008) (Table 1).

3.1.1. Radiocarbon Reservoir Effects

Previous studies have demonstrated the potential uncertainty in using ^{14}C ages from tufa and shell to define the age of shoreline features and deposits because these types of carbonate materials can be contaminated by either younger, post-depositional carbon from either meteoric water and pedogenic processes or by syndepositional older carbon in ground-water fed spring and lake waters (e.g., Lubetkin and Clark, 1988; Benson, 1993; Bischoff et al., 1993; Brennan and Quade, 1997; Pigati et al., 2004; Rosenthal et al., 2017). Previously published lake-level curves for Owens Lake (e.g., Bacon et al., 2006; Reheis et al., 2014), Searles Lake (Smith, 2009; Knott et al., 2019), and Panamint Lake (Jayko et al., 2008) did not incorporate a reservoir correction to ^{14}C ages because of the uncertainty and lack of confident reservoir corrections for each lake basin.

A detailed analysis on the paleoenvironmental conditions and suitability of aquatic and semi-aquatic mollusks for ^{14}C dating was performed on samples from China

Lake basin and Salt Wells Valley by Rosenthal et al. (2017; Figure 1). Their study provides important paleoenvironmental information and insight on the potential reservoir correction required to account for the hard water effects from ambient ^{14}C-depleted carbon for the overall paleo-Owens River system. The study of Rosenthal et al. (2017) concluded that ^{14}C determinations from tufa and aquatic and semi-aquatic mollusk shells may be as much as 140–350 years older than the true age of the samples. The magnitude of reservoir effects for China Lake basin and Salt Wells Valley tufa and shell is similar to the reservoir correction of 330 years for tufa at the highstand shoreline in nearby Searles Lake basin based on comparisons between ^{14}C and $^{230}Th/^{234}U$ ages (Peng et al., 1978; Lin et al., 1998) (Figure 1). In addition to tufa and shell requiring a reservoir correction, bulk samples of carbonate-rich lacustrine mud (marl) ^{14}C dated in several Owens Lake sediment cores (OL-84B and OL-97) had a reservoir effect of 600–1000 yr (Benson et al., 1998a; Smoot et al., 2000; Benson et al., 2002; Benson, 2004).

We accept the reservoir corrections of Lin et al. (1998) and Rosenthal et al. (2017) as reasonable estimates for the magnitude of reservoir effects in the paleo-Owens River system. A uniform reservoir correction of 300 years was applied prior to calibrating ^{14}C ages for aquatic and semi-aquatic mollusk shells, ostracod valves, tufa, and oolitic sand samples used in our study, and the dates previously used in Bacon et al. (2006) and Reheis et al., (2014). A reservoir correction of ~1000 yr has also been confirmed for bulk samples of mud-rich lacustrine sediments of Owens Lake by temporal correspondence between the age of lake expansion inferred from lake cores and the Late Holocene shoreline chronology that was determined by ^{14}C ages from charcoal and luminescence ages from sands in beach ridge deposits (Bacon et al., 2018). Therefore, we apply a

300-yr correction to shell, tufa, and oolitic material and accept the previously applied 600-yr correction to bulk samples of lacustrine mud in lake cores to account for reservoir effects during closed lake conditions for the construction of the lake-level curve herein and for the lake-core stratigraphic modeling described in a later section. Corrections were applied to conventional ^{14}C ages prior to calibration. Conventional ^{14}C dates are reported in radiocarbon years before present (^{14}C yr BP) and have been calibrated to calendar years before present (cal yr BP) using the CALIB7.1 program (Stuiver and Reimer, 1993; Stuiver et al., 2017) with the IntCal13 data set (Reimer et al., 2013) (Table 1).

3.2. Luminescence Analysis

Luminescence dating determines the last process of sediment reworking and therefore enables the direct age determination of the depositional age of sediment (Rhodes, 2011). Two methods of luminescence dating were used in this study including: post-infrared infrared stimulated luminescence (post-IR-IRSL) and optically stimulated luminescence (OSL) that require sand-sized mineral grains of feldspar and quartz, respectively. We also used previously published post-IR-IRSL dates from several Owens Lake shorelines that are Late Holocene in age (Bacon et al., 2018) and Late Pleistocene in age (~40 ka) (Bacon et al., 2019a).

3.2.1. Post-Infrared Infrared Stimulated Luminescence Dating

We used post-IR-IRSL analysis to directly date sediments of a previously undated suite of five prominent beach ridges at Centennial Flat (Table 2). The crests of the sampled beach ridges are at elevations of ~1114, 1120, 1127, 1129, 1131 m. A total of

10 samples were collected in light-resistant plastic tubes driven horizontally into sand-rich horizons in cleaned, natural exposures along shallow channels cut across each beach ridge. Duplicate samples were taken from the ~1114, 1120, 1127, and 1129 m beach ridges, whereas a single sample could only be recovered from the ~1131 m beach ridge due to hard consistency of sediment, in addition to an additional sample from the ~1127 m beach ridge. Samples were prepared and processed at the University of California, Los Angeles (UCLA) Luminescence Laboratory. Dating was based on the post-$IRSL_{225}$ single-grain luminescence dating method (Rhodes, 2015). This method has been used recently in Owens Lake basin to date aaeolian and shoreline deposits lacking suitable quartz (e.g., Bacon et al., 2018; Bacon et al., 2019a) and enables accurate dating of feldspar grains with a precision equal in many cases to radiocarbon analysis of detrital charcoal for Holocene deposits – thereby allowing the dating of previously undateable strata and landforms. Rhodes (2015) and Appendix B provide descriptions of the post-$IRSL_{225}$ technique and analysis.

3.2.2. Optically Stimulated Luminescence Dating

OSL analysis of sediment sampled during a geotechnical investigation in the northern end of the Owens Lake overflow channel (Black and Veatch, 2013; Goetz et al., 2016), and prepared and processed at the Luminescence Dating Laboratory at the University of Cincinnati, are used to define the age of potential overflow episodes. The samples were collected from fluvial-deltaic (channel fill) sedimentary facies of undisturbed cores from a deep borehole drilled within the overflow channel (Samples HD 1, 2, and 3), as well as alluvial/colluvial sedimentary facies in steel tubes driven

horizontally into sand-rich horizons in cleaned, deep excavations on colluvial slopes along the eastern margin of the overflow channel (Samples HD 6, 7-1, 7-2, and 9) (Table 3). Dating was based on the single-aliquot regenerative-dose (SAR) OSL dating method (e.g., Murray and Wintle, 2000, 2003). Appendix C provides detailed descriptions of the OSL technique and analysis.

3.3. Paleolake Water-Level Reconstruction

Sedimentologic and geomorphic indicators of former lake levels can be preserved for millennia and accurately measured across broad areas, thus allowing reconstruction of long paleoclimate records provided tectonic effects and/or isostatic rebound can also either be assessed or corrected (Reheis et al., 2014). Most geomorphic and geologic studies focused on reconstructing lake levels are either limited to periods with relative highstands because of a lack of preserved landforms and outcrop evidence for lower water levels (e.g., Adams, 2007; Bartov et al., 2007) or rely on inferences from stratigraphy exposed in lower parts of lake basins without shoreline data (e.g., Negrini et al., 2006). Lacustrine sediment cores are also useful in identifying changes in relative lake levels from proxy evidence (e.g., sediment size, geochemistry, biology) (e.g., Benson, 2004), but there is large uncertainty in use of proxy evidence to infer corresponding water depths and associated water levels (e.g., Smith, 1997; Reheis et al., 2014). As a result, we applied the methods of Bacon et al. (2018) to estimate lake levels in the absence of shoreline evidence by integrating new shoreline data and previously published shoreline and lake core data sets from Owens Lake with threshold lake-water depth estimates from wind-wave and sediment entrainment modeling of lake core

sedimentology. This integrated approach was previously shown to be suitable in producing a continuous ~4000-yr lake-level record of Owens Lake during the Late Holocene that agreed well with proxy evidence of wet and dry periods from tree-ring and glacial records within the watershed, as well as showed the timing, duration, and magnitude of hydroclimate variability.

3.3.1. Geomorphic Shoreline and Sedimentary Datasets

Documentation of shoreline features in Owens Lake basin and channel fill and alluvium at the overflow channel were based on field observations and mapping of the lacustrine and alluvial geomorphology and bedrock geology at each site. The aerial extent and identification of landforms and related features (e.g., wave-formed scarps, beach ridge crests), as well as subsurface stratigraphy were confirmed from georeferenced satellite imagery in a geographic information systems (GIS) platform, from numerous natural exposures, several exploratory trenches, and several deep geotechnical borings. Lacustrine landforms were classified following the categorization schemes of Peterson (1981) and Otvos (2000). We made field descriptions of deposits from cleaned, natural exposures to establish lacustrine and alluvial sequence stratigraphy and sedimentological characteristics. Lithofacies and facies associations were classified in the field according to grain size, sedimentary structure, and as lateral and vertical stratigraphic position (e.g., Einsele, 2000).

Elevation control at new and previously published shoreline sites in Owens Lake basin (Table 2) was determined in our study with a Trimble GPS Pathfinder® ProXRT receiver with differential correction services. Measurements of elevation during

surveying had a vertical accuracy of ±80 cm. Landforms reported in previous studies were resurveyed to keep elevation data within the same georeferenced frame and to minimize the error associated with different surveying methods. Previous studies had elevation control based on either total-station surveys (Orme and Orme, 2008; Slemmons et al., 2008) or hand-held GPS units cross-checked with 1:24,000 topographic quadrangle maps and 10-m-digital elevation models (DEMs) (Bacon et al., 2006; Jayko and Bacon, 2008; Reheis et al., 2014). Elevation control of exploratory trenches and geotechnical borings at the overflow channel site was made by a licensed surveyor (Black and Veatch, 2013; Goetz et al., 2016). All reported elevations are relative to mean sea level.

Previously published sedimentologic descriptions and interpretations of depositional environments commonly reported with numerical ages and elevations were used to reconstruct water levels (e.g., Table 1). These sedimentologic descriptions were made from both natural exposures (e.g., Bacon et al., 2006; Orme and Orme, 2008) and exploratory pits and trenches excavated on key landforms (e.g., Bacon and Pezzopane, 2007).

3.3.2. Lake Sediment Core Datasets

Sediment cored from beneath the playa surface of Owens Lake includes up to a ~370 m record of climate change over the past 800 ka (Smith and Bischoff, 1997). Sedimentologic characteristics were used in combination with a simple method for calculating deterministic wind-wave characteristics for deep water sediment entrainment (USACE, 1984; 2002) to estimate threshold lake-water depth, which in turn was used to reconstruct lake level (e.g., Bacon et al., 2018). We used stratigraphic and geochemical

proxy information from sediment cores in the depocenter of the lake basin including the ~320-m-long core OL-92, ~28-m-long core OL-90, and ~9-m-long core OL-84B from of Owens Lake basin (Benson et al., 1996, 1997, 1998; Smith and Bischoff, 1997) (Figure 2).

A range of geochronological techniques have been used to date sediment cores from Owens Lake including dating methods consisting of radiocarbon and uranium-series, plus correlation methods involving tephrochronology, paleomagnetic analysis, and pollen assemblages (Benson et al., 1996; Smith and Bischoff, 1997; Bischoff and Cummins, 2001; Phillips, 2008; Li et al., 2000; Smoot et al., 2002). At shallow depths, sediment cores from Owens Lake (~2–30 m) yielded ^{14}C ages from wood, disseminated carbon (i.e., humate), carbonate, and shell that range from ~4 to 50 ka (Benson et al., 1996, 1997, 1998, 2002; Smith and Bischoff, 1997). A revised age-depth model was developed for the last 230 ka of core OL-92 that is based on the correlation between palynostratigraphies defined by U-Th ages from salt layers in Searles Lake core LDW-6 and similar pollen assemblages identified in Owens Lake sediments (Litwin et al., 1999). In our study we use the revised age-depth model of Litwin et al. (1999) for age control of the lithologic log of core OL-92 in Smith and Bischoff (1997).

3.3.3. Tectonic Ground Deformation

Understanding the rates and style of tectonic deformation within seismically active lake basins provides information to correlate shoreline features, as well as to accurately reconstruct past lake levels. Shoreline features and associated lacustrine deposits can be correlated within lake basins based on their elevation and characteristics if the geomorphic and geologic processes that created them are understood, and if ground

deformation is considered (Oviatt, 2000; Reheis et al., 2014). Previously published water-level reconstructions of Owens Lake or other lakes in the paleo-Owens River system did not include corrections for tectonic ground deformation (e.g., Bacon et al., 2006; Jayko et al., 2008; Phillips, 2008; Smith, 2009; Rosenthal et al., 2017). The approach we used to reconstruct the depositional position of terrestrial and lacustrine features and deposits is after a simple method of Bacon et al. (2019a) that was used to reconstruct deformed shorelines in Owens Lake basin to absolute elevations based on a differential fault-block model. In contrast to other regional tectonic lake basins in the western U.S. (e.g., Lahonton and Bonneville basins), where slip and vertical ground deformation are principally accommodated solely by single fault systems, plus isostatic crustal flexure and rebound of relatively thin crust (e.g., Adams et al., 1999; Hampel and Hetzel, 2006), the approach of Bacon et al. (2019a) is applicable for tectonically complex and seismically active lake basins where isostatic rebound from loading of lakes is negligible, but vertical ground deformation is accommodated by distributed slip on two or more primary normal and dextral-oblique faults (Figure 2).

We used previously published information on the locations, style of faulting, and vertical slip rates for primary faults in Owens Lake basin to correct the elevations of geomorphic and outcrop study sites, lake-core sites, and spillways for tectonic ground deformation (Table 4; Figure 2). The location and sense of motion for primary faults in Owens Lake basin are from geologic and fault map databases (Slemmons et al., 2008; Jayko, 2009; USGS, 2016). Vertical slip rates on faults in Owens Lake basin are from studies on the tectonic geomorphology of the Sierra Nevada frontal fault (SNFF; Le et al., 2007), paleoseismology on the southern Owens Valley fault (OVF; Bacon and

Pezzopane, 2007) and Sage Flat fault (SFF; Amos et al., 2013), as well as tectonic-geomorphology of other faults in the lake basin including the Keeler fault and Owens River-Centennial Flat fault (KF and OR-CFF; Bacon et al., 2019a) (Table 4 and Figure 2).

3.3.4. Wind-Wave and Lake Bottom Sediment Entrainment Modeling

Application of wind-wave and sediment entrainment models are commonly used to estimate erosion potential within intertidal to open water coastal environments for coastal protection and habitat rehabilitation (e.g., USACE, 1984, 2002; Teeter et al., 2001; Rohweder et al., 2008; Fagherazzi and Wiberg, 2009). These types of models have also been used in lacustrine environments to estimate the distribution of sediment texture at the lake bottom (e.g., Håkanson, 1977), as well as to quantify potential impacts to water quality and clarity from resuspension of sediment, plus nutrients, heavy metals, and other toxic substances for water resource management (e.g., Reardon et al., 2016; Ji, 2017). In this study, we apply a similar approach to model the wind-wave characteristics and threshold lake-water depths required for the sedimentology described in sediment core OL-92 (Smith and Bischoff, 1997). The approach we use is based on Bacon et al. (2018) that was previously calibrated and verified by modeling the sedimentology described in the historical section in core OL-97 (Li et al., 2000; Smoot et al., 2000) with limnological conditions for the period AD 1872–1878 when Owens Lake was at its historical maximum water level. Appendix D provides descriptions of the wind-wave and lake bottom sediment entrainment modeling of lake-core OL-92 (Smith and Bischoff, 1997).

4. RESULTS

4.1. Owens Lake Basin Study Sites

4.1.1. Post-IR-IRSL Dating of Centennial Flat Beach Ridges

The best preserved and most complete geomorphic record of historical to late Pleistocene shorelines in Owens Valley is located in the southeastern sector of the lake basin along the northwestern flank of the Coso Range near Centennial Flat wash (Jayko and Bacon, 2008; Orme and Orme, 2008; Jayko, 2009; Figure 2). The Centennial Flat site consists of a well-preserved and isolated beach plain comprised of a suite of ten well-developed, tectonically undeformed beach ridges and shoreline scarps at elevations between ~1096 and 1131 m, and a tectonically deformed beach ridge, locally at ~1165 m (Orme and Orme, 2008; Bacon et al., 2019a) (Figure 3). The second highest shoreline in Owens Lake basin is vertically deformed up to 9.8 ± 1.8 m with a maximum elevation of ~1166 m that has a post-IR-IRSL date of 40.0 ± 5.8 ka from beach ridge deposits (Bacon et al., 2019a; Figure 3). Sediment and erosional features of the highest shoreline preserved in the valley are nearby at elevations of ~1174–1180 m and are 160 ± 32 ka from a ^{36}Cl age from a lithoid tufa mound (F. Phillips, personal commun. in Jayko and Bacon, 2008).

We performed the first post-IR-IRSL analysis to estimate direct ages on sediment from Centennial Flat beach ridges at elevations of ~1114, 1120, 1127, 1129, 1131 m (Table 2; Figure 3). Freshly cleaned surfaces were made in natural exposures along active channels that were locally filled with windblown sand. Deposits at sample sites consisted of well-rounded, spherical to disk-shaped, sandy to gravelly beach ridge facies with either basinward, horizontal or landward dipping tabular beds that formed based on their

position within the beach ridge (i.e., foresets, topsets or backsets, respectively; e.g., Adams and Wesnousky, 1998). The soil-geomorphic characteristics of all the beach ridges indicate that they are relatively younger and not recessional shorelines associated with the higher late Pleistocene (~40 ka) highstand beach ridge at the site because the lower beach ridges lack well-developed soil indices typical of late Pleistocene landforms in Owens Valley (e.g., Zehfuss et al., 2001) (Figure 2). The lower beach ridges are sparsely covered by shrubs with coppice dunes and gravel-sized ventifacts from active aeolian sand transport across the area (Orme and Orme, 2008). The surfaces of the beach ridges have moderately developed desert pavement with weakly developed desert varnish and subsurface rubification (i.e., reddening) coatings on gravel clasts, a thin vesicular A (Av) horizon (e.g., McFadden et al., 1998), and a ~20- to 40-cm thick, weakly developed soil with carbonate (k) and Avk/Bwk/Ck profile lacking soil structure, plus very few and patchy carbonate coatings on bottom of gravel clasts (e.g., Birkeland, 1999). These soil characteristics are similar to descriptions made on gravelly Holocene alluvial fans in the southwestern U.S. (e.g., McDonald et al., 2003), and slightly better developed compared to nearby Late Holocene beach ridges below elevations of ~1108 m in Owens Valley (Bacon et al., 2018).

The post-IR-IRSL samples were taken from depths between 0.4 and 1.55 m within stratified sandy layers that lacked evidence of bioturbation. A single sample from the 1131 m beach ridge at a depth of 1.14 m from a hard, silty sand bed within topsets yielded an age of 8.4 ± 0.6 ka. Two samples from the 1129 m beach ridge were taken in a vertical profile at depths of 0.8 and 1.55 m from loose, sandy beds within topsets that were separated by a clear and horizontal boundary defined by a hard and thin, sandy silt

layer overlain by a concentration of disk-shaped gravel (Figure 3). Samples from the 1129 m beach ridge returned ages in stratigraphic order of 12.8 ± 1.1 and 8.1 ± 0.6 ka (Table 2). A total of three samples were recovered from the 1127 m beach ridge. Two closely spaced samples from near the crest of the beach ridge at depths of 0.4 and 0.6 m within the same loose, sandy backset yielded ages of 6.0 ± 0.5 and 6.7 ± 0.5 ka that are within their uncertainties, having a mean age of 6.4 ± 0.7 ka (Table 2). The third sample was taken ~15 m basinward of the crest at a depth of 0.5 m from a loose, sandy bed within foresets that returned an age of 7.6 ± 0.6 ka (Table 2; Figure 3). The ~1120 m shoreline at the Centennial Flat site consists of two closely spaced beach ridges with GPS crest elevations of 1120.9 and 1121.2 m for the inner (basinward) and outer (landward) ridges, respectively (Figure 3). Two closely spaced samples from below the crest of the inner ridge at depths of 0.9 and 1.0 m within the same loose, sandy foreset returned ages of 5.9 ± 0.5 and 6.5 ± 0.5 ka that are within their uncertainties, having a mean age of 6.2 ± 0.6 ka.

The lowest sample site was of the ~1114 m beach ridge. Here, two samples below the crest of the ridge at similar depths of 1.15 m and separated by ~0.6 m yielded ages of 5.8 ± 0.4 and 8.8 ± 0.6 ka from different loose, sandy backsets underlain by a massive, hard silty sand in the bottom of the exposure (Table 2; Figure 3). These post-IR-IRSL ages are not within their uncertainties and not in stratigraphic order given that the younger sample was situated basinward and stratigraphically below the forests of the older sample (Figure 3). This relation is confirmed by how backsets are formed by a process called barrier rollover. Barrier rollover occurs when storm waves wash sand and gravel from the beach face over the crest of a barrier (i.e., ridge) and onto the backside

depositing younger backsets over older ones (e.g., Adams and Wesnousky, 1998; Reheis et al., 2014). Evidence of possible reworking of older sediment at the site is from the presence of detrital shells found within deposits of the ~1114 m beach ridge and the active wash that dissects it. The sediment of the beach ridge contained less than 5% mollusk shell fragments of up to ~2 cm long from an aquatic mussel (*Anodonta californiensis*) concentrated within the coarser fraction along the tabular beds of backsets. Similar shells of *Anodanta* sp. from deposits of the same ~1114 m beach ridge, but in a different wash ~250 m to the southwest, have a ^{14}C age of ~14,600 cal yr BP (Orme and Orme, 2008), as well as from articulated shells from sites along the northeast sector of the lake basin at Keeler with ^{14}C ages of ~24,000 to 25,000 cal yr BP (Bacon et al., 2006) (Table 1; Figure 2). There were also detrital shell fragments of *Anodanta* sp. in deposits of the inner beach ridge at ~1120 m sampled for post-IR-IRSL analysis. In addition, a nearby exposure of a concentration of shells of a semi-aquatic snail (*Helisoma* (*Carinifex*) *newberryi*) at an elevation of ~1130 m has a ^{14}C age of ~38,700 cal yr BP (Table 1; Figure 3). The range in age of sediment associated with the ~1114 m beach ridge, and presence of older shell fragments in deposits indicates possible reworking of older deposits from later water-level fluctuations, where the lowest elevations of past water levels appear to have all stabilized near an elevation of ~1111–1113 m.

4.1.2. Swansea Shoreline Stratigraphic Site

New shoreline and stratigraphic investigations were performed at additional sites in the lake basin to refine the lake-level record of Owens Lake. These new investigations included GPS surveys and ^{14}C dating of tufa and mollusk shells at sites near Swansea in

the northeastern sector of the lake basin (Figure 2). The Swansea site includes a well-developed beach ridge complex composed of stratified sand and gravel with common mollusk-rich beds that formed at the base of steep bedrock cliffs within the Swansea embayment (Orme and Orme, 2000, 2008; Figure 2). There are three well-developed beach ridges at the site with crest elevations of ~1119, 1123, and ~1128–1129 m that yielded latest Pleistocene ages from ^{14}C ages on mollusk shells from deeper sections (Orme and Orme, 2000, 2008; Bacon et al., 2006; Table 1). We performed a GPS survey to confirm beach ridge elevations at the site. Our new survey identified that the previously surveyed beach ridge at ~1119 m (e.g., Orme and Orme, 2008) is not a single ridge across the embayment, but occurs primarily as a pair of closely spaced ridges. The crests have GPS elevations of 1120.4 and 1120.7 m for the inner and outer ridges, respectively, which are at similar elevations to the paired beach ridges at the Centennial Flat site (e.g., Figure 3).

The Swansea site also has a lower beach ridge and shoreline scarps at ~1108 m that truncate the beach plain with higher beach ridges, which is at a similar elevation of the shoreline scarp at the Centennial Flat site (e.g Figure 3). The soil-geomorphic characteristics of the ~1108 m beach ridge deposit indicate a Late Holocene age, which is supported by duplicate post-IR-IRSL samples that returned a mean age of 3.6 ± 0.4 ka (Bacon et al., 2018). The continuity in shoreline elevations between the Swansea and Centennial Flat sites indicates there has been negligible vertical tectonic ground deformation between the sites in the eastern sectors of the basin during the latest Quaternary (Bacon et al., 2019a).

In addition to evaluating the shoreline geomorphology at the site, tufa and mollusk shells were sampled to define lower water levels in the basin. The northwestern margin of the Swansea embayment has a cliff headland with several wave-formed notches on bedrock. Surfaces of the lowest notch, as well as on an accumulation of clast supported 0.5–1.5 m boulders have thick coatings of dense tufa at an elevation of 1108.1 m. The morphology and depositional environment of the tufa coatings is similar to encrusting tufa described at Pyramid Lake, Nevada (e.g., Benson, 1994). A tufa sample from a bedrock surface returned an age of 10,280 ± 40 ^{14}C yr BP (11,620–11,260 cal yr BP) with a median probability age of 11,400 cal yr BP (Table 1). A nearby site of shoreline sediment exposed in a road cut at an elevation of ~1109 m was also investigated at the base of the cliff headland at the Swansea embayment. The exposure consisted of a thin cover of alluvial sediment and windblown sand that was underlain by a ~1.0–1.5 m thick sequence of well stratified and interbedded sands and gravels with a concentration of mollusk shells within foreset beds. The shell-rich bed contained a mixed mollusk assemblage composed mostly of disarticulated bivalves consisting of the mussel *Anodonta* sp. and the clam *Pisidium* sp., as well as snails *Heliosoma newberryi* and *Vorticifex effusa*. Of this assemblage, a snail shell of *Heliosoma newberryi* with preserved pigment was sampled and yielded an age of 14,460 ± 45 ^{14}C yr BP (17,450–17,060 cal yr BP) with a median probability age of 17,200 cal yr BP (Table 1). The shell-rich deposit is typical of a relatively high-energy beach face depositional environment. The mixed mollusk assemblage includes species that live below the shoreline within different lacustrine environments ranging from relatively deep to shallow water (e.g., Koehler, 1995). As a result we interpret the mixed mollusk

assemblage as likely reworked from older deposits sourced nearby. Nonetheless, the ^{14}C age provides a maximum determination, as well as is likely close to the depositional age of the shoreline deposit given similar shell ages from sediment nearby.

4.1.3. Dirty Socks and OVF Shoreline Stratigraphic Sites

New shoreline and stratigraphic investigations were performed at sites in the lake basin to refine the lake-level record of Owens Lake. These investigations included ^{14}C dating of tufa and mollusk shells at sites near Dirty Socks and the Owens Valley fault in the southeastern sector of the lake basin (Figure 2). The Dirty Socks and OVF sites are located in areas of the lake basin that previously lacked stratigraphic investigations to define lake levels. The Dirty Socks site is located near Dirty Socks hot spring ~2 km northeast of the trace of the OVF between the elevations of ~1103 and ~1107 m, whereas the OVF site is located within the fault zone between ~1105 and 1122 m (Figure 2). A total of ten mollusk shells from shoreline deposits were collected for ^{14}C dating, four at the OVF site and six at the Dirty Socks site (Table 1). Sample sites were from natural exposures in active channels cut across a broad beach plain with shoreline scarps that is locally overlain by recent alluvium and windblown sand (Jayko, 2009). The shoreline geomorphology of the Dirty Socks and OVF stratigraphic sites is not straightforward because of active faulting and related ground deformation on the OVF in the form of distributive faulting and localized anticlinal growth structures (Slemmons et al., 2008). The five historical to late Holocene shorelines between ~1096 and ~1108 m identified in other parts of the lake basin are present in the area of the Dirty Socks and OVF sites. The number and elevations of several higher shoreline scarps between ~1109 and 1160 m,

however, do not match with dated shorelines identified in other areas of the lake basin, therefore are interpreted to be tectonically deformed. The beach plain in the area shows geomorphic evidence for mostly erosional shoreline processes along the mapped trace of the OVF, with the latest period of surface modification up to an elevation of ~1131 m associated with the Latest Pleistocene-Early Holocene water levels that constructed the Centennial Flat beach ridges, as well as the lower Late Holocene lake-level fluctuations at and below ~1108 m (e.g., Figure 3).

4.1.4. Dirty Socks Site

The Dirty Socks stratigraphic site included sampling in two ~1–1.5-m-deep active channels separated ~25 m from each other. One channel exposed a sequence of faulted shore to nearshore sedimentary facies composed of stratified and interbedded silty to sandy deposits with mollusk-rich beds, where the other channel exposed similar stratigraphy without faults. The channel with faults included deposits juxtaposed against dissimilar beds on either side of a single vertical fault, typical of strike-slip faulting (e.g., McCalpin, 1996). Mollusk shells were sampled for ^{14}C dating at two sites along the channel. Two bivalve shells were sampled on both sides of a fault at different depths below an elevation of ~1103 m. An articulated mussel sample of *Anodonta* sp. at a depth of ~0.3 m from a silty sand bed returned an age of 34,700 ± 320 ^{14}C yr BP (39,700–38,300 cal yr BP) with a median probability age of 38,900 cal yr BP (Table 1). In addition, an articulated clam sample of *Sphaerium striatinum* at a depth of ~1.0 m from a silty sand bed mixed with shells of articulated *Anodonta* sp. returned an age of 35,160 ± 340 ^{14}C yr BP (40,150–38,640 cal yr BP) with a median probability age of

39,400 cal kyr BP (Table 1). The other site in the same channel consisted of a sequence of mostly shore stratigraphic facies. Single samples of bivalve and gastropod shells were sampled on both sides of a fault at different depths below an elevation of ~1104 m. A disarticulated clam sample of *Sphaerium* sp. at a depth of ~0.4 m from a cross-bedded sandy layer returned an age of 42,560 ± 840 ^{14}C yr BP (47,270–44,040 cal yr BP) with a median probability age of 45,600 cal yr BP (Table 1). In addition, a snail sample at a depth of ~1.0 m from a sandy bed returned an age of 31,730 ± 230 ^{14}C yr BP (35,850–34,800 cal yr BP) with a median probability age of 35,300 cal yr BP (Table 1). The apparent ages and corresponding depths of samples from the ~1104 m site are not in stratigraphic order because sample locations are separated by several fault strands in exposures, therefore the deposits have been faulted.

Sites in the channel without faults were sampled at higher elevations of ~1106 and 1108 m. An articulated mussel of *Anodonta* sp. at a depth of ~1 m from a mollusk-rich sandy layer returned an age of 36,910 ± 420 ^{14}C yr BP (41,920–40,340 cal yr BP) with a median probability age of 41,200 cal yr BP (Table 1). The articulated shells of *Anodonta* sp. in the mollusk-rich bed were commonly filled with smaller clams of *Sphaerium* sp. and *Pisidium* sp., plus small gastropods. In addition, the higher site consisted of stratified sands and gravels in the upper section of shoreline sediment associated with ~3.6 ka beach ridge deposits. The Late Holocene gravelly deposits were underlain by a depositional boundary composed of a layer of tufa over a sandy layer with articulated *Anodonta* sp. shells. The tufa at the site resembles palmate tufa, which commonly forms in nearshore environments where thermal springs discharge (e.g.,

Benson, 1994). A sample of *Anodonta* sp. from a depth of ~1 m from the mollusk-rich sandy layer returned an age of 10,345 ± 30 ^{14}C yr BP (11,750–11,300 cal yr BP) with a median probability age of 11,500 cal yr BP (Table 1).

4.1.5. OVF Site

The OVF stratigraphic site included sampling in ~1–1.5-m-deep active channels across a gravelly beach plain. All four sample sites consisted of a 0.5–1-m-thick gravelly beach plain deposit underlain by shore to nearshore sedimentary facies composed of stratified, shell-rich silts and sands. The lowest elevation site at ~1106 m included an exposure of gravelly deposits underlain by gastropod-rich sandy sediment. A snail sample from a depth of ~1 m returned an age of 24,200 ± 130 ^{14}C yr BP (28,270–27,690 cal yr BP) with a median probability age of 27,900 cal yr BP (Table 1). At a higher elevation of ~1108 m, an abrasion surface underlain by a sandy layer with articulated *Anodonta* sp. shells were sampled at a depth of ~0.5 m. The articulated *Anodonta* sp. yielded an age of 11,630 ± 35 ^{14}C yr BP (13,270–13,090 cal yr BP) with a median probability age of 13,200 cal yr BP (Table 1). The other two samples sites were at higher elevations of ~1116 and 1123 m. The sample site at ~1116 m included a surface locally covered by densely packed palmate tufa underlain by a sequence of thinly interbedded silts and sands. An ostracode sample from a ostracode-rich lens interbedded with silt layers at a depth of ~1.3 m returned an age of 16,900 ± 50 ^{14}C yr BP (20,200–19,830 cal yr BP) with a median probability age of 20,000 cal yr BP (Table 1). The site at ~1123 m included an exposure of gravelly beach plain deposits underlain by thick mollusk-rich sandy sediment. An articulated *Anodonta* sp. sample from a depth of ~1 m returned an age of

11,435 ± 35 ^{14}C yr BP (13,100–12,900 cal yr BP) with a median probability age of 13,000 cal yr BP (Table 1). The articulated shells of *Anodonta* sp. in the mollusk-rich bed were partly filled with sand and smaller clams of *Sphaerium* sp. and *Pisidium* sp., plus small gastropods and ostracods. The ^{14}C ages from tufa and mollusk shells from the stratigraphic sites in the eastern and southern sectors of Owens Lake basin provide new shoreline ages to revise the latest Pleistocene (~13 ka) and define the late Pleistocene (~45 to 16 ka) part of the lake-level record of Owens Lake.

4.1.6. Previously Published Data from Owens Lake Basin

Owens Lake has been the focus of numerous paleohydrologic studies because of a robust record of climate change is preserved in lacustrine sediments and shoreline geomorphic features. Most of these studies have focused on resolving the late Pleistocene history of pluvial Owens Lake through analyses of sediment cores with records going back ~800 ka (e.g., Smith and Pratt, 1957; Newton, 1991; Lund et al., 1993; Benson et al., 1996, 1997, 2004; Smith et al., 1997 and references therein; Mensing, 2001) and shoreline features as old as ~140 ka (Carver, 1970; Beanland and Clark, 1994; Bacon et al., 2006; 2018; in press; Bacon and Pezzopane, 2007; Jayko and Bacon, 2008; Orme and Orme, 2008). The previously developed lake-level record of Owens Lake was constructed from a total of 42 ^{14}C ages on tufa, mollusk shell, charcoal, and organic-rich sediment over the last 27 ka (Bacon et al., 2006; Reheis et al., 2014). The stratigraphic context and elevation of ^{14}C ages that were sampled from different sedimentary facies ranging from terrestrial, delta plain to lacustrine (shore, nearshore), plus proxy information from sediment cores were collectively used to define the position of water

levels. In our study, we refine the previous lake-level curve for Owens Lake and extend the record to 50 ka by including the previously unpublished data presented in sections 4.1.1.–4.1.5. with the previously published shoreline and outcrop stratigraphic sites used in Bacon et al. (2006) (Table 1).

The majority of the data previously used to develop the lake-level record came from paleoseismic trench sites (AGPS and QPS) on the OVF north of Lone Pine (Beanland and Clark, 1994; Bacon and Pezzopane, 2007), as well as stratigraphic sites along bluffs of the Owens River (ORB) in northern Owens Lake basin, plus additional sites along the northeastern sector of the basin at Swansea and Keeler (Bacon et al., 2006) (Figure 2). All these sites were used to collectively define latest Pleistocene to Early Holocene lake levels based on integrating sequence stratigraphy of interbedded nearshore, shore, delta, and delta plain depositional environments from numerous natural and trench exposures and ^{14}C ages from charcoal, organic sediment, tufa, and mollusk shells. In addition, the latest Pleistocene ages of mollusk shells in beach ridge deposits used to define maximum oscillations in lake level were from detailed stratigraphic studies previously performed at the Swansea and Centennial Flat sites (Orme and Orme, 2000; 2008). Furthermore, other investigations at the Owens River delta site characterized a mixed assemblage of bivalves and gastropods that yielded ^{14}C ages from mollusk shells in areas at the mouth of the Owens River to define relatively low lake levels during the latest Pleistocene (Koehler, 1995; Orme and Orme, 2008; Figure 2). Maximum lake-levels were also estimated from the age and elevation of soluble pack rat middens preserved at the base of the Inyo Mountains at the Haystack site (Koehler and Anderson, 1994; Table 1; Figure 2).

4.2. Owens Lake Overflow Channel and Sill

The overflow channel (i.e., spillway) of Owens Lake is a prominent, north-south axial channel that has incised across distal piedmont slopes of the Sierra Nevada and Coso Range in the southern end of the lake basin (Figures 3 and 5). The overflow channel crosses dissected late Pliocene to Pleistocene alluvium that is underlain by gently dipping, interbedded lacustrine sandstone and siltstone with volcanic tuff and flow rocks of the ~3–6 Ma Coso Formation (Jayko, 2009). The channel is bounded on the west by the east-dipping normal SNFF and on the northeast by the east-dipping dextral-oblique OVF. The normal SFF locally forms a graben in the northern reach of the overflow channel (Figure 4). The modern sill has formed at an elevation of ~1145 m associated with recent alluvial fan aggradation in the central confined reaches of the overflow channel at the confluence of two of the larger streams draining the Sierra Nevada and Coso Range (Figure 4). The lowest elevations within the overflow channel near the drainage divide have been submerged since AD 1913 by construction of Haiwee Reservoir. The reservoir is part of the Los Angeles Aqueduct system and consists of two dams (North and South Haiwee Dams) that impound water on both sides of the drainage divide (Figure. 4). As a result, there has been a lack of detailed studies of the sill area since construction of the reservoir.

Prior to our study, the sill was considered to be relatively stable at ~1145 m, therefore the age of either shorelines identified below this elevation or proxies for closed basin conditions from sediment lake cores were interpreted to be associated with no overflow conditions at or below this level (Smith and Street-Perrot, 1983; Smith and Bischoff, 1997; Bacon et al., 2006). Conversely, Orme and Orme (2008) speculated that

an earlier spillway of Owens Lake was ~1 km west of its current position at unknown elevations from ground deformation from either faulting or volcanism. We present previously published and unpublished subsurface geologic evidence and chronologic ages of sediment from geotechnical investigations of the Haiwee Reservior area to characterize the morphometry of the entire overflow channel and directly date the latest episodes of overflow, thereby resolving the apparent asynchrony between the latest Pleistocene overflow records of Owens Lake (Bacon et al., 2006; Orme and Orme, 2008; Reheis et al., 2014) and China-Searles Lake (Phillips, 2008; Rosenthal et al., 2017).

4.2.1. Geomorphology and Geology of the Overflow Channel

Pre-construction topographic surveys of the overflow channel and geological observations of foundation materials of the South Haiwee Dam site were used to characterize the geomorphology of the entire overflow channel, as well as the thickness of channel fill and depth to bedrock in the southern reach of the channel (Los Angeles Board of Public Service Commissioners, 1916). A longitudinal profile along the axis of the overflow channel from digitized contours of the georeferenced map of pre-construction topography shows the transverse profiles of four coalescing alluvial fans that have formed within the confined reaches of the channel, where the highest alluvial fan controls the position of the modern sill at an elevation of ~1145 m (A–A'; Figures 4 and 6). In the vicinity of the South Haiwee dam site, three deep test wells along with a deep trench were excavated to depths of up to 36 m into bedrock across a constriction in the overflow channel prior to and during construction in AD 1911. The excavations were logged and a survey-controlled geologic cross section of the proposed dam site was

produced by the City of Los Angeles engineers. The cross section and geologic descriptions demonstrate that channel fill is composed of up to 33.5-m-thick sequence of poorly consolidated and poorly sorted, sandy to bouldery alluvial fan deposits sourced from nearby granitic bedrock of the Sierra Nevada and basalt from either the Coso Formation or Coso Range. The channel fill is underlain by a sharp depositional contact developed on indurated bedrock of the Coso Formation that is composed of gently tilted siltstone across most of the bottom of the channel and volcanic flow rocks on the eastern margin of the channel, whereas hard, cemented sandy to gravelly alluvial fan sediment also underlain by Coso Formation bedrock is on the upper western margin of the channel (Los Angeles Board of Public Service Commissioners, 1916). The depositional contact over the width of the bottom of the channel has planar topography with an elevation as low as 1097.3 m that we interpret to be a strath terrace (A–A'; Figure 5).

A geotechnical investigation of foundation materials at the toe of the North Haiwee Dam site was also used to characterize the stratigraphy and thickness of channel fill, depth to bedrock, and age of sediment from OSL dating in the northern reach of the channel (Black and Veatch, 2013; Goetz et al., 2016; Kemp et al., 2016). A transect of 10 exploratory sonic boreholes, 31 cone penetration testing probes, and seismic reflection surveys across the overflow channel (B–B') show channel fill is composed of up to ~35-m-thick sequence of poorly consolidated and moderately sorted, interbedded silty sand to sandy silt with lesser gravel alluvial-type deposits sourced mostly from nearby granitic bedrock of the Sierra Nevada. The base of the channel fill consists of a ~1.5-m-thick moderately-sorted, subrounded to rounded, elliptical- to disk-shaped basal gravel deposit that is underlain by a sharp depositional contact on indurated interbeds of

siltstone and sandstone of the Coso Formation. The depositional contact over the width of the bottom of the channel has planar to wavy topography with a mean elevation of 1112.8 ± 2.7 m that we interpret to be a strath terrace. The upper margins of the channel are composed of sandy to gravelly alluvial fan deposits with varying degrees of pedogenic carbonate development that also overly a higher strath terrace formed on Coso Formation bedrock (Goetz et al., 2016) (B–B'; Figures 4 and 6).

4.2.2. Age of Channel Fill and Colluvial Slope Deposits

The northern reach of the overflow channel in the vicinity of North Haiwee Dam is relatively wide and consists of a pair of prominent terraces between the elevations of ~1162 and 1165 m that are inset with older alluvial fan deposits along upper channel margins (Beanland and Clark, 1994; Goetz et al., 2016). The pair of terraces become narrow in width and grade to a channel constriction ~2 km south of North Haiwee Dam. The elevation and geomorphology of the terraces suggest that they are likely beach plains formed near the outlet of the lake based on the presence of spit-like features and shoreline scarps at similar elevations of the ~40 ka shoreline at ~1165 m (e.g., Jayko, 2009; Bacon et al., 2019a) (Figure 4). The upper alluvial fan deposits along the channel margins are estimated to be Pleistocene in age based on soil-geomorphologic characteristics and geologic mapping (Jayko, 2009). Exposures of alluvial fan deposits on the eastern margin of the channel show pedogenic carbonate stage IV development and other soil indices within soil profiles (e.g., Birkeland, 1999) indicating a likely age of ~100 ka, whereas lower sections with buried soils, in addition to alluvial fan deposits on the western margin of the channel, collectively have better developed soil indices, suggest relatively older

ages of >100 ka (Goetz et al., 2016) (B–B'; Figure 6). Modification of alluvial fan surfaces and development of the beach terrace within the upper overflow channel near the outlet of the lake provide minimum ages for the alluvial fan deposits to older than ~40 ka, thereby supporting the inferred ages of ≥100 ka (Figure 5).

Geochronologic dating included ^{14}C and OSL analyses to determine the age of sediment exposed in exploratory trenches and encountered in deep boreholes in the northern reach of the overflow channel (Black and Veatch, 2013; Goetz et al., 2016). An ~85-m-long and up to 4.6-m-deep trench was excavated along the B-B' transect between boring SB-12-09 and North Haiwee Dam to characterize the upper section of channel fill (Figure 5). The trench exposed a continuous section of horizontally stratified alluvial sediment consisting of poorly-sorted, angular to subangular sandy silt to silty sand with gravel. Detrital charcoal sampled from near the base of the trench at an elevation of 1135.5 m returned an age of 5060 ± 30 ^{14}C yr BP (5900–5740 cal yr BP) with a median probability age of 5800 cal yr BP (Black and Veatch, 2013) (Table 1; Figure 5). Sediment from a deeper section of channel fill was also sampled for dating from a ~21-m-deep sonic boring. Three OSL samples were taken from boring SB-12-09 at depths of 9.4, 13.4, and 16.4 m below an elevation of 1136.9 m in an area ~330 m north of North Haiwee Dam near the eastern channel margin. The samples consisted of well-sorted, fine- to medium-grained sand that lacked angular to subangular gravel typical of alluvium encountered in the upper ~5 m of sediment at the borehole site and nearby trench exposures. The OSL samples yielded ages in stratigraphic order of 6.9 ± 1.1, 7.6 ± 1.3, and 11.6 ± 1.8 ka (Black and Veatch, 2013; Goetz et al., 2016; Table 3; Figure 5). The luminescence signals for samples from the channel fill (HD 1, 2, and 3) were well

behaved having tightly clustered distributions of equivalent doses, thereby providing confidence in the ages (see Appendix C).

The colluvial slopes along the eastern channel margin were also sampled for OSL dating by Black and Veatch (2013) at sites ~0.7 km south of North Haiwee Dam. Colluvial slopes in this area are derived from weathered late Pliocene to early Pleistocene alluvial sediment that locally fringe the overflow channel and cap an erosion surface developed on Coso Formation bedrock (Jayko, 2009). Three ~4–5 m deep trenches spaced up to ~45 m from each other were excavated across the transition between the footslope and midslope of the eastern channel wall where it steepens between the elevations of ~1150 and 1166 m (e.g., B–B'; Figure 5). Trenches exposed colluvial deposits consisting of loose, massive and poorly sorted, angular to subangular silty sand with gravel to cobbles. The colluvial deposits have an unconformable depositional contact over slightly hard to very hard, moderately stratified and poorly-sorted, angular to subangular sandy silt to silty sand with gravel and cobbles alluvial fan deposits of likely late Pliocene to early Pleistocene age based on geologic mapping in the area (Jayko, 2009), morpho-stratigraphic position with nearby alluvial surfaces, and soil-geomorphologic characteristics of deposits.

The OSL samples were taken from depths between 0.6 and 2.1 m within gently dipping, matrix supported sandy deposits typical of colluvial wedge stratigraphy. Sample sites are from depths that also show evidence of pedogenic processes and bioturbation. Three OSL samples taken from colluvium in a trench at depths of 1.4 and 2.1 m returned ages of 22.8 ± 8.4 ka for a single sample and 29.1 ± 8.0 and 21.4 ± 9.5 ka for duplicates samples, respectively. Samples at shallower depths of 0.6 and 0.8 in colluvium from

different trenches yielded ages of 7.7 ± 1.5 and 35.9 ± 13.7 ka, respectively (Black and Veatch, 2013) (Table 3). The luminescence signal for the youngest sample (HD 8) was well behaved with a tightly clustered distribution of equivalent doses, thereby providing confidence in the age. The other signals, however, had poorly clustered distributions of equivalent does and the confidence level for these samples is low (see Appendix C). The poor behavior of the samples (HD 6, 7-1, 7-2, and 9) might be the consequence of significant volcanic quartz within samples derived from ash flow tuff units in the Coso Formation. This would produce a high residual level and decay pattern for the OSL signal that is sluggish, and not characteristic of the normal shine down curve for quartz (Black and Veatch, 2013). As a result, samples from deeper depths with ages of ~21 to 29 ka (HD 6, 7-1, and 7-2) are considered to be generally reasonable, but likely underestimate the age of the deposits, therefore are interpreted to be minimum ages. The oldest sample with an age of ~36 ka derived from near surface colluvium (HD 9) is considered problematic because of its older age and shallow depth (Black and Veatch, 2013). Therefore, the age of sampled HD 9 is uncertain and considered unreliable rather than a minimum age and not used in our study.

4.2.3. Spillway of Owens Lake Basin

Previous studies that addressed the location and character of sills in Owens Lake basin were either somewhat limited in scope (Bacon et al., 2006; Jayko and Bacon, 2008) or did not include site-specific data to support proposed overflow models (Orme and Orme, 2008). Two of the highest documented shorelines in Owens Valley are tectonically deformed at elevations of ~1155–1165 m from a ~40 ka lake level (Bacon et al., 2019a)

and ~1180–1200 m from a ~160 ka lake level (Jayko and Bacon, 2008). The bottom of the overflow channel of Owens Lake is characterized as a stable (i.e., hard) sill at ~1113 m below North Haiwee Dam that would control spill when there is a lack of channel fill. At elevations above ~1113 m the sill of Owens Lake is controlled by the level of unconsolidated sediment confined in the narrow reach of the channel, thereby forming an unstable and erodible (i.e., soft) sill. We performed an assessment of potential areas within the overflow channel that may have controlled the latest highstand water levels of Owens Lake that formed the ~40 and 160 ka shorelines.

Several transverse topographic profiles across the entire length of the overflow channel from a 10-m-resolution DEM were used to identify landforms that coincide with the range of elevations of the deformed ~40 and 160 ka shorelines in Owens Lake basin. Two of the profiles at the outlet of the overflow channel along transects C–C' and D–D' provided the best evidence for landforms related to the highstand shorelines (Figure 4A). The upstream transect crosses dissected alluvial fans with a suite of terraces down to the channel bottom on the western margin and a large landslide feature developed on pervasively jointed and moderately dipping volcanic flow rock of the Coso Formation on the eastern margin of the channel (C–C'; Figures 4 and 6). Given the uncertainties with the 10-m-resolution DEMs, the geomorphic profile shows sharp breaks-in-slope, benches, and channel features between the elevations of ~1172 and 1180 m, as well as another set of breaks-in-slope and a bench between ~1156 and 1165 m that coincide with the elevations of the ~160 and ~40 ka shorelines, respectively (C–C'; Figure 6). The downstream transect crosses dissected alluvial fans on the western margin of the channel similar to transect C–C', but also crosses a steeper and narrower canyon within volcanic

flow rock of the Coso Formation (D–D'; Figures 4 and 6). There is no obvious evidence of landforms associated with ~160 ka shoreline at elevations near ~1180 m along the D–D' profile. The profile does, however, show sharp breaks-in-slope, benches, and a channel feature at elevations between ~1140 and 1165 m that may be associated with down-cutting from spill at the ~40 ka water level (D–D'; Figure 6).

The fluvial geomorphology of the outlet indicates that the spillway of the ~40 and ~160 ka shorelines may have been located in the southern reaches of the overflow channel, whereas the more recent outlet during the latest Pleistocene and Early Holocene was likely in the northern reach. Prior to ~160 ka, it is possible that the position of a paleo-spillway channel was where the large landslide mass is today (Figures. 4 and 6). This implies there has been several subsequent episodes of cut-and-fills since the lake was impounded at this time. The height of the sill was likely influenced by channel filling with alluvial fan sedimentation during inter-pluvials (i.e., inter-glaciations) followed by contemporaneous alluvial sedimentation during highstand water levels at ~40 and 160 ka. The sills during the highstands were likely soft, similar to the modern configuration, but reaching greater thickness and height, and would have had minor spillway channels along channel margins, such as the inset terraces and elevated channel features developed on more stable older alluvial fans, the large landslide feature, and bedrock. The area of the outlet that is currently devoid of sediment was likely plugged with sediment during the highstands at ~40 and 160 ka. This plug would be reflected downstream of the spillway outlet as an alluvial fan in Rose Valley with an alluvial fan apex graded to areas of transects C–C' and D–D' (Figures 4 and 6). Remnants of this alluvial fan appear to be preserved on the western margin of the outlet in the form of a broad and prominent inset

terrace with a bouldery surface along the toe of dissected older alluvial fans (Figures 6 and 7). A reconnaissance-level investigation of the degree of surface boulder weathering and subsurface soil-geomorphic characteristics of the broad inset terrace indicates an age older than ~20–25 ka when compared to similar alluvial fans in Owens Valley (e.g., Zehfuss et al., 2001).

4.3. Lake-Level Reconstruction

4.3.1. Elevation of Shoreline Features and Lacustrine Deposits

The differential fault-block model we use to reconstruct water levels for Owens Lake is applicable for tectonically complex and seismically active lake basins where vertical ground deformation is accommodated by distributed slip on two or more normal and strike-slip fault systems. We account for vertical deformation by identifying the absolute elevations of landforms and deposits on individual fault blocks because differential motion occurs on closely spaced faults with different vertical slip rates (e.g., Bacon et al., 2019a). Calculating a net vertical slip rate across the lake basin and overflow area (sill) that are bounded by two or more faults produces more accurate estimates of the absolute magnitude of vertical deformation of individual study sites. A net vertical slip rate is calculated by either using a single mean slip rate if the study site is on a fault block adjacent to a single fault or using the sum of two or more mean slip rates if the study site is situated on a fault block bounded by two or more parallel faults. The location of study sites relative to individual faults determines if vertical slip rates are either positive values representing footwall deformation (i.e., uplift rates) or negative values for hanging-wall deformation (i.e., subsidence rates) for both normal and dextral-

oblique faults. The approach used to estimate tectonic ground deformation was to multiply the net vertical slip rate of the fault block containing landforms and deposits with their age to solve for the magnitude and direction of vertical deformation. If the sign is negative then the value of vertical deformation is then added to the observed field elevation, whereas if the sign is positive then the value is subtracted from the observed field elevation to correct the elevation of study sites to pre-deformed positions (Bacon et al., 2019a). The datum for elevations of geomorphic and stratigraphic sites is mean sea level, therefore the application of fault slip rates to adjust contemporary elevations for tectonic deformation produced elevations having a frame of reference relative to mean sea level.

Owens Lake basin contains five subparallel faults, including the primary SNFF and OVF systems, as well as the less active normal Keeler fault (KF), normal Owens River-Centennial Flat fault (OR-CFF), and the dextral-oblique southern Inyo Mountains fault (SIMF) (Figure 2). Spatiotemporal changes in the distribution of slip in the lake basin are defined by the ~40 ka highstand beach ridge that is vertically deformed ~10 m and undeformed suite of ~11–16 ka beach ridge deposits at elevation of ~1114–1129 m. Integration of paleoseismic records in Owens Valley with the tectonic geomorphic record of deformed beach ridges and alluvial fans indicates that both normal and strike-slip faulting occurred between ~11–16 and 40 ka across all faults in the lake basin, whereas strike-slip faulting on the OVF and SIMF has been the predominant style of slip since ~16 ka (Bacon et al., 2019a). In general, the apparent slip distributed in the lake basin is accommodated by two structural domains, a western domain including fault blocks between the SNFF, OVF and OR-CFF and an eastern domain consisting of fault blocks between the OR-CFF, KF, and SIMF (Figure 2).

Study sites in the western structural domain (AGPS, ORB, QPS, Owens River delta, Haystack, Dirty Socks, and OVF) required accounting for vertical deformation on the SNFF and OVF (Figure 2). The majority of sample locations at these sites are located on the hanging walls of the OVF and SNFF, therefore sample sites were corrected to higher elevations based on a net subsidence rate of 0.37 m/ka from the summation of mean rates for the OVF and SNFF of –0.12 and –0.25 m/ka, respectively (Table 4). In contrast, all sample locations at the OVF study site, as well as a single sample location at the QPS study site are located on the footwall of the OVF and hanging wall of the SNFF. As a result, sample sites were corrected to higher elevations based on a net subsidence rate of 0.13 m/ka from the summation of mean rates for the OVF and SNFF of 0.12 and – 0.25 m/ka, respectively (Table 4). Study sites in the eastern structural domain (Swansea, Keeler, and Centennial Flat) are situated within a sector of the lake basin that requires accounting for net subsidence. The sample locations at these sites are located in an area where 9–10 m of ground deformation resulted from the cumulative effects of faulting, uniform tilting, and basin-wide subsidence since ~40 ka (Bacon et al., 2019a). As a result, sample sites in the eastern sector of the lake basin were corrected to higher elevations using a uniform, mean net subsidence rate of 0.24 m/ka (Table 4). The corrected elevations of previously reported sample sites with ^{14}C ages and new ^{14}C, post-IR-IRSL, and OSL ages of our study are shown in Tables 1–3.

4.3.2. Lake Bottom Elevation

The absolute elevation of the lake bottom during the time of deposition is required to perform the threshold lake-water depth analysis of sediment in lake cores described in

the following section. Estimating the absolute elevations of sediment layers at lake-core sites involves accounting for settlement from consolidation and subsidence from active faulting (e.g., Bacon et al., 2018). Sediment in lacustrine settings consolidates with burial, requiring normalization of sediment thickness based on dry density or water content to allow direct comparison of recent and ancient sedimentation rates (e.g., Martin and Rice, 1981; Davidson et al., 2004). To reconstruct the lake bottoms to depositional elevations by accounting for consolidation, we used the water contents of ~62.7–44.0 wt.% at depths of 1–70.8 m for silty clay layers reported in Owens Lake core OL-92 (Friedman et al., 1997). We modeled down to a depth of ~71 m in sediment cores because this depth corresponded to ages older than 50 ka. A natural logarithm function was developed from water content and depth data in core OL-92. The normalized water content versus depth data was fitted by a logarithmic trend line ($r^2 = 0.95$), similar to the presentation of compression test data of soil, where the void ratio of a soil decreases linearly with the logarithm of pressure (e.g., Handy and Spangler, 2007). Normalized water content (W_w) was calculated as:

$$W_w = -0.062\ln(d)+0.998 \quad (1)$$

where the bottom of sediment layer depth (d) in meters is the variable. Settlement due to consolidation (δ_c) of sediment layers in lake cores was estimated as:

$$\delta_c = t - (t * W_w) \quad (2)$$

where thickness of each layer (t) in meters is the variable.

Estimating rates of subsidence from active faulting at core sites was done similar to the approach used to vertically correct the elevations of shoreline features and deposits

for tectonic ground deformation. The reconstruction of ground deformation at the core OL-92 site was based on a maximum net subsidence rate of 0.46 m/ka from combining the maximum vertical slip rates for the SNFF of –0.30 m/ka and for the OVF of –0.16 m/ka, given that the core site is located on the hanging wall of both faults (Table 4; Figure 2). We used a maximum subsidence rate because this value was used in the calibration of the threshold lake-water depth analysis with historical shoreline and sediment core data from core OL-97 (Bacon et al., 2018). The absolute elevations of sediment layers in lake cores were calculated by multiplying the subsidence rate with the duration of time between individual sediment layers to derive values of tectonic subsidence, which was followed by adding this value to the magnitude of consolidation of each sediment layer. The cumulative value of the total consolidation and tectonic subsidence for each sediment layer since ~ 50 ka was then added to its corresponding field elevation. The magnitude of correction for consolidation and subsidence at a depth of ~28 m in core OL-92 are ~4 and 18 m, respectively.

4.3.3. Threshold Lake-Water Depth Analysis

The erosion potential of lake bottom sediments was assessed by modeling the threshold lake-water depths required to best match sedimentology described in core OL-92. The wind wave-generated bottom shear stress at the water-sediment boundary and critical shear stress for bottom erosion were calculated after the methods of USACE (1984, 2002). The hourly average wind speeds of 7 and 18 m/s for strong breeze and whole gale conditions, respectively, along with fetch lengths up to 70 km were used in the model to simulate two wind event scenarios that would potentially define the

effective wave base at core sites (Appendix D; Figure 8). The wave characteristic calculated by the wind-wave model include significant wave height (H_s), spectral peak wave period (T_p), and wave length (L). The wave characteristics driven by wind speeds of 7 and 18 m/s over a fetch of up to 70 km have values ranging from (H_s=1.1 m; T_p=4.6 s; L=32.6 m) to (H_s=2.9 m; T_p=6.3 s; L=62.3 m), respectively. The critical bottom shear stresses at fetches between 0 and 70 km were calculated to entrain four particle sizes ranging from clay (2 μm) to coarse pebble (32 mm) that coincide with the boundaries between the size classes of the Wentworth (1922) scale.

The threshold lake-water depth to initiate sediment entrainment was determined by iterating water depth until the ratio between the bottom shear stress below the wave crest and the critical bottom shear stress to entrain a given particle size exceeded 1. Potential sediment entrainment for a range of particles sizes described in the sediment core were modeled. The modeling shows that the threshold lake-water depth of the finer sediment with clay-sized particles (2 μm) can potentially be entrained at depths of ~20 and 44 m under waves driven by wind events of 7 and 18 m/s over a fetch of up to 70 km, respectively (Figure 8). The modeling also shows that coarser sediment of pebble-sized particles up to 32 mm under the same two wind events and fetch can potentially be entrained at depths of ~2.7 and 8.6 m, respectively (Figure 8). The threshold lake-water depth analysis was used in conjunction with sedimentology described in the lake core to estimate minimum potential water levels in the absence of shoreline positions.

4.3.4. Spillway Elevations

Spillways and sills composed of alluvium in seismically active lake basins are especially dynamic because they are relatively more erodible compared to bedrock and can occupy different positions through time. Changing sill positions are mostly controlled by channel down-cutting—influenced by the combination of fluctuating rates of base-level changes, headward erosion, and tectonic or isostatic ground deformation. Understanding the types of ground deformation in sill areas affords an assessment of potential processes and accurate reconstruction of overflow levels. We reconstructed spillway elevations by accounting for differential fault-block deformation in sill areas similar to the approach used to correct the elevations of shoreline features and deposits, and lake core sites. Given the uncertainty of the absolute position of alluvial-filled spillways without information, we reconstructed the elevations of bedrock sills at 1 ka time steps to provide minimum estimates of the absolute elevations of periods with overflow conditions since 50 ka.

The northern half of the spillway channel of Owens Lake is bounded by the normal SNFF and dextral-oblique OVF, as well as situated within a graben of the normal SFF (Goetz et al., 2016; Kemp et al., 2016; Figures 2 and 4). Total vertical deformation in the area of the overflow channel and sill was estimated by accounting for distributed slip between normal and dextral-oblique faulting. Paleoseismic investigations on the SFF indicate the most recent event on the fault occurred at ~28 ka (Amos et al., 2013). Furthermore, dextral-oblique faulting on the OVF has also been the primary source of deformation in Owens Valley over the last ~16 ka, which was preceded by a period that included both normal and dextral-oblique faulting from all faults in the basin between

~16 and 40 ka (Bacon et al., 2019a). As a result, we accounted for spatiotemporal patterns of the distribution of slip at the overflow channel by reconstructing the elevation of the lowest strath terrace in the channel at an elevation of ~1113 m with two net vertical slip rates (B–B'; Figure 5). Ground deformation at the spillway during the most recent period between 0 and 28 ka was estimated by accounting for only footwall deformation on the OVF, which required a mean uplift rate of 0.12 m/ka (Table 4). The uplift rate of the OVF yielded as much as ~3.4 m of correction to lower elevations in the last 28 ka. The period from 28 to 50 ka, however, required a mean net subsidence rate of 0.22 m/ka from the summation of mean vertical rates for hanging wall deformation on the SNFF and SFF, and footwall deformation on the OVF of –0.25, –0.09, and 0.12 m/ka, respectively (Table 4). The net subsidence rate resulted in as much as ~4.8 m of correction to higher elevations during the earlier 22 ka period. The reconstruction shows the bottom of the northern reach of the spillway channel has been relatively stable with a net ~1.4 m of mean subsidence in the last 50 ka when accounting for net vertical deformation, as well as earthquake cycles and distributed slip on bounding faults.

4.4. Lake-Level Indicators

Reconstructing accurate lake-level curves requires detailed knowledge of how the lake surface has fluctuated through time. Lake-level curves are typically constructed from the ages and elevations of samples that were deposited above, at or near, or below lake level (Reheis et al., 2014, and references therein). The lake-level curve in this study was constructed from shoreline elevations and ages of a variety of indicators for depositional environments, but also included threshold lake-water depth modeling of lake-core

sedimentology to produce continuous estimates of water-level variations in the absence of shoreline information (Bacon et al., 2018). The curve also includes reconstructions of lake bottom and spillway elevations to produce a fully integrated model of lake-level variations that are corrected for vertical ground deformation (Figure 9). The elevation of lake levels shown on the curve was developed from the type of depositional environment indictor and assigned water depths based on conservative estimates to minimize errors in modeled lake size.

4.4.1. Beach Ridges and Depositional Carbonate

Beach ridges are the most precise indictor for the location of water level at the time of deposition, and as a result, the position of lake level shown on the curve corresponds to the reported elevation of ridge crests. A variety of calcium carbonate materials have also been used in lake-level reconstructions (e.g., Benson et al., 2013; Hudson et al., 2017), but there are large uncertainties in the absolute water depth at the time of deposition if the material is either depositional (i.e., tufa, marl, oolites) or faunal (i.e., gastropod, bivalve, ostracode). Studies in Pyramid Lake subbasin and Lahontan basin, Nevada identified several conditions or processes to explain the occurrence and uneven spatial distribution of tufa deposits, beginning with the most important process as follows: (1) stable lake level; (2) proximity to a source of calcium; (3) existence of a hydrologically closed system; (4) presence of a stable substrate; and (5) elevated water temperature (Benson, 1994). The morphology of tufa accumulations commonly indicate lake-level dynamics during the time of deposition. Large accumulations commonly occur at elevations that coincide with lake levels stabilized by either relative changes in

bathymetry of the lake basin or spill levels into adjoining basin or sub-basins, whereas relatively thinner sheet-like tufa deposits form during fluctuating lake levels in response to climate change (Benson, 1994).

The uncertainty of water depth for tufa ages in Owens Lake basin was accounted for by assigning a depth of 3 m. Other carbonate deposits including oolitic sand and marl (mud) were also used to define water levels in this study. These types of lacustrine sediment form in shallow (i.e., high-energy) and deep (i.e., low-energy) depositional environments, respectively (Ehlers and Blatt, 1982). Field observations of modern lacustrine oolitic sand deposits are commonly restricted to a depth of 0 to 5 m (e.g., Davaud and Girardclos, 2001). Therefore, a typical water depth of 2 m was assigned to oolitic sand samples to define water levels. Sample sites of marl, however, were assigned variable water depths from the threshold lake-water depth analysis using a study site's fetch and a range of particle sizes of coarse silt to clay for muddy sediment.

4.4.2. Fossil Mollusk and Crustacean Shells

Additional carbonate materials including shells from mollusks were used to define water levels of Owens Lake. Deposits with either articulated bivalve shells or well-preserved gastropod shells have the highest confidence in representing the substrate utilized by mollusk species while living, whereas deposits with either disarticulated bivalve shells or a mixed assemblage of species is evidence of post-mortem transport and reworking. A variety of mollusk taxa associated with different aquatic habitats have been identified and dated in the paleo-Owens River system (Miller, 1989; Koehler, 1995; Smith, 2009; Rosenthal et al., 2017). We only used mollusk species from lacustrine

deposits as lake-level indicators in an effort to not include species typically associated with terrestrial environments disconnected from a large water body, such as springs and ponds. Up to four species of bivalve have been documented in Owens Lake lacustrine sediment (Miller, 1989; Koehler, 1995), however, only two species (*Sphaerium striatinum* and *Anodonta californiensis*) have been dated from samples collected from shore to nearshore depositional environments (Table 1). In general, living *Sphaerium* sp. throughout North America and Northern California are found mostly in clean permanent lakes at depths of several cm to ~20 m and prefers sandy to gravelly substrates. Living *Anodonta* sp. in the western U.S. also predominantly live in large perennial lakes, but require a specific host fish during its larval stage and prefers sandy to muddy substrates (e.g., Koehler, 1995). A water depth of 4 m was assigned to bivalve lake-level indicators in this study given the wide range of water depths associated with living *Sphaerium* sp. and *Anodonta* sp., in conjunction with sample sites consisting mostly of silty sand to gravelly sand sediment that are deposited in relatively shallow water.

Many more gastropod species have been identified and dated in the paleo-Owens River system with up to twenty-two species of aquatic and semi-aquatic gastropod identified in deposits associated with either terrestrial or lacustrine depositional environments (Miller, 1989; Koehler, 1995; Smith, 2009; Rosenthal et al., 2017). Only two species have been dated from samples collected from deposits in Owens Lake basin interpreted to be from shore to nearshore depositional environments (Table 1). One of the gastropods *Amnicola* is a gilled species and the other *Helisoma* is a pulmonate. Interpreting the depositional environment of pulmonate species is complicated because many of them are found in both terrestrial (i.e., spring, delta plain) and lacustrine (i.e.,

back-barrier lagoon, wetlands) environments. We reduce this uncertainty by using gastropods that are sampled from both deltaic and lacustrine deposits, as well as from elevations with other supporting stratigraphic and geomorphic lake-level indictors. In general, the gastropods including *Helisoma newberryi* live in large perennial lakes and streams. This species prefers muddy substrate with or without vegetation (e.g., Koehler, 1995). The other dated gastropod including *Amnicola palustris* is commonly found in waters with a wide range of water qualities and temperatures and can tolerate seasonal fluctuations in water level within wetlands, small streams, and ponds. These species commonly prefer densely vegetated shallow water environments (e.g., Koehler, 1995). A uniform water depth of 2 m was assigned to the gastropod lake-level proxy in this study given that most shells were sampled from deposits interpreted to be from wetlands to shoreline depositional environments.

In addition to mollusk species, ostracod valves were also identified in lacustrine deposits of Owens Lake. We use ostracods to define lake levels by assigning variable water depths to the elevation of sample locations from the threshold lake-water depth analysis using a fetch for the lake core site and a range of particle sizes of coarse silt to clay for muddy sediment.

4.4.3. Terrestrial Landforms and Deposits

Landforms and deposits associated with terrestrial depositional environments were also used to define maximum lake level. Most of the materials dated were sampled from deposits associated with environments adjacent to or distant to the water's edge, including delta and alluvial plains, wetlands, and springs. The materials include organic

sediment, plant material, peat, carbonized wood, charcoal, and soluble pack rat middens (Table 1). Sandy deposits from colluvial slopes in the Owens Lake overflow channel were also dated by OSL and used to define maximum lake levels (Table 3). The elevation of sample sites associated with terrestrial environments were used to limit the position of water levels shown on curves to below their respective elevations.

4.4.4. Sediment Core Proxy Records

Proxy evidence in lake cores from Owens Lake including variations of total organic carbon (TOC), total inorganic carbon (TIC) and $\delta^{18}O$ values (Benson et al., 1996; 1997; 1998) and presence of thick oolitic sand deposits (Smith and Bischoff, 1997) were collectively used as proxy indicators of relative evaporation in the lake system to represent either drops in lake level or hypersaline lake conditions. Reconstructed depths of proxy data in lake cores were also used in this study to constrain the direction of lake-level oscillations in the absence of shoreline data (e.g. Bacon et al., 2006).

5. DISCUSSION

5.1. Revised Owens Lake Water-Level Record

We revised the Owens Lake water-level record with new ages from stratigraphic sections, shoreline features, and from threshold lake-water depth modeling of sedimentology in core OL-92 which serves as a proxy for near shore or shallow lacustrine water depths. We also provide new ages for episodes of spill of Owens Lake based on geotechnical investigations and reconstructions of sill elevations within the overflow channel. Integration of these new data offers a comprehensive and continuous

characterization of the lake-level history of Owens Lake. This in turn, allows refinement of previous work and extension of the lake-level curve from ~28–30 to 50 ka (Figure 9). The following discussion includes descriptions of modeled water-level variations of Owens Lake and periods of potential overflow in relation to periods of rapid climate change and general comparisons with Owens Lake sediment core records and lake-level records of downstream China and Searles Lakes basins, and other nearby river-lake systems of the Sierra Nevada.

5.1.1. Overflow Record (50 to 6.4 ka)

Many basins in the western U.S. were hydrologically integrated by streams or coalescing lakes during pluvial periods (Smith and Street-Perrott, 1983; Jannik et al., 1991; Reheis, 1999; Phillips, 2008). In general, sills and associated overflow channels controlled the absolute water level of hydrologically open lakes, which could either be characterized as stable (i.e., hard) or unstable (i.e., soft) in terms of erodibility (e.g., Pengelly et al., 1997). Sill areas in seismically active lake basins in the Basin and Range are commonly affected by either uniform tilt related to isostatic rebound or normal faulting from a single fault system (e.g., Mifflin and Wheat, 1979; Adams et al., 1999) or vertical ground deformation related to distributed slip between parallel oblique-normal faults in lake basins that are within the southern WLB, such as in Owens Valley (e.g., Bacon et al., 2019a, Figure 2). Accounting for distributed slip at the Owens Lake overflow channel and sill in our study afforded reconstruction of overflow levels, as well as provided limiting elevations to constrain the timing of potential overflow episodes.

The stratigraphic and geochronologic data showed the spillway of Owens Lake basin is dynamic and currently composed of up to ~40 m of unconsolidated fluvial-deltaic and alluvial sediment, rather than a stable bedrock sill, as previously interpreted (e.g., Smith and Street-Perrott, 1983; Bacon et al., 2006). When characterization of the overflow channel is combined with the reconstruction of sill elevations altered by vertical tectonic deformation we are able to constrain the elevations of potential overflow levels of Owens Lake (Figure 9). The position of the strath terrace in the northern reach of the overflow channel provides minimum elevations for potential overflowing water levels. Presence of prominent shorelines features and evidence of both in situ and reworked shoreline deposits at ~1114 m, plus mollusk-rich deposits from many sites encompassing the lake basin at ~1111–1113 m were assigned corrected elevations that corroborate sill-controlled and mostly overflowing water levels at strath terrace positions between ~46 to 13 ka (Table 1; Figure 9).

Geotechnical investigations of the Owens Lake sill area (Black and Veatch, 2013; Goetz et al., 2016; Kemp et al., 2016) provided a well dated stratigraphic section that we have been able to correlate with dated shoreline and nearshore deposits in order to establish a chronology for recent episodes of overflow above the modern strath terrace (i.e., hard sill) at 1112.8 ± 2.7 m. The well sorted and rounded sandy sedimentology described in the overflow channel with OSL ages of ~11.6, 7.6, and 6.9 ka suggests that the channel fill was deposited as the fluvial-deltaic sedimentary facies of an overflowing lake. Accounting for tectonic ground deformation at the borehole site results in corrected elevations between ~1119 and 1127 m for water levels associated with the fluvial-deltaic sediment (Table 3; Figure 9). The range of elevations and OSL ages of the fluvial-deltaic

sediment are similar to the higher beach ridges at the Centennial Flat site that developed at elevations between ~1127.9 and 1131.3 m at 12.8 to ~6.2 ka (Tables 2 and 3; Figure 9). The new OSL ages from the overflow channel provide direct evidence of latest Pleistocene spill as recently as 11.6 ± 1.8 ka. The data also indicates that Owens Lake last overflowed during the Holocene between 7.6 ± 1.3 and 6.9 ± 1.1 ka ka, which is ~4–5 ka later than previously inferred (Figure 9). A change to alluvial deposition above ~1134.8 m in the overflow channel beginning at ~5800 cal yr BP from a ^{14}C age on wood in trenches is the same age as the youngest and lowest beach ridge at the Centennial Flat site, as well as the beginning of oolitic sand deposition and shallow conditions at Owens Lake indicating a lack of overflow and change to dryer hydroclimatic conditions by this time (Figure 9). Data from the overflow channel indicated that the soft sill of the basin is dynamic and has ranged in elevation from ~1113 to 1165 m during the late Pleistocene to Early Holocene, thereby suggesting far more recent hydrologic connections between Owens Lake via the Owens River and downstream lake basins than previously understood.

The revised overflow record of Owens Lake is consistent with previous inferences that Panamint Lake was likely the terminal lake in the system for brief periods between ~28 and 12 ka (Jayko et al., 2008; Hoffman, 2009; Kirby and McDonald, 2016) at a time when Searles Lake lacks stratigraphic evidence of hypersaline lake conditions. Otherwise, Searles Lake was predominantly the terminal lake in the paleo-Owens River system based on thick sequences of lacustrine mud and interbedded evaporate layers in sediment cores of late Pleistocene age combined with a lack of stratigraphic evidence for complete desiccation of Owens Lake between ~50 and 6 ka (e.g., Smith, 1979; Benson et al., 1996; Smith and Bischoff, 1997; Phillips, 2008).

5.1.2. Lake-Level Record (50 to 12.8 ka)

The new mollusk and ostracod ages from the Dirty Socks, OVF, and Swansea sites of our study and previously published lake-level ages from other sites that encompass the lake basin were used to revise the lake-level record of Owens Lake from 50 to 10.5 ka (Table 1; Figure 9). Relatively low reconstructed elevations of ten mollusk sample sites show good elevation correspondence with reconstructed sill elevations for periods of overflow at 45.6, 41.2, 39.4, 38.9, 35.3, 27.9, 17.2, 13.3, 13.2, and 11.5 ka (Table 1; Figure 9). Seven of the mollusk used are bivalves, and in particular five are *Anadonta* sp., which is an indicator taxa for a "fresh" aquatic environment and open lake system (i.e., overflowing) because it relies on fish for its reproductive cycle, whereas palmonate gastropods indicate relatively less open and likely a more saline aquatic environment (Firby et al., 2008; Table 1; Figure 9). Although three of the ten mollusks are gastropods, their presence in mostly shoreline deposits are interpreted as indicating relatively stable water levels controlled by spill. Without performing the elevation reconstruction of the these sample sites with mostly aquatic mollusks it would have been difficult to reconcile their field elevations, because all sites are located well below the hard sill level, thereby suggesting a closed lake system. The remarkable correspondence of the positions of lacustrine mollusk species requiring open basin (overflowing lake) conditions at sites adjusted for faulting faulting and the hard sill elevations determined from the geotechnical studies provides confidence in the published slip rate values and application of the differential fault-block model to reconstruct paleo-elevations of critical geomorphic and stratigraphic sites (Figure 9).

Moderate to high water levels above the hard sill were also identified from mollusk and tufa ages of this study and previously reported luminescence ages for highstand lake levels. A major transgression of Owens Lake up to an elevation of ~1165 m was previously dated by post-IR-IRSL analysis. Duplicate samples from sandy beach ridge deposits at an elevation of ~1156 m returned a mean age of 40.8 ± 4.9 ka and a single sample from ~1163 m yielded an age of 40.1 ± 3.0 ka (Bacon et al., 2019a). The mean ages and elevations show that the second highest shoreline in the lake basin was constructed by a major transgression that was relatively short lived (~700 yr) prior to falling to low, but overflowing lake levels near the hard sill (Figure 9). Maximum overflow defined from OSL ages of colluvial slope deposits along the overflow channel and soluble packrat middens near Lone Pine support the older age (~40 ka) of the ~1165 m highstand shoreline (Figure 9). Bounding ages from mollusks near the hard sill level suggest the ~40.5 ka lake-level oscillation and major transgression was controlled by high rates of alluvial fan deposition in the overflow channel to out compete down-cutting from discharge of the lake during this time.

The timing of seven low lake levels between 37.0 and 28.6 ka inferred from TOC proxy data in lake core OL-92 combined with threshold lake-water depth analysis were also used to estimate episodes with little to no overflow during this time (Figure 9). Moderate oscillations in lake level centered at ~26–23, 20.0–19.3, 17.5, 15.6, 14.6, and 13.8 ka reached elevations up to ~5–20 m above the hard sill from mollusk and tufa indictors (Figure 9). The last four of these transgression centered at ~17.5, 15.6, 14.6, and 13.8 ka have good offset temporal correspondence with the ages of lake-level fluctuations

to lower levels at 16.9, 15.1, 14.2, and 13.2 ka inferred from $\delta^{18}O$ proxy data in lake core OL-84B that collectively define the magnitude of complete lake-level cycles above and below the hard sill during this period (Table 1; Figure 9).

5.1.3. Lake-Level Record (12.8 to 5.8 ka)

The stratigraphy and post-IR-IRSL ages of beach ridges (Table 2) at the Centennial Flat site provide evidence for at least two lake-level cycles between the elevations of ~1114 and 1133 m from ~12.8 to 5.8 ka that had not been previously recognized at such high temporal and elevational resolutions in Owens Lake basin (Figure 9). Sediment dated within the deeper section of the ~1129 m beach ridge below a clear depositional boundary indicates the first transgression reached an elevation up to ~1131 m by ~12.8 ka (Table 2; Figures 3 and 10). Additional sediment of latest Pleistocene age was not dated in other beach ridges at the site, because sediment was either reworked into younger deposits by subsequent alluvial and lacustrine processes or is present at deeper depths than sampled. Tufa and mollusks from several other sites (Dirty Socks, OVF, Swansea) at similar elevations to the Centennial Flat site support a transgression at ~13 ka, and two lower transgressions up to ~1119 and 1121 m that were centered at ~11.6 and ~10.6 ka, respectively (Table 1; Figures 3 and 10). The two oscillations in lake level between ~13.0 and 11.4 ka are well constrained with post-IR-IRSL and OSL ages from beach ridges in the lake basin and fluvial-deltaic deposits in the overflow channel, as well as many mollusk and tufa ages across the lake basin that show lake levels fluctuated between elevations of ~10–20 m above the hard sill to as low as ~10 below the hard sill during this period.

The timing of three transgressions centered at ~12.8, 11.6, and 10.6 ka also have temporal correspondence with the ages of preceding lake regressions from wood and organic sediment in delta plain deposits at sites north of Lone Pine (AGPS, ORB, QPS), in addition to lake-level fluctuations to lower levels centered at 11.9 and 10.4 ka inferred from $\delta^{18}O$ proxy data in lake core OL-84B (Tables 1 and 2; Figures 3 and 10). An additional dry period is also indicated by the threshold lake-water depth analysis of silty sediment in core OL-92 that shows low water levels below the sill between ~10.5 and 9.0 ka (Figure 9). This major drop in lake level also appears to have significantly impacted mollusk population structure because mollusks have not been identified in lacustrine deposits younger than ~10.5 ka, suggesting possible extirpation of aquatic mollusk species in the lake basin during sustained and low lake levels.

The ~1.5 ka period with low lake levels was followed by a major Early Holocene transgression. The Early–Middle Holocene post-IR-IRSL ages from our study from the upper sections of all the beach ridges at the Centennial Flat site are supported by soil-geomorphologic characteristics observed in each beach ridge. The post-IR-IRSL ages define the magnitude and duration of the second and last significant lake-level cycle of Owens Lake. The ~8.8 ka age for sediment from the lowest beach ridge at ~1114 m indicates it was subsequently reworked into younger deposits, but that it may also represent the age of older deposits associated with lower water levels at this elevation prior to an Early Holocene transgression. A rise in water level of ~17 m to an elevation of ~1131 m is indicated by the construction of the highest beach ridge at ~8.4 ka that was short lived before dropping ~2 m to construct the ~1129 m beach ridge at ~8.1 ka (Figures 3 and 10). Water level was relatively stable with minor lake-level variations for

~2 ka after the initial transgression. Stable lake levels during this period is from the age of sediment from the lower beach face of the ~1127 m beach ridge that indicates that a water level reached an elevation of up to ~1126 m by ~7.6 ka, prior to a subsequent rise in water level that formed the ~1127 m beach ridge at ~6.4 ka (Figures 3 and 10). A major regression with no overflow after ~6.4 ka is indicated by a large drop in water level of ~7 m that briefly stabilized to form the inner ~1120 m beach ridge at ~6.2 ka, followed by an additional drop in water level of ~6 m which formed the ~1114 m beach ridge at ~5.8 ka (Figures 3 and 10).

Geomorphic and stratigraphic analysis of paleoseismic trench sites (AGPS, QPS, ORB) north of Lone Pine previously identified an Early Holocene transgression of Owens Lake that reached elevations ranging from 1113 to 1128 m, with a maximum estimate of up to 1135 m (Bacon et al., 2006; Bacon and Pezzopane, 2007; Figure 2). The ages of carbonized wood and organic sediment from interbedded delta plain layers with lacustrine deposits exposed in both fault trenches and banks of the Owens River were previously used to define the beginning of the Early Holocene transgression to after ~10.2 ka. Shore and nearshore stratigraphy in fault trenches combined with tufa ages provided the first information on the elevations and timing of the Early Holocene transgression above elevations of ~1122 and 1117 m between ~8.4 and 7.5 ka, respectively (Bacon et al., 2006; Bacon and Pezzopane, 2007) (Table 1; Figure 9). The geomorphology and post-IR-IRSL ages of beach ridges of this study have revised the maximum elevation of the Early Holocene transgression up to ~1133 m after accounting for tectonic ground deformation, as well as providing additional lake-level indicators on the timing of the regression to a much later period extending into the Middle Holocene (Figure 9).

5.1.4. Lake-Level Record (5.8 ka to 1872 AD)

The Owens Lake water-level record during the beginning of the Middle Holocene warm period reflects extreme hydroclimatic variability in the form of persistent, multi-centennial to multi-millennial drought conditions. Shallow and hypersaline lake conditions between ~5.8 and 3.2 ka are shown by many ^{14}C ages from a well-sorted oolitic sand deposit in core OL-92 (Smith and Bischoff, 1997), which is supported by a post-IR-IRSL age of 5.0 ± 0.2 ka on alluvial deposits at an elevation as low as 1099 m in the lake basin (Bacon et al., 2018; Figure 9). The recently revised Late Holocene lake-level history of Owens Lake based on post-IR-IRSL analysis on sandy sediment that define the age of four major transgressions up to elevations of ~1108, 1103, and 1099–1101 m provides information to better understand hydroclimate variability in the southern Sierra Nevada during the this period (Bacon et al., 2018). Furthermore, up to eighteen oscillations were estimated from threshold lake-water depth analysis of interbedded muddy and sandy layers in core OL-97, thereby showing Owens Lake had significantly lower water levels not reflected in the geomorphic record from ~3.6 ka to AD 1872–1878 (Bacon et al., 2018) (Figure 9). Integration of the Owens Lake shoreline and lake-core proxy data records show a hydrologic response of the Owens River-Lake system to two general patterns of hydroclimatic forcing during the Late Holocene. The analysis of Bacon et al. (2018) demonstrated that sand deposition (i.e., low stands) and glacial maxima occurred mostly during periods with persistent and higher hydroclimate variability, whereas mud deposition (i.e., high stands) occurred primarily during times with persistent and lower hydroclimate variability.

5.2. Spatiotemporal Patterns of Owens Lake Water-Level Fluctuations with Regional and Global Climate Variability

Past studies in the western U.S. have correlated the age of Holocene lake-level fluctuations to regional climate variability (e.g., Enzel et al., 1989; Stine, 1990; Enzel and Wells, 1997; Adams, 2003; Kirby et al., 2014, 2015; Bacon et al., 2018) and late Pleistocene highstands to changes in North Atlantic climatic phases (e.g., Benson et al., 1996, 1997; 1998b, Negrini, 2002; Zic et al., 2002; Munroe and Laabs, 2013; Garcia et al., 2014; Reheis et al., 2015; Hudson et al., 2019; Knott et al., 2019). The North Atlantic climatic phases were reflected by periods of high-frequency warm air and sea surface temperatures referred to as Dansgaard–Oeschger (D–O) cycles that were followed by relatively cold phases that expanded the Laurentide Ice Sheet and influenced the discharge of icebergs to float further to the south, known as Hienrich events or stadials (e.g., Heinrich, 1988; Bond et al., 1992; Dansgaard et al., 1993; Hemming, 2004). Shoreline and speleothem records in the southwestern U.S. and majority of the Great Basin demonstrate during the last deglaciation wetter conditions in the region were coincident with cool periods in the North Atlantic, such as Heinrich 1 and Younger Dryas stadials, and drier conditions coincident with warm periods, such as the Bølling and Allerød interstadials (i.e., D–O cycles) (e.g., Asmerom et al., 2010; Munroe and Laabs, 2011; Oster et al., 2015). Furthermore, older shoreline, speleothem, and groundwater recharge records mostly from the southern Great Basin and Mojave Desert in eastern California also demonstrate lake-level fluctuations and cool wet conditions between ~45 and 25 ka coincided with Heinrich stadials 3 and 4 (Garcia et al., 2014; Oster et al., 2014; Reheis et al., 2015; Wendt et al., 2018; Knott et al., 2019).

Studies of Owens Lake sediment cores have also linked $\delta^{18}O$, TOC, and TIC proxy data of rapid climate change to D–O cycles and Heinrich stadials 4–1 between ~53 and 18 ka, thereby indicating nearly synchronous climate change in the northern Hemisphere (Benson et al., 1996). The synchronous climate change is generally reflected in proxy lake-core records in the western Great Basin as high lake levels during warm North Atlantic climatic phases (D–O cycles) and low lake levels during cold ones (Heinrich stadials) (e.g., Benson et al., 1996, 1997; 1998b; Negrini, 2002; Zic et al., 2002) in contrast to correlations made using shoreline and speleothem records that show the opposite relations. The apparent discrepancy between the different types of records maybe related to uncertainty in age-depth models used in lake cores (Munroe and Laabs, 2011; Reheis et al., 2015; Franke and Donner, 2019) or related to a north-south dipole in hydroclimatic patterns during the last deglaciation across the western U.S. (McGee et al., 2018; Hudson et al., 2019). Potential errors are also likely associated with uncertainty in accurate reservoir corrections applied to ^{14}C ages (Benson et al., 1997), as well as a lack of correction for sediment compaction in age-depth models which would also overestimate the age of progressively deeper sediment containing proxy indicators. Although Benson et al. (1996, 1997) acknowledged errors in their age-depth model that prohibit absolute synchroneity between Owens Lake and North Atlantic climate records, they did show a similar number of large and abrupt climate signals in the proxy data to major latest Pleistocene climatic phases in the Northern Hemisphere.

5.2.1. Comparison between Owens Lake Shoreline and Lake-Core Proxy Records

We performed a comparison of the revised lake-level record of Owens Lake from our study with the $\delta^{18}O$ ice-core record from the North Greenland Ice Core Project (NGICP; Andersen et al., 2004) to verify correlations between rapid climate change in the Northern Atlantic and the Owens River watershed (Figure 10A–B). We also compared the $\delta^{18}O$, TOC, and TIC proxy records from Owens Lake cores OL-84B and OL-90 of Benson et al. (1996, 1997, 2002) to the water-level record of Owens Lake to understand potential differences or limitations in comparing these types of lacustrine datasets (Figure 10C–E). Initial comparison of the datasets produced poor temporal correspondence between periods with either high lake levels (wet conditions) or low lake levels (dry conditions). We corrected for compaction in the core proxy records to assess if this adjustment increased the temporal correspondence with the shoreline and ice-core records. The reported age-depth models for cores OL-84B and OL-90 included a uniform 600-yr reservoir correction (Benson et al., 1996, 1997, 2002). The Late Holocene shoreline and Owens Lake core OL-97 records demonstrate that the carbonate-rich mud in lake cores used for ^{14}C dating had a reservoir effect of ~1000 yr (Smoot et al., 2000; Bacon et al., 2018). While a 600–1000-yr correction is well justified for periods when Owens Lake was hydrologically closed and highly saline, it is likely not applicable for periods with mostly overflowing and dilute lake conditions subject to strong wind mixing and atmospheric exchange (Phillips, 2016). Therefore, we revised the age-depth models of cores OL-84B and OL-90 by applying no reservoir correction to ^{14}C dates and accounted for compaction. The two cores collectively form a composite lake-core record where core OL-84B has a length of 8.88 m, ranging in depth from 0.50–9.43 m and core

OL-90 has a length of 27.91 m, ranging in depth from 5.37–33.28 m (Benson et al., 1996, 1997, 2002).

The upper 2.2 m of the Late Holocene section of core OL-84B was not revised because the 600-yr reservoir correction produced good temporal correspondence with the shoreline record (Figure 10). The age-depth model of a subsection of core OL-84B with ^{14}C ages at depths from 2.2–9.43 m was refined by accounting for consolidation using equations 1 and 2, which yielded an increase of 0.84 m in the overall length of the core. The age-depth model of a subsection of core OL-90 with ^{14}C ages was also refined by recalculating the depths from 5.37–22.38 m, which yielded an increase of 2.81 m in the overall length of the core. The refined age-depth models were developed from regression analysis by developing empirical relations between corrected depths and corresponding calibrated ^{14}C dates in core OL-84B (n=18) and OL-90 (n=21). Linear trend lines were used to best match data in core OL-84B (R^2 = 0.95) and OL-90 (R^2 = 0.97). The empirical relations were used to interpolate the age of horizons with proxy data by corresponding depth. The revised age-depth models produced younger ages for proxy indicators in the deeper section of core compared to previous age-depth models. The $\delta^{18}O$ data used to identify four extremely dry (closed-basin) intervals (D_1 to D_4) in core OL-84B were previously estimated at 15.1, 13.2, 12.2, and 11.3 ka, respectively (Benson et al., 1997). The revised age-depth model for the same core yielded younger ages of 14.5, 12.9, 11.9, and 10.4 ka for the same $\delta^{18}O$ data, respectively (Figures 9 and 10). The adjusted $\delta^{18}O$, TOC, and TIC proxy records produced good temporal correspondence between the Owens Lake shoreline and North Atlantic ice records, where decreases in $\delta^{18}O$ and TIC (wet conditions), commonly agree with the age of relative highstands and timing of

Heinrich stadials and increases in TOC (dry conditions) generally coincide with relative lowstands and D–O interstadials, similar to other shoreline and speleothem records in the southwestern U.S. (e.g., Asmerom et al., 2010; Munroe and Laabs, 2011; Oster et al., 2014, 2015; Reheis et al., 2015; Figure 10).

5.2.2. Owens Lake Highstands

There is good temporal correspondence of water-level variations between transgressions of Owens Lake and hydroclimate variability during the late Pleistocene and Holocene. The major transgressions of Owens Lake at ~41–40 ka and minor transgression at ~38.7 ka, plus corresponding variations in the geochemical proxy records of core OL-90 coincide with Heinrich stadial 4 (HS4; Figure 10). Supporting stratigraphic evidence for moderate to deep lakes and high sedimentation rates in the overflow channel of Owens Lake during HS4 is from additional core proxy data, plus alluvial and glacial stratigraphy in the Sierra Nevada. Core OL-92 shows the highest weight percent of clay deposition since ~130 ka occurred at ~39.5–43 ka indicating a deep lake during this time (Smith and Bischoff, 1997; Litwin et al., 1999). In addition, the rock flour record of composite core OL-90/92 shows evidence of two glacier advances at 49.0–45.1 and 42.8–39.0 ka, with the latter advance coinciding with the ~40 ka transgression of Owens Lake (Bischoff and Cummins, 2001). Geomorphic evidence of increased runoff in the watershed at 32–44 ka from surface exposure dating of wide-spread alluvial fan deposits in Owens Valley near Line Pone indicates an increase in runoff to the lake during a broadly defined period encompassing HS4 (Benn et al., 2006). The two major oscillations in lake level during HS4 reached elevations of

~45 and 20 m above the hard sill prior to major glacial advances in the Sierra Nevada during the Tioga glaciation (MIS 2) from 30.5 to 15.0 ka that encompassed HS3–HS1 (Clark and Gillespie, 1997; Bischoff and Cummins, 2001; Phillips et al., 2009; Gillespie and Clark, 2011; Rood et al., 2011; Moore and Moring, 2013; Phillips, 2016, 2017; Figure 10).

Given the geomorphic and numerical age uncertainties of lake-level indicators used in our study, six later transgressions that reached 10–20 m above the hard sill at ~26–23, 19.3, 17.5, 15.6, 13.8, and 12.8 ka coincided with periods of global-scale climate change (Figure 10). The age of highstands at ~26–23, 19.3, and 15.6 ka are within the range of ages for Tioga glacial fluctuations and deglaciation in the Owens River watershed (Phillips et al., 1996, 2009; Gillespie and Clark, 2011; Rood et al., 2011). There is good temporal correspondence between the ~26–23, 17.5 and 15.6 ka transgressions of Owens Lake and HS2 and HS1, respectively, whereas the period of HS3 is reflected by little to no overflow (Figure 10). The major transgression that started at 20.1 and terminated at ~19 ka did not occur during a Hienrich stadial, but instead coincided with a glacial advance (Tioga 3) (Rood et al., 2011; Phillips, 2017). Corresponding variations in the $\delta^{18}O$, TIC, and TOC proxy records of core OL-90 indicate mostly overflowing conditions during the Tioga glaciation from ~28.5–17.2 ka (Benson et al., 1996). The core proxy records generally show good temporal correspondence with lake-level fluctuations, where the $\delta^{18}O$ record exhibits the greatest correspondence during the Tioga glaciation (Figure 10). Furthermore, the broad transgression of Owens Lake with overflowing water levels ending by ~15.6 ka during HS1 coincides with the age of high lake levels of downstream China-Searles Lake

(Rosenthal et al., 2017) and the highstand of Lake Lahontan in the central Great Basin at ~15.7 ka (Adams and Wesnousky, 1999; Munroe and Laabs, 2011; Benson et al., 2013). In contrast, Lake Chewaucan in the northwestern Great Basin had relatively low lake levels during this time (Negrini, 2002; Zic et al., 2002; Hudson et al., 2019).

The post-glacial highstands of Owens Lake at ~13.8 and 12.8 ka also occurred during periods of climate change in the Sierra Nevada coinciding with the Recess Peak glaciation. The timing of the Recess Peak glaciation is bounded by ages ranging from 14–13 ka during the Older Dryas stadial based on glacial and alpine lake records in the Sierra Nevada (Clark and Gillespie, 1997; Phillips et al., 2009) to 14–12 ka corresponding to the beginning of cold and wet climate during the Younger Dryas stadial based on glacial records (Phillips et al., 2009; Phillips, 2016, 2017; Marcott et al., 2019) and lake-core proxy indicators at Owens Lake and alpine lakes in the Sierra Nevada (Mensing, 2001; MacDonald et al., 2008; Street et al., 2012). The transgressions of Owens Lake at ~13.8 and 12.8 ka also have good temporal correspondence with the ages of a coalesced China-Searles Lake (Rosenthal et al., 2017). The ages of ~13.8 ka for the transgression of Owens Lake and ~14 ka for a deep China-Searles Lake is similar to the highstand of Lake Chewaucan centered at ~13.8 ka (Hudson et al., 2019). The similarity in the ages of deep lakes at latitudes ranging from 42.8°N for Lake Chewaucan and 36°N for Owens and China-Searles Lakes suggests the north-south wet/dry dipole atmospheric circulation pattern across the western U.S. during this time was not as robust as previously proposed (e.g., Hudson et al., 2019).

The last two transgressions with overflowing lake conditions during the latest Pleistocene occurred at ~11.6 and 10.7 ka that coincided with the end of the Younger

Dryas stadial and beginning of the Holocene during relatively wet and brief periods inferred from pollen and algal proxy data in core OL-84B (Mensing, 2001). Changes in hydroclimate variability at the Pleistocene-Holocene transition (~14.6–8 ka) in the southwestern U.S. has been linked to semi-permanent El Niño-like conditions in the Tropical Pacific, which enhanced the frequency of winter frontal storms and increased penetration of tropical cyclones that influenced alluvial fan aggradation in most of the region (Antinao and McDonald, 2013). The magnitude of post-glacial highstands of Owens Lake were likely controlled, in part, by variations in alluvial fan aggradation in the overflow channel that created soft sills that impounded Owens Lake during this period.

An Early-Middle Holocene transgression of Owens Lake attained high and stable water levels between 8.8 and 5.8 ka (Figure 9). Overflow likely occurred between ~8.4 and 6.4 ka at elevations from ~1132–1129 m. Spill was probably characterized by relatively low-energy surface flows, based on the type of fluvial stratigraphy and paleoenvironmental conditions described in Rose Valley during this period (e.g., Rosenthal et al., 2017; Figure 1). The only stratigraphic and geologic evidence of Holocene lakes in downstream basins is at Searles Lake basin based on composite lake core LDW-6 and geologic mapping encompassing the playa margin (Smith, 1979, 2009). An ~10 m-thick section of interbedded mud and salt with a radiocarbon age of ~3,800 cal yr BP from wood sampled at a depth of 2.4 m indicates a period of perennial and ephemeral lakes that followed an earlier period of mostly ephemeral lakes that deposited an ~10 m-thick accumulation of salt after 11.7 ka (Smith, 1979, 2009). The sediment core data provides direct evidence of shallow and fluctuating lakes in Searles basin that would

have required hydraulic connections of either the Owens River or the Indian Wells Valley watersheds or both given the small size and low elevations of the Searles Valley watershed (Figure 1).

The beginning of the Early Holocene transgression at ~9 ka documented by shoreline data in Owens Lake basin coincides with changes in $\delta^{18}O$, TIC, and TOC values in core OL-84B (Figure 10). In particular, the high-amplitude oscillations in TIC values between ~8.4 and 6 may indicate Owens Lake had strong oscillations in hydrologic balance during this period (Benson et al., 2002; Figure 10). The Early Holocene highstand attained its highest level at ~8.4 ka coincident with an Early Holocene cooling event at ~8.4–8.0 ka identified in Greenland ice-core proxies (e.g., Alley et al., 1997; Figure 10B) and towards the end of a period with enhanced winter sub-Tropical moisture flux across the southwestern U.S., commonly referred as atmospheric rivers (Enzel et al., 1989, 2003; Antinao and McDonald, 2013; Kirby et al., 2015; Steponaitis et al., 2015). The Early-Middle Holocene Owens Lake transgressions are characterized by two distinct oscillations and associated highstands at ~9.2–7.6 and ~7.6–5.8 ka, also similar to the lake-level records of nearby Mono and Tulare Lakes. The watersheds of Mono and Tulare Lakes share common drainage divides with the Owens River watershed (Figure 1). Mono Lake on the north had two early Holocene lake-level oscillations and associated highstands at ~9.4–7.2 and ~7.2–5.5 ka (Stine, 1990). Tulare Lake on the west side of the southern Sierra Nevada in the San Joaquin Valley is directly west of Owens Lake and also had two early Holocene highstands and evidence of deep lakes at ~9.5–8.0 and ~6.9–5.8 ka (Negrini et al., 2005; Blunt and Negrini, 2015).

Owens Lake had mostly shallow to near desiccation water levels since ~6.4 ka that were punctuated with transgressions of up to ~11–25 m. Post-IR-IRSL ages of major transgressions at elevations of ~1108, 1103, and 1099–1101 m coincided with wetter and cooler climate during the Neopluvial (~3.6 ka), Medieval Pluvial (~0.8 cal kyr BP), and Little Ice Age (~0.35 ka), respectively (Figure 10). The Late Holocene ages of lake-level oscillations shown on the lake-level curve of Owens Lake have good temporal correspondence with variations in proxy indicators of wet and dry conditions in sediments of core OL-84B (Benson et al., 2002; Figure 10); and alpine lakes in the watershed (Street et al., 2013). These lake-level oscillations were likely driven by renewed hydroclimatic variability from enhanced winter sub-Tropical moisture in the region (e.g., Kirby et al., 2014; Hatchett et al., 2019).

Late Holocene water-level variations of Owens Lake also have good temporal correspondence to the Late Holocene lake-level records of nearby Mono Lake (Stine, 1990) and Walker Lake (Adams and Rhodes, 2019a) on the east side of the central Sierra Nevada (Figure 1). Comparison of shoreline records of large lakes on the west and east sides of the Sierra Nevada shows good temporal correspondence during the latest Pleistocene and Holocene indicating that even with inherited geologic uncertainties and dating methods in the different studies, all records show that each lake basin responded in a similar manner to hydroclimatic forcing coinciding with periods of global-scale climate change (Figure 10).

5.2.3. Owens Lake Lowstands

The lake-level and sill reconstructions of Owens Lake show several periods of low lake levels during little to no overflow conditions that also correspond to variations in regional and global hydroclimate. The timing of episodes with little to no overflow have good temporal correspondence with periods of major lake-level oscillations in downstream lakes. Seven of the earlier episodes are inferred from a lack of shoreline data at and above sill levels combined with TOC proxy data from core OL-90 for the age of changes in Owens Lake levels between ~37 and 28.5 ka (Figures 9 and 10). Major lake-level oscillations at Searles Lake from U-Th and ^{14}C ages of salt layers and bounding muddy sediment in lake core X-52 collectively show playa lake environments to near desiccation at ~36.9, 33.8, 32.3, 30.3 and 28.5 ka (Lin et al., 1998; Phillips, 2008). The ages of salt deposition at Searles Lake have good temporal correspondence with the TOC proxy data from Owens Lake supporting little to no overflow during these times (Benson et al., 1996). The ages of little to no overflow of Owens Lake and shallow conditions at Searles Lake occurred primarily during warm phases in the North Atlantic during numerous D–O cycles between HS4 and HS2 (Figure 10).

Three well defined episodes of little to no overflow of Owens Lake also occurred between ~18 and 11 ka that are indicated by both shoreline and lake-core proxy indicators (Figures 9 and 10). A lowstand at ~17.8 ka reached ~10–12 m below hard sill levels based on threshold lake-water depth analysis of a thin sandy layer in core OL-92 (Smith and Bischoff, 1997) (Figure 9). The lowstand coincided with a dry episode during the early Mystery Interval in the Great Basin centered at ~17.5 ka prior to HS1 (e.g., Broecker et al., 2009) (Figure 10). Low water levels at ~15.5–14.5 ka also are defined by

$\delta^{18}O$ proxy data and shoreline indicators that coincided with termination of the Tioga deglaciation by 15.7–15.5 ka (Clark and Gillespie, 1997; Phillips et al., 2009; Phillips, 2016, 2017) and the last major D–O cycle in the North Atlantic region (Figure 10). The last major lowstand during this period was centered at ~13.1 ka based on mollusk ages from sites near the mouth of the Owens River. The Low lake levels at ~13.0 ka is supported by geochemical, as well as pollen and algal proxy data in core OL-84B that indicate low lake levels and drought conditions at ~12.9 ka (Benson et al., 1997; Mensing, 2001), which occurred near the transition between the Bølling interstadial and Younger Dryas stadial (Figure 10).

A steady decrease in spill from Owens Lake and dryer and more variable hydroclimatic conditions at the Pleistocene-Holocene transition is indicated by the progressive age of desiccation of downstream lakes in the paleo-Owens River system. The downstream lakes desiccated between ~0.6 and 1.1 ka of each other with Panamint Lake first desiccating at ~12.8 ka followed by Searles Lake at 11.7 ka and then China Lake by 11.1 ka (Jayko et al., 2008; Phillips, 2008; Hoffman, 2009; Smith, 2009; Rosenthal et al., 2017). Owens Lake attained fluctuating, but overflowing levels between ~12.8 and 10.5 ka with discharge insufficient to support large perennial lakes, but great enough to provide a source of low-energy surface flow to support extensive perennial wetland habitats documented in Rose Valley and the delta plain area of China Lake during this period (Rosenthal et al., 2017). The wetland habitats were previously inferred to be supported by mountain block recharge, however, evidence of overflow as recently as ~10.5 ka is a more plausible source of groundwater recharge through inundation and channel loss of the paleo-Owens River. Owens Lake followed the trend of progressive

desiccation by dropping below sill levels for ~1–2 ka beginning at 10.5 ka that is also reflected in the $\delta^{18}O$ and TOC proxy records (Figure 10). The onset of low lake levels corresponds to a period of maximum solar insolation between 11 and 10 ka that appears to have resulted in a warm and dry climate, as indicated by pollen evidence in core OL-84B of a modern vegetation assemblage in Owens Valley at this time (Mensing, 2001), as well as lake-core proxy evidence in the Mojave Desert (Enzel and Wells, 1997; Kirby et al., 2015), and speleothem records in the Great Basin (Lachniet et al., 2014; Steponaitis et al., 2015).

Owens Lake had mostly shallow to near desiccation water levels since the Middle Holocene highstand ending at ~6.4 ka. This highstand was followed by near desiccation of Owens Lake between ~5.8 and 4.2 ka during the global-scale Mid-Holocene warm period (e.g., Bartlein et al., 2011). The frequency and duration of Owens Lake lowstands after ~4.2 ka are also in general agreement with periods of severe multidecadal to multicentennial droughts (i.e., megadroughts) documented in the western Great Basin and south-central Sierra Nevada during the early part of the Late Holocene and the Medieval Climatic Anomaly centered at ~0.89 and 0.67 ka (e.g., Stine, 1994; Benson et al., 2002; Mensing et al., 2008, 2013; Cook et al., 2010; Hatchett et al., 2016; Bacon et al., 2018; Figure 10).

6. CONCLUSIONS

We refined the lake-level history of Owens Lake for the past 50 ka by applying a method to construct a continuous lake-level curve. New studies of several sites in the lake basin and subsurface geotechnical investigations within the overflow channel yielded

stratigraphic and geochronologic information to define the timing of potential episodes of overflow. New post-IR-IRSL ages of beach ridges and OSL ages from fluvial-deltaic and alluvial sediment filling the overflow channel established the first spatiotemporal connections between Early-Middle Holocene and latest Pleistocene shorelines and overflow levels of Owens Lake, thereby reducing the uncertainty between the late Pleistocene overflow records of Owens Lake (Bacon et al., 2006; Reheis et al., 2014) and downstream lake basins (Orme and Orme, 2008; Phillips, 2008; Smith, 2009; Rosenthal et al., 2017). Geotechnical and lake-level data demonstrated that the overflow area is a dynamic and deeply entrenched channel with soft sill elevations that ranged from the ~40 ka highstand at ~1165 m to the hard sill at ~1113 m from variable infilling of fluvial-deltaic and alluvial sediment. The lake-level curve shows temporal correspondence in the frequency of oscillating water levels that is controlled by spill of Owens Lake. The record indicates Owens Lake spilled most of the time at or near minimum sill levels that supported moderately sized water levels of Searles Lake between 50 and ~11.5 ka (e.g., Phillips, 2008; Smith, 2009).

Given the range of numerical dating methods used to define water levels, the lake-level curve and reconstruction of sill/spillway levels show the entire system of lakes between Owens and Searles basins were hydrologically connected most of the time with major transgressions of Owens Lake corresponding to sediment aggradation in the overflow channel that coincided with documented periods of glaciations in the Sierra Nevada, global-scale hydroclimate variability associated with abrupt cold/warm oscillations in the North Atlantic region, and timing of enhanced post-glacial subtropical moisture. A steady decrease in spill from Owens Lake at the Pleistocene-Holocene

transition influenced progressive desiccation of downstream lakes over a period of ~0.6 to 1.1 ka, with China Lake the last to desiccate by 11.1 ka (e.g., Rosenthal et al., 2017). Owens Lake last spilled from ~8.4 to 6.4 ka during an Early-Middle Holocene transgression that was during a time when other lakes in the southern Sierra Nevada watershed (i.e., Mono and Tulare Lakes) and on the east side of the northern Sierra Nevada (i.e., Pyramid Lake) also expanded.

Previous sediment core age-depth models for cores OL-84B and OL-90 were revised by accounting for sediment compaction and using no reservoir correction for open basin conditions, which reduced discrepancies between Owens Lake shoreline and lake-core proxy records. The good temporal correspondence between the reconstruction of shoreline indictors and spillway and lake bottom positions from this analysis also provides confidence in the approach developed in this study to produce an integrated lake-level curve to accurately identify overflow episodes, as well as to estimate the timing, duration, and magnitude of regional climate change. Our integrated approach to generate a continuous lake-level record of Owens Lake with well-defined oscillating water levels is an important step in performing accurate hydrologic water-balance modeling of the paleo-Owens River system and quantifying the pattern of hydroclimate variability along south-central Sierra Nevada over the past 50 ka.

7. ACKNOWLEDGEMENTS

Many discussions with Thomas Bullard throughout the study are gratefully appreciated. The authors acknowledge Ken Adams for field discussions and assistance with luminescence sampling at the Centennial Flat site. The authors thank John Umek for

discussions on mollusk aquatic ecology. We also thank the Los Angeles Department of Water and Power (LADWP) for providing access to the Black and Veatch (2013) report and all the geologists from LADWP, Black and Veatch, URS, and Lettis Consultants International, Inc. who worked on the comprehensive assessment of local faulting in the Haiwee Reservoir area. We thank Fred Phillips and an anonymous reviewer for providing constructive and thoughtful reviews that improved the manuscript. Funding for this work was partially provided by U.S. Government Contract #N68936–09–D–0040, National Science Foundation EAR #1252225, Great Basin Unified Air Pollution Control District (GBUAPCD), and Vice President for Research Office of the Desert Research Institute to S. Bacon.

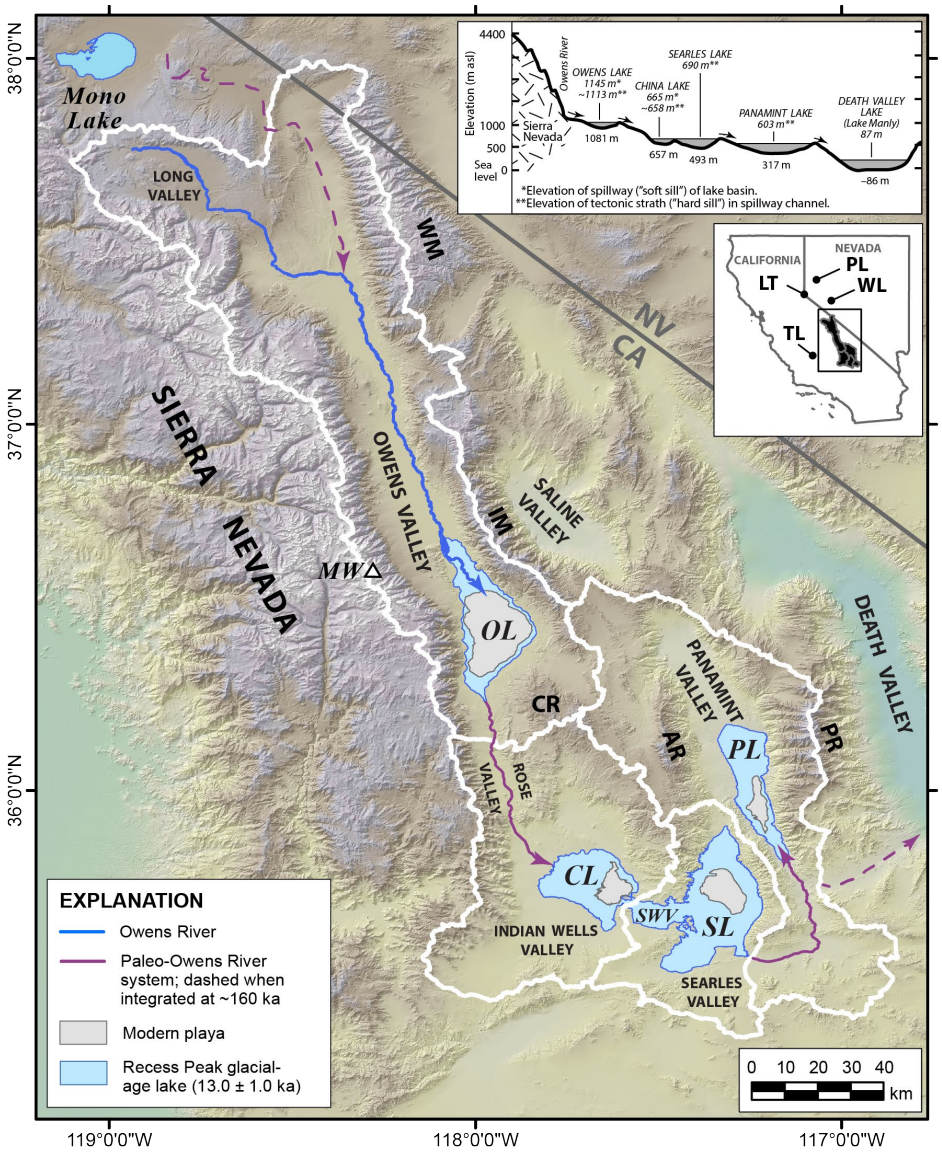

Figure 1. Major physiographic features along the eastern escarpment of the southern Sierra Nevada, eastern California in relation to modern playas and pluvial Owens Lake, and other lakes of the paleo-Owens River system during the Recess Peak glaciation (Bacon et al., 2006; Orme and Orme, 2008; Hoffman, 2009; Rosenthal et al., 2017). Age of Recess Peak glaciation is from Phillips (2016, 2017). Inset is graphical profile of the chain of lakes downstream of Owens Lake showing the elevations of hard and soft sills, plus playa bottoms of each lake basin (modified after Smith and Bischoff, 1997). Watershed boundaries of lake basins are shown for: CL – China Lake; OL – Owens Lake; PL – Panamint Lake; SL – Searles Lake; and SWV – Salt Wells Valley. Mountain ranges are also shown on the map: AR – Argus Range CR – Coso Range; IM – Inyo Mountains; PR – Panamint Range; WM – White Mountains. Other lakes discussed in text include: LT – Lake Tahoe; TL – Tulare Lake; PL – Pyramid Lake; and WL – Walker Lake.

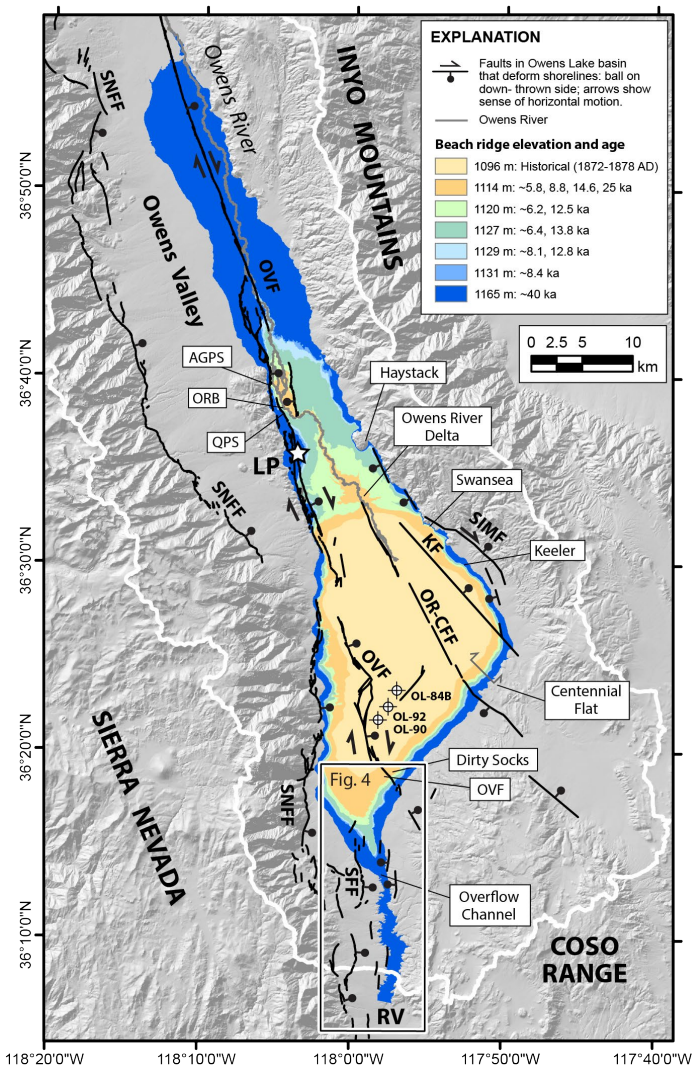

Figure 2. Map of the southern Owens River watershed showing the elevations of prominent beach ridges with Holocene and late Pleistocene post-IR-IRSL (~12.8 ka) and ^{14}C ages for shoreline deposits at similar elevations. Beach ridges with Late Holocene post-IRSL and ^{14}C ages at 1108 m (~3.6 ka), 1103 m (~0.8 ka), 1099–1101 m (~0.35 ka) are not shown (Bacon et al., 2018). The extent of the late Pleistocene highstand shoreline (~1165 m) with a post-IR-IRSL age of 40 ± 5.8 ka is also shown (Bacon et al., 2019a). The modern extent of the playa below an elevation of ~1096 m and location of lake-core sites OL-84B, OL-90, and OL-92 are shown with white circles. The name and location of study sites described in text are shown by white boxes and leader lines. Rectangle shows areal extent of map on Figure 5A. Faults shown on map include: KF – Keeler fault; OR-CFF – Owens River-Centennial Flat Fault; OVF – Owens Valley fault; SFF – Sage Flat fault; SIMF – Southern Inyo Mountains fault; SNFF – Sierra Nevada frontal fault. Major physiographic features and towns shown on map include: LP – Lone Pine; I – Independence; RV – Rose Valley.

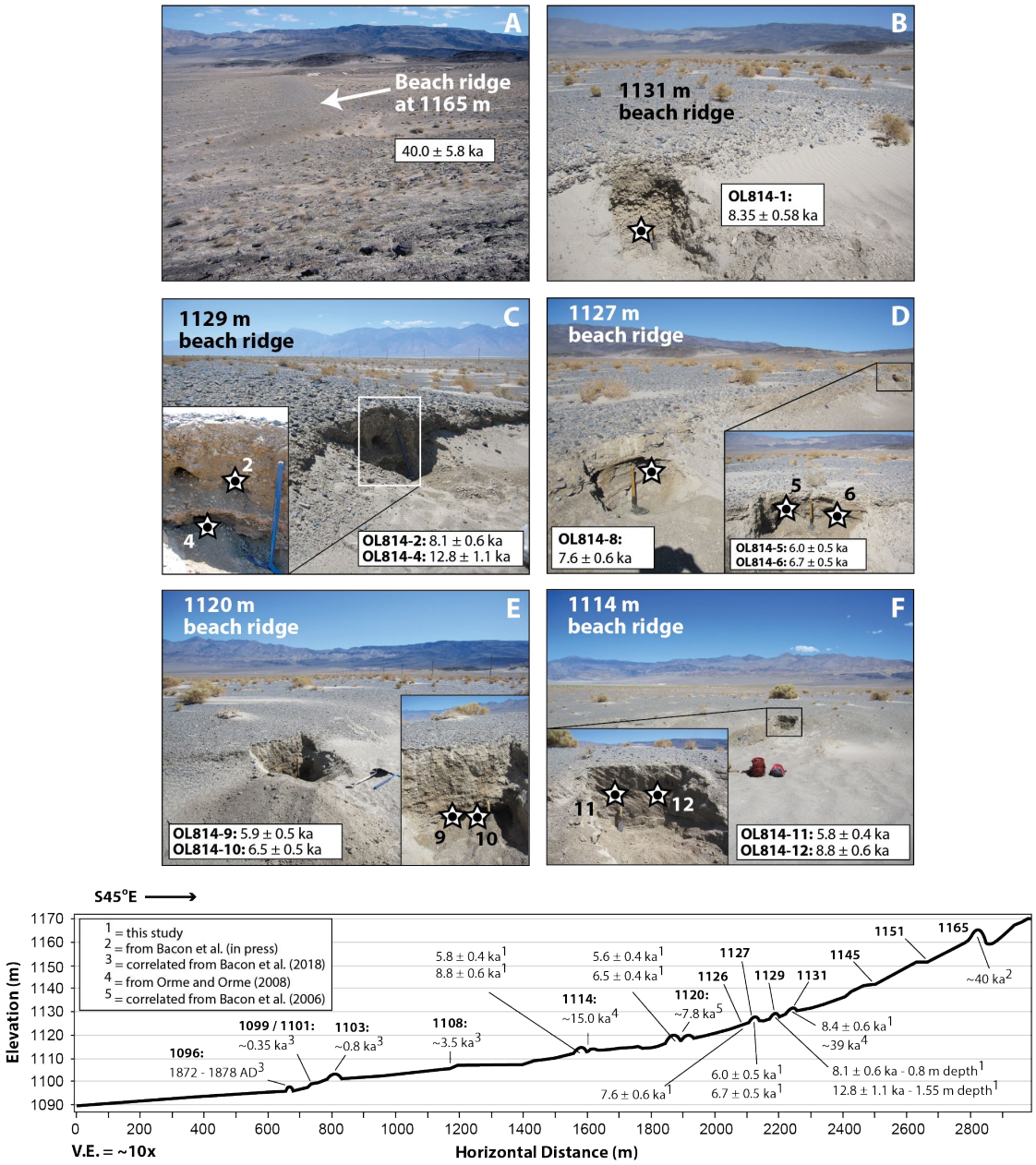

Figure 3. Views of the ~40 ka highstand beach ridge at ~1165 m and location of infrared-stimulated luminescence (IRSL) sampling of five beach ridges between ~1114 and 1131 m at the Centennial Flat site (Figure 2). Stars and numbers of sample sites are shown with associated post-IR-IRSL ages. Below is geomorphic profile across the site showing up to twelve shoreline features between the highstand beach ridge at ~1165 m and lowest shorelines at ~1096 m (see Figure 2 for location of transect). The lower five shoreline features range from historical (AD 1872–1878) beach ridges along the playa margin to Neopluvial (~3.5 ka) beach ridges and shoreline scarps formed up to ~1108 m (Bacon et al., 2018). Correlated ages from previously published studies for shoreline features at ~1114 and 1120 m are also shown.

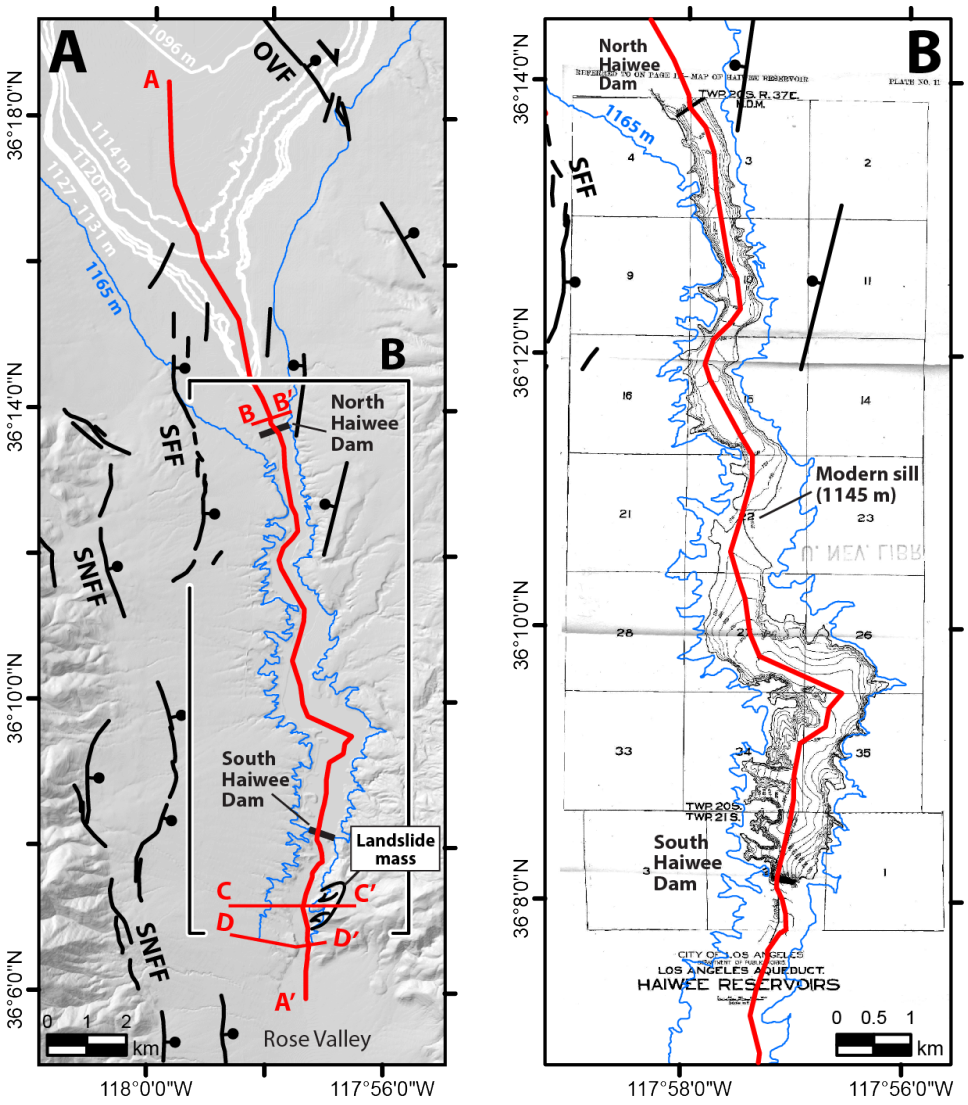

Figure 4. Owens Lake overflow channel: (A) hillshade map and elevation contours of the ~40 ka highstand shoreline (~1165 m), Early-Middle Holocene beach ridges of the Centennial Flat site (1114–1131 m), and historical (AD 1872–1878) lake level at ~1096 m. The location of the north and south dams of Haiwee Reservoir and a large landslide feature in the southern reach of the channel are shown. Generalized location of faults are also shown including: OVF – Owens Valley fault; SFF – Sage Flat fault; SNFF – Sierra Nevada frontal fault (e.g., Geotz et al., 2016; Kemp et al., 2016). Location of geomorphic profiles A–A', B–B', and C–C' are shown; and (B) pre-construction topography of the Haiwee Reservoir dam site (Los Angeles Board of Public Service Commissioners, 1916). The location of the modern sill of the lake basin at ~1145 m and nearby faults are shown.

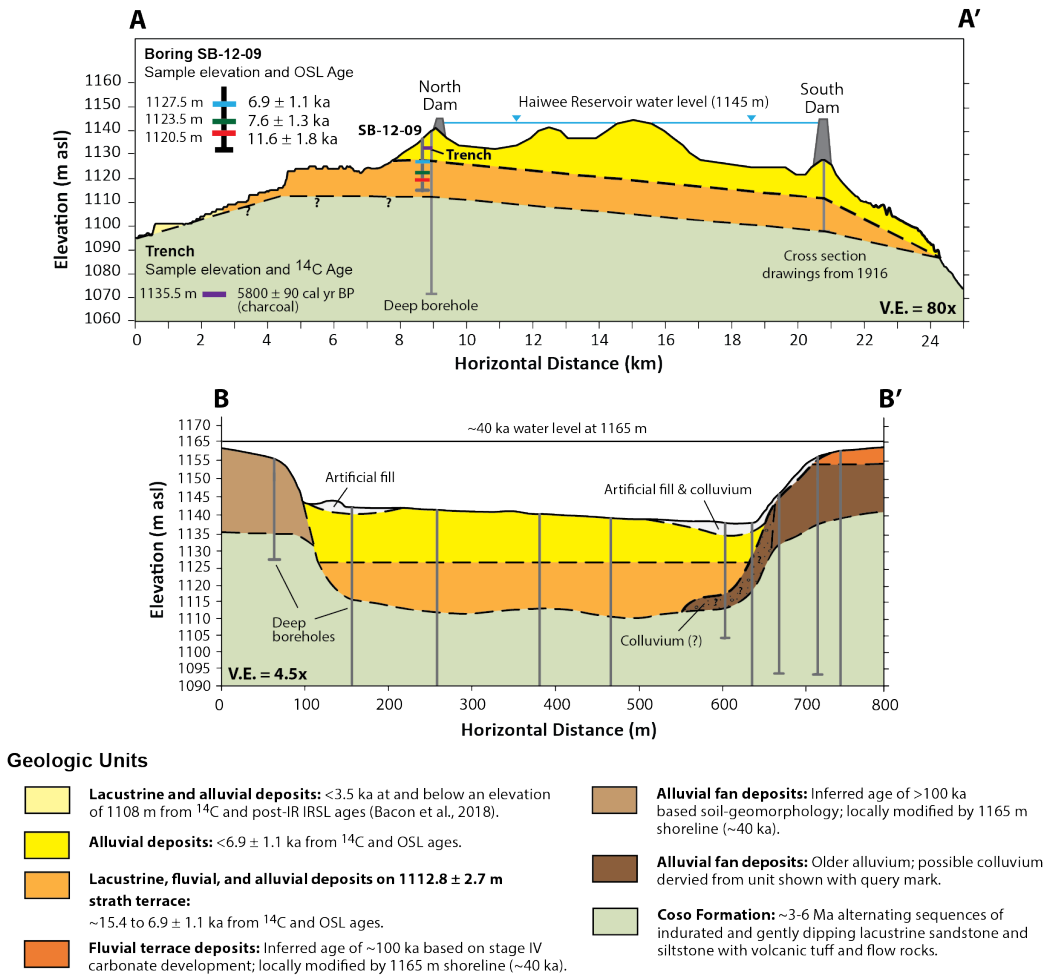

Figure 5. Geologic cross sections along longitudinal (A–A') and transverse (B–B') transects of the Owens Lake overflow channel showing the morphometery and position of strath surfaces (see Figure 4A for positions of section lines). The topographic profile shown on A–A' within the limits of Haiwee Reservoir is from pre-construction topography (Figure 4B) and shows the transverse profiles of four coalescing alluvial fans that have formed within the confined reaches of the channel. Geology shown on cross section B–B' is based on a geotechnical investigation that included a transect of 10 exploratory sonic borings, 31 cone penetration testing probes, and seismic reflection surveys across the width of the channel (Black and Veatch, 2013; Goetz et al., 2016). Geology shown at the southern reach of the channel is from a geologic cross section of foundation materials from exploratory excavations prior to construction of the south dam (Los Angeles Board of Public Service Commissioners, 1916). Age control is from ^{14}C dating of wood in trenches and OSL dating of sands collected in situ from boring SB-12-09 that yielded latest Pleistocene to middle Holocene ages for channel fill (Black and Veatch, 2013). The bottom of the channel at transect B–B' is a hard sill that provides minimum elevation constraints for potential overflowing water levels of Owens Lake at 1112.8 ± 2.7 m.

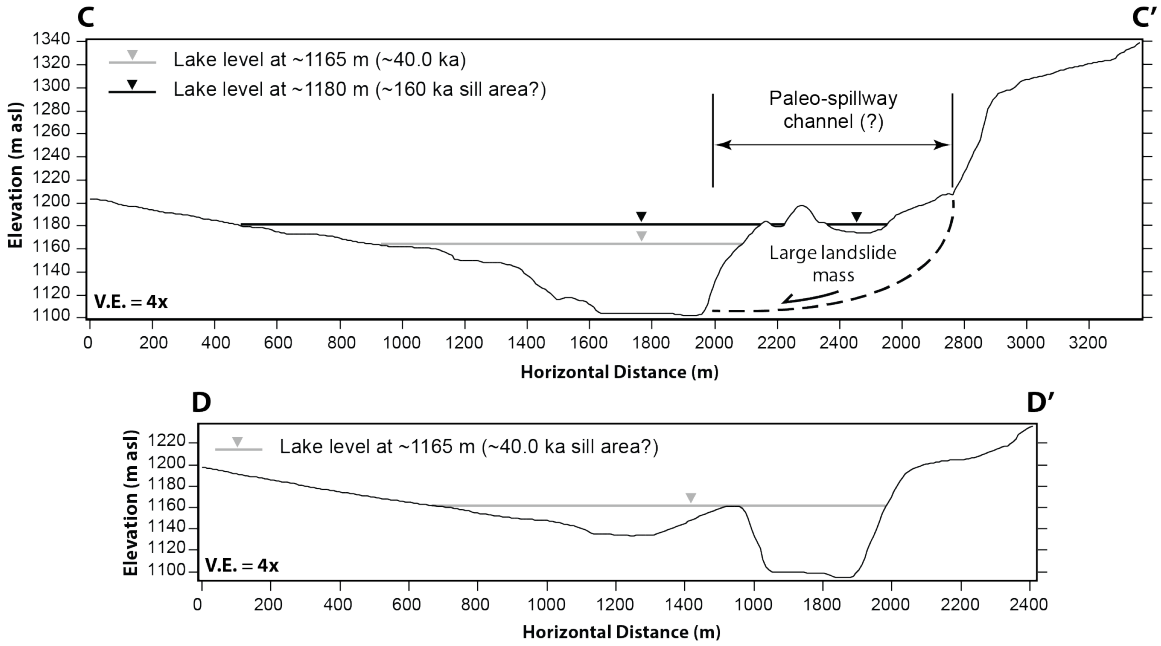

Figure 6. Geomorphic profiles across the southern reach of the Owens Lake overflow channel at transects C–C' and D–D' (see Figure 4A for positions of section lines) showing sharp breaks-in-slope, benches, and channel features. These features may be evidence of potential sill areas associated with late Pleistocene highstands of Owens Lake that reached elevations of ~1145 m at ~40 ka (Bacon et al., 2019a) and up to ~1180 m at ~160 ka (Jayko and Bacon, 2008). Profiles were developed from USGS 10-m-resolution DEM.

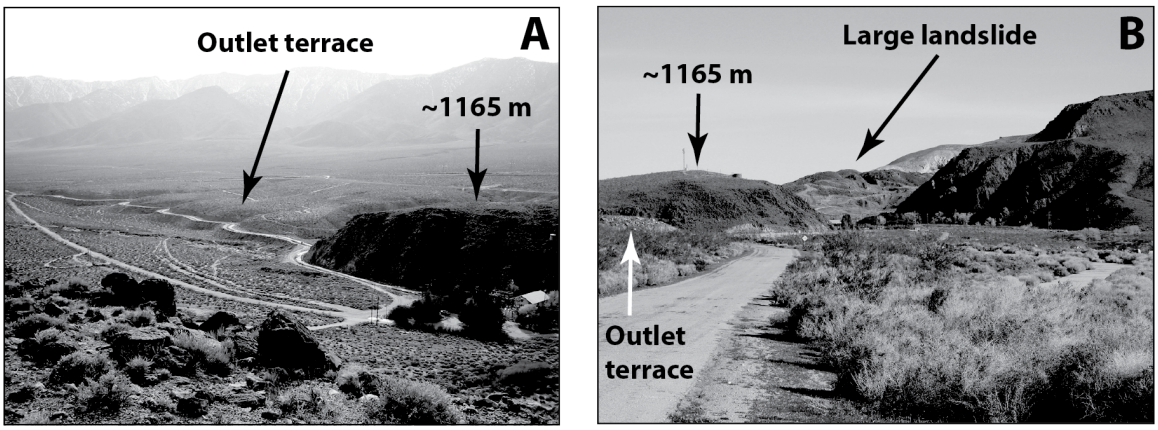

Figure 7. Views of the outlet of the Owens Lake overflow channel showing: (A) broad inset terrace formed across the toe of older alluvial fans and a knob underlain by resistant volcanic rock of the Coso Formation with a surface elevation of ~1165 m, view to the south-southwest into Rose Valley; and (B) large landslide feature, as well as same features described in part A, view to north-northeast. The elevation of the knob coincides with the elevation of the ~40 ka shoreline of Owens Lake. The geomorphology of the outlet terrace appears to be a remnant of the distal portion of an alluvial fan that formed within the overflow channel.

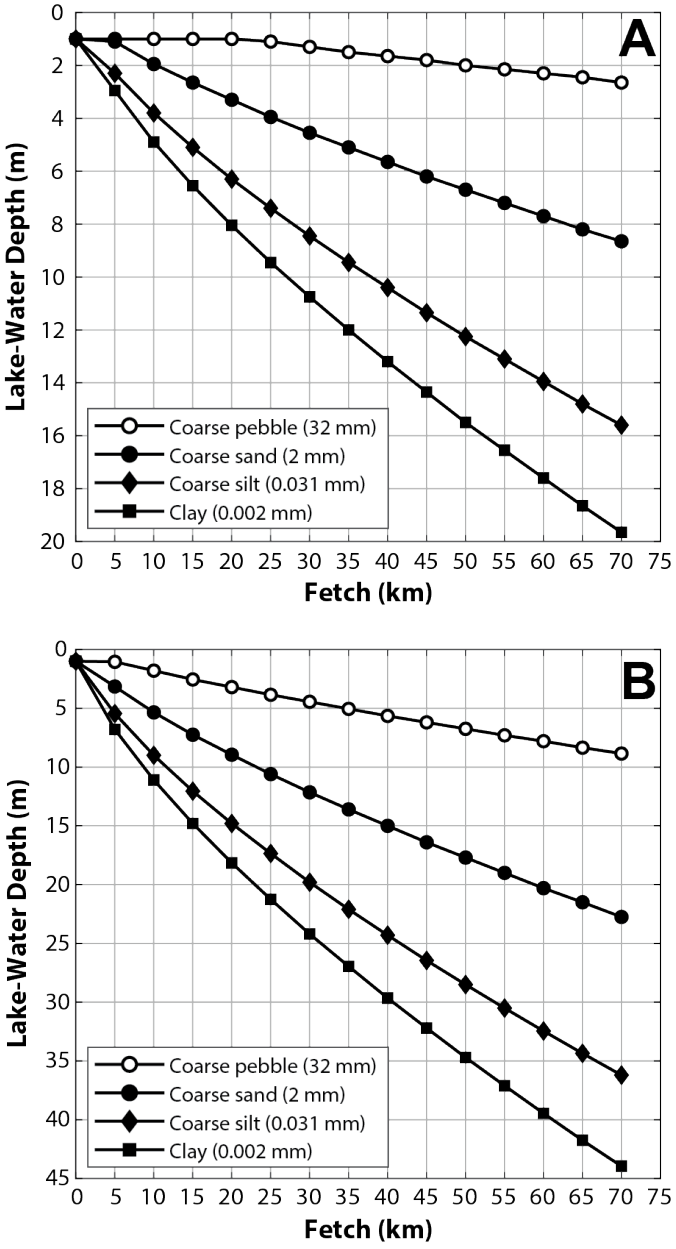

Figure 8. Threshold lake-water depth curves for particle entrainment of coarse pebble, coarse sand, coarse silt, and clay corresponding to fetch at wind speeds of (A) 7 m/s and (B) 18 m/s. The depth and corresponding fetch at which there is no particle entrainment is shown for each particle size.

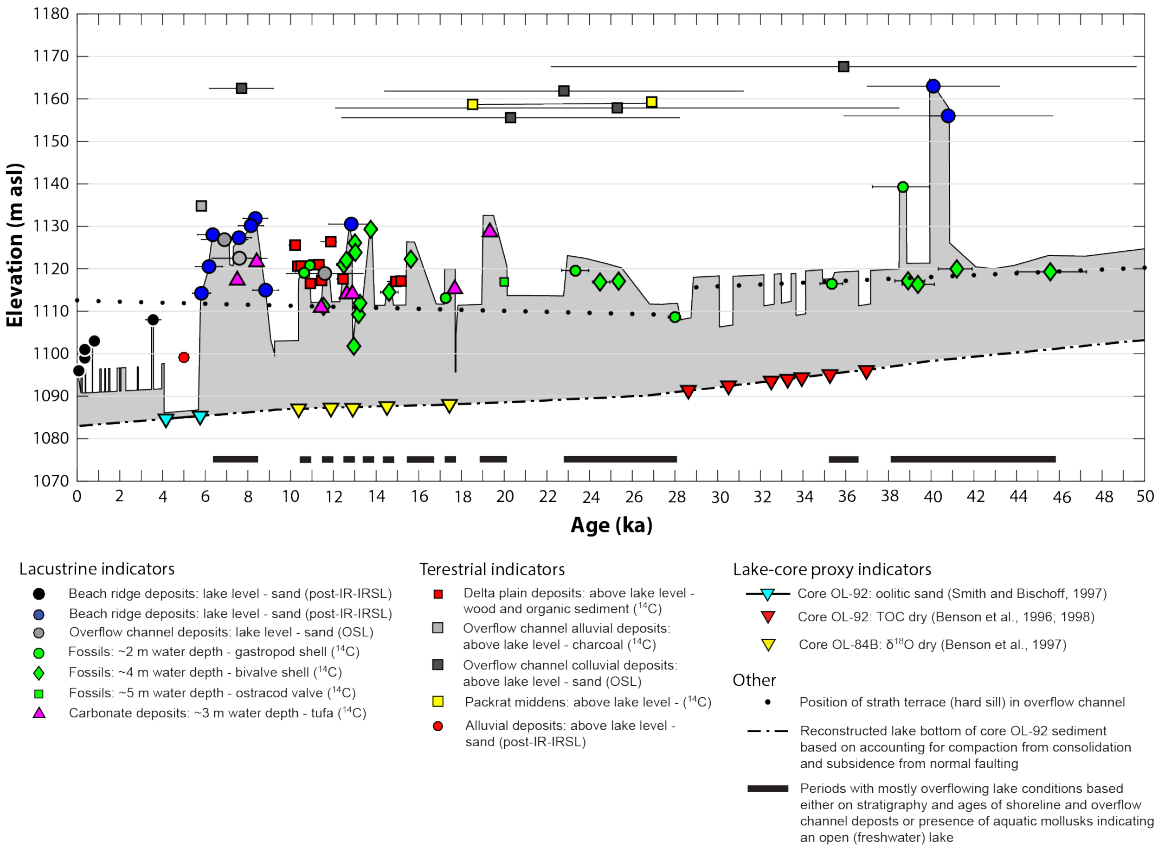

Figure 9. Refined lake-level curve and reconstructions of sill and lake bottom elevations of Owens Lake since 50 ka. The lake-level curve is a compilation of stratigraphic, geomorphic, and lake core data from new investigations of this study and previously published studies (e.g., Bacon et al., 2006, 2018, in press; Orme and Orme, 2008; Reheis et al., 2014). Reconstruction of the lake bottom is based on accounting for settlement from compaction and subsidence from active faulting (see Tables 1–3 and Figure 2 for ages and study sites, and text for a more complete description of data and methods).

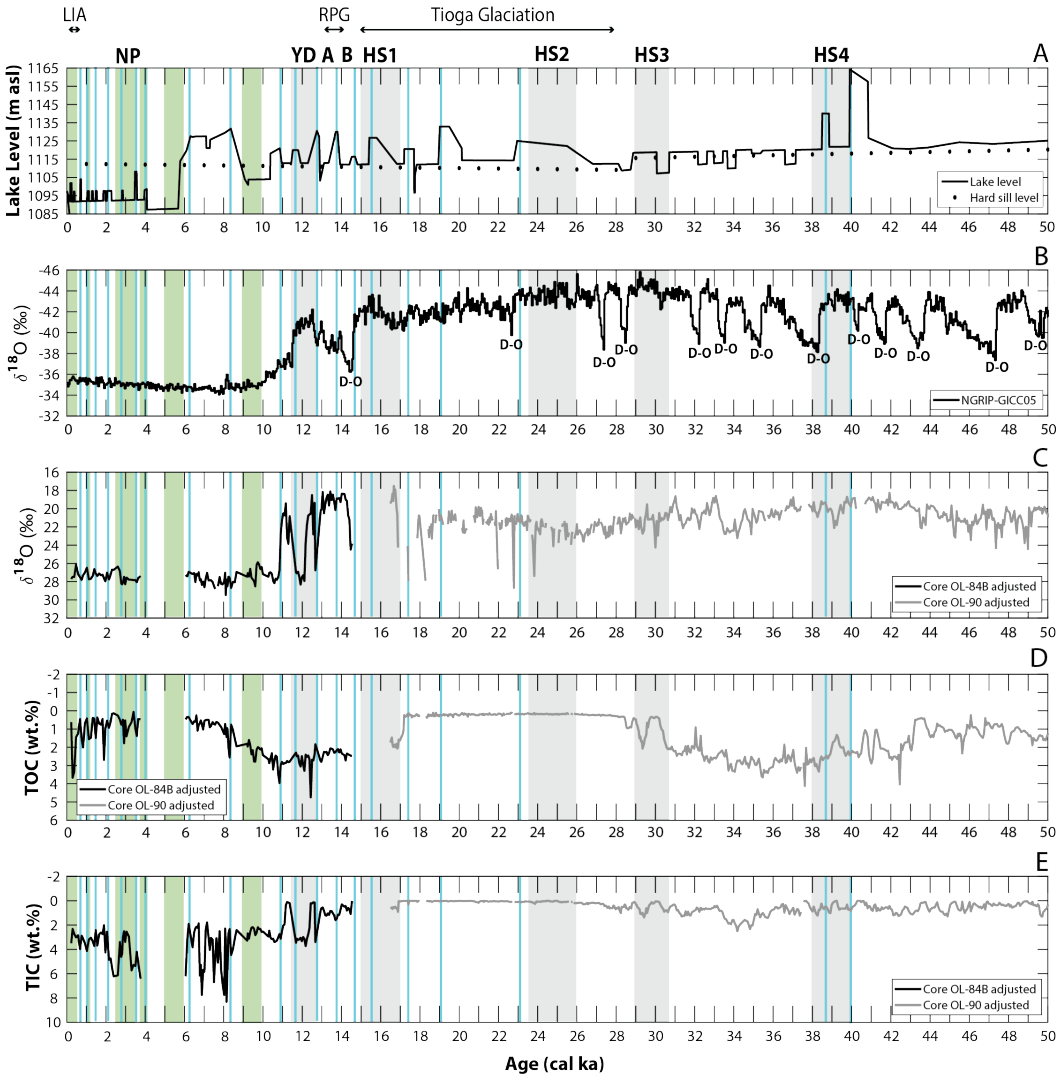

Figure 10. Comparison of shoreline and proxy records since 50 ka including: (A) Owens lake-level curve; (B) $\delta^{18}O$ ice core record from the North Greenland Ice Core Project (NGICP; Andersen et al., 2004); and Owens Lake OL-84B and OL-90 lake core proxy record. The lake core records were adjusted by developing revised age-depth models that account for sediment compaction and no reservoir corrections during periods with mostly open basin conditions from 6–50 ka. The adjusted lake core records show variations in (C) $\delta^{18}O$; (D) total organic carbon (TOC); and (E) total organic carbon (TIC) (Benson et al., 1996, 1997, 2002). Blue lines represent Owens Lake transgressions. Gray vertical bars are Heinrich stadials (or events) 1–4 (HS1–4) and Younger Dryas (YD) stadial. Green vertical bars are periods of Holocene global climate change (Mayewski et al., 2004). Interstadials related to Dansgaard–Oeschger (D–O) cycles, Allerød (A), and Bølling (B) are shown. Glaciations in the Sierra Nevada are also shown: RPG – Recess Peak glaciation and LIA – Little Ice Age. Relative cool and wet period in the Sierra Nevada referred to as the Neopluvial (NP) is also shown.

Table 1. Radiocarbon ages from carbonized wood, charcoal, organic sediment, mollusk, ostracode, and tufa from sites in Owens Lake basin used in this study.

Sample Locality	Sample Elevation (meters)	Corrected Elevation[a] (meters)	Material Dated	^{14}C yr BP	$\delta^{13}C/\delta^{12}C$ (‰)	cal yr BP[b]		Lab No.	Ref.
						Median Probability[c]	2-σ Range		
Dirty Socks	1102.8	1117.2	*Anodonta californiensis*	34,700 ± 320	0	38,920	38,300–39,700	USGS-WW8661	1
Dirty Socks	1101.8	1116.3	*Sphaerium striatinum*	35,160 ± 340	0	39,380	38,640–40,150	USGS-WW8662	1
Dirty Socks	1102.4	1119.3	*Sphaerium striatinum*	42,560 ± 840	0	45,580	44,040–47,270	USGS-WW8663	1
Dirty Socks	1103.4	1116.5	gastropod	31,730 ± 230	0	35,310	34,800–35,850	USGS-WW8664	1
Dirty Socks	1104.7	1120.0	*Anodonta californiensis*	36,910 ± 420	0	41,200	40,340–41,920	USGS-WW8665	1
Dirty Socks	1106.9	1111.1	*Anodonta californiensis*	10,345 ± 30	0	11,540	11,300–11,750	USGS-WW8667	1
OVF	1105.0	1108.7	gastropod	24,200 ± 130	–3.0	27,940	27,690–28,270	USGS-WW8693	1
OVF	1107.5	1109.2	*Anodonta californiensis*	11,630 ± 35	–2.6	13,180	13,090–13,270	USGS-WW8695	1
OVF	1114.4	1117.0	ostracodes	16,900 ± 50	0	20,030	19,830–20,200	USGS-WW8669	1
OVF	1122.1	1123.8	*Anodonta californiensis*	11,435 ± 35	0	13,030	12,900–13,100	USGS-WW8672	1
Swansea	1109.0	1113.1	*Helisoma newberryi*	14,460 ± 45	–3.2	17,240	17,060–17,450	USGS-WW8697	1
Swansea	1108.1	1110.8	carbonate, tufa	10,280 ± 40	–1.8	11,430	11,260–11,620	Beta-299115	1
Overflow Ch.	1135.5	1134.8	charcoal	5060 ± 30	–11.2	5820	5740–5900	Beta-335354	2
Swansea	1118.9	1121.5	*Helisoma newberryi*	9870 ± 90	–2.3	10,920	10,610–11,190	Beta-158755	3
Swansea	1118.5	1122.3	*Anodonta californiensis*	13,340 ± 40	0	15,630	15,370–15,810	USGS-WW4782	3
Keeler	1124.0	1128.6	carbonate, tufa	16,320 ± 90	+3.5	19,330	19,060–19,580	Beta-166887	3
Keeler	1111.0	1114.1	carbonate, tufa	11,320 ± 70	+2.2	12,890	12,740–13,040	Beta-166888	3
Keeler	1111.0	1116.9	*Anodonta californiensis*	20,680 ± 120	–2.8	24,490	24,140–24,960	Beta-166889	3
Keeler	1111.0	1114.0	carbonate, tufa	10,970 ± 70	+2.2	12,630	12,440–12,730	Beta-166890	3
Keeler	1111.0	1117.1	*Anodonta californiensis*	21,300 ± 100	0	25,360	25,080–25,610	USGS-WW4044	3
Keeler	1111.0	1115.2	carbonate, tufa	14,810 ± 40	0	17,690	17,520–17,880	USGS-WW4045	3
ORB; OR-2B	1113.0	1117.2	carbonized wood	9990 ± 40	–22.1	11,450	11,270–11,700	Beta-163551	3

Table 1. Radiocarbon ages from carbonized wood, charcoal, organic sediment, mollusk, ostracode, and tufa from sites in Owens Lake basin used in this study (Continued).

Sample Locality	Sample Elevation (meters)	Corrected Elevation[a] (meters)	Material Dated	^{14}C yr BP	$\delta^{13}C/\delta^{12}C$ (‰)	cal yr BP[b]		Lab No.	Ref.
						Median Probability[c]	2-σ Range		
ORB; OR-2A	1113.0	1117.6	organic sediment	10,480 ± 40	–26.1	12,450	12,150–12,570	Beta-163552	3
ORB; OR-4	1112.5	1116.5	organic sediment	9560 ± 40	–25.4	10,930	10,730–11,090	Beta-163553	3
AGPS; T2	1121.8	1125.6	carbonized wood	9060 ± 40	–23.9	10,220	10,180–10,260	Beta-163554	3,4
AGPS; T2	1121.8	1125.6	organic sediment	9030 ± 60	–25.4	10,200	9920–10,290	Beta-163555	3,4
QPS; T4	1116.8	1120.6	organic sediment	9160 ± 50	–25.2	10,330	10,230–10,490	Beta-163556	3,4
QPS; T4	1116.8	1120.9	organic sediment	9680 ± 50	–25.1	11,110	10,790–11,220	Beta-163557	3,4
QPS; T4	1116.8	1121.0	charcoal	9920 ± 50	–24.7	11,330	11,230–11,600	Beta-163558	3,4
QPS; T4	1116.8	1120.7	charcoal	9300 ± 60	–25.3	10,490	10,280–10,660	Beta-163500	3,4
QPS; T5	1120.5	1121.6	carbonate, tufa	7910 ± 60	–3.2	8,410	8330–8540	Beta-163561	3,4
QPS; P4	1114.5	1117.3	carbonate, tufa	6910 ± 60	–1.2	7,500	7430–7580	Beta-168599	3,4
QPS; P4	1111.5	1117.0	carbonized wood	12,580 ± 60	–27.8	14,920	14,530–15,180	Beta-168600	3,4
QPS; P4	1111.5	1117.0	carbonized wood	12,590 ± 60	–28.2	14,940	14,580–15,200	Beta-168601	3,4
QPS; P4	1111.5	1117.1	carbonized wood	12,730 ± 60	–28.7	15,170	14,910–15,360	Beta-168602	3,4
Swansea	1117.0	1119.5	*Helisoma newberryi*	9580 ± 100	n/r	10,470	10,240–10,700	Beta-58386	5
Swansea	1118.0	1121.0	*Anodonta californiensis*	10,840 ± 80	n/r	12,490	12,150–12,690	Beta-82063	5
Swansea	1119.0	1122.0	*Anodonta californiensis*	10,940 ± 70	n/r	12,610	12,430–12,720	Beta-52398	5
Swansea	1123.0	1126.1	*Anodonta californiensis*	11,450 ± 70	n/r	13,010	12,810–13,130	Beta-54341	5
Owens River delta	1107.0	1111.9	*Anodonta californiensis*	11,700 ± 110	n/r	13,250	13,070–13,450	Beta-82061	5
Swansea	1126.0	1129.3	*Anodonta californiensis*	12,210 ± 130	n/r	13,750	13,470–14,060	Beta-51957	5
Swansea	1114.0	1119.6	*Amnicola paluustris*	19,670 ± 260	n/r	23,330	22,690–23,960	Beta-61076	5
Centennial Flat	1111.0	1114.5	*Anodonta californiensis*	12,760 ± 80	n/r	14,610	14,210–15,040	Beta-82062	5

Table 1. Radiocarbon ages from carbonized wood, charcoal, organic sediment, mollusk, ostracode, and tufa from sites in Owens Lake basin used in this study (Continued).

Sample Locality	Sample Elevation (meters)	Corrected Elevation[a] (meters)	Material Dated	^{14}C yr BP	$\delta^{13}C/\delta^{12}C$ (‰)	cal yr BP[b]		Lab No.	Ref.
						Median Probability[c]	2-σ Range		
Centennial Flat	1130.0	1139.3	*Helisoma newberryi*	34,540 ± 500	n/r	38,730	37,250–39,920	Beta-82062	5
AGPS; T3	1122.0	1126.4	charcoal	10,190 ± 70	n/r	11,880	11,410–12,150	USGS-2339	6
Owens River delta	1097.0	1101.8	*Anodonta californiensis*	11,400 ± 60	n/r	12,960	12,810–13,080	Beta-67673	7
Haystack	1155	1161 - 1163	Packrat midden; wood	14,870 ± 130 to 22,900 ± 270	n/r	18,090 to 27,200	17,770 to 27,650	Beta-39274; 39273	8

Notes: n/r = not reported; Radiocarbon dates determined based on accelerator mass spectrometry (AMS) by Jack McGeehin, US Geological Survey (USGS-WW), Reston, Virginia and Beta Analytical Inc. (Beta), Miami, Florida, USA. References: (1) this study; (2) Black and Veatch (2013); (3) Bacon et al. (2006); (4) Bacon and Pezzopane (2007); (5) Orme and Orme (2008); (6) Beanland and Clark (1994); (7) Koehler (1995); (8) Koehler and Anderson (1994).

[a]Elevation corrected for tectonic deformation based on fault rates and tectonic block model of Bacon et al. (in review).

[b]A 300-yr reservoir correction is applied to radiocarbon dates from mollusk, ostracodes, and tufa based on study of Lin et al. (1998) in Searles Lake basin; radiocarbon dates are calibrated at ±2σ using CALIB7.1 program (Stuiver and Reimer, 1993) with the IntCal13 data set (Reimer et al., 2013).

[c]Median probability of the calibrated age falling within the reported range as calculated by CALIB7.1 program.

Table 2. Results of single-grain post-IR-IRSL dating of fine sand in beach ridge deposits at the Centennial Flat study site in Owens Lake basin.

Site	Landform	Latitude (°N)	Longitude (°W)	Elevation[a] (m)	Field Sample Number	Depth (m)	Sample Elevation[b] (m)	Dose rate (Gy/ka)	Mean Equivalent Dose (Gy)	Age[c] (ka)
Centennial Flat	Beach ridge	36.4018	-117.8518	1131.3	OL814-1	1.14	1132.2	3.91 ± 0.18	32.6 ± 1.7	8.4 ± 0.6
Centennial Flat	Beach ridge	36.4017	-117.8529	1129.4	OL814-2	0.80	1130.6	4.13 ± 0.20	33.6 ± 1.8	8.1 ± 0.6
Centennial Flat	Beach ridge	36.4017	-117.8529	1129.4	OL814-4	1.55	1130.9	3.96 ± 0.18	50.8 ± 3.5	12.8 ± 1.1
Centennial Flat	Beach ridge	36.4021	-117.8531	1127.5	OL814-5	0.40	1128.5	4.59 ± 0.25	27.5 ± 1.7	6.0 ± 0.5
Centennial Flat	Beach ridge	36.4021	-117.8531	1127.5	OL814-6	0.60	1128.5	4.21 ± 0.22	28.2 ± 1.7	6.7 ± 0.5
Centennial Flat	Beach ridge	36.4022	-117.8533	1126.7	OL814-8	0.50	1128.0	4.25 ± 0.22	32.2 ± 1.8	7.6 ± 0.6
Centennial Flat	Beach ridge	36.4033	-117.8555	1120.9	OL814-9	0.90	1121.4	3.67 ± 0.16	21.5 ± 1.3	5.9 ± 0.5
Centennial Flat	Beach ridge	36.4033	-117.8555	1120.9	OL814-10	1.00	1121.5	4.05 ± 0.19	26.4 ± 1.4	6.5 ± 0.5
Centennial Flat	Beach ridge	36.4063	-117.8565	1113.6	OL814-11	1.15	1113.8	4.12 ± 0.20	24.0 ± 1.3	5.8 ± 0.4
Centennial Flat	Beach ridge	36.4063	-117.8565	1113.6	OL814-12	1.15	1114.6	4.10 ± 0.20	36.2 ± 1.8	8.8 ± 0.6

Note: Analysis performed at University of California Los Angeles Luminescence Laboratory, Los Angeles, California. Uncertainty reported at 1σ.

[a]Elevation of surface of sample site. Elevation surveyed with GPS with real-time differential correction with 18–69 cm vertical accuracy.

[b]Elevation of sample is corrected for tectonic ground deformation.

[c]Ages are presented as years before AD 2015.

Table 3. Results of single-grain OSL dating of fine quartz sand at the Owens Lake overflow channel.

Sample Site[a]	Sedimentary Facies	Latitude (°N)	Longitude (°W)	Field Sample #	Elevation[c] (m)	Depth (m)	Sample Elevation[d] (m)	Dose Rate (Gy/ka)	Mean Equivalent Dose (Gy)	Age[f](ka)
Boring SB-12-09	Fluvial-deltaic	36.2331	-117.9649	HD 1	1136.9	9.4	1126.9	4.20 ± 0.21	28.93 ± 4.19	6.9 ± 1.1
Boring SB-12-09	Fluvial-deltaic	36.2331	-117.9649	HD 2	1136.9	13.4	1122.5	3.81 ± 0.21	28.87 ± 4.58	7.6 ± 1.3
Boring SB-12-09	Fluvial-deltaic	36.2331	-117.9649	HD 3	1136.9	16.4	1118.9	4.25 ± 0.25	49.22 ± 7.21	11.6 ± 1.8
Eastern channel	Colluvium	36.2246	-117.9597	HD 6[b]	1166	1.4	1161.9	5.16 ± 0.23	106.33 ± 33.52	22.8 ± 8.4
Eastern channel	Colluvium	36.2246	-117.9597	HD 7-1[b]	1163	2.1	1157.4[e]	4.97 ± 0.23	144.73 ± 86.00	29.1 ± 8.0
Eastern channel	Colluvium	36.2246	-117.9597	HD 7-2[b]	1163	2.1	1157.4[e]	4.97 ± 0.23	12.83 ± 2.01	21.4 ± 9.5
Eastern channel	Colluvium	36.2251	-117.9597	HD 8	1164	0.6	1162.5	5.00 ± 0.23	38.28 ± 7.06	7.7 ± 1.5
Eastern channel	Colluvium	36.2247	-117.9598	HD 9[b]	1170	0.8	1167.6	5.17 ± 0.23	134.07 ± 17.45	35.9 ± 13.7

Note: Analysis performed at University of Cincinnati Luminescence Dating Laboratory, Cincinnati, Ohio.

[a]Samples from sites of geotechnical study at Owens Lake basin overflow area by Black and Veatch (2013) and Goetz et al. (2016).

[b]Sample group does not behave well and their age estimation has large error.

[c]Elevation of surface of sample site. All elevations surveyed by licensed land surveyor.

[d]Elevation of sample is corrected for tectonic ground deformation.

[e]Elevation of sample corrected for tectonic ground deformation based on mean age of 25.3 ka for samples HD 7-1 and 7-2.

[f]Ages are presented as years before AD 2012.

Table 4. Vertical slip and subsidence rates used to account for tectonic ground deformation in Owens Lake basin.

Fault system	Type of fault	Vertical slip rate (m/ka)	Source
Eastern lake basin subsidence	n/a	0.24 ± 0.06	Bacon et al. (2019a)
Southern Owens Valley fault	dextral-oblique	0.12 ± 0.04	Bacon and Pezzopane (2007)
Southern Sierra Nevada frontal fault	normal	0.25 ± 0.05	Le et al. (2007)
Sage Flat fault	normal	0.09 ± 0.01	Amos et al. (2013)

Note: n/a = not applicable.

8. REFERENCES

Adams, K.D., 2003. Age and paleoclimatic significance of late Holocene lakes in the Carson Sink, NV, USA. Quaternary Research 60, 294–306.

Adams, K.D., 2007. Late Holocene sedimentary environments and lake-level fluctuations at Walker Lake, Nevada, USA. Geological Society of America Bulletin 119, 126–139.

Adams, K.D., and Wesnousky, S.G., 1998. Shoreline processes and the age of the Lake Lahontan highstand in the Jessup embayment, Nevada. Geological Society of America Bulletin 110, 1318–1332.

Adams, K.D., and Rhodes, E.J., 2019a. Late Holocene paleohydrology of Walker Lake and the Carson Sink in the western Great Basin, Nevada, USA. Quaternary Research 92, 165–182.

Adams, K.D., and Rhodes, E.J., 2019b. Late Pleistocene to present lake-level fluctuations at Pyramid and Winnemucca Lakes, Nevada, USA. Quaternary Research 92, 146–164.

Adams, K.D., Wesnousky, S.G., and Bills, B.G., 1999. Isostatic rebound, active faulting, and potential geomorphic effects in the Lake Lahontan basin, Nevada and California. Geological Society of America Bulletin, 111, 1739–1756.

Alley, R.B., Mayewski, P.A., Sowers, T., Stuiver, M., Taylor, K.C., Clark, P.U., 1997. Holocene climatic instability: a prominent, widespread event 8200 yr ago. Geology 25, 483–486.

Amos, C.B., Lutz, A.T., Jayko, A.S., Mahan, S.A., Burch Fisher, G., and Unruh, J.R., 2013a. Refining the southern extent of the 1872 Owens Valley earthquake rupture through paleoseismic investigations in the Haiwee Area, southeastern California. Bulletin of the Seismological Society of America 103, 1022–1037.

Antinao, J.J., and McDonald, E., 2013. An enhanced role for the Tropical Pacific on the humid Pleistocene-Holocene transition in southwestern North America. Quaternary Science Reviews 78, p. 319–341.

Asmerom, Y., Polyak, V.J., Burns, S.J. 2010. Variable winter moisture in the southwestern United States linked to rapid glacial climate shifts. Nature Geoscience 3, 114–117.

Bacon, S.N., and Pezzopane, S.K., 2007. A 25,000-year record of earthquakes on the Owens Valley fault near Lone Pine, California: Implications for recurrence intervals, slip rates, and segmentation models. Geological Society of America Bulletin 119, 823–847.

Bacon, S.N., Jayko, A.S., and McGeehin, J.P., 2005. Holocene and latest Pleistocene oblique dextral faulting on the southern Inyo Mountains fault, Owens Lake basin, California. Bulletin Seismological Society of America 95, 2472–2485.

Bacon, S.N., Burke, R.M., Pezzopane, S.K., and Jayko, A.S., 2006. Last glacial maximum and Holocene lake levels of Owens Lake, eastern California, USA. Quaternary Science Reviews 25, 1264–1282.

Bacon, S.N., Lancaster, N., Stine, S., Rhodes, E.J., and McCarley Holder, G.A., 2018. A continuous 4000-year lake-level record of Owens Lake, south-central Sierra Nevada, California, USA. Quaternary Research 90, 276–302.

Bacon, S.N., Bullard, T.F., Keen-Zebert, A.K., Jayko, A.S., and Decker, D.L., in press. Spatiotemporal patterns of distributed slip in southern Owens Valley indicated by deformation of late Pleistocene shorelines, eastern California. Geological Society of America Bulletin. doi.org/10.1130/B35247.1.

Bartlein, P.J., and 18 others, 2011. Pollen-based continental climate reconstructions at 6 and 21 ka: a global synthesis. Climate Dynamics 37, 775–802.

Bartov, Y., Enzel, Y., Porat, N., Stein, M., 2007. Evolution of the late Pleistocene-Holocene Dead Sea Basin from sequence stratigraphy of fan deltas and lake-level reconstruction. Journal of Sedimentary Research 77, 680–692.

Basagic, H.J., and Fountain, A.G., 2011. Quantifying 20th century glacier change in the Sierra Nevada, California. Arctic, Antarctic, and Alpine Research 43, 317–330.

Beanland, S., and Clark, M.M., 1994. The Owens Valley fault zone, eastern California, and surface rupture associated with the 1872 earthquake. U.S. Geological Survey Bulletin 1982, 29 p.

Benn, D.I., Owens, L.A., Finkel, R.C., and Clemmens, S., 2006. Pleistocene lake outburst floods and fan formation along the eastern Sierra Nevada, California: implications for the interpretation of intermontane lacustrine records. Quaternary Science Reviews 25, 2729–2748.

Benson, L.V., 1993. Factors affecting 14C ages of lacustrine carbonates: timing and duration of the last highstand lake in the Lahontan basin. Quaternary Research 39, 163–174.

Benson, L.V., 1994. Carbonate deposition, Pyramid Lake Subbasin, Nevada: 1. Sequence of formation and elevational distribution of carbonate deposits (Tufas). Palaeogeography, Palaeoclimatology, Palaeoecology 109, 55–87.

Benson, L., 2004. Western Lakes. In: Gillespie, A.R., Porter, S.C., Atwater, B.F. (Eds.), The Quaternary Period in the United States. Elsevier, New York, pp. 185–204.

Benson, L.V., Currey, D.R., Dorn, R.I., Lajoie, K.R., Oviatt, C.G., Robinson, S.W., Smith, G.I., and Stine, S., 1990. Chronology of expansion and contraction of four Great Basin lake systems during the past 35,000 years. Palaeogeography, Palaeoclimatology, Palaeoecology 78, 241–286.

Benson, L., Kashgarian, M., Rubin, M., 1995. Carbonate deposition, Pyramid Lake subbasin, Nevada: 2. Lake levels and polar jet stream positions reconstructed from radiocarbon ages and elevations of carbonates (tufas) deposited in the Lahontan basin. Palaeogeography, Palaeoclimatology, Palaeoecology 117, 1–30.

Benson, L.V., Burdett, J.W., Kashgarian, M., Lund, S.P., Phillips, F.M., Rye, R.O., 1996. Climatic and hydrologic oscillations in the Owens Lake basin and the adjacent Sierra Nevada, California. Science 274, 746–749.

Benson, L., Burdett, J., Lund, S., Kashgarian, M., Mensing, S., 1997. Nearly synchronous climate change in the Northern Hemisphere during the last glacial termination. Nature 388, 263–265.

Benson, L.V., May, H.M., Antweiler, R.C., Brinton, T.I., Kashgarian, M., Smoot, J.P., and Lund, S.P., 1998a. Continuous lake-sediment records of glaciation in the Sierra Nevada between 52,600 and 12,500 ^{14}C yr B.P. Quaternary Research 50, 113–127.

Benson, L.V., Lund, S.P., Burdett, J.W., Kashgarian, M., Rose, T.P., Smoot, J.P., Schwartz, M., 1998b. Correlation of Late-Pleistocene lake-level oscillations in Mono Lake, California, with North Atlantic climate events. Quaternary Research 49, 1–10.

Benson, L., Kashgarian, M., Rye, R., Lund, S., Paillet, F., Smoot, J., Kester, C., Mensing, S., Meko, D., Lindstrom, S., 2002. Holocene multidecadal and multicentennial

droughts affecting northern California and Nevada. Quaternary Science Reviews 21, 659–682.

Benson, L.V., Smoot, J.P., Lund, S.P., Mensing, S.A., Foit Jr., F.F., Rye, R.O., 2013. Insights from a synthesis of old and new climate-proxy data from the Pyramid and Winnemucca lake basins for the period 48 to 11.5 cal ka. Quaternary International 310, 62–82.

Birkeland, P.W., 1999. Soils and Geomorphology, 3rd ed., Oxford Univ. Press, New York, p. 372 p.

Bischoff, J.L., Rosenbauer, R.H., and Smith, G.I., 1985. Uranium-series dating of sediments from Searles Lake: differences between continental and marine climate records. Science 227, 1222–1224.

Bischoff, J.L., and Cummins, K., 2001. Wisconsin glaciation of the Sierra Nevada (79,000-15,000 yr B.P.) as recorded by rock flour in sediments of Owens Lake, California. Quaternary Research 55, 14–24.

Black and Veatch, 2013. Local fault considerations for proposed North Haiwee Dam Number 2, Inyo County, California. Project No. 169501 Final Report prepared by Black & Veatch, URS, and Lettis Consultants International for Los Angeles Department of Water and Power, dated September 24, 2013, 95 p. plus appendices.

Blunt, A.B., and Negrini, R.M., 2015. Lake levels for the past 19,000 years from the TL05-4 cores, Tulare Lake, California, USA: Geophysical and geochemical proxies. Quaternary International 387, 122–130.

Bond G.C., Heinrich H., Broecker W.S., et al. 1992. Evidence for massive discharges of icebergs into the North Atlantic Ocean during the last glacial period. Nature 360, 245–249.

Bowerman, N.D., and Clark, D.H., 2011. Holocene glaciation of the central Sierra Nevada, California. Quaternary Science Reviews 30, 1067–1085.

Brennan, R., Quade, J., 1997. Reliable late-Pleistocene stratigraphic ages and shorter groundwater travel times from ^{14}C fossil snails from the southern Great Basin. Quaternary Research 47, 329–336.

Broecker, W.S., McGee, D., Adams, K.D., Cheng, H., Lawrence Edwards, R., Oviatt, C.G., and Quade, J., 2009. A Great Basin-wide dry episode during the first half of the Mystery Interval? Quaternary Science Reviews 28, 2557–2563.

Clark, D.H., and Gillespie, A.R., 1997. Timing and significance of late-glacial and Holocene cirque glaciation in the Sierra Nevada, California. Quaternary International 38/39, 21–38.

Cohen, A.S., 2003. Paleolimnology: The History and Evolution of Lake Systems. Oxford University Press, New York, NY 500 p.

Cook, E.R., Seager, R., Heim, R.R. Jr., Vose, R.S., Herweijer, C., Woodhouse, C., 2010. Megadrought in North America: placing the IPCC projections of hydroclimate change in a long-term paleoclimate context. Journal of Quaternary Science 25, 48–61.

Dansgaard, W., Johnsen, S.J., Clausen, H.B., Dahl-Jensen, D., Gunderstrup, N.S., Hammer, C.U., Steffensen, J.P., Svein-björnsdottir, A., Jouzel, J., and Bond, G., 1993. Evidence for general instability of past climate from a 250-kyr ice-core record. Nature 364, 218–220.

Davaud, E., and Girardclos, S., 2001. Recent freshwater ooids and oncoids from western Lake Geneva (Switzerland): Indications of a common organically mediated origin. Journal of Sedimentary Research 71, 423–429.

Davidson, G.R., Carnley, M., Lange, T., Galicki, S.J., Douglas, A., 2004. Changes in sediment accumulation rate in oxbow lake following late 9th century clearing of land for agricultural use: A 210Pb, 137Ce, and 14C study in Mississippi, USA. Radiocarbon 46, 755–764.

Dettinger, M.D., Cayan, D.R., Diaz, H.F., Meko, D.M., 1998. North-south precipitation patterns in western North America on interannual-to-decadal timescales. Journal of Climate 11, 3095–3111.

Ehlers, E.G., and Blatt, H., 1982. Petrology: Igneous, Sedimentary, and Metamorphic. W.H Freeman and Company, New York, 732 p.

Einsele, G., 2000. Sedimentary Basins: Evolution, Facies, and Sediment Budget, second ed. Springer, New York, NY 804 p.

Enzel, Y., and Wells, S.G., 1997. Extracting Holocene paleohydrology and paleoecology information from modern extreme flood events: An example from southern California. Geomorphology 19, 203–226.

Enzel, Y., Cayan, D.R., Anderson, R.Y., Wells, S.G., 1989. Atmospheric circulation during Holocene lake stands in the Mojave Desert: evidence of regional climate change. Nature 341, 44–48.

Enzel, Y., Wells, S.G., Lancaster, N., 2003. Late Pleistocene lakes along the Mojave River, southeast California. In: Enzel, Y., Wells, S.G., Lancaster, N. (Eds.), Paleoenvironments and Paleohydrology of the Mojave and Southern Great Basin Deserts, Geological Society of America Special Paper 368, pp. 61–77.

Fagherazzi, S., Wiberg, P.L., 2009. Importance of wind conditions, fetch, and water levels on wave-generated shear stresses in shallow intertidal basins. Journal of Geophysical Research 114, F03022. http://dx.doi.org/ 10.1029/2008JF001139.

Firby, J.R., Sharpe, S.E., Whelan, J.F., Smith, G.R., and Spaulding, W.G., 1997. Paleobiotic and isotopic analysis of mollusks, fish, and plants from core OL-92: Indicators for an open or close lake system. In: Smith, G.I., and Bischoff, J.L., eds., An 800,000-year paleoclimatic record from core OL-92, Owens Lake, southeast California. Geological Society of America Special Paper 317, p. 127–142.

Forester, R.M., Lowenstein, T.K., and Spencer, R.J., 2005. An ostracode based paleolimnologic and paleohydrologic history of Death Valley: 200 to 0 ka. Geological Society of America Bulletin 117, 1379–1386.

Franke, J.G., and Donner, R.V., 2019. Correlating paleoclimate time series: Sources of uncertainty and potential pitfalls. Quaternary Science Reviews 212, 69–79.

Friedman, I., Bischoff, J.L., Johnson, A., Tyler, S.W., Fitts, J.P., 1997. Movement and diffusion of pore fluids in Owens Lake sediment: An 800-k.y. record of saline/fresh cycles in core OL-92. In: Smith, G.I., Bischoff, J.L. (Eds.), An 800,000-year Paleoclimatic Record from Core OL-92, Owens Lake, Southeast California. Geological Society of America Special Paper 317, pp. 49–66.

Gale, H.S., 1914. Salines in the Owens, Searles, and Panamint basins, southeastern California. U.S. Geology Survey Bulletin 580-L, 251-323.

Garcia, A.L., Knott, J.R., Mahan, S.A., Bright, J., 2014. Geochronology and paleoenvironment of pluvial Harper Lake, Mojave Desert, California, USA. Quaternary Research 81, 305–317.

Gillespie, A.R., and Clark, D., 2011. Glaciations in the Sierra Nevada, California, USA. Developments in Quaternary Science 15, 447–462.

Goetz, C.W., Heron, C.W., Kemp, C.D., Lindvall, S.C., Mass, K., Olson, M., 2016. Fault rupture hazard assessment for North Haiwee Dam No. 2, Owens Valley,

California. In: Anderson R., Ferriz, H. (Eds.), Applied Geology in California. Star Publishing Company, pp. 63–76.

Haddon, E.K., Amos, C.B., Zielke, O., Jayko, A.S., Bürgmann, R., 2016. Surface slip during large Owens Valley earthquakes. Geochemical, Geophysical, Geosystems 17, 2239–2269.

Håkanson, L., 1977. The influence of wind, fetch, and water depth on the distribution of sediments in Lake Väern, Sweden. Canadian Journal of Earth Sciences 14, 397–412.

Hampel, A., and Hetzel, R., 2006. Response of normal faults to glacial-interglacial fluctuations of ice and water masses on Earth's surface. Journal of Geophysical Research 111, B06406.

Handy, R.L., and Spangler, M.G., 2007. Geotechnical Engineering: soil and foundation principles and practice, 5th ed. McGraw-Hill, New York, NY, 904 p.

Hatchett, B.J., Boyle, D.P., Putnam, A.E., Bassett, S.D., 2015. Placing the 2012–2015 California-Nevada drought into a paleoclimatic context: Insights from Walker Lake, California-Nevada, USA. Geophysical Research Letters 42, doi:10.1002/2015GL065841.

Hatchett, B. J., Boyle, D. P., Garner, C. B., Kaplan, M. L., Putnam, A. E., Bassett, S., 2016. Magnitude and frequency of wet years under a megadrought climate in the western Great Basin, USA, Quaternary Science Reviews 152, 197-202.

Hatchett, B.J., Boyle, D.P., Garner, C.B., Kaplan, M.L., Bassett, S.D., Putnam, A.E., 2019. Sensitivity of a western Great Basin terminal lake to winter northeast Pacific storm track activity and moisture transport. In Starratt, S.W., and Rosen, M.R., (Eds.), From Saline to Freshwater: The Diversity of Western Lakes in Space and Time: Geological Society of America Special Paper 536, doi.org/10.1130/2018.2536(05).

Heinrich H., 1988. Origin and consequences of cyclic ice rafting in the northeast Atlantic Ocean during the past 130,000 years. Quaternary Research 29, 142–152.

Hemming S.R., 2004. Heinrich events; massive late Pleistocene detritus layers of the North Atlantic and their global climate imprint. Reviews of Geophysics 42: RG1005.1–RG1005.43.

Hoffman, W.R., 2009. Late Pleistocene slip rate along the Panamint Valley fault zone, eastern California. Unpublished M.Sc. Thesis, The Pennsylvania State University, 81 p.

Hollett, K.J., Danskin, W.R., McCafferey, W.F., Walti, C.L., 1991. Geology and water resources of Owens Valley, California. U.S. Geological Survey Water-Supply Paper 2370-B, 77 p.

Hough, S.E., and K. Hutton, 2008. Revisiting the 1872 Owens Valley, California, earthquake. Bulletin Seismological Society of America 98, 931–949.

Hudson, A.M., Quade, J., Ali, G., Boyle, D., Bassett, S., Huntington, K.W., De los Santos, M.G., Cohen, A.S., Lin, K., Wang, X., 2017. Stable C, O and clumped isotope systematics and 14C geochronology of carbonates from the Quaternary Chewaucan closed-basin lake system, Great Basin, USA: Implications for paleoenvironmental reconstructions using carbonates. Geochim. Cosmochim. Acta. 212, 274–302.

Hudson, A.M., Hatchett, B.J., Quade, J., Boyle, D.P., Bassett, S.D., Ali, G., and De los Santos, M.G., 2019. North-south dipole in winter hydroclimate in the western United States during the last deglaciation. Scientific Reports 9, 4826, doi.org/10.1038/s41598-019-41197-y.

Ibarra, D.E., Egger, A.E., Weaver, K.L., Harris, C.R., Maher, K., 2014. Rise and fall of late Pleistocene pluvial lakes in response to reduced evaporation and precipitation: Evidence from Lake Surprise, California. Geological Society of America Bulletin 126, 1387–1415.

Jannik, N.O., Phillips, F.M., Smith, G.I., Elmore, D., 1991. A ^{36}Cl chronology of lacustrine sedimentation in the Pleistocene Owens River system. Geological Society of America Bulletin 103, 1146–1159.

Jayko, A.S., 2009, Surficial geologic map of the Darwin Hills 30' x 60' quadrangle, Inyo County, California: U.S. Geological Survey Scientific Investigations Map 3040, 20 p. pamphlet, 2 plates, scale 1:100,000.

Jayko, A.S., Bacon, S.N., 2008. Late Quaternary MIS 6-8 shoreline features of pluvial Owens Lake, Owens Valley, eastern California. In: Reheis, M.C., Hershler, R., Miller, D.M. (Eds.), Late Cenozoic drainage history of the southwestern Great Basin and lower Colorado River Region: geologic and biotic perspectives, Geol. Soc. Amer. Spec. Paper 439, pp. 185–206.

Jayko, A.S., Forester, R.M., Kaufman, D.S., Phillips, F.M., Yount, J.C., McGeehin, J., Mahan, S.A., 2008. Late Pleistocene lakes and wetlands, Panamint Valley, Inyo County, California. In: Reheis, M.C., Hershler, R., Miller, D.M. (Eds.), Late Cenozoic Drainage History of the Southwestern Great Basin and Lower Colorado River Region: Geologic and biotic perspectives, Geol. Soc. Amer. Spec. Paper 439, pp. 151–184.

Ji, Z.G., 2017. Hydrodynamics and Water Quality: Modeling Rivers, Lakes, and Estuaries. John Wiley & Sons Inc., New Jersey.

Kemp, C.D., Lindvall, S.C., Heron, C.W., Goetz, C.W., 2016. LiDAR based fault mapping in southern Owens Valley, California. In: Anderson R., Ferriz, H. (Eds.), Applied Geology in California. Star Publishing Company, pp. 77–100.

Kirby, E. and McDonald, E., 2016. (Eds.), Friends of the Pleistocene, Pacific Cell 2016 Field Trip – Panamint Valley, CA, October 7–9.

Kirby, M.E., Feakins, S.J., Hiner, C.A., Fantozzi, J., Zimmerman, S.R.H., Dingemans, T., Mensing, S.A., 2014. Tropical Pacific forcing of Late-Holocene hydrologic variability in the coastal southwest United States. Quaternary Science Reviews 102, 27–38.

Kirby, M.E., Knell, E.J., Anderson, W.T., Lachniet, M.S., Silveira, E., Palermo, J.,Hiner, C.A., Eeg, H., Arevalo, A., Lucero, R., Murrieta, R., 2015. Evidence for Insolation and Pacific Forcing of Late Glacial through Holocene Climate in the Central Mojave Desert (Silver Lake, CA), Quaternary Research 84, 174–186.

Knott, J.R., Liddicoat, J.C., Coe, R.S., and Negrini, R.M., 2019, Radiocarbon and paleomagnetic chronology of the Searles Lake Formation, San Bernardino County, California, USA. In: Starratt, S.W., Rosen, M.R. (Eds.), From Saline to Freshwater: The Diversity of Western Lakes in Space and Time: Geological Society of America Special Paper 536, doi.org/10.1130/2018.2536(06).

Koehler, P.A., 1995. Late Pleistocene mollusks from the Dolomite site, Owens Lake playa, California. The Veliger 38, 312–318.

Koehler, P.A., and Anderson, R.S., 1994. Full-glacial shoreline vegetation during the maximum highstand at Owens Lake, California. Great Basin Naturalist 54, 142–149.

Lachniet, M.S., Denniston, R.F., Asmerom, Y., Polyak, V.J., 2014. Orbital control of western North America atmospheric circulation and climate over two glacial cycles. Nat. Commun. 5, 3805.

Le, K., Lee, J., Owen, L.A., and Finkel, R., 2007, Late Quaternary slip rates along the Sierra Nevada frontal fault zone, California: Evidence for slip partitioning across the western margin of the Eastern California shear zone/Basin and Range Province: Geological Society of America Bulletin, v. 119, p. 240–256.

Lee, C.H., 1915. Report on hydrology of Owens Lake basin and the natural soda industry as affected by the Los Angeles Aqueduct diversion. Hydraulic Engineer, Los Angeles, California.

Licciardi, J.M., 2001. Chronology of latest Pleistocene lake-level fluctuations in the pluvial Lake Chewaucan basin, Oregon, USA. Journal of Quaternary Science 16, 545–553.

Litwin, R.J., Smoot, J.P., Durika, N.J., and Smith, G.I., 1999. Calibrating Late Quaternary terrestrial climate signals: radiometrically dated pollen evidence from the southern Sierra Nevada, USA. Quaternary Science Reviews 18, 1151–1171.

Li, H., Bischoff, J.L., Ku, T., Lund, S.P., Stott, L.D., 2000. Climate variability in east-central California during the past 1000 years reflected by high-resolution geochemical and isotopic records from Owens Lake sediments. Quaternary Research 54, 187–197.

Lin, J.C., Broecker, W.S., Hemming, S.R., Hajdas, I., Anderson, R.F., Smith, G.I., Kelley, M., Bonani, G., 1998. A reassessment of U-Th and 14C ages for late-glacial high-frequency hydrological events at Searles Lake, California. Quaternary Research 49, 11–23.

Los Angeles Board of Public Service Commissioners, 1916. Complete report on the construction of the Los Angeles Aqueduct. California Department of Public Service, city of Los Angeles, 331 p.

Lubetkin, L.K.C., and Clark, M.M., 1988, Late Quaternary activity along the Lone Pine fault, eastern California: Geological Society of America Bulletin, v. 100, p. 755–766.

Lund, S.P., Newton, M.S., Hammond, D.E., Davis, O.K., Bradbury, J.P., 1993. Late Quaternary stratigraphy of Owens Lake, California. In: Benson, L.V., (Ed.),

Proceedings on the Workshop “Ongoing Paleoclimatic Studies in the Northern Great Basin. U.S. Geological Survey Circular 1119, p. 47–52.

Lyle, M., Heusser, L., Ravelo, C., Yamamoto, M., Barron, J., Diffenbaugh, N.S., Herbert, T., and Andreasen, D., 2012. Out of the tropics: The Pacific, Breat Basin lakes, and late Pleistocene water cycle in the western United States. Science 337, 1629–1633.

MacDonald, G.M., Moser, K.A., Bloom, A.M., Porinchu, D.F., Potito, A.P., Wolfe, B.B., Edwards, A.P., Orme, A.R., and Orme, A.J., 2008. Evidence of temperature depression and hydrological variations in the eastern Sierra Nevada during the Younger Dryas state. Quaternary Research 70, 131–140.

Marcott, S.A., Clark, P.U., Shakun, J.D., Brook, E.J., Davis, P.T., Caffee, M.W., 2019. 10Be age constraints on latest Pleistocene and Holocene cirque glaciation across the western United States. npj Climate and Atmospheric Science 2, 10.1038/s41612-019-0062-z.

Martin, E.A., and Rice, C.A., 1981. Sampling and analyzing sediment cores for 210Pb geochronology. U.S. Geological Survey Open-File Report 81–983.

Mayewski, P.A., and 15 others, 2004. Holocene climate variability. Quaternary Research 62, 243–255.

McDonald, E.V., McFadden, L.D., Wells, S.G., 2003. Regional response of alluvial fans to the Pleistocene-Holocene climatic transition, Mojave Desert, California: In Enzel, Y., Wells, S.G., Lancaster, N., (Eds.), Paleoenvironments and paleohydrology of the Mojave and southern Great Basin Deserts. Geological Society of America Special Paper 368, p. 189–205.

McFadden, L.D., McDonald, E.V., Wells, S.G., Anderson, K., Quade, J., Forman, S.L., 1998. The vesicular layer and carbonate collars of desert soils and pavements: formation, age and relation to climate change. Geomorphology 24, 101–145.

McGee, D., Moreno-Chamarro, E., Wetlandsall, J., Galbraith, E.D., 2018. Western U.S. lake expansions during Heinrich stadials linked to Pacific Hadley circulation. Science Advances 4, eaav0118, DOI: 10.1126/sciadv.aav0118.

Menking, K.M., 1995. Paleoclimate reconstructions from Owens Lake core OL-92, southeastern California. Unpublished Ph.D. Thesis, University of California Santa Cruz, 169 pp.

Mensing, S.A., 2001. Late-glacial and early Holocene vegetation and climate change near Owens Lake, eastern California. Quaternary Research 55, 57–65.

Mensing, S.A., Sharpe, S.E., Tunno, I., Sada, D.W., Thomas, J.M., Starratt, S., Smith, J., 2013. The Lake Holocene Dry Period: multiproxy evidence for an extended drought between 2800 and 1850 cal yr BP across the central Great Basin, USA. Quaternary Science Reviews 78, 266–282.

Mensing, S.A., Smith, J., Norman, K.B., Allen, M., 2008. Extended drought in the Great Basin of western North America in the last two millennia reconstructed from pollen records. Quaternary International 188, 79–89.

Mifflin, M.D., and Wheat, M.M., 1979. Pluvial lakes and estimated pluvial climates of Nevada: Nevada Bureau of Mines and Geology Bulletin 94, p. 57.

Miller, W., 1989. Pleistocene freshwater mollusks on the floor of Owens Lake playa, eastern California. Tulane Studies in Geology and Paleontology 22, 47–54.

Moore, J.G., and Moring B.C., 2013. Range wide glaciation in the Sierra Nevada, California. Geosphere 9, 1804–1818.

Morrill, C., Lowry, D.P., Hoell, A., 2018. Thermodynamic and dynamic causes of pluvial conditions during the Last Glacial Maximum in western North America. Geophysical Research Letters 45, 335–345.

Munroe, J.S., Laabs, B.J.C., 2013. Temporal correspondence between pluvial lake highstands in the southwestern US and Heinrich Event 1. Journal of Quaternary Sciences 28, 49–58.

Murray, A.S. and Wintle, A.G., 2000. Luminescence dating of quartz using an improved single-aliquot regenerative-dose protocol. Radiation Measurements 32, 57–73.

Murray, A.S. and Wintle, A.G., 2003. The single aliquot regenerative dose protocol: potential for improvements in reliability. Radiation Measurements 37, 377–381.

Negrini, R.M., 2002. Pluvial lake sizes in the northwestern Great Basin throughout the Quaternary period. In: Hershler, R., Madsen, D.B., Currey, D. (Eds.), Great Basin Aquatic Systems History: Smithsonian Contributions to the Earth Sciences, vol. 33. Smithsonian Institution Press, Washington, D.C, pp. 11e52.

Negrini, R.M., Wigand, P.E., Draucker, S., Gobalet, K., Gardner, J.K., Sutton, M.Q., Yohe, R.M., 2006. The Rambla highstand shoreline and the Holocene lake-level

history of Tulare Lake, California, USA. Quaternary Science Reviews 25, 1599–1618.

Neponset Geophysical Company and Aquila Geosciences, Inc., 1997, Final Report Phase 3 and Phase 4 seismic program, Owens Lake, Inyo County, California. Unpublished report prepared for the Great Basin Unified Air Pollution Control District, Bishop, California, 55 p.

Newton, M.S., 1991. Holocene stratigraphy and magnetostratigraphy of Owens and Mono Lakes, eastern California. Unpublished Ph.D. Thesis, University of Southern California, Los Angeles, 330 pp.

Orme, A.R., and Orme, A.J., 1993. Late Pleistocene oscillations of Lake Owens, eastern California. Geological Society of America Abstracts with Programs 25, 129–130.

Orme, A.R., and Orme, A.J., 2008. Late Pleistocene shorelines of Owens Lake California, and their hydroclimatic and tectonic implications, in Reheis, M.C., Hershler, R., and Miller, D.M., eds., Late Cenozoic Drainage History of the Southwestern Great Basin and Lower Colorado River Region: Geologic and Biotic Perspectives: Geological Society of America Special Paper 439, p. 207–226.

Oster, J.L., Montanez, I.P., Mertz-Kraus, R., Sharp, W.D., Stock, G.M., Spero, H.J., Tinsley, J., Zachos, J.C., 2014. Millennial-scale variations in western Sierra Nevada precipitation during the last glacial cycle MIS 4/3 transition. Quaternary Research 82, 236–248.

Oster, J.L., Ibarra, D.E., Winnick, M.J., and Maher, K., 2015. Steering of westerly storms over western North America at the Last Glacial Maximum. Nature Geoscience 8, 201–205.

Oster, J.L., Montañez, I.P., Santare, L.R., Sharp, W.D., Wong, C., Cooper, K.M., 2015. Stalagmite records of hydroclimate in central California during termination 1. Quaternary Science Reviews 127, 199–214.

Otvos, E.G., 2000. Beach ridges – definitions and significance. Geomorphology 32, 83–108.

Oviatt, C.G., 1997. Lake Bonneville fluctuations and global climate change. Geology 25, 155–158.

Oviatt, C.G., 2000. Lacustrine features and global climate change, in Noller, J.S., Sowers, J.M., and Lettis, W.R., eds., Quaternary Geochronology: Methods and

Applications: AGU Reference Shelf Volume 4: Washington D.C., American Geophysical Union, p. 470–478.

Oviatt, C.G., 2015. Chronology of Lake Bonneville, 30,000 to 10,000 yr BP. Quaternary Science Reviews 110, 166–171.

Pakiser, L.C., Kane, M.F., and Jackson, W.H., 1964, Structural geology and volcanism of Owens Valley region, California—a geophysical study: U.S. Geological Survey Professional Paper 438, 65 p.

Peng, T.H., Goddard, J.G., and Broecker, W.S., 1978. A direct comparison of 14C and 230^{Th} ages at Searles Lake, California. Quaternary Research 9, 319–329.

Pengelly, J.W., Tinkler, K.J., Parkins, W.G., and McCarthy, F.M., 1997. 12,600 years of lake level changes, changing sills, ephemeral lakes and Niagara Gorge erosion in the Niagara Peninsula and Eastern Lake Erie basin. Journal of Paleolimnology, 17, 377–402.

Peterson, F.F., 1981. Landforms of the Basin and Range province: defined for soil surveys: Nevada agriculture experiment station, University of Nevada, Reno, Technical Bulletin 28, 52 p.

Phillips, F.M., 2008. Geological and hydrological history of the paleo-Owens River drainage since the late Miocene, in Reheis, M.C., Hershler, R., and Miller, D.M., eds., Late Cenozoic Drainage History of the Southwestern Great Basin and Lower Colorado River Region: Geologic and Biotic Perspectives: Geological Society of America Special Paper 439, p. 115–150.

Phillips F.M., 2016. Constraints on cosmogenic nuclide production rates by samples from the Sierra Nevada, California: I. Late Pleistocene glacial chronology. Quaternary Geochronology 35, 119–129.

Phillips F., 2017. Glacial chronology of the Sierra Nevada, California, from the Last Glacial Maximum to the Holocene. Geographical Research Letters 43, 527–552, doi:10.18172/cig.3233.

Phillips, F.M., Zreda, M.G., Benson, L.V. Benson, Plummer, M.A., Elmore, D., and Sharma, P., 1996. Chronology for fluctuations in late Pleistocene Sierra Nevada glaciers and lakes. Science 274, 749–751.

Phillips, F.M., Zreda, M., Plummer, M.A., Elmore, D., and Clark, D.H., 2009. Glacial geology and chronology of Bishop Creek and vicinity, eastern Sierra Nevada, California. Geological Society of America Bulletin 121, 1013–1033.

Pigati, J.S., Quade, J., Shahanan, T.M., Haynes Jr., C.V., 2004. Radiocarbon dating of minute gastropods and new constraints on the timing of late Quaternary spring-discharge deposits in southern Arizona, USA. Palaeogeography, Palaeoclimatology, Palaeoecology 204, 33–45.

Rades, E.F., Tsukamoto, S., Frechen, M., Xu, Q., Ding, L., 2015. A lake-level chronology based on feldspar luminescence dating beach ridges at Tangra Yum Co (southern Tibet). Quaternary Research 83, 469–478.

Reardon, K.E., Moreno-Casas, P.A., Bombardelli, F.A., Schladow, S.G., 2016. Seasonal nearshore sediment resuspension and water clarity at Lake Tahoe. Lake and Reservoir Management 32, 132–145.

Redmond, K.T., Koch, R.W., 1991. Surface climate and streamflow variability in the western United States and their relationship to large scale circulation indices. Water Resources Research 27, 2381–2399.

Reheis, M.C., 1999. Highest pluvial-lake shorelines and Pleistocene climate of the western Great Basin. Quaternary Research 52, 196–205.

Reheis, M.C., Adams, K.D., Oviatt, C.G., Bacon, S.N., 2014. Pluvial lakes in the Great Basin of the western United States – A view from the outcrop. Quaternary Science Reviews 97, 33–57.

Reheis, M.C., Miller, D.M., McGeehin, J.P., Redwine, J.R., Oviatt, C.G., Bright, J., 2015. Directly dated MIS 3 lake-level record from Lake Manix, Mojave Desert, California, USA. Quaternary Research 83, 187–203.

Rhodes, E.J., 2011. Optically stimulated luminescence dating of sediments over the past 200,000 years. Annual Review of Earth and Planetary Sciences 39, 461–488.

Rhodes, E.J., 2015. Dating sediments using potassium feldspar single-grain IRSL: Initial methodological considerations. Quaternary International 362, 14–22.

Rohweder, J., Rogala, J.T., Johnson, B.L., Anderson, D., Clark, S., Chamberlin, F., Runyon, K., 2008. Application of wind fetch and wave models for habitat rehabilitation and enhancement projects. U.S. Geological Survey Open-File Report 2008–1200. United States Government Printing Office, Washington.

Rood, D.H., Burbank, D.W., and Finkel, R.C., 2011. Chronology of glaciations in the Sierra Nevada, California, from ^{10}Be surface exposure dating. Quaternary Science Reviews 30, 646–661.

Rosenthal, J.S., Meyer, J., Palacios-Fest, M.R., Young, D.C., Ugan, A., Byrd, B.F., Goblet, K., and Giacomo, J., 2017. Paleohydrology of China Lake basin and the context of early human occupation in the northwestern Mojave Desert, USA. Quaternary Science Reviews 176, 112–139.

Slemmons, D.B., Vittori, E., Jayko, A.S., Carver, G.A., and Bacon, S.N., 2008, Quaternary fault and lineament map of Owens Valley, Inyo County, eastern California: Geological Society of America Map and Chart 96, 25 p.

Smith, G.I., 1979, Subsurface stratigraphy and geochemistry of Late Quaternary evaporates, Searles Lake, California. U.S. Geological Survey Professional Paper 1043, 130 p.

Smith, G.I., 2009, Late Cenozoic geology and lacustrine history of Searles Valley, Inyo and San Bernardino Counties, California. U.S. Geological Survey Professional Paper 1727, 115 p.

Smith, G.I. and Pratt, W.P., 1957. Core logs from Owens, China, Searles, and Panamint Basins, California. US Geological Survey Bulletin 1045-A, 1–62.

Smith, G.I., and Street-Perrott, F.A., 1983. Pluvial lakes of the western United States. In: Porter, S.C. (Ed.), The Late Pleistocene. Univ. Minn. Press, Minneapolis, pp. 190–212.

Smith, G.I., and Bischoff, J.L., eds., 1997. An 800,000-year paleoclimatic record from core OL-92, Owens Lake, southeast California. Geological Society of America Special Paper 317, 165 p.

Smoot, J.P., Litwin, R.J., Bischoff, J.L., and Lund, S.P., 2000, Sedimentary record of the 1872 earthquake and ‘‘Tsunami’’ at Owens Lake, southeast California: Journal of Sedimentary Geology, 135, 241–254.

Steponaitis, E., Andrews, A., McGee, D., Quade, J., Hseih, Y.-T., Broecker, W.S., Shuman, B.N., Burns, S.J., Cheng, H., 2015. Mid-Holocene drying of the U.S. Great Basin recorded in Nevada speleothems. Quat. Sci. Rev. 127, 174–85.

Stine, S., 1990. Late Holocene fluctuations of Mono Lake, eastern California. Palaeogeogrrarphy, Palaeoclimatology, Palaeoecology 78, 333–381.

Stine, S., 1994. Extreme and persistent drought in California and Patagonia during Medieval time. Nature 339, 546–549.

Street, J.H., Anderson, R.S., Paytan, A., 2012. An organic geochemical record of Sierra Nevada climate since the LGM from Swamp Lake Yosemite. Quaternary Science Reviews 40, 89–106.

Street, J.H., Anderson, R.S., Rosenbauer, R.J., Paytan, A., 2013. *n*-Alkane evidence for the onset of wetter conditions in the Sierra Nevada, California (USA) at the mid-Holocene transition, ~3.0 ka. Quaternary Research 79, 14–23.

Teeter, A.M., Johnson, B.H., Berger, C., Stelling, G., Scheffner, N. W., Garcia, M.H., Parchure, T.M., 2001. Hydrodynamic and sediment transport modeling with emphasis on shallow-water, vegetated areas (lakes, reservoirs, estuaries and lagoons). Hydrobiologia 444, 1–23.

U.S. Army Corps of Engineers (USACE), 1984. Shore Protection Manual, Volume 1. U.S. Army Engineer Waterways Experiment Station, Vicksburg, MS, U.S.A., 502 p.

U.S. Army Corps of Engineers (USACE), 2002. Coastal Engineering Manual. Washington D.C., U.S. Corps of Engineers, Engineer Manual 1110-2-1100, Part II and III.

U.S. Geological Survey (USGS) and California State Geological Survey, 2016. Quaternary fault and fold database for the United States, accessed June, 2016 from USGS web site: https://earthquake.usgs.gov/hazards/qfaults/.

Wendt, K.A., Dublyansky, Y.V., Moseley, G.E., Edwards, R.L., Cheng, H., Spötl, C. 2018. Moisture availability in the southwest United States over the last three glacial-interglacial cycles. Science Advances 4, eaau1375. DOI: 10.1126/sciadv.aau1375

Wentworth, C.K., 1922. A scale of grade and class terms for clastic sediments. *Journal of* Geology 30, 377–392.

Wesnousky, S.G., 2005a. Active faulting in the Walker Lane. Tectonics 24, 1–35.

Wesnousky, S.G., 2005b. The San Andreas and Walker Lane fault systems, western North America: transpression, transtension, cumulative slip and the structural evolution of a major transform plate boundary. Journal of Structural Geology 27, 1505–1512.

Wesnousky, S.G., and Jones, C.H., 1994. Oblique slip, slip partitioning, spatiotemporal changes in the regional stress field, and the relative strength of active faults in the Basin and Range, western United States: Geology, 1031–1034.

Zehfuss, P.H., Bierman, P.R., Gillespie, A.R., Burke, R.M., and Caffe, M.W., 2001, Slip rates on the Fish Springs fault, Owens Valley, California, deduced from cosmogenic 10Be and 26Al and soil development on fans: Geological Society of America Bulletin, v. 113, p. 241–255.

Zic, M., Negrini, R.M., Wigand, P.E., 2002. Evidence of synchronous climate change across the Northern Hemisphere between the Northern Atlantic and the Northwestern Great Basin, United States. Geology 30, 635–638.

CHAPTER 4

11,500-YEAR PRECIPITATION AND SNOWPACK RECONSTRUCTION OF THE SOUTH-EASTERN SIERRA NEVADA FROM HYDROLOGIC MODELING OF THE PALEO-OWENS WATERSHED-LAKE SYSTEM

1. INTRODUCTION

Terminal lakes in the western U.S. record regional climate as lake levels encode a watershed's water balance (Reeves, 1968; Cohen, 2003). Precipitation computed from paleohydrologic modeling of watershed-lake systems provide quantitative estimates of long-term moisture patterns that in turn are commonly used as input data to support regional- to global-scale paleoclimate atmospheric models (e.g., McGee et al., 2018). Previous watershed-lake modeling approaches in the Great Basin have included either greatly simplified and annually resolved water budgets at equilibrium that are governed by runoff, precipitation, and evaporation (Mifflin and Wheat, 1979; Benson and Paillet, 1989; Menking, 1995; Clement, 2005; Matsubara and Howard, 2009; Broecker, 2010; Ibarra et al., 2014), water-balance and linear models controlled by observed input variables (Huybers et al., 2016) or extremely complex and distributed water balance models that require gauged streamflow and measured groundwater levels as input data to forecast monthly lake stage for water resource management (e.g., Niswonger et al., 2014).

Recent paleohydrologic modeling of watershed-lake systems in the western U.S. have been based on adjustment of 800-meter gridded, historical monthly precipitation and

temperature datasets until a water-level simulation achieves a target steady-state hydrologic solution. This monthly modeling approach has put paleoclimate into a modern hydroclimatic context for systems along the eastern escarpment of the Sierra Nevada and in northern Nevada (Hatchett et al., 2015; Barth et al., 2016). Coupled watershed-lake hydrologic models similar in principle to the monthly models mentioned above have also been developed for the paleo-Owens River-Lake system in the south-eastern Sierra Nevada (Matsubara and Howard, 2009; Yu et al., 2015) (Figure 1). The paleohydrologic models of Matsubara and Howard (2009) and Yu et al. (2015) also included modeling of the water balance within downstream China and Searles lake basins of the system for periods during the late Pleistocene. The lake histories that Matsubara and Howard (2009) relied on for each basin, however, are not current because of recent refinement of the shoreline histories of Owens Lake (Bacon et al., 2018, 2020), China-Searles Lake (Rosenthal et al., 2017), and Panamint Lake (Hoffman, 2009; Choi, 2016). Although the Yu et al. (2015) model is relatively new, the lake histories they used for each basin were also not current at the time of their study that were primarily based on shoreline data of Smith and Perrott (1983) and sediment core proxy evidence of Benson et al. (1990).

Coupled watershed-lake hydrologic models are commonly controlled by discontinuous lake stage records derived from either dated landforms or inferences from outcrop evidence. These hydrologic models typically include simulations encompassing short time periods during which lakes were at their relative highstands (e.g., Matsubara and Howard, 2009; Yu et al., 2015; Barth et al., 2016) or in rare cases during relative lowstands (e.g., Hatchett et al., 2015; 2016). As a result, most of the model simulations are restricted to discrete periods that lack a complete record of a given lake-level cycle,

thereby offering discontinuous estimates of paleoclimate variability in the context of climate change at multidecadal to multicentennial scales. Although the application of monthly watershed-lake water balance models have recently been used for the Sierra Nevada and Great Basin, these models simulated discrete or relatively short periods of time (e.g., 0–1, 6, 9, 12, 15 or 18 thousand years ago (ka)) and all did not account for glacial ice or perennial snow accumulation, and only one study (Yu et al., 2015) accounted for changes in solar insolation driven by Earth's natural orbital oscillations (i.e., Milankovitch cycles).

The goal of this study is to reconstruct post-glacial precipitation patterns and the build up of snowpack in the south-eastern Sierra Nevada by performing paleohydrologic modeling of the paleo-Owens River-Lake system in eastern California over the past 11,500 years (Figure 1). The water balance model developed in this study improves on existing paleohydrologic models for the region through:

(1) controlled by a continuous lake-level (i.e., stage) and overflow record of Owens Lake that is corrected for tectonic deformation (Bacon et al., 2018, 2019a, 2020);

(2) use of a mean global paleo-temperature dataset adjusted to local temperature depression estimates from glacial deposits in the watershed;

(3) accounting for changes in paleo-solar insolation driven by Milankovitch cycles;

(4) inclusion of a paleo-equilibrium line altitudes (ELAs)-based glacial ice/perennial snow accumulation component;

(5) incorporation of the effects of variable paleolake water salinity; and

(6) inclusion of surface runoff gains and losses based on an 81-year record of observed data in the Owens River watershed.

The simulations of the water balance of the paleo-Owens River-Lake system between the Pleistocene-Holocene transition and pre-historical period provide a continuous estimate of moisture flux at 100-year time steps along the eastern escarpment of the southern Sierra Nevada. This temporal resolution can be used as a high-resolution dataset to evaluate the accuracy of multiproxy records and paleoclimate models used to characterize moisture variability in the region.

2. STUDY AREA

The Owens River watershed includes Owens Valley, an ~15–40 km wide and 200 km long tectonically-active graben within the southwestern Great Basin in eastern California (Figure 1). The watershed extends along the eastern escarpment of the south-central Sierra Nevada, which is a seismically active region that has experienced several moderate to large earthquakes, during the latest Quaternary, including the historical M_w7.5–7.9 Owens Valley earthquake in 1872 (e.g., Beanland and Clark, 1994). The Sierra Nevada forms one of the principal rain shadows in the western U.S. with its highest crest elevations of 3400–4300 m occurring between ~36°N and 38°N. The watershed has a drainage area of ~8515 km^2 and is bounded by the crests of the Sierra Nevada Range to the west, White-Inyo Mountains to the east, and the Coso Range to the south and east (Figure 1). The northern and southern parts of the watershed share drainage divides with the watersheds of Mono and China Lake basins, respectively. The northern reach of the Owens River is within the Long Valley caldera and its central and

southern reaches are in the form of a prominent meander belt bounded by steep alluvial fans that ultimately drains to the south in Owens Lake basin (Figure 1). The Sierra Nevada receives over 70% of its annual precipitation during the cool season (October–April) with approximately 40–50% derived from sub-Tropical moisture in the form of atmospheric rivers (e.g., Dettinger et al., 2011; Hatchett, 2018). Contemporary mean annual precipitation on the eastern slope of the Sierra Nevada at ~37°N ranges from up to ~150 cm/yr at the crest, to ~25 cm/yr at the range front, to ~13 cm/yr at Owens Lake playa; plus annual streamflow is primarily derived from snowmelt runoff from ~20% of the watershed along the eastern escarpment (Hollett et al., 1991; Danskin, 1998).

During the period 1872–1878, Owens Lake was a perennial, closed-basin lake that covered >280 km^2 with a historical maximum lake level at 1096.4 m and a water depth of 14.9 m (Gale, 1914; Lee, 1915). Major water diversions in Owens Valley began after 1913 with construction of the Los Angeles aqueduct system that transported surface water from the Owens River watershed and Mono Lake basin (since 1941) >320 km to the south for distribution (Hollett et al., 1991). Owens Lake first began depositing salts onto the lake floor in ~1920 because of these diversions, and by ~1930, Owens Lake had desiccated and become a playa (Smith and Bischoff, 1997).

The Owens River watershed is very sensitive to arid to semi-arid hydroclimate variability. It is the single largest watershed draining the eastern Sierra Nevada and contains over 230 km of range crest spanning the highest elevations. Owens Lake basin is relatively shallow because of high sedimentation from the Owens River and surrounding alluvial fans. Therefore, small changes in streamflow inputs associated with changes in the magnitude of snowpack and rate of snowmelt are amplified in the lake basin because

of its shallow hypsometric configuration compared to other east side lakes that are deeper, such as Lake Tahoe, Pyramid Lake, Walker Lake, and Mono Lake.

3. Geologic and Paleohydrologic Setting

During the Tioga glaciation (30–15 ka) the entire western boundary of the Owens River watershed was extensively glaciated with lobes of ice extending past the range front of the Sierra Nevada as far south as the latitude 36.8°N (Kaufman et al., 2004; Phillips et al., 2009; Gillespie and Clark, 2011; Rood et al., 2011; Moore and Moring, 2013). Since the Tioga glaciation there have been several minor post-glacial cirque advances during the Recess Peak glaciation (~13.6 ka) and early Younger Dryas (~12.4 ka), as well as the Little Ice Age (~0.60–0.15 ka), which was limited to the highest parts of the range above elevations of ~3700 m (Clark and Gillespie, 1997; Kaufman et al., 2004; Phillips et al., 2009; Bowerman and Clark, 2011; Marcott et al., 2019).

Owens Lake occupies a topographically closed basin contained by a modern spillway across its drainage divide (i.e., sill) at the south end of the basin (Figure 1). During much of the Pleistocene when periods with greater moisture flux and cooler temperatures occurred across the region, Owens Lake was a perennial freshwater lake that periodically overflowed its sill to form a chain of pluvial lakes occupying one or more of four successively lower-elevation lake basins (China, Searles, Panamint, and Death Valley) (e.g., Gale, 1914; Smith and Street-Perrott, 1983; Jannik et al., 1991; Menking, 1995; Phillips, 2008; Knott et al., 2019) (Figure 1B). Shoreline and sediment-core records from lakes in the paleo-Owens River system indicate that pluvial Owens Lake had relatively high-water levels during the late Pleistocene coinciding with

deglaciations and exceptionally wet periods in the Sierra Nevada. Owens Lake has previously been inferred to have overflowed into China-Searles and Panamint Lakes, as many as 2 to 3 times between ~20 and 12 ka (Benson et al., 1996, 1997; 1998; 2002; Phillips et al., 1996; Smith et al., 1997; Bishoff and Cummins, 2001; Jayko et al., 2008; Orme and Orme, 2008; Phillips, 2008; Hoffman, 2009; Kirby and McDonald, 2016; Rosenthal et al., 2017; Knott et al., 2019) (Figure 1).

Earlier studies also indicated that overflow from Owens Lake to support downstream lakes likely ceased after 11–12 ka based on shoreline stratigraphic studies in China Lake basin and sediment lake core data in Searles Lake basin (Phillips, 2008; Smith, 2009; Rosenthal et al., 2017). Owens Lake was also previously considered to be the terminal lake in the system during the entire Holocene with mostly moderate to shallow water levels into historical times according to geomorphic shoreline records (Bacon et al., 2006; 2018; Orme and Orme, 2008) and lake-core evidence (Newton, 1991; Smith et al., 1997; Li et al., 2000; Smoot et al., 2000; Benson et al., 2002). New studies of the shoreline geomorphology and subsurface geotechnical investigations within the overflow channel of Owens Lake basin, however, have yielded stratigraphic and geochronologic information to revise previous inferences of latest Pleistocene and early-middle Holocene lake levels and episodes of overflow. New numerical ages from beach ridges and fluvial-deltaic sediment filling the overflow channel established the first spatiotemporal connections between latest Pleistocene (12.8–11.6 ka) and early-middle Holocene (~8.4–6.4 ka) shorelines and overflow levels of Owens Lake, thereby demonstrating far more recent hydrologic connections between Owens Lake via the

paleo-Owens River and downstream China and Searles Lakes than previously understood (Bacon et al., 2020) (Figure 1).

4. Paleo-Owens Watershed-Lake Water Balance Model

The goal of this study is to develop a 11,500-year time-series of reconstructed changes in precipitation and temperature relative to historical average (normal) precipitation and temperature from a coupled watershed-lake water balance model. This hydrologic model is controlled by refined and continuous water-level records from Owens, China, and Searles Lakes. The watershed-lake water balance model consists of four simplified hydrologic model components that include: (1) watershed runoff; (2) energy-balance and snow melt; (3) glacial ice/perennial snow accumulation; and (4) open-water evaporation. The model domain consists of 800 x 800 m grid cells, each of which is considered an independent modeling unit in terms of physiographic elements, hydroclimatic conditions, and hydrologic processes (e.g., Barth et al., 2016). The Owens River watershed model domain consists of 12,969 grid cells, and when the downstream watersheds of China and Searles lake basins are included, the entire model domain consists of 20,898 grid cells (Figure 1). The monthly water balance solution for each grid cell is aggregated at an annual time step in order to compare to available measured/observed hydrologic data from the watershed for calibration. Historical precipitation and temperature time-series data for water years (WY) 1896 to 2015 from the Parameter elevation Regression on Independent Slopes Model (PRISM) historical climate (Daly et al., 1994) were used as inputs in the Owens watershed-lake hydrologic model. The same climate dataset from 1896 to 2015 was adjusted to match

paleohydroclimate conditions during simulations at 100-yr time steps between 0 (present day) and 11,500 years ago, thereby modeling lake-level oscillations with natural annual to decadal hydroclimate variability. Modern temperature was adjusted by adding a uniform paleotemperature anomaly to gridded data (e.g., -1.16 or 0.31ºC). Modern precipitation was also adjusted by iterating a uniform multiplier to gridded data until target lake levels were achieved (e.g., 0.85 or 1.15). The paleo-simulations are controlled by geologically determined lake-level records of Owens, China, and Searles Lakes. The model framework and computations were performed within the MATLAB numerical computing environment.

4.1. Watershed Runoff

Runoff in the paleo-Owens River watersheds was calculated using a modified Thornthwaite (1948)-based water balance model (McCabe and Markstrom 2007) that has previously been applied to other watershed-lake systems in the Sierra Nevada and Great Basin (Hatchet et al. 2015; 2016, Barth et al. 2016). The Thornthwaite model includes a monthly accounting procedure that simulates the main components of a hydrologic system and their seasonal distribution. The model uses mean monthly temperature (T), mean monthly precipitation (P), and latitude as input variables. It partitions precipitation into frozen (P_{snow}) and liquid (P_{rain}) components, snow storage (snostor), snow melt (SM) based on a predefined melt rate, soil-moisture storage capacity (SMSC), actual evapotranspiration (AET1) based on the Hamon equation (Hamon, 1961), and runoff in the form of direct runoff (DRO) and surplus runoff (RO) (Figure 2). The climatic input variables for the model includes 120-years of mean monthly values from minimum and

maximum temperature, plus precipitation estimates for WY1896 to 2015 from the 800-metereter PRISM historical climate data (Figure 3). Static parameters required for the Thornthwaite model include subsurface hydraulic properties in the form of soil-moisture storage capacity (SMSC) or available water capacity. The soil data used in the model was from the 1:250,000-scale NRCS State Soil Geographic (STATSGO) database (Figure 2). The SMSC map unit polygons were converted to a raster dataset at 800-meter grid resolution to match the PRISM dataset (Figure 3). The computation of Thornthwaite runoff is based on MATLAB code of Raleigh (2010).

To accommodate relevant Owens River watershed hydrologic components not included in the Thornthwaite runoff model new model components were developed for this study. These include (Figure 2):

1. fraction of channel bed leakage along the Owens River (OR_loss_F);
2. fraction of leakage along alluvial fans ($Alluv\_loss_F$);
3. actual evapotranspiration (AET2) from riparian vegetation;
4. groundwater baseflow contributions mostly from the Sierra Nevada mountain block (BF1); and
5. return flow (BF2) commonly associated with valley tributary streams and the Owens River, and
6. perennial snow and/or glacial ice accumulation (ELA_{snotor}).

The resulting watershed-lake water balance model is more appropriate for a high-elevation mountainous watershed that contains modern glaciers and perennial snowfields, as well as minor cirque glacial advances during the last 11,500 years.

4.2. Simplified Energy-Balance Snow Melt

The Thornthwaite runoff model requires mean monthly temperature and a specified melt rate that melts all snow at the end of the season. An energy-balance model was added for use in this study to account for the influence of solar radiation to better approximate snowmelt and model perennial snow and/or glacial ice persistence in the Owens River watershed (Figure 2). The energy budget of seasonal snowpacks and glaciers is frequently used to compute rates of snowmelt and sublimation (e.g., Orleans, 2001; DeWalle and Rango, 2008; MacDougall et al., 2011). The energy-balance model component was used to estimate the magnitude of snow and ice accumulation in the upper elevations of the watershed above the annual snowline (Figure 2). It also was used to account for melt at lower elevations when mean monthly temperatures are below the threshold temperature parameter for snow storage in the Thornthwaite runoff model, thereby initiating melt from solar radiation across the watershed during months with temperatures below freezing.

The simplest mass balance model of snow or ice must at least include incoming solar radiation (S_n) and air temperature (T_a). Because the net longwave radiation budget is strongly related to air temperature, the simplest possible parameterization of the energy flux of melting snowpack or glacier surfaces include these parameters (Oerlemans, 2001). Mean monthly temperature PRISM data was used for air temperature. The simplified energy-balance model of Oerlemans (2001) takes the form:

$$Q_M = \left(S_n\,(1-\alpha)\right) + C_0 + C_1 T_a, \quad (1)$$

$$M = \frac{Q_M}{L_f \rho_w B} \quad (2)$$

where Q_M is the energy available to melt snow or ice, M is the snow or ice melt rate (m), L_f = 3.34 x 10^5 J kg^{-1} is the latent heat of fusion, ρ_w = 1000 kg m^{-3} is the density of water, and C_0 = -38 and C_1 = 1.5 are typical empirical factors that together take into account net longwave radiation and turbulent heat fluxes, respectively (e.g., Orleans, 2001; MacDougall et al., 2011). In addition, B = 0.97 is a typical dimensionless value for the thermal quality of the snowpack that represents the fraction of snowpack that is ice rather than liquid water (Wilson, 1942; Dewalle and Range, 2008). Similar to temperature-index models of snowmelt, the treatment of S_n and albedo (α) was determined during the calibration processes of the glacial ice/perennial snow accumulation component of the hydrologic model (e.g., MacDougall et al., 2011).

In mountainous terrain, the value of potential S_n varies in time and space due to the combined effects of the position of the sun, surface slope, surface aspect, and shading from surrounding topography (MacDougall et al., 2011). To account for this, monthly solar irradiance (Wh m^{-2}) were calculated from the USGS NED 30-meter digital elevation model (DEM) data set for each watershed using the "Area Solar Radiation" tool in ArcGIS (Figure 4). The analysis was performed using the settings of "clear skies" for each month of the year in a uniform sky model with default diffusivity and transmissivity values of 0.3 and 0.5, respectively. The mean 30-meter solar irradiance values were calculated for each 800-meter grid cell using zonal statistics in ArcGIS and then converted to mean monthly S_n (W m^{-2}) values.

4.3. Glacier and Perennial Snow Accumulation

The regional snowline is the altitude that separates perennial snow from seasonal (annual) snow. At this altitude, glaciers will form or perennial snowfields will persist, although the altitudes of these ice/snow features will be subject to large topographic and climatic variations. The equilibrium line altitude (ELA), the effective regional snowline on a glacier, is a climate-sensitive parameter marking the upper limit reached by the snowline on a glacier at the end of the summer ablation season. Along this line across the glacier the annual net mass balance equals zero (Paterson, 1994). When the glacier is in a steady state, snowline elevations averaged over many years give the position of the ELA, which is the average position of the snowline for the glacier to remain in equilibrium over a given period (Meier and Post, 1962). Temperature and precipitation are the primary variables that control the altitude of the equilibrium line, although topography, wind, and humidity are among the many other influences (Porter, 1975; Graf, 1976). Small valley and cirque glaciers are increasingly influenced by local orography as their size decreases. In contrast, as the size of a glacier increases, its mass balance and ELA become less influenced by local topography and are more strongly controlled by regional hydroclimatic conditions (e.g., Graf, 1976; Bowerman and Clark, 2011).

The glacier and perennial snow accumulation component of the watershed model is a simplified approach to estimate the storage of snow water equivalent (SWE) in the Sierra Nevada at 800-meter grid resolution. This approach does not account for redistribution of snow from avalanching, wind scour, and blowing snow from areas west of the crest, nor does it account for glacial flow. The model component is principally intended to estimate the annual ELA within the model domain and resultant storage of

SWE at and above this elevation across model time steps. Extensive research has been done to reconstruct ELAs associated with glaciations in the Sierra Nevada (Burbank, 1991; Clark and Gillespie, 1997; Kaufman et al., 2004; Bowerman and Clark, 2011) (Table 1; Figure 5). The paleo-ELAs are estimated using the highest occurrence of lateral moraines in the watershed because the area below the ELA is the zone of net ablation and deposition of glacial sediment. In contrast, the modern ELA is estimated by identifying the elevation of the boundary across a glacier or perennial snowfield that separates the area with clean ice or snow from the area with dirty ice or snow. This line is also referred to as the firn line and is typically well defined and measured in late summer (Figure 5).

By plotting the mean summer (June–September) temperature at modern ELAs on glaciers, one can resolve the climate required to sustain the glaciers at their current extent. The same can be done for reconstructed ELAs of past glaciations to estimate the temperature change or temperature depression relative to modern that was required to sustain glaciers at their maxima. Following the methods of Bowerman and Clark (2011) for estimating the modern mean summer temperature at former ELAs and the historical annual ELA in the southern Sierra Nevada, a revised environmental adiabatic lapse rate for the Owens River watershed was developed (Figure 6A).

An environmental lapse rate is the rate of decrease of temperature with altitude in a stationary dry atmosphere at a given time and location (e.g., Shuttleworth, 2012). A general environmental lapse rate that does not account for changes in humidity was computed from mean monthly PRISM data along a west to east transect extending from the highest point in the watershed and the conterminous U.S. at Mount Whitney (elev. 4421 m) to the lowest elevation point in North America at Bad Water in Death Valley

(elev. -85 m) (Figure 6A). The mean summer temperature change of historical and past ELAs were estimated relative to the 1974 modern ELA measured at ~3860 m (Bowerman and Clark, 2011) using the adiabatic lapse rate of this study and published elevations of paleo-ELAs (Tables 1 and 2; Figure 6B). Although, the paucity of long-term climate records in mountain environments makes validation of PRISM algorithms across diverse regions a challenge, a recent study in the nearby Walker basin in the central Sierra Nevada demonstrated that daily observations of minimum and maximum temperatures had mean absolute error variations ranging from 1.1 to 3.7°C with better performance observed during summertime as opposed to winter (Stratchon and Daly, 2017). The better performance of summer PRISM temperature estimates provides insight in the potential uncertainty of the environmental adiabatic lapse rate in the Owens River watershed for the summer in 1974.

The approximation of SWE or snow remaining in the last month of the water year (September) above the annual ELA was accounted for and added to the proceeding year's ELA snow storage (ELAsnotor) to calculate the mass balance of glacial ice/perennial snow fields in the watershed and associated ELA snowmelt (ELASM) (Figure 2). The annual ELA snow storage above a specified range of elevations that correspond to changes in mean summer temperature relative to 1974 were calculated based on the adiabatic lapse rate developed for the watershed (Table 2; Figure 6A).

The long-term cumulative ELA snow storage input was computed to estimate the volume of glacial ice and/or perennial snow in the model domain. The volume of annual ELA snow storage of SWE was converted to ice-volume equivalent to account for ice expansion and air inclusions to aid in the calibration of observed data. An ice density of

866 kg/m^3 for small alpine glaciers and perennial snowfields was used by taking the mean of ice densities of 815 kg/m^3 for ice rich in air inclusions, typical of firn and thin glaciers, and 916.7 kg/m^3 for pure ice devoid of air inclusions, typical of older and thick glaciers (e.g., Shumskiy, 1960; Huss, 2013). The ratios of 0.87 and 1.13 between the mean ice density of 866 kg/m^3 and pure water of 1000 kg/m^3 was taken to convert between ELA snowmelt and ELA snow storage, respectively. The glacial ice accumulation and melt model takes the form:

$$\Delta V_i = [V_{i-1} + V_i] \cdot ELA\ Sublim_F \quad (3)$$

where ΔV_i is net SWE above the ELA (m^3) and V_i is annual SWE (m^3) above the ELA of the *i* year. The simple model does not consider variations in topography that would limit the accumulation of snow on steep slopes. The model is intended to represent the snow storage potential within 800-meter grid cells. An ELA sublimation factor (*ELA Sublim*$_F$), however, was developed to account for basin-specific topographic and climatic influences on melt and used to calibrate the historical 120-year simulation of ice accumulation. The accumulation and melt of annual SWE above the ELA occur when ΔV_i is positive and negative, respectively.

The simulated annual ELA snow storage with units of m^3/yr were converted to area with units of km^2/yr in order to calibrate to observed data. Because the total thickness of the modeled ELA snow storage is unknown, the small glacier volume model of Chen and Ohmura (1990) that is empirical and based on studies of small glaciers in the western U.S. (Bahr et al., 1997) was used to estimate the area of modeled SWE snow

storage in order to compare to measured areas of small alpine glaciers and perennial snowfields in the Owens River watershed (Raub et al., 2006; Basagic and Fountain, 2011). The small glacier volume model takes the form:

$$V = \alpha A^{\beta} \rightarrow$$

$$A = \left(\frac{V}{\alpha}\right)^{\beta^{-1}} \quad (4)$$

where an estimate of glacier thickness (h) is also in the form:

$$h = \alpha A^{\beta-1} = \frac{V}{A} \quad (5)$$

where V (km^3) is glacier/perennial snowfield volume, A (km^2) is glacier/perennial snowfield area, α and β are empirical factors of 0.021346 and 1.145, respectively (Chen and Ohmura, 1990). The empirical relations were developed from small glaciers in the Cascade Range, Washington that also have been applied to estimate the thickness of glaciers in the Sierra Nevada from measured glacier areas to evaluate potential for movement (Basagic and Fountain, 2011).

4.4. Open-Water Evaporation

Open-water evaporation for lakes in the watershed-lake hydrologic model of the paleo-Owens River system was estimated using the Priestley-Taylor equation (Priestley and Taylor, 1972) (Figure 2). The Priestley-Taylor equation is applicable to large water

bodies in mountainous and semiarid regions (e.g., Assouline et al., 2015). The equation has also been used in previous watershed-lake paleohydrologic models in the Great Basin (Hatchett et al., 2015; Barth et al., 2016). The monthly evaporation of open water was estimated at the centroid of lake basins using the Priestley-Taylor equation:

$$E_{LK} = Salt_f \left(\alpha \left[\frac{s}{s+\gamma} \right] \left[\frac{R_n - G}{L_v} \right] \right) \quad (6)$$

where E_{LK} (m) is open-water evaporation from the lake, L_v is the latent heat of vaporization, R_n is net radiation, G is the soil heat flux (considered zero for water), s is the slope of the saturation vapor pressure-temperature relationship calculated from the Clausius-Clapeyron relationship, γ is the psychometric constant, and α is the dimensionless Priestley-Taylor coefficient. A salt suppression factor ($Salt_f$) was also included to decrease the freshwater evaporation derivation because of the saline to hypersaline water conditions of historical Owens Lake that ranged from as low as 60.4 g/L in 1872–1878 to as high as 213.6 g/L by 1913 (Winkle and Eaton, 2010; Lee, 1915; Harbeck, 1955; Langbein, 1961; Mihevc et al., 1997).

Net radiation was calculated from taking the difference between net shortwave radiation and net longwave radiation $R_n = (S_n - L_n)$ (Figure 2). Shortwave radiation was estimated using the ArcGIS-derived incoming solar radiation for the grid cell at the centroid of the lake basin and a typical albedo value of 0.08 for open water surfaces.

The longwave radiation was calculated using the following equations (Shuttleworth, 2012):

$$L_n = f\varepsilon'\sigma {T_{avg}}^C \quad (7)$$

$$\varepsilon' = 0.34 - 0.14\sqrt{e} \quad (8)$$

where ${T_{avg}}^C$ is mean monthly temperature, σ is the Stefan-Boltzman constant of 5.67×10^{-8} W/m^{2}K^4, ε′ is effective emissivity to account for humidity content of air or vapor pressure (e), and f is an empirical cloud factor. The empirical cloud factor was derived from the following equation for arid environments (Shuttleworth, 2012):

$$f = 1.35\,\frac{a_s + \left(\frac{n}{N}\right)b_s}{a_s + b_s} - 0.35 \quad (9)$$

where a_s and b_s are empirical factors having typical values of 0.25 and 0.5, respectively, which correspond to 25% and 75% loss of energy in clear sky and overcast ($a_s + b_s$) conditions, respectively. The typical number of days with bright sunshine (n) in a month lasting N day across the watersheds was from the Western Regional Climate Center climate data summary for Bishop in northern Owens Valley for the period of record from 1961–1990.

The calculation of L_n requires estimates of vapor pressure. The calculation of α also requires vapor pressure, plus vapor pressure deficit and wind speed at 2 m height.

Seventeen years of hourly temperature and relative humidity data from 1994–2011, plus twenty years of hourly wind speed data at 2 m height from 1991–2011 collected at the Great Basin Unified Air Pollution Control District's A-Tower meteorological station at Owens Lake playa were used to estimate vapor pressure and vapor pressure deficit (Figure 7A). The PRISM vapor pressure and vapor pressure deficit dataset was not used in this study because it was assumed by using the high-resolution, site-specific meteorological data from the centroid of Owens Lake basin and developing empirical relations between the meteorological data and PRISM temperature data that potential errors in the estimate of vapor pressure deficient would be minimized.

The meteorological data were aggregated into monthly minimum and maximum temperature and mean monthly wind speed to match the time step in the watershed runoff model. Empirically derived relative humidity was used to estimate vapor pressure from the seventeen years of measured relative humidity and calculated saturated vapor pressure from measured temperature at the A-Tower meteorological station (Figure 7B). Saturated vapor pressure was calculated from temperature based on the following empirically determined equations (Shuttleworth, 2012):

$$e_s(T_{max}) = 0.6108exp\left(\frac{17.27{T_{max}}^C}{237.3 + {T_{max}}^C}\right) \quad (10)$$

$$e_s(T_{min}) = 0.6108exp\left(\frac{17.27{T_{min}}^C}{237.3 + {T_{min}}^C}\right) \quad (11)$$

$$e_s = \left(\frac{e_s(T_{max}) + e_s(T_{min})}{2}\right) \quad (12)$$

where $T_{max}{}^{C}$ and $T_{min}{}^{C}$ are monthly maximum and minimum temperatures (°C), $e_s(T_{max})$ and $e_s(T_{min})$ are maximum and minimum saturated vapor pressure, and e_s is mean monthly saturated vapor pressure. There is a relatively strong correlation (R^2=0.75) between the A-Tower derived mean monthly relative humidity (RH_{avg}) and mean monthly calculated e_s (Figure 7B). The equations for deriving the Priestley-Taylor coefficient (α) are in the form (Shuttleworth, 2012):

$$s = \frac{4098 e_s}{(237.3 + T_{avg}{}^{C})} \tag{13}$$

$$e = \left(\frac{RH_{avg}}{100}\right) e_s \tag{14}$$

$$D = e_s - e \tag{15}$$

$$r_{clim} = \left(\frac{187219 \gamma D}{(275 + T_{avg}{}^{C}) s R_n}\right) \tag{16}$$

$$\alpha = \frac{(R_n + \gamma)\left[\left(\frac{208}{u_2}\right) + r_{clim}\right]}{(R_n + \gamma)\left[\left(\frac{208}{u_2}\right) + 70\gamma\right]} \tag{17}$$

where s is the slope of the saturation vapor pressure-temperature relationship, e is vapor pressure, D is vapor pressure deficit, r_{clim} is climatological resistance factor when R_n is in mm/d, and u_2 (m/s) is monthly wind speed at 2-m height. The power function derived

from the data on Figure 7B was used to estimate *RH* from the calculation of e_s using the 800-meter PRISM temperature data during model simulations.

4.5. Change in Storage

The net positive or negative change in storage of the lake basin was determined by computing the annual cumulative sum of the input and output components of the water balance model plus the initial lake volume at the beginning of the simulation. The basic hydrologic mass balance model for a closed-basin lake must balance inputs from direct precipitation on the lake and runoff to the lake with output through evaporation from the lake to maintain a lake level at steady state and the development of a well-developed shoreline (e.g., Kutzbach, 1980; Huth et al., 2015). This mass balance model is in the form of:

$$\Delta V_i = V_{i-1} + [In]_i - [Out]_i, i > 0 \quad (18)$$

$$\Delta V_i = V_{i-1} + \left[P_{LK_i} \cdot a_{LK_i} + V_{OR_i} + V_{GW_i}\right] - \left[E_{LK_i} \cdot a_{LK_i}\right] \quad (19)$$

where ΔV_i (m^3) is net lake storage of year i, P_{LK} (m) is annual precipitation to the lake, V_{OR} (m^3) is annual Owens River discharge (i.e., watershed runoff) to the lake, V_{GWD} (m^3) is annual groundwater discharge to the lake, E_{LK} (m) is annual evaporation from the lake surface, and a_{LK} (m^2) is lake area (Figure 2).

Precipitation to the lake is from historical mean monthly precipitation PRISM data from the grid cell at the centroid of the playa lake for the entire period of record

(WY1896–2015). Groundwater discharge to the lake is from hydrogeologic studies of spring and seep discharge into Owens Lake basin (Feeney Hall, 1996; Conway, 1997; Mihevc et al., 1997; Schumer, 1997). Groundwater information from other downstream watersheds were estimated using analogous hydrologic conditions documented in Owens Lake basin.

4.5.1. Hypsometry of Lake Basins

Hypsometric curves of the lake basins were used to calculate equivalent water-level elevation from ΔV_i of the water balance model. A high resolution DEM of Owens Lake basin was constructed in a GIS platform from a DEM that was previously created from contours digitized by Mihevc et al. (1997) between the elevations of 1082 and 1097 m from the bathymetric map of Owens Lake surveyed in February, 1913 (Gale, 1914; Lee; 1915) (Figure 8). The hypsometry of Owens Lake basin was expanded between the elevations of 1097 and 1165 m using the USGS NED 10-meter DEM. The 10-meter DEM was also used in the other watersheds to construct hypsometric curves. The basin area and volume at 1-meter elevation intervals were calculated in ArcGIS for each lake basin (Figure 8). Two hypsometric relations were used to simulate lake-level elevation and area from volume at annual time steps based on the following:

$$Z_i = Z(V_i) \tag{20}$$

$$A_i = A(Z_i) \tag{21}$$

where Z_i (m) is elevation of lake level, V_i (m^3) is lake storage, and A_i (m^2) is surface area of lake of the *i* year. The interpolation function in MATLAB was used to calculate changes in lake level and area from tabulated hypsometric relations at 1-meter elevation intervals during each annual time step.

5. UNCERTAINTY AND SENSITIVITY ANALYSES

Uncertainty and sensitivity analyses are used to produce a robust assessment of the strength and weakness of a model (e.g., Peeters et al., 2014; Borgonovo et al., 2017). Numerical models (e.g., water-balance hydrological models) consist of independent variables, dependent variables, and relationships between these quantities. These types of models typically include parameters whose actual values cannot be directly measured in nature with sufficient accuracy, therefore are commonly estimated through inverse modeling to generate a specific range of probable values (Borgonovo et al., 2017). As a result, the effects of such errors and/or parameter variations must be quantified in order to asses a model's range of validity. Furthermore, the effects of uncertainties in the model's parameters on the uncertainty in the calculated results (i.e., output) must also be quantified (Cacuci, 2003).

The objective of uncertainty analysis is to understand the reliability of model predictions, given various sources of uncertainty in model input and design. In contrast, the objective of sensitivity analysis is to identify the variable(s) that have the greatest influence on the model output (e.g., Zhang et al., 2015). The purpose of sensitivity analysis is to : (1) understand the relation between model inputs and outputs; (2) determine which model input contributes most to the variability of the model output; (3)

identify the important and influential parameters that drive model outputs and magnitudes; and (4) guide future model design (Zhang et al., 2015; Borgonovo et al., 2017).

5.1. Uncertainty Analysis

5.1.1. Precipitation and Temperature

Uncertainties in hydrologic model outputs commonly stem from errors in model structure, or uncertainties in model inputs: forcing data, model parameters, and initial conditions (Gupta et al., 2012; Seck et al., 2014). An uncertainty analysis was performed on the precipitation and temperature input variables of the watershed-lake hydrologic model prior to and during model calibration. Precipitation and temperature from the 800-meter, monthly historical PRISM gridded dataset does not include model errors (Daly et al., 1994). An uncertainty analysis was previously performed to assess the accuracy of PRISM precipitation in a mountainous watershed in North Carolina that determined historical PRISM national grids matched closely (within 5%) with similarly gridded observed rain gauge data from a dense network over the period 1951–1958 (Daly et al., 2017). However, the uncertainty of the PRISM grids used for the Owens River watershed are likely much larger than ~5% identified in the relatively moderate-relief mountainous watershed in North Carolina, because the Owens River watershed is dominated by alpine environments of the relatively high-relief and complex mountain terrain of the Sierra Nevada (e.g., Stratchon and Daly, 2017).

Hydrologic model input uncertainty within a Bayesian framework (e.g., Kuczera et al., 2006; Kavetski et al., 2006; Vrugt et al., 2008; Thyer et al., 2009) recognize that

hydroclimatic inputs in watershed-hydrologic models are uncertain, despite having rain gauge and/or radar data, in addition to other parameters and model structure being uncertain. One-way to deal with this uncertainty is to assume that rainfall error varies from event to event, and that this can be treated using a positive multiplier that is drawn from a random distribution with moderate variance and centered on one (Kavetski et al., 2006; Vrugt et al., 2008). The rationale of the application of a rainfall multiplier is that by allowing the multipliers to very between hydrologically reasonable ranges, systematic errors in rainfall forcing can be corrected, and parameter inference and streamflow predictions can be improved (Vrugt et al., 2008). In this study, parameter multipliers were applied to the monthly precipitation, as well as temperature PRISM grids of the Owens River watershed during calibration to account for potential large errors associated with alpine environments and orographic effects along the eastern escarpment of the Sierra Nevada.

A simple Gaussian multiplier model (e.g., Kavetski et al., 2006) was used that randomly selected 1440 monthly (i.e., 120 years) precipitation and temperature multiplier values from a Beta probability distribution ranging from 0.5 to 1.5 constructed in MATLAB. The Beta distribution was developed using shape parameters of 7, 7, which produced a pseudo Gaussian distribution that best fit observed data during calibration (Figure 9). Each randomly selected monthly multiplier was applied to the entire 12,969 cell model domain to assign a model uncertainty to PRISM precipitation and temperature values for each specific month. The monthly multiplier values from a 1000-run simulation were aggregated into mean annual, plus maximum and minimum

monthly values to show the distribution of values used during the 120-yr period of record from WY1896 to 2015 during calibration of the watershed-lake hydrologic model.

5.2. Sensitivity Analysis Background

Several sensitivity analysis methods have been developed recently that have contributed to a vast and growing literature (Borgonovo and Plishke, 2016). In general, there are two types of sensitivity analysis: (1) local and (2) global. Local sensitivity analysis evaluates changes in the model outputs with respect to variations in a single parameter input by changing parameters with relatively small increments (e.g., 0.1%) at which individual parameter perturbations on model output is calculated using local sensitivity indices. Local sensitivity analysis may only be used when the model output is linearly related to the parameters near a specific nominal value. The one-at-a-time method and regression analysis are commonly used to calculate local sensitivity indices that provide a general sensitivity measure of complex models (e.g., Hamby, 1994). In contrast, global sensitivity analysis includes the variation of all parameters simultaneously over the entire parameter space, which allows to simultaneously evaluate the relative contributions of each individual parameter, as well as the interactions between parameters to the model output variance (Zhang et al., 2015).

The two most widely used approaches used for global sensitivity analysis are Fourier amplitude sensitivity analysis (FAST) and Sobol method. Both FAST and Sobol methods are variance-based techniques. The methods differ in that FAST uses a sinusoidal function to search patterns through the parameter space, while the Sobol method is based on a Monte Carlo integration of quasi-random sequence of numbers (Sobol, 1976; 1993;

2001). Of all the global sensitivity methods that are commonly used, the variance-decomposition based Sobol sensitivity analysis is one of the most powerful techniques used for evaluating nonlinear models (e.g., Homma and Saltelli, 1996; Zhang et al., 2015).

New techniques have recently been used in global sensitivity analysis that include probability density function (PDF)-based and cumulative density function (CDF)-based sensitivity analyses (e.g., Peeters et al., 2014; Borgonovo and Plischke, 2016; Borgonovo et al., 2017). The PDF- and CDF-based sensitivity analyses differ from the variance-based methods (e.g., Sobol) in that it does not require nearly as much computational execution time, it does not require any assumptions on the shape of the distribution, and it is independent of the parameter sampling scheme (Plischke et al., 2013). This is an improvement in global sensitivity analysis because the variance-based methods assume the entire effect of a parameter can be summarized by the variance, and as a result, the variance-based indices will be less reliable if the response to a parameter has a skewed or multi-modal distribution (e.g., Peeters et al., 2014).

5.2.1. Runoff and Ice Melt Models

A sensitivity analysis was performed on the Thornthwaite runoff model (McCabe and Markstrom, 2007), as well as the simplified energy-balance ice melt model (Orleans, 2001) to identify the input parameter or set of input parameters that have the greatest influence on the model output of runoff and ice melt. A global sensitivity analysis was performed in the study based on variance-based Sobol sensitivity indices and an ensemble of probability density function (PDF)- and cumulative density function (CDF)-based on sensitivity indices after Plischke et al. (2013). The sensitivity analysis was

divided into five steps: (1) pre-analysis – define parameters lower and upper bounds; (2) generate parameter sets using Sobol sequences; (3) run the parameter sets through the model; (4) calculate sensitivity indices; and (5) analyze correlation coefficients by evaluating the first-, second-, and total-order global sensitivity indices.

Parameter sets were generated using the Sobol sequence technique based on MATLAB code of Cannavo' (2011). A Sobol sequence is a quasi-randomized, low-discrepancy random number generator that involves sampling parameter space more uniformly than complete random number sequences. A sequence with a sample size of N = 9000 and dimensions of d = X (i.e., number of model parameters) were used. Of note, a sample size of N = 1000 typically provides a minimum sequence of realizations needed for the calculation of Sobol indices (Homma and Saltelli, 1996).

5.2.2. Thornthwaite Runoff Model

The Thornthwaite model includes a total of nine parameters. The assignment of the lower and upper bounds for the parameters of precipitation (Pmm), mean temperature (Tmean), latitude (lat), and soil-moisture storage capacity (SMSC) are from the range of values from the PRISM climate, geographic, and NRCS soil datasets within the model domain of the Owens River watershed. The range of the other parameters of the runoff model including: runoff factor (Rf), direct runoff factor (DRf), rain temperature threshold (TempRain), snow temperature threshold (TempSnow), and snow melt rate (Maxmelt) were based on an arbitrary assignment of a wide range of all possible variations (Table 3). The Sobol normalized values from 0 to 1 in each dimension were adjusted to the specific range for each of the nine parameters. The adjusted Sobol sequence (i.e.,

matrix = 9000 x 9) was then used with the Thornthwaite model to calculate runoff (e.g., model output = y) (Figure 10A). The analysis shows that the modeled runoff output had a maximum frequency of zero runoff, whereas the distribution of modeled runoff greater than zero had a distribution ranging from ~1 to 430 mm, centered at 160 mm (Figure 10A).

5.2.3. Simplified Energy-Balance Ice Melt Model

The simplified energy-balance ice melt model includes a total of six parameters. The assignment of the lower and upper bounds for the parameters of incoming shortwave radiation and mean temperature (Tmean) are from the range of ArcGIS-derived values from the DEM and PRISM climate data within the model domain of the Owens River watershed, respectively (Table 4). The range of the other parameters used including: albedo and thermal quality of snowpack (B), plus the empirical factors used with the simplified energy-balance ice melt model of net longwave radiation (C_0) and turbulent heat fluxes (C_1) are based on the wide range of possible variations directly measured or previously used in glacial ice melt models (e.g., Wilson, 1942; Paterson, 1994; Orleans, 2001; DeWalle and Rango, 2008; MacDougall et al., 2011; Shuttleworth, 2012) (Table 4). The Sobol normalized values from 0 to 1 in each dimension were adjusted to the specific range for each of the six parameters. The adjusted Sobol sequence (i.e., matrix = 9000 x 6) was then used with the simplified energy-balance ice melt model to calculate ice melt (e.g., model output = y) (Figure 10B). The analysis shows that the modeled ice melt output had a maximum frequency of zero runoff, whereas the distribution of modeled runoff greater than zero had a distribution ranging from ~0.1 to 2.4 m, centered at less than 0.25 m (Figure 10B).

5.2.4. Global Sensitivity Analysis

5.2.4.1. Sobol Sensitivity Indices

A Sobol sensitivity analysis was performed to evaluate if the Sobol analysis would result in more insight on the sensitivity of the input parameters than a local sensitivity analysis based on simple, linear regression approaches. In general, the Sobol method generates three sensitivity indices that include first-, second-, and total-order sensitivity indices. The first-order indices are the main effect and used to measure the fractional contribution of a single parameter to the output variance. The second-order indices are used to measure the fractional contributions of parameter interactions to the output variance. Lastly, the total-order indices consider both the main and second-order effects, which involves the evaluation over a full range of parameter space. The higher the sensitivity indices value, the more influential the parameter is to the output. Also, an arbitrary value of 0.05 is frequently accepted as a distinct cutoff for distinguishing important from unimportant parameters (Zhang et al., 2015). Therefore, only the parameters in each model with indices of greater than 0.05 are the most sensitive in influencing model output. The Sobol sensitivity analysis typically produces results that are relatively more insightful than simple linear regression analysis. The first- and total-order Sobol indices for the runoff model indicated that mean temperature (T_{mean} = 0.65 and 0.66) and precipitation (P_{mm} = 0.10 and 0.11) were the two most sensitive parameters in influencing the model output (Figure 11a). The first- and total-order Sobol indices for the ice melt model indicated that radiation (0.34 and 0.34) and albedo (0.32 and 0.32) were the two most sensitive parameters in influencing the model output (Figure 11B).

5.2.4.2. Probability Density Function (PDF)-Based and Cumulative Density Function (CDF)-Based Sensitivity Indices

An ensemble approach that includes several different sensitivity analysis techniques are becoming more widely used in global sensitivity analysis to evaluate complex models with numerous input parameters (e.g., Plischke et al., 2013; Peeters et al., 2014; Borgonovo et al., 2017). The ensemble approach typically includes the use of Sobol indices, but also includes several density-based sensitivity indices. In general density-based sensitivity techniques requires an assessment of the unconditional and conditional probability densities of model output, which have been shown to significantly reduce computational burden and improving estimation accuracy by accounting for the shape of the probability distribution (i.e., moment).

An ensemble of first-order density-based sensitivity indices from seven different PDF- and CDF-based correlation techniques after Plischke et al. (2013) were used in conjunction with the same parameter values generated from the Sobol sequences. The purpose of performing the density-based sensitivity analysis was to assess if these types of techniques would provide higher resolution and distinguish the relative sensitivity of the other less sensitive parameters than the Sobol method. A total of seven different PDF- and CDF-based correlation techniques from the MATLAB database of Plischke et al. (2013) were used.

The ensemble of density-based sensitivity techniques collectively produced results that were much more insightful than the Sobol method. Although the Sobol method, shows mean temperature and precipitation are the two most sensitive parameters for the runoff model, the density-based sensitivity techniques also captured the relative

influence of the other six parameters. For example, the density-based techniques identified direct runoff and snow temperature threshold as other parameters that are relatively sensitive in controlling runoff (Figure 12A). In contrast, the ensemble of density-based sensitivity techniques yielded from the ice melt model collectively produced results that were similar to the Sobol method (Figure 12B).

The global sensitivity analysis performed for the runoff model provided insightful information on which parameters were sensitive to the model output. The ensemble of density-based sensitivity analysis techniques provided a more complete evaluation of the relative influence of all input parameters compared to the Sobol method. The result of the density-based sensitivity analysis indicated that the four most sensitive input parameters (from highest to lowest) that influences runoff are mean temperature, precipitation, direct runoff, and snow temperature threshold. These results make sense given that discharge within the Owens River watershed is primarily controlled by snowmelt runoff. In addition, the global sensitivity analysis performed for the ice melt model also provided insightful information on which parameters were relatively sensitive to the model output. The results of both the Sobol and density-based sensitivity analyses indicated that the four most sensitive input parameters (from highest to lowest) that influences ice melt are radiation, albedo, mean temperature, and turbulent heat fluxes. It is likely that both global sensitivity analysis methods yielded similar results because the parameters in the ice melt model are principally dependent on either radiation or temperature, thereby returning relatively higher sensitivity indices for all parameters compared to the runoff model that included a larger range of independent parameters (Figure 12). The sensitivity of temperature in the runoff model and solar radiation in the ice melt model is reflected by

the sensitivity analysis of modeled output, where the lack of runoff output is mostly related to the combination of temperatures below freezing and little precipitation and the lack of ice melt output is associated with the combined effects of differing solar radiations and albedo (e.g., Figure 10).

6. MODEL CALIBRATION

The process of calibration is performed to parameterize a model in order to accurately simulate the physical environment. There are over a hundred years of surface hydrologic, groundwater, and evapotranspiration investigations of the Owens River watershed related to development of the Los Angeles aqueduct system that provide a large resource of historical observed data (Lee, 1906; 1912; 1915; 1932; Gale, 1915; Williams, 1966; 1978; Hollett et al., 1987; 1991; Danskin, 1998; Dileanis and Groeneveld, 1989; Duell, 1990; Sorenson et al., 1989; 1991; Conway, 1997; Schumer, 1997; Tyler et al., 1997; 2006; and Groeneveld et al., 2010). In addition, because Owens Lake desiccated in the 1930s, there have been several studies performed to estimate post-1913 water balances of Owens Lake basin (Blevens et al., 1976; Lopes, 1986), and in particular, simulate lake levels without Los Angeles aqueduct diversions based on monthly measured runoff and a simplified lake evaporation model between 1913 and 1995 (Mihevc et al., 1997). A variety of surface runoff, groundwater, and evaporation datasets, along with snow survey data from investigations in the watershed were used to calibrate the watershed-lake water balance model. The simulated lake levels of Mihevc et al. (1997) were also used to evaluate the accuracy of the watershed-lake water balance model and resultant lake-level simulation of this study.

The Owens River watershed-lake hydrologic model includes four model components comprising of snow accumulation, runoff, groundwater, and lake evaporation that collectively contain a total of fifteen model parameters (Table 5). Model calibration involved either assigning a range of values to select parameters that previously demonstrated to be sensitive to model output or assigning a range of values from measured hydrologic data. In addition, some parameters either were assigned a single value if the parameter demonstrated low sensitivity in influencing model output or were assigned a mean value from a range of observed data if shown to be a highly sensitive parameter. Similar to that performed during the sensitivity analysis, parameter sets were generated using the Sobol sequence technique for parameters with a range of assigned values (Table 5). Model calibration included several iterations of 1000-run simulations with varying model parameters and mean monthly precipitation and temperature PRISM data with uncertainty multiplier values to identify the best fit to observed data (e.g., Figure 9). Three model parameters including snow temperature threshold (TempSnow) in the snow accumulation model component, plus direct runoff (DRf) and runoff fraction (Rf) in the runoff model component were adjusted during calibration given the uncertainty in these input parameters in influencing snow accumulation and runoff, whereas the remaining parameters included randomly generated values from measured hydrologic data or single values from published sources (Table 5).

6.1. Snow Accumulation

6.1.1. Annual Snow Storage

Annual snow storage was estimated using the Thornthwaite runoff model (snowstor) for areas below the ELA and the simplified energy-balance snow melt model (ELAsnotor) for areas above and below the ELA (Figure 2). The model parameters for TempRain of 3.3ºC and Maxmelt of 0.5 were used in the runoff model. These values are the same as the default values previously used by McCabe and Markstrom (2007), and slightly different from the values used by Barth et al. (2016) (Table 5). A value of 0.55 was assigned to the albedo model parameter in the snow melt model (Equation 1; Table 5). This value was selected to represent a generalized albedo throughout the water year that typically ranges from 0.2 to 0.95 for glacier ice to fresh snow, respectively (e.g., Singh and Singh, 2001; Paterson, 1994; Shuttleworth, 2012). Calibration of the snow accumulation and energy-balance snow melt model components was performed by comparing the distribution of April 1st SWE storage from WY2004–2015 estimated from the model output of this study and from the snow data assimilation system (SNODAS) model (Barrett, 2003) (Figure 13). A mean model parameter of -1.96ºC for TempSnow based on randomly generated values ranging from -1.0 to -3.0ºC and a threshold SWE depth of 4 cm yielded the best fit to SNODAS derived SWE storage during several iterations of 1000-run simulations (Table 5). These parameter values returned a $R^2 = 0.80$ and mean absolute error (MAE) = 32.1% when all twelve years of the SNODAS dataset was compared (Figure 14A). Water year 2008 yielded the largest discrepancy between the modeled snowpack of this study and SNODAS snowpack. The snow accumulation model of this study simulated nearly 2.5 times more SWE storage than the SNODAS

dataset. The error could be associated with the gridded mean monthly precipitation and temperature PRISM data for this particular year, although the other years correlated very well with SNODAS. When WY2008 is omitted from the comparison, the correlation coefficient increased and the model error decreased having values of R^2 = 0.94 and MAE = 24.1%, respectively (Figure 14A). The calibrated snow accumulation component of the watershed hydrologic model enabled reconstruction of April 1st SWE storage, area, and snowline elevation across the watershed during the 120-year simulation (Figure 15). The trends of modeled April 1st SWE storage, area, and snowline from WY2008–2015 of this study are similar to the trend of winter snow level rise documented in the northern Sierra Nevada associated with the partitioning of snowfall to rainfall in snow-dominated mountain watersheds during mostly warm and drought climatic conditions during this period (e.g., Hatchett et al., 2017).

6.1.2. Glacier and Perennial Snow Accumulation

The Owens River watershed hydrologic model includes an element to estimate the accumulation and melt of glacial ice and perennial snow in the upper elevations of the watershed. The ELA is the datum or elevation in the watershed that is used to control the position and magnitude of snow accumulation (ELAsnotor) and melt (ELASM) at or above the annual snowline (Figure 2). The ELA is determined by estimating the change in annual mean summer temperature relative to the temperature of the ELA in 1974 and converting it to an associated elevation based on the adiabatic lapse rate developed for the watershed (Table 1; Figures 6 and 16A). All model domain grids with mean elevations at or above the annual ELA are included in the estimate of annual ELA snow storage.

Calibration of the glacial ice and perennial snow accumulation component was made by using the percent change in the area of mapped small glaciers and perennial snowfields in the Owens River watershed. Calibration involved adjusting the ELA sublimation factor (*ELA Sublim$_F$*) in Equation 3 until the difference in cumulative SWE storage over the 120-year simulation matched the -55% change in glacier area (e.g., Equation 4) between 1903 and 2004 (Basagic and Fountain, 2011) (Figure 16B). An *ELA Sublim$_F$* of 0.981 was required to simulate the observed historical change in SWE storage (Table 5). The SWE storage in WY1896 was estimated by increasing the starting volume of the 120-year simulation until the total area of SWE storage within the watershed equaled the total area of 10.551 km^2 for mapped glaciers and snowfields in 1972 (Raub et al., 2006) (Figure 16C).

An evaluation of the method used to determine the starting volume of SWE storage in the model simulation was made by performing a similar simulation for the Big Pine Creek subbasin (Figures. 1 and 5). The Big Pine Creek subbasin was selected because it contains the largest glacier in the Sierra Nevada (Middle Palisades Glacier) and detailed mapping of Matthes (Little Ice Age: ~150-600 cal yr B.P.) and Recess Peak (~13.6 ka) glacial deposits (Figure 5). The upper parts of the subbasin also contain some of the highest elevations in the Sierra Nevada with North Palisade and Norman Clyde Peak having elevations of ~4300 m, about 100 m lower in elevation than Mt. Whitney (Figure 5). Calibration involved adjusting *ELA Sublim$_F$* in Equation 3 until the difference in cumulative SWE storage over the 120-year simulation matched the -44% change in glacier area (e.g., Equation 4) between 1903 and 2004 (Basagic and Fountain, 2011) (Figure 17A). An *ELA Sublim$_F$* of 0.9915 was required to simulate the observed historical

change in SWE storage in the Big Pine Creek subbasin (Table 5). A starting SWE storage of 1.9 x 10^8 m^3/yr in WY1896 was required to match the total area of 4.56 km^2 for mapped glaciers and snowfields within the subbasin in 1972 (Raub et al., 2006) (Figure 17B).

Early surveys and photographs of prominent glaciers in the Sierra Nevada documented a rapid re-advance of post-LIA glaciers that were in contact with Matthes (LIA) moraines between 1883 and 1908 (e.g., Basagic and Fountain, 2011). The total area of Matthes glacial deposits in the Big Pine Creek subbasin is 5.4 km^2 (Bowerman and Clark, 2011) (Figure 5). The modeled starting SWE storage in 1896 yielded an area of 6.3 km^2 by 1908 at the termination of the glacial re-advance (Figure 17B). The area of mapped glacial deposits is considered a minimum estimate for the extent of glacial ice and snow accumulation during the Matthes glaciation because the geologic mapping does not adequately characterize the extent of perennial snowfields, whereas the model of this study was calibrated to observed changes in the extent of total snow accumulation including glaciers and perennial snowfields.

6.2. Modeled Runoff and Measured Groundwater Contributions

The Owens River watershed hydrologic model includes a runoff component based on the Thornthwaite runoff and a groundwater component from measured hydrogeologic data that collectively are used to provide a more representative simulation of a coupled surface and groundwater system (Table 5). Stream losses and baseflow groundwater contribution are accounted for in the watershed runoff model (Figure 2). Estimates of channel loss from alluvial fan stream bed leakage ($Alluv\_loss_F$) and actual

evapotranspiration (AET2) by riparian vegetation are based on measurements from gauged tributary stream reaches between the Sierra Nevada range front and the Los Angeles aqueduct from WY1935–1984. Measurements from several of the larger tributary streams showed losses of 16–53% that averaged ~30% of the observed annual discharge (Hollett et al., 1991; Danskin, 1998). Estimates of stream gains along the lower Owens River (ORG) from groundwater contributions were also used from measurements that range from 3.70×10^6 to 1.36×10^7 m^3/yr between WY1946 and 1986 (Hollett et al., 1991; Danskin, 1998) (Table 5; Figure 2). In addition, spring discharge (GWD) into Owens Lake basin was also accounted for by using the range of values estimated from surface measurements and groundwater modeling in the lake basin (Conway, 1997; Schumer, 1997) (Table 5; Figure 2). The fractional values of 0.7–0.8 were used to simulate the typical channel loss from the Owens River and tributary streams on alluvium. Runoff within grid cells of the model domain that correspond with younger and older alluvial geologic map units of Jennings et al. (2010) was reduced to account for alluvial fan channel loss by the fraction values. The total Owens River (OR_loss_F) discharge was also reduced to account for channel loss prior to input in the lake basin (Table 5; Figure 2). Soil-moisture storage capacity was not part of the parameterization of the model because it is static input data.

The watershed runoff model was calibrated using Los Angeles Department of Water and Power (LADWP) annual runoff of the Owens River watershed from WY1934–2015. The observed runoff was measured from 34 stream gauges located at tributary reaches along the Sierra Nevada range front, thereby demonstrating that runoff within the watershed is primarily sourced from the Sierra Nevada mountain block. Prior

to calibration, the annual runoff for the Owens River watershed was corrected for imported water contributions from Mono Basin. Water imports began in 1937 during construction of the Mono Basin extension of the Los Angeles aqueduct. Completion and full operation of the Mono Basin extension began in 1944. In this study, the imported runoff from Mono Basin and groundwater gains from the Mono Tunnel were omitted from the reported annual runoff to provide a representative estimate of runoff for the Owens River watershed (Vorster, 1985; LADWP, 1987; Mihevc et al., 1997; Mono Lake Committee, 2017). Estimates of open-water evaporation from Crowley Lake reservoir in the upper reach of the Owens River in Long Valley was also made in this study to account for potential loss of water from reservoir storage (Figure 1). Open-water evaporation for Crowley Lake was estimated using the same methods for Owens Lake described in the following section. The period from WY1937–2015 was corrected to account for reservoir evaporative loss and gains from Mono Basin. The net correction resulted in a mean decrease of 9.5% of reported annual runoff.

Mountain rivers controlled by glacier melt and snowmelt have hydrographs that consist of two components: (1) a baseflow component supplied by groundwater discharge, runoff from storage zones within ice during the summer (e.g., Figures 16D and 17C), and regular drainage from alpine lakes; and (2) a flood component commonly influenced by late spring/early summer snowmelt runoff (e.g., Wohl, 2000). Total baseflow (BF1 and BF2) was indirectly estimated in this study by separating the annual hydrograph of measured discharge of the Owens River into two parts during calibration. Calibration of runoff to measured data required a nearly uniform addition of discharge ranging from 8.192×10^7 to 1.229×10^8 m^3/yr (Table 5). This addition of discharge is

interpreted to be total baseflow, while the runoff from the Thornthwaite model effectively represents discharge from seasonal precipitation and snowmelt runoff.

Calibration of modeled runoff was performed by using the Sobol sequence technique to generate a range of runoff (DRf and Rf) and groundwater (Total baseflow [BF1 and BF2], ORG, channel loss) parameter values during several iterations of 1000-run simulations (Table 5; Figure 18). Collectively, the range of parameters shown in Table 5 returned the best fit to observed runoff with a $R^2 = 0.84$ and mean absolute error (MAE) = 16.9% over the calibration period from WY1934–2015 (Figures 14B and 19A). The uncertainty of modeled runoff during the final 1000-run simulation ranged from 1.07 x 10^6 to 5.04 x 10^6 m^3/yr, averaging 2.13 x 10^6 m^3/yr at 95% confidence level. The parameter values used during calibration for the Owens River watershed differ from the studies of McCabe and Markstrom (2007) and Barth et al. (2016), because of the different physiographic, soil-geomorphic, and hydroclimatic characteristics of each of the modeled watersheds (Table 5).

6.3. Open-Water Evaporation

Calibration of open-water evaporation was made by comparing model results of this study with direct measurements made at Owens Lake, as well as with evaporation estimates made by other analytical approaches. Evaporation of freshwater was estimated in this study for the period WY1896–2015 by applying the Priestley-Taylor equation, combined with observed wind speed data from a meteorological station at Owen Lake playa to represent typical wind conditions, and mean monthly temperature data from the PRISM grid at the centroid of the lake basin (Figure 20). An evaluation of the accuracy

of the method used to estimate open-water evaporation was made by comparing estimates to other approaches. A mean annual evaporation of ~1.8 m/yr based on the Penman-Monteith method and meteorological station data at the playa was previously calculated for the lake basin for the year 2009 (Groeneveld et al., 2010). The annual evaporation for the same year in 2009 based on the Priestley-Taylor equation yielded an estimate of 1.96 m/yr (Figure 20). A difference of 8.2% of evaporation between the two analytical approaches is similar to other studies that showed the Priestley-Taylor equation commonly produces estimates that are 10.6% greater than the Penman-Monteith method (e.g., McJannet et al., 2013).

In addition to the analytical approaches used to characterize the potential of freshwater evaporation, direct measurements made at Owens Lake prior to major stream diversions in the watershed were used to calibrate open-water evaporation from a saline lake. Calibration of evaporation was performed by using estimates of lake evaporation from a water balance budget of Owens Lake between WY1906 and 1914 (Lee, 1915). Prior to these measurements, the water level of Owens Lake dropped ~6 m during a severe drought between 1895 and 1905 (Lee, 1915). Owens Lake became hypersaline during the drought having a salinity of 213.6 g/L (Winkle and Eaton, 1910; Gale, 1914).

The evaporation rate from saline water is less than from fresh water under the same climate. The decrease is due to a lowering of the vapor pressure of a liquid by the solute (i.e., specific gravity). Although the net effect on evaporation depends on the relative humidity of the atmosphere and on the kind of salt in solution, the lowering in the evaporation rate in percent is roughly equal to the percentage of salt in solution (Langbein, 1961). A mean gross annual evaporation of 1.545 m/yr between WY1906 and

1914 was previously calculated from direct measurements of Owens River discharge into the lake and survey-controlled volume-elevation hypsometric relations of the lake basin (Lee, 1915; Figure 8C). Simulation of mean annual evaporation of freshwater for the same nine-year period yielded 1.864 m/yr based on the Priestley-Taylor equation (Figure 20). The percent difference between the mean gross annual evaporation from a hypersaline Owens Lake calculated by Lee (1915) and the theoretical evaporation of freshwater based on the Priestley-Taylor equation is 17.1% during this period, thereby resulting in an evaporation suppression of 0.829 relative to freshwater at a salinity of 213.6 g/L. A uniform value of 0.829 was used as the salinity suppression factor ($Salt_f$) in Equation 6 to adjust freshwater evaporation estimates based on the Priestley-Taylor equation during periods with low water levels and saline conditions for the entire 120-year calibration period (Table 5; Figure 20).

Previous estimates of evaporation suppression were made for a study that performed lake-level simulations from WY1913–1995 when Owens Lake desiccated and became a playa (Mihevc et al., 1997). The study of Mihevc et al. (1997) estimated evaporation suppression from regression analysis by developing an empirical relation using original experimental data of Lee (1915) that consisted of comparing evaporation of freshwater and brine samples (n = 14) from Owens Lake with salinity of less than 400 g/L, where paired samples were exposed to the exact same conditions. The equation Mihevc et al. (1997) developed was used to convert reservoir evaporation to evaporation from Owens Lake in their model, which is in the form:

$$Esup = (TDS \times -7.653 \times 10^{-7} + 0.9929) \quad (22)$$

where *Esup* is evaporation suppression and TDS is total dissolved solids (mg/L). A comparison of the salinity suppression factor of this study based on both the Priestley-Taylor equation and water balance data of Lee (1915) and the empirical approach of Mihevc et al. (1997) based on the Lee (1915) salinity data yielded the same value of 0.829 at a salinity of 213.6 g/L measured in 1905 by Winkle and Eaton (1910). The comparison of the different approaches and data sources used to estimate evaporation suppression of Owens Lake water demonstrates that both independent methods produced a surprisingly similar result.

6.4. Lake-Level Simulation

Simulation of Owens Lake water levels from WY1896–2015 was performed during the parameterization of the snow accumulation, runoff, groundwater, and evaporation components of the watershed-lake hydrologic model. The 120-year simulation of Owens Lake water levels represents annual lake-level variations without Los Angeles aqueduct stream diversions (Figure 19B). The starting volume of the simulation was based on an elevation of 1091.75 m measured in 1896 (Gale, 1914; Lee, 1915). The uncertainty of modeled water-level elevation during the final 1000-run simulation ranged from 0.02–0.17 m, averaging 0.14 m at 95% confidence level (Figure 19B). Major stream diversions in the Owens River watershed began after completion of the Los Angeles aqueduct in 1913. The stream diversions produced low lake levels and complete desiccation of Owens Lake by ~1930 (Smith and Bischoff, 1997). As a result, there is no observed water-level record of Owens Lake after 1913 (Figure 20B). Therefore, the lake-level simulation of Mihevc et al. (1997) from

WY1913–1995 was compared to evaluate the accuracy of the modeled water levels of this study. The Mihevc et al. (1997) lake-level simulation is based on monthly discharge data measured by LADWP and a simple evaporation model based on empirical relations of measured salinity of Owens Lake water.

A lake-level simulation was performed from WY1913–1995 to compare with the simulation of Mihevc et al. (1997). The starting volume of the simulation was based on an elevation of 1090.4 m measured in 1913 (Gale, 1914; Lee, 1915) (Figure 21). Comparison of the simulated lake levels of this study and Mihevc et al. (1997) resulted in a $R^2 = 0.79$ and MAE = 0.08% (Figure 14C). The largest disparities between the two simulations are during the period from WY1969–1988, where differences in water-level elevation ranged from 0.8–2.6 m, averaging 1.8 m (Figure 21). During this 20-year period, the Sierra Nevada experienced up to nine years with weak to strong temperature and precipitation anomalies associated with El Niño atmospheric climatic patterns that influenced the magnitude of snowpack accumulation and snowmelt runoff in the region (e.g., Redmond and Koch, 1991; McCabe and Dettinger, 2002). Differences in the water-level elevations may be related to errors associated with the coarse resolution of the mean monthly precipitation and temperature PRISM data used in the watershed-lake hydrologic model during periods with moderate to strong El Niño events, as opposed to the dataset used in Mihevc et al. (1997) that is based on measured monthly discharge data.

Apparent differences are also evident in the comparison of the hydrographs of modeled and measured runoff. The hydrographs show the modeled runoff was underestimated in WY1969 during a strong El Niño, whereas the modeled runoff was overestimated during the strong El Niño in WY1983 (Figure 19A). Conversely, the

modeled runoff during the strong El Niño in WY1998 yielded a relatively closer match to measured runoff (Figure 19A). Given the range of model elements and number of parameters, along with the 800-meter resolution PRISM input data, the Owens watershed-lake hydrologic model produced a water-level simulation that closely paralleled the simulation based on measured runoff. This provides a relative measure of the accuracy of the watershed-lake hydrologic model and confidence in the simulation of Owens Lake water levels without Los Angeles aqueduct stream diversions for the entire period from WY1896–2015 (Figure 21).

7. PALEOCLIMATE HYDROLOGIC MODEL

The calibrated model of the Owens watershed-lake system served as a platform for the development of the watershed-lake hydrologic models for China and Searles Lakes. The same dataset of gridded mean monthly precipitation and temperature PRISM data from WY1896–2015 and mean parameterized values of watershed input data for the entire model domain were used for paleohydrologic modeling of all lakes in the paleo-Owens River-Lake system (Table 5; Figures 1, 3–4). The paleoclimate model for the paleo-Owens watershed-lake system includes three primary model variables that include precipitation, temperature, and solar insolation. Of the three variables, precipitation has the most uncertainty followed by temperature over the last 11,500 years. A long record of solar insolation has previously been computed that is based on analytical solutions of changes in the astronomical positions of the Earth's orbit and rotation following Milankovitch theory (Berger and Loutre, 1991), therefore the uncertainty in this record is considered negligible and used in the paleoclimate model. In addition, global- and

watershed-scale temperature records were integrated to produce a continuous record of temperature change applicable for the south-eastern Sierra Nevada. The primary goal of this study is to reconstruct post-glacial precipitation patterns and extent of snowpack in the south-eastern Sierra Nevada. As a result, precipitation was the only variable adjusted during simulations of the watershed-lake hydrologic model until targeted lake levels were reached.

7.1. Lake-Level Records

Reconstruction of precipitation and snowpack in the paleo-Owens watershed-lake hydrologic model was controlled by matching modeled water levels to geologically determined lake-level records of Owens, China, and Searles Lakes. The lake-level and overflow record of Owens Lake that is corrected for tectonic deformation was used in the paleoclimate model. A continuous lake-level curve of Owens Lake was constructed from integrating lake-core data and dated shoreline geomorphology with wind-wave and sediment entrainment modeling of lake core sedimentology (Bacon et al., 2018, 2020) (Figure 22A). The downstream lake-level and overflow record of China Lake that is based mostly on shoreline geomorphology and dated deposits (Rosenthal et al., 2017) and the lake-level record of Searles Lake that is principally based on outcrop and sediment lake-core data (Smith, 1979, 2009; Phillips, 2008) were also used. The downstream lake-level records, however, primarily characterize the extent of moderate to deep lakes during the latest Pleistocene and show Searles Lake desiccated by ~11.7 ka followed by China Lake by 11.1 ka (Smith, 1979, 2009; Phillips, 2008; Rosenthal et al., 2017).

The lake-level record of Owens Lake is the only complete archive that shows the magnitude of lake-level variations of high and low water levels, as well as the duration of overflowing lake conditions controlled by soft sills characterized by easily erodible sediment since 11.5 ka (Bacon et al., 2018; 2020) (Figure 22A). A linear interpolation function was used to calculate the position of water-level and soft sill elevations for Owens Lake at 100-year time steps during simulations. In contrast, there are no directly dated shorelines in China and Searles basins to constrain water levels for deep and shallow lakes. The overflow history of China Lake is also poorly known because there is a lack of direct ages from sediment in the modern sill area (i.e., overflow divide) at an elevation of 665 m. Boreholes drilled in the sill area, however, demonstrate the subsurface geology in the sill area is in the form of an entrenched overflow channel on bedrock (i.e., hard sill) at an elevation of 657 m that is overlain by a ~8 m-thick section of poorly consolidated and easily erodible sediment that forms a soft sill (e.g., Rosenthal et al., 2017) (Figure 22B). The youngest terrestrial deposits in China Lake basin with ages ranging from ~11.1 to 9.5 ka are from elevations above the soft sill of the basin at 665 m. These deposits provide no information on the existence of shallow lakes that may have formed below an elevation of 665 m at times when either Owens Lake was overflowing during the latest Pleistocene to middle-early Holocene or when the Indian Wells Valley and Searles Valley watersheds were the primary source of runoff that supported shallow China and Searles Lakes since 11.5 ka.

The composite lake core (LDW-6) from Searles Valley provides the only stratigraphic evidence of Holocene lakes in downstream basins. An ~10 m-thick section of interbedded mud and salt with a radiocarbon age of ~3,800 cal yr BP from wood

sampled at a depth of 2.4 m indicates a period of perennial and ephemeral lakes that followed an earlier period of mostly ephemeral lakes that deposited an ~10 m-thick accumulation of salt after 11.7 ka (Smith, 1979, 2009). The sediment core data provides direct evidence of shallow and fluctuating lakes in Searles basin that would have required a hydraulic connection with the Indian Wells Valley watershed given the small size and low elevations in the Searles Valley watershed (Figure 1). As a result, a geomorphic evaluation of areas adjacent to playa margins in China and Searles basins was performed to identify potential shoreline features associated with shallow Holocene lakes that could be used to validate lake-level simulations of the paleo-Owens watershed-lake hydrologic model.

7.1.1. Holocene China Lake Strandlines

Inspection of satellite imagery and DEM data for China Lake basin was performed to identify Holocene strandlines and to determine their maximum extent. A high-resolution geomorphic map for areas below an elevation of 700 m in China Lake basin was also used to determine the maximum elevation of lakes that may have formed during the Holocene (Bacon et al., 2019b; Bullard et al., 2019). Geomorphic mapping shows no evidence of prominent shorelines at the elevation of the China Lake basin sill (665 m). The mapping does show the lowest prominent shoreline features encompassing the lake basin are at elevations of ~670 m that likely formed ~13 ka, based on a date from tufa sampled at an elevation of ~666 m (Rosenthal et al., 2017). Evidence of discontinuous recessional shorelines and wave-formed notches in the eastern sector of the lake basin have also been documented between ~665 and 660 m that may be

related to lakes that were present at ~12 ka, based on dates from gastropod and bivalve shells sampled at an elevation of ~658 m (Giambastiani and Bullard, 2007; Rosenthal et al., 2017).

The lowest strandlines that encompass the margins of China Lake playa were identified in this study as youthful wave-formed scarps and low-relief beach ridges at elevations of ~662 and 660 m, about 4 and 2 m above the modern playa, respectively (Figure 22B). The strandlines commonly occur along the playa margin and truncate the distal ends of alluvial fans with a range of ages from ~8.2–4.2 to <4.2 ka, indicating shoreline erosion in the Holocene (Bacon et al., 2019b; Bullard et al., 2019). In addition, eolian deposits in the form of isolated dunes and dune fields in the lake basin and sand ramps in the sill area have previously been dated by luminescence analysis. Eolian deposits in the western sector of the lake basin have ages of 0.92–2.14 ka (Lancaster et al., 2019), whereas deposits near the sill area returned a mean age of ~1.6 ka (Bullard et al., 2019). Given the geomorphic shoreline evidence in China Lake basin, it is plausible that the sill was at lower elevations during much of the Holocene, which would have permitted shallow lakes to overflow and provide input to sustain shallow lakes in Searles basin. In addition, the geomorphic mapping and luminescence ages support a possible conceptual model of the recent development of the soft sill of China Lake basin that includes the deposition of ~5 m of eolian sand within the overflow channel up to an elevation of the modern sill at 665 m from the migration of sand ramps beginning at ~2 ka. The filling of the overflow channel with mostly eolian sediment would have terminated overflow of China Lake during relatively dryer climate in the late Holocene (Figure 22B).

7.1.2. Holocene Searles Lake Strandlines

Inspection of satellite imagery and DEM data for Searles Lake basin was performed to identify Holocene strandlines and to determine their maximum extent. The surficial geologic map of Searles Valley was also used to determine the maximum elevation of lakes that may have formed during the Holocene (Smith, 2009). Three of the lowest strandlines that encompass the margins of Searles Lake playa were identified as wave-formed scarps and low-relief beach ridges at elevations of ~505, 500, and 496 m, about 15, 10, and 6 m above the modern playa, respectively (Figure 22C). The ~500 m strandline consists mostly of wave-formed scarps that forms the margin of the playa, whereas the 496 m strandline is on the lakebed and defines a change from a channelized playa surface above the strandline to relatively smoother playa surfaces extending to the depocenter of the basin at 490 m. The area between the playa margin and up to an elevation of ~510 m was previously mapped to be composed of middle Holocene coarse-grained alluvial or nearshore lacustrine deposits (Smith, 2009). The ~505 m strandline is within this geologic map unit and consists of mostly youthful wave-formed scarps that commonly truncate distal alluvial fans previously mapped as late to middle Holocene (Smith, 2009). The geologic mapping and stratigraphic evidence from lake cores, plus the presence of geomorphically youthful strandlines encompassing the playa margins provide strong evidence for the existence of shallow lakes in Searles basin and hydrologic connection in the paleo-Owens watershed-lake system during the Holocene.

7.2. Solar Insolation Records

The total energy received by the Earth from the Sun changes with time due to collective effects of changes in the Earth's movement around the Sun. These changes are known as Milankovitch cycles, which consist of variations in eccentricity (shape of orbit around sun), obliquity (axial tilt), and precession (wobble of axis) of the Earth's orbit. These orbital changes result in cyclical variation in the solar radiation (insolation) reaching the Earth that in turn influence climatic patterns on Earth (Milankovitch, 1941). As a result, changes in solar radiation across the paleo-Owens River watersheds were accounted for during the 11,500-year model timeframe. Accounting for paleochanges in solar radiation relative to historical conditions afforded representative estimates of the energy-balance derived snowmelt, evapotranspiration, and open-water evaporation model components of the paleo-Owens watershed-lake hydrologic model.

A long record of changes in solar radiation based on Milankovich cycles have been computed that consists of Earth's obliquity and monthly solar insolation for intervals of 10 degrees of latitude at 1000-year time steps (Berger and Loutre, 1991). This record was used to estimate changes in Earth's obliquity and solar radiation at a mean latitude of 37°N for the Owens River watershed (Table 6; Figure 1). The gridded latitude and solar insolation input data of the model domain were adjusted at specific time steps by taking the difference relative to modern values (Table 7). A linear interpolation function was used to calculate changes in the differences of obliquity and solar radiation from tabulated data (e.g., Table 7) to produce 100-year time steps for paleoclimate simulations. Correction for changes in orbital forcing on energy balance of a Sierra Nevada/Great Basin paleohydrologic model was implemented by Yu et al. (2015). Other

studies either applied constant evaporation rates based on mean observed values (Graham and Hughes, 2007), randomly selected evaporation rates from a range of observed values (Adams et al., 2015), or the Priestley-Taylor equation with modern radiation and latitude values (Hatchett et al., 2015; Barth et al., 2016).

7.3. Paleotemperature Records

Temperature is the most sensitive parameter in the Thornthwaite runoff model because the Owens River watershed is a snowmelt-runoff dominated hydrologic system (Figures 11A and 12A). Alpine summer temperature in the Sierra Nevada controls the elevation of the annual snowline and persistence of glaciers and perennial snowfields. As a result, it was important to use an accurate paleotemperature dataset to characterize temperature changes during paleohydrologic modeling. Global-scale temperature changes over the last 22 ka have been estimated from a variety of land- and marine-based proxy data (Shakun et al., 2012; Marcott et al., 2013). Proxy records of temperature change at a regional scale have also been developed for the period 567.7–4.5 ka based on stable oxygen isotopes ($\delta^{18}O$) from dated vein calcite at Devil's Hole, Nevada (Winograd et al., 1992; 2006). In addition, there are watershed-scale discontinuous records of paleotemperature depression from glacial deposits in the Owens River watershed (Table 1), as well as proxy records of temperature anomalies as long as 4000 years from tree rings in the south-eastern Sierra Nevada (Scuderi, 1987a, 1987b, 1993) and White Mountains (Salzer et al., 2014).

The record of global mean temperature anomaly for the last 22 ka was used in the paleo-Owens watershed-lake hydrologic model (Shakun et al., 2012; Marcott et al.,

2013). This record was chosen because it is at 100-year resolution and generally follows the trend of paleotemperature depression estimates from glacial deposits during the ~0.35 ka Matthes (LIA), ~13.6 ka Recess Peak, and ~19 ka Tioga (retreat) glaciations in the south-central Sierra Nevada (Table 1; Figure 23). The global mean temperature dataset, however, shows temperature anomalies that are higher than the temperature depression estimates from glacial landforms (i.e., moraines), where differences in the two datasets include: 0.88°C for the Matthes, 0.85°C for the Recess Peak, and 1.92°C for the Tioga (retreat) (Figure 23A). The global mean temperature dataset was adjusted to coincide with the lower paleotemperature depression estimates from glacial landforms in order to produce a representative temperature change record for the paleo-Owens watershed-lake system. Two functions were developed from regression analysis of the two paleotemperature records to adjust the global mean temperature dataset to fit paleotemperature depression from glacial deposits. A polynomial function was applied to the global mean temperature data between 0.1 and 0.8 ka to fit temperature change associated with the cooler period of the Matthes glaciation during the Little Ice Age and the Medieval Climate Anomaly in the Sierra Nevada (Figure 23B). A linear function was applied to the remaining dataset from 0.8–22 ka to match cooler periods of temperature change associated with the Recess Peak glaciation and termination of the Tioga glaciation in the Sierra Nevada (Figure 23C). The linear function also corrected the global mean temperature dataset by decreasing warm (positive) temperature anomalies by 0.12–0.32°C between 2.8 and 10.8 ka (Figure 23A). The corrected global mean temperature record was used in the paleo-Owens watershed-lake hydrologic model for the period 0–11.5 ka.

7.4. Paleolake Salinity Records

Multi-proxy data consisting of total inorganic carbon (TIC) and aquatic crustaceans (ostracodes) in sediment lake-cores of Owens Lake provide information for the salinity of the lake during the Holocene. The proxy information is used to estimate the salinity suppression factor of open-water evaporation in the paleoclimate hydrologic model. The TIC record from Owens Lake indicates that the early part of the early Holocene (11.6–10 ka) was characterized by a drying trend that was interrupted by a brief (200 yr) wet oscillation centered at ~10.3 ka that was followed by a long-term wet trend from 10.0–7.7 ka (Benson et al., 2002). Paleo-ecological information for the period from ~12–10 ka from an ostracode assemblage co-dominated by *Candona caudate and Limnocythere ceriotuberosa* indicates the lake salinity at this time ranged from 0.3–1.5 g/L (Forester, 2000). The period with a long-term wet trend from ~10–8.3 ka contains an ostracode assemblage dominated by *L. ceriotuberosa*, indicating strong seasonal changes in salinity, with minima around 0.75 g/L, but likely higher, and with maxima upwards of 10 g/L. An unusual ostracode assemblage in sediment cores existed in the lake from ~8.3–6.8 ka that was dominated by *Limnocythere sappaensis* with moderate occurrences of *L. ceriotuberosa* and rare occurrences of *C. caudate* (Forester, 2000). This mixed assemblage indicates strong seasonal variability with low flow from the Owens River and a lake salinity of 10–20 g/L and perhaps up to 80 g/L, but the occurrences of *C. caudate* and *L. ceriotuberosa* imply that there were wet decades and perhaps centuries during this period, when seasonal flow in the river was greater and lake salinity could have been as low as 0.3–1.5 g/L (Forester, 2000; Sharpe and Forester, 2008). The salinity of Owens Lake significantly increased during the middle Holocene

from 5.8–4.2 ka based on high-amplitude oscillations in TIC and presence of shallow-water oolite deposits (Smith and Bischoff, 1997; Benson et al., 2002). The last ostracode assemblage in cores existed from ~4.5–3.8 ka and represented by only abundant *L. sappaensis* that is indicative of a very saline lake, and after ~3.5 ka brine and ephemeral lakes with salinity from 25–213.6 g/L were likely common (Forester, 2000; Sharpe and Forester, 2008; Winkle and Eaton, 1910).

The ostracode record indicates the salinity of Owens Lake during overflow conditions ranged from 0.3 to 80 g/L and during non-overflow conditions ranged from 20 to 213.6 g/L. These values have an equivalent range in salinity suppression factors of 0.93–0.99 for overflowing conditions and 0.83–0.98 for non-overflowing conditions based on Equation 22 of Mihevc et al. (1997). Two general salinity suppression factors were used to simulate open-water evaporation of Owens Lake during non-steady overflow (0.93) and non-overflow (0.83) lake conditions in the paleoclimate hydrologic model during the Holocene (Table 5). A salinity suppression factor of 0.83 was used to simulate evaporation of saline and shallow China and Searles Lakes. Minimum values were selected to provide conservative estimates of open-water evaporation to not overestimate simulated precipitation during calculations of the water balance of the watershed-lake system.

7.5. Initial Conditions

Hydrologic model initial conditions, and the complex relationship among initial moisture, rainfall, and soil characteristics have a major role in accurately reproducing hydrologic response. It is common to start both groundwater and surface water models

from an initial state that has reached dynamic equilibrium based on data availability and model input needs (Seck et al., 2015). The paleo-Owens River watershed-lake model consists primarily of static input parameters associated with the snow accumulation, runoff, and groundwater model components (Table 5). Therefore, initialization of the static parameters was not required. The starting water level of Owens Lake and volume of glacial ice and perennial snow (SWE storage), however, were required for the start of the simulation at 11.5 ka. The starting water level and non-overflowing conditions of Owens Lake at 11.5 ka are from the lake-level curve developed from dated shoreline deposits in the lake basin and fluvial-deltaic sediments in the overflow channel (Bacon et al., 2020) (Figure 22A).

In contrast, there is no geologic evidence for the extent of glacial ice and perennial snowfields in the Sierra Nevada at 11.5 ka. The age of the Recess Peak glaciation is broadly constrained between 14 and 12 ka (Clark and Gillespie, 1997; Phillips et al., 2009; Phillips, 2016, 2017). It is likely glaciers began to recede from their Recess Peak maximum extent sometime after ~12 ka. The initial condition for SWE storage at 11.5 ka was determined by iterating both the starting volume of SWE storage and precipitation until a dynamic equilibrium between snow accumulation and melt was reached over the 100-year time step at the targeted lake level. Boundary conditions for the initial condition of SWE storage included a starting volume of Owens Lake based on an elevation of 1113.8 m (Figure 22A), an adjusted global mean temperature anomaly of -1.5°C (Figure 23A), and adjustment of Earth's obliquity and monthly solar insolation for 11.5 ka (Table 7). Under these boundary conditions, 124.4% of normal (i.e., average) precipitation relative to the historical record from WY1896–2105 was required to sustain

a SWE storage of 8.3 x 10^8 m^3/yr at equilibrium (Figure 25A). In addition, the starting volumes of China and Searles Lakes were set to zero to represent playa conditions, and a soft sill and overflow level of 662.9 m for China Lake was used at the start of the simulation (Figures 22B and C).

8. DISCUSSION

8.1. Uncertainties in Model Boundary Conditions

Tree rings and other high-resolution paleoproxies that are resolved to annual time scales have been used with hydrologic models to provide a range of continuous hydroclimate scenarios used in climate impact assessments (e.g., Gray and McCabe, 2010; Saito et al., 2008; 2015). Although tree rings are annually resolved, they typically consist of relatively short chronologies (relative to geological scales) that are typically less than 2000 years (e.g., Scuderi, 1987a, 1987b, 1993) with a few covering the past 5000 and 8000 years from the Owens River watershed (Hughes and Graumlich, 1996; Salzer et al., 2009; 2014). In contrast to annually resolved climate records, the uncertainties with dating geologic materials can be hundreds to thousands of years and the geologic record of sediments within the shore zone of the lacustrine environment used to reconstruct lake level may be discontinuous due to erosion associated with fluctuations in water level. Because of uncertainties in shoreline records, only discrete periods in the past, where there is good preservation of shoreline landforms and/or deposits with numerical age control, have been used as model calibration points in previous watershed-lake paleohydrologic models (e.g., Matsubara and Howard, 2009; Hatchett et al., 2015, 2016; Yu et al., 2015; Barth et al., 2016). The watershed-lake hydrologic modeling in this

study, however, relied on a continuous lake-level curve developed from the integration of shoreline geomorphology and lake-core data with wind-wave and sediment entrainment modeling of lake-core sedimentology that are corrected for tectonic ground deformation (Bacon et al., 2018, 2019a, 2020). This afforded the simulation of periods with both high and low water levels at a high resolution (100-yr time step) over the past 11,500 years (Figure 22A).

Although the use of a continuous lake-level record will ultimately reduce the uncertainty in modeling centennial-scale hydroclimate change, there is large uncertainty in the timing, duration, and magnitude of discharge during overflow episodes at the decadal-scale of the adjusted historical PRISM climate input data. To account for this uncertainty, a boundary condition was used to limit overflow contributions to downstream lake basins by ending the simulation when the mean water level of Owens Lake over the 120-year period of historical data reached 1.0 ± 0.02 m below the target lake level from geologic evidence (e.g., Figure 22A). This boundary condition was intended to produce conservative estimates of overflow by reducing the potential for continuous overflow conditions, which is unrealistic given the variation in the simulation of historical water levels of Owens Lake (e.g., Figure 19B). In addition, simulation of non-overflowing conditions for all lakes in the paleo-Owen River system were terminated when mean water level reached to within ± 0.02 m of the target lake level from geologic evidence. The use of the continuous lake-level record will ultimately reduce the inherited geologic uncertainty that is typically associated with past studies of lake-level reconstructions, thereby further reducing the uncertainty in model boundary conditions used in this study to reconstruct precipitation and snowpack in the Sierra Nevada.

The record of mean global temperature anomaly for the past 22,000 years based on paleoclimate proxy reconstruction was also used as continuous input data for model boundary conditions (Shakun et al., 2012; Marcott et al., 2013). The Holocene part of the record that shows early Holocene warmth followed by a cooling trend through the middle to late Holocene (Marcott et al., 2013) has previously been examined because it is opposite from the trend of expected and simulated global warming in climate models due to retreating of ice sheets and rising naturally-occurring atmospheric greenhouse gases (Liu et al., 2014). This discrepancy poses an important test for understanding the uncertainty of paleoclimate models and their climate sensitivity to atmospheric greenhouse gases, ice sheets, orbital insolation, and volcanic forcings, as well as the uncertainty of multi-proxy records in accurately recording climate change (Liu et al., 2014). An overall decrease in Holocene temperatures, however, can also be explained by orbiting forcing, where an overall change to less obliquity in the Earth's axial tilt and less solar radiation occurred at the latitude of the Owens River watershed (e.g., Wanner et al., 2008; Tables 6 and 7).

Glacial landforms are useful measures of paleotemperature because they preserve the physical record of the hydroclimatic process directly associated with snow accumulation and melt. Uncertainty in paleotemperature estimates from glacial landforms is low compared to biological proxy data, such as tree-rings and pollen for air temperature and planktonic foraminifera for sea surface temperature, because they are not influenced by antecedent environmental conditions (e.g., Clark et al., 1999). The minimum late Holocene cooling of -1.16°C during the Little Ice Age shown in the adjusted mean global temperature anomaly dataset used in paleoclimate simulations in

this study (Figure 23A) is similar in magnitude to the zonal mean temperature anomaly for the 90°N to 30°N latitude bands at this time from multi-proxy records (Marcott et al., 2013). Also, the relatively low temperatures of the adjusted mean global dataset for the early to middle Holocene are generally similar to the magnitude of simulated global surface temperatures from paleoclimate models (Liu et al., 2014), as well as a temperature reconstruction from multi-proxy datasets from mid-latitude regions of North America (e.g., Wanner et al., 2008; Shuman and Marsicek, 2016). These relations indicate the approach used to adjust the mean global temperature anomaly data by integrating ELA estimates and glacial chronology of the Sierra Nevada share common traits to other land- and marine-based proxy records and global climate models.

8.2. Paleoclimate Simulation from 11.5–0 ka

The calibrated Owens River-Lake hydrologic model was used to infer paleoclimate conditions required to match geologically determined control points from lake-level and glacial records. The downstream watersheds of China and Searles Lake basins were also included in paleoclimate simulations, which increased the model domain to 20,898 grid cells and created a fully integrated watershed-lake hydrologic model of the paleo-Owens River system. Paleoclimate simulations for the period 11.5–0 ka were performed at 100-yr time steps using adjusted 800-meter PRISM historical climate data. The adjustment of modern climate baseline data was used to place paleoclimate simulations within a historical (WY1896–2015) context. As previously mentioned, modern baseline temperature was adjusted during simulations by adding a uniform temperature anomaly from the adjusted global mean paleotemperature dataset to gridded

data (e.g., Figure 23A). Modern baseline precipitation was also adjusted by iterating a uniform multiplier to gridded data until target lake levels were achieved. Furthermore, changes in the Earth's axial tilt and monthly solar insolation were also accounted for by adjusting latitude and solar radiation values relative to fraction of present-day during each time step (e.g., Tables 6 and 7). Simulations span the majority of the Holocene Series/Epoch, a time interval from 11.7 ka to present day. The Holocene is subdivided into three sub-series/sub-epochs based on global-scale natural climatic/environmental events that are clearly defined in ice-core, marine, and terrestrial records (Mayewski et al., 2004; Walker et al., 2012). The subdivisions of the Holocene include the early Holocene (11.7–8.2 ka), middle Holocene (8.2–4.2 ka), and late Holocene (4.2 ka to present day) (Walker et al., 2012).

8.3. Early Holocene (11.5–8.2 ka)

8.3.1. Lake-Level Simulation

The simulation of lakes in the paleo-Owens River system shows large changes in the magnitude of water levels and snowpack from 11.5–8.2 ka (Figures 24 and 25A). Owens Lake had two major oscillations in lake level during the early Holocene with highstands centered at 10.9 and 8.4 ka, and a sustained lowstand from 10.4–9.2 ka (Figure 22A). The simulation of precipitation during the early Holocene to sustain Owens Lake water depths of ~17–45 m ranges from 109–159% of historical baseline with a mean of 127% (Figure 25B). Owens Lake had two episodes of mostly overflowing lake conditions at highstand water levels for ~400–600 years with freshwater conditions ($Salt_f$ = 0.930) that supported shallow and saline ($Salt_f$ = 0.829) downstream lakes (Table 5;

Figure 22A). Simulation of downstream lakes during overflow episodes yields an average water depth of ~1 m for a spilling China Lake and an average depth of ~5 m and maximum depth of up to ~14 m for Searles Lake (Figure 24). Water depths during simulations with no overflow from Owens Lake are much less, averaging ~1 m with maximum depths of 1–7 m for both China and Searles Lakes (Figure 24). The corresponding elevations of ~496 and 504 m from simulated maximum water depths of Searles Lake are similar to the elevations of strandlines at ~496 and 505 m adjacent to the margins of Searles playa (Figures 22C and 24C). The geomorphic evidence provides an independent control point to validate the accuracy of the early Holocene simulation. The maximum range in simulated water levels of Searles Lake also demonstrates the importance of overflow contributions from both Owens and China Lakes even when the watersheds of Indian Wells and Searles Valleys independently experience 3300 years of precipitation ~110–160% of historical baseline.

8.3.2. Snowpack Simulation

Simulation of snowpack in the Owens River model domain during the early Holocene shows a decrease in SWE storage that closely corresponds with an overall warming trend with temperature anomalies ranging from -1.5°C to 0.25°C (Figure 25A). The volume of SWE storage in equilibrium at the start of the simulation is about 52% less than the equivalent SWE storage for the Recess Peak glaciation and about 22% greater than the equivalent SWE storage for the Matthes glaciation during the Little Ice Age based on mean ELA estimates (Table 1 and Figure 25A). The snowpack reconstruction shows hydroclimatic conditions were sufficient to support two short periods of snowpack

expansion. Snowpack expansion at 10.9 ka was simulated with precipitation 151% of historical baseline and a temperature anomaly of -0.32°C and the expansion at 8.4 ka was simulated with precipitation 159% of historical baseline and temperature anomaly of 0.14°C that both coincided with transgressions of Owens Lake (Figure 25A). The two peaks of snowpack expansion during the early Holocene reached levels less than the extent of snowpack during the Little Ice Age, but mean snowpack centered at 8.4 ka is nearly the same as present day (Figure 25A).

8.3.3. Hydrologic Response to Orbital Forcing

The simulation of precipitation ~110–160% of historical baseline required to offset open-water evaporation and sustain deep and overflowing Owens Lake water levels was not enough to support extensive glaciers and perennial snowfields during the early Holocene. The effects of orbital forcing during the early Holocene played a major role in reducing the extent of snowpack in the Sierra Nevada and contributing to Recess Peak deglaciation, thereby effecting the hydrologic balance of the watershed-lake system. Even though the amount of total annual solar insolation within the model domain decreased 0.45% during the early Holocene simulation, the Earth's obliquity peaked from ~10–9 ka that produced conditions equivalent to a southerly latitudinal shift of ~0.78° compared to present day. The early Holocene was a period with strong seasonality reflected by minimum solar insolation during the winter (December, January, February) up to ~10% lower than present day and maximum during the summer (June, July, and August) up to 8.4% greater than present day (Tables 6 and 7). Simulation of the orbital changes coupled with a long-term warming trend produces summer conditions favorable

for melting glacier ice and large seasonal snowpacks that accumulated during the winter, even with precipitation ~110–160% of historical baseline.

The highest Owens Lake water levels on record were in the early Holocene. The ~8 m transgression of Owens Lake from 11.5–9.0 ka is controlled by an increase in precipitation of up to ~25% and a rapid increase of ~1.7°C from negative to positive temperature anomalies by the end of the period (Figure 25). This highstand was followed by ~15 m regression to a sustained lowstand from ~10.4–9.2 ka that is controlled by a decrease in precipitation of up to ~40% and a change to positive temperature anomalies after 10.5 ka. The period of sustained lowstands controlled by precipitation ~110% of historical baseline and positive temperature anomalies is also reflected in pollen records in sediment core OL-84B indicating a modern vegetation assemblage in Owens Valley at this time (Mensing, 2001). The lowstand was followed by a return to wetter conditions from 9.1–8.4 ka with a 50% increase in precipitation up to ~160% of historical baseline that coincided with a short cooling trend of positive temperature anomalies that is reflected by a major ~27 m transgression to highstand and overflowing water levels (Figures 24 and 25).

8.3.4. Hydrologic Response to Hydroclimate Variability

Although it is beyond the scope of this dissertation to perform a thorough analysis of the forcing mechanisms that drive changes in atmospheric circulation patterns in the region, I do provide a general review of the notable factors that likely controlled Holocene hydroclimate variability to place the modeling results into a regional- to global-scale context. Present-day interannual hydroclimate variability in the southwestern U.S.

is linked to decadal scale changes of sea-surface temperatures (SST) (the Pacific Decadal Oscillation, or PDO), in the form of prolonged dry and wet episodes (Mantua and Hare, 2002). Increases in SST and pressure gradients across the Pacific Ocean promote an El Niño-Southern Oscillation (ENSO) climatic pattern that is commonly reflected in the western U.S. as wetter winters and springs associated with southerly shifts in north Pacific frontal storm tracks (El Niño pattern), whereas decreases in SST and pressure gradients typically produces dryer winter and springs from northerly shifts in frontal storm tracks (La Niña pattern) (e.g., Dettinger et al., 1995; Cayan et el., 1999). Paleohydrologic studies in the western U.S. have also correlated the age of late Pleistocene lake-level fluctuations to changes in North Atlantic climatic phases to infer atmospheric climate patterns (e.g., Benson et al., 1997; Munroe and Laabs, 2013). The North Atlantic climatic phases were reflected by periods of high-frequency warm air and SST referred to as Dansgaard–Oeschger cycles that were followed by relatively cold phases that expanded the Laurentide Ice Sheet and influenced the discharge of icebergs to float further to the south, known as Hienrich events (e.g., Heinrich, 1988; Bond et al., 1992; Dansgaard et al., 2013; Hemming, 20014). Shoreline and speleothem records in the southwestern U.S. and majority of the Great Basin demonstrate during the last deglaciation wetter conditions in the region were coincident with cool periods in the North Atlantic and drier conditions coincident with warm periods (e.g., Asmerom et al., 2010; Munroe and Laabs, 2011; Oster et al., 2015).

The large hydrologic change in the Owens watershed-lake system from 9.1–8.4 ka with an increase in precipitation patterns coincided with a period of global-scale rapid climate change between 9 and 8 ka (Mayewski et al., 2004) (Figure 25B). The highstand

of Owens Lake centered at ~8.4 ka is also coincident with a cooling event at ~8.4–8.0 ka identified in Greenland ice-core proxies (e.g., Alley et al., 1997), thereby demonstrating a potential link between cool conditions in the North Atlantic and wet conditions in the western U.S. during the early Holocene. A wet early Holocene in the southwestern U.S. has also been attributed to a period of enhanced winter sub-Tropical moisture flux across the region related to strengthening of ENSO and atmospheric river climatic patterns driven by variations in equatorial Pacific SST (e.g., Enzel et al., 1989, 2003; Antinao and McDonald, 2013; Kirby et al., 2015). This enhanced atmospheric circulation pattern in the western U.S. may have in part been controlled by the southerly deflection of winter storm tracks by the early Holocene position and topography of the Laurentide Ice Sheet over Hudson Bay that would have focused precipitation into the Great Basin (Steponaitis et al., 2015). Although the early-middle Holocene orbital configuration favors a minimum in ENSO variance because of a more northerly position of the Northern Hemisphere summer position of the Intertropical Convergence Zone (ITCZ) (e.g., Braconnot et al., 2011), the freshwater fluxes from the melting of the Laurentide Ice Sheet into the North Atlantic Ocean during the early Holocene could have offset this orbital control, leading to near-modern ENSO variance and wetter conditions in the southwestern U.S. at this time (Steponaitis et al., 2015).

8.4. Middle Holocene (8.2–4.2 ka)

8.4.1. Lake-Level Simulation

The simulation of lakes during the middle Holocene shows a single rapid and extreme oscillation in hydrologic balance in the paleo-Owens River system (Figures 24

and 25A). The extreme change is reflected by sustained overflowing water levels of Owens Lake during the period from 8.2–6.4 ka and sustained low to near desiccation water levels from 6.4–4.2 ka (Figure 22A). The simulation of precipitation to match two minor oscillations of highstand water levels with freshwater lake conditions from 8.2–6.4 ka ranges from 139 to 158% of historical baseline. During this period, Owens Lake had mostly overflowing lake conditions for ~1800 years that supported shallow downstream lakes up to 6.4 ka (Figure 22). Simulation of downstream lakes during overflow episodes yields an average water depth of ~1 m for a spilling China Lake and an average depth of ~5 m and maximum depth of up to ~14 m for Searles Lake (Figure 24).

The simulation of precipitation from 6.4–4.2 ka to match a major regression to sustained lowstand water levels requires a ~74% decrease in precipitation to ~74–77% of historical baseline (Figure 25B). Water depths of downstream lakes during simulations with no overflow from Owens Lake after 6.4 ka average ~1 m for both China and Searles Lakes and up to ~5 m for Searles Lake (Figure 24). The simulated maximum water depths of Searles Lake from 8.2–6.4 ka with corresponding elevations of ~495 and 503 m are similar to levels reached during the early Holocene that also correspond well with the elevations of strandlines at ~496 and 505 m based on geomorphic evidence (Figures 22C and 24C).

8.4.2. Snowpack Simulation

Simulation of snowpack in the Owens River model domain during the middle Holocene shows both rapid and extreme variations influenced by changes in precipitation from ~152 to 74% of historical baseline coupled with mostly positive but decreasing

temperature anomalies from 0.31 to -0.01°C (Figure 25). The snowpack reconstruction shows hydroclimatic conditions were sufficient to support a relatively continuous snowpack from 8.2–6.4 ka that was sustained at volumes nearly the same as present day (Figure 25A). The magnitude of snowpack storage from 6.4–4.2 ka, however, was controlled by simulated precipitation 74–89% of historical baseline. Persistent below normal precipitation for 1400 years coupled with mostly positive temperature anomalies produces the lowest amount of snowpack during the entire Holocene that is ~56% less than present day (Figure 25A).

8.4.3. Hydrologic Response to Orbital Forcing

Glaciers from the mid- to high latitudes in the Northern Hemisphere were reduced in extent in the early to middle Holocene due to elevated summer solar insolation during this time (Wanner et al., 2008). The amount of simulated glacial ice and perennial snow in the Sierra Nevada from 8.2–6.4 ka was similar to present day, however, the effects of orbital forcing and positive temperature anomalies played a major role in reducing the extent of snowpack, even with simulated precipitation 139–158% of historical baseline that supported a deep and overflowing Owens Lake. Strong seasonality was slightly changing at this time where solar insolation during the winter was slightly increasing (December, January, February), but 6.0–8.6% lower than present day, and maximum solar insolation during the summer was slightly decreasing (June, July, August), but at values of 4.1–7.7% greater than present day (Tables 6 and 7).

The highest and lowest water levels of Owens Lake were during the middle Holocene from 6.4–5.7 ka. The major ~40 m regression in Owens Lake water levels was

driven by a ~74% decrease in precipitation and positive temperature anomalies over a 700-year period (Figures 24 and 25). Although the effects of orbital forcing together with positive temperature anomalies were steadily decreasing after ~6.4 ka, a rapid change to persistent drought conditions with precipitation 74–89% of historical baseline effected the hydrologic balance of the watershed-lake system by producing shallow to near desiccation water levels of Owens Lake and reducing the extent of snowpack well below present day.

8.4.4. Hydrologic Response to Hydroclimate Variability

The mostly low water levels of Owens Lake with depths of up to ~5 m from 5.7–4.3 ka occurred during the broadly recognized mid-Holocene Warm Period (e.g., Bartlein et al., 2011) and coincided with a period of global-scale rapid climate change between 6 and 5 ka (Mayewski et al., 2004) (Figure 25B). At the global scale, orbital forcing during the middle Holocene influenced large scale atmospheric patterns in the Northern Hemisphere, even with slow and steady reductions in summer solar insolation over the period. The redistribution of solar energy during the middle Holocene caused a progressive southward shift of the Northern Hemisphere summer position of the ITCZ, thereby by weakening the ENSO atmospheric pattern and causing persistent La Niña conditions and summer aridity in the western U.S. (e.g., Clement et al., 2000; Diffenbaugh et al., 2006; Wanner et al., 2008). A lack of significant ice cover in North America resulting in no meltwater discharge after 8 ka may have permitted the middle Holocene orbital forcing to drive a minimum in ENSO variance and produce dry conditions in the Great Basin (Steponaitis et al., 2015). The reconstruction of reduced

precipitation and snowpack in the Owens watershed-lake system during the middle Holocene provides quantified estimates of the combined effects of global- to watershed-scale orbital forcing, plus changing atmospheric climate patterns in controlling the hydrologic balance of the watershed-lake system.

8.5. Late Holocene (4.2 ka to present day)

8.5.1. Lake-Level Simulation

The simulation of lakes in the paleo-Owens River hydrologic model shows many rapid and extreme changes in the hydrologic balance of the watershed-lake system during the late Holocene (Figures 24 and 25A). During the period from 4.1–2.4 ka, Owens Lake had mostly sustained lowstands, whereas water levels from 2.4 ka to present day were also low but reflected as mostly high frequency (100-year) fluctuations (Figure 22A). The simulation of precipitation from 4.1–2.4 ka to match sustained shallow water depths of ~7–8 m ranges from 90.8 to 92.3% of historical baseline. During this same period, two minor transgressions in water level occurred at 4.1 and 3.0 ka, and a major late Holocene transgression at 3.6 ka (Figure 24A). Simulation of precipitation during the three transgressions with water depths of ~13–24 m ranges from 100.3 to 111.6% of historical baseline (Figure 25B). In contrast, the simulation of precipitation from 2.3 ka to 0.2 ka to match relatively short duration lowstand water levels with depths of ~6–8 m ranges from 82.4 to 90.2% of historical baseline (Figure 25B). During this same period, seven minor transgressions occurred, and two notable highstands at 0.8 and 0.3 ka (Figure 24A). Simulation of precipitation for the nine transgressions from 2.3 ka to 0.3 ka with water depths of ~14–20 m ranges from 98.0 to 104.7% of historical baseline (Figure 25B).

Simulation of downstream lakes with no overflow contributions from Owens Lake during the late Holocene yields average water depths of ~1 m for a spilling China Lake prior to 2.2 ka and maximum depths up to 3–4 m after 2.2 ka during non-overflowing conditions (Figure 24B). Searles Lake has average water depths of ~1 m and maximum depths of ~5–6 m when China Lake is spilling and average water depths of ~0.5 m and maximum depths of 2–3 m when China Lake ceases to overflow (Figure 24). The simulated maximum water depth of Searles Lake during the late Holocene with corresponding elevations of ~492 and 495–496 m is similar to elevations of the modern playa and the lowest strandline at ~496 m based on geomorphic evidence (Figures 22C and 24C).

8.5.2. Snowpack Simulation

Simulation of snowpack in the Owens River model domain shows both an increase during the early part of the late Holocene and major expansion throughout the latter half of the period (Figure 25). An increase of simulated SWE storage from 4.1–2.4 ka is predominately influenced by a steady decrease in negative temperature anomalies ranging from -0.08 to -0.38°C with precipitation at mostly 90.8–92.3% of historical baseline. Simulation of snowpack from 2.4–0.9 ka shows a peak in SWE storage followed by a slight decrease with minor variations driven by a short increase in negative temperature anomalies and changes in precipitation 89.4–100.9% of historical baseline. Mean snowpack from 2.4–0.9 ka reaches volumes of 70–75% of present day extent (Figure 25A).

Initial simulations of SWE storage beginning at 0.8 ka resulted in insufficient accumulation of SWE storage to match the Little Ice Age maximum (6.5×10^8 m^3) by 0.3 ka (Figure 25A). The hydroclimate and orbital forcing boundary conditions of precipitation, temperature anomaly, and solar insolation were controlled by independent records. As a result, snow albedo was the only parameter in the hydrologic model changed to simulate SWE storage during the Little Ice Age to best match geologic evidence. A change in albedo value from 0.55 to 0.65 was required to simulate glacial conditions with relatively fresh snow surfaces, thereby increasing the reflectance of incoming solar radiation by 15% and decreasing snowmelt in areas above the seasonal ELA (Table 5). The change to a higher albedo coincides with temperature anomalies that are less than -1°C, as well as increases the volume of simulated mean SWE storage to within 1.2% of the estimated Little Ice Age maximum from geological evidence (Figure 25A).

Simulation of SWE storage during the Little Ice Age shows a greater than 200% increase in snowpack over a 600-year period from 0.8 to 0.3 ka (Figure 25A). A major expansion in snowpack at the beginning of the glacial advance at 0.8 ka is driven by an increase in precipitation 104.7% of historical baseline and a decrease in temperature anomaly of -1.02°C. A steady increase in SWE storage from 0.7 to 0.4 ka is driven by variable precipitation 87.1–98.0% of historical baseline and continued decrease in temperature anomalies from -1.06 to -1.14°C. The culmination of simulated mean SWE storage of 6.42×10^8 m^3 coinciding with the maximum extent of Matthes glaciers is reached with precipitation 102.5% of historical baseline and a middle-late Holocene minimum temperature anomaly of -1.16°C (Figure 25). Simulation of periods after the

Little Ice Age shows major variations in precipitation reaching a Holocene minimum of 82.4% of historical baseline at 0.2 ka followed by precipitation 100% of historical baseline at 0.1 ka with a slight increase in temperature anomalies from -1.13 to -1.08°C, respectively. A major decrease in mean SWE storage during present day of ~33% from the Little Ice Age maximum is driven by a rise in temperature anomaly of ~1°C, precipitation 100% of historical baseline, and a decrease in snow albedo to 0.55 for interglacial conditions. The ~33% decrease in simulated mean SWE storage from 0.1 ka to present day parallels the measured 55% decrease in glacier area within the Owens River watershed between 1903 and 2004 (Basagic and Fountain, 2011).

8.5.3. Hydrologic Response to Orbital Forcing

The late Holocene SWE storage reconstruction shows hydroclimatic conditions were sufficient to support a steady increase of snowpack from 4.2–0.9 ka and a peak in expansion of snowpack during the Little Ice Age maximum by 0.3 ka. The expansion of the snowpack from 4.2–0.3 ka was controlled by negative temperature anomalies despite a mean precipitation 94% of historical baseline over this period which was reflected by mostly persistent periods with high-frequency fluctuations of low Owens Lake water levels. Seasonality during the late Holocene was generally similar to present day where solar insolation during the winter was up to 2.1% less than present and maximum solar insolation during the summer was up to 2.1% greater than present day, but annual solar insolation was at a Holocene minimum, about 0.07% less than present day (Tables 6 and 7). Although the effects of mostly below normal precipitation produced highly variable and low water levels of Owens Lake, the continuous negative temperature anomalies

ranging from -0.08°C to -1.16°C together with a decreasing trend to minimum annual solar insolation collectively were sufficient to reduce high elevation snowmelt and promote a minor glacial advance in south-eastern Sierra Nevada during the Little Ice Age.

8.5.4. Hydrologic Response to Hydroclimate Variability

Many studies in the western U.S. have used lake-level and multiproxy records from the Great Basin to infer the timing of droughts across the region because there is a rich record of paleoclimate change for the late Holocene (e.g., Benson et al., 2002; Mensing et al., 2008, 2013; Cook et al., 2010). Other studies have also performed paleo-hydrological modeling along the north-central Sierra Nevada of megadrought climatic conditions to reconstruct precipitation (e.g., Graham and Hughes, 2007; Kleppe et al., 2011; Hatchett et al., 2015) and to identify potential storm track activity and moisture transport in the central Sierra Nevada during the late Holocene (e.g., Hatchett et al., 2016; 2018) that commonly use tree-ring proxy records for information on the magnitude of either precipitation or temperature or both. The hydrologic modeling of the Owens watershed-lake system of this dissertation was performed to produce a continuous reconstruction of coupled lake-level and snowpack to provide high-resolution estimates of the duration and magnitude of hydroclimate change in the region. A lack of input data from tree-ring records in paleoclimate simulations provides estimates of late Holocene hydroclimate variability for the region that are not directly biased by biological archives, which commonly have an inherent environmental uncertainties and relatively poor correlations to historical precipitation and moderate correlations to temperature (e.g., Salzer et al., 2009; Tolwinski-Ward et al., 2015; Tran et al., 2017).

The lake-level record of Owens Lake shows predominately low water levels that were ~4–11 m below the historical maximum in 1872–1878 during the majority (~75%) of the late Holocene (Figure 22A). The lowstands from 4.1–2.4 ka are controlled by extended 400–600-year periods with simulated precipitation ranging from 90.8 to 92.3% of historical baseline and a steady decrease in temperature anomalies from -0.08 to - 0.38°C that are interrupted by three short periods with precipitation of at least 100% of historical baseline. The period of mostly cool and persistent drought conditions with lowstands from 4.1–2.4 ka coincided with two periods of global-scale rapid climate change from 4.2–3.8 ka and 3.5–2.5 ka (Mayewski et al., 2004) (Figure 25B). An additional 300-year period of sustained lowstands from 1.9–1.7 ka is controlled by simulated precipitation ~90% of historical baseline and a short drop in temperature anomalies of -0.44 to -0.48°C. This period of drought in the Owens River watershed coincided with the end of extended drought across the central Great Basin from 2.8–1.85 ka inferred primarily from pollen records and referred to as the Late Holocene Dry Period (Mensing et al., 2013). Persistent drought in the Owens River watershed was terminated from 1.7–1.2 ka by a precipitation pattern consisting of 100-year changes in simulation of precipitation between ~90 and 100% of historical baseline and negative temperature anomalies that controlled high-frequency oscillations in lake level over a 500-year period (Figures 24A and 25B).

A return to sustained low lake levels during two periods at 1.1–0.9 and 0.7–0.6 ka is controlled by mean precipitation ~90 and 88% of historical baseline, respectively (Figure 25B). The low lake levels of Owens Lake from 1.1–0.9 ka occurred during the first episode of extreme and persistent drought during the Medieval Climatic Anomaly

(MCA-1 or Stine #1) identified in the south-central Sierra Nevada and western U.S. (e.g., Stine, 1994; Cook et al., 2010). Similarly, the later period of low lake levels from 0.7–0.6 ka that followed a short interpluvial period occurred during the second episode of extreme and persistent drought during the MCA-2 or Stine #2. An ~0.57°C drop in negative temperature anomaly from -0.45 to -1.02°C defines a major hydroclimatic change between 0.9 and 0.8 ka near the beginning of the MCA-1. A rapid change to precipitation ~90% of historical baseline and ~0.57°C drop in temperature anomaly in the Owens River watershed coincided with a short period of global-scale rapid climate change between 1.2 and 1.0 ka defining the beginning of the MCA (Mayewski et al., 2004) (Figure 25B).

The sustained lowstands of Owens Lake between ~1.1 and 0.6 ka controlled by simulated precipitation 88–90% of historical baseline and temperature anomalies of around -1°C provides insight to the range of hydroclimatic conditions in the south-eastern Sierra Nevada during the MCA that produced severe and persistent multidecadal to multicentennial droughts (i.e., megadroughts) documented in other parts of the western Great Basin from lake-level, pollen, and tree-ring records (e.g., Stine, 1990,1994; Benson et al., 2002; Mensing et al., 2008, 2013; Cook et al., 2004, 2010; Swetnam et al., 2009). Many of the multiproxy records, such as tree rings, used to infer hydroclimate conditions in the western Great Basin during the MCA are typically more sensitive to changes in effective moisture than temperature (e.g., Cook et al., 2010), whereas pollen records are typically more sensitive to temperature variations (e.g., Mensing et al., 2008, 2013). As a result, many studies of megadroughts during the MCA in the western U.S. have inferred that aridity at this time was primarily related to warm and dry hydroclimatic conditions

that controlled soil moisture variability and evaporative demand (e.g., Swetnam et al., 2009; Cook et al., 2016). Although the period of the MCA-1 is known as the Medieval Warm Period in Europe, global-scale comparisons of paleoclimatic data indicate it was not a uniformly warm period across the planet (Hughes and Diaz 1994; Bradley et al., 2003). The simulation of lake levels and snowpack in the Owens watershed-lake system from 0.8–0.3 ka suggests it was both relatively drier and cooler during the MCA compared to present day with temperature anomalies of about -1°C required to support a major expansion in snowpack during the Medieval Pluvial and the beginning of the Little Ice Age. This relatively cool period in the south-eastern Sierra Nevada with a steady expansion of snowpack has temporal correspondence with other glacial records in Europe that show up to four episodes of glacier advances centered at ~0.72, 0.57, 0.37, and 0.17 ka during the MCA-2 in the Sierra Nevada (e.g., Wanner et al., 2008).

The last period of low lake levels of Owens Lake occurred at 0.2 ka with a simulated mean drop in lake level of ~11.9 m from the Little Ice Age highstand at 0.3 ka (Figure 24A). Simulation of the 0.2 ka lowstand is controlled by precipitation 82% of historical baseline which is lower than the entire MCA and a minimum since 4.2 ka (Figure 25).

The remaining 25% of the Owens Lake record during the late Holocene was characterized by eleven transgressions in lake level that reached to within ~1 m and up to ~12 m above the historical maximum in 1872–1878 at an elevation of ~1096 m (Figure 24A). Four of the late Holocene transgressions coincided with above normal precipitation and periods of global-scale climate change. The first transgression from 4.3–4.1 ka occurred over a 200-year period with a mean rise in simulated lake level of

10.9 ± 3.7 m to an elevation of ~1098 m (Figure 24A). Simulation of the 4.1 ka highstand is controlled by precipitation 103.3% of historical baseline and -0.08°C temperature anomaly. The change in hydroclimate at this time began an overall expansion of snowpack and termination of the severe and persistent drought during the mid-Holocene Warm Period (Figure 25).

The second transgression at 3.6 ka occurred over a 100-year period with a mean rise in simulated lake level of 15.5 ± 3.9 m to an elevation of ~1108 m (Figure 24A). Simulation of the 3.6 ka highstand is controlled by precipitation 111.6% of historical baseline and -0.19°C temperature anomaly (Figure 25). The simulation in hydroclimate produced a minor expansion in snowpack and a late Holocene highstand with a water depth of ~24 m. Around this time, alpine lakes and rock glaciers expanded in the south-central Sierra Nevada that were previously inferred to be associated with wetter conditions commonly referred to as the Neopluvial (or Neoglacial) (e.g., Stine, 1990; 1994; Konrad and Clark, 1998; Bowerman and Clark, 2011; Street et al., 2012; 2013).

The third transgression at 0.8 ka occurred over a 100-year period with a mean rise in simulated lake level of 11.9 ± 3.7 m to an elevation of ~1104 m (Figure 24A). Simulation of the 0.8 ka highstand is controlled by precipitation 104.7% of historical baseline and -1.02°C temperature anomaly (Figure 25). The simulation in hydroclimate produces ~40% increase in snowpack and the second highest lake level with a water depth of ~21 m. Around this time, other areas in the western Great Basin also had a major wet interval during the MCA, known as the Intervening Pluvial (Cook et al., 2010) or Medieval Pluvial (Adams et al., 2015; Hatchett et al., 2015). The bristlecone pine tree-ring chronologies in the White Mountains support a short period of extreme hydroclimate

variability at this time with a 10–49 year wet and anomalously cold interval centered at ~840 cal yr B.P. (Leavitt, 1994; Hughes and Graumlich, 1996; Cook et al., 2010; Bale et al., 2011; Salzer et al., 2014).

The fourth and last notable transgression at 0.3 ka occurred over a 100-year period with a mean rise in simulated lake level of 10.2 ± 3.7 m to an elevation of ~1102 m (Figure 24A). Simulation of the 0.3 ka highstand is controlled by precipitation 102.5% of historical baseline and a middle-late Holocene minimum temperature anomaly of - 1.16°C (Figure 25). The simulated hydroclimate produces the maximum extent of snowpack and the third highest lake level with a water depth of ~19 m. This period generally corresponds to a time of glacier advance in the south-central Sierra Nevada and across North America during the Little Ice Age (e.g., Bowerman and Clark, 2011; Solomina et al., 2016) that also coincided with a period of rapid global-scale climate change from 0.6–0.15 ka (Figure 25).

A rapid increase in simulated precipitation from 82.4% to 100% of historical baseline from 0.1 ka to present day coupled with an increase in temperature anomalies from -1.08 to 0°C produces lake levels with average elevations of 1096.0 m, ranging from 1090.0 to 1100.2 m (Figures 24 and 25). The average lake level simulated over the last two 100-year periods is similar to the historical maximum water levels of ~1096 m measured in 1856 and 1872–1878 (Lee, 1915), as well as several minor transgressions of Owens Lake centered at WY1916, 1943, 1983–1985, 1998, and 2006 in the calibrated Owens watershed-lake hydrologic model that coincide with the 20th century North American pluvial from 1905–1917 (Cook et al., 2011) and later times with moderate to

strong ENSO activity (e.g., Redmond and Koch, 1991; McCabe and Dettinger, 2002) (Figure 21).

Although the increase in temperatures associated with the end of the Little Ice Age and beginning of anthropogenic forcing reduces the extent of glaciers and perennial snowfields in the Sierra Nevada, the historical water levels of Owens Lake are sustained at relatively high levels compared to most of the record since 5.8 ka (Figure 24). The pattern of hydroclimate over the last 0.8 ka is characterized by mean precipitation 94.4% of historical baseline during most of the MCA and Little Ice Age. This implies that the overall decrease in the extent of modeled snowpack over the last ~200 years is primarily associated with a sharp increase in temperature and not with a reduction in precipitation during the historical period (Figure 25).

The frequency and intensity of ENSO variability increased from the middle to late Holocene, promoting a shift from dryer to wetter conditions in the southwestern U.S., based on climate model results that are corroborated by marine and terrestrial proxy records (e.g., Liu et al., 2000). A steady change in ENSO activity since the middle Holocene was mainly driven by orbital forcing where steady decreases in Northern Hemisphere solar insolation continued to influence the southerly shift of the ITCZ that in turn increased the zonal SST contrast between the equatorial western Pacific warm pool and the equatorial eastern Pacific cold tongue, a pattern that is similar to present day (e.g., An et al., 2018). Much attention has been focused on understanding the drivers that control persistent droughts and pluvials over western North America during the late Holocene and the Common era by performing climate modeling of tropical forcing with internal atmospheric variability and SST, as well as accounting for land surface and dust

aerosol feedbacks (e.g., Ault et al., 2014; Seager et al., 2005, 2014; Cook et al., 2016; Routson et al., 2016). Although global-scale orbital forcing has been shown to have controlled the overall strength of ENSO activity during the late Holocene, other climate drivers including solar and volcanic forcings have also contributed to influencing the timing and duration of major periods of rapid climate change during the last 4200 years (e.g., Wanner et al., 2008).

Solar forcing caused by changes in the radiation emitted from the Sun produces subtle changes that can either increase or decrease solar insolation over centennial time scales (e.g., Lean et al., 1995). Volcanic forcing from large eruptions can also reduce solar insolation and cool the Earth's surface from the absorption of incoming solar radiation by volcanic aerosols in the troposphere and stratosphere (e.g., Zielinski, 2000). Periods of coeval solar activity minima and volcanic eruptions combined with lower summer solar insolation commonly have good temporal correspondence with minor glacial advances since ~3.0 ka, including the globally recognized Holocene glacial maximum during the Little Ice Age (e.g., Wanner et al., 2008). In contrast to cold periods, past megadroughts in the southwest U.S., such as during the MCA, were likely driven by unusually frequent and cold central tropical Pacific SST excursions in conjunction with anomalously warm Atlantic SSTs and solar activity maxima that collectively weakened ENSO activity and produced a dryer climate in the southwestern U.S. (Steiger et al., 2019). Furthermore, volcanic forcings have also been shown to have favored the occurrence of a moderate-to-strong El Niño event amid persistent La Niña–like conditions induced by increased solar activity during the MCA (Emile-Geay et al., 2008). The occurrence of coeval solar and volcanic forcing events appear to have played

a large role in modulating past ENSO activity during the late Holocene, thereby influencing a higher propensity of wetter and cooler conditions in the southwest U.S. at this time. The paleohydrologic modeling of the Owens watershed-lake system provides high-resolution estimates on the timing, duration, and magnitude of hydroclimate variations that can be used to provide better insight on the patterns of climate change and ENSO activity during the late Holocene.

9. SUMMARY AND CONCLUSIONS

A 11,500-year time-series of reconstructed changes in precipitation and snowpack was produced from a calibrated watershed-lake water balance model of the paleo-Owens River-Lake system. The paleohydrologic model is principally controlled by continuous water-level records from Owens Lake. The continuous lake-level record of Owens Lake afforded the simulation of periods with both high and low water levels at a high resolution that differs with previous paleoclimate hydrologic models for the region. The watershed-lake water balance model also differs from most other paleoclimate hydrologic models by: (1) using a mean global paleotemperature dataset that is adjusted to correspond with local paleotemperature depression estimates from glacial deposits in the watershed; (2) accounting for changes in paleo-solar insolation driven by Milankovitch cycles; (3) including a glacial ice/perennial snow accumulation component based on modeling paleo-ELAs; (4) accounting for changes in salinity of paleolake water to suppress evaporation; and (5) accounting for surface runoff gains and losses based on an 81-year record of observed data.

The paleoclimate simulation for the period 11.5–0 ka was performed at 100-yr time steps using adjusted 800-meter PRISM historical climate data for the period WY1896–2015. The historical climate data was used so that interannual to decadal hydroclimate variability was captured, as well as to place paleoclimate simulations within a historical context. The historical dataset used to simulate paleohydroclimate consisted of precipitation that was below the 120-year mean about 55% of the record, as well as a steady increase in alpine temperatures of 1.0–1.5ºC from 1980–2015. The variability in the climate data enabled a realistic simulation of hydroclimate as oppose to using a range of probabilistic precipitation and temperature scenarios for the Holocene. The overall trend of higher precipitation variability and increased temperatures towards the latter part of the historical record produced cyclic changes from wetter and cooler to dryer and warmer that is considered representative of a signal of climate change over centennial scales. Although the historical data includes a strong signal of anthropogenic forcing in the latter half of the record, the adjustment of temperature input based on local glacial deposits along with accounting for changes in solar insolation from orbital forcing dampens the signal.

The calibrated watershed-lake hydrologic model was used to simulate paleoclimate conditions required to match geologically determined control points from lake-level and glacial records. The simulation of hydroclimate of the south-eastern Sierra Nevada during the Holocene is summarized by:

- The early Holocene simulation of lakes shows large changes in hydroclimate with precipitation ranging from 109 to 159% of historical baseline with temperature

anomalies ranging from -1.5°C to 0.25°C. Millennial-scale changes in precipitation and temperature over the period produces a broad range in snowpack extent compared to present day from ~200% at 11.5 ka during Recess Peak deglaciation to 65% from 10.5–8.9 ka to 100% by 8.2 ka.

- The middle Holocene simulation of lakes shows extreme changes in hydroclimate with precipitation ranging from ~139–158% of historical baseline from 8.2–6.4 ka to precipitation ~74–77% of historical baseline from 6.4–4.2 ka along with mostly positive temperature anomalies ranging from -0.01 to 0.31°C. The hydroclimatic conditions are sufficient to support continuous snowpack nearly the same as present day from 8.2–6.4 ka, but persistent and below historical baseline precipitation from 6.4–4.2 ka during the mid-Holocene Warm Period produces the lowest alpine snowpack during the Holocene that is ~56% less than present day, a result that provides perspective on future projections of declining seasonal snowpack in the Sierra Nevada driven by a warming climate (e.g., Pierce and Cayan, 2013).

- The late Holocene simulation of lakes shows hydroclimate variability in the form of an early period from 4.1–2.4 ka with persistent droughts (400–600-year) and short wet intervals (100-year) with changes in precipitation ~91–112% of historical baseline, and a later period from 2.4 ka to present day with higher frequency changes between extended droughts (100–300 year) and short wet intervals (100-year) with variations in precipitation ~82–105% of historical

baseline. Snowpack is reflected by a steady increase to near present-day extent from 4.2–0.8 ka that is interrupted by a greater than 200% increase in snowpack extent over a 600-year period from 0.8 to 0.3 ka. The large increase in snowpack is controlled by mean precipitation 94.4% of historical baseline during most of the MCA and persistent low temperature anomalies from -1.16 to -1.02°C throughout the Little Ice Age. The historical period from 0.2 ka to present day is characterized by hydroclimate variability with changes in precipitation ~82–100% of historical baseline and an increase of ~1°C temperature anomaly to present day associated with the termination of the Little Ice Age and beginning of anthropogenic forcing.

The effects of watershed-scale orbital forcing during the early to middle Holocene played a major role in reducing the extent of simulated snowpack in the Sierra Nevada from strong seasonality reflected by winters with less solar insolation and summers with more compared to present day, coupled with positive temperature anomalies, even during periods with significantly above (~150–160%) historical baseline precipitation. This is in sharp contrast to an increase in simulated snowpack during the late Holocene that is influenced by low winter and summer solar insolation and mostly negative temperature anomalies. These boundary conditions along with mostly below (~82–105%) historical baseline precipitation patterns culminated in maximum snowpack reaching ~60% greater than present day during a Little Ice Age glacial advance. Simulation of open-water evaporation based on minimum estimates of salinity suppression factors produces conservative estimates of evaporative loss, thereby producing conservative estimates of

precipitation in the watershed-lake water balance solution for a given targeted lake level. The conservative estimates of simulated precipitation coupled with negative temperature anomalies were still sufficient to accumulate snowpack reaching the Little Ice Age maximum extent, as well as provide minimum estimates of the severity of droughts during the MCA and mid-Holocene Warm Period.

The simulation of the water balance of the paleo-Owens River-Lake system between the Pleistocene-Holocene transition and historical period provides a continuous estimate of the moisture variability in the south-eastern Sierra Nevada. This record is at a resolution that has good temporal correspondence with other records of regional- to global-scale rapid climate change. As a result, the record can be used to support other moisture sensitive archives in the western U.S. by providing quantitative estimates of regional hydroclimate and insight to previous inferences and qualitative interpretations of hydroclimate conditions and moisture variability from multi-proxy records. This in turn can be used to support new or refine previous regional- to global-scale paleoclimate atmospheric models for the past 11,500 years.

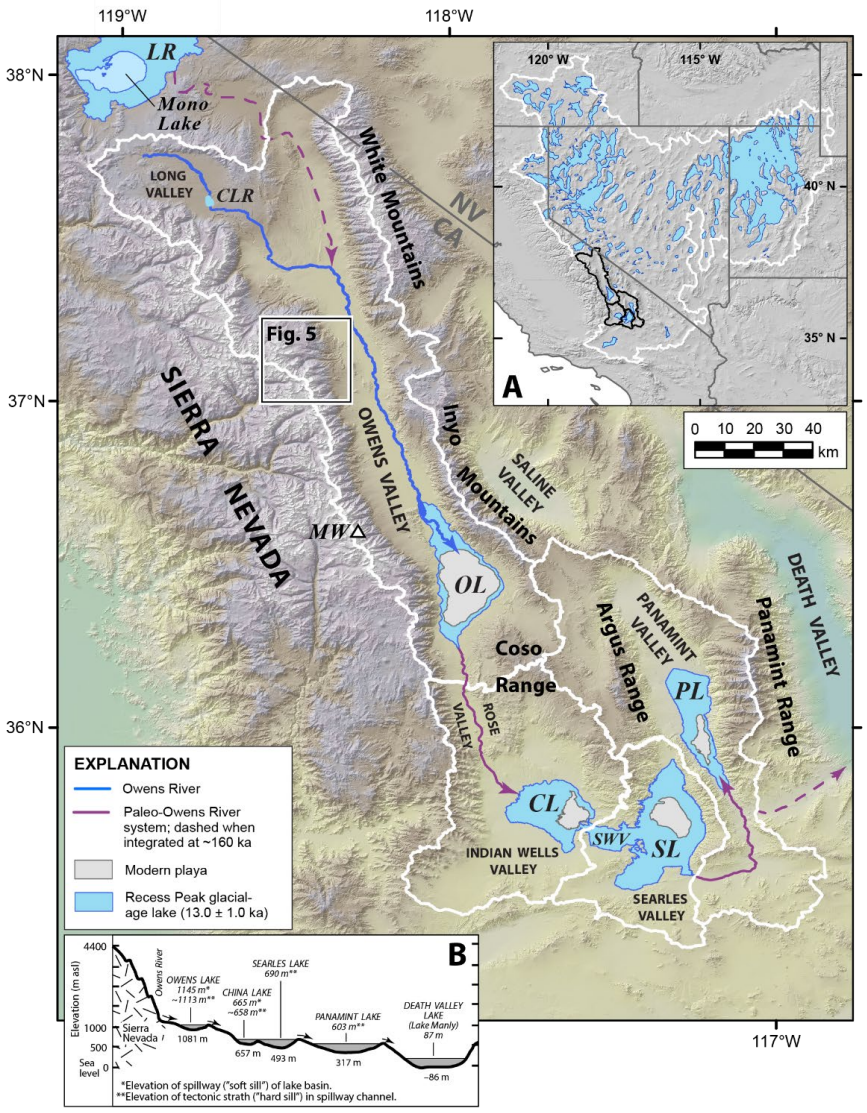

Figure 1. Major physiographic features along the eastern escarpment of the southern Sierra Nevada, eastern California in relation to modern playas and pluvial Owens Lake, and other lakes of the paleo-Owens River system during the Recess Peak glaciation (Bacon et al., 2006; Orme and Orme, 2008; Hoffman, 2009; Rosenthal et al., 2017). Age of Recess Peak glaciation is from Phillips (2016, 2017). Inset A is map of pluvial lakes in the hydrologically closed Great Basin (white line) and paleo-Owens River watershed (black lines). Inset B is graphical profile of the chain of lakes downstream of Owens Lake showing the elevations of hard and soft sills, plus playa bottoms of each lake basin (modified after Smith and Bischoff, 1997). Square shows aerial extent of map on Figure 5. Watershed boundaries of lake basins are shown for: CL – China Lake; OL – Owens Lake; PL – Panamint Lake; SL – Searles Lake; and SWV – Salt Wells Valley. Other physiographic features discussed in text include: CLR – Crowley Lake Reservoir; LR – pluvial Lake Russel; and MW – Mount Whitney.

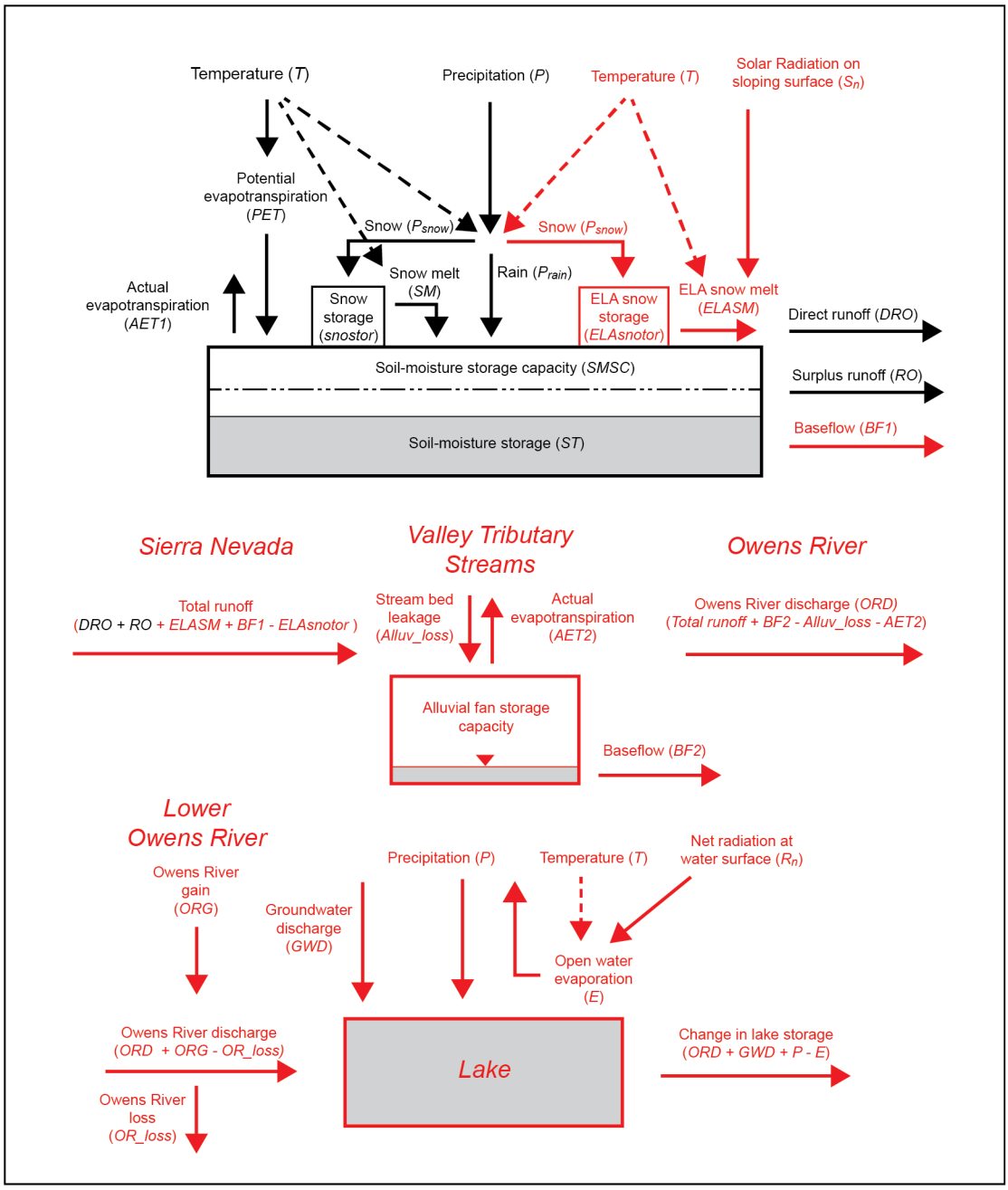

Figure 2. Diagram showing the four main components in the watershed-lake hydrologic model used for lake basins in the paleo-Owens River system comprising snow accumulation, runoff, groundwater, and lake evaporation. Snow accumulation and watershed runoff based on the Thornthwaite runoff model is shown in black (McCabe and Markstrom, 2007). Other model elements shown in red include snow accumulation and melt above the equilibrium line altitude (ELA) based on the simplified energy-balance snow melt model (Oerlemans, 2001), groundwater information (Hollet et al., 1991; Danskin, 1998), and open water evaporation based on the Priestly-Taylor equation (Priestly and Taylor, 1972).

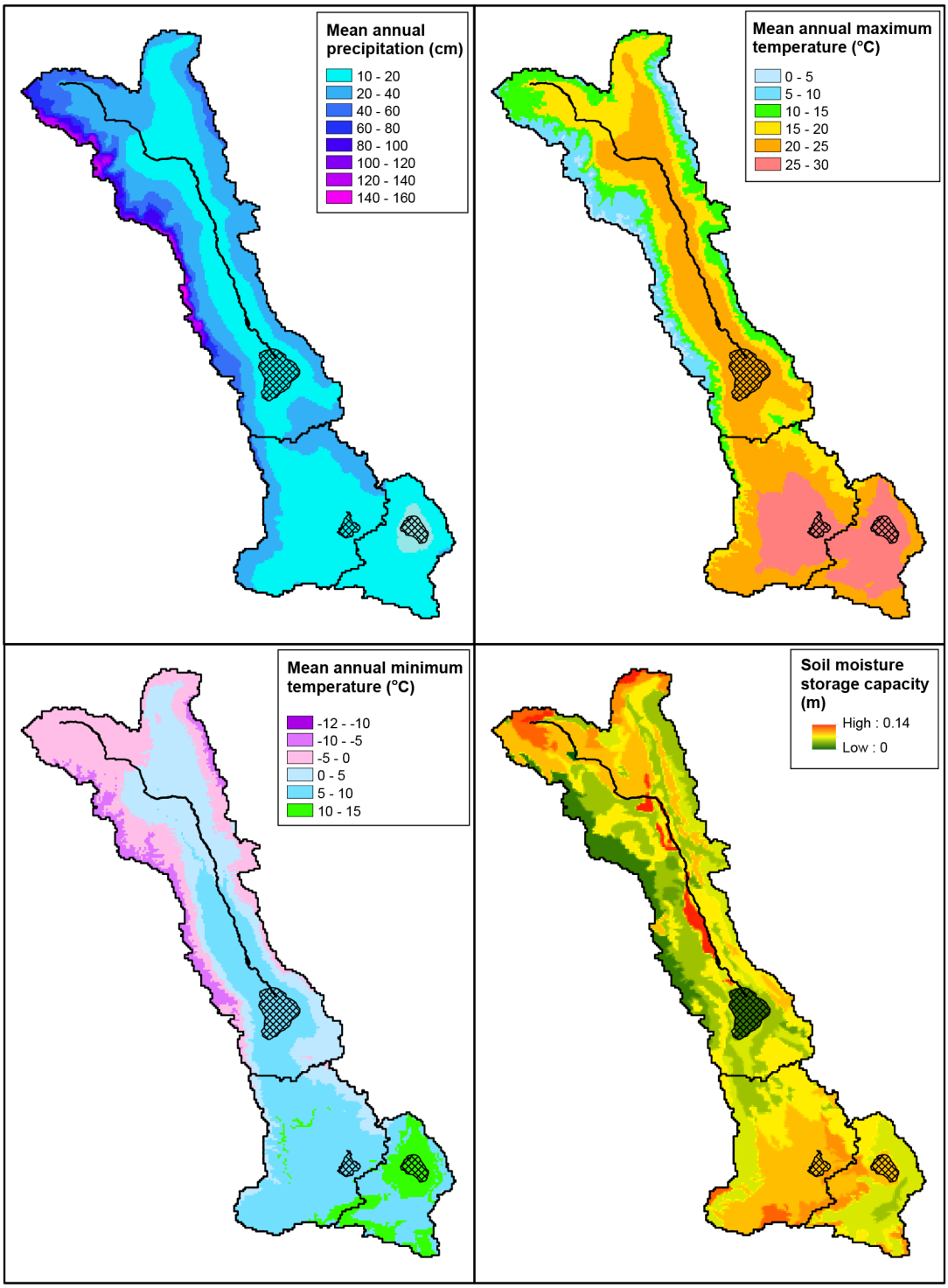

Figure 3. Maps showing the distribution of input data used in the 800-meter paleo-Owens River model domain of 20,898 grid cells. Mean annual precipitation, plus maximum and minimum temperature is from 800-meter PRISM historical climate data (Daly et al., 1994). Soil moisture capacity is from the 1:250,000-scale NRCS State Soil Geographic (STATSGO) database.

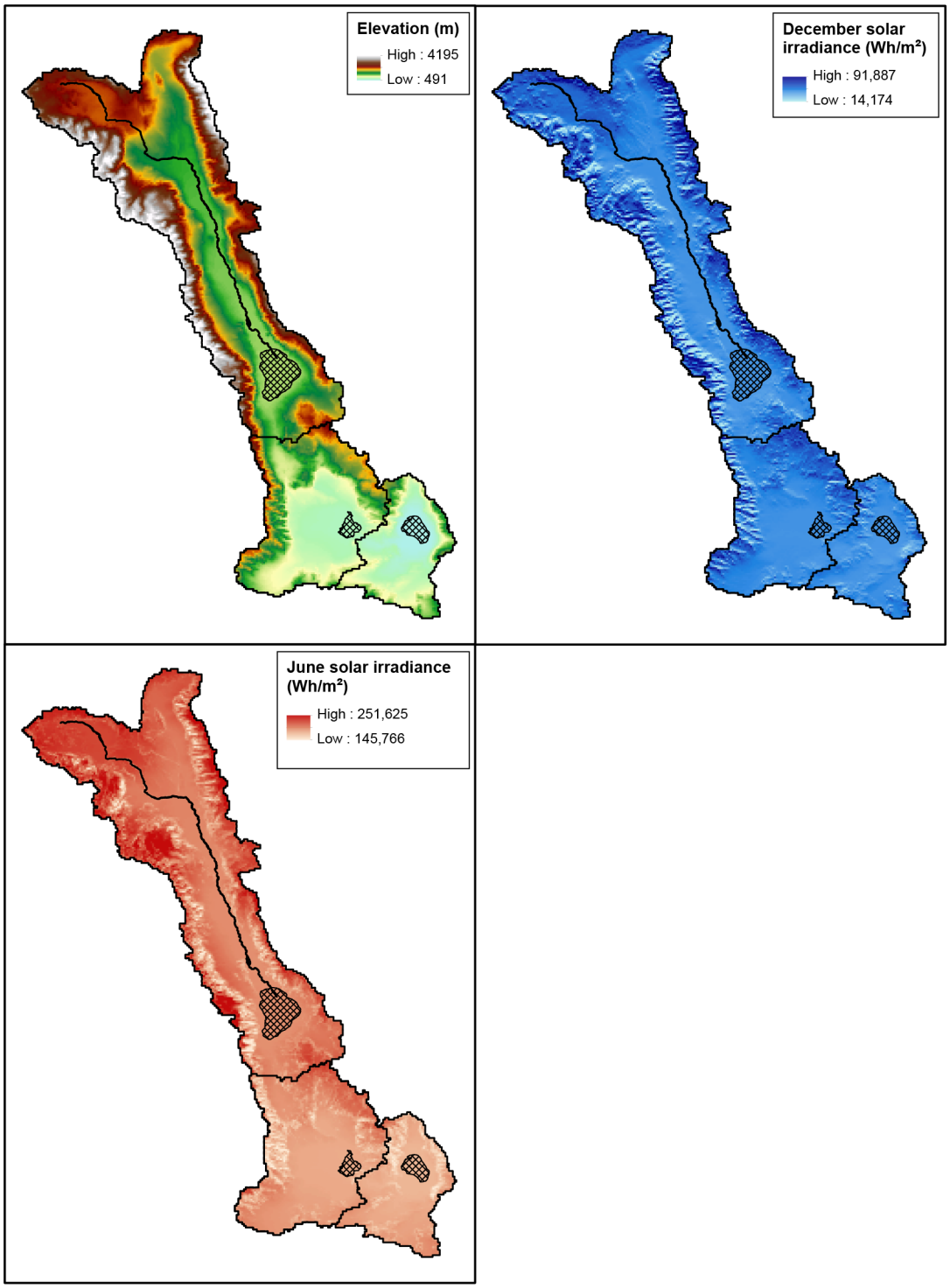

Figure 4. Maps showing the distribution of input data used in the 800-meter paleo-Owens River model domain of 20,898 grid cells. Elevation data is from the USGS NED 30-meter digital elevation model dataset. Examples of monthly solar irradiance for December and June used in the watershed-lake hydrologic model. Solar irradiance was calculated from elevation data using the Area Solar Radiation tool in ArcGIS.

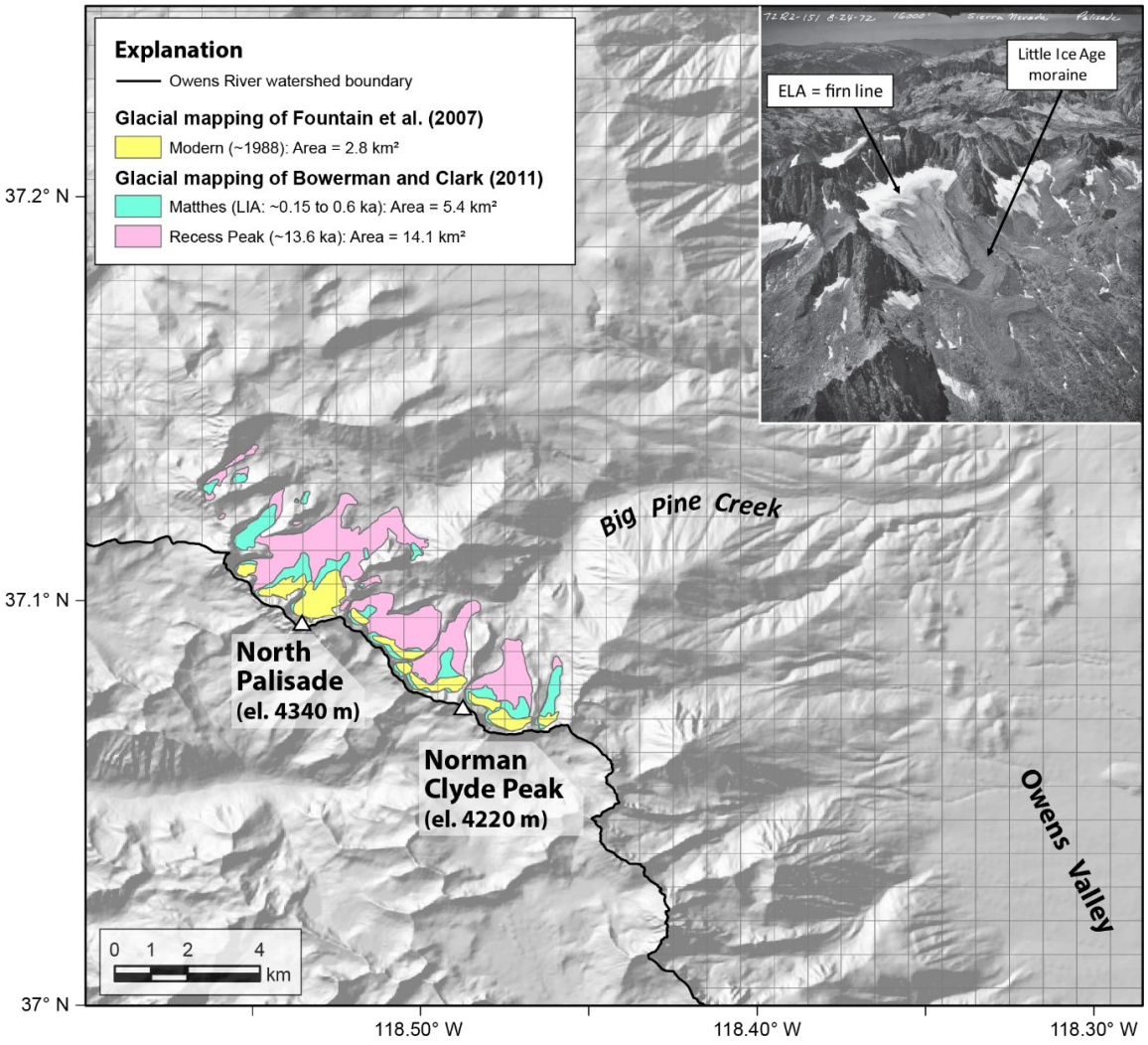

Figure 5. Map of the distribution of glacial deposits and modern glaciers and perennial snowfields in the Big Pine Creek subbasin of the Owens River watershed (Figure 1). Inset photograph showing the position of the equilibrium line altitude (ELA) in late August 1972 on the North Palisade glacier and well-preserved Matthes (Little Ice Age) lateral and terminal moraines (from Bowerman and Clark, 2011). The areal extent of Matthes glacial deposits and modern glaciers and perennial snowfields were used in the calibration of snow water equivalent (SWE) storage above the ELA component of the watershed-lake hydrological model.

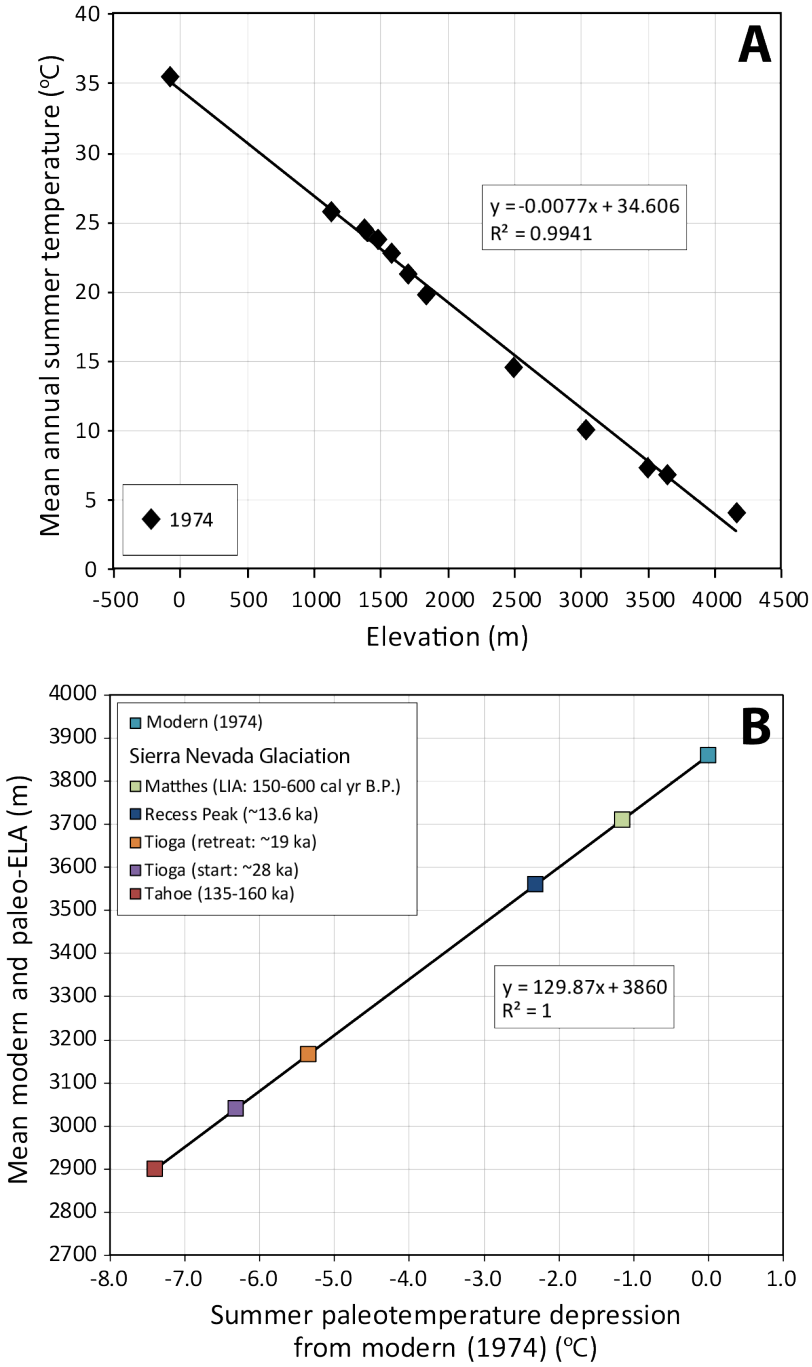

Figure 6. Plots showing: (A) mean summer (June–September) environmental adiabatic lapse rate in 1974 for the Owens River watershed computed from mean monthly PRISM data along a west to east transect from Mount Whitney (elev. 4421 m) in Owens Valley to Bad Water in Death Valley (elev. -85 m); and (B) summer paleotemperature depression relative to 1974 based on environmental adiabatic lapse rate and published paleo-equilibrium line altitude (ELA) estimates from glacial deposits (see Table 1).

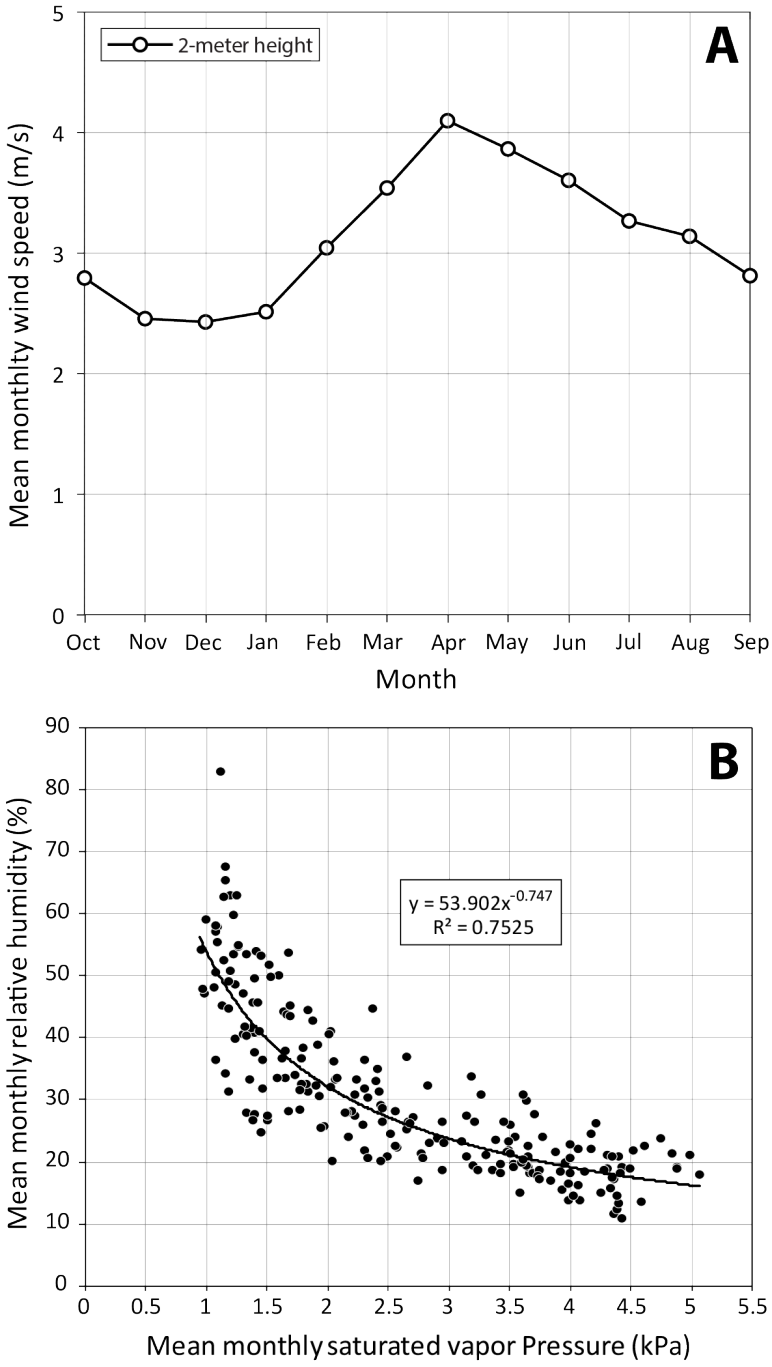

Figure 7. Mean monthly meteorological data from the Great Basin Unified Air Pollution Control District A-Tower station at Owens Lake playa. Plots showing: (A) twenty years of wind speed data from 2-meter height for the period 1991–2011; and (B) seventeen years of measured relative humidity versus saturated vapor pressure calculated from measured mean monthly 800-meter PRISM maximum and minimum temperature data at the centroid of the playa for the period 1994–2011.

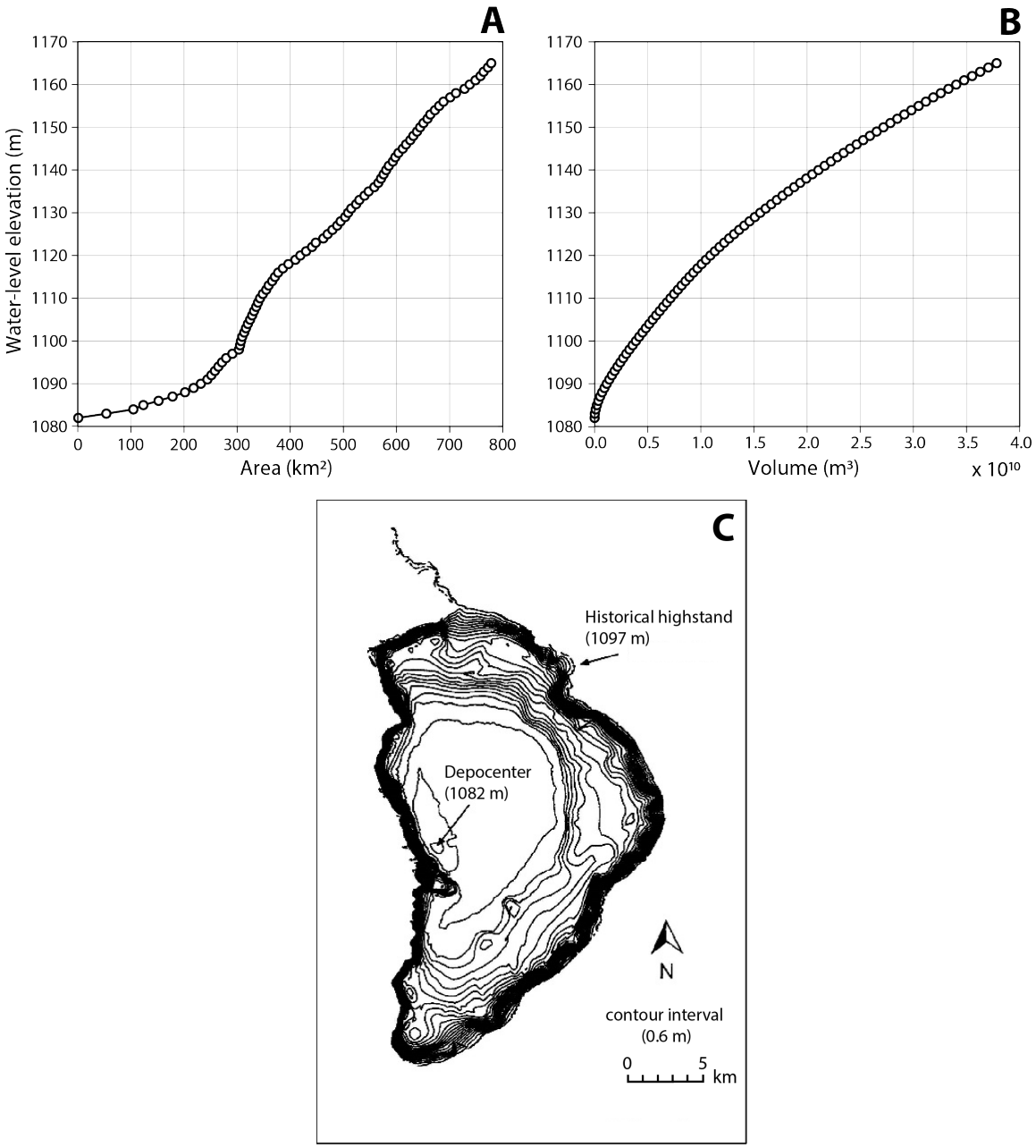

Figure 8. Hypsometric relations used in the watershed-lake hydrologic model to calculate equivalent water-level elevation from changes in: (A) lake area; and (B) lake volume. Hypsometric curves for Owens Lake were developed from a high-resolution digital elevation model based on the integration of digitized contours of the bathymetric map of Owens Lake surveyed in February 1913 (Gale, 1914) (C) and USGS NED 10-meter digital elevation model dataset.

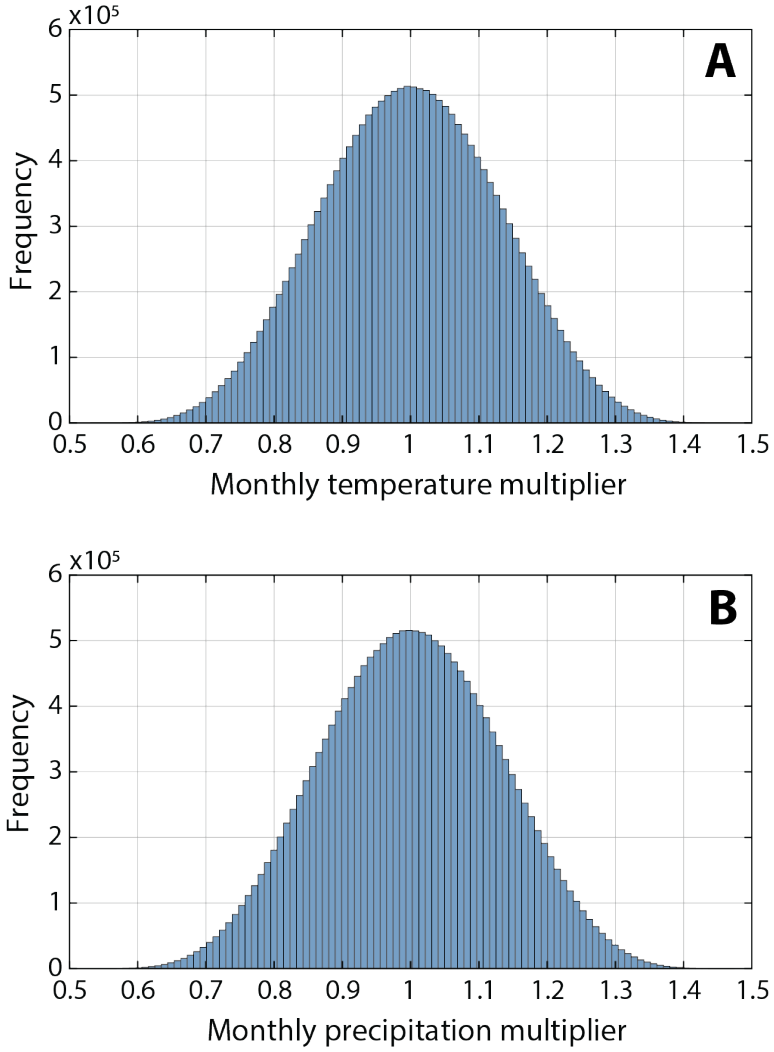

Figure 9. Histogram plots showing the distribution of multiplier values applied to 800-meter PRISM mean monthly temperature (A) and monthly precipitation (B) data for the uncertainty analysis of the Owens watershed-lake hydrologic model for the period WY1896–2015.

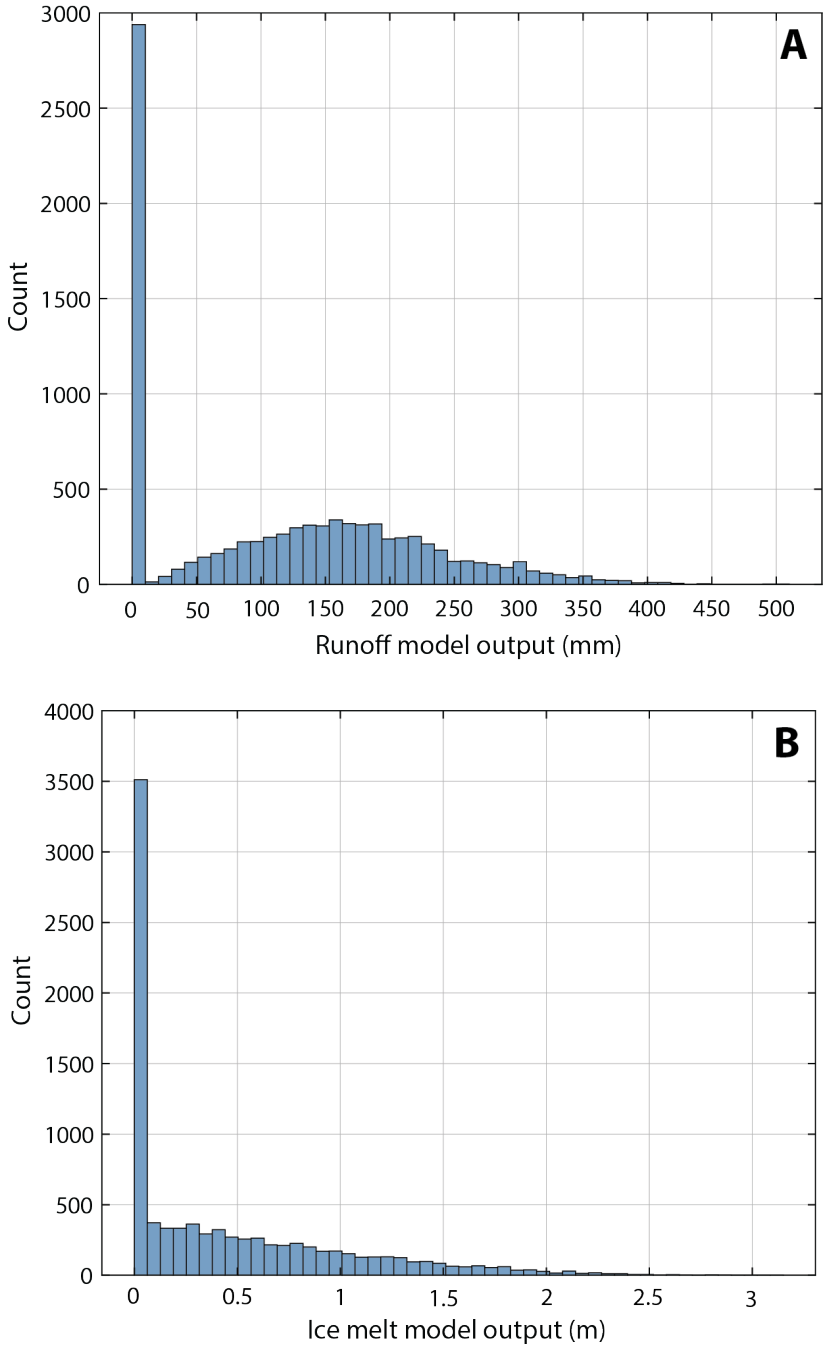

Figure 10. Histogram plots showing the distribution and magnitude of model outputs generated from a sample size of $N = 9000$ and application of the Sobol random number sequence technique for: (A) runoff from the Thornthwaite watershed model (McCabe and Markstrom, 2007) and (B) ice melt from the simplified energy-balance ice melt model (Oerlemans, 2001).

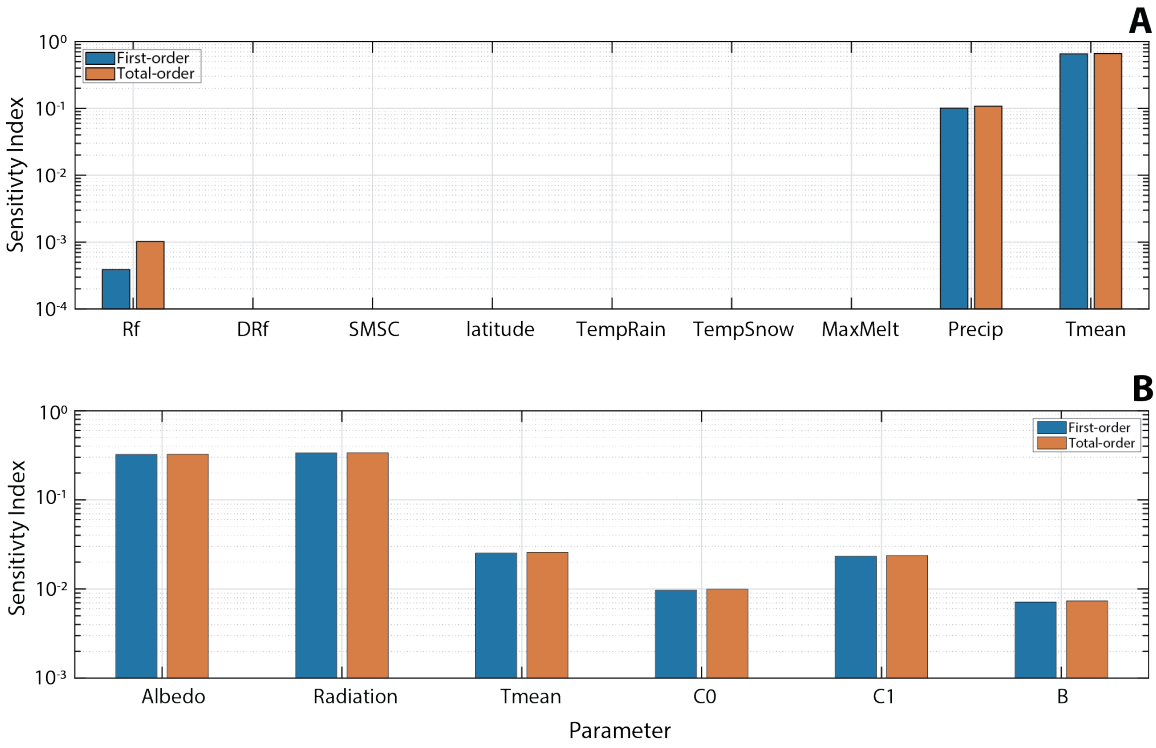

Figure 11. Bar plots showing the first- and total-order Sobol sensitivity indices for model parameters in relation to model output of: (A) the nine parameters in the Thornthwaite watershed runoff model (McCabe and Markstrom, 2007) and (B) the six parameters in the simplified energy-balance ice melt model (Oerlemans, 2001). Of note the greater the sensitivity value, the greater the dependence of the input parameter to model output. Rf – runoff fraction; DRf – direct runoff fraction; SMSC – soil moisture storage capacity; TempRain – temperature threshold for rain; TempSnow – temperature threshold for snow; MaxMelt – maximum snow melt rate; Precip – precipitation; Tmean – mean temperature; C0 – net longwave radiation empirical factor; C1 – turbulent heat fluxes empirical factor; B – thermal quality of snowpack.

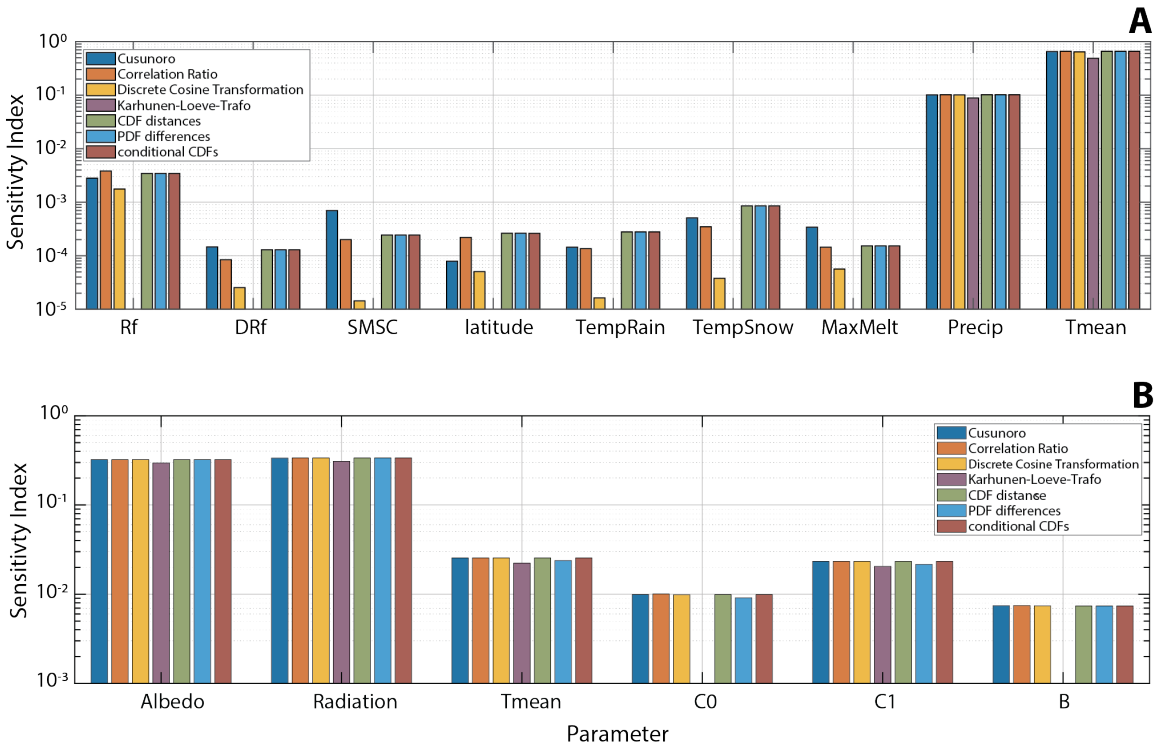

Figure 12. Bar plots showing an ensemble of first-order density-based sensitivity indices from seven different probability density function (PDF)- and cumulative density function (CDF)-based correlation techniques after Plischke et al. (2013) for model parameters in relation to model output of: (A) the nine parameters in the Thornthwaite watershed runoff model (McCabe and Markstrom, 2007) and (B) the six parameters in the simplified energy-balance ice melt model (Oerlemans, 2001). Of note the greater the sensitivity value, the greater the dependence of the input parameter to model output. Rf – runoff fraction; DRf – direct runoff fraction; SMSC – soil moisture storage capacity; TempRain – temperature threshold for rain; TempSnow – temperature threshold for snow; MaxMelt – maximum snow melt rate; Precip – precipitation; Tmean – mean temperature; C0 – net longwave radiation empirical factor; C1 – turbulent heat fluxes empirical factor; B – thermal quality of snowpack.

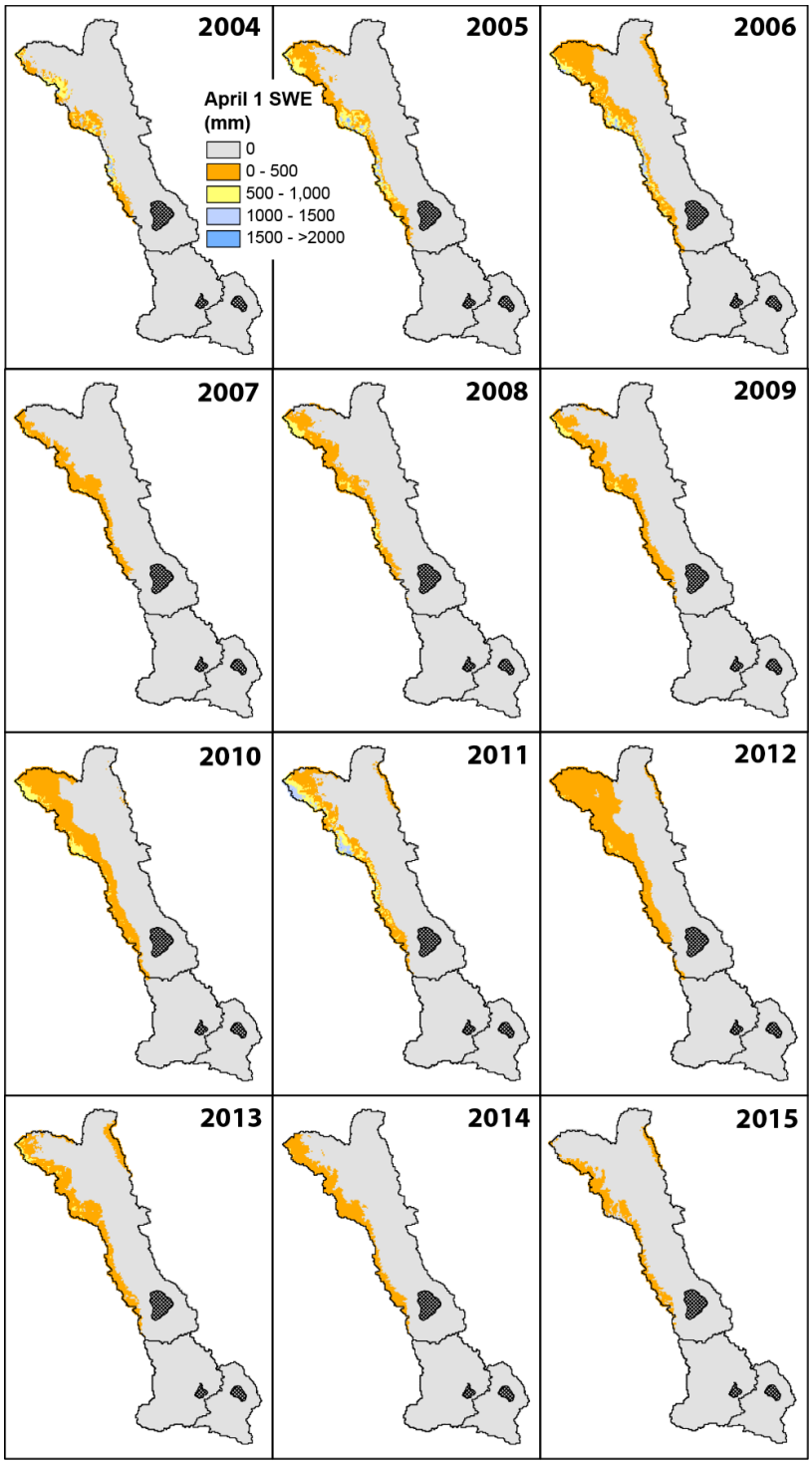

Figure 13. Maps showing the distribution of Snow Data Assimilation System (SNODAS) April 1st snow water equivalent (SWE) in the 800-meter paleo-Owens River model domain for the years 2004–2015 (Barrett, 2003). SNODAS dataset is used to calibrate the snow accumulation and energy-balance snow melt components of the watershed runoff model.

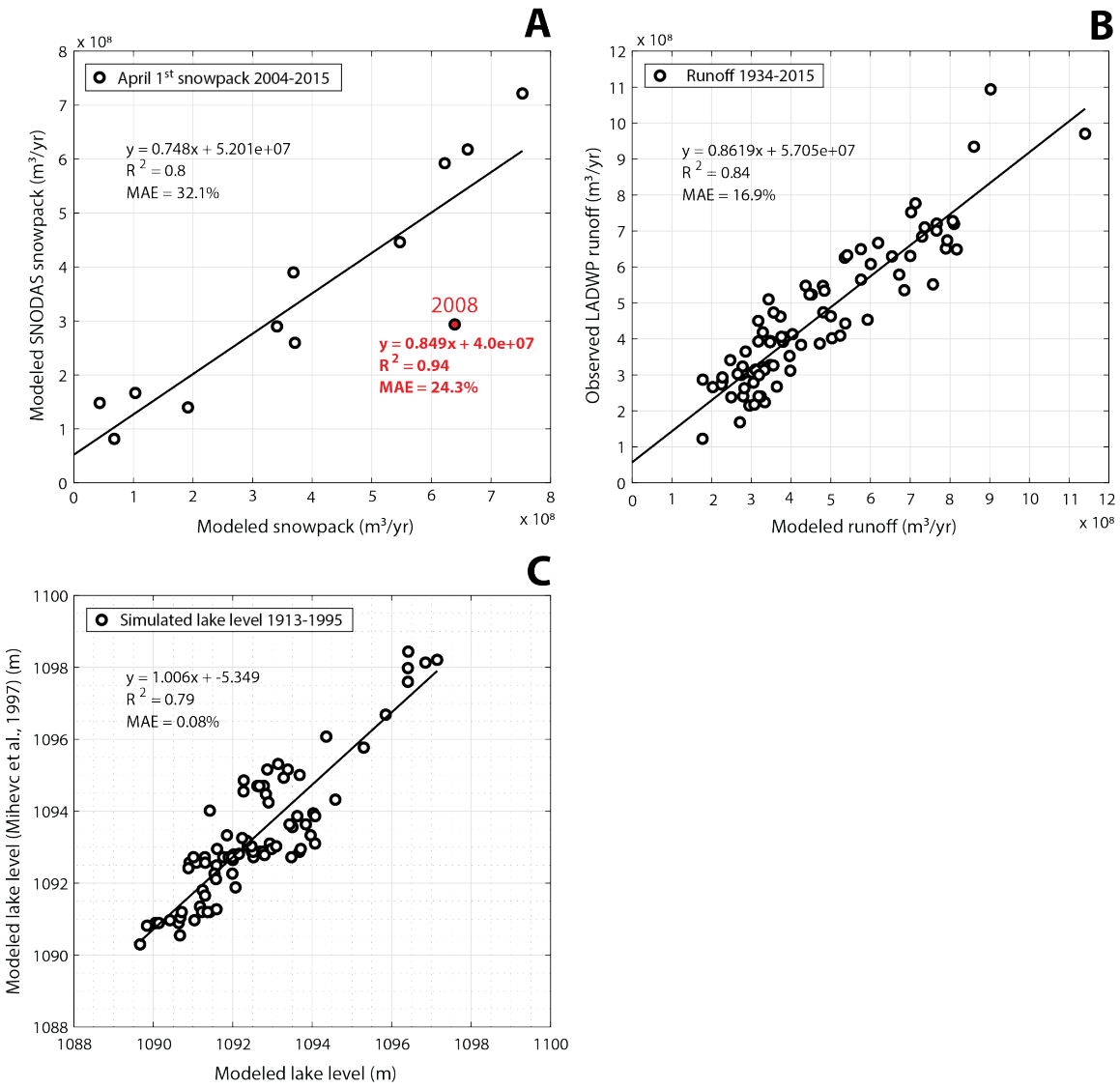

Figure 14. Plots used to evaluate accuracy of the calibrated Owens watershed-lake hydrologic model outputs of: (A) April 1st snowpack from 2004–2015 between this study and Snow Data Assimilation System (SNODAS) data. If the disparate data in 2008 is omitted from the comparison the correlation of determination (R^2) value increases and mean absolute error (MAE) value decreases; (B) runoff from 1934–2015 between this study and runoff measured by the Los Angeles Department of Water and Power (LADWP); and (C) lake level without Los Angeles aqueduct diversions from 1913–1995 between this study and modeled lake level of Mihevc et al. (1997).

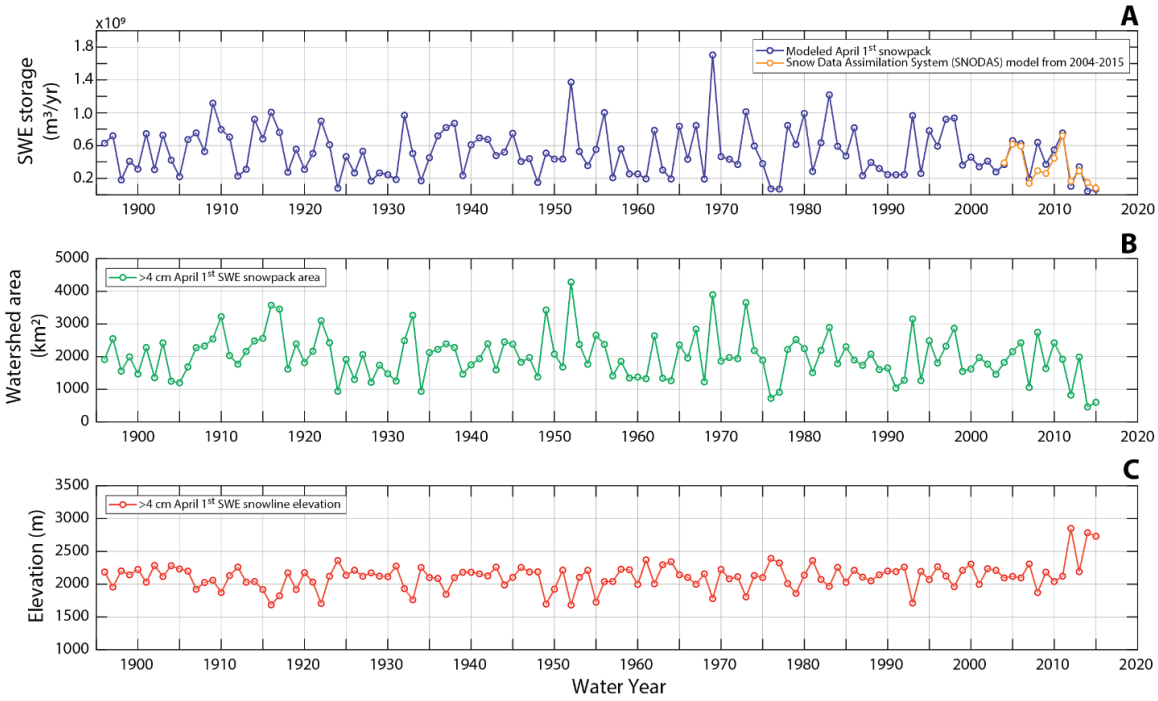

Figure 15. Plots showing characteristics of simulated April 1st snowpack from the calibrated Owens watershed-lake hydrologic model for the period WY1896–2015. Simulated characteristics include: (A) snow water equivalent (SWE) storage of this study in comparison with Snow Data Assimilation System (SNODAS) data from 2004–2015; (B) areal extent of equivalent SWE storage in the Owens River watershed; and (C) changes in equivalent SWE storage shown as spring snowline elevation.

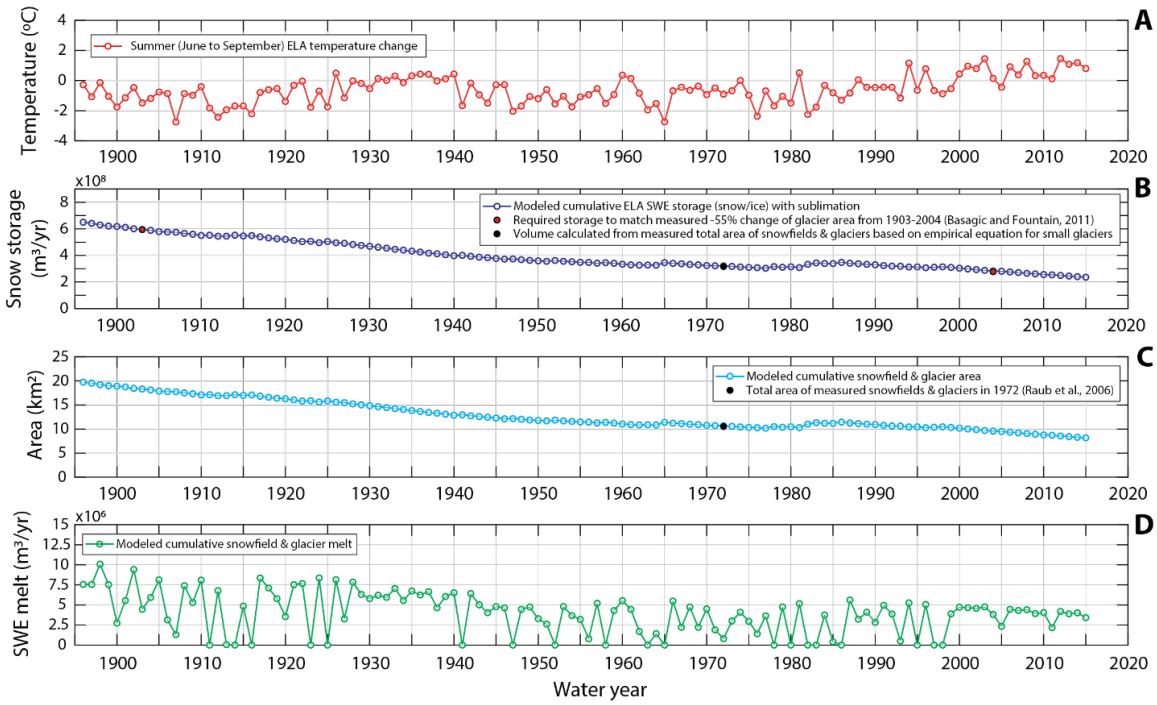

Figure 16. Plots showing characteristics of simulated glacier and perennial snow accumulation and melt above the equilibrium line altitude (ELA) from the calibrated Owens watershed-lake hydrologic model for the period WY1896–2015. Simulated characteristics include: (A) summer ELA temperature change relative to measured ELA in 1974; (B) snow water equivalent (SWE) storage above the ELA of this study and calibration control points from measured data; (C) areal extent of SWE storage above the ELA in the Owens River watershed and control point from measured data in 1972; and (D) melt from SWE storage above the ELA.

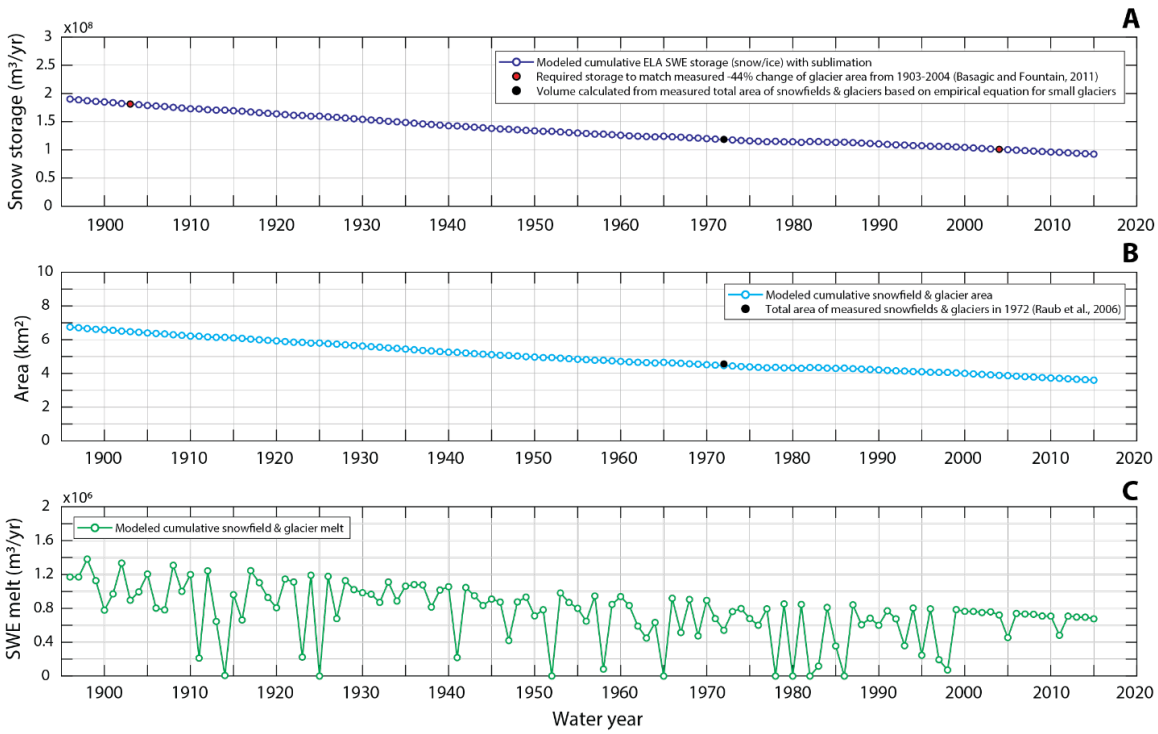

Figure 17. Plots showing characteristics of simulated glacier and perennial snow accumulation and melt above the equilibrium line altitude (ELA) in the Big Pine Creek subbasin from the calibrated Owens watershed-lake hydrologic model for the period WY1896–2015. Simulated characteristics include: (A) snow water equivalent (SWE) storage of this study and calibration control points; (B) areal extent of SWE storage in the Owens River watershed and control point from measured data in 1972; and (C) melt from SWE storage above the ELA.

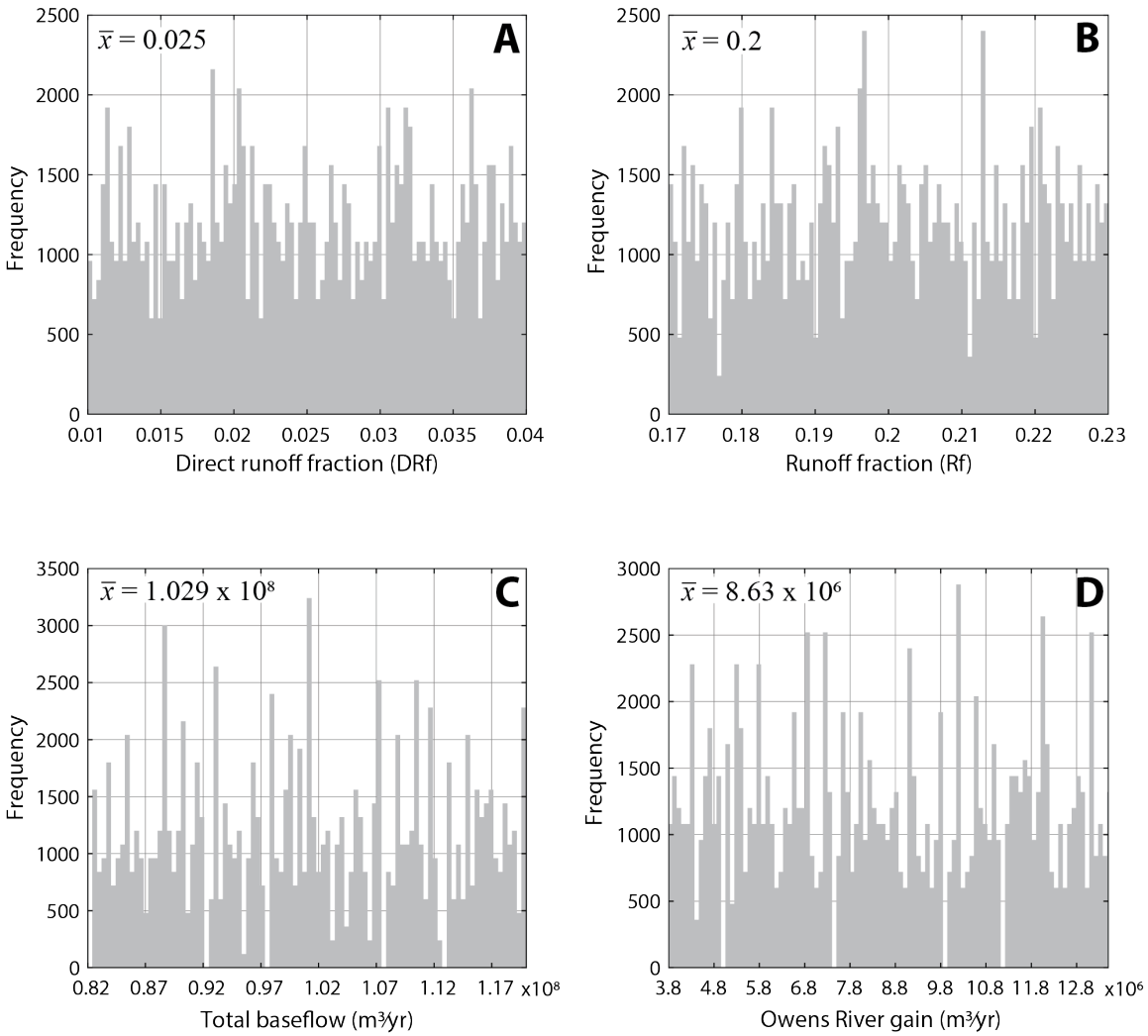

Figure 18. Histogram plots showing the distribution of model parameter values derived from the Sobol sequence technique used during the calibration of the runoff component of the Owens watershed-lake hydrologic model. The technique was used to generate a range of parameter values during several iterations of 1000-run simulations to account for parameter uncertainty for: (A) direct runoff fraction (DRf); (B) Runoff fraction (Rf); (C) Total baseflow (BF1 and BF2); and (D) Owens River gain (ORG) (see Table 5).

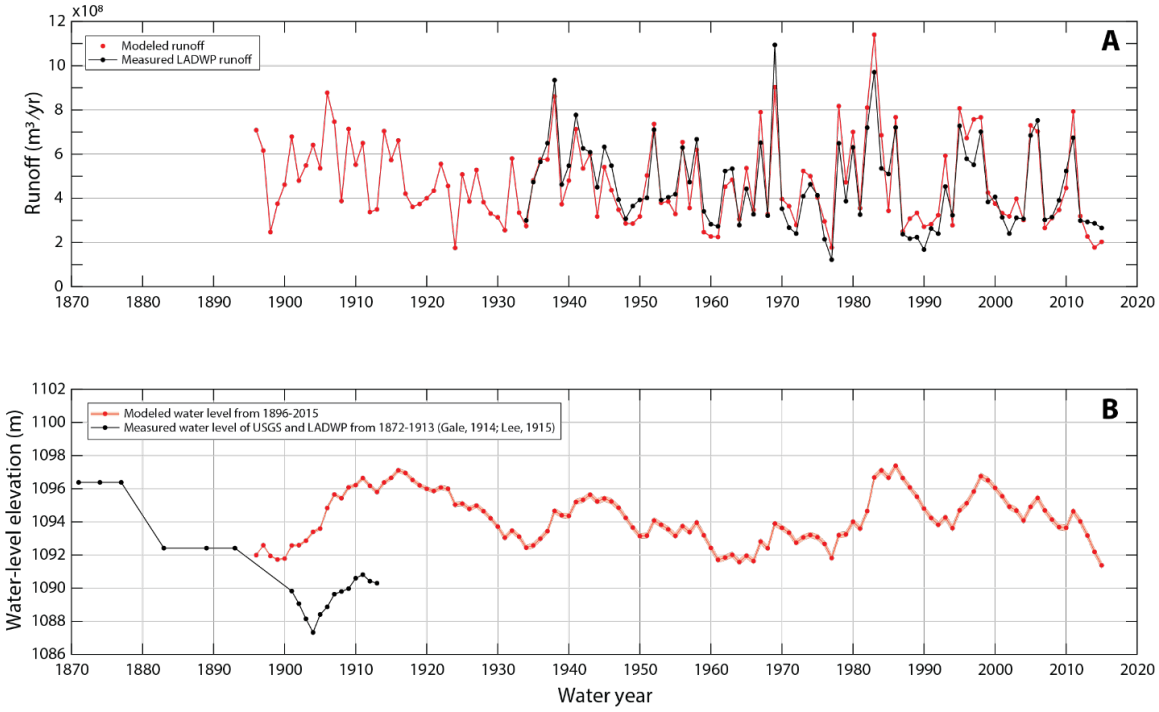

Figure 19. Plots showing output from the calibrated Owens watershed-lake hydrologic model for the period WY1896–2015. The output includes: (A) simulated runoff of this study in comparison with runoff measured by the Los Angeles Department of Water and Power (LADWP) from 1934–2015; and (B) simulated water level of Owens Lake without Los Angeles aqueduct diversion of this study in comparison with measured water level from 1913–1972.

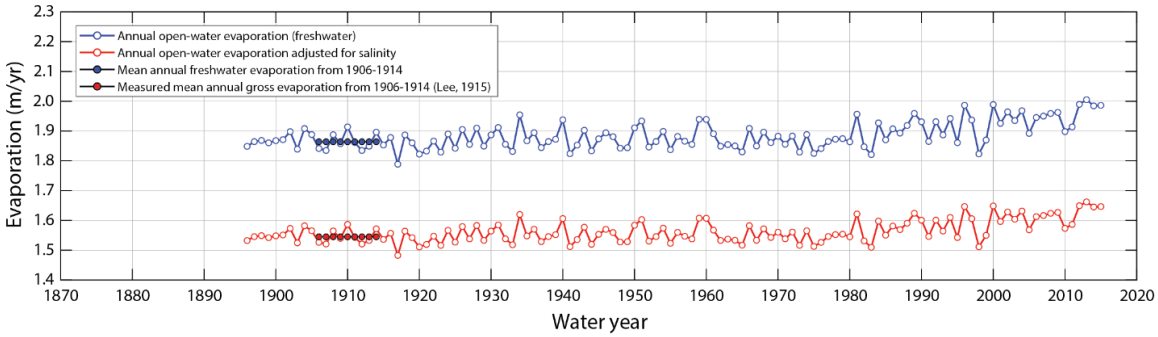

Figure 20. Simulated open water evaporation from the calibrated Owens watershed-lake hydrologic model for the period WY1896–2015. Calibration points from measured gross evaporation based on the water-balance between measured Owens River discharge and hypsometry of lake basin from 1906–1914 were used to adjust evaporation for salinity. The adjustment required a salinity suppression factor of 0.829 to lower simulated open water evaporation of freshwater to equivalent saline water.

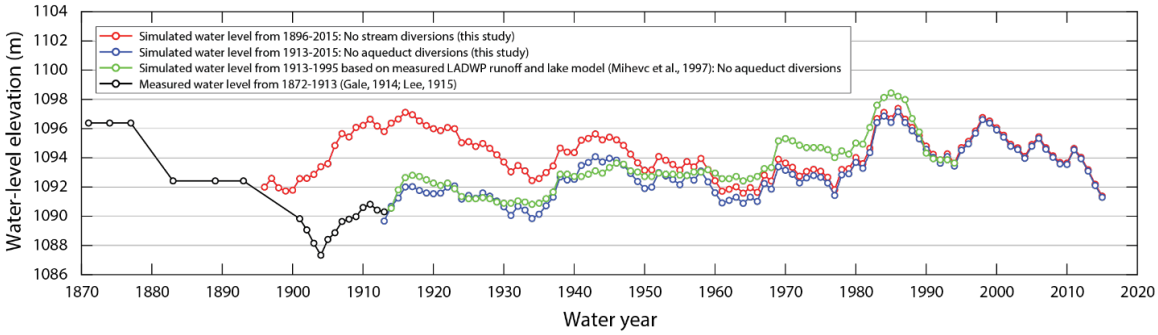

Figure 21. Simulated Owens Lake water levels from the calibrated Owens watershed-lake hydrologic model for the period WY1896–2015. Two simulations with no Los Angeles aqueduct diversions were performed beginning in WY1896 and 1913. Simulated water levels of Mihevc et al. (1997) beginning in WY1913 based on measured runoff by the Los Angeles Department of Water and Power (LADWP) and a simple lake evaporation model is also shown.

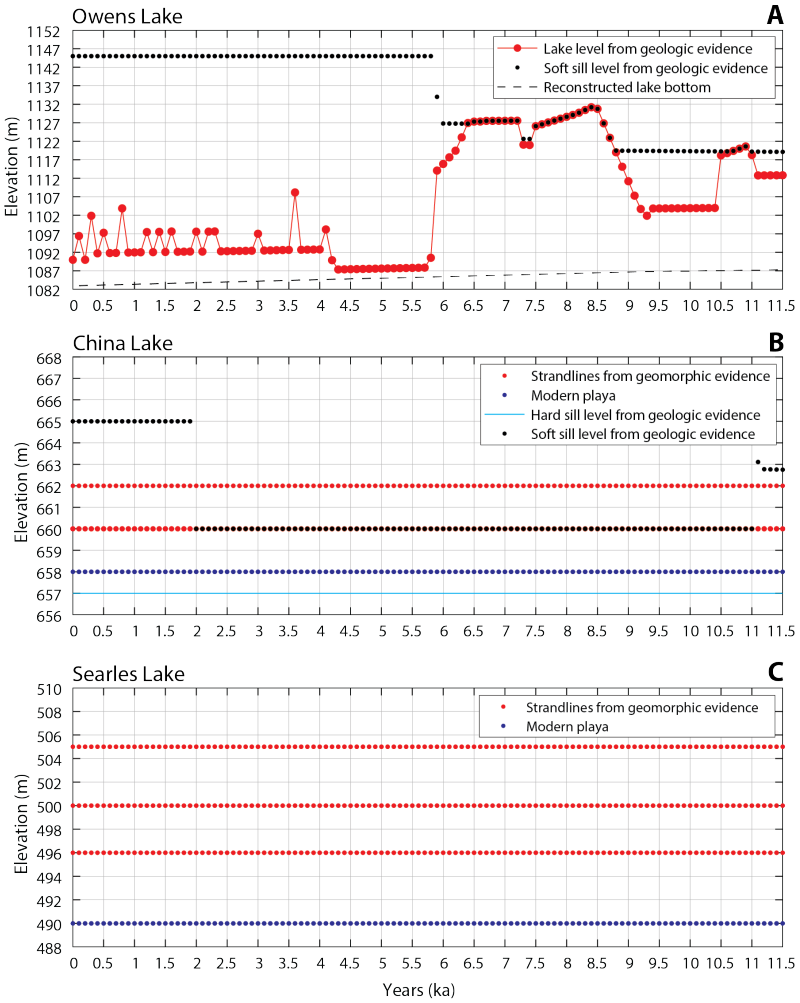

Figure 22. Geologically determined lake-level curves at 100-year time steps used for control points in the paleo-Owens watershed-lake hydrologic model from 11.5 ka to present day. (A) Continuous lake-level record of Owens Lake developed from the integration of shoreline geomorphology and lake-core data with wind-wave and sediment entrainment modeling of lake-core sedimentology that is corrected for tectonic ground deformation (Bacon et al., 2018, 2019a, 2020). The position of reconstructed soft sills and lake bottom at each time step is also shown; (B) Elevation of potential Holocene water levels of China Lake based on the identification of youthful strandlines encompassing the playa basin (this study) and geologic evidence from the sill area (e.g., Rosenthal et al., 2017). Periods of inferred Holocene overflow are from dated eolian deposits in the lake basin and near the overflow area (Bullard et al., 2019; Lancaster et al., 2019) combined with geologic evidence of shallow lakes in Searles Valley; and (C) Elevation of potential Holocene water levels of Searles Lake based on the identification of youthful strandlines encompassing the playa basin (this study) and evidence of Holocene lakes from sediment cores and geologic mapping (Smith, 1979, 2009). Note: overflow conditions occur when water level is at elevations at or above soft sills.

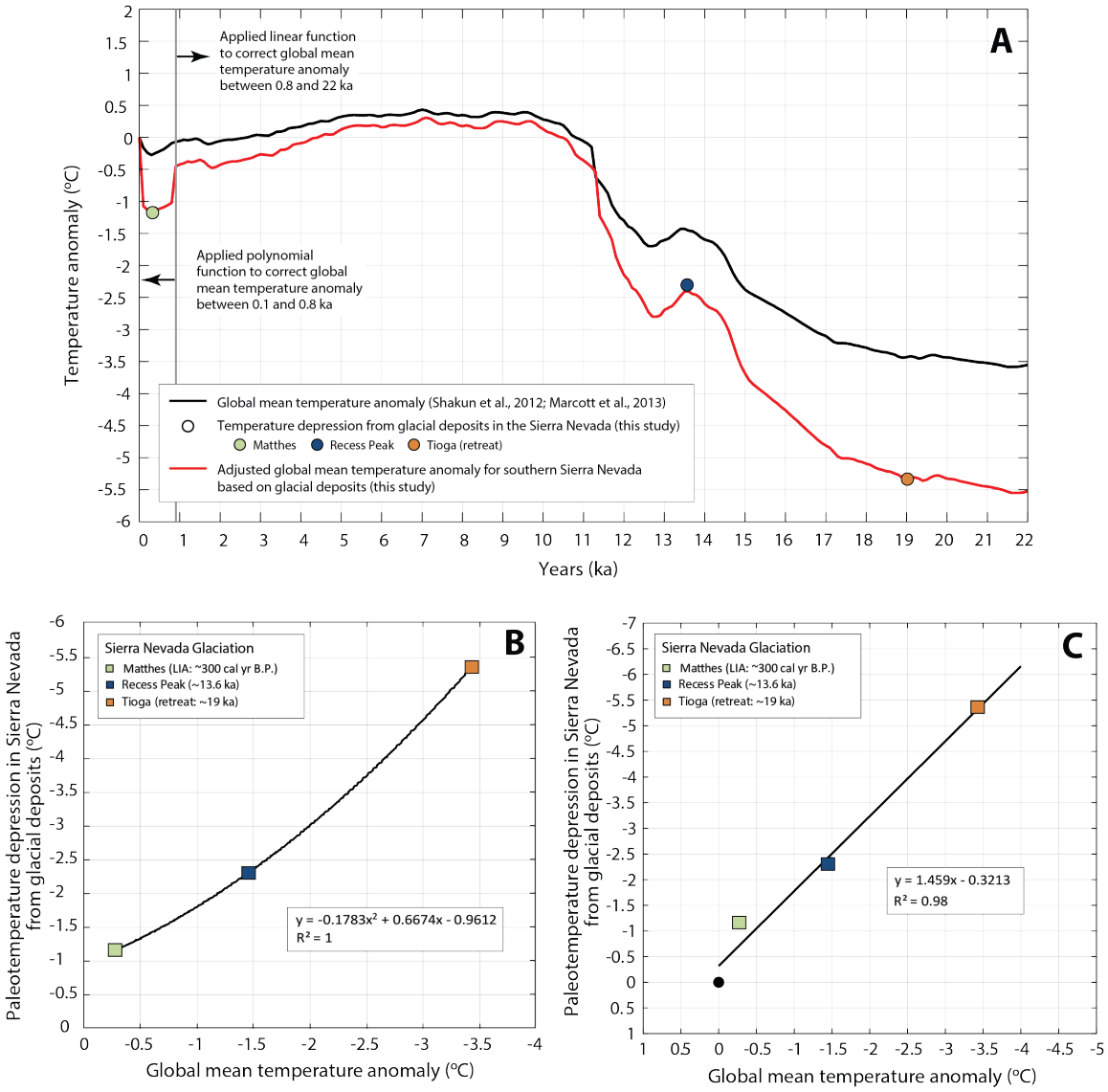

Figure 23. Paleotemperature data used in the paleo-Owens watershed-lake hydrologic model at 100-year time steps. (A) Adjusted mean global temperature anomaly to correspond with local paleotemperature depression estimates from glacial deposits in the Owens River watershed. Two functions were developed to best match paleotemperature depression during the Matthes (Little Ice Age), Recess Peak, and Tioga (retreat) glaciations in the south-central Sierra Nevada (see Table 1; Figure 6). Adjustment required the application of: (B) second-order polynomial function to global mean temperature anomaly from 0.1–0.8 ka during the Medieval Climate Anomaly and Little Ice Age; and (C) linear function to global mean temperature anomaly from 0.8–22 ka during a minor glacial advance and deglaciation in the Sierra Nevada (e.g., Gillespie and Clark, 2011; Phillips, 2016, 2017).

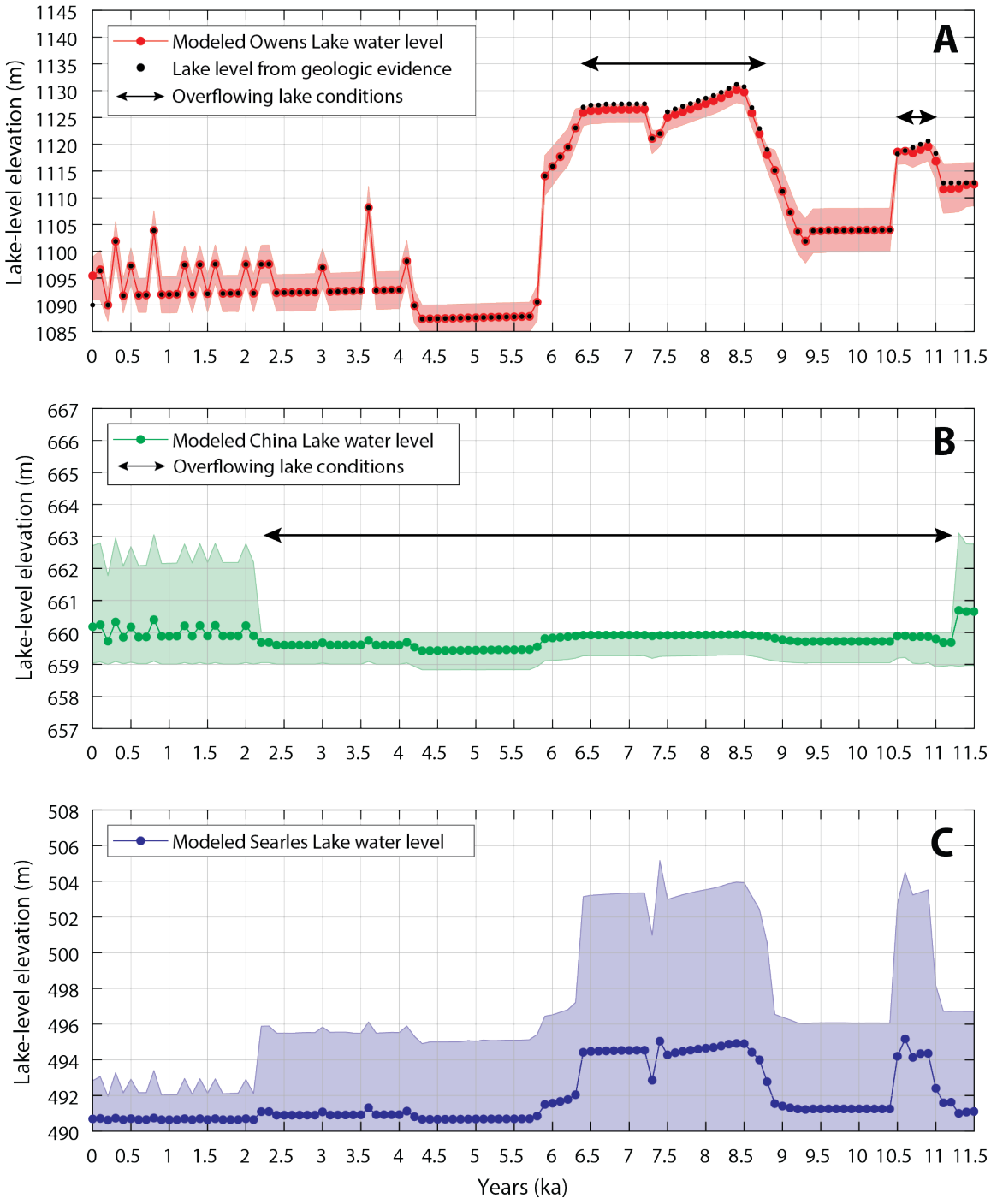

Figure 24. Simulated water levels of lakes of the paleo-Owens River-Lake system between 11.5 ka and present day at 100-year times steps from the paleo-Owens watershed-lake hydrologic model. (A) mean and range of Owens Lake water levels and targeted lake level from geologic evidence; (B) mean and range of China Lake water levels; and (C) mean and range of Searles Lake water levels. Periods with overflow from Owens and China Lakes into terminal Searles Lake are also shown.

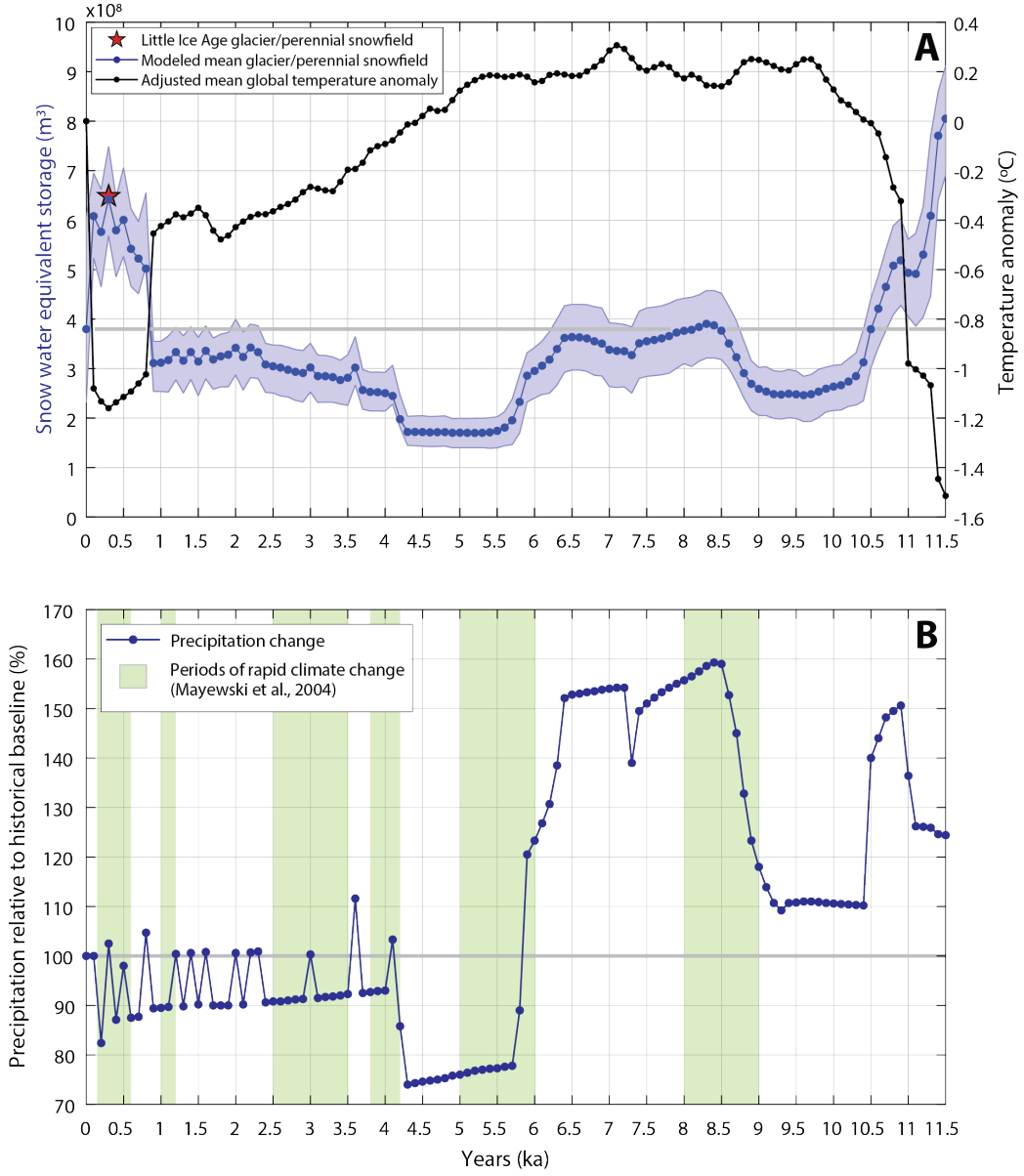

Figure 25. Simulated hydroclimate of the south-eastern Sierra Nevada between 11.5 ka and present day at 100-year times steps from the paleo-Owens watershed-lake hydrologic model. (A) Snow water equivalent storage (i.e., snowpack) representing the volume of glaciers and perennial snowfields and adjusted mean global temperature anomaly used in the simulation (see Figure 23). Maximum volume of Little Ice Age glaciers and perennial snowfields used as a geologic-based control point at 0.3 ka is shown; and (B) Percent precipitation relative to historical baseline (WY1896–2015) required to match simulation of geologically determined lake-level records of Owens, China, and Searles Lakes (see Figure 24). Periods of global-scale rapid climate change that commonly coincide with extreme changes in simulated precipitation and temperature in the watershed are also shown. Thick horizonal gray lines represent present day snowpack and baseline precipitation.

Table 1. Mean equilibrium line altitude in 1974 and during past glaciations in the Sierra Nevada with their associated mean summer paleotemperature change.

Paleosnowline change			Paleotemperature change	
Sierra Nevada Glaciation	**Mean age[1]**	**Mean ELA (m)[1]**	**Mean 1974 Summer Temperature (ºC)[2]**	**Mean Summer Paleotemperature Depression (ºC)**
Modern	1974 A.D.	3860	4.88	0.00
Matthes (Little Ice Age)	100-600 cal yr B.P.	3710	6.04	-1.16
Recess Peak	~13.6 ka	3560	7.19	-2.31
Tioga – retreat (MIS 2)	~19 ka	3165	10.24	-5.35
Tioga -start (MIS 2)	~28 ka	3040	11.20	-6.31
Tahoe 1 (MIS 6)	135 - 165 ka	2940	11.97	-7.08

Notes: NA - not applicable; ELA - equilibrium line altitude; MIS - marine isotope stage.

[1]Burbank (1991); Clark and Gillespie (1997); Phillips et al. (2009); Kaufman et al. (2004); Bowerman and Clark (2011); Gillespie and Clark (2011); Rood et al. (2011).

[2]This study - paleotemperature change calculated relative to 1974 using adiabatic lapse rate from PRISM climate data (see Table 2 and Figure 6A).

Table 2. Range of mean summer paleotemperature change and associated equilibrium line altitude (ELA) used to estimate ELA snow storage relative to 1974.

ELA (m)[1]	Mean 1974 Summer Temperature (ºC)[2]	Mean Summer Paleotemperature Change from Modern (ºC)
4200	2.27	2.62
4100	3.04	1.85
4000	3.81	1.08
3900	4.58	0.31
3860	4.88	0.00
3800	5.35	-0.46
3700	6.12	-1.23
3600	6.89	-2.00
3500	7.66	-2.77
3400	8.43	-3.54
3300	9.20	-4.31
3200	9.97	-5.08
3100	10.74	-5.85
3000	11.51	-6.62
2940	11.97	-7.08

Notes:

[1]ELA at 3860 m in 1974 from Bowerman and Clark (2011).

[2]This study - paleotemperature change calculated relative to 1974 using adiabatic lapse rate from PRISM climate data (see Figure 6A).

Table 3. Range of parameter values used in the sensitivity analysis of the Thornthwaite runoff model.

Parameter No.	Parameter descriptor	Parameter description	Units	Lower limit	Upper limit
X_1	Rf	Runoff factor from soil surplus storage	mm	0.1	0.5
X_2	DRf	Direct runoff factor from impervious surfaces/infiltration-excess overflow	mm	0.01	0.1
X_3	SMSC	Soil-moisture storage capacity	mm	0.0	140.0
X_4	TempRain	Rain temperature threshold	°C	0.1	5.0
X_5	TempSnow	Snow temperature threshold	°C	-5.0	0.0
X_6	Maxmelt	Snow melt rate	Decimal fraction	0.25	0.75
X_7	lat	Latitude	°N	36.0	38.00
X_8	Pmm	Precipitation	mm	0.0	1100.0
X_9	Tmean	Mean temperature	°C	-19.0	32.0

Table 4. Range of parameter values used in the sensitivity analysis of the simplified energy-balance ice melt model.

Parameter No.	Parameter descriptor	Parameter description	Units	Lower limit	Upper limit
X_1	Albedo	Reflected shortwave radiation from snow/ice surface	Decimal fraction	0.2	0.95
X_2	Radiation	Incoming shortwave radiation	W/m^2	17.2	348.3
X_3	Tmean	Mean temperature	°C	-19.0	32.0
X_4	C0	Net longwave radiation empirical factor	W/m^2	-30.0	-60.0
X_5	C1	Turbulent heat fluxes empirical factor	$W/m^2/K$	-2.0	3.5
X_6	B	Thermal quality of snowpack	Decimal fraction	0.7	1.0

Table 5. Description of Owens River watershed-lake water-balance model components and parameters.

Model component	Parameter	Description	Default value of McCabe & Markstrom (2007)	Calibrated value range of Barth et al. (2016)	Calibrated value range (this study)	Value in paleohydrologic simulation (this study)	Units
Snow accumulation	TempRain	Threshold temperature for all precipitation as rain	3.3	3.3	3.3	3.3	ºC
	TempSnow	Threshold temperature for all precipitation as snow	-1.0	-9.0	-1.0 to -3.0	-1.96	ºC
	Maxmelt	Maximum melt rate below equilibrium line altitude (ELA)	0.5	0.75	0.5	0.5	Decimal fraction
	albedo_snow	Snow/glacier albedo	NA	NA	0.55	0.55 and 0.65[1]	Unitless
	$ELAsublim_F$	Snow/glacier sublimation fraction above equilibrium line altitude (ELA)	NA	NA	0.981	0.981	Unitless
Runoff	SMSC	Soil-moisture storage capacity	150	20 - 210	0 - 140	0 - 140	mm
	DRf	Direct runoff fraction from impervious surfaces/infiltration-excess overflow	0.05	0.02	0.01 - 0.04	0.025	Decimal fraction
	Rf	Runoff fraction from soil surplus storage	0.5	0.08	0.17 - 0.23	0.2	Decimal fraction
	rfactor_q	Quick runoff from surplus storage	NA	0.15	NA	NA	Decimal fraction

Table 5. Description of Owens River watershed-lake water-balance model components and parameters (Continued).

Model component	Parameter	Description	Default value of McCabe & Markstrom (2007)	Calibrated value range of Barth et al. (2016)	Calibrated value range (this study)	Value in paleohydrologic simulation (this study)	Units
Groundwater	BF1 and BF2	Total baseflow	NA	NA	0.8192 - 1.229	1.029	10^8 m^3/yr
	ORG	Lower Owens River gain along channel	NA	NA	3.70 - 13.60	8.63	10^6 m^3/yr
	GWD	Spring discharge into Owens Lake basin	NA	NA	1.37	1.37	10^7 m^3/yr
	OR_loss_F	Owens River channel loss fraction	NA	NA	0.7 - 0.8	0.75	Decimal fraction
	$Alluv\_loss_F$	Runoff loss fraction in alluvium from percolation and evapotranspiration along streams	NA	NA	0.7 - 0.8	0.75	Decimal fraction
Lake evaporation	$Salt_f$	Salinity suppression factor	NA	NA	0.829	0.829 (saline lake) 0.930 (fresh lake)	Decimal fraction

Note: NA = not applicable.

Table 6. Earth's obliquity and monthly solar insolation for the Owens River Watershed from 0 to 12,000 years ago after Berger and Loutre (1991).

Years B.P.	Earth's Obliquity (deg)	Solar insolation (W/m^2) at 37°N latitude												
		Oct	Nov	Dec	Jan	Feb	Mar	Apr	May	Jun	Jul	Aug	Sep	Annual
0	23.45	263.56	200.79	177.16	202.05	266.75	347.24	418.87	465.41	480.04	462.02	413.88	342.25	4040.03
1000	23.58	265.30	200.94	176.33	200.45	264.19	343.71	415.34	462.99	480.23	464.44	417.42	345.79	4037.12
2000	23.70	266.90	201.08	174.88	198.37	261.13	340.17	412.28	461.88	481.68	468.17	421.78	349.33	4037.66
3000	23.82	268.01	200.26	173.43	195.80	258.08	337.12	410.35	462.36	484.45	473.02	426.62	352.72	4042.21
4000	23.93	268.50	199.14	171.35	193.24	255.03	334.70	409.38	464.15	488.80	478.20	431.46	355.28	4049.23
5000	24.03	268.01	197.55	169.12	190.52	252.32	332.76	409.86	467.06	493.99	484.01	435.82	356.88	4057.90
6000	24.11	267.04	195.46	166.55	188.30	250.38	332.13	411.32	471.27	499.65	489.19	438.87	357.85	4068.02
7000	24.17	264.96	192.90	164.32	186.21	248.78	332.28	414.22	476.26	505.46	494.03	441.15	357.36	4077.95
8000	24.21	262.88	190.67	162.58	184.76	248.30	333.73	418.10	481.93	510.98	497.42	442.12	356.25	4089.72
9000	24.23	259.83	188.59	160.98	183.65	248.78	336.15	422.45	487.25	515.34	499.36	441.15	353.68	4097.23
10,000	24.23	257.11	186.84	160.01	183.65	249.90	339.20	426.96	492.10	518.73	499.85	439.21	350.29	4103.86
11,000	24.20	254.55	185.24	159.53	184.28	251.98	342.74	431.80	495.97	520.19	498.39	435.82	346.76	4107.25
12,000	24.15	251.98	184.62	159.87	185.73	254.55	346.76	435.82	498.39	519.85	495.63	431.80	343.08	4108.07

Table 7. Difference from modern Earth's obliquity and percent change from modern monthly solar insolation for the Owens River Watershed from 0 to 12,000 years ago after Berger and Loutre (1991).

Years B.P.	Difference from modern Earth's obliquity (deg)	Percent change from modern solar insolation at 37°N latitude												
		Oct	Nov	Dec	Jan	Feb	Mar	Apr	May	Jun	Jul	Aug	Sep	Annual
0	0.00	0.00	0.00	0.00	0.00	0.00	0.00	0.00	0.00	0.00	0.00	0.00	0.00	0.00
1000	0.13	0.66	0.07	-0.46	-0.79	-0.96	-1.02	-0.84	-0.52	0.04	0.52	0.85	1.03	-0.07
2000	0.26	1.27	0.14	-1.28	-1.82	-2.11	-2.04	-1.57	-0.76	0.34	1.33	1.91	2.07	-0.06
3000	0.38	1.69	-0.27	-2.10	-3.09	-3.25	-2.91	-2.03	-0.66	0.92	2.38	3.08	3.06	0.05
4000	0.48	1.87	-0.82	-3.28	-4.36	-4.39	-3.61	-2.27	-0.27	1.83	3.50	4.25	3.81	0.23
5000	0.58	1.69	-1.62	-4.54	-5.70	-5.41	-4.17	-2.15	0.35	2.91	4.76	5.30	4.27	0.44
6000	0.66	1.32	-2.65	-5.99	-6.81	-6.14	-4.35	-1.80	1.26	4.09	5.88	6.04	4.56	0.69
7000	0.72	0.53	-3.93	-7.24	-7.84	-6.74	-4.31	-1.11	2.33	5.30	6.93	6.59	4.41	0.94
8000	0.76	-0.26	-5.04	-8.23	-8.56	-6.92	-3.89	-0.18	3.55	6.45	7.66	6.82	4.09	1.23
9000	0.78	-1.41	-6.08	-9.13	-9.11	-6.74	-3.19	0.86	4.69	7.35	8.08	6.59	3.34	1.42
10,000	0.78	-2.44	-6.95	-9.68	-9.11	-6.32	-2.32	1.93	5.73	8.06	8.19	6.12	2.35	1.58
11,000	0.75	-3.42	-7.74	-9.95	-8.80	-5.54	-1.30	3.09	6.57	8.36	7.87	5.30	1.32	1.66
12,000	0.71	-4.39	-8.06	-9.76	-8.08	-4.58	-0.14	4.05	7.09	8.29	7.27	4.33	0.24	1.68

10. REFERENCES

Adams, K.D. (2007). Late Holocene sedimentary environments and lake-level fluctuations at Walker Lake, Nevada, USA. *Geological Society of America Bulletin* 119, 126–139.

Adams K.D., and Wesnousky S.G. (1998). Shoreline processes and the age of the Lake Lahontan highstand in the Jessup embayment, Nevada. *Geological Society of America Bulletin* 110: 1318–1332.

Adams, K.D., Goebel, T., Graf, K., Smith, G.M., Camp, A.J., Briggs, R.W., Rhode, D. (2008). Late Pleistocene and early Holocene lake-level fluctuations in the Lahontan Basin, Nevada: implications for the distribution of archaeological sites. *Geoarchaeology* 23, 608-643.

Adams, K. D., Negrini, R. M., Cook, E. R., Rajagopal, S. (2015). Annually-Resolved Late Holocene Paleohydrology of the Southern Sierra Nevada and Tulare Lake, California, *Water Resources Research*, 51, 1–17.

Alley, R.B., Mayewski, P.A., Sowers, T., Stuiver, M., Taylor, K.C., and Clark, P.U. (1997). Holocene climate instability: a prominent, widespread event 8200 yr ago. *Geology* 25, 483–486.

An, S.I., Im, S.H., and Jun, S.Y. (2018). Changes in ENSO activity during the last 6,000 years modulated by background climate state. *Geophysical Research Letters* 45, 2467–2475.

Antinao, J.J., and McDonald, E. (2013). An enhanced role for the Tropical Pacific on the humid Pleistocene-Holocene transition in southwestern North America. *Quaternary Science Reviews* 78, 319–341.

Asmerom, Y., Polyak, V.J., and Burns, S.J. (2010). Variable winter moisture in the southwestern United States linked to rapid climate shifts. *Nature Geoscience* 3, 114–117.

Assouline, S., Li, D., Tyler, S., Tanny, J., Cohen, S., Bou-Zeid, E., Parlange, M., and Katul, G.G. (2016). On the variability of the Priestley-Taylor coefficient overwater bodies. *Water Resources Research*, 52, 150–163.

Ault T.R., Cole, J.E., Overpeck, J.T., Pederson, G.T., Meko, D.M. (2014). Assessing the risk of persistent drought using climate model simulations and paleoclimate data. Journal of Climate 27, 7529–49.

Bacon, S.N., Burke, R.M., Pezzopane, S.K., and Jayko, A.S. (2006). Last glacial maximum and Holocene lake levels of Owens Lake, eastern California, USA. *Quaternary Science Reviews* 25/11-12, 1264-1282.

Bacon, S.N., and Pezzopane, S.K. (2007). A 25,000-year record of earthquakes on the Owens Valley fault near Lone Pine, California: Implications for recurrence intervals, slip rates, and segmentation models. *Geological Society of America Bulletin*, 119/7, 823–847.

Bacon, S.N., Lancaster, N., Stine, S., Rhodes, E.J., and McCarley Holder, G.A. (2018). A continuous 4000-year lake-level record of Owens Lake, south-central Sierra Nevada, California, USA. *Quaternary Research* 90, 276–302.

Bacon, S.N., Bullard, T.F., Keen-Zebert, A.K., Jayko, A.S., and Decker, D.L. (2019a). Spatiotemporal patterns of distributed slip in southern Owens Valley indicated by deformation of late Pleistocene shorelines, eastern California. *Geological Society of America Bulletin*, (in press) doi.org/10.1130/B35247.1.

Bacon, S.N., Bullard, T.F., Adams, K.D., and Decker, D.L. (2019b). Geomorphic map of China Lake basin below 700 m elevation, Inyo, Kern, and San Bernardino Counties, California. Prepared by Naval Earth Sciences and Engineering Program, Desert Research Institute for Naval Air Warfare Center, Weapons Division, China Lake, NAWCWD TP 8839, 1:50,000-scale.

Bacon, S.N., Jayko, A.S., Owen, L.A., Lindvall, S.C., Rhodes, E.J., Schumer, R.A., and Decker, D.L. (2020). A 50,000-year record of lake-level variations and overflow from Owens Lake, eastern California, USA. *Quaternary Science Reviews* (in press).

Bahr, D.B., Meier, M.F., and Peckham, S.D. (1997). The physical basis of glacier volume-area scaling. *Journal of Geophysical Research* 102(B9), 20,355–20,362.

Bale, R.J., Robertson, I., Salzer, M.W., Loader, N.J., Leavitt, S.W., Gagen, M., Harlan, T.P., and McCarroll, D. (2011). An annually resolved bristlecone pine carbon isotope chronology for the last millennium. *Quaternary Research* 76, 22–29.

Barrett, A. (2003). National Operational Hydrologic Remote Sensing Center SNOw Data Assimilation System (SNODAS) Products at NSIDC. NSIDC Special Report 11. Boulder, CO, USA: National Snow and Ice Data Center. Digital media.

Barth, C., Boyle, D.P., Hatchett, B.J., Bassett, S.D., Garner, C.B., and Adams, K.D. (2016). Late Pleistocene climate inferences from a water balance model of Jakes Valley, Nevada (USA). *Journal of Paleolimnology*, DOI 10.1007/s10933-016-9897-z.

Bartlein, P.J., and 18 others. (2011). Pollen-based continental climate reconstructions at 6 and 21 ka: a global synthesis. *Climate Dynamics* 37, 775–802.

Bartov, Y., Enzel, Y., Porat, N., Stein, M. (2007). Evolution of the late Pleistocene-Holocene Dead Sea Basin from sequence stratigraphy of fan deltas and lake-level reconstruction. *Journal of Sedimentary Research* 77, 680–692.

Basagic, H.J., and Fountain, A.G. (2011). Quantifying 20th century glacier change in the Sierra Nevada, California. *Arctic, Antarctic, and Alpine Research* 43, 317–330.

Belmecheri, S., Babst, F., Wahl, E.R., Stahle, D.W., Trouet, V. (2015). Multi-century evaluation of Sierra Nevada snowpack. *Nature Climate Change* 6(2–3), doi:10.1038/nclimate2809.

Benson, L. (1994). Carbonate deposition, Pyramid Lake subbasin, Nevada; 1, Sequence of formation and elevational distribution of carbonate deposits (tufas). *Palaeogeography, Palaeoclimatology, Palaeoecololgy* 109, 55–87.

Benson, L. (2004). Western Lakes. In: Gillespie, A.R., Porter, S.C., Atwater, B.F. (Eds.), The Quaternary Period in the United States. Elsevier, New York, pp. 185–204.

Benson, L.V., and Thompson, R.S. (1987). The physical record of lakes in the Great Basin. In: Ruddiman, W.F., Wright Jr., H.E. (Eds.), North America and Adjacent Oceans during the Last Deglaciation. Geological Society of America, Boulder, CO, United States, pp. 241–260.

Benson, L.V., and Paillet, F.L. (1989). The use of total lake-surface area as an indicator of climatic change: examples from the Lahontan basin. *Quaternary Research* 32, 262–275.

Benson, L.V., Currey, D.R., Dorn, R.I., Lajoie, K.R., Oviatt, C.G., Robinson, S.W., Smith, G.I., and Stine, S. (1990). Chronology of expression and contraction of four Great Basin lake systems during the past 35000 years, *Palaeogeography, Palaeoclimatology, Palaeoecology* 78, 241–286.

Benson, L.V., Burdett, J.W., Kashgarian, M., Lund, S.P., Phillips, F.M., and Rye, R.O. (1996). Climatic and hydrologic oscillations in the Owens Lake basin and the adjacent Sierra Nevada, California. *Science* 274, 746–749.

Benson, L., Burdett, J., Lund, S., Kashgarian, M., and Mensing, S. (1997). Nearly synchronous climate change in the Northern Hemisphere during the last glacial termination. *Nature* 388, 263–265.

Benson, L., Kashgarian, M., Rye, R., Lund, S., Paillet, F., Smoot, J., Kester, C., Mensing, S., Meko, D., and Lindstrom, S. (2002). Holocene multidecadal and multicentennial droughts affecting northern California and Nevada. *Quaternary Science Reviews* 21, 659–682.

Berger A. and Loutre M.F. (1991). Insolation values for the climate of the last 10 million years. *Quaternary Science Reviews* 10(4), 297–317.

Berkelhammer, M., and Stott, L.D. (2008). Recent and dramatic changes in Pacific storm trajectories recorded in $\delta^{18}O$ from bristlecone pine tree ring cellulose. *Geochemistry, Geophysics, Geosystems* 9, Q04008.

Blevins, M.L., Pagan, R.J., and Haw, R.D. (1976). Report on Owens Lake water balance water year 1968-69. Los Angeles Department of Water and Power, Internal Report.

Blunt, A., and Negrini, R.M. (2016). Latest Pleistocene through Holocene lake levels from the TL05-4 cores, Tulare Lake, CA. *Quaternary International* 387, 122–130.

Bond, G.C., Heinrich, H., and Broecker, et al. (1992). Evidence for massive discharges of icebergs into the North Atlantic Ocean during the last glacial period. *Nature* 360, 245–249.

Borgonovo, E., and Plischke, E. (2016). Sensitivity analysis: A review of recent advances. *European Journal of Operational Research* 248, 869–887.

Borgonovo, E., Lu, X., Plischke, E., Rakovec, O, and Hill, M.C. (2017). Making the most out of a hydrological model data set: Sensitivity analyses to open the model black-box. *Water Resources Research* 53, 7933–7950.

Bowerman, N.D., and Clark, D.H. (2011). Holocene glaciation of the central Sierra Nevada, California. *Quaternary Science Reviews* 30, 1067–1085.

Braconnot, P., Luan, Y., Brewer, S., and Zheng, W. (2011). Impact of Earth's orbit and freshwater fluxes on Holocene climate mean seasonal cycle and ENSO characteristics. *Climate Dynamics* 38, 1081–1092.

Bradley, R.S., Hughes, M.K., and Diaz, H.F. (2003). Climate in medieval time. *Science* 302, 404–405.

Broecker, W. (2010). Long-term water prospects in the western United States. *Journal of Climate* 23, 6669–6683.

Bullard, T.F., Bacon, S.N., Adams, K.D., and Decker, D.L. (2019). Geomorphic Map of the China Lake Basin below 700 m in Support of Cultural Resource Management at Naval Air Weapons Station China Lake. Prepared by Naval Earth Sciences and Engineering Program, Desert Research Institute for Naval Air Warfare Center, Weapons Division, China Lake, NAWCWD TP 8839, 24 pp. including appendices and 1:5,000-scale map.

Burbank, D.W. (1991). Late Quaternary snowline reconstructions for the southern and central Sierra Nevada, California and a reassessment of the "Recess Peak Glaciation". *Quaternary Research* 36, 297–306.

Cacuci, D.G. (2003). Theory. In: Sensitivity and Uncertainty Analysis, vol. 1. Chapman and Hall Publisher.

Cannavo', F., 2011. Get Sobol Sequence. https://www.mathworks.com/matlabcentral/mlc-downloads/downloads/submissions/40759/versions/12/previews/fnc_getSobolSequence.m/index.html.

Cayan, D.R., Redmond, K.T., and Riddle, L.G. (1999). ENSO and hydrologic extremes in the western United States. *Journal of Climate* 12, 2881–2893.

Cayan, D., Das, T., Pierce, D., Barnett, T., Tyree, M., and Gershunov, A., (2010). Future dryness in the southwest United States and the hydrology of the early 21st century drought. *Proc. Natl. Acad. Sci. U.S.A.*, 107(50), 21,271–21,276.

Chen, J., and Ohmura, A. (1990). Estimation of alpine glacier water resources and their change since the 1870s. in Hydrology in mountainous regions: hydrologic measurements, the water cycle. *International Association of Hydrological Sciences Publication* 193, 127–135.

Choi, N.H. (2016). Late Pleistocene slip rate along the Panamint Valley Fault System, Eastern California. Unpublished Master's Thesis, Oregon State University, Corvallis, Oregon, 72 p.

Clark, D.H., and Gillespie, A.R. (1997). Timing and significance of late-glacial and Holocene cirque glaciation in the Sierra Nevada, California. *Quaternary International* 38/39, 21–38.

Clark, P.U., Webb, R.S., and Keigwin, L.D. (1999). Mechanisms of global climate change at millennial time scales. Geophysical Monograph 112, American Geophysical Union, Washington, D.C., 394 p.

Clement, A.C., Seager, R., and Cane, M.A. (2000). Suppression of El Niño during the mid-Holocene by changes in the Earth's orbit. *Paleoceanography* 15, 731–737.

Clement, S.M. (2005). Modeling of the Great Basin pluvial lakes during the Last Glacial Maximum. Unpublished Ph.D. thesis, Kent State University, Ohio, USA.

Cohen, A.S., (2003). Paleolimnology: The History and Evolution of Lake Systems. Oxford University Press, New York, NY 500 p.

Conway, C.J. (1997). Observation of ephemeral flows and estimation of recharge from the Inyo and Coso Mountains, Owens Dry Lake, California. Unpublished Master's Thesis, University of Nevada, Reno.

Cook, B.I., Seager, R., and Miller, R.L. (2011). On the causes and dynamics of the early twentieth-century North American pluvial. *Journal of Climate* 24, 5043–5060.

Cook, B.I., Cook, E.R., Smerdon, J.E., Seager, R., Williams, A.P., Coats, S., Stahle, D.W., and Díaz, J.V. (2016). North American megadroughts in the Common Era: reconstructions and simulations. *WIREs Climate Change*. doi: 10.1002/wcc.394.

Cook E.R., Meko D.M., Stahle D.W., and Cleaveland, M.K. (1999). Drought reconstructions for the continental United States. *Journal of Climate* 12, 1145–1162.

Cook, E.R., Woodhouse, C., Eakin, C.M., Meko, D.M., and Stahle, D.W. (2004). Long-term aridity changes in the western United States. *Science* 306, 1015–1018.

Cook, E.R., Seager, R., Heim, Jr. R.R., Vose, R.S., Herweijer, C., and Woodhouse, C. (2010). Megadrought in North America: placing the IPCC projections of hydroclimate change in a long-term paleoclimate context. *Journal of Quaternary Science* 25, 48–61.

Dai, A. (2013). Increasing drought under global warming in observations and models. *Nat. Clim. Change*, 3(1), 52–58.

Dai, A., Trenberth, K.E., and Qian, T., (2004). A global dataset of Palmer Drought Severity Index for 1870–2002: Relationship with soil moisture and effects of surface warming. *Journal of Hydrometeorology* 5(6), 1117–1130.

Daly, C., Nelson, R.P., and Philips, D.L. (1994). A statistical-topographic model for mapping climatological precipitation over mountain terrain. *Journal of Applied Meteorology* 33, 140–158.

Daly, C., Slater, M.E., Roberti, J.A., Laseter, S.H., and Swift, L.W., Jr. (2017). High-resolution precipitation mapping in a mountainous watershed: ground truth for evaluation uncertainty in a national precipitation dataset. *International Journal of Climatology*. DOI: 10.1002/joc.4986.

Dansgaard, W., Johnsen, S.J., Clausen, H.B., Dahl-Jensen, D., Gunderstrup, N.S., Hammer, C.U., Steffensen, J.P., Svein-björnsdottir, A., Jouzel, J., and Bond, G. (1993). Evidence for general instability of past climate from 250-kyr ice-core record. *Nature* 364, 218–220.

Danskin, W.R. (1998). Evaluation of the hydrologic system and selected water-management alternatives in the Owens Valley, California. U.S. Geological Survey Water-Supply Paper 2370-H, 175 p.

DeRose, J.R., Wang, S., Buckley, B.M., and Bekker, M.F. (2014). Tree-ring reconstruction of the level of Great Salt Lake, USA. *The Holocene* 24, 805-813.

Dettinger, M.D. and Cayan, D.R., (1995). Large-scale atmospheric forcing of recent trends toward early snowmelt runoff in California. *Journal of Climate*, 8(3), 606–623.

Dettinger, M.D., Ralph, F.M., Das, T., Neiman, P.J., Cayan, D.R. (2011). Atmospheric rivers, floods and the water resources of California. *Water* 3, 445–478.

DeWalle, D.R., and Rango, A. (2008). Principles of Snow Hydrology. Cambridge University Press, New York. 410 p.

Diffenbaugh, N.S., Ashfaq, M., Bryan, S., Williams, J.W., and Bartlein, P.J. (2006). Summer aridity in the United States: response to mid-Holocene changes in insolation and sea surface temperature. *Geophysical Research Letters* 33, L22712.

Dileanis, P.D. and Groeneveld, D.P. (1989). Osmotic potential and projected drought tolerance of four phreatophytic shrub species in Owens Valley, California. U.S. Geological Survey Water-Supply Paper 2370-D, 21 p.

Duell, L.F.W., Jr. (1991). Estimates of evapotranspiration in alkaline scrub and meadow communities of Owens Valley, California, using the Bowen-ratio, eddy-correlation, and Penman-combination methods: U.S. Geological Survey Water-Supply Paper 2370-E, 39 p.

Ehlers, E.G., and Blatt, H. (1982). Petrology: Igneous, Sedimentary, and Metamorphic. W.H Freeman and Company, New York. 732 p.

Emile-Geay, J., Seager, R., Cane, M.A., and Cook, E.R. (2008). Volcanoes and ENSO over the past millennium. *Journal of Climate* 21, 3134–3148.

Enzel, Y., and Wells, S.G. 1997. Extracting Holocene paleohydrology and paleoecology information from modern extreme flood events: An example from southern California. *Geomorphology* 19, 203–226.

Enzel, Y., Cayan, D.R., Anderson, R.Y., Wells, S.G. (1989). Atmospheric circulation during Holocene lake stands in the Mojave Desert: evidence of regional climate change. *Nature* 341, 44–48.

Enzel, Y., Wells, S.G., Lancaster, N. (2003). Late Pleistocene lakes along the Mojave River, southeast California. In: Enzel, Y., Wells, S.G., Lancaster, N. (Eds.), Paleoenvironments and Paleohydrology of the Mojave and Southern Great Basin Deserts, Geological Society of America Special Paper 368, pp. 61–77.

Epstein, S., and Yapp, C.J. (1976). Climatic implications for paleoclimate reconstruction based on isotopic analysis of wood cellulose. *Geochem. Cosmochim. Acta.* 53, 2573–2580.

Feeney Hall, M.P. (1996). Investigation of spring and seep discharge at Owens Lake, California. Unpublished Master's Thesis, University of Nevada, Reno, 117 p.

Forester, R.M. (2000). An ostracode record of Holocene climate change from Owens Lake, California. In: Jayko, A.S., Miller, C.I. (eds.), Impacts of Climate Change on Landscapes of the Eastern Sierra Nevada and Western Great Basin. U.S. Geological Survey Open-File Report 01-202, pp. 7–8.

Fountain, A.G., Hoffman, M., Jackson, K., Basagic, H., Nylen, T., and Percy, D. (2007). Digital outlines and topography of the glaciers of the American West: U.S. Geological Survey Open-File Report 2006–1340, 23 p.

Gale, H.S. (1914). Salines in the Owens, Searles, and Panamint basins, south-eastern California. U.S. Geology Survey Bulletin 580-L, 251-323.

Giambastiani, M.A., Bullard, T.F. (2007). Terminal Pleistocene-early Holocene occupations on the eastern shoreline of China Lake, California. Pac. Coast Archaeol. Soc. Q. 43, 51–70 (printed 2010).

Gillies, R.R., Chung, O., Wang, S., DeRose, J.R., and Sun, Y. (2015). Added value from 576 years of tree-ring records in the prediction of the Great Salt Lake level. *Journal of Hydrology* 529, 962–968.

Graf, W.L. (1976). Cirques as glacier locations. *Arctic and Alpine Research* 8, 79–90.

Graham, N.E., and Hughes, M.K. (2007). Reconstructing the medieval low stands of Mono Lake, Sierra Nevada, California, USA. *The Holocene* 17(8), 1197–1210.

Gray, S.T., and McCabe, G.J. (2010). A combined water balance and tree ring approach to understanding the potential hydrologic effects of climate change in the central Rocky Mountain region. *Water Resources Research* 46, W05513 (13 pp).

Groeneveld, D.P., Huntington, J.L., and Barz, D.D. (2010). Floating brine crusts, reduction of evaporation and possible replacement of fresh water to control dust from Owens Lake bed, California. *Journal of Hydrology* 392, 211–218.

Gupta, H.V., Clark, M.P., Vrugt, J.A., Abramowitz, G., and Ye, M. (2012). Towards a comprehensive assessment of model structure adequacy. *Water Resources Research* 48, W08301.

Hamon, W.R. (1961). Estimating potential evapotranspiration. *Journal of the Hydraulics Division, Proceedings of the American Society of Civil Engineers* 87, 107–120.

Hamby, D.H. (1994). A review of techniques for parameter sensitivity analysis of environmental models. *Environmental Monitoring and Assessment* 32, 135–154.

Harbeck, G.E. (1955). The effect of salinity on evaporation. U.S. Geological Survey Professional Paper 272-A, 6 p.

Harpold, A.A., Dettinger, M., and Rajagopal, S. (2017). Defining snow drought and why it matters. *Eos* 98, doi:10.1029/2017EO068775.

Hatchett, B.J. (2018). Snow level characteristics and impacts of a spring typhoon-originating atmospheric river in the Sierra Nevada, USA. *Atmosphere* 9, 233, doi:10.3390/atmos9060233.

Hatchett, B.J., and McEvoy, D.J. (2018). Exploring the origins of snow droughts in the northern Sierra Nevada, California. *American Meteorological Society* 22, 1–13.

Hatchett, B.J., Boyle, D.P., Putnam, A.E., and Bassett, S.D. (2015). Placing the 2012-2015 California-Nevada drought into a paleoclimatic context: Insights from Walker Lake, California-Nevada, USA. *Geophysical Research Letters* 42, doi:10.1002/2015GL065841.

Hatchett, B. J., Boyle, D. P., Garner, C. B., Kaplan, M. L., Putnam, A. E., and Bassett, S. (2016). Magnitude and frequency of wet years under a megadrought climate in the western Great Basin, USA, *Quaternary Science Reviews* 152, 197–202.

Hatchett, B.J., Daudert, B., Garner, C.B., Oakley, N.S., Putnam, A.E., and White, A.B. (2017). Winter snow level rise in the northern Sierra Nevada from 2008 to 2017. *Water* 9, 899, doi:10.3390/w9110899.

Hatchett, B.J., Boyle, D.P., Garner, C.B., Kaplan, M.L., Bassett, S.D., and Putnam, A.E. (2019). Sensitivity of a western Great Basin terminal lake to winter northeast Pacific storm track activity and moisture transport. In Starratt, S.W., and Rosen, M.R., (Eds.), From Saline to Freshwater: The Diversity of Western Lakes in Space and Time: Geological Society of America Special Paper 536, doi.org/10.1130/2018.2536(05).

Heinrich, H. (1988). Origin and consequences of cyclic ice rafting in the northeast Atlantic Ocean during the past 130,000 years. *Quaternary Research* 29, 142–152.

Hemming, S.R. (2004). Heinrich events; massive late Pleistocene detritus layers of the North Atlantic and their global climate imprint. *Reviews in Geophysics* 42, RG1005.1–RG1005.43.

Hoffman, W.R. (2009). Late Pleistocene slip rates along the Panamint Valley Fault Zone, Eastern California. Unpublished Master's Thesis, The Pennsylvania State University, 81 p.

Hollett, K.J. (1987). Additional studies, *in* Rogers, L.S., and others. Overview of water resources in Owens Valley, California: U.S. Geological Survey Water-Resources Investigations Report 86-4357, p. 34–35.

Hollett, K.J., Danskin, W.R., McCafferey, W.F., and Walti, C.L. (1991). Geology and water resources of Owens Valley, California. U.S. Geological Survey Water-Supply Paper 2370-B, 77 p.

Homma, T., and Saltelli, A. (1996). Importance measures in global sensitivity analysis of nonlinear models. *Reliability Engineering and System Safety* 52, 1–17.

Howat, I.M., and Tulaczyk, S. (2005). Trends in spring snowpack over a half-century of climate warming in California, USA. *Annals of Glaciology* 40, 151–156.

Hughes, M.K., and Graumlich, L.J., (1996). Multimillennial dendroclimatic studies from the western United States. *in*: (eds.) R.S. Bradley, P.D. Jones, and J. Jouzel. Climatic variations and forcing mechanisms of the last 2000 years. Berlin: Springer Verlag, p. 109–124.

Hughes, M.K., and Diaz, H.R. (1994). Was there a Medieval Warm Period, and if so, where and when? *Climatic Change* 26, 109–142.

Hughes, M.K., Funkhouser, G., and Ni, F. (2002). The ancient bristlecone pines of Methuselah Walk, California, as a natural archive of past environment. *PAGES News* 10(1), 16–17.

Huss, M. (2013). Density assumptions for converting geodetic glacier volume change to mass change. *The Cryosphere* 7, 877–887.

Huth, T., Hudson, A.M., Quade, J., Guoliang, L., and Hucai, Z. (2015). Constraints on paleoclimate from 11.5 to 5.0 ka from shoreline dating and hydrologic budget modeling of Baqan Tso, southwestern Tibetan Plateau. *Quaternary Research* 83, 80–93.

Huybers, K., Rupper, S., and Roe, G.H. (2016). Response of closed basin lakes to interannual climate variability. *Climate Dynamics* 46, 3709–3723.

Ibarra, D.E., Egger, A.E., Weaver, K.L., Harris, C.R., and Maher, K. (2014). Rise and fall of late Pleistocene pluvial lakes in response to reduced evaporation and precipitation: Evidence from Lake Surprise, California. *Geological Society of America Bulletin,* doi:10.1130/B31014.1

Jayko, A.S. and Bacon, S.N. (2008). Late Quaternary MIS 6-8 shoreline features of pluvial Owens Lake, Owens Valley, eastern California, in Reheis, M.C., Hershler, R., and Miller, D.M., eds., Late Cenozoic Drainage History of the Southwestern Great Basin and Lower Colorado River Region: Geologic and Biotic Perspectives: Geological Society of America Special Paper 439, p. 185-206.

Jennings, C.W., with modifications by Gutierrez, C., Bryant, W., Saucedo, G., and Wills, C. (2010). Geologic map of California: California Geological Survey, Geologic Data Map No. 2, scale 1:750,000.

Kaufman, D.S., Porter, S.C., and Gillespie, A.R. (2004). Quaternary alpine glaciations in Alaska, the Pacific Northwest, Sierra Nevada, and Hawaii. In: A.R. Gillespie,

S.C. Porter, and B.F. Atwater (Eds.), The Quaternary Period in the United States. Developments in Quaternary Science 1, Elsevier Publishing, pp. 77–104.

Kavetski, D., Kuczera, G., and Franks, S. (2006). Bayesian analysis of input uncertainty in hydrological modeling: 2. Application. *Water Resources Research* 42. 10.1029/2005WR004376.

Kirby, M.E., Zimmerman, S.R.H., Patterson, W.P., and Rivera, J.J. (2012). A 9170-year record of decadal-to-multi-centennial scale pluvial episodes from the coastal Southwest United States: a role for atmospheric rivers? *Quaternary Science Reviews* 46, 57–65.

Kirby, M.E., Knell, E.J., Anderson, W.T., Lachniet, M.S., Silveira, E., Palermo, J.,Hiner, C.A., Eeg, H., Arevalo, A., Lucero, R., Murrieta, R. (2015). Evidence for Insolation and Pacific Forcing of Late Glacial through Holocene Climate in the Central Mojave Desert (Silver Lake, CA), *Quaternary Research* 84, 174–186.

Kleppe, J.A., Brothers, D.S., Kent, G.M., Biondi, F., Jensen, S., and Driscoll, N.W. (2011). Duration and severity of Medieval drought in the Lake Tahoe Basin. *Quaternary Science Reviews* 30, 3269–3279.

Konrad, S.K., and Clark, D.H. (1998). Evidence for an early Neoglacial glacier advance from rock glaciers and lake sediments in the Sierra Nevada, California, USA. *Arctic and Alpine Research* 30, 272–284.

Kuczera, G., Kavetski, D., Franks, S., and Thyer, M. (2006). Towards a Bayesian total error analysis of conceptual rainfall-runoff models: Characterising model error using storm-dependent parameters. *Journal of Hydrology* 331, 161–177.

Kutzbach, J.E. (1980). Estimates of past climate at Paleolake Chad, North Africa, based on a hydrological and energy-balance model. *Quaternary Research* 14, 210–223.

LADWP [Los Angeles Department of Water and Power] (1987). Mono Basin geology and hydrology. Report prepared by the Aqueduct Division – Hydrology Section, May, 1987, 123 p. figures, tables, plus appendices.

LaMarche,V.C. Jr. (1973). Holocene climatic variations inferred from tree line fluctuations in the White Mountains, California. *Quaternary Research* 3, 632–660.

LaMarche, V.C. Jr. (1974). Paleoclimatic inferences from long tree-ring records. *Science* 183, 1043–1048.

Lancaster, N., Bacon, S.N., Baker, S., and Holder, G.A.M. (2015). Owens Lake dune fields: composition, sources of sand, and transport pathways. *Catena* 134, 41–49.

Lancaster, N., Bacon, S.N., Bullard, T.F., and Decker, D.L. (2019). Eolian Hazard Assessment for the SNORT Facility. Prepared by Naval Earth Sciences and Engineering Program, Desert Research Institute for Naval Air Warfare Center, Weapons Division, China Lake, NAWCWD TP 8840, 40 pp. including appendices.

Landwehr, J.M., Sharp, W.D., Coplen, T.B., Ludwig, K.R., and Winograd, I.J. (2011). The chronology for the $\delta^{18}O$ record from Devils Hole, Nevada, extended into the mid-Holocene: U.S. Geological Survey Open-File Report 2011–1082, 5 p.

Langbein, W.B. (1961). Salinity and hydrology of closed lakes. U.S. Geological Survey Professional Paper 412, 20 p.

Lean, J., Beer, J., and Bradley, R.S. (1995). Reconstruction of solar irradiance since 1610: implications for climate change. *Geophysical Research Letters* 22, 3195–3198.

Lee, C.H. (1912). An intensive study of the water resources of a part of Owens Valley, California. U.S. Geological Survey Water-Supply Paper 294, 135 p.

Lee, C.H. (1915). Report on hydrology of Owens Lake basin and the natural soda industry as affected by the Los Angeles Aqueduct diversion. Hydraulic Engineer, Los Angeles, California.

Lee, W.T. (1906). Geology and water resources of Owens Valley, California: U.S. Geological Survey Water- Supply Paper 181, 28 p.

Lee, W.T. (1932). Report on the physical and economic limits of the underground water resources of Owens Valley: Los Angeles Department of Water and Power, unpublished report, 23 p.

Leavitt, S.W. (1994). Major wet interval in White Mountains medieval warm period evidenced in $\delta^{13}C$ of bristlecone pine tree rings. *Climate Change* 26, 299–307.

Li, H., Bischoff, J.L., Ku, T., Lund, S.P., Stott, L.D. (2000). Climate variability in east-central California during the past 1000 years reflected by high-resolution geochemical and isotopic records from Owens Lake sediments. *Quaternary Research* 54, 187–197.

Liu, Z., Kutzbach, J., and Wu, L. (2000). Modeling climate shift of El Niño variability in the Holocene. *Geophysical Research Letters* 27, 2265–2268.

Liu, Z., Zhu, J., Rosenthal, Y., Zhang, X., Otto-Blienser, B.L., Timmermann, A., Smith, R.S., Lohmann, G., Zheng, W., and Timm, O.E. (2014). The Holocene temperature conundrum. *Proceedings of the National Academy of Sciences* 111, E3501–3505.

Lopes, T.J. (1988). Hydrology and water budget of Owens Lake, California: University of Nevada, Reno, Desert Research Institute, Water Resources Center Publication 41107, 104 p.

MacDonald, G.M., Moser, K.A., Bloom, A.M., Porinchu, D.F., Potito, A.P., Wolfe, B.B., Edwards, A.P., Orme, A.R., and Orme, A.J. (2008). Evidence of temperature depression and hydrological variations in the eastern Sierra Nevada during the Younger Dryas state. *Quaternary Research* 70, 131–140.

MacDougall, A.H., Wheler, B.A., and Flowers, G.E. (2011). A preliminary assessment of glacier melt-model parameter sensitivity and transferability in a dry subarctic environment. *The Cryosphere* 5, 1011–1028.

Mantua, N.J., and Hare, S.R. (2002). The Pacific decadal oscillation. *Journal of Oceanography* 58, 35–42.

Marcott, S.A., Shakun, J.D., Clark, P.U., and Mix, A.C. (2013). A Reconstruction of regional and global temperature for the past 11,300 years. *Science* 339, 1198–1201.

Marks, D., and Dozier, J. (1992). Climate and energy exchange at the snow surface in the alpine region of the Sierra Nevada 2: snow cover energy balance. *Water Resource Research* 28, 3043–3054.

Matsubara, Y., and Howard, A.D. (2009). A spatially explicit model of runoff, evaporation, and lake extent: Application to modern and late Pleistocene lakes in the Great Basin region, western United States. *Water Resources Research* 45, W06425.

Mayewski, P.A. et al., (2004). Holocene climate variability. *Quaternary Research* 62, 243–255.

McCabe, G.J., and Dettinger, M.D. (2002). Primary modes and predictability of year-to-year snowpack variations in the western United States from teleconnections with Pacific Ocean Climate. *Journal of Hydrometeorology* 3, 13–25.

McCabe, G.J., and Markstrom, S.L. (2007). A monthly water-balance model driven by a graphical user interface. U.S. Geological Survey Open-File Report 2007-1088, 6 p.

McGee, D., Moreno-Chamarro, E., Wetlandsall, J., Galbraith, E.D. (2018). Western U.S. lake expansions during Heinrich stadials linked to Pacific Hadley circulation. Science Advances 4, eaav0118, DOI: 10.1126/sciadv.aav0118.

McJannet, D.L., Cook, F.J., and Burn, S. (2013). Comparison of techniques for estimating evaporation from an irrigation water storage. *Water Resource Research* 49, 1415–1428.

Meier, M.F., and Post, A.S. (1962). Recent variations in mass net budgets of glaciers in western North America. IUGG/IASH Committee on Snow and Ice, General Assembly, Obergurgl. *International Association of Science and Hydrology* 58: 63–77.

Meko, D.M., Cook, E.R., Stahle, D.W., Stockton, C.W., and Hughes, M.K. (1993). Spatial patterns of tree-growth anomalies in the United States and south-eastern Canada: *Journal of Climate* 6, 1773–1786.

Meko, D.M., Therrell, M.D., Baisan, C.H., and Hughes, M.K. (2001). Sacramento River flow reconstructed to A.D. 869 from tree rings: *Journal of the American Water Resources Association* 37(4) 1029–1040.

Meko, D.M. and Woodhouse, C.A. (2011). Application of streamflow reconstruction to water resources management, *in* Dendroclimatology: Progress and Prospects (eds. M.K. Hughes, T.W. Swetnam, H.F. Diaz). Springer, pp. 231-261.

Menking, K.M. (1995). Paleoclimatic reconstructions from Owens Lake core OL-92, south-eastern California. Unpublished Ph.D. Thesis, University of California, Santa Cruz, 169 pp.

Mihevc, T.M., Cochran, G.F., and Hall, M. (1997). Simulation of Owens Lake water levels. Report prepared by Desert Research Institute for the Great Basin Unified Air Pollution Control District, June 1997, 71 p.

Mifflin M.D., and Wheat M.M. (1979). Pluvial lakes and estimated pluvial climates of Nevada. Nevada Bureau of Mines and Geology Bulletin 94: 57 pp; University of Nevada, Reno.

Milankovitch, M. (1941). Kanon der Erdbestrahlung, R. Serbian Academy Special Publication 132, Sect. Math. Nat. Sci., 33. (Canon of insolation and the ice-age problem, English translation by Israel Program for Scientific Translations, Jerusalem, 1969.)

Mono Lake Committee (2017). Mono Basin Clearinghouse. http://www.monobasinresearch.org/ onlinereports/index.php (accessed 2017).

Munroe, J.S. and Laabs, B.J.C. (2013). Late Pleistocene history of Pluvial Lake Franklin, Northeastern Nevada, U.S.A., *Geological Society of America Bulletin* 125, 322–342.

Negrini, R.M., Erbes, D.B., Faber, K., Herrera, A.M., Roberts, A.P., Cohen, A.S., Wigand, P.E., Foit, F.F.J. (2000). A paleoclimate record for the past 250,000 years from Summer Lake, Oregon, USA: I. Chronology and magnetic proxies for lake level. *Journal of Paleolimnology* 24, 125–149.

Negrini, R.M., Wigand, P.E., Draucker, S., Gobalet, K., Gardner, J.K., Sutton, M.Q., Yohe, R.M. (2006). The Rambla highstand shoreline and the Holocene lake-level history of Tulare Lake, California, USA. *Quaternary Science Reviews* 25, 1599–1618.

Niswonger, R.G., Allander, K.K., and Jeton, A.E. (2014). Collaborative modelling and integrated decision support system analysis of a developed terminal lake basin. *Journal of Hydrology* 517, 521–537.

Noble, P.J., Ball, G.I., Zimmerman, S.H., Maloney, J., Smith, S.B., Kent, G., Adams, K.D., Karlin, R.E., and Driscoll, N. (2016). Holocene paleoclimate history of Fallen Leaf Lake, CA, from geochemistry and sedimentology of well-dated sediment cores. *Quaternary Science Reviews* 131, 193–210.

Oerlemans, J. (2001). Glaciers and Climate Change, Swets & Zeitlinger, BV, Lisse, 1st ed., 148 p.

Orme, A.R. and Orme, A.J. (2008). Late Pleistocene shorelines of Owens Lake, California, and their hydroclimatic and tectonic implication, in Reheis, M.C., Hershler, R., and Miller, D.M., eds., Late Cenozoic Drainage History of the Southwestern Great Basin and Lower Colorado River Region: Geologic and Biotic Perspectives: Geological Society of America Special Paper 439, p. 207-226.

Orndorff, R.L. (1994). Development of a surface hydrologic model and its application to modern and last glacial conditions within the Great Basin. Unpublished Ph.D. thesis, Kent State University, Ohio, USA.

Oster, J.L., Montañez, I.P., Santare, L.R., Sharp, W.D., Wong, C., and Cooper, K.M. (2015). Stalagmite records of hydroclimate in central California during termination 1. *Quaternary Science Reviews* 127, 199–214.

Paterson, W.S.B. (1994). The physics of glaciers (3rd ed.). Pergamon Press. 480 p.

Peeters, L.J.M., Podger, G.M., Smith, T., Pickett, et al., Bark, R.H., and Cuddy, S.M. (2014). Robust global sensitivity analysis of a river management model to assess nonlinear and interaction effects. *Hydrology and Earth System Sciences* 18, 3777–3785.

Phillips, F.M. (2008). Geological and hydrological history of the paleo-Owens River drainage since the late Miocene, in Reheis, M.C., Hershler, R., and Miller, D.M., eds., Late Cenozoic Drainage History of the Southwestern Great Basin and Lower Colorado River Region: Geologic and Biotic Perspectives: Geological Society of America Special Paper 439, p. 115-150.

Phillips F.M. (2016). Constraints on cosmogenic nuclide production rates by samples from the Sierra Nevada, California: I. Late Pleistocene glacial chronology. *Quaternary Geochronology* 35, 119–129.

Phillips F. (2017). Glacial chronology of the Sierra Nevada, California, from the Last Glacial Maximum to the Holocene. *Geographical Research Letters* 43, 527–552.

Phillips, F.M., Zreda, M., Plummer, M.A., Elmore, D., and Clark, D.H. (2009). Glacial geology and chronology of Bishop Creek and vicinity, eastern Sierra Nevada, California. *Geological Society of America Bulletin* 121, 1013–1033.

Pierce, D.W., and Cayan, D.R. (2013). The uneven response of different snow measures to human-induced climate warming. *Journal of Climate* 26, 4148–4167.

Plishke, E., Borgonovo, E., and Smith, C.L. (2013). Global sensitivity measures from given data. *European Journal of Operational Research* 226, 536–550.

Porter, S.C. (1975). Equilibrium-line altitudes of late Quaternary glaciers in the Southern Alps, New Zealand. *Quaternary Research* 5, 27–47.

Priestley, C.H.B., and Taylor, R.J. (1972). On the assessment of surface heat flux and evaporation using large-scale parameters. *Monthly Weather Review* 100, 81–92.

Reeves, C.C. Jr. (1968). Introduction to Paleolimnology. Elsevier Publishing Company, New York, 228 p.

Raleigh, M. (2010). Matlab Code for Thornthwaite Monthly Water Balance Model. Coded on 4/17/2010, http://depts.washington.edu/mtnhydr/people/mraleig1/toolbox2.html#Top.

Raub, W.B., Brown, C.S., and Post, A. (2006). Inventory of glaciers in the Sierra Nevada, California. U.S. Geological Survey Open-File Report, 2006-1239, 232 p.

Redmond, K.T., and Koch, R.W. (1991). Surface climate and streamflow variability in the western United States and their relationship to large scale circulation indices. *Water Resources Research* 27, 2381–2399.

Reheis, M.C., Adams, K.D., Oviatt, C.G., and Bacon, S.N. (2014). Pluvial lakes in the Great Basin of the western United States – A view from the outcrop. *Quaternary Science Reviews* 97, 33–57.

Rice, J., Woodhouse, C., and Lukas, J. (2009). Science and decision-making: Water management and tree-ring data in the western United States. *Journal of the American Water Resources Association* 45(5): 1248–1259.

Rosenthal, J.S., Meyer, J., Palacios-Fest, M.R., Young, D.C., Ugan, A., Byrd, B.F., Goblet, K., and Giacomo, J. (2017). Paleohydrology of China Lake basin and the context of early human occupation in the northwestern Mojave Desert, USA. *Quaternary Science Reviews* 176, 112–139.

Routson C.C., Overpeck, J.T., Woodhouse, C.A., and Kenney, W.F. (2016). Three millennia of southwestern North American dustiness and future implications. *PLOS ONE* 11, doi:10.1371/journal.pone.0149573.

Roza, J., Jackson, B., Heaton, E., and Negrini, R. (2016). Paleomagnetic secular variation and environmental magnetism of Holocene-age sediments from Tulare Lake, CA. *Quaternary Research* 85, 391–398.

Saito, L., Biondi, F., Salas, J.D., Panorska, A.K., Kozubowski, T.J. (2008). A watershed modeling approach to streamflow reconstruction from tree-ring records. *Environmental Research Letters* 3 (2), 024006 (6pp).

Saito, L., Biondi, F., Devkota, R., Vittori, J., and Salas, J.D. (2015). A water balance approach for reconstructing streamflow using tree-ring proxy records. *Journal of Hydrology* 529, 535–547.

Salzer M.W., Hughes M.K., Bunn A.G., and Kipfmueller K.F. (2009). Recent unprecedented tree-ring growth in bristlecone pine at the highest elevations and possible causes. *Proceedings of the US National Academy of Sciences* 106, 20348–20353

Salzer, M.W., Bunn, A.G., Graham, N.E., and Hughes, M.K. (2014). Five millennia of paleotemperatures from tree-rings in the Great Basin, USA. *Climate Dynamics* 42, 1517–1526.

Schumer, R. (1997). Extension and refinement of the Owens Lake groundwater basin numerical simulation. Unpublished Master's Thesis, University of Nevada, Reno.

Shakun, J., Clark, P., He, F., Marcott, S.A., Mix, A.C., Liu, Z., Otto-Bliesner, B., Schmittner, A., and Bard, E. (2012). Global warming preceded by increasing carbon dioxide concentrations during the last deglaciation. *Nature* 484, 49–54.

Sharpe, S.E., and Forester, R.M. (2008). Continental-aquatic mollusk hydrochemical occurrence patterns: Implications for population dynamics and paleoenvironmental reconstruction. *Quaternary International* 188, 105–116.

Shuman, B.N., and Marsicek, J. (2016). The structure of Holocene climate change in the mid-latitude North America. *Quaternary Science Reviews* 141, 38–51.

Scuderi, L.A. (1987a). Glacier variations in the southern Sierra Nevada, California, as related to a 1200-year tree-ring chronology. *Quaternary Research* 27, 220–231.

Scuderi, L.A. (1987b). Late-Holocene upper timberline variation in the southern Sierra Nevada. *Nature* 325, 242–244.

Scuderi, L.A. (1993). A 2000-year tree ring record of annual temperatures in the Sierra Nevada Mountains. *Science* 259, 1433–1436.

Seager, R., Kushnir, Y., Herweijer, C., Naik, N., and Velez, J. (2005). Modeling of tropical forcing of persistent droughts and pluvials over western NorthAmerica:1856–2000. *Journal of Climate* 18, 4065–4088.

Seager, R. et al., (2007). Model projections of an imminent transition to a more arid climate in southwestern North America. *Science* 316, 1181–1184.

Seager, R., Neelin, D., Simpson, I., Liu, H., Henderson, N., Shaw, T., Kushnir, Y., Ting, M., and Cook, B. (2014). Dynamical and thermodynamical causes of large scale changes in the hydrological cycle over North America in response to global warming. *Journal of Climate* 27, 7921–7948.

Seck, A., Welty, C., and Maxwell, R.M. (2015). Spin-up behavior and effects on initial conditions for an integrated hydrologic model. *Water Resources Research* 51, 2188–2210.

Serreze, M.C., Clark, M.P., Armstrong, R.L., McGinnis, D.A., and Pulwarty, R.S. (1999). Characteristics of the western United States snowpack from snowpack telemetry (SNOTEL) data. *Water Resource Research* 35, 2145–2160.

Shumskiy, P.A. (1960). Density of glacier ice. *Journal of Glaciology* 3, 568–573.

Shuttleworth, W.J. (2012). Terrestrial Hydrometeorology. Wiley-Blackwell, United Kingdom. 448 p.

Smith, G.I. (1979). Subsurface stratigraphy and geochemistry of Late Quaternary evaporates, Searles Lake, California. U.S. Geological Survey Professional Paper 1043, 130 p.

Smith, G.I. (2009). Late Cenozoic geology and lacustrine history of Searles Valley, Inyo and San Bernardino Counties, California. U.S. Geological Survey Professional Paper 1727, 115 p.

Smith, G.I., Street-Perrott, F.A. (1983). Pluvial lakes of the western United States. (H. E. Jr. Wright, Ed.), In "Late-Quaternary environments of the United States vol. 1" (S. C. Porter, Ed.), pp. 190-212. Minneapolis, University of Minnesota Press.

Smith, G.I., and Bischoff, J.L. (1997). Core OL-92 from Owens Lake: project rationale, geologic setting, drilling procedures, and summary. In: Smith, G.I., Bischoff, J.L. (Eds.), An 800,000-year Paleoclimatic Record from Core OL-92, Owens Lake, southeast California, Geological Society of America Special Paper 317, pp. 1-8.

Smith, G.I., Bischoff, J.L., and Bradbury, J.P. (1997). Synthesis of the paleoclimatic record from Owens Lake Core OL-92. In: Smith, G.I., Bischoff, J.L. (Eds.), An 800,000-year Paleoclimatic Record from Core OL-92, Owens Lake, southeast California, Geologic Society of America Special Paper 317, pp. 143-160.

Smoot, J.P., Litwin, R.J., Bischoff, J.L., and Lund, S.P. (2000). Sedimentary record of the 1872 earthquake and ''Tsunami'' at Owens Lake, southeast California. *Journal of Sedimentary Geology* 135, 241–254.

Sobol, I.M. (1976). On the distribution of points in a cube and the approximate evaluation of integrals. *USSR Computational Mathematics and Mathematics Physics* 7, 86–112.

Sobol, I.M. (1993). Sensitivity estimates for nonlinear mathematical models. *Mathematical Model and Computational Experiments* 1, 407–414.

Sobol, I.M. (2001). Global sensitivity indices for nonlinear mathematical models and their Monte Carlo estimates. *Mathematical Computational Simulations* 55, 271–280.

Solomina, O.N., Bradley, R.S., Jomelli, V., Geirsdottir, A., Kaufman, D.S., Koch, J., McKay, N.P., Masiokas, M., Miller, G., Nesje, A., Nicolussi, K., Owen, L.A., Putnam, A.E., Wanner, H., Wiles, G., and Yang, B. (2016). Glacier fluctuations during the past 2000 years. *Quaternary Science Reviews* 149, 61–90.

Sorenson, S.K., Miller, R.F., Welch, M.R., Groeneveld, D.P., and Branson, F.A. (1989). Estimating soil matric potential in Owens Valley, California: U.S. Geological Survey Water-Supply Paper 2370-C, 18 p.

Sorenson, S.K., Dileanis, P.D., and Branson, F.A. (1991). Soil water and vegetation responses to precipitation and changes in depth to ground water in Owens Valley, California: U.S. Geological Survey Water-Supply Paper 2370-G, 54 p.

Stakhiv, E.Z. (2011). Pragmatic approaches for water management under climate change uncertainty. *Journal of the American Water Resources Association* 47(6), 1183–1196.

Steiger, N.J., Smerdon, J.E., Cook, B., and Seager, R., Williams, A.P., Cook, E.R. (2019). Oceanic and radiative forcing of medieval megadroughts in the American Southwest. *Science Advances* 5, eaax0087.

Steponaitis, E., Andrews, A., McGee, D., Quade, J., Hseih, Y.-T., Broecker, W.S., Shuman, B.N., Burns, S.J., Cheng, H. (2015). Mid-Holocene drying of the U.S. Great Basin recorded in Nevada speleothems. *Quaternary Science Reviews* 127, 174–85.

Stine, S. (1990). Late Holocene fluctuations of Mono Lake, eastern California. *Paleogeography, Paleoclimatology, and Paleoecology* 78, 333–381.

Stine, S. (1994). Extreme and persistent drought in California and Patagonia during Medieval time. *Nature* 339, 546–549.

Stockton, C.W., and Meko, D.M. (1975). A long-term history of drought occurrence in western United States as inferred from tree rings: *Weatherwise* 28, 245–249.

Stratchon, S. and Daly, C. (2017). Testing the daily PRISM air temperature model on semiarid mountain slopes. *Journal of Geophysical Research: Atmospheres* 122, 5697–5715.

Street, J.H., Anderson, R.S., Paytan, A. (2012). An organic geochemical record of Sierra Nevada climate since the LGM from Swamp Lake Yosemite. *Quaternary Science Reviews* 40, 89–106.

Street, J.H., Anderson, R.S., Rosenbauer, R.J., Paytan, A. (2013). n-Alkane evidence for the onset of wetter conditions in the Sierra Nevada, California (USA) at the mid-Holocene transition, ~3.0 ka. *Quaternary Research* 79, 14–23.

Street-Perrott, F.A., and Harrison, S.P. (1985). Lake levels and climate reconstruction, *in*: Paleoclimate Analysis and Modeling, ed., Hecht, A.D., John Wiley and Sons, New York, pp. 291–340.

Swetnam, T.W., Baisan, C.H., Caprio, A.C., Brown, P.M., Touchan, Anderson, R.S., and Hallett, D.J. (2009). Multi-millennial fire history of the giant forest, Sequoia National Park, California, USA. *Fire Ecology* 5, doi: 10.4996/fireecology.0503120.

Thornthwaite, C.W. (1948). An approach toward a rational classification of climate. *Geographical Review* 38, 55-94.

Thyer, M., Renard, B., Kavetski, D., Kuczera, G., Franks, S., and Srikanthan, S. (2009). Critical evaluation of parameter consistency and predictive uncertainty in hydrological modeling: A case study using Bayesian total error analysis. *Water Resources Research* 45. 10.1029/2008WR006825.

Tolwinski-Ward, S.E., Tingley, M.P., Evans, M.N., Hughes, M.K., Nychka, D.W. (2015). Probabilistic reconstructions of local temperature and soil moisture from tree-ring data with potentially time-varying climatic response. *Climate Dynamics* 44, 791–806.

Tran, T.J., Bruening, J.M., Bunn, A.G., Salzer, M.W., and Weiss, S.B. (2017). Cluster analysis and topoclimate modeling to examine bristlecone pine tree-ring growth signals in the Great Basin, USA. *Environmental Research Letters* 12, 014007.

Tyler, S.W., Kranz, S., Parlange, M.B., Albertson, J., Katul, G.G., Cochran, G.F., Lyles, B.A., and Holder, G. (1997). Estimation of groundwater evaporation and salt flux from Owens Lake, California, USA. *Journal of Hydrology* 200, 110–135.

Tyler, S.W., Muňoz, J.F., and Wood, W.W. (2006). The response of playa and sabkha hydraulics and mineralogy to climate forcing. *Ground Water* 44, 329–338.

Vorster, P., (1985). A water balance forecast model for Mono Lake, California. Unpublished Master's Thesis, California State University, Hayward, California.

Vrugt, J.A., ter Braak, C.J.F., Clark, M.P., Hyman, J.M., and Robinson, B.A. (2008). Treatment of input uncertainty in hydrologic modeling: Doing hydrology backward with Markov chain Monte Carlo simulation. *Water Resources Research*, 44, W00B09, doi:10.1029/2007WR006720.

Walker, M.J.C., et al. (2012). Formal subdivision of the Holocene Series/Epoch: a Discussion Paper by a Working Group of INTIMATE (Integration of ice-core, marine and terrestrial records) and the Subcommission on Quaternary Stratigraphy (International Commission on Stratigraphy). Journal of *Quaternary Science* 27, 649–659.

Wanner, H., Beer, J., Bütikofer, J., et al. (2008). Mid- to Late-Holocene climate change: and overview. *Quaternary Science Reviews* 27, 1791–1828.

Williams, D.E. (1966). Water resources development study for proposed Los Angeles Aqueduct second barrel: Los Angeles Department of Water and Power (unpublished report), 62 p.

Wilson, W.T. (1942). Some observations of the thermal quality of snow. *Transactions of the American Geophysical Union*, p. 553–556.

Winkle, W.V., and Eaton, F.M. (1910). Quality of the surface waters of California. United States Geological Survey, Water-Supply Paper 237. United States Government Printing Office, Washington.

Winograd, I.J., Coplen T.B., Landwehr, J.M., Riggs, A.C., Ludwig, K.R., Szabo, B.J., Kolesar, P. T., and Revesz, K.M. (1992). Continuous 500,000-year climate record from vein calcite in Devils Hole, Nevada. *Science*, 258, 255–260.

Winograd, I.J., Landwehr, J.M., Coplen, T.B., Sharp, W.D., Riggs, A.C., Ludwig, K.R., and Kolesar, P.T. (2006). Devils Hole, Nevada, $\delta^{18}O$ record extended into the mid-Holocene. *Quaternary Research* 66, 202–212.

Wohl, E., (2000). Mountain Rivers. Water Resources Monograph 14, American Geophysical Union, Washington D.C., 320 p.

Yu, Z, Dong, W., and Jiang, P. (2015). Temperature and rainfall estimates for past 18000 years in Owens Valley, California with a coupled catchment-lake model. *Hydrology and Earth Systems Sciences Discussions* 12, 6505–6539.

Zhang, X.Y., Trame, M.N., Lesko, L.J., and Schmidt, S. (2015). Sobol sensitivity analysis: A tool to guide the development and evaluation of systems pharmacology models. *Pharmacometrics Systems Pharmocology* 4, 69–79.

Zielinski, G.A. (2000). Use of paleo-records in determining variability within the volcanism-climate system. *Quaternary Science Reviews* 19, 417–438.

Zhong, S., Li, J., Whiteman, C.D., Bian, X., and Yao, W. (2008). Climatology of high wind events in the Owens Valley, California. *Monthly Weather Review* 136, 3536–3552.

Zimmerman, S.R.H., Hemming, S.R., Hemming, N.G., Tomascak, P.B., Pearl, C. (2011). High-resolution chemostratigraphic record of late Pleistocene lake-level variability, Mono Lake, California. *Geological Society of America Bulletin* 123, 2320–2334.

DISSERTATION CONCLUSIONS

RESEARCH OBJECTIVES

This research quantifies changes in precipitation and snowpack in the south-eastern Sierra Nevada over the last 11,500 years from water-balance modeling of the Owens watershed-lake system. Research was focused in two areas: (1) production of a high-resolution time series of water-level changes of late Pleistocene and Holocene Owens Lake; and (2) simulation of Holocene hydroclimate variability in this snow-dominated hydrologic system using a water balance model calibrated to lake-level and glacial records.

The geologic and geomorphic investigations (Chapters 1, 2, 3) led to a continuous lake-level curve of Owens Lake for the last 50,000 years. Characterization of the slip history of five primary faults in the lake basin and development of a differential fault-block model led to reconstruction of the vertical tectonic ground deformation and correction of modern shoreline, lake bottom, and spillway elevations. New ages were estimated for ten beach ridges, shoreline deposits at seven other study sites in the lake basin, and alluvial fill recently identified in the overflow channel between Owens Lake and China Lake basins. The reconstructed elevations and new ages, combined with shoreline geology, sediment lake-core proxy data, as well as wind-wave and sediment entrainment modeling of lake-core sedimentology, led to a continuous lake-level curve for use in calibrating a paleo-hydrologic model. This multi-disciplinary approach produced a record of absolute hydrologic change of both high and low water levels at a resolution much greater than previous outcrop- and lake-core-based lake-level records in

the western U.S. (e.g., Benson, 2004; Reheis et al., 2014). Combining all available geologic, geomorphic, and tectonic information into an integrated 50,000-year record of lake-level variations and overflow from Owens Lake was the first step in producing a high-resolution dataset that could be used to control paleoclimate simulations of the water balance of the entire paleo-Owens River-Lake system.

The Thornthwaite-based Owens watershed-lake water balance model with 800-meter grid resolution accurately simulated observed changes in snowpack and runoff, as well as matched another lake-level simulation of Owens Lake based on measured monthly discharge (Chapter 4). The calibrated model was expanded to include areas of the entire paleo-Owens River-Lake system. The historical climate data for the period WY1896–2015 was used in paleoclimate simulations so that interannual to decadal hydroclimate variability could be captured, and model results could be put in historical context. The paleoclimate model developed in this research is novel because it accounts for primary hydrologic elements of a snow-dominated hydrologic system that, in turn, influence the response of terminal lakes to hydroclimate variability. These primary paleohydrologic elements include: (1) alpine glacial ice and perennial snow accumulation; (2) paleotemperature controlled by local glacial deposits; (3) changes in solar insolation from orbital forcing; and (4) salinity of paleolake water. The use of a continuous lake-level curve of Owens Lake and downstream basins combined with a temperature dataset constrained by glacial evidence is also novel in watershed-lake hydrologic modeling because it affords the opportunity to perform high-resolution reconstruction of precipitation and snowpack at 100-year time steps.

CONTRIBUTIONS TO KNOWLEDGE

The use of a continuous lake-level curve and temperature anomaly dataset that corresponds to paleotemperature depression from local glacial deposits is a new approach in watershed-lake hydrologic modeling in general, and specifically in the Sierra Nevada. This new approach reduced the uncertainty of paleoclimate simulations for the past 11,500 years by providing well-constrained boundary conditions directly connected to the water balance of a snow-dominated watershed-lake hydrologic system. This contrasts with previous Sierra Nevada precipitation reconstructions which have been restricted to the last ~2000 years and rely on paleo-discharge and/or paleotemperature estimates from tree-ring proxy records without incorporation of glacial ice/perennial snow accumulation or orbital forcing (e.g., Graham and Hughes, 2007; Kleppe et al., 2011; Adams et al., 2015; Hatchet et al., 2015; 2016).

This research suggests a cooler south-eastern Sierra Nevada during the late Holocene with less severe drought periods than previously reported. While tree ring-based hydrologic models have inferred warmer temperatures (1–2ºC) and less precipitation (60 to 70% of baseline) during the Medieval Climate Anomaly (MCA) compared with the last ~100 years (Graham and Hughes, 2007; Kleppe et al., 2011; Hatchet et al., 2015), I suggest that these conditions could not support the extent of alpine glaciers recorded in the geomorphic record. Instead, reproduction of lake level and snowpack build up in the Owens River watershed during the MCA, requires cooler average temperature (anomalies of -1 to -0.4ºC) and precipitation 87 to 90% of historical baselines. This pattern is supported by global temperature data that indicates an overall steady decrease in temperatures since the middle Holocene driven by long-term

reductions in solar insolation (e.g., Wanner et al., 2008) and previous paleotemperature depression estimates from glacial deposits in the Sierra Nevada (e.g., Bowerman and Clark, 2011).

A corollary to the conclusions above is the significance of explicitly representing snow accumulation and loss when developing water balance models for snow-dominated watersheds. For example, incoming solar radiation in the southern Sierra Nevada accounts for 66–90% of the energy available for snowmelt and sublimation accounts for approximately 20% of snowpack mass loss (Marks and Dozier, 1992). Only by considering snowpack mass balance, including losses from sublimation and glacial ice or perennial snow storage in combination with runoff losses from channel percolation, can the amount of precipitation and runoff to sufficiently simulate paleolake levels be calculated. The reduction in drought severity shown in this dissertation is related to increases in simulated precipitation required to balance the losses from snow sublimation and storage, along with channel percolation across the watershed, in combination with accounting for changes in solar insolation.

This work demonstrates that hydroclimate during the Holocene (11.5 ka to present day) is summarized by precipitation ranging from ~74 to 159% of historical baseline (WY1896–2015) with temperature anomalies ranging from -1.5 to 0.31°C. Simulations indicate that alpine snowpack was present in the Sierra Nevada during the entire Holocene and that the period with the most severe and persistent drought conditions occurred during the Mid-Holocene Warm Period. My simulations suggest that hydroclimate during this period had positive temperature anomalies of up to 0.31ºC and precipitation ranging from 74 to 78% of historical baseline, about twice that of the MCA.

RECOMMENDATIONS

To better understand the implications of the paleoclimate modeling results of this dissertation, future paleohydrologic modeling studies in the Sierra Nevada would benefit by accounting for losses in the alpine hydrologic system from snow sublimation and glacial ice/perennial snow storage, plus losses from channel percolation, as well as accounting for the long-term changes in seasonality driven by orbital forcing. The inclusion of these additional model components combined with a paleotemperature dataset that is supported by alpine geologic constraints will likely reduce the uncertainty of paleoclimate simulations for the region. Furthermore, the use of a continuous lake-level curve corrected for tectonic ground deformation also affords a better understanding of the absolute hydrologic change in watershed-lake systems, as well as provide more accurate estimates of the timing, duration, and magnitude of hydroclimate change.

REFERENCES

Adams, K. D., Negrini, R. M., Cook, E. R., and Rajagopal, S. (2015). Annually-Resolved Late Holocene Paleohydrology of the Southern Sierra Nevada and Tulare Lake, California, *Water Resources Research*, 51, 1–17.

Barth, C., Boyle, D.P., Hatchett, B.J., Bassett, S.D., Garner, C.B., and Adams, K.D. (2016). Late Pleistocene climate inferences from a water balance model of Jakes Valley, Nevada (USA). *Journal of Paleolimnology*, DOI 10.1007/s10933-016-9897-z.

Benson, L. (2004). Western Lakes. In: Gillespie, A.R., Porter, S.C., Atwater, B.F. (Eds.), The Quaternary Period in the United States. Elsevier, New York, pp. 185–204.

Bowerman, N.D., and Clark, D.H. (2011). Holocene glaciation of the central Sierra Nevada, California. *Quaternary Science Reviews* 30, 1067–1085.

Graham, N.E., and Hughes, M.K. (2007). Reconstructing the medieval low stands of Mono Lake, Sierra Nevada, California, USA. *The Holocene* 17(8), 1197–1210.

Hatchett, B.J., Boyle, D.P., Putnam, A.E., and Bassett, S.D. (2015). Placing the 2012-2015 California-Nevada drought into a paleoclimatic context: Insights from Walker Lake, California-Nevada, USA. *Geophysical Research Letters* 42.

Hatchett, B. J., Boyle, D. P., Garner, C. B., Kaplan, M. L., Putnam, A. E., and Bassett, S. (2016). Magnitude and frequency of wet years under a megadrought climate in the western Great Basin, USA, *Quaternary Science Reviews* 152, 197–202.

Kleppe, J.A., Brothers, D.S., Kent, G.M., Biondi, F., Jensen, S., and Driscoll, N.W. (2011). Duration and severity of Medieval drought in the Lake Tahoe Basin. *Quaternary Science Reviews* 30, 3269–3279.

Marcott, S.A., Shakun, J.D., Clark, P.U., and Mix, A.C. (2013). A Reconstruction of regional and global temperature for the past 11,300 years. *Science* 339, 1198–1201.

Marks, D., and Dozier, J. (1992). Climate and energy exchange at the snow surface in the alpine region of the Sierra Nevada 2: snow cover energy balance. *Water Resource Research* 28, 3043–3054.

Matsubara, Y., and Howard, A.D. (2009). A spatially explicit model of runoff, evaporation, and lake extent: Application to modern and late Pleistocene lakes in the Great Basin region, western United States. *Water Resources Research* 45, W06425.

Reheis, M.C., Adams, K.D., Oviatt, C.G., and Bacon, S.N. (2014). Pluvial lakes in the Great Basin of the western United States – A view from the outcrop. *Quaternary Science Reviews* 97, 33–57.

Wanner, H., Beer, J., Bütikofer, J., et al. (2008). Mid- to Late-Holocene climate change: and overview. *Quaternary Science Reviews* 27, 1791–1828.

Yu, Z, Dong, W., and Jiang, P. (2015). Temperature and rainfall estimates for past 18000 years in Owens Valley, California with a coupled catchment-lake model. *Hydrology and Earth Systems Sciences Discussions* 12, 6505–6539.

APPENDICES

APPENDIX A: IRSL DATA REPOSITORY TEXT - SAMPLE PREPARATION AND DATING METHODS

Samples were opened and prepared in the University of California, Los Angeles (UCLA) luminescence laboratory under low-intensity red and amber lighting. Potassium feldspar grains of 175–200µm were separated from the central, unexposed, portion of each sample; following wet sieving to isolate the correct grain size range, samples were treated in dilute HCl to remove carbonate, dried, and the potassium feldspar component floated off using a lithium metatungstate (LMT) solution with a density of 2.58 g/cm^3. After rinsing, samples were treated in 10% hydrofluoric acid for 10 minutes to etch the outer surfaces of each feldspar grain, dried, and sieved at 175µm to remove small fragments.

Between 200 and 600 K-feldspar grains of each sample were measured using a post-IR IRSL SAR (single aliquot regenerative-dose) protocol modified for single grains from Buylaert et al. (2009), documented in Rhodes (2015). Measurements were made in a Risø TL-DA-20CD automated luminescence reader, fitted with an XY single grain attachment incorporating a 150 mW 830 nm IR laser passed through a single RG-780 filter to reduce resonance emission at 415 nm, used at 90% power for 2.5 s. All measurements were made using a BG3 and BG39 filter combination, allowing transmission around 340–470 nm to an EMI 9235QB photomultiplier tube. For the natural measurement, and following each regenerative-dose and test dose application, a preheat of 250º C for 60 s was administered. IRSL was measured (for 2.5 s for each grain) at 50º C, and then subsequently at 225º C (for the post-IR determination).

Following a test dose of 9 Gy, an identical preheat, IRSL at 50º C and post-IR IRSL at 225ºC were administered. Each SAR cycle was completed with a hot bleach treatment using an array of Vishay TSFF 5210 870 nm IR diodes at 90% power for 40 s at 290º C. The SAR sequence incorporated measurement of the natural IRSL, between four and six regenerative dose points, a zero dose point to assess thermal transfer, and a repeat of the first regenerative dose point, to assess recycling behavior.

Growth curves were constructed for the post-IR IRSL signal measured at 225º C using an integral of the background-subtracted sensitivity-corrected IRSL from the first 0.5 s, fitted with an exponential plus linear function. For most samples, around 5 to 10% of measured K-feldspar grains provided a useful post-IR IRSL signal, typically providing between 20 and 60 single grain results for each sample; other grains were either insensitive, associated with large uncertainties, or in the case of a few grains, the post-IR IRSL signal was in saturation. Samples typically displayed a uniform minimum equivalent dose value, with other grains displaying higher dose values, interpreted as grains incompletely zeroed before or during transport owing to rapid deposition in water under high energy shoreline conditions. Isolation of a population of grains for age estimation used a “discrete minimum” procedure in which higher values were excluded until the remaining grains were consistent with an overdispersion (OD) value of 15%, based on experience from quartz single grain OSL dating (e.g. Rhodes et al., 2010). Fading correction was based on detailed determination of single grain post-IR IRSL fading rates for key samples, and involve an increase in apparent age of 11%. Of note, although fading uncorrected PIR-IR_{225} has been shown to agree with independent age control in several studies, in some cases, residuals associated with thermal transfer arising from high pre-heat temperatures can result in age

overestimation (Buyalert et al., 2011; Chen et al., 2013; Li et al., 2014). Gamma dose rates were based on in- situ NaI spectrometer measurements; external beta dose rates were calculated from ICP-MS (U, Th) and ICP-OES (K) measurements of sediment from the end of each sample tube, internal beta dose rate was based on 12.5% internal K content, cosmic dose rates were based on measured overburden depth, and moisture correction used contemporary water content values.

References

Buylaert, J.P., Murray, A.S., Thomsen, K.J., Jain, M. (2009). Testing the potential of an elevated temperature IRSL signal from K-feldspar: *Radiation Measurements* 44, 560–565.

Buyalert, J., Thiel, C., Murray, A.S., Vendenberghe, D.A.G., Yi, S., Lu, H. (2011). IRSL and post-IR IRSL residual doses recorded in modern dust samples from the Chinese loess plateau. *Geochronometria* 38, 432–440.

Chen, Y., Sheng-Hua, L., Li, B. (2013). Residual doses and sensitivity change of post IR IRSL signals from potassium feldspar under different bleaching conditions. *Geochronometria* 40, 229–238.

Li, B., Roberts, R.G., Jacobs, Z. (2013). On the dose dependency of the bleachable and non-bleachable components of IRSL from K-feldspar: Improved procedures for luminescence dating of Quaternary Sediments. *Quaternary Geology* 17, 1–13.

Rhodes, E.J. (2015). Dating sediments using potassium feldspar single-grain IRSL: Initial methodological considerations: *Quaternary International* 362, 14–22.

Rhodes, E.J., Fanning, P.C., Holdaway, S.J. (2010). Developments in optically stimulated luminescence age control for geoarchaeological sediments and hearths in western New South Wales, Australia: *Quaternary Geochronology* 5, 348–352.

APPENDIX B: IRSL SAMPLE PREPARATION AND DATING METHODS

Samples were opened and prepared in the University of California, Los Angeles (UCLA) luminescence laboratory under low-intensity red and amber lighting. Potassium feldspar grains of 175–200µm were separated from the central, unexposed, portion of each sample; following wet sieving to isolate the correct grain size range, samples were treated in dilute HCl to remove carbonate, dried, and the potassium feldspar component floated off using a lithium metatungstate (LMT) solution with a density of 2.58 g/cm^3. After rinsing, samples were treated in 10% hydrofluoric acid for 10 minutes to etch the outer surfaces of each feldspar grain, dried, and sieved at 175µm to remove small fragments.

Between 200 and 600 K-feldspar grains of each sample were measured using a post-IR IRSL SAR (single aliquot regenerative-dose) protocol modified for single grains from Buylaert et al. (2009), documented in Rhodes (2015). Measurements were made in a Risø TL-DA-20CD automated luminescence reader, fitted with an XY single grain attachment incorporating a 150 mW 830 nm IR laser passed through a single RG-780 filter to reduce resonance emission at 415 nm, used at 90% power for 2.5 s. All measurements were made using a BG3 and BG39 filter combination, allowing transmission around 340–470 nm to an EMI 9235QB photomultiplier tube. For the natural measurement, and following each regenerative-dose and test dose application, a preheat of 250º C for 60 s was administered. IRSL was measured (for 2.5 s for each grain) at 50º C, and then subsequently at 225º C (for the post-IR determination). Following a test dose of 9 Gy, an identical preheat, IRSL at 50º C and post-IR IRSL at 225ºC were administered. Each SAR cycle was completed with a hot bleach treatment

using an array of Vishay TSFF 5210 870 nm IR diodes at 90% power for 40 s at 290º C. The SAR sequence incorporated measurement of the natural IRSL, between four and six regenerative dose points, a zero dose point to assess thermal transfer, and a repeat of the first regenerative dose point, to assess recycling behavior.

Growth curves were constructed for the post-IR IRSL signal measured at 225º C using an integral of the background-subtracted sensitivity-corrected IRSL from the first 0.5 s, fitted with an exponential plus linear function. For most samples, around 5 to 10% of measured K-feldspar grains provided a useful post-IR IRSL signal, typically providing between 20 and 60 single grain results for each sample; other grains were either insensitive, associated with large uncertainties, or in the case of a few grains, the post-IR IRSL signal was in saturation. Samples typically displayed a uniform minimum equivalent dose value, with other grains displaying higher dose values, interpreted as grains incompletely zeroed before or during transport owing to rapid deposition in water under high energy shoreline conditions. Isolation of a population of grains for age estimation used a "discrete minimum" procedure in which higher values were excluded until the remaining grains were consistent with an overdispersion (OD) value of 15%, based on experience from quartz single grain OSL dating (e.g. Rhodes et al., 2010). Fading correction was based on detailed determination of single grain post-IR IRSL fading rates for key samples, and involve an increase in apparent age of 11%. Of note, although fading uncorrected PIR-IR_{225} has been shown to agree with independent age control in several studies, in some cases, residuals associated with thermal transfer arising from high pre-heat temperatures can result in age overestimation (Buyalert et al., 2011; Chen et al., 2013; Li et al., 2014). Gamma dose rates were based on in- situ NaI

spectrometer measurements; external beta dose rates were calculated from ICP-MS (U, Th) and ICP-OES (K) measurements of sediment from the end of each sample tube, internal beta dose rate was based on 12.5% internal K content, cosmic dose rates were based on measured overburden depth, and moisture correction used contemporary water content values.

References

Buylaert, J.P., Murray, A.S., Thomsen, K.J., Jain, M. (2009). Testing the potential of an elevated temperature IRSL signal from K-feldspar: *Radiation Measurements* 44, 560–565.

Buyalert, J., Thiel, C., Murray, A.S., Vendenberghe, D.A.G., Yi, S., Lu, H. (2011). IRSL and post-IR IRSL residual doses recorded in modern dust samples from the Chinese loess plateau. *Geochronometria* 38, 432–440.

Chen, Y., Sheng-Hua, L., Li, B. (2013). Residual doses and sensitivity change of post IR IRSL signals from potassium feldspar under different bleaching conditions. *Geochronometria* 40, 229–238.

Li, B., Roberts, R.G., Jacobs, Z. (2013). On the dose dependency of the bleachable and non-bleachable components of IRSL from K-feldspar: Improved procedures for luminescence dating of Quaternary Sediments. *Quaternary Geology* 17, 1–13.

Rhodes, E.J. (2015). Dating sediments using potassium feldspar single-grain IRSL: Initial methodological considerations. *Quaternary International* 362, 14–22.

Rhodes, E.J., Fanning, P.C., Holdaway, S.J. (2010). Developments in optically stimulated luminescence age control for geoarchaeological sediments and hearths in western New South Wales, Australia. *Quaternary Geochronology* 5, 348–352.

APPENDIX C: OSL SAMPLE PREPARATION AND DATING METHODS

Optically Stimulated Luminescence (OSL) dating determines the time elapsed since a sediment sample was last exposed to daylight (Aitken, 1998). The method relies on the interaction of ionizing radiation with electrons in semi-conducting minerals within buried sediment, which results in metastable accumulation of charge. Illumination of the sediment releases the charge as a measurable emission of photons (luminescence). The methods assume that mineral grains during or immediately prior to the transport were exposed to daylight to set them to their geological zero residual level. On burial, day light exposure ceased and essentially the luminescence signal begins to accumulate due to the radiation arising from the decay of ambient radioisotopes that include U, Th, and K. Given that, as a first approximation, the radiation exposure (the dose rate - DR) is constant over the timescales of interest, the luminescence buildup (equivalent dose – DE) in the minerals in proportion to the duration of burial and the concentration of the radioisotopes in the sample environment. The depositional age (A) of the sample is thus a ratio of luminescence acquired and the rate of luminescence acquisition (i.e., A=DE/DR)(Murray and Olley, 2002; Singhvi and Porat, 2008).

Samples HD1, HD2 and HD3 were from core samples in a deep borehole with approximate length of 20-24 inches. Only the middle 10 inches of each core sample was used for quartz extraction and a 1 inch thick sample from each side of 10 inches was used for dose-rate estimation. The other OSL samples were collected by hammering 10 inch-long, 2 inch-diameter steel tubes into cleaned, logged sediment faces in trenches. The tubes remained sealed until opened in the luminescence laboratory at the University of Cincinnati. A 1 inch- thick layer of sediment was removed from each end to obtain

sediment from the center of the tube for processing and to reduce the possibility of any sampled sediment being exposed to daylight while sampling. The sediment from the end of the tubes was dried to determine the water content of each sample. The sediment was then crushed and sent to the Activation Laboratories Limited in Ancaster, Ontario, Canada for Major Elements Fusion ICP/MS/Trace Elements analysis to determine the U, Th and K concentrations for DR calculations (Table A1).

The sediment from the center of the tubes and cores was pretreated with 10% HCl and 10% H2O2 to remove carbonates and organic matter, respectively. The pretreated samples were rinsed in water, dried and sieved to attract the 90–150 μm particle size fraction. A low field controlled Frantz isodynamic magnetic separator (LFC Model-2) was used to separate feldspar and magnetic minerals from quartz in the 90-150 μm particle size fraction following the methods of Porat (2006) and Jain et al. (2008) and the forward and side slopes were set at 100° and 10°, respectively, within a variable magnetic field. The quartz-rich separate was etched using 44% HF acid for 80 minutes to remove the outer alpha irradiated layer from quartz particles and any feldspars that were removed during the magnetic separation. Any fluoride precipitates were removed using concentrated HCl. The quartz sample was then rinsed in distilled water and acetate, and dried and sieved to obtain grain size 90-150 μm in diameter.

An automated Risoe OSL reader model TL-DA-20 was used for OSL measurements and irradiation. Aliquots, containing approximately several hundred grains of the samples, were mounted onto ~6 mm- diameter stainless steel discs as a small central circle ~3 mm in diameter. Aliquots for each sample were first checked for feldspar contamination using IRSL at room temperature before the main OSL

measurements were undertaken (Jain & Singhvi, 2001). If the aliquots did not pass the IRSL test the samples were etched in 40% HF for further 30 minutes to remove any feldspar, followed by 10% HCl treatment and sieving again. Samples that passed the IRSL test were used for OSL dating. Aliquots of samples were illuminated with blue LEDs stimulating at a wavelength of 470 nm (blue light stimulated luminescence – BLSL). The detection optics comprised Hoya U-340 and Schott BG-39 color glass filters coupled to an EMI 9235 QA photomultiplier tube. The samples were irradiated using a 90Sr/90Y beta source. The single aliquot regeneration (SAR) method of Murray and Wintle (2000), Murray and Wintle (2003) and Jain et al. (2008) were used to determine the DE for age estimation. Only aliquots that satisfied the criterion of a recycling ratio not more than 10% were used in determining DE. A preheat of 240 °C for 10s was used and the OSL signal was recorded for 40 s at 125 °C. OSL sensitivity of the samples had a high signal to noise ratio. Dose recovery tests (Wintle and Murray, 2006) indicate that a laboratory dose could be recovered to within 2% by the SAR protocol suggesting that the protocol was appropriate (Figure A1).

The OSL ages are presented in Table 3 in the article. Luminescence signals for samples HD1, HD2, HD3, and HD8 are well behaved, with the fast component dominating, providing confident ages. Figure A2a and illustrate the typical shine down curves for all well behaved samples showing that the fast component dominates in samples HD1, HD2, HD3, and HD8. The fast component is most easily bleached and thus its presence helps provide confidence that samples with it would have been bleached quickly during exposure to sunlight. In contrast, Figure A2b shows the luminescence characteristics for all poorly behaved samples HD5, HD6, HD7-1, HD7-2, and HD9 were

not typical for quartz (as a fast component is not dominant) and they had high background signals providing much less confidence in these ages. Probability graphs for the equivalent doses for aliquots of each sample are shown in Figure A3. The distribution of equivalent doses for samples HD1, HD2, HD3, and HD8 are relatively tightly clustered providing confidence in these ages (Figure A3a). However, the distribution of equivalent doses for samples HD5, HD6, HD7-1, HD7-2 and HD9 are poorly clustered and the confidence level for these samples is low and may have underestimation in ages because of the presence of an ultrafast component (Jain et al., 2008; Figure A3b).

The poor behavior of samples HD5, HD6, HD7-1, HD7-2 and HD9 might be the consequence of significant volcanic quartz within the samples. This would produce high residual level and decay pattern for the OSL signal that is sluggish, and not characteristic of the normal shine down curve for quartz. Volcanic quartz has thermally unstable component and anomalous fading problem at room temperature. Tsukamoto et al. (2007) reports that volcanic quartz OSL dates are severely underestimated. For this reason we are not confident about the ages for samples HD5, HD6, HD7-1, HD7-2 and HD9. Every sample was examined using an optical microscope for the presence for of zircon grains, which is indicative of a volcanic component within the sediment. In the ~1 gram of each sample (couple of thousands grain) examined there were 10 grains present in samples HD7 and HD9 for each slide, while other samples have less than 2-4 zircon grains. This supports the view that these samples might be problematic because of the presence of volcanic material, specifically volcanic glass.

References

Aitken, M.J. (1998). An introduction to Optical dating: The Dating of Quaternary Sediments by the Use of Photon-stimulated Luminescence. Oxford University press, USA, New York, 280 pp.

Grün, R. (1991). Age Calculation software for Riso Laboratories.

Jain, M., Choi, J.H. and Thomas, P.J. (2008). "The ultrafast OSL component in quartz: Origins and implications". *Radiation Measurements* (doi:10.1016/j.radmeas.2008.01.005).

Murray, A.S. and Olley, J.M. (2002). "Precision and accuracy in the optically stimulated luminescence dating of sedimentary quartz: a status review". *Geochronometria* 21, pp11-16.

Murray, A.S. and Wintle, A.G. (2000). "Luminescence dating of quartz using an improved single-aliquot regenerative-dose protocol". *Radiation Measurements* 32(1): pp57-73.

Murray, A.S. and Wintle, A.G. (2003). "The single aliquot regenerative dose protocol: potential for improvements in reliability". *Radiation Measurements* 37(4-5): pp 377-381.

Porat, N. (2006). "Use of magnetic separation for purifying quartz for luminescence dating". Ancient TL 24(2): pp33-36.

Prescott, J.R. and Hutton, J.T. (1994). "Cosmic ray contributions to dose rates for luminescence and ESR dating: Large depths and long-term time variations". *Radiation Measurements* 23(2-3): pp497-500.

Singhvi, A.K. and Porat, N. (2008). "Impact of luminescence dating on geomorphological and palaeoclimate research in drylands". *Boreas* 37(4): pp536-558.

Wintle, A.G. and Murray, A.S. (2006). "A review of quartz optically stimulated luminescence characteristics and their relevance in single-aliquot regeneration dating protocols". *Radiation Measurements* 41(4): pp369-391.

Table A1. Radioisotope, water content, and cosmic dose data and the calculated dose rate for samples. Water content used is that for the time sample collection and cosmic dose rate is estimated using Prescott and Hutton's (1994) formulation. Complete dose rate was estimated using software written by Grün (1991).

Sample name	U (ppm)	Th (ppm)	K (%)	Water Content (%)	Cosmic dose (µGy/a)	Dose Rate (Gy/ka)
HD 1	1.30 ± 0.13	3.4 ± 0.34	4.06 ± 0.20	8.0 ± 1.6	60 ± 12	4.20 ± 0.21
HD 2	1.70 ± 0.17	5.1 ± 0.51	3.52 ± 0.18	9.6 ± 1.9	39 ± 8	3.81 ± 0.21
HD 3	3.90 ± 0.39	11.9 ± 1.19	3.24 ± 0.16	12.5 ± 2.5	30 ± 6	4.25 ± 0.25
HD 6	2.20 ±0.22	7.2 ± 0.72	4.05 ± 0.20	1.3 ± 0.3	188 ± 38	5.16 ± 0.23
HD 7-1	2.80 ± 0.28	9 ± 0.90	3.53 ± 0.18	0.9 ± 0.2	167 ± 33	4.97 ± 0.23
HD 7-2	2.80 ± 0.28	9 ± 0.90	3.53 ± 0.18	0.9 ± 0.2	167 ± 33	4.97 ± 0.23
HD 8	2.00 ± 0.20	8.5 ± 0.85	3.75 ± 0.19	0.3 ± 0.1	217 ± 43	5.00 ± 0.23
HD 9	3.50 ± 0.35	11.1 ± 1.11	3.47 ± 0.17	1.7 ± 0.3	210 ± 42	5.17 ± 0.23

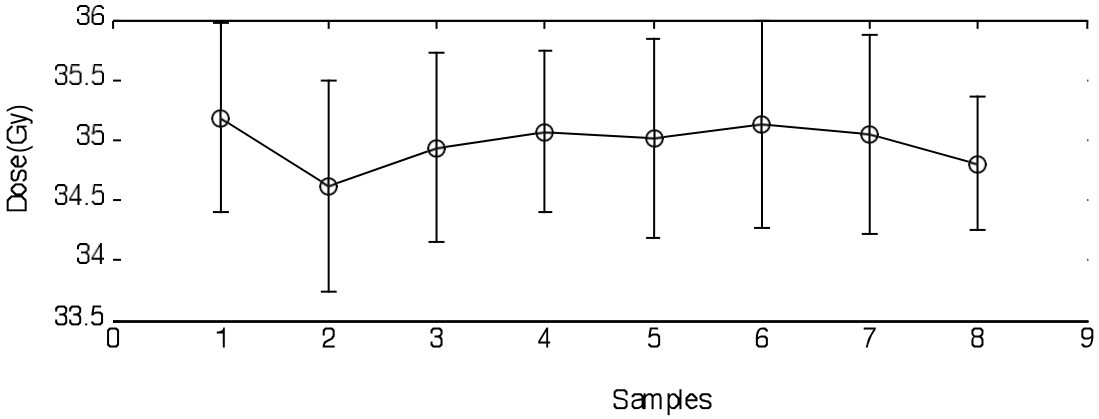

Figure A1. Dose recovery for all HD samples except HD4 samples. A 35 Gy dose was recovered for each sample and the error bar signifies a standard deviation of 5 aliquots.

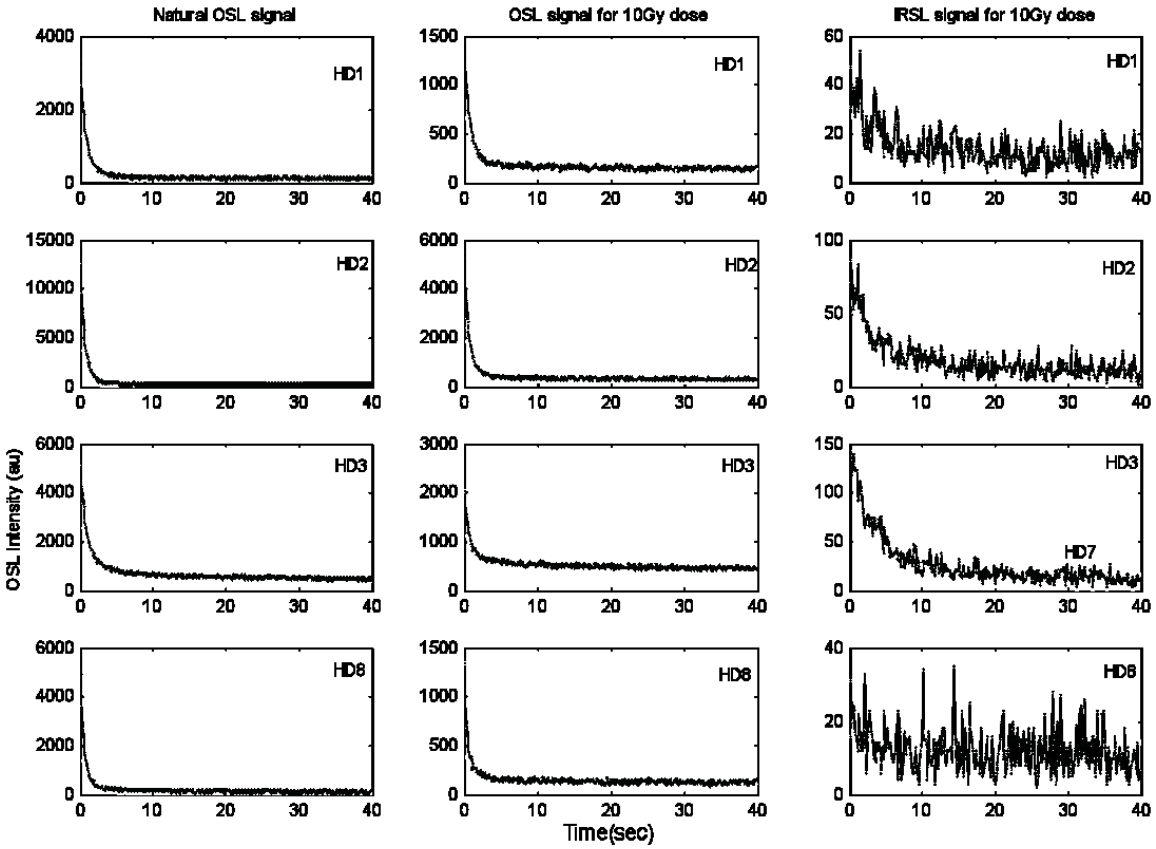

Figure A2a. Typical shine down curves for a group of samples that behaved well and do not show large variation in ages. Left to right every sample shows natural BLSL, for 10 Gy beta dose BLSL and infrared stimulated luminescence (IRSL), which confirms the absence of any feldspar in the sample.

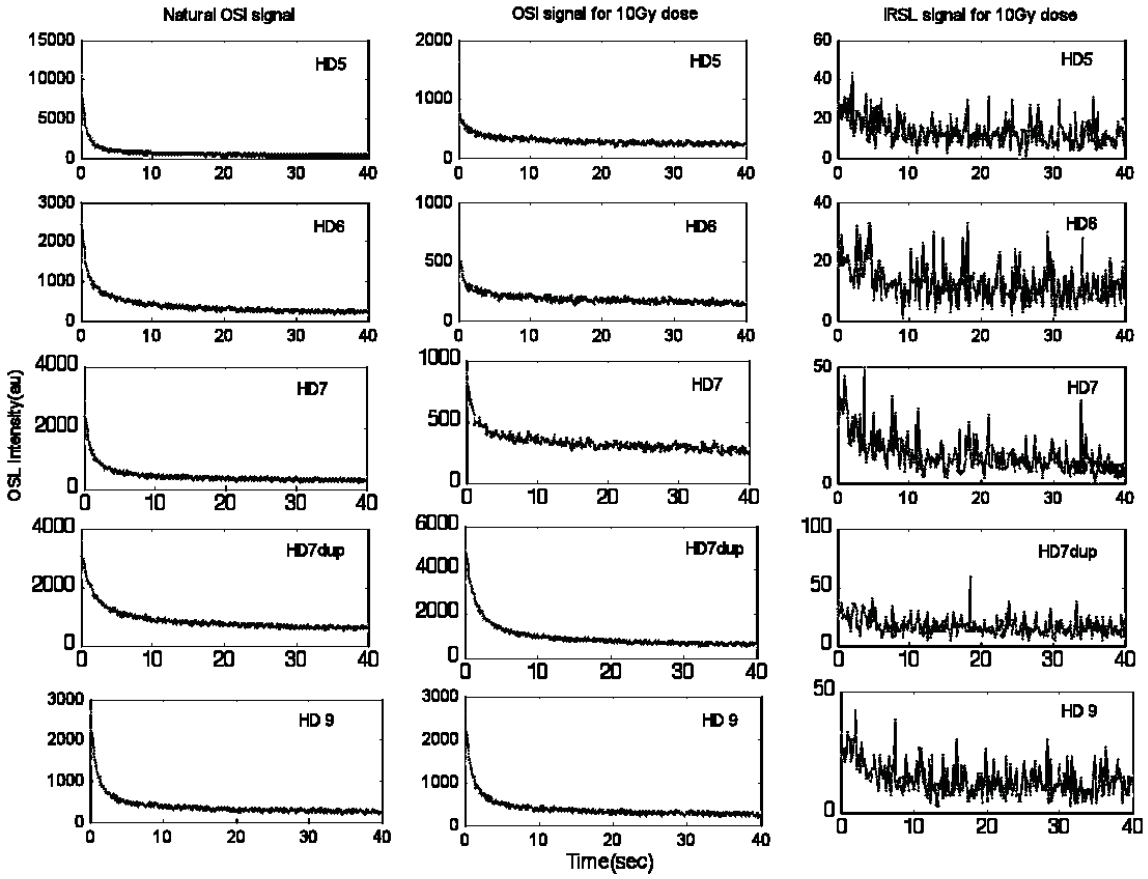

Figure A2b. Shine down patterns for poorly behaved samples HD5, HD6, HD7 (HD 7-1), HD7dup (HD 7-2), and HD9. Left to right for every sample shown natural BLSL, for 10 Gy beta dose BLSL and infrared stimulated luminescence (IRSL), which shows the absence of any feldspar in the sample. But the OSL decay pattern does not decay sharply as compare to other samples; all samples are having high residual level of signal. And this group of samples has a large variation in age. The nature of OSL for 10Gy dose shows the presence of an ultrafast component, which may lead to less confident age estimations. These sample were measured according using the methods of Jain et al. (2008).

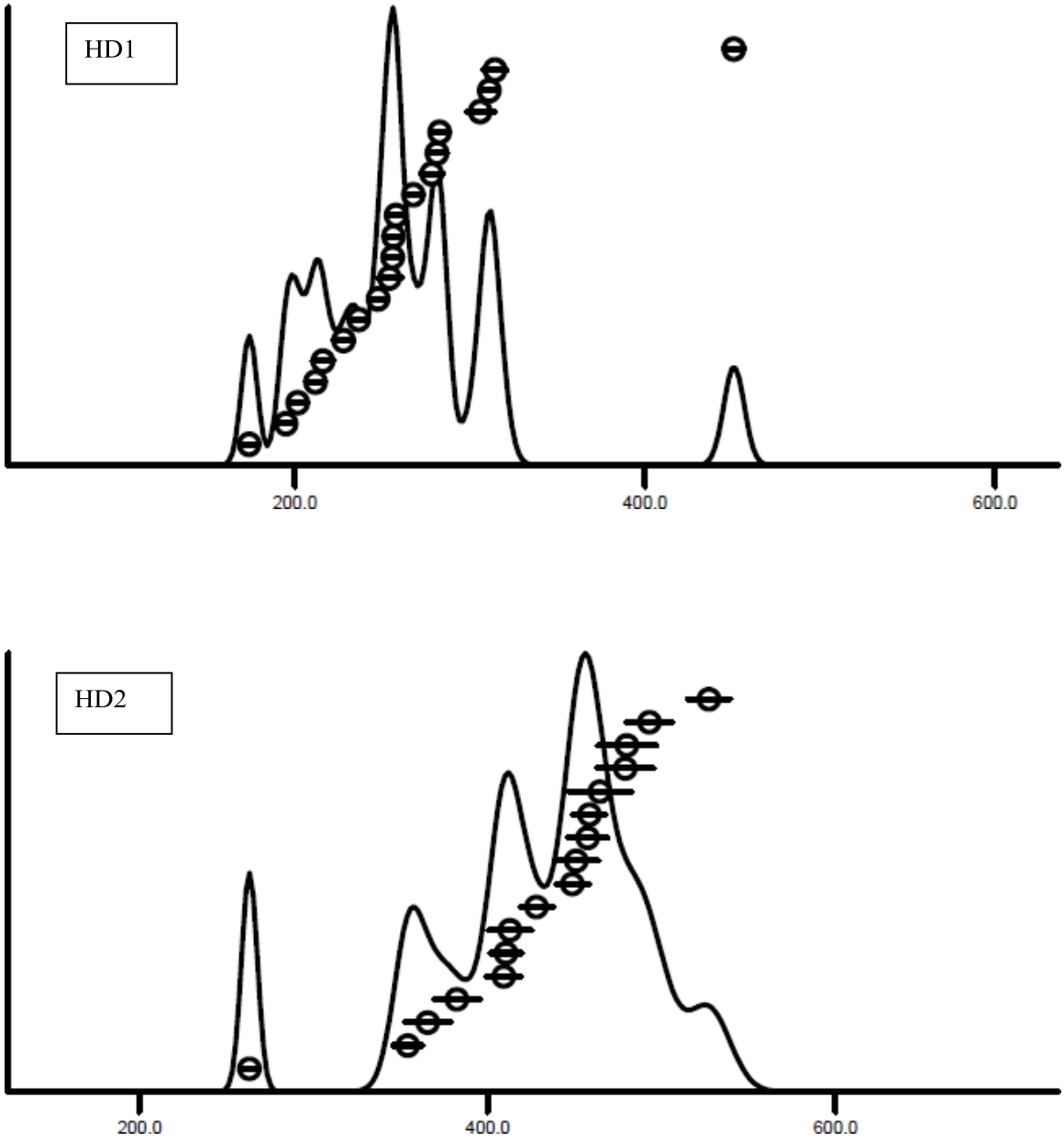

Figure A3a. Probability graphs for all well-behaved samples (HD1, HD2, HD3 and HD8), which show that most of the aliquots are inside of the probability curve, arguing for cluster of ages, and a confident age. Here the number of aliquots is plotted against equivalent dose (in seconds equivalent for beta source of Riso reader). These graphs were plotted using Riso Analyst software.

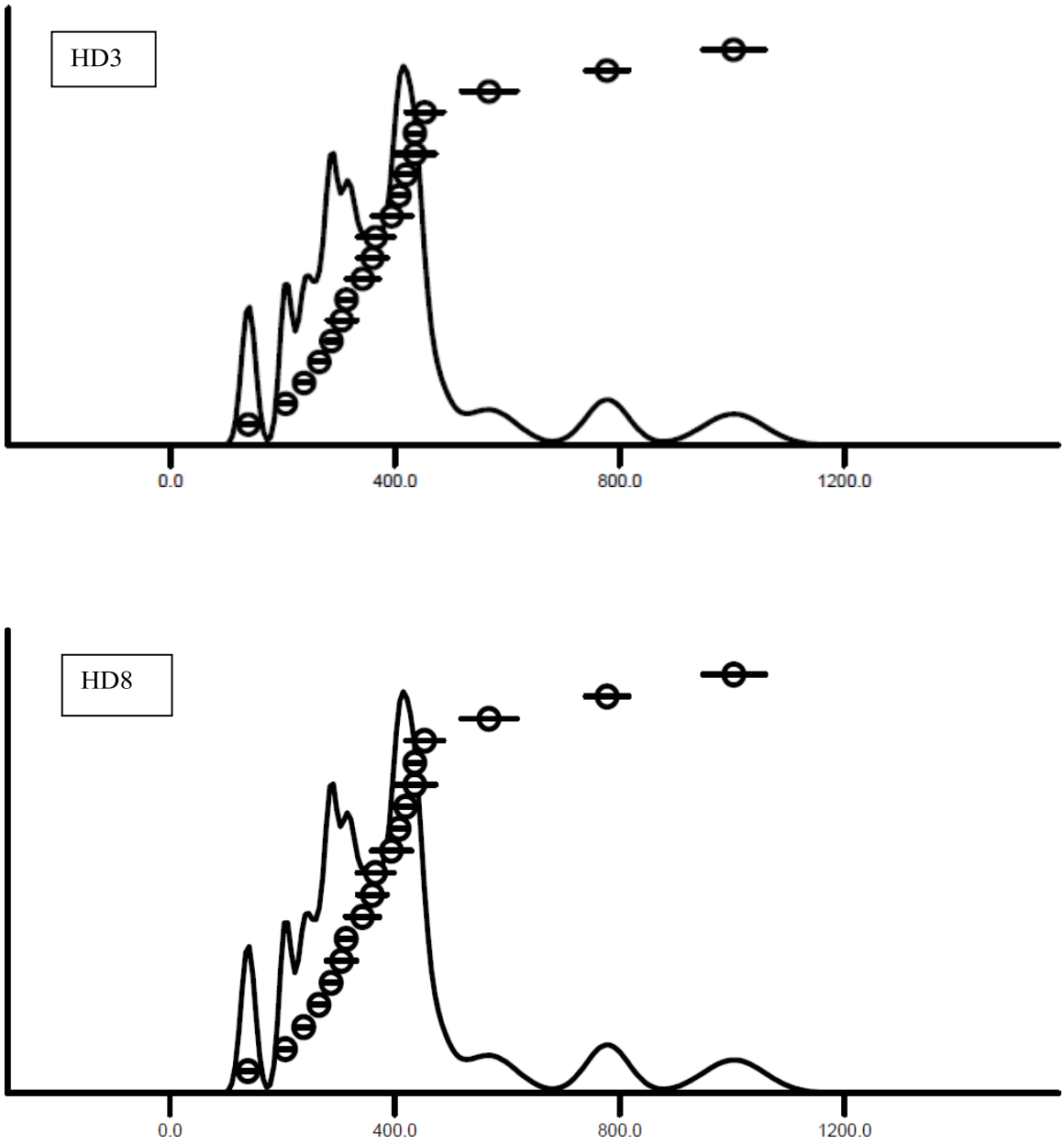

Figure A3a. Probability graphs for all well-behaved samples (HD1, HD2, HD3 and HD8), which show that most of the aliquots are inside of the probability curve, arguing for cluster of ages, and a confident age. Here the number of aliquots is plotted against equivalent dose (in seconds equivalent for beta source of Riso reader). These graphs were plotted using Riso Analyst software (Continued).

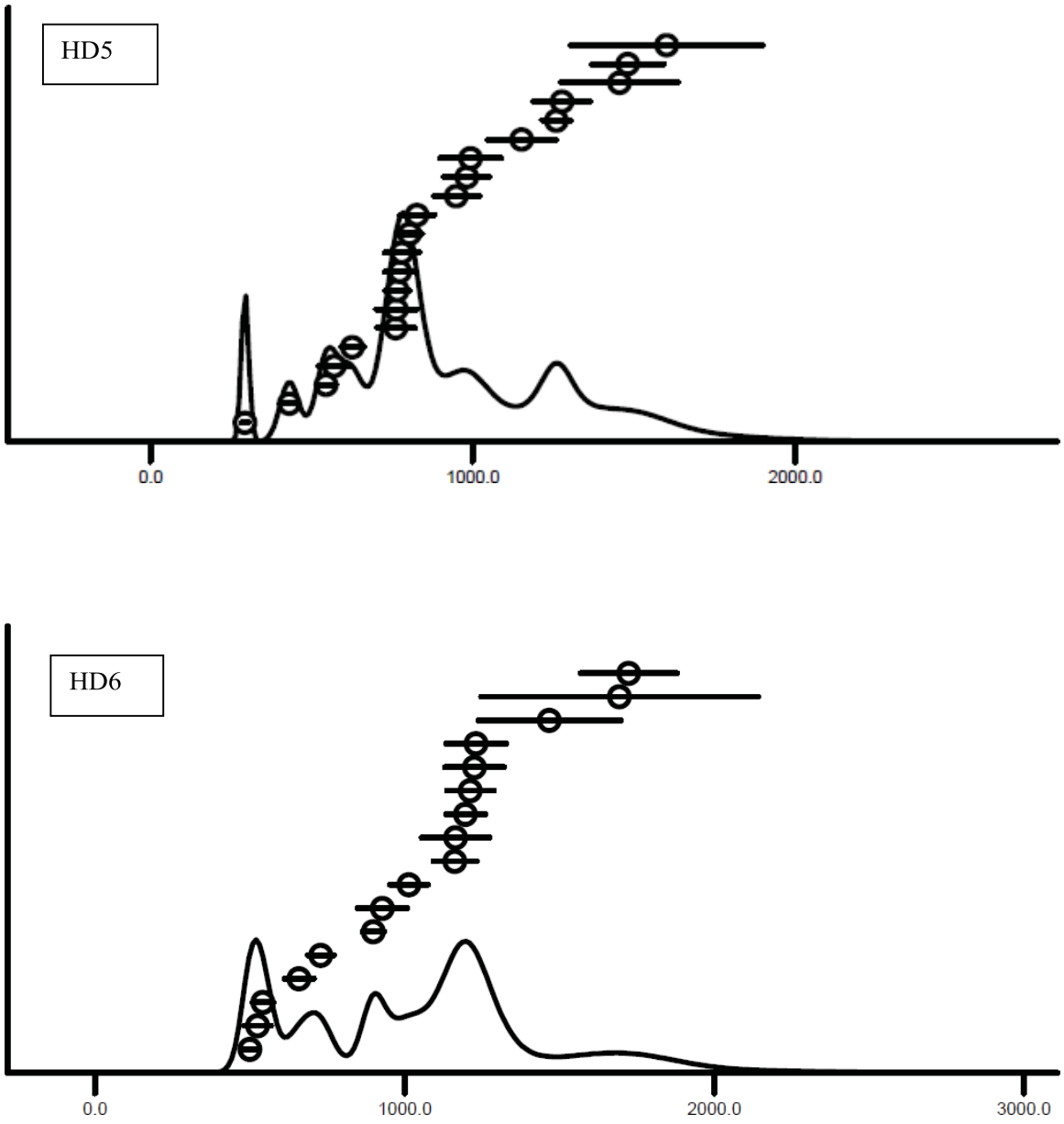

Figure A3b. Probability graphs for all poorly behaved samples (HD5, HD6, HD7-1, HD7-2, and HD9), which show most of the aliquots are outside of the probability curve, arguing for low confidence in the ages. Here the number of aliquots is plotted against equivalent dose (in seconds equivalent for beta source of Riso reader). These graphs were plotted using Riso Analyst software.

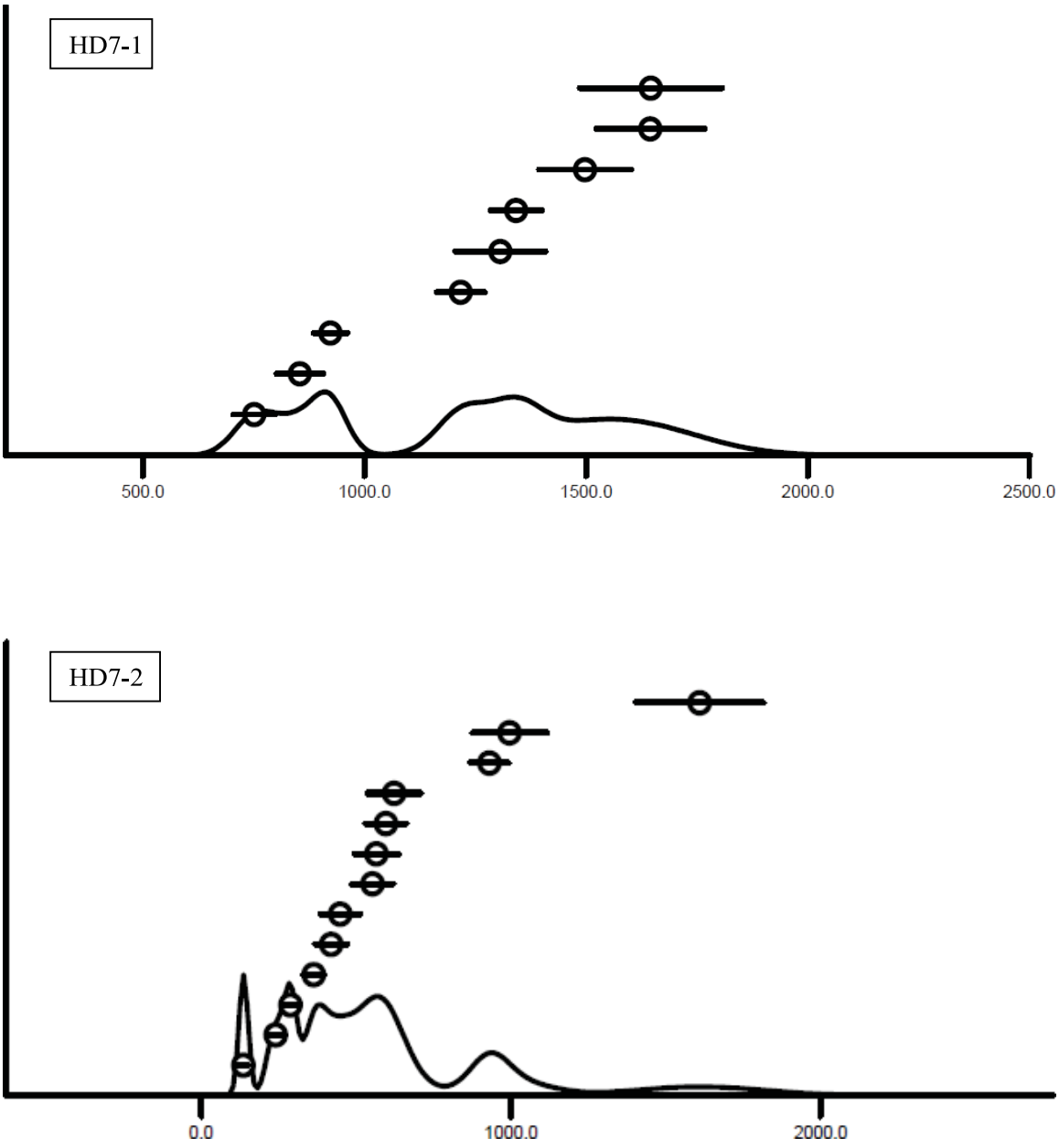

Figure A3b. Probability graphs for all poorly behaved samples (HD5, HD6, HD7-1, HD7-2, and HD9), which show most of the aliquots are outside of the probability curve, arguing for low confidence in the ages. Here the number of aliquots is plotted against equivalent dose (in seconds equivalent for beta source of Riso reader). These graphs were plotted using Riso Analyst software (Continued).

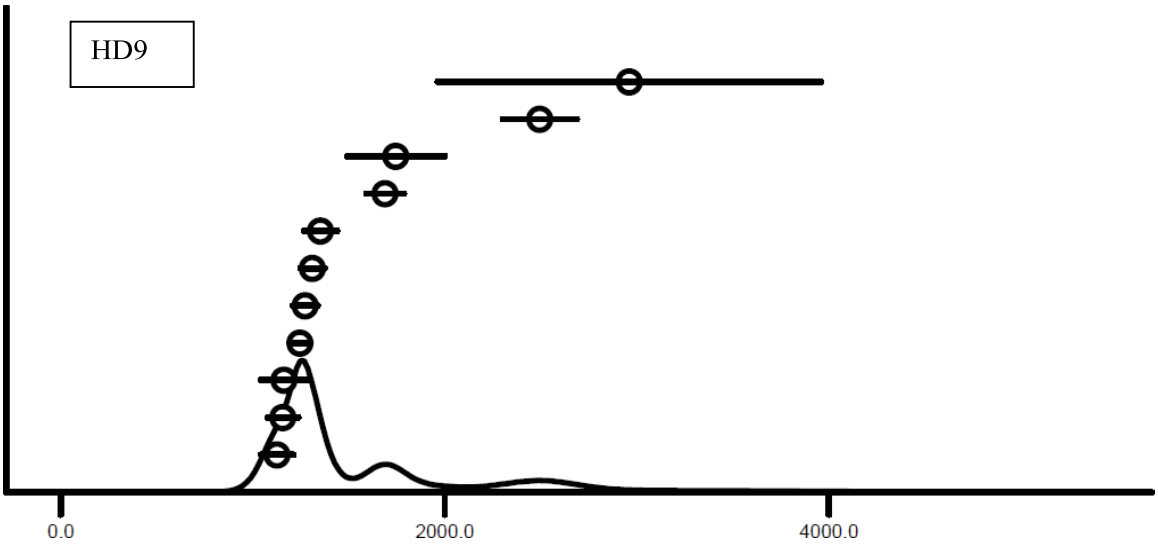

Figure A3b. Probability graphs for all poorly behaved samples (HD5, HD6, HD7-1, HD7-2, and HD9), which show most of the aliquots are outside of the probability curve, arguing for low confidence in the ages. Here the number of aliquots is plotted against equivalent dose (in seconds equivalent for beta source of Riso reader). These graphs were plotted using Riso Analyst software (Continued).

APPENDIX D: WIND-WAVE AND LAKE BOTTOM SEDIMENT ENTRAINMENT MODELING

We apply an approach to model the wind-wave characteristics and threshold lake-water depths required for the sedimentology described in Owens Lake core OL-92 (Smith and Bischoff, 1997). The approach is based on Bacon et al. (2018) that was previously calibrated and verified by modeling the sedimentology described in the historical section in core OL-97 (Li et al., 2000; Smoot et al., 2000) with limnological conditions for the period AD 1872–1878 when Owens Lake was at its historical maximum water level.

Wind-driven sediment entrainment occurs when water depth is shallow enough to effectively transfer the momentum of wind-waves from the water surface to the sediment-water interface (Håkanson and Jansson, 2002; Reardon et al., 2016). Wind waves and the fluid shear stresses they produce within the water column are the main mechanism responsible for sediment erosion and resuspension when the critical shear stress of bottom sediment is exceeded (e.g., Fagherazzi and Wiberg, 2009). The wind-wave model we used is based on linear wave theory and consists of a series of analytical solutions for estimating deep-water wave characteristics, including: significant wave height, wave length, spectral peak wave period, maximum orbital wave velocity, and critical shear stress (USACE, 1984, 2002; Rohweder et al., 2008).

An initial step in the modeling procedure is to determine the wave characteristics of wave height, period, and length in deep water. The shape of wind waves is predominately controlled by the intensity and duration of wind shear across open water surfaces, therefore wind velocity and fetch are the principal variables used to determine wave characteristics that control the magnitude of the boundary velocity below the wave

crest at a specified depth. Modeling of intermediate to shallow wind-waves (e.g., USACE, 2002; Le Roux, 2010) was not performed in this study because sediment cores were extracted from the depocenter area.

Wind

Wind direction is strongly controlled by the orientation and topography of its surrounding mountain ranges, e.g., Owens Lake basin has a wind regime with two primary directional sectors of N-NNW and S-SSE (Lancaster et al., 2015) (Figure 1). We used the classification of wind potential to produce dust raising events from a study in Owens Lake basin to characterize wind in the wind-wave model. Data from three continuous meteorological stations around Owens Lake playa operating from AD 1988 to 1991 show that high and extreme-high wind events in the lake basin have hourly average wind speeds of ≥7 and ≥18 m/s, respectively, with extreme-high wind events occurring only a few times per year having wind gusts in excess of 22 m/s mostly from the N-NNW (Zhong et al., 2008). Furthermore, measured wind speeds of 15–17 m/s for fetch-limited water bodies have previously been used in wind-wave models because these magnitudes generate waves causing sediment erosion and resuspension (e.g., Rohweder et al., 2008; Fagherazzi and Wiberg, 2009).

Fetch

Fetch is the unobstructed distance traveled by wind or waves across open water (e.g., Fagherazzi and Wiberg, 2009). Limited fetch conditions existed at Owens Lake even at highstand water levels because of its relatively small and linear lake size with

fetches of up to ~70 km. Fetch was determined by using the distance between study sites (shoreline, outcrop, lake cores) and corresponding elevation from either N-NNW or S-SSE directed winds. The measured fetch is a minimum estimate because there is an unknown height of water above the sites (i.e., depth), which is the purpose of the threshold lake-water depth modeling procedure to calculate. A minimum fetch input variable in the model also produces lower lake-water depth relations because relatively smaller waves are simulated, therefore it is considered a conservative approximation.

Critical Shear Stress

Critical shear stress represents the threshold for the initiation of potential particle motion when the drag force of flowing water against a particle exceeds the gravitational force holding it in place. The routine used to calculate the critical shear stress is based on the methods described in USACE (2002), which accounts for laminar flow along a flat lake bottom surface, as well as particle size and density in water with a specific density and viscosity. Salinity of large lakes along the eastern Sierra Nevada between ~1876 and 1886 AD ranged from ~0.07 g/l at Lake Tahoe (freshwater), ~3 g/l at Walker Lake (slightly saline), to ~50–70 g/l at Mono and Owens Lakes (brine) (Russel, 1885; Winkle and Eaton, 1910; Figure 1). We used a salinity of 2 g/l to simulate slightly saline lake conditions, which is a typical value commonly associated with living and fossil molluscan and microcrustacean (ostracode) assemblages identified in the paleo-Owens River system during the late Pleistocene to Early Holocene (e.g., Sharpe and Forester, 2008; Rosenthal et al., 2017). This value was used to calculate a water density of 1000.5 kg/m^3 and kinematic viscosity of 1.1414 x 10^{-6} m^2/s at an elevation of 1096 m asl

(Owens Lake historical shoreline) and temperature of 15°C based on MATLAB code of the MIT seawater thermophysical properties library (Sharqawy et al., 2010; Nayar et al., 2016). General sediment characteristics were assumed to have a density of quartz (2.65 g/cm^3), well sorted, and rounded with particle diameters of clay (2 μm), coarse silt (31 μm), coarse sand (2 mm), and up to coarse pebble (32 mm) that coincide with the boundaries between the size classes of the Wentworth (1922) scale.

References

Bacon, S.N., Lancaster, N., Stine, S., Rhodes, E.J., and McCarley Holder, G.A., 2018. A continuous 4000-year lake-level record of Owens Lake, south-central Sierra Nevada, California, USA. Quaternary Research 90, 276–302.

Fagherazzi, S., Wiberg, P.L., 2009. Importance of wind conditions, fetch, and water levels on wave-generated shear stresses in shallow intertidal basins. Journal of Geophysical Research 114, F03022. http://dx.doi.org/ 10.1029/2008JF001139.

Håkanson, L., Jansson, M., 2002. Principles of Lake Sedimentology. The Blackburn Press, New Jersey.

Li, H., Bischoff, J.L., Ku, T., Lund, S.P., Stott, L.D., 2000. Climate variability in east-central California during the past 1000 years reflected by high-resolution geochemical and isotopic records from Owens Lake sediments. Quaternary Research 54, 187–197.

Lancaster, N., Baker, S., Bacon, S., McCarley-Holder, G., 2015. Owens Lake dune fields: Composition, sources of sand, and transport pathways. Catena 134, 41–49.

Le Roux, J.P., 2010. Sediment entrainment under fully developed waves as a function of water depth, boundary layer thickness, bottom slope and roughness. Sedimentary Geology 223, 143–149.

Nayar, K.G., Sharqawy, M.H., Banchik, L.D., Lienhard V., J.H., 2016. Thermophysical properties of seawater: A review and new correlations that include pressure dependence. Desalination 390, 1– 24.

Reardon, K.E., Moreno-Casas, P.A., Bombardelli, F.A., Schladow, S.G., 2016. Seasonal nearshore sediment resuspension and water clarity at Lake Tahoe. Lake and Reservoir Management 32, 132–145.

Rohweder, J., Rogala, J.T., Johnson, B.L., Anderson, D., Clark, S., Chamberlin, F., Runyon, K., 2008. Application of wind fetch and wave models for habitat rehabilitation and enhancement projects. U.S. Geological Survey Open-File Report 2008–1200. United States Government Printing Office, Washington.

Russell, I.C., 1885. Geological history of Lake Lahontan, a Quaternary lake of northwestern Nevada. U.S. Geo-logical Survey Monograph 11, 288 p.

Sharpe, S.E., and Forester, R.M., 2008. Continental-aquatic mollusk hydrochemical occurrence patterns: Implications for population dynamics and paleoenvironmental reconstruction. Quaternary International 188, 105–116.

Sharqawy, M.H., Lienhard, J.H., Zubair, S.M., 2010. Thermophysical properties of seawater: a review of existing correlations and data. Desalination and Water Treatment 16, 354–380.

Smith, G.I., and Bischoff, J.L., eds., 1997. An 800,000-year paleoclimatic record from core OL-92, Owens Lake, southeast California. Geological Society of America Special Paper 317, 165 p.

Smoot, J.P., Litwin, R.J., Bischoff, J.L., and Lund, S.P., 2000, Sedimentary record of the 1872 earthquake and ‘‘Tsunami’’ at Owens Lake, southeast California: Journal of Sedimentary Geology, v. 135, p. 241–254.

U.S. Army Corps of Engineers (USACE), 1984. Shore Protection Manual, Volume 1. U.S. Army Engineer Waterways Experiment Station, Vicksburg, MS, U.S.A., 502 p.

U.S. Army Corps of Engineers (USACE), 2002. Coastal Engineering Manual. Washington D.C., U.S. Corps of Engineers, Engineer Manual 1110-2-1100, Part II and III.

Wanner, H., and 17 others (2008). Mid- to Late Holocene climate change: an overview. *Quaternary Science Reviews* 27, 1791–1828.

Wentworth, C.K., 1922. A scale of grade and class terms for clastic sediments. *Journal of* Geology 30, 377–392.

Winkle, W.V., and Eaton, F.M., 1910. Quality of the surface waters of California. U.S. Geological Survey, Water-Supply Paper 237, 142 p.

Zhong, S., Li, J., Whiteman, C.D., Bian, X., Yao, W., 2008. Climatology of high wind events in the Owens Valley, California. Monthly Weather Review 136, 3536–3552.